Study of the dark components of the Universe with the Euclid mission

Isaac Tutusaus Lleixa

THÈSE

En vue de l'obtention du

DOCTORAT DE L'UNIVERSITÉ DE TOULOUSE

Délivré par : *l'Université Toulouse 3 Paul Sabatier (UT3 Paul Sabatier)*

Présentée et soutenue le *20 septembre 2018* **par :**

ISAAC TUTUSAUS LLEIXA

Étude des composantes noires de l'Univers avec la mission Euclid

---

JURY

PROF. A. BLANCHARD	Professeur des universités	UPS/IRAP (France)
DR. A. EALET	Directeur de recherche	IPNL (France)
DR. P. FOSALBA	*Científico titular*	ICE, IEEC-CSIC (Espagne)
DR. S. HENROT-VERSILLÉ	Directeur de recherche	LAL (France)
DR. T. KITCHING	*Reader*	MSSL/UCL (Royaume-Uni)
PROF. M. KUNZ	Professeur associé	UNIGE (Suisse)
DR. B. LAMINE	Maître de conférences	UPS/IRAP (France)

École doctorale et spécialité :
SDU2E : Astrophysique, Sciences de l'Espace, Planétologie

Unité de Recherche :
Institut de Recherche en Astrophysique et Planétologie (UMR 5277)

Directeur(s) de Thèse :
Prof. Alain BLANCHARD et *Dr. Brahim* LAMINE

Rapporteurs :
Dr. Sophie HENROT-VERSILLÉ et *Prof. Martin* KUNZ

"*Everything should be as simple as it can be,*
Says Einstein,
But not simpler."

Louis Zukofsky (1978)

UNIVERSITÉ TOULOUSE 3 PAUL SABATIER

Résumé

Étude des composantes noires de l'Univers avec la mission Euclid[1]

par Isaac Tutusaus Lleixa

Le modèle de concordance de la cosmologie, appelé ΛCDM, est un succès de la physique moderne, car il est capable de reproduire les principales observations cosmologiques avec une grande précision et très peu de paramètres libres. Cependant, il prédit l'existence de matière noire froide et d'énergie sombre sous la forme d'une constante cosmologique, qui n'ont pas encore été détectées directement. Par conséquent, il est important de considérer des modèles allant au-delà de ΛCDM et de les confronter aux observations, afin d'améliorer nos connaissances sur le secteur sombre de l'Univers. Le futur satellite Euclid, de l'Agence Spatiale Européenne, explorera un énorme volume de la structure à grande échelle de l'Univers en utilisant principalement le regroupement des galaxies et la distorsion de leurs images due aux lentilles gravitationnelles. Dans ce travail, nous caractérisons de façon quantitative les performances d'Euclid vis-à-vis des contraintes cosmologiques, à la fois pour le modèle de concordance, mais également pour des extensions phénoménologiques modifiant les deux composantes sombres de l'Univers. En particulier, nous accordons une attention particulière aux corrélations croisées entre les différentes sondes d'Euclid lors de leur combinaison et estimons de façon précise leur impact sur les résultats finaux. D'une part, nous montrons qu'Euclid fournira d'excellentes contraintes sur les modèles cosmologiques qui définitivement illuminera le secteur sombre. D'autre part, nous montrons que les corrélations croisées entre les sondes d'Euclid ne peuvent pas être négligées dans les analyses futures et, plus important encore, que l'ajout de ces corrélations améliore grandement les contraintes sur les paramètres cosmologiques.

[1] Cette thèse est basée sur, ou contient des documents non-publics du consortium Euclid ou des résultats qui n'ont pas encore été approuvés par le consortium Euclid.

UNIVERSITÉ TOULOUSE 3 PAUL SABATIER

Abstract

Study of the dark components of the Universe with the Euclid mission[2]

by Isaac Tutusaus Lleixa

The concordance model of cosmology, called ΛCDM, is a success, since it is able to reproduce the main cosmological observations with great accuracy and only few parameters. However, it predicts the existence of cold dark matter and dark energy in the form of a cosmological constant, which have not been directly detected yet. Therefore, it is important to consider models going beyond ΛCDM, and confront them against observations, in order to improve our knowledge on the dark sector of the Universe. The future Euclid satellite from the European Space Agency will probe a huge volume of the large-scale structure of the Universe using mainly the clustering of galaxies and the distortion of their images due to gravitational lensing. In this work, we quantitatively estimate the constraining power of the future Euclid data for the concordance model, as well as for some phenomenological extensions of it, modifying both dark components of the Universe. In particular, we pay special attention to the cross-correlations between the different Euclid probes when combining them, and assess their impact on the final results. On one hand, we show that Euclid will provide exquisite constraints on cosmological models that will definitely shed light on the dark sector. On the other hand, we show that cross-correlations between Euclid probes cannot be neglected in future analyses, and, more importantly, that the addition of these correlations largely improves the constraints on the cosmological parameters.

[2]This thesis is based on, or contains non-public Euclid Consortium material or results that have not yet been endorsed by the Euclid Consortium.

Acknowledgements

I would like to take this opportunity to sincerely thank many people without whom it would not have been possible to write this thesis.

My first huge thank you goes to my thesis advisors Alain Blanchard and Brahim Lamine. I can still remember the day, three years ago, that Brahim told me the verdict of the jury awarding me with the scholarship. I was excited to start my career as a researcher, but I was also afraid in front of the blurry path that was waiting for me. I would like to thank both of them for welcoming me with open arms and help in all my problems during these years. I will not forget the freedom that they have given me. In particular, I really appreciate their support when I decided to completely change the initial subject of the thesis. They have always been there for all my doubts; not only from a research point-of-view, but also on personal aspects, which has made my stay away from home definitely much easier. For all of this, and the beautiful scientific discussions we have had in all this time, I really hope we can continue working together in the future.

Following my acknowledgements, I would like to express my gratitude to all the people from the *Institut de Recherche en Astrophysique et Planétologie*, as well as the *Université de Toulouse III - Université Paul Sabatier* as a whole. To my office-mate Safir Yahia-Cherif, with whom it has been a pleasure to share the office for nearly two years. I have really enjoyed our discussions, even when we were the last ones remaining in the lab. I would also like to thank Arnaud Dupays and Ziad Sakr, for the nice discussions we have had during these years at home or abroad. I am also grateful to Natalie Webb and Thierry Contini, for (together with Alain and Brahim) allowing we to go to as many conferences and workshops as I could have ever hoped. With respect to this point, I would also like to thank Carole Gaïti, Emilie Dupin, and Josette Garcia for perfectly managing all the administrative details of my travels, even if I was nearly always late for my documents. I am very grateful to Geneviève Soucail and Marie-Claude Cathala, for always answering my questions concerning the doctoral school, and all the GAHEC group for the nice discussions and for transmitting me the feeling of having belonged to a great institute.

I want to express my gratitude to Alain, Natalie, Martin Kilbinger, and Matteo Martinelli for writing all the reference letters I asked them to, sometimes in a incredibly short time scale.

I am very grateful to the Euclid Collaboration. In particular to the IST group and, even more in particular, to the cross-correlations group within the IST. It has been a pleasure to work in a huge collaboration like Euclid, but I have been even more fortunate to work with the people I have met there. I would like to specially thank Martin Kilbinger for helping me in all the troubles

I have had with `CosmoSIS`, and Matteo, for all the time we have spent comparing codes and trying to agree on the final results. Their help has been invaluable, and a large part of this work relies on it. I would also like to warmly thank the people from the weak lensing code comparison: Marco Raveri, Santiago Casas, Stefano Camera, and Vincenzo Cardone, for all the hours spent trying to obtain compatible results. My gratitude also goes to Martin Kunz, Stéphane Ilić, and Fabien Lacasa for all their help in Euclid-related doubts or beyond it, and to the IST leads Valeria Pettorino, Tom Kitching, and Ariel Sánchez, as well as Peter Schneider, for allowing me to present my work in multiple places.

Still within the Euclid Collaboration, I would like to thank the organizers of the French Euclid summer schools, as well as all the professors and students that participated in the last editions, for the nice debates that took place in them, and for all the cosmology I learned from them.

I would also like to express my gratitude to the people from the COBESIX group for the scientific discussions we have had over the years and that led to a part of the work presented here. In particular, I would like to thank Anne Ealet, Stéphane Plaszczynski, and Yves Zolnierowski for our discussions, as well as André Tilquin for his help on the DEC cluster. Part of this work has been carried out thanks to the support of the OCEVU Labex (ANR-11-LABX- 0060) and of the Excellence Initiative of Aix-Marseille University - A*MIDEX, part of the French “Investissements d’Avenir” programme.

Moreover, I would like to sincerely thank Anne, Pablo Fosalba, Sophie Henrot-Versillé, Tom, and Martin Kunz for having accepted to be members of my jury, despite their tight schedules. It is very important to me that they have accepted to evaluate this work, and I am very grateful for it. Also, I would like to thank again Martin Kunz and Sophie for being my *rapporteurs* and reading my thesis well in advance. Their help has been really appreciated.

I want to thank Enrique Fernández and Ramon Miquel for allowing me to start working in cosmology when I was still an undergraduate student, as well as my bachelor and MSc cosmology professors, Francisco Castander, Pablo, Enrique Gaztañaga, Martín Crocce, Géraldine Servant, and Eduard Massó, for transmitting me the passion for this branch of Physics.

I would also like to take this opportunity to thank my friends, who have supported me even if we have been a few hundred kilometers apart and it has not been always easy to see one another. Special thanks go to Jonathan, Jennifer, Sara, and Isidro, for always asking how was I doing, and for always trying to find a moment to meet, even if that implied coming to Toulouse to see me. I want to thank Sergi and Dani for keeping our friendship since we were kids. Despite the fact that we have spent weeks or months without seeing one another, they have always tried to stay in contact, and I am proud to call

them my friends. I want to specially thank Sergi, Dani, and Sara for expressly coming to Toulouse for attending my defense. I will not forget it.

Last, but obviously not least, I would like to thank all my family for their support and for continuously checking on me. I want to specially thank those who were able to attend my defense, Àngela, Òscar, Foix, and Dídac, even if it implied a long trip during working days. Their effort have been very valuable to me.

I am happy to thank my little brother, Miquel, for our relationship. Even if we do not live together anymore, I feel that our trust is as strong as always, and it has clearly helped me over these years to finish this work. I only hope that I can continue helping him in all the steps of his life.

I want to lovely thank my partner, Alba, who has supported me from the very beginning. She had the courage to push me to follow my dream when I was hesitating, and she convinced me to take this opportunity, even if it was not the easiest choice. During these years, she has been next to me every single day, even if they were hundreds of kilometers between us. She has celebrated all my successes, and this thesis exists thanks to her support and understanding. I just want to thank her for being by my side, and I wish we will keep drawing our path together.

Finally, I owe everything to my parents, Miquel and Regina, for the family they have given me. They have supported me all my life, and they have fought for giving me the best education possible, such that I would eventually be able to follow my dream, whatever it was. They have always been by my side, helping me all the times I needed it. I would not have been able to get here without their love and their work. Because all of it, this thesis is as much mine as theirs.

To all the people cited above, and all the others that I have, for sure, forgot to mention (I apologize for that), a big, sincere, and warm thank you.

Contents

List of Abbreviations

ΛCDM	Λ and **C**old **D**ark **M**atter concordance model
ΛGDM	Λ and **G**eneralized **D**ark **M**atter model
***w*CDM**	***w*** (dark energy) and **C**old **D**ark **M**atter model
***w*$_0$*w*$_a$CDM**	***w*$_0$**-***w*$_a$** (dark energy) and **C**old **D**ark **M**atter model
2dFGRS	**2**-**d**egree **F**ield **G**alaxy **R**edshift **S**urvey
2PCF	**2**-**p**oint-**c**orrelation **f**unction
6dFGS	**6**-**d**egree **F**ield **G**alaxy **S**urvey
AGN	**A**ctive **G**alactic **N**uclei
AIC	**A**kaike **I**nformation **C**riterion
AICc	**A**kaike **I**nformation **C**riterion - **c**orrected
AP	**A**lcock-**P**acyznski effect
BAO	**B**aryon **A**coustic **O**scillations
BBN	**B**ig **B**ang **N**ucleosynthesis
BIC	**B**ayesian **I**nformation **C**riterion
BOSS	**B**aryon **O**scillation **S**pectroscopic **S**urvey
CCDs	**C**harge **C**oupled **D**evice**s**
CDM	**C**old **D**ark **M**atter
CFHTLenS	**C**anada **F**rance **H**awaii **Len**sing **S**urvey
CMB	**C**osmic **M**icrowave **B**ackground
COBE	**CO**smic **B**ackground **E**xplorer
CPL	**C**hevallier-**P**olarski-**L**inder parametrization
CS	**C**oasting **S**plines
DE	**D**ark **E**nergy
DES	**D**ark **E**nergy **S**urvey
DESI	**D**ark **E**nergy **S**pectroscopic **I**nstrument
eBOSS	**e**xtended **B**aryon **O**scillation **S**pectroscopic **S**urvey
EC	**E**uclid **C**onsortium
ECB	**E**uclid **C**onsortium **B**oard
ECL	**E**uclid **C**onsortium **L**ead
eNLA	**e**xtended **N**on-**L**inear **A**lignment model for IA
ESA	**E**uropean **S**pace **A**gency
FLRW	**F**riedmann-**L**emaître-**R**obertson-**W**alker metric
FoG	**F**ingers-**o**f-**G**od

FoM	**F**igure **o**f **M**erit
GC	**G**alaxy **C**lustering
GCp	**G**alaxy **C**lustering - **p**hotometric
GCs	**G**alaxy **C**lustering - **s**pectroscopic
GDM	**G**eneralized **D**ark **M**atter
GTD	**G**eneralized **T**ime **D**ependent galaxy bias model
`halofit`	**halofit** non-linear prescription
`HaloModel`	**Halo Model** non-linear prescription
HST	**H**ubble **S**pace **T**elescope
IA	**I**ntrinsic **A**lignment of galaxies
IST	**I**nter-**S**cience **T**askforce for forecasting
JLA	**J**oint **L**ight-curve **A**nalysis
LRGs	**L**uminous **R**ed **G**alaxie**s**
LSST	**L**arge **S**ynoptic **S**urvey **T**elescope
MCMC	**M**onte **C**arlo **M**arkov **C**hain
NALPL	**N**on-**A**ccelerated **L**ocal **P**ower **L**aw
NASA	**N**ational **A**eronautics and **S**pace **A**dministration
OUs	**O**rganizational **U**nit**s**
PLM	**P**ay**L**oad **M**odule
PPF	**P**arametrized **P**ost-**F**riedmann framework
QSO	**Q**uasi-**S**tellar **O**bject
RPT	**R**enormalized **P**erturbation **T**heory
RSD	**R**edshift-**S**pace **D**istortions
SDCs	**S**cience **D**ata **C**enter**s**
SDSS	**S**loan **D**igital **S**ky **S**urvey
SGS	**S**cience **G**round **S**egment
SNIa	**S**uper**N**ovae of type **Ia**
SNIa+ev	**S**uper**N**ovae of type **Ia** with luminosity **ev**olution
SOC	**S**cience **O**peration **C**enter
SPT	**S**tandard **P**erturbation **T**heory
SVM	**S**er**V**ice **M**odule
SWGs	**S**cience **W**orking **G**roup**s**
VIPERS	**VI**MOS **P**ublic **E**xtragalactic **R**edshift **S**urvey
WL	**W**eak **L**ensing
WMAP	**W**ilkinson **M**icrowave **A**nisotropy **P**robe
XC	Cross (**X**) - **C**orrelations

List of Symbols

a	scale factor
$\mathcal{A}_{\rm IA}$	IA multiplicative nuisance parameter
A_s	amplitude of the initial matter power spectrum
b	galaxy bias
c	speed of light in vacuum
c_a	adiabatic sound speed
$\mathcal{C}_{\rm IA}$	IA multiplicative nuisance parameter
$C_{ij}^{\delta_{\rm g}\delta_{\rm g}}$	GCp tomographic angular spectra
$C_{ij}^{\delta_{\rm g}\gamma}$	XC tomographic angular spectra
$C_{ij}^{\gamma\gamma}$	WL tomographic angular spectra
c_s	rest-frame sound speed
$c_{\rm vis}$	GDM viscosity parameter
D_1	growth factor
$d_{\rm A}$	angular diameter distance
$d_{\rm L}$	luminosity distance
E	dimensionless Hubble parameter
f	growth rate
$f\sigma_8$	weighted growth rate
$f_{\rm sky}$	fraction of the sky observed
G	Newton's gravitational constant
h	reduced Hubble constant
H	Hubble parameter
H_0	Hubble constant
k	modulus of the wave mode in Fourier space
$k_\parallel$	$\boldsymbol{k}$ component along the line-of-sight
$k_\perp$	$\boldsymbol{k}$ component perpendicular to the line-of-sight
$m_{\rm B}^*$	SNIa observed peak magnitude in the rest-frame B band
$M_{\rm B}^1$	SNIa absolute magnitude in the rest-frame B band nuisance parameter
n_e	free electron number density
$N_{\rm eff}$	effective number of relativistic degrees of freedom
n_i	galaxy number density in the ith redshift bin
$N_{ij}^{\delta_{\rm g}}$	GCp shot-noise
N_{ij}^{ϵ}	WL shot-noise

n_s	slope of the initial matter power spectrum (spectral index)
$N_{\rm ur}$	number of ultra-relativistic species
p	pressure
$P_{\rm dw}$	de-wiggled power spectrum
$P_{\rm g}$	galaxy power spectrum
$P_{\rm m}$ (& $P_{\delta\delta}$)	matter power spectrum
$P_{\rm nw}$	no-wiggles power spectrum
P_s	GCs shot-noise
q_0	deceleration parameter present value
R	scaled distance to recombination
$r_{\rm d}$	BAO standard ruler
$r_{\rm s}$	co-moving sound horizon
t	cosmic time
T	transfer function
$T_{\rm CMB}$	temperature of the CMB
w	equation of state parameter
$W_i^{\delta_g}$	GCp window function in the ith redshift bin
$\mathcal{W}_i^{\delta_g}$	GCp window function in the ith redshift bin divided by χ
W_i^{γ}	shear window function in the ith redshift bin
$\mathcal{W}_i^{\gamma}$	shear window function in the ith redshift bin including the IA
$W_i^{\rm IA}$	IA window function in the ith redshift bin
X_e	free electron fraction
z	redshift
z_*	redshift of the last scattering epoch
$z_{\rm d}$	redshift of the baryon drag epoch
α	SNIa stretch nuisance parameter
β	SNIa color nuisance parameter
$\beta_{\rm IA}$	IA luminosity nuisance parameter
χ	co-moving distance
$\Delta_{\rm M}$	SNIa host galaxy nuisance parameter
$\Delta m_{\rm evo}$	SNIa luminosity evolution nuisance term
δp	pressure perturbation
ℓ_a	angular scale of the sound horizon at recombination
ϵ	ellipticity
$\eta_{\rm IA}$	IA redshift nuisance parameter
γ	shear
κ	convergence
Λ	cosmological constant
μ	distance modulus
$\omega_{\rm b}$	baryon reduced present energy density parameter

$\Omega_{\rm b}$	baryon present energy density parameter
$\omega_{\rm cdm}$	cold dark matter reduced present energy density parameter
$\Omega_{\rm cdm}$	cold dark matter present energy density parameter
$\omega_{\rm dm}$	dark matter reduced present energy density parameter
$\Omega_{\rm dm}$	dark matter present energy density parameter
$\Omega_{\rm K}$	curvature present energy density parameter
Ω_{Λ}	Λ present energy density parameter
$\omega_{\rm m}$	matter reduced present energy density parameter
$\Omega_{\rm m}$	matter present energy density parameter
$\Omega_{\rm r}$	radiation present energy density parameter
ρ	energy density
$\rho_{0,\rm crit}$	critical present energy density
σ	anisotropic stress
σ_8	Root mean square mass fluctuations amplitude on $8\,{\rm Mpc}/h$ scales at $z = 0$
$\sigma_{\rm p}$	GCs non-linear nuisance parameter
$\sigma_{\rm v}$	GCs non-linear nuisance parameter
τ	re-ionization optical depth

A la meva família

Introduction

[Version française]

La cosmologie est la branche de la science qui étudie l'Univers, ou le cosmos, dans son ensemble. Son objectif principal est d'aborder des questions fondamentales pour la nature humaine, comme d'où venons-nous, où sommes-nous, où allons-nous et à quel rythme ? Fondamentalement, la cosmologie essaie de comprendre l'Univers dans lequel nous vivons en observant notre passé et finalement, de prédire notre avenir. Il y a un siècle, cela ressemblait à des questions philosophiques et il semblait impossible d'y répondre par l'approche scientifique. Cependant, grâce à l'amélioration de nos connaissances théoriques et, dans les dernières décennies, l'amélioration de la technologie et des techniques d'observation, nous sommes maintenant en mesure de proposer des modèles théoriques pour expliquer notre Univers et, surtout, de les tester grâce aux observations. Ce fut le début de la cosmologie moderne. Une brève revue, fournissant les bases du cadre cosmologique, est présentée dans le chapitre 1 de cette thèse.

Encore plus récemment, nous avons atteint une si bonne précision sur nos observations cosmologiques que nous pouvons dire que nous vivons dans l'ère de la cosmologie de précision. Nous avons ainsi clairement besoin d'outils statistiques robustes pour analyser les données. Nous présentons les bases des principaux outils utilisés dans ce travail dans le chapitre 2. Il est intéressant de noter que nous disposons d'un modèle théorique très simple (avec seulement 7 paramètres), appelé ΛCDM, capable de reproduire presque toutes les observations actuelles avec une grande précision. Cependant, ce modèle suppose l'existence d'un fluide sombre appelé matière noire froide et d'un second fluide sombre appelé énergie sombre sous la forme d'une constante cosmologique. Le premier est nécessaire pour expliquer le manque de matière suggéré par nos observations, tandis que le second est nécessaire pour expliquer la nature accélérée observée de l'expansion de l'Univers. Le problème est qu'il n'y a pas de détection directe de la matière noire froide, ou d'une constante cosmologique et, dans le cadre du modèle ΛCDM, ils ont une contribution d'environ 95 % de la densité totale d'énergie de l'Univers. Il est donc impératif d'essayer de comprendre ces composantes sombres en proposant de nouveaux modèles théoriques et de les tester par rapport aux observations.

Depuis le début de la cosmologie moderne, de nombreux télescopes observent le ciel pour obtenir des mesures pour différentes sondes cosmologiques, comme les supernovae de type Ia, les oscillations acoustiques de baryons, le fond cosmologique micro-onde, le groupement de galaxies ou les lentilles faibles. Il y a beaucoup de sondages en cours dont les données sont en train d'être analysées et qui semblent pointer vers des tensions dans le modèle standard ΛCDM qui pourraient éventuellement conduire à de la nouvelle physique. Il existe par ailleurs plusieurs projets qui verront le jour dans les années qui viennent avec le but de fournir d'excellentes observations et l'espoir d'illuminer le secteur sombre de l'Univers. Les données de certains de ces sondages passés et actuels sont décrites dans le premier chapitre de cette thèse. Mais, ce travail est largement axé sur le futur satellite Euclid de l'Agence Spatiale Européenne, qui va sonder un énorme volume de la structure à grande échelle de l'Univers avec des groupements de galaxies et des lentilles faibles. Par conséquent, nous présentons la mission de manière beaucoup plus détaillée dans le chapitre 3 de la thèse.

L'objectif principal de cette thèse est de prédire le pouvoir contraignant d'Euclid pour le modèle de concordance ΛCDM et des extensions simples au-delà. Cependant, la principale différence par rapport à de nombreuses études dans la littérature est le traitement spécifique que nous utilisons pour la combinaison des différentes sondes. Il est bien connu que la combinaison de différentes sondes cosmologiques est un moyen très puissant de contraindre les modèles cosmologiques. La raison en est que les différentes sondes sont généralement sensibles à différents aspects dans la façon dont la gravité agit dans le cosmos; par conséquent, les combiner peut casser certaines dégénérescences entre différents paramètres cosmologiques et améliorer sensiblement nos contraintes. Les sondes sont généralement combinées en supposant qu'elles sont statistiquement indépendantes, ce qui peut être vrai dans certains cas, mais ce n'est certainement pas le cas pour le regroupement de galaxies et les lentilles faibles si nous sondons le même volume de l'Univers. Dans ce travail, nous quantifions l'impact des corrélations croisées entre ces sondes pour le futur satellite Euclid et estimons l'amélioration de nos connaissances cosmologiques si nous prenons ces corrélations croisées en compte. Toute cette analyse est présentée dans le chapitre 6 de la thèse.

Au-delà de la prédiction de la capacité contraignante d'Euclid pour ΛCDM (et certaines extensions), cette thèse aborde également les composantes sombres de l'Univers au-delà du modèle de concordance. Nous utilisons une approche phénoménologique pour décrire à la fois la matière noire et l'énergie sombre. En commençant par la matière noire, on suppose généralement qu'elle est sans collision et sans pression, même lorsque nous considérons des modèles au-delà de ΛCDM. Dans le chapitre 7, nous considérons un modèle généralisé pour la

matière noire, où nous lui permettons d'avoir une certaine pression et une certaine vitesse du son, qui lissent essentiellement le groupement de galaxies à petite échelle. Nous présentons les contraintes obtenues avec les observations actuelles et nous prédisons également la capacité d'Euclid à contraindre la nature de cette matière noire.

Concernant l'énergie sombre, nous considérons un modèle phénoménologique exotique pour lequel le taux d'expansion de l'Univers est donné par une loi de puissance. Il y a eu quelques désaccords dans la communauté concernant ce modèle entre ceux qui prétendent qu'il peut reproduire les observations jusqu'au redshift $z \sim 2$ et ceux qui prétendent le contraire. Dans ce travail, nous incluons, pour la première fois, des informations provenant du fond diffus cosmologique lors du test de ce modèle. C'est le sujet du chapitre 4.

En dernier lieu, nous étudions la possible corrélation entre des systématiques astrophysiques dans les supernovae de type Ia et l'information cosmologique que nous en tirons. Plus en détail, nous étudions comment une dépendance de la luminosité intrinsèque des supernovae de type Ia avec le redshift peut influencer nos conclusions sur la nature accélérée de l'expansion de l'Univers. Cette étude est l'objet du chapitre 5 de cette thèse.

En résumé, l'objectif principal de cette thèse est de prédire la puissance contraignante du futur satellite Euclid pour le modèle de concordance (et des extensions simples, chapitre 6) et les modèles de matière noire exotique (chapitre 7), avec une attention particulière portée sur l'impact des corrélations croisées quand on combine différentes sondes cosmologiques. En plus, nous analysons également un modèle d'énergie sombre exotique où le taux d'expansion de l'Univers est donné par une loi de puissance dans le chapitre 4 et nous étudions l'impact d'une dépendance de luminosité intrinsèque des supernovae de type Ia avec le redshift sur les conclusions que nous pouvons tirer sur la nature accélérée de l'expansion cosmique dans le chapitre 5.

Nous suivons la notation standard dans la littérature, sauf indication contraire. Les indices latins correspondent aux trois coordonnées spatiales, tandis que les indices grecs correspondent aux quatre coordonnées d'espace-temps. Les indices répétés sont sommés. Les vecteurs sont indiqués par des lettres en caractères gras. Un point sur toute quantité désigne la dérivée temporelle de celle-ci. Un indice 0 indique le temps présent et nous utilisons des unités naturelles avec $\hbar = c = 1$.

[English version]

Cosmology is the branch of science studying the Universe, or cosmos, as a whole. Its main goal is to address questions that are fundamental to human nature, like where do we come from, where are we, where are we going and at what pace. Basically, cosmology tries to understand the Universe we are living in by observing our past, and eventually predict our future. A century ago these interrogations looked like philosophical questions and it seemed impossible to answer them with the scientific approach. However, thanks to the improvement on our theoretical knowledge and, especially in the last decades, the improvement of technology and observational techniques, we are now able to propose theoretical models trying to explain our Universe and, more importantly, we can test them against the observations. This was the beginning of modern cosmology. A brief review of it, providing the basics of the cosmological framework, is presented in Chapter 1 of this thesis.

Even more recently, we have reached such a good precision on our cosmological observations that we can say we live in the precision cosmology era. Therefore, we are in clear need of robust statistical tools to analyze the data. We present the basics of the main tools used in this work in Chapter 2. Interestingly enough, we have a very simple (only 7 parameters) theoretical model, called ΛCDM, that is able to reproduce nearly all the current observations with great accuracy. However, this model assumes the existence of a dark fluid called cold dark matter and a second dark fluid called dark energy in the form of a cosmological constant. The former is needed in order to explain the lack of matter in our observations, while the latter is required in order to explain the observed accelerated nature of the expansion of the Universe. The problem is that there is no direct detection of cold dark matter, or a cosmological constant, and in the ΛCDM framework they have a contribution of roughly 95 % of the total energy density of the Universe. It is therefore mandatory to try to understand these dark components by proposing new theoretical models and confront them with the observations.

Since the beginning of modern cosmology, there have been many telescopes observing the sky to obtain measurements for different cosmological probes, like type Ia supernovae, baryon acoustic oscillations, the cosmic microwave background, galaxy clustering, or weak lensing. There are many ongoing surveys whose data is currently being analyzed, and which seem to point to some tensions within the standard ΛCDM model that could eventually lead to some new physics. And there are several projects that will occur in the future with the goal of providing exquisite observations, and the hope of shedding light on the dark sector of the Universe. Data from some of these past and current surveys is described in the first chapter of this thesis. But, this work is largely focused

on the future Euclid satellite from the European Space Agency, which is going to probe a huge volume of the large-scale structure of the Universe with galaxy clustering and weak lensing. We present this mission in much more detail in Chapter 3 of the thesis.

The main goal of this thesis is to predict the constraining power of Euclid for the concordance ΛCDM model, and simple extensions beyond it. However, the key difference with respect to many studies in the literature is the special treatment we use for the combination of the different probes. It is well known that combining different cosmological probes is a very powerful way to constrain cosmological models. The reason being that different probes are usually sensitive to different aspects of how gravity acts in the cosmos; therefore, combining them can break some degeneracies between different cosmological parameters and noticeably improve our constraints. Probes are usually combined assuming they are statistically independent, which might be true in some cases, but is definitely not true for galaxy clustering and weak lensing if we probe the same volume of the Universe. In this work we quantify the impact of the cross-correlations between these probes for the future Euclid satellite, and estimate the improvement on our cosmological knowledge if we take these cross-correlations into account. All this analysis is presented in Chapter 6 of the thesis.

Beyond predicting the constraining ability of Euclid for ΛCDM (and simple extensions of it), this thesis also tackles the dark components of the Universe beyond the concordance model. We use a phenomenological approach to describe both dark matter and dark energy. Starting with dark matter, it is usually assumed to be collision-less and pressure-less, even when we consider models beyond ΛCDM. In Chapter 7 we consider a generalized model for dark matter, where we allow it to have some pressure and some sound speed, which essentially smoothes out the clustering at small scales. We present the constraints obtained with state-of-the-art observations, and we also predict the ability of Euclid to constrain the nature of dark matter.

Concerning dark energy, we consider an exotic phenomenological model for which the expansion rate of the Universe is given by a power law. There has been some disagreement in the community concerning this model between those claiming that it can reproduce the observations up to redshift $z \sim 2$, and those who claim the contrary. In this work we include, for the first time, information coming from the cosmic microwave background when testing this model. This is the subject of Chapter 4.

As a last point, we study the possible correlation between type Ia supernovae astrophysical systematics and the cosmological information we derive from them. More in detail, we study how a redshift dependence of the type Ia

supernovae intrinsic luminosity may impact our conclusions about the accelerated nature of the expansion of the Universe. This is the subject of Chapter 5 of this thesis.

Summarizing, the main goal of this thesis is to predict the constraining power for the future Euclid satellite for the concordance model (and simple extensions of it, Chapter 6) and general dark matter models (Chapter 7), paying special attention to the impact of cross-correlations when we combine different cosmological probes. In addition, we also analyze an exotic dark energy model where the expansion rate of the Universe is given by a power law in Chapter 4, and we study the impact of type Ia supernovae intrinsic luminosity redshift dependence on the conclusions we can draw on the accelerated nature of cosmic expansion in Chapter 5.

We follow the standard notation in the literature unless stated otherwise. Latin indices run over the three spatial coordinates, while greek indices run over the four spacetime coordinates. Repeated indices are summed. Vectors are indicated by letters in boldface. A dot over any quantity denotes the time-derivative of it. A subscript 0 denotes the present time, and we use natural units with $\hbar = c = 1$.

Chapter 1

Cosmological framework

In this chapter we present a broad overview of the cosmological framework, with the goal of providing the main cosmological tools required to follow the rest of this thesis. More in particular, we divide this first chapter in four different sections. In Sec. 1.1 we introduce the standard model in cosmology focusing on its background expansion. In Sec. 1.2, Sec. 1.3, and Sec. 1.4 we describe the large-scale structure of the Universe commenting both on the formation of structures, and the distortion of light because of these structures. Finally, in Sec. 1.5 we present the main cosmological probes used nowadays in cosmology to constrain our models.

1.1 Modern cosmology

Cosmology is the branch of physics that studies the Universe, or cosmos, as a whole. Its ultimate goal is to understand the origin, the evolution, and the structure of the Universe. In order to achieve this goal, cosmology needs to consider all the structures of the Universe on a huge range of scales; planets orbiting stars, stars forming galaxies, galaxies gravitationally bound into clusters, or even clusters within superclusters. Moreover, a lot of particle physics are required to properly understand the origins of our Universe. Because of it, and the difficulty of studying the Universe (theoretically or observationally), cosmology used to be close to philosophy. However, in the past decades we have started to be able to give quantitative answers to some of the most important questions concerning our Universe, like why is it so smooth? Or how did structures form? We have been able to start providing these answers by combining our knowledge on fundamental physics and the precise astronomical observations that we have nowadays. This shift from philosophy to science and our ability to propose theoretical models that can be tested quantitatively against observations has led us to the modern era of cosmology.

In the XIX century the Universe was considered a static system where bright objects where fixed in the sky, because of their lack of apparent motion. In 1915 Albert Einstein published his theory of General Relativity [Einstein, 1915],

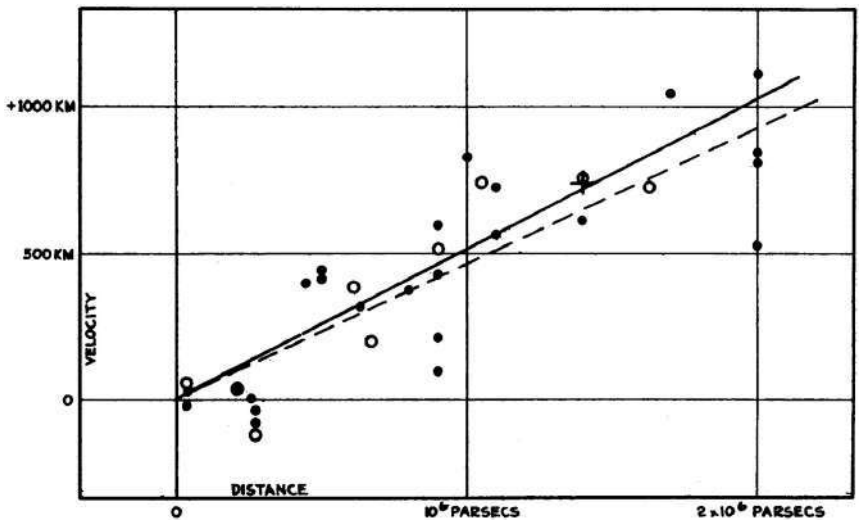

FIGURE 1.1: Original plot of Edwin Hubble from Hubble, 1929, showing the velocity along the line-of-sight as a function of the distance for the observed galaxies. Notice the typographical error in the velocity units being km/s.

describing gravity as the consequence of the curvature of spacetime generated by the distribution of mass and energy. A couple of years later, he applied his theory to cosmology for the first time [Einstein, 1917] and, in order to get a static Universe from it, he was forced to introduce a constant in his equations: the cosmological constant Λ. However, in 1929 Edwin Hubble was able to measure the velocity along the line-of-sight for a few galaxies with known distances, and he found that most of these galaxies were actually moving away from us, the faster the further they were [Hubble, 1929] (see the original plot in Fig. 1.1).

After realizing that the Universe was not static, but expanding, Einstein retracted from the introduction of the cosmological constant, and a new theoretical model for the history of the Universe was developed: the Big Bang theory, where the Universe expands from an initial extremely high density and temperature state. This model is supported by astronomical observations, like the photons coming from the early Universe, or the abundance of primordial elements, and it is still one of the pillars of the standard model of cosmology.

Assuming the General Relativity theory of Einstein, the expansion of the Universe is only sensitive to the energy content, curvature, and pressure. Thus, for a Universe filled with matter (and radiation), there are only two final fates for the Universe: either the gravitational interaction is larger than the expansion originated from the Big Bang, leading to a Big Crunch where all the Universe comes back to a singularity, or it continues expanding forever but asymptotically converging to a static Universe (Big Chill). Surprisingly, in 1998 two different groups measured the distances to type Ia supernovae and found out that the

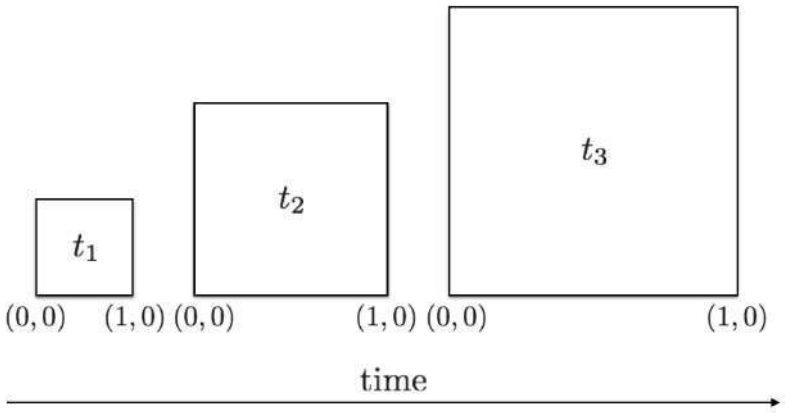

FIGURE 1.2: Intuitive interpretation of the scale factor. The co-moving distance between points on a hypothetical grid remains constant as the Universe expands, while the physical distance gets larger as time evolves.

Universe is not only expanding, but in an accelerated way [Riess et al., 1998; Perlmutter et al., 1999]. In the standard model of cosmology this acceleration is associated to an exotic fluid that only interacts through gravity and whose pressure is less than minus one third of its energy density. For the case where the pressure is exactly minus the energy density this fluid is equivalent to the cosmological constant first introduced by Einstein in 1917. More than 100 years later we have not been able to understand the nature of this constant (or fluid), if it is really there. This acceleration may also be due to a modification of the theory of gravity at cosmological scales, but, if we trust the theory of Einstein, current measurements tell us that the nature of about 95% of the energy content of the Universe remains still unknown.

1.1.1 A smooth and expanding universe

Scale factor and the FLRW metric

Thanks to the measurements performed since Hubble [Hubble, 1929], we have very good evidence to think that our Universe is expanding. This effect is commonly described by the so-called scale factor a, whose present value is set to one and was smaller in the past. In Fig. 1.2 we can see an intuitive picture of the definition of the scale factor. Let us imagine the space as a grid expanding uniformly as a function of time. Two different points of this grid maintain their coordinates, so the co-moving distance (or difference between coordinates) remains constant. However, the physical distance is proportional to the scale factor, which evolves with time.

In addition to the scale factor, the Universe is usually also characterized by its geometry: flat, closed or open, that, according to General Relativity, is related to the energy content of the Universe.

Let us first consider the geometry of a three-dimensional homogeneous and isotropic space. Geometry is essentially encoded in the metric $g_{ij}(\boldsymbol{x})$ (with the indices i, j running over the three spatial coordinate labels), which gives the line element $\mathrm{d}l^2 \equiv g_{ij}\,\mathrm{d}x^i\,\mathrm{d}x^j$ (with summation over repeated indices). The easiest metric for a homogeneous, isotropic, three-dimensional space is given by flat space, with line element $\mathrm{d}l^2 = \mathrm{d}\boldsymbol{x}^2$. Another possibility is a spherical (or hyper-spherical) surface in four-dimensional Euclidian (pseudo-Euclidian) space with some arbitrary positive constant radius a. The line elements are then given by

$$\mathrm{d}l^2 = \mathrm{d}\boldsymbol{x}^2 \pm \mathrm{d}z^2, \qquad z^2 \pm \boldsymbol{x}^2 = a^2\,. \tag{1.1}$$

Rescaling these coordinates by the constant a, the line elements in the spherical and hyper-spherical cases are

$$\mathrm{d}l^2 = a^2\left[\mathrm{d}\boldsymbol{x}^2 \pm \mathrm{d}z^2\right], \qquad z^2 \pm \boldsymbol{x}^2 = 1\,. \tag{1.2}$$

Computing the differential of the last equation we can write the line elements as

$$\mathrm{d}l^2 = a^2\left[\mathrm{d}\boldsymbol{x}^2 \pm \frac{(\boldsymbol{x}\cdot\mathrm{d}\boldsymbol{x})^2}{1 \mp \boldsymbol{x}^2}\right]. \tag{1.3}$$

We can then extend this to the Euclidian space by

$$\mathrm{d}l^2 = a^2\left[\mathrm{d}\boldsymbol{x}^2 + K\frac{(\boldsymbol{x}\cdot\mathrm{d}\boldsymbol{x})^2}{1-\boldsymbol{x}^2}\right], \tag{1.4}$$

where

$$K\begin{cases} > 0 & \text{spherical,} \\ < 0 & \text{hyper-spherical,} \\ = 0 & \text{Euclidian.} \end{cases} \tag{1.5}$$

It can also be easily extended to the geometry of space-time by writing the line element as

$$\mathrm{d}s^2 \equiv -g_{\mu\nu}\,\mathrm{d}x^\mu\,\mathrm{d}x^\nu = \mathrm{d}t^2 - a^2(t)\left[\mathrm{d}\boldsymbol{x}^2 + K\frac{(\boldsymbol{x}\cdot\mathrm{d}\boldsymbol{x})^2}{1-\boldsymbol{x}^2}\right], \tag{1.6}$$

where $a(t)$ is now the scale factor of the Universe presented in Fig. 1.2.

If the Universe appears spherically symmetric and isotropic to a set of freely falling observers, this is the unique metric of the Universe (up to a coordinate transformation). The components of this metric are then given by

$$g_{ij} = a^2(t)\left(\delta_{ij} + K\frac{x^i x^j}{1 - K\boldsymbol{x}^2}\right), \quad g_{i0} = 0, \quad g_{00} = -1\,, \tag{1.7}$$

where x^0 stands for the time coordinate, and the speed of light c has been set to 1. Notice that another convention with an overall minus sign in the metric is also used in the literature.

In spherical polar coordinates we can write

$$\mathrm{d}\boldsymbol{x}^2 = \mathrm{d}r^2 + r^2\,\mathrm{d}\Omega, \quad \mathrm{d}\Omega \equiv \mathrm{d}\theta^2 + \sin^2\theta\,\mathrm{d}\phi^2\,, \tag{1.8}$$

giving

$$\mathrm{d}s^2 = \mathrm{d}t^2 - a^2(t)\left[\frac{\mathrm{d}r^2}{1 - Kr^2} + r^2\,\mathrm{d}\Omega\right]. \tag{1.9}$$

In this case the metric becomes diagonal,

$$g_{rr} = \frac{a^2(t)}{1 - Kr^2}, \quad g_{\theta\theta} = a^2(t)r^2, \quad g_{\phi\phi} = a^2(t)r^2\sin^2\theta, \quad g_{00} = -1\,. \tag{1.10}$$

This is the so-called Friedmann-Lemaître-Robertson-Walker (FLRW) metric, and it is the standard one used in cosmology. It is important to notice that this metric is built on the cosmological principle, which states that the Universe is homogeneous and isotropic. Particularly, it states that the average properties of the Universe are the same in all locations and in all directions.

Dynamics of expansion

To understand the expansion of the Universe we need to determine the evolution of the scale factor, a, as a function of cosmic time, t. General Relativity tells us that this evolution is sensitive to the energy content of the Universe. In order to understand the dynamics of the expansion we need to apply the gravitational field equations of Einstein's theory to the Universe. These equations can be written as

$$R_{\mu\nu} = -8\pi G S_{\mu\nu}\,, \tag{1.11}$$

where $R_{\mu\nu}$ is the Ricci tensor,

$$R_{\mu\nu} = \frac{\partial\Gamma^\lambda_{\lambda\mu}}{\partial x^\nu} - \frac{\partial\Gamma^\lambda_{\mu\nu}}{\partial x^\lambda} + \Gamma^\lambda_{\mu\sigma}\Gamma^\sigma_{\nu\lambda} - \Gamma^\lambda_{\mu\nu}\Gamma^\sigma_{\lambda\sigma}\,, \tag{1.12}$$

with $\Gamma^{\mu}_{\nu\kappa}$ being the affine connection,

$$\Gamma^{\mu}_{\nu\kappa} = \frac{1}{2} g^{\mu\lambda} \left[\frac{\partial g_{\lambda\nu}}{\partial x^{\kappa}} + \frac{\partial g_{\lambda\kappa}}{\partial x^{\nu}} - \frac{\partial g_{\nu\kappa}}{\partial x^{\lambda}} \right] , \tag{1.13}$$

and $S_{\mu\nu}$ can be expressed as a function of the energy-momentum tensor $T_{\mu\nu}$

$$S_{\mu\nu} \equiv T_{\mu\nu} - \frac{1}{2} g_{\mu\nu} T^{\lambda}_{\lambda} . \tag{1.14}$$

If we take into account the standard FLRW metric, we can use several symmetries of it and simplify these equations. For instance, the components of the affine connection with two or three time indices all vanish, as well as the $R_{i0} = R_{0i}$ components of the Ricci tensor. After some algebra we can write the Ricci tensor as

$$R_{00} = 3\frac{\ddot{a}}{a}, \qquad R_{ij} = -\left[2K + 2\dot{a}^2 + a\ddot{a}\right] \tilde{g}_{ij} , \tag{1.15}$$

where $\tilde{g}_{ij}$ is the three-dimensional metric.

In a homogeneous and isotropic universe the components of the energy-momentum tensor must take everywhere the form

$$T^{00} = \rho(t), \qquad T^{0i} = 0, \qquad T^{ij} = \tilde{g}^{ij}(\boldsymbol{x}) a^{-2}(t) p(t) , \tag{1.16}$$

where $\rho(t)$ stands for the proper energy density and $p(t)$ represents the proper pressure. We can then write the tensor $S_{\mu\nu}$ as

$$S_{ij} = T_{ij} - \frac{1}{2}\tilde{g}_{ij} a^2 \left(T^k_k + T^0_0\right) = \frac{1}{2}(\rho - p) a^2 \tilde{g}_{ij} , \tag{1.17}$$

$$S_{00} = T_{00} + \frac{1}{2}\left(T^k_k + T^0_0\right) = \frac{1}{2}(\rho + 3p) , \tag{1.18}$$

$$S_{i0} = 0 , \tag{1.19}$$

and finally obtain the Einstein equations

$$-\frac{2K}{a^2} - \frac{2\dot{a}^2}{a^2} - \frac{\ddot{a}}{a} = -4\pi G(\rho - p) , \tag{1.20}$$

$$\frac{3\ddot{a}}{a} = -4\pi G(3p + \rho) . \tag{1.21}$$

Adding three times the first equation to the second we find the fundamental Friedmann-Lemaître equation [Friedmann, 1922; Friedmann, 1924; Lemaître, 1927], which provides the evolution of the expansion of the Universe as a function of the energy content

$$\dot{a}^2 + K = \frac{8\pi G\rho a^2}{3}\,. \tag{1.22}$$

From the Einstein equations (Eq. (1.21) is also sometimes know as the acceleration equation) we can also extract the so-called conservation equation

$$\dot{\rho} = -\frac{3\dot{a}}{a}(\rho + p)\,. \tag{1.23}$$

Although Eqs. (1.21, 1.22, 1.23) are not independent because they all come from Einstein equations, all of them are very useful in cosmology. For instance, given p as a function of ρ we can solve Eq. (1.23) to get ρ as a function of a, and plug it into Eq. (1.22) to find a as a function of t.

Even without knowing the dependence of ρ as a function of a, we can define from Eq. (1.22) the critical present energy density

$$\rho_{0,\mathrm{crit}} \equiv \frac{3H_0^2}{8\pi G}\,. \tag{1.24}$$

Independently of the contents of the Universe, the curvature constant K will be > 0, equal to 0, or < 0, if the present energy density ρ_0 is greater, equal to, or smaller than $\rho_{0,\mathrm{crit}}$.

Using Eq. (1.21) we can define the deceleration parameter today q_0 as

$$q_0 \equiv -\frac{\ddot{a}(t_0)a(t_0)}{\dot{a}^2(t_0)} = \frac{4\pi G}{3H_0^2}(\rho_0 + 3p_0)\,, \tag{1.25}$$

where the subscript 0 denotes the present value, and t_0 is the age of the Universe today.

Cosmic inventory

In order to fully understand the expansion of the Universe we need to know the evolution of ρ as a function of a. Although it is difficult to solve Eq. (1.23) in a general way, we can consider some frequently encountered extreme cases. Let us first assume that the pressure is related to the energy density through the equation of state parameter, w

$$p = w\rho\,, \tag{1.26}$$

and let us further assume w to be time-independent. Then Eq. (1.23) tells us that

$$\rho \propto a^{-3-3w}\,. \tag{1.27}$$

In particular, for cold matter (or dust) we have

$$p = 0 \Rightarrow \rho \propto a^{-3} \,. \tag{1.28}$$

For radiation we get

$$p = \frac{1}{3}\rho \Rightarrow \rho \propto a^{-4} \,. \tag{1.29}$$

And for a cosmological constant

$$p = -\rho \Rightarrow \rho = \text{constant} \,. \tag{1.30}$$

With these relations between ρ and a, and assuming a flat Universe, we can use Eq. (1.22) to easily get the scale factor dependence on cosmic time. For instance, for a cold matter dominated universe $a(t) \propto t^{2/3}$, while $a(t) \propto t^{1/2}$ for a radiation dominated universe.

In general we do not have a single constituent of the Universe. For a mixture of cold matter, radiation, and a cosmological constant, the total energy density is given by

$$\rho = \frac{3H_0^2}{8\pi G}\left[\Omega_\Lambda + \Omega_\mathrm{m} a^{-3} + \Omega_\mathrm{r} a^{-4}\right] \,, \tag{1.31}$$

where $\Omega_\Lambda, \Omega_\mathrm{m}, \Omega_\mathrm{r}$ stand for the present energy density parameter of the cosmological constant, cold matter, and radiation, respectively, which is defined as the ratio of the present energy density and the critical present energy density. We can then rewrite the Friedmann-Lemaître equation (1.22) for an arbitrary value of K as

$$H^2(a) = H_0^2\left[\Omega_\Lambda + \Omega_\mathrm{m} a^{-3} + \Omega_\mathrm{r} a^{-4} + (1 - \Omega_\Lambda - \Omega_\mathrm{m} - \Omega_\mathrm{r}) a^{-2}\right] \,, \tag{1.32}$$

where $H(a) \equiv \dot{a}/a$ is the Hubble parameter, and the term $(1 - \Omega_\Lambda - \Omega_\mathrm{m} - \Omega_\mathrm{r})a^{-2}$ can be associated to the curvature of the Universe

$$(1 - \Omega_\Lambda - \Omega_\mathrm{m} - \Omega_\mathrm{r}) = \Omega_\mathrm{K} \equiv -\frac{K}{H_0^2} \,. \tag{1.33}$$

1.1.2 Distances in the Universe

Measuring distances in the Universe is inherently tricky since, because of the expansion of the Universe, the distance to a given object varies with the propagation time of the emitted light. Looking back at Fig. 1.2 we can immediately see two different definitions of distance: the co-moving distance, that remains fixed as the Universe expands; and the physical distance, which grows because of the expansion. In the following we will present different definitions for the

distance that will be useful depending on the observations that we have. All of them can be calculated from the fundamental distance measure: the distance on the co-moving grid.

Redshift

Since the speed of light is finite, when we measure the distance to a certain object we are looking at the past. Therefore, there is in intrinsic duality between time and distance. It is characterized by a quantity called redshift. It is an observational phenomenon that indicates that the spectrum of a source is shifted towards red sequences because of the expansion of the Universe. It is a very interesting quantity from an observational point of view because it can be measured by atomic emission and absorption wavelengths. Notice that when objects have peculiar velocities their spectra can also be shifted (red if they are receding or blue if they are approaching us). This contribution to the redshift is then associated to the Doppler effect.

The redshift z can be related to the scale factor a. Let us consider a light ray emitted at time t_e with wavelength λ_e, and received at time t_r with wavelength λ_r. Since light travels in geodesics, $\mathrm{d}s^2 = 0$, using Eq. (1.9) we can write

$$\int_{t_e}^{t_r} \frac{\mathrm{d}t}{a(t)} = \int_R^0 \frac{\mathrm{d}r}{\sqrt{1-Kr^2}} = \int_{t_e+\lambda_e}^{t_r+\lambda_r} \frac{\mathrm{d}t}{a(t)}\,, \tag{1.34}$$

which lead to

$$\int_{t_e}^{t_e+\lambda_e} \frac{\mathrm{d}t}{a(t)} = \int_{t_r}^{t_r+\lambda_r} \frac{\mathrm{d}t}{a(t)}\,. \tag{1.35}$$

Assuming that the scale factor is constant over the small period of one cycle of a light wave we can write

$$\frac{1}{a_e}(t_e+\lambda_e-t_e) = \frac{1}{a_r}(t_r+\lambda_r-t_r) \Rightarrow \frac{\lambda_r}{\lambda_e} = \frac{a_r}{a_e}\,, \tag{1.36}$$

where $a_e = a(t_e)$ and equivalently for t_r.

We can now define the redshift as

$$z \equiv \frac{\lambda_r - \lambda_e}{\lambda_e}\,. \tag{1.37}$$

Taking $a_r = a_0 = 1$ and a_e just as an arbitrary a value, the redshift is then given by

$$1 + z = \frac{1}{a}\,. \tag{1.38}$$

Co-moving distance

The co-moving distance measures the distance between two objects in a coordinate system that expands with the Universe; thus, if these objects do not have peculiar velocities the distance between them will remain constant. We can define the co-moving distance between an object at scale factor a and us as

$$\chi = \int_{t(a)}^{t_0} \frac{dt'}{a(t')} = \int_a^1 \frac{da'}{a'^2 H(a')} = \int_0^z \frac{dz'}{H(z')} \,. \tag{1.39}$$

We can see objects typically with redshifts $z \lesssim 6$. At these late times the radiation content can be ignored, so for a flat, matter-dominated Universe this integral can be solved analytically, giving

$$\chi(a) = \frac{2}{H_0} \left[1 - a^{1/2}\right] \,. \tag{1.40}$$

Angular diameter distance

It is relatively easy in astronomy to measure the angle θ subtended by an object. We can measure the distance to an object by measuring this angle and knowing its physical size l. It will be given by (assuming θ is small)

$$d_\mathrm{A} = \frac{l}{\theta} \,. \tag{1.41}$$

In an expanding universe the co-moving size of the object is l/a. The co-moving distance to the object is given by Eq. (1.39), so the angle subtended will be given by $\theta = (l/a)/\chi(a)$, giving the angular diameter distance

$$d_\mathrm{A} = a\chi = \frac{\chi}{1+z} \,. \tag{1.42}$$

This expression is only valid for a flat universe. It can be generalized to arbitrary non-vanishing values of Ω_K with

$$d_\mathrm{A} = \frac{a}{H_0\sqrt{|\Omega_\mathrm{K}|}} \begin{cases} \sinh\left(\sqrt{\Omega_\mathrm{K}} H_0 \chi\right) & \Omega_\mathrm{K} > 0 \\ \sin\left(\sqrt{-\Omega_\mathrm{K}} H_0 \chi\right) & \Omega_\mathrm{K} < 0 \end{cases} \,. \tag{1.43}$$

Luminosity distance

Another way of measuring distances in cosmology is through the flux of an object with known luminosity. Let us first recall that the observed flux F at a distance d from a source of luminosity L is given by (in a static universe)

$$F = \frac{L}{4\pi d^2} \,, \tag{1.44}$$

since the total luminosity through a spherical shell with area $4\pi d^2$ is constant.

Let us now focus on the co-moving grid again and center the source at the origin. The observed flux will be given by

$$F = \frac{L(\chi)}{4\pi\chi^2(a)}\,, \tag{1.45}$$

where $L(\chi)$ is the luminosity through a co-moving spherical shell of radius $\chi(a)$. Let us also assume that all photons have been emitted with the same energy. The luminosity is then multiplied by the number of photons passing through a co-moving spherical shell per unit time. In a fixed time interval, photons travel farther on the co-moving grid at early times than at late times, since the associated physical distance at early times is smaller. Therefore, the number of photons crossing a shell in a fixed time interval will be smaller today than at emission by a factor a. In the same way, the energy of the photons will be smaller today than at emission. Thus, the energy per unit time passing through a co-moving shell a distance $\chi(a)$ from the source will be smaller than the luminosity at the source by a factor a^2. The observed flux will then be

$$F = \frac{La^2}{4\pi\chi^2(a)}\,, \tag{1.46}$$

where L is the luminosity at the source, and the luminosity distance will be given by

$$d_{\rm L} \equiv \frac{\chi}{a}\,. \tag{1.47}$$

1.1.3 Dark matter

The idea of having a non-baryonic contribution to matter in our Universe was first proposed in 1933 by Zwicky [Zwicky, 1933]. He measured the velocity dispersion of galaxies inside the Coma cluster, and he inferred from them a mass much smaller than the gravitational mass necessary for the galaxies random motion. Even by considering non-luminous baryonic matter to compensate for this deficit, it cannot be fully explained because the baryonic fraction is well constrained by baryon acoustic oscillations (see Sec. 1.5).

Since Zwicky first proposal, there have been many observational evidence pointing towards the existence of a contribution to matter with a non-baryonic origin, from galactic to cosmological scales. In the following we will provide some examples at different scales, but a detailed compilation of dark matter evidence can be found in the review from Bertone, Hooper, and Silk, 2005.

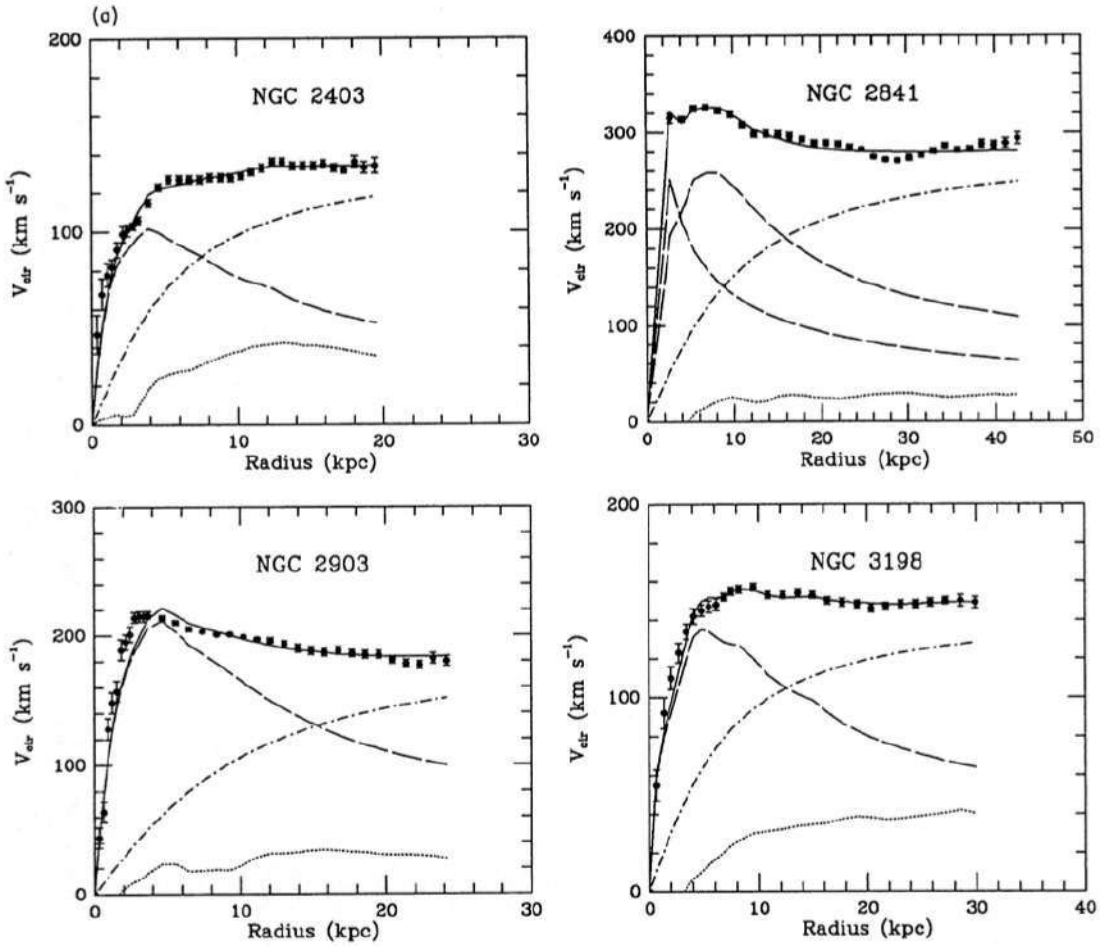

FIGURE 1.3: Original rotation curves of different galaxies (circular velocity as a function of the distance to the galactic center) from Begeman, Broeils, and Sanders, 1991. The dotted, dashed, and dash-dotted lines are the contributions of gas, disk, and dark matter, respectively.

Galactic scales

The most convincing evidence of dark matter on galactic scales comes from the analyses of the rotation curves of galaxies; i.e. the circular velocities of stars (and gas) as a function of their distance to the center of the galaxy. In Newtonian dynamics the circular velocity is given by

$$v(r) = \sqrt{\frac{GM(r)}{r}}\,, \tag{1.48}$$

where $M(r) \equiv 4\pi \int \rho(r) r^2 \, \mathrm{d}r$ and $\rho(r)$ the mass density profile. The velocity should then be falling as $1/\sqrt{r}$ beyond the optical disk. However, it has been observed (see Fig. 1.3 with the original rotation curves from Begeman, Broeils, and Sanders, 1991) that $v(r)$ is approximately constant, implying the existence

of a halo with $M(r) \propto r$ and $\rho \propto 1/r^2$.

Other arguments for dark matter on sub-galactic and inter-galactic scales come from:

- Strong lensing around individual massive elliptical galaxies, which provides evidence for substructure on scales of $\sim 10^6$ solar masses [Metcalf et al., 2004; Moustakas and Metcalf, 2003].
- Inconsistency between the amount of stars in the solar neighborhood and the gravitational potential implied by their distribution [Bahcall, Flynn, and Gould, 1992].
- Velocity dispersions of dwarf spheroidal galaxies, that imply mass-to-light ratios larger than those observed in our neighborhood [Mateo, 1998; Vogt et al., 1995].
- Velocity dispersions of spiral galaxy satellites, that suggest the existence of dark halos around spiral galaxies behind the optical disc [Azzaro, Prada, and Gutiérrez, 2004; Zaritsky et al., 1997].

Galaxy cluster scales

The mass of a cluster can be determined using different approaches, like applying the virial theorem to the observed distribution of radial velocities, using weak lensing analyses, or studying the X-ray emission profile that traces the distribution of hot gas in rich clusters.

Let us consider the equation of hydrostatic equilibrium for a spherically symmetric system

$$\frac{1}{\rho}\frac{\mathrm{d}P}{\mathrm{d}r} = -a(r)\,, \tag{1.49}$$

where P, ρ, and a are the pressure, density, and gravitational acceleration of the gas, respectively, at radius r. For an ideal gas it can be rewritten in terms of the temperature T. It can then be shown that for a baryonic mass of a typical cluster the temperature should obey the relation [Bertone, Hooper, and Silk, 2005]

$$kT \approx (1.3 - 1.8)\,\mathrm{keV}\left(\frac{M_r}{10^{14}M_\odot}\right)\left(\frac{1\,\mathrm{Mpc}}{r}\right)\,, \tag{1.50}$$

where k is the Boltzmann's constant, $M_\odot$ is the solar mass, and M_r is the mass enclosed within the radius r. The disparity between this temperature and the observed one ($T \approx 10\,\mathrm{keV}$), suggests the existence of a substantial amount of dark matter in clusters.

These conclusions have been checked using gravitational lensing data [Tyson, Kochanski, and Dell'Antonio, 1998]. According to General Relativity, photons propagate along geodesics that deviate from straight lines when passing near intense gravitational fields. Measuring the distortion of background objects due to the gravitational mass of a cluster enables us to determine its mass.

Cosmological scales

Many different cosmological probes are sensitive to the total quantity of baryonic matter, or the total matter contribution to our Universe, like the photons coming from the early Universe (the cosmic microwave background), gravitational analyses at cosmological scales (weak lensing), the structure of visible matter in the Universe (baryon acoustic oscillations), or even type Ia supernovae analyses. All these probes will be presented in detail in Sec. 1.5. We just focus here on one of the fundamental cosmological observations known as the Big Bang nucleosynthesis (BBN).

Since the Universe is expanding, its temperature was higher in the past. Just extrapolating, we can imagine a moment when the temperature was high enough for nuclear reactions to take place, as it is the case in the core of the stars. These nuclear reactions allow for the formation of light elements, like Helium or Lithium, from the combination of protons and neutrons. We refer to this process as BBN. Knowing the conditions of the early Universe and the relevant nuclear cross-sections, we can predict the expected primordial abundances of these light elements. In Fig. 1.4 we show the predictions of BBN for these abundances and the agreement with the observations.

Interestingly enough, the BBN predictions for the abundances depend on the density of protons and neutrons at that time. The combined proton plus neutron density is the baryon density, so BBN gives us a way to measure the baryon density in the Universe. Since we know how those densities scale as a function of the scale factor, we can turn the measurements of light element abundances into measures of the baryon density today. BBN measurements tell us that nowadays baryonic matter contributes only around 5% to the critical density of the Universe. Since the total matter density today is certainly larger than this, BBN provides an extra evidence for the existence of dark matter.

1.1.4 Cosmic acceleration: a cosmological constant and dark energy

Measuring distances at redshifts $z > 0.1$ are cosmologically interesting because these redshifts are large enough to have a small contribution from peculiar motions of the sources, and they are also large enough to be forced to take

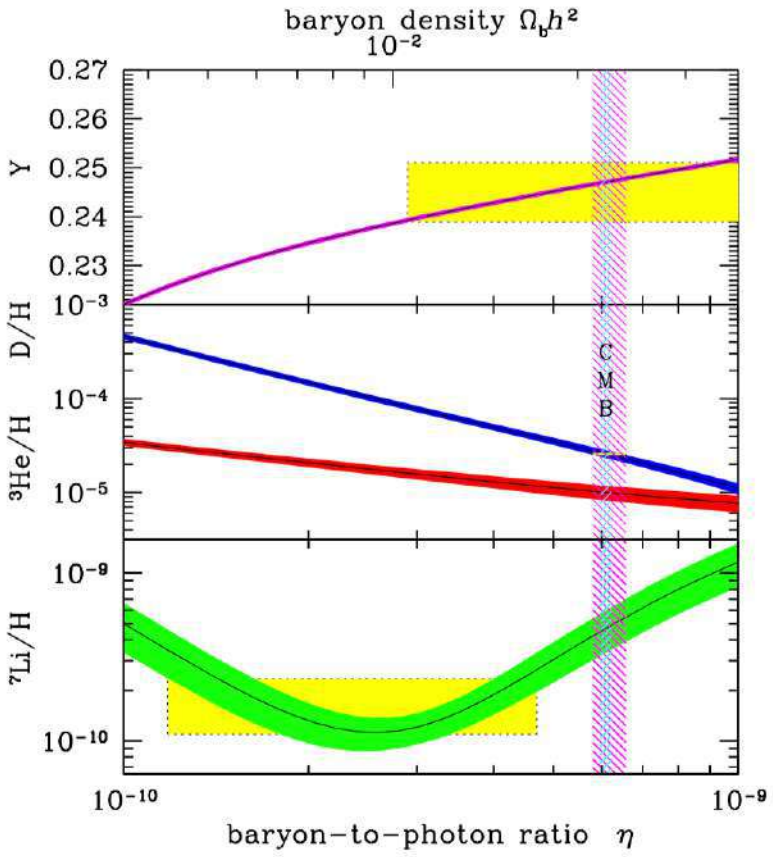

FIGURE 1.4: Original plot from the Particle Data Group 2016 (and 2017 update) Review [Patrignani et al., 2016]. The BBN predictions for the primordial abundances of ^{4}He, D, ^{3}He, and ^{7}Li are shown (as bands) as a function of the baryon-to-photon ratio. The corresponding observations are represented by yellow boxes. The vertical narrow band corresponds to the cosmic microwave background measurement of the baryon-to-photon ratio, while the wider vertical band represents the constraints from the combination of the different abundance measurements.

into account the effects of the cosmological expansion when determining the distances. In order to measure these distances we look for "standard candles" in the sky. These are objects with known absolute luminosity, so we can extract the luminosity distance by measuring their flux. For many years, the standard candles used were the brightest galaxies in rich galaxy clusters, but it is now well known that their absolute luminosity evolves significantly over cosmological time scales.

Fortunately, type Ia supernovae (SNIa) are nice candidates to replace these bright galaxies. SNIa are very bright objects easy to spot even at high redshifts, and, although they are not directly standard candles, they can be standardized by correcting for empirical effects (see Sec. 1.5.1 for a more detailed discussion

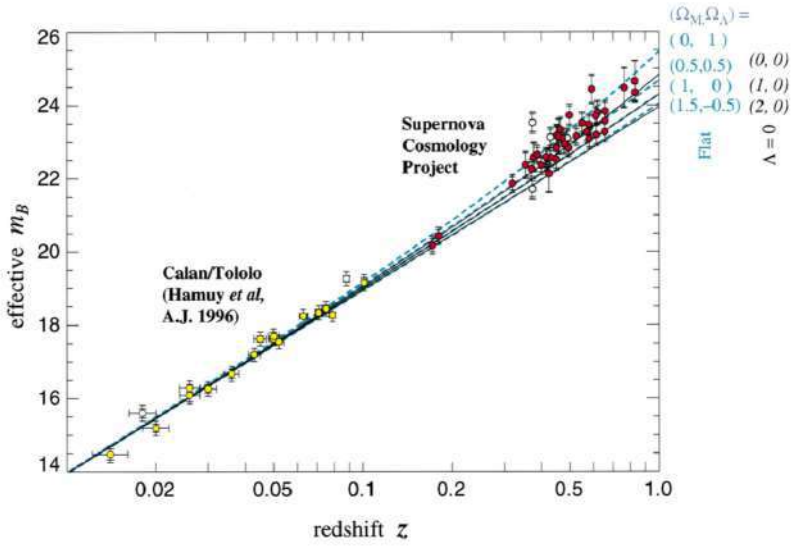

FIGURE 1.5: Original plot from Perlmutter et al., 1999, showing the effective apparent magnitude in the B-band (corrected for variations in the absolute magnitude by SNIa light-curves) as a function of the redshift, for the 42 SNIa observed by the Supernova Cosmology Project. 18 low-redshift SNIa from the Calán/Tololo Supernova Survey are also added into the analysis. Horizontal bars indicate the uncertainty in redshift due to an assumed peculiar velocity uncertainty of 300 km/s. Dashed and solid lines give the theoretical predictions for cosmological models with $\Omega_K = 0$ or $\Omega_\Lambda = 0$, respectively, and different Ω_m values.

on their standardization). More in detail, a SNIa occurs when a white dwarf member of a binary system has accreted enough mass to go beyond the Chandrasekhar limit, so the nature of the explosion does not depend too much on when in the history of the expansion of the Universe it happens, or on the initial mass of the white dwarf, or on the nature of the companion.

In the last years of the past century, two different groups, The Supernova Cosmology Project [Perlmutter et al., 1999] and the High-z Supernova Search Team [Riess et al., 1998], were the first to analyze high-redshift SNIa ($z > 0.1$). The Supernova Cosmology Project analyzed the relation between apparent luminosity and redshift for 42 SNIa from $z = 0.18$ to $z = 0.83$, together with low-redshift ($z < 0.1$) SNIa available at that moment from another survey. This group claimed (see their results in Fig. 1.5) that a vanishing (or negative) cosmological constant contribution to the total energy density of the Universe was ruled out with a confidence level of 99%. For a flat universe the group found a value for Ω_m close to 0.28, which gives a value for the deceleration parameter close to $q_0 = -0.58$, indicating the accelerated nature of the expansion of the Universe.

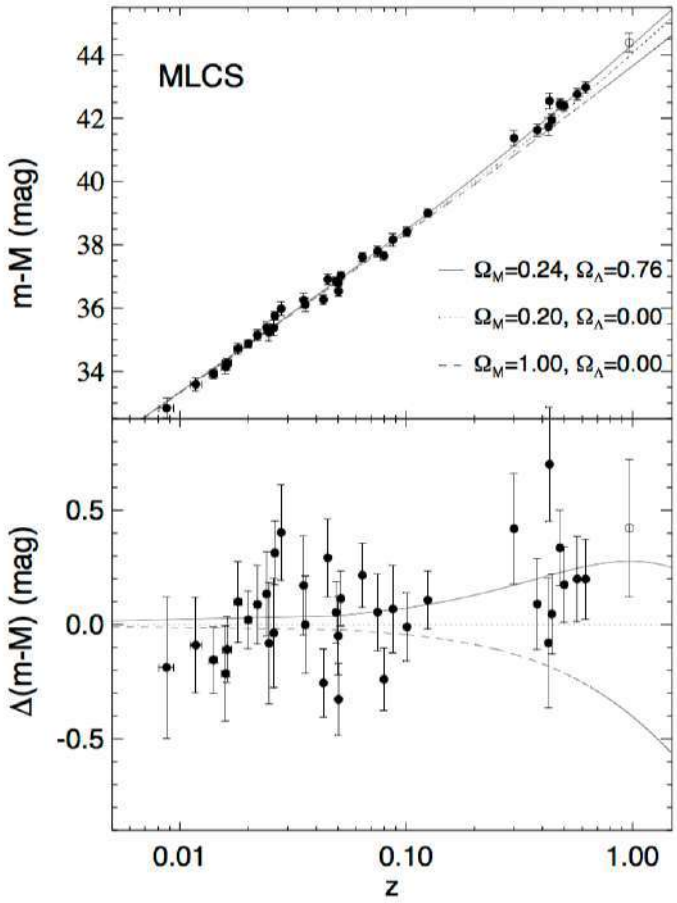

FIGURE 1.6: Original plot from Riess et al., 1998. In the upper panel the distance modulus (apparent magnitude minus absolute magnitude) is plotted as a function of the redshift for a sample of SNIa. The curves give the theoretical predictions for two cosmologies with $\Omega_\Lambda = 0$ and a good-fit flat cosmology with $\Omega_m = 0.24$ and $\Omega_\Lambda = 0.76$. The bottom panel shows the difference between data and a model with $\Omega_m = 0.2$ and $\Omega_\Lambda = 0$, represented by the horizontal dotted line.

The High-z Supernova Search Team studied 16 high-redshift SNIa with redshifts ranging from 0.16 to 0.97, including 2 SNIa from the Supernova Cosmology Project, and 34 low-redshift SNIa. They concluded that $\Omega_\Lambda > 0$ at the 99.7% confidence level, without assumptions about spatial curvature (see their results in Fig. 1.6). Assuming only $\Omega_m \geq 0$, and with a conservative fitting method, they concluded that $q_0 < 0$ with a 99.5% confidence level, indicating also that the Universe is expanding in an accelerated way.

The work of these two groups (confirmed by more precise and recent data, and also other cosmological probes (see Sec. 1.5)), provided the first empirical evidence for the existence of an exotic fluid, with a negative pressure, that accelerates the expansion of the Universe. It was the first observational evidence

supporting the existence of dark energy. More precisely, a cosmological constant Λ. However, the fact that the accelerated nature of the expansion relies on a constant, which suffers from fine-tuning problems (see Sec. 1.1.5), is not very satisfying from a theoretical point of view. Because of this, a large literature addressing different theoretical and phenomenological models for dark energy beyond a cosmological constant has appeared in the past two decades. We just present a few cases in the following and refer the reader to Amendola et al., 2013, for a detailed review on dark energy models.

Phenomenological and model-independent approaches

The most common phenomenological parametrization beyond a cosmological constant is the CPL parametrization [Chevallier and Polarski, 2001; Linder, 2003], where the equation of state for dark energy is given by

$$w(a) = w_0 + w_a(1-a)\,. \tag{1.51}$$

In this case we do not assume any specific dark energy model. It is frequently used to check if the data prefers a dynamically evolving dark energy fluid in front of a cosmological constant. Notice also that it only models the background expansion of dark energy, without specifying the perturbation behavior of the fluid.

Alternatively, we can directly measure the dark energy density, or the expansion rate of the Universe in different redshift bins [Wang and Garnavich, 2001], which is closer to observations; or even use a principal component approach [Huterer and Starkman, 2003] or Gaussian processes analysis [Seikel, Clarkson, and Smith, 2012] to reconstruct any of these functions in a model-independent way. Notice that in these cases a choice of the perturbation evolution for dark energy is also needed (see next section).

Quintessence

We define by quintessence models the scalar field models with canonical kinetic energy in General Relativity. Scalar fields are good candidates for dark energy because they are the simplest fields, do not introduce preferred directions, are usually weakly clustered, and can easily provide us with an accelerated expansion. Because of all this, quintessence models [Wetterich, 1988; Ratra and Peebles, 1988; Caldwell, Dave, and Steinhardt, 1998] are the most studied dark energy models. They are described by the action (neglecting radiation)

$$S = \int \mathrm{d}^4x\sqrt{-g}\left(\frac{1}{16\pi G}R + \mathcal{L}_\phi\right) + S_\mathrm{m}\,, \tag{1.52}$$

where

$$\mathcal{L}_\phi = -\frac{1}{2} g^{\mu\nu} \partial_\mu \phi \partial_\nu \phi - V(\phi) \,, \tag{1.53}$$

R is the Ricci scalar, and S_m is the matter action.

In a FLRW background, the energy density and the pressure of the scalar field ϕ are given by

$$\rho_\phi = \frac{1}{2}\dot{\phi}^2 + V(\phi) \,, \tag{1.54}$$

$$p_\phi = \frac{1}{2}\dot{\phi}^2 - V(\phi) \,, \tag{1.55}$$

which give the equation of state

$$w_\phi = \frac{\dot{\phi}^2 - 2V(\phi)}{\dot{\phi}^2 + 2V(\phi)} \,. \tag{1.56}$$

In a flat universe, Einstein's equations give

$$H^2 = \frac{8\pi G}{3}\left(\frac{1}{2}\dot{\phi}^2 + V(\phi) + \rho_M\right) \,, \tag{1.57}$$

$$\dot{H} = -\frac{8\pi G}{2}\left(\dot{\phi}^2 + \rho_M + p_M\right) \,. \tag{1.58}$$

Notice that the condition $w_\phi < -1/3$ is required in order to have late-time cosmic acceleration. This can be translated into $\dot{\phi}^2 < V(\phi)$.

Concerning the perturbations (see next section), it has been shown that they correspond to those of a fluid with sound speed equal to 1, which means that quintessence models do not cluster significantly inside the horizon [Sapone and Kunz, 2009; Sapone, Kunz, and Amendola, 2010].

K-essence

In the quintessence model, it is the potential energy of the scalar field which leads to cosmic acceleration. If we ask for the kinetic energy to dominate we obtain the k-essence models [Armendariz-Picon, Mukhanov, and Steinhardt, 2000; Armendariz-Picon, Mukhanov, and Steinhardt, 2001]. They are characterized by the action

$$S = \int \mathrm{d}^4x \sqrt{-g} p(\phi, X) \,, \tag{1.59}$$

where $X = (1/2) g^{\mu\nu} \nabla_\mu \phi \nabla_\nu \phi$. The energy density of the scalar field is given by

$$\rho_\phi = 2X\frac{\mathrm{d}p}{\mathrm{d}X} - p\,, \tag{1.60}$$

while the pressure is $p_\phi = p(\phi, X)$.

If we treat the k-essence scalar as a perfect fluid, its equation of state is given by

$$w_\phi = -\frac{p}{p - 2X\frac{\mathrm{d}p}{\mathrm{d}X}}\,. \tag{1.61}$$

With the appropriate choice of p, the scalar can act as dark energy.

Modified gravity

Although the terms dark energy and modified gravity are usually used in the literature, there is no consensus on where is the line between these two classes of models.

In general, when we consider standard dark energy models of minimally coupled scalar fields, with standard kinetic energy in Einstein gravity, and the scalar potential as only degree of freedom, we refer to it as quintessence. However, once we go beyond this, different models can have the same observational signatures both at the background and perturbations levels [Kunz and Sapone, 2007]. Any modification of Einstein's equations can be interpreted as standard General Relativity with a modified matter source containing a mixture of scalars, vectors, and tensors [Hu and Sawicki, 2007; Kunz, Amendola, and Sapone, 2008]. It seems therefore impossible to distinguish between dark energy and modifications to the theory of gravity. However, a classification largely used in the literature is the following:

- Standard dark energy: Models with standard General Relativity and dark energy that does not cluster significantly inside the horizon. The main example of these models is a minimally coupled scalar field with standard kinetic energy and sound speed equal to 1, or quintessence.

- Clustering dark energy: In these models there is an extra contribution to the Poisson equation due to the dark energy perturbations, and no extra effective anisotropic stress. The main example is the k-essence model with a low sound speed.

- Explicit modified gravity: Models where from the start the Einstein equations are modified. Some examples could be the scalar-tensor theories (see e.g. Wetterich, 1988; Hwang, 1990), $f(R)$ (see e.g. Amendola and Tsujikawa, 2010), or interacting dark energy (see e.g. Kodama and Sasaki,

1984; Amendola, 2000), in which a fifth force is effectively introduced in addition to gravity.

Phantom crossing

One of the most important quantities that phenomenologically characterize dark energy is its equation of state parameter w. Current observations point to the fact that our Universe is compatible with a cosmological constant; thus $w \approx -1$. However, the region of the parameter space given by $w < -1$ (and called phantom energy) is not excluded. Although there is not any problem on allowing w to be smaller than -1 for the background evolution, there are apparent divergences that appear at the level of perturbations when a model tries to cross the limit $w = -1$ (see e.g. Amendola et al., 2013). This may be a problem when analyzing data from Euclid, since it will directly probe the perturbations through measurements of galaxy clustering and weak lensing. However, at the level of cosmological first-order perturbation theory, some regularization can be performed to allow an effective fluid to cross the phantom divide (see Amendola et al., 2013, and references therein for a detailed description on the regularization of the phantom divergences).

From a more phenomenological point of view, like when we use the CPL parametrization, the equation of state parameter for dark energy can cross the phantom divide. Since we only specify the background evolution with this parametrization it should not introduce any problem. However, when considering cosmological probes sensitive to perturbations, as it is the case in Euclid, we need to take into account the perturbation behavior of our fluid. A standard approach in the literature is to use the parametrized post-Friedmann (PPF) framework [Hu and Sawicki, 2007] on top of our Boltzmann code. This framework is based on the requirements of a metric theory, with small deviations from the FLRW metric, and covariant conservation of the stress energy tensor. It allows us to study models beyond a cosmological constant and capture their perturbation behavior inside modifications of the theory of gravity. In this way, we can phenomenologically consider the CPL parametrization without providing a full theoretical model for dark energy perturbations.

1.1.5 The standard model

The current standard (or concordance) model of cosmology is the so-called ΛCDM model, since it is a model in which the main contribution to matter is cold and dark; i.e. collision-less and only interacting through gravity, hence the CDM part of the model. The other key ingredient accounts for the the majority of the energy density of the Universe today, and it behaves like vacuum energy;

TABLE 1.1: Values of the ΛCDM cosmological parameters obtained from the combination of CMB, BAO, SNIa, and H_0 data [Planck Collaboration, 2016b]. The CMB temperature comes from the analysis of the CMB monopole data [Fixsen, 2009].

Parameter	Symbol	Value
Physical baryon density	$\Omega_{\rm b}h^2$	0.02230 ± 0.00014
Physical cold dark matter density	$\Omega_{\rm cdm}h^2$	0.1188 ± 0.0010
Dimensionless Hubble constant	h	0.6774 ± 0.0046
Power spectrum amplitude	$\ln(10^{10}A_s)$	3.064 ± 0.023
Power spectrum slope	n_s	0.9667 ± 0.0040
Re-ionization optical depth	τ	0.066 ± 0.012
CMB temperature	$T_{\rm CMB}$ [K]	2.72548 ± 0.00057

i.e. like the cosmological constant Λ. The ability of this model to fit many cosmological observations of different origin with an incredible precision has been decisive to consider it the standard model of cosmology.

Parameters and assumptions

Being a bit more specific about the ΛCDM model, it can be fully parametrized by 7 parameters, that are listed (with current constraints from the cosmic microwave background (CMB), baryon acoustic oscillations (BAO), SNIa and H_0 measurements) in Table 1.1. The first two parameters correspond to the physical densities for baryonic, $\Omega_{\rm b}h^2$ and cold dark matter, $\Omega_{\rm cdm}h^2$, while the third parameter, h, stands for the dimensionless Hubble constant $h \equiv H_0/100\,\mathrm{km/(s{\cdot}Mpc)}$. The following three parameters correspond to the amplitude of the initial power spectrum of matter fluctuations, A_s, the slope of this initial power spectrum as a function of the wavenumber, n_s, and the re-ionization optical depth, τ, describing how much the primary CMB anisotropies are scattered by the re-ionized medium at low redshifts. The last parameter of the ΛCDM model is the present temperature of the CMB, $T_{\rm CMB}$, but, because of the exquisite precision of this measurement, it is usually fixed in the analyses giving 6 free parameters for the ΛCDM model. Other parameters are usually used in the literature, like the total critical density of matter, $\Omega_{\rm m}$, or the root mean square mass fluctuation amplitude on scales of $8h^{-1}$ Mpc at redshift $z = 0$, σ_8, but they can all be derived from the seven parameters presented.

It is important to notice that the ΛCDM model implies some assumptions, like the cosmological principle (homogeneous and isotropic universe), spatial flatness, dark energy behaving as a cosmological constant, or dark matter being

collision-less and cold (see Scott, 2018, for a detailed list of the assumptions behind the standard model). Many assumptions have been investigated, checking if the data prefers a model without them, like evolving dark energy, or curved universes. Our current measurements do not provide (yet) any evidence towards a model beyond ΛCDM.

Background equations

The flat ΛCDM model assumes a Robertson-Walker metric and Friedmann-Lemaître dynamics leading to the co-moving distance, $\chi(z)$, and Friedmann-Lemaître equation,

$$\chi(z) = \int_0^z \frac{\mathrm{d}z'}{H(z')}\,, \tag{1.62}$$

$$\frac{H^2(z)}{H_0^2} = \Omega_\mathrm{r}(1+z)^4 + \Omega_\mathrm{m}(1+z)^3 + (1-\Omega_\mathrm{r}-\Omega_\mathrm{m})\,. \tag{1.63}$$

We can compute the radiation contribution as in Planck Collaboration, 2016b,

$$\Omega_\mathrm{r} = \Omega_\gamma \left[1 + N_\mathrm{eff}\,\frac{7}{8}\left(\frac{4}{11}\right)^{4/3}\right]\,, \tag{1.64}$$

where N_eff is the effective number of relativistic degrees of freedom and the photon contribution, Ω_γ, is given by

$$\Omega_\gamma = 4 \cdot 5.6704 \times 10^{-8} \frac{T_\mathrm{CMB}^4}{c^3} \frac{8\pi G}{3H_0^2}\,. \tag{1.65}$$

Fine-tuning problems and tensions

Despite the ability of the ΛCDM model to fit the observations, there are some problems around this model coming from observations. In a first place, measurements from the CMB [Planck Collaboration, 2016b] tell us that our Universe is nowadays very close to being spatially flat. Extrapolating back in time, this means that the initial density of the different components of the Universe should have been set to a specific value with high precision. This is known as the flatness problem. Another issue is the so-called horizon problem. We can see, observationally, that our Universe is very homogeneous at very large scales. These scales are so large that light has not had the time to travel from one place to the other. One of the most accepted solutions to both problems is the cosmological inflation [Guth, 1981]. This would be an era just after the Big Bang where the flatness would be forced very close to zero and the anisotropies would

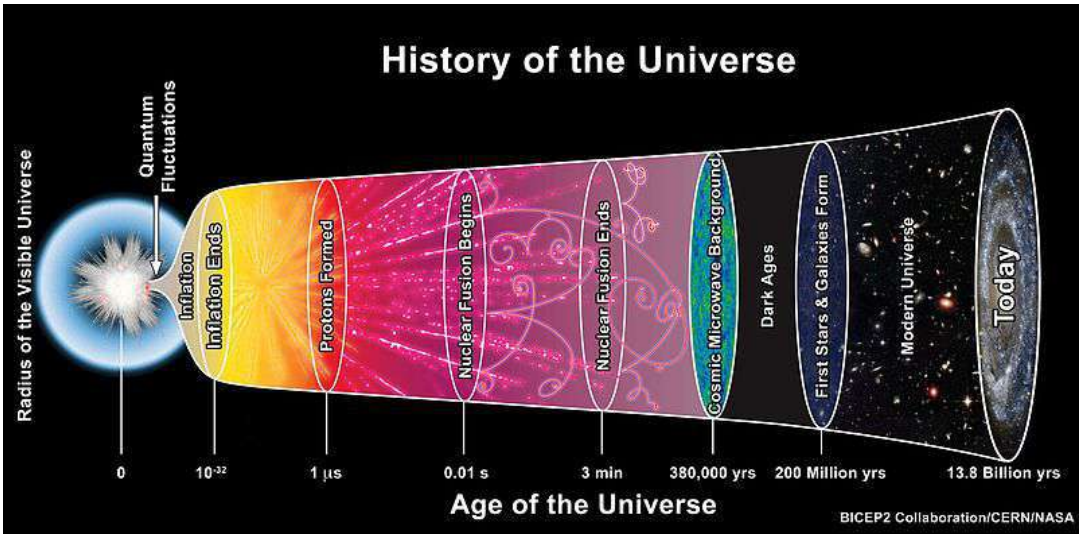

FIGURE 1.7: Illustration of the history of the Universe, from the Big Bang singularity to today. Credit: BICEP2 Collaboration/CERN/NASA.

be suppressed, so that the Universe would become flat and homogenous as we observe it now. Many observational attempts are being done to probe this era of the history of the Universe and, although it has not been confirmed yet, all the predictions coming from inflation are in agreement with our observations.

Also, in the past few years, different cosmological analyses using different probes have given values for the ΛCDM parameters that are slightly in tension. For example, the amplitude σ_8 obtained from CMB measurements is in tension with the value obtained from cluster abundance. Another example can be the value of the Hubble constant, H_0. Direct measurements from SNIa give significantly higher values than the indirect value obtained from CMB data. These tensions might be the sign of new physics beyond the standard model, or observational systematics that are not fully under control, or even just a statistical fluctuation. There is a huge effort in the community to propose theoretical models that could explain these tensions, as well as trying to better understand the different systematics of the measurements. We must remember that, even if the ΛCDM model is able to fit the current cosmological observations, the nature of about 95% of the content of the Universe remains still unknown.

A very brief history of the Universe

Just before finishing this first section of the chapter we provide here an intuitive picture of the history of the Universe under the standard cosmological model.

Looking at Fig. 1.7 we can see the origin of the Universe with the Big Bang

singularity in space-time. Nearly immediately afterwards, cosmological inflation occurs, generating an exponential expansion of the Universe. With this expansion the primordial quantum fluctuations remain in the Universe. After inflation the Universe keeps expanding, so the temperature drops enough for symmetries between fundamental forces to break. Successively, anti-baryons annihilate, neutrinos decouple, and BBN takes place, forming then the first atomic nuclei.

After these first minutes of history of the Universe, it continues to expand and the temperature continues to drop, until the matter-radiation equality is achieved ($z \approx 3600$). After that, at $z \approx 1100$, the temperature of the Universe is low enough to enable the plasma of photons, electrons and protons to be no longer in thermal equilibrium. Electrons and protons start forming hydrogen atoms, which is called recombination, and photons start to travel freely since they are no longer coupled to matter. This are the photons from the CMB that we observe today.

After recombination, only the CMB radiation is emitted (dark ages), and structures start to be formed due to gravity. At $z \approx 20$, highly dense regions start to form stars and galaxies. These objects emit new light, which is able to rip electrons from the neutral atoms (re-ionization). At lower redshifts ($z \approx 6$) clusters of galaxies start to appear due again to gravity. At $z \approx 0.4$ the contribution of matter is roughly equal to the contribution of dark energy to the total energy content of the Universe, and the latter is increasingly more important than the former until today.

1.2 Structure formation

The Universe is very homogeneous at very large scales, but when we look at smaller scales (galaxy cluster, galaxy, or Solar system scales) we can see some structures following a net with filaments, walls and voids. Look for example at Fig. 1.8, where we can see the structures that galaxies form in the Universe from the Sloan Digital Sky Survey data. The formation of these structures depends on the cosmology; therefore, studying the large-scale structure of the Universe can provide information on the underlying cosmological model.

It is important to mention that if the Universe were perfectly homogeneous and isotropic there would not be any anisotropy in the CMB, or structures in the low-redshift Universe. The cosmological inflation was first proposed to explain the flatness and horizon problems, but interestingly, it provides a simple mechanism to explain these anisotropies. Intuitively, the initial quantum fluctuations were magnified due to the exponential expansion from inflation, and they were able to remain in the Universe with a cosmic size. These fluctuations

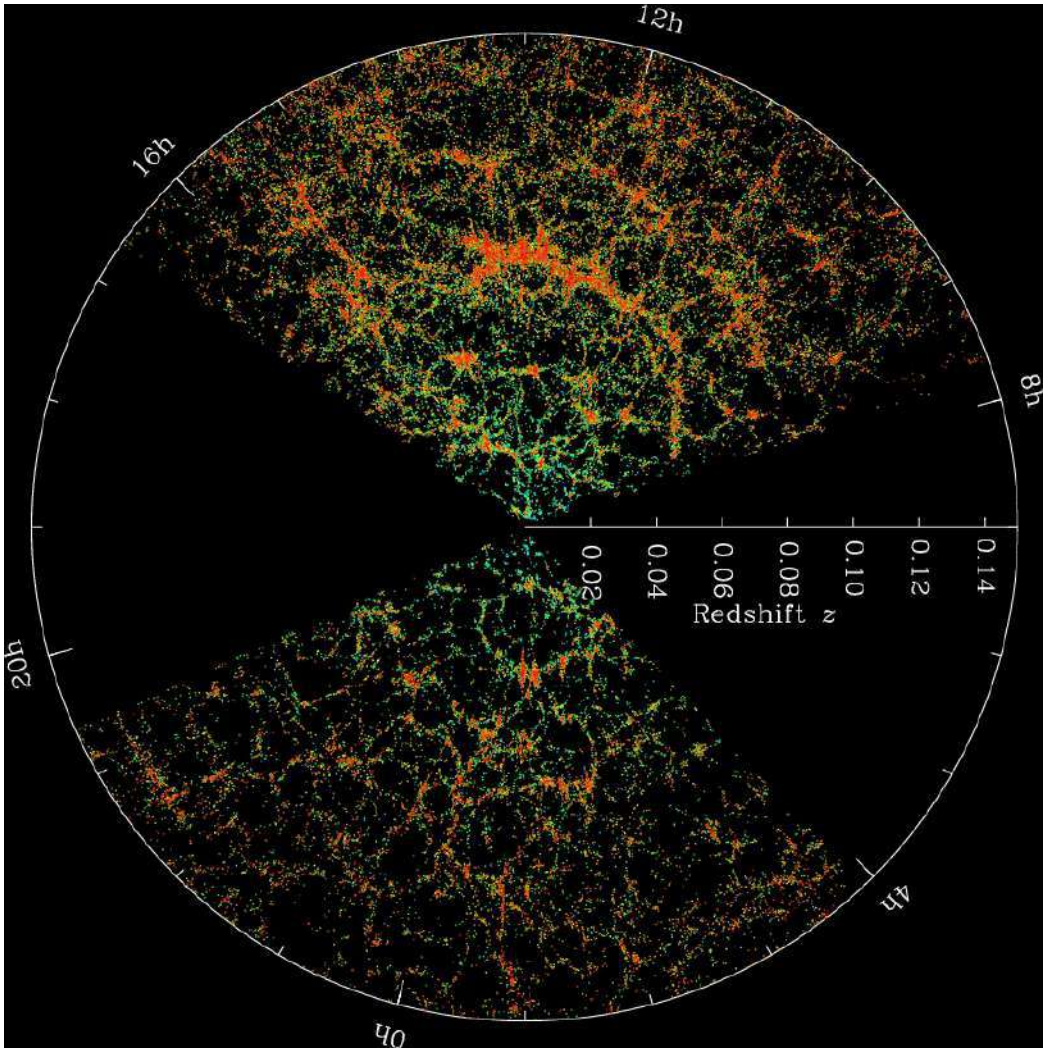

FIGURE 1.8: Map of the galaxies in the Universe from the SDSS. Each dot represents a galaxy. Credit: M. Blanton and SDSS. [http://www.sdss.org/science/orangepie/].

became then the seed of the anisotropies that we observe today in the CMB and the large-scale structure of the Universe.

1.2.1 Two-point-correlation function, power spectrum, and angular correlations

Before entering into the evolution of structures, we will first remind the notion of Fourier space and define the two-point-correlation function, the power spectrum, and angular correlations.

Let us first consider a three-dimensional field $f(\boldsymbol{r})$ defined in real space position $\boldsymbol{r}$. We can then define the Fourier transform of this field as

$$\tilde{f}(\boldsymbol{k}) \equiv \int_{\mathbb{R}^3} \mathrm{d}^3\boldsymbol{r} e^{-i\boldsymbol{k}\boldsymbol{r}} f(\boldsymbol{r})\,, \tag{1.66}$$

where $\boldsymbol{k}$ is a wave vector in Fourier space. Let us also define the inverse Fourier transform as

$$f(\boldsymbol{r}) \equiv \int_{\mathbb{R}^3} \frac{\mathrm{d}^3\boldsymbol{k}}{(2\pi)^3} e^{i\boldsymbol{k}\boldsymbol{r}} \tilde{f}(\boldsymbol{k})\,. \tag{1.67}$$

Let us now consider two different fields f_1 and f_2, and their convolution product

$$(f_1 * f_2)(\boldsymbol{r}) \equiv \int \mathrm{d}^3\boldsymbol{r}' f_1(\boldsymbol{r}-\boldsymbol{r}') f_2(\boldsymbol{r}')\,. \tag{1.68}$$

Using the fact that the Fourier transform of 1 is a Dirac delta function, it can be shown that this convolution is equivalent to a product in Fourier space

$$(f_1 * f_2)(\boldsymbol{r}) = \int \frac{\mathrm{d}^3\boldsymbol{k}}{(2\pi)^3} e^{i\boldsymbol{k}\boldsymbol{r}} \left(\tilde{f}_1 \cdot \tilde{f}_2\right)(\boldsymbol{k})\,. \tag{1.69}$$

For a given three-dimensional field f we can define the two-point-correlation function (2PCF) $C(\boldsymbol{r})$ as

$$C(\boldsymbol{r}) = \langle f(\boldsymbol{r}') f(\boldsymbol{r}'+\boldsymbol{r})\rangle_{\boldsymbol{r}'} \equiv \int_{\mathbb{R}^3} \mathrm{d}^3\boldsymbol{r}' f(\boldsymbol{r}') f(\boldsymbol{r}'+\boldsymbol{r})\,, \tag{1.70}$$

where the subscript $\boldsymbol{r}'$ implies averaging over $\boldsymbol{r}'$. The intuitive interpretation of a 2PCF is the expectation valor of the product of two field points separated by a distance $\boldsymbol{r}$.

We can also define the contrast δ of a field f and its variance σ by

$$\delta(\boldsymbol{r}) \equiv \frac{f(\boldsymbol{r})-\bar{f}}{\bar{f}} \quad \text{with} \quad \bar{f} \equiv \lim_{V\to+\infty} \frac{1}{V}\int_V \mathrm{d}^3\boldsymbol{r} f(\boldsymbol{r}) \tag{1.71}$$

$$\sigma^2 \equiv \langle \delta^2(\boldsymbol{r})\rangle_{\boldsymbol{r}} = \int_{\mathbb{R}^3} \mathrm{d}^3\boldsymbol{r}\delta^2(\boldsymbol{r})\,. \tag{1.72}$$

We can now define the power spectrum as the average of $|\tilde{\delta}(\boldsymbol{k})|^2$ over all directions

$$P(k) \equiv \frac{1}{4\pi}\int \mathrm{d}^2\Omega |\tilde{\delta}(\boldsymbol{k})|^2\,, \tag{1.73}$$

which is completely equivalent to another extensively used definition

$$\langle \tilde{\delta}(\boldsymbol{k})\tilde{\delta}^*(\boldsymbol{k}')\rangle_\Omega \equiv (2\pi)^3 P(k)\delta_D^{(3)}(\boldsymbol{k}-\boldsymbol{k}')\,, \tag{1.74}$$

where $\delta_D^{(3)}$ stands for the three-dimensional Dirac function.

Let us now focus on the case of the matter field, with δ being the matter density contrast of the Universe. Depending on the field, the integral from Eq. (1.72) can diverge. When it concerns the matter field, it is convenient to regularize this integral by filtering the field. If we denote as $W_R(\boldsymbol{r})$ the filter function, characterized by a physical size R, then Eq. (1.72) becomes

$$\sigma^2(R) \equiv \langle (W_R * \delta)^2(\boldsymbol{r}) \rangle_{\boldsymbol{r}} \,. \tag{1.75}$$

If W_R has a finite support we can express this new quantity as

$$\sigma^2(R) = \int \frac{k^2 \,\mathrm{d}k}{2\pi^2} P(k) |\tilde{W}_R(\boldsymbol{k})|^2 \,. \tag{1.76}$$

For the specific case of a three-dimensional top-hat filter function with radius $R = 8\,\mathrm{Mpc}/h$, we obtain the commonly used σ_8 parameter, which represents the variance of the matter density contrast smoothed with a spherical top-hat filter of physical radius $8\,\mathrm{Mpc}/h$.

The power spectrum (or the two-point correlation function) includes information in three-dimensions. However, sometimes we might be interested (or forced due to the available data) to project all the information into two dimensions, like in an angular survey of galaxies. The simplest statistic to be computed in two dimensions is the two-point angular correlation function, $\omega(\theta)$, or its Fourier transform: the two-dimensional power spectrum $C(\ell)$.

Let us consider a given galaxy at co-moving distance $\chi(z)$. In the plane perpendicular to the line pointing to the center of the distribution of galaxies, a galaxy position is determined by the two-dimensional vector $\vec{\theta} = (\theta_1, \theta_2)$; thus, the three-dimensional position of the galaxy is given by

$$\boldsymbol{x}(\chi(z), \vec{\theta}) = \chi(z)(\theta_1, \theta_2, 1) \,. \tag{1.77}$$

We measure all galaxies along the line-of-sight; therefore, an over-density at $\vec{\theta}$ is

$$\delta_2(\vec{\theta}) = \int_0^{\chi_\infty} \mathrm{d}\chi W(\chi) \delta(\boldsymbol{x}(\chi, \vec{\theta})) \,, \tag{1.78}$$

where the subscript $_2$ stands for a two-dimensional contrast, and $W(\chi)$ is the selection function, containing the probability of observing a galaxy a co-moving distance χ away from us, normalized so that $\int_0^{\chi_\infty} \mathrm{d}\chi W(\chi) = 1$.

We can now express the Fourier transform of $\delta_2(\vec{\theta})$ as

$$\tilde{\delta}_2(\vec{\ell}) = \int \mathrm{d}^2\theta e^{-i\vec{\ell}\cdot\vec{\theta}} \delta_2(\vec{\theta}) \,. \tag{1.79}$$

And we can define the two-dimensional power spectrum analogous to the three-dimensional case

$$\langle\tilde{\delta}_2(\vec{\ell})\tilde{\delta}_2^*(\vec{\ell'})\rangle = (2\pi)^2\delta_D^2(\vec{\ell}-\vec{\ell'})C(\ell)\,. \tag{1.80}$$

Integrating, we can write the $C(\ell)$ as

$$\begin{aligned} C(\ell) &= \frac{1}{(2\pi)^2}\int \mathrm{d}^2\ell'\,\langle\delta_2(\vec{\ell})\delta_2^*(\vec{\ell})\rangle = \\ &= \frac{1}{(2\pi)^2}\int \mathrm{d}^2\ell' \int \mathrm{d}^2\theta \int \mathrm{d}^2\theta' e^{-ie\vec{l}l\cdot\vec{\theta}} e^{i\vec{\ell'}\cdot\vec{\theta'}} \\ &\quad \times \int_0^{\chi_\infty} \mathrm{d}\chi W(\chi) \int_0^{\chi_\infty} \mathrm{d}\chi' W(\chi')\,\langle\delta(\boldsymbol{x}(\chi,\vec{\theta}))\delta(\boldsymbol{x}'(\chi',\vec{\theta'}))\rangle\,. \end{aligned} \tag{1.81}$$

Using the properties of the Dirac delta functions, and introducing the power spectrum we can rewrite it as

$$C(\ell) = \int_0^{\chi_\infty} \mathrm{d}\chi \frac{W(\chi)}{\chi^2} \int_0^{\chi_\infty} \mathrm{d}\chi' W(\chi') \int_{-\infty}^{\infty} \frac{\mathrm{d}k_3}{(2\pi)} P\left(\sqrt{k_3^2+\frac{\ell^2}{\chi^2}}\right) e^{ik_3(\chi-\chi')}\,. \tag{1.82}$$

With the approximation that the only modes that contribute to the integral are those with $k_3 \ll \ell/\chi$ we can express the $C(\ell)$ by

$$C(\ell) = \int_0^{\chi_\infty} \mathrm{d}\chi \frac{W^2(\chi)}{\chi^2} P\left(\frac{\ell}{\chi}\right) = \frac{1}{\ell}\int_0^{\infty} \mathrm{d}k P(k) W^2\left(\frac{\ell}{k}\right)\,. \tag{1.83}$$

1.2.2 Linear structure formation

On large scales, perturbations remain small and we can use linear theory to derive the formation of the structures. Therefore, linear theory is enough to analyze the observations from the large-scale structure. However, if we go to smaller and smaller scales the perturbations become more important and the linear theory breaks down. We will briefly discuss this regime in Sec. 1.2.3.

Let δ be the matter density contrast of the Universe, and let us consider the gravitational potential in Fourier space, $\Phi(\boldsymbol{k}, a)$. The evolution of cosmological perturbations can be then divided in three different stages. At early times, all of the modes are outside the horizon and they evolve identically. At intermediate times, the wavelengths fall within the horizon and the Universe evolves from radiation domination to matter domination. The order of the matter-radiation equality and the epoch of the horizon crossing have an important role on the evolution of the modes. At late times, all the modes evolve identically again. We mainly observe the distribution of matter at late epochs, in the third stage of evolution, where all the modes evolve identically. However, we can relate

the gravitational potential to the primordial one set up by inflation, $\Phi_{\rm p}(\boldsymbol{k})$. Neglecting anisotropic stress, the relation is given by

$$\Phi(\boldsymbol{k},a) = \frac{9}{10}\Phi_{\rm p}(\boldsymbol{k})T(k)\frac{D_1(a)}{a}\,, \tag{1.84}$$

where $T(k)$ is the transfer function, describing the evolution of perturbations through the epochs of horizon crossing and radiation-matter transition, and $D_1(a)$ is the growth factor, that describes the wavelength-independent growth at late times.

We can now express the power spectrum of the matter distribution in terms of the primordial power spectrum coming from inflation, the transfer function, and the growth function. Let us remind Poisson's equation

$$\Phi = \frac{4\pi G\rho_{\rm m}a^2\delta}{k^2}\,, \tag{1.85}$$

which relies the matter over-density to the potential at late times. Since the background density of matter is $\rho_{\rm m} = \Omega_{\rm m}\rho_{\rm cr}a^{-3}$ and $4\pi G\rho_{\rm cr} = (3/2)H_0^2$ we can write

$$\delta(\boldsymbol{k},a) = \frac{k^2\Phi(\boldsymbol{k},a)a}{(3/2)\Omega_{\rm m}H_0^2} = \frac{3}{5}\frac{k^2}{\Omega_{\rm m}H_0^2}\Phi_{\rm p}(\boldsymbol{k})T(k)D_1(a)\,. \tag{1.86}$$

In the context of inflation the primordial potential is drawn from a Gaussian distribution with mean 0 and variance

$$P_\Phi = \frac{50\pi^2}{9k^3}\left(\frac{k}{H_0}\right)^{n_s-1}\delta_{\rm H}^2\left(\frac{\Omega_{\rm m}}{D_1(a=1)}\right)^2\,, \tag{1.87}$$

where $\delta_{\rm H}$ stands for the amplitude of the perturbations at horizon crossing. So the power spectrum of matter at late times is given by

$$P(k,a) = 2\pi^2\delta_{\rm H}^2\frac{k^{n_s}}{H_0^{n_s+3}}T^2(k)\left(\frac{D_1(a)}{D_1(a=1)}\right)^2\,. \tag{1.88}$$

At late times ($z \lesssim 10$) all modes of interest have entered the horizon. Considering the Boltzmann equations governing the dark matter evolution, and the Poisson equation we can derive a second order differential equation for the matter perturbations

$$\frac{{\rm d}^2\delta}{{\rm d}a^2} + \left(\frac{{\rm d}\ln(H)}{{\rm d}a} + \frac{3}{a}\right)\frac{{\rm d}\delta}{{\rm d}a} - \frac{3}{2}\frac{\Omega_{\rm m}H_0^2}{a^5H^2}\delta = 0\,. \tag{1.89}$$

There are two different solutions to this equation. One is $\delta \propto H$, but all current models of the Universe have a non-increasing Hubble rate. This is the

so-called decaying solution. We are interested in the other solution. To obtain the growing mode we can try a solution of the form $u = \delta / H$

$$\frac{\mathrm{d}^2 u}{\mathrm{d}a^2} + 3\left[\frac{\mathrm{d}\ln(H)}{\mathrm{d}a} + \frac{1}{a}\right]\frac{\mathrm{d}u}{\mathrm{d}a} = 0\,. \tag{1.90}$$

Integrating this first-order differential equation for $\mathrm{d}u/\mathrm{d}a$ we obtain

$$\frac{\mathrm{d}u}{\mathrm{d}a} \propto (aH)^{-3}\,. \tag{1.91}$$

Integrating again, and using the initial condition that when matter still dominates ($z \approx 10$) D_1 should be equal to a, we obtain the growth factor given by

$$D_1(a) = \frac{5\Omega_\mathrm{m}}{2}\frac{H(a)}{H_0}\int_0^a \frac{\mathrm{d}a'}{(a'H(a')/H_0)^3}\,. \tag{1.92}$$

Concerning the transfer function $T(k)$, there has been some analytic fitting formulas provided in the literature (see e.g. Bardeen et al., 1986). But nowadays the majority of the cosmological analyses rely on numerical Boltzmann solvers like `CAMB` [Howlett et al., 2012; Lewis, Challinor, and Lasenby, 2000] or `CLASS` [Lesgourgues, 2011a; Blas, Lesgourgues, and Tram, 2011; Lesgourgues, 2011b; Lesgourgues and Tram, 2011] to derive the transfer function including not only dark matter, but baryons, and relativistic species.

1.2.3 Non-linear regime

When we focus on smaller and smaller scales, the perturbations of the matter density field are no longer small and the linear theory for the evolution of structures, discussed in the previous section, starts to give biased predictions. In the standard cosmological model, structures are formed in a hierarchical way: small structures form around the first over-densities of the matter density field. Because of gravity, these structures collapse into virialized dark matter halos, and larger structures form even later from accretion of nearby mass, or merging of different halos. Because of the different nature of dark and baryonic matter, the latter falls into the already formed halos of dark matter. The reason being that the temperature of cold dark matter decreases faster than the temperature of baryonic matter. Because of the non-gravitational interactions of baryonic matter, it is very difficult to study the evolution of structures at the scales of a galactic halo or inside it. There are different theoretical approaches to extend the theoretical predictions to smaller scales, but in order to reach very small scales we need to rely on prescriptions fitted from cosmological simulations, which will then depend on the cosmological model used for the simulations.

Theoretical approach

The standard method to go beyond linear theory is the so-called standard perturbation theory (SPT) (see Bernardeau et al., 2002, for a detailed review). Let us recall that for linear theory we can write the contrast of the matter field, δ, as

$$\delta(\boldsymbol{k}, z) = \frac{D_1(z)}{D_1(z_i)}\delta_i(\boldsymbol{k})\,. \tag{1.93}$$

In SPT we develop it as a power series

$$\delta(\boldsymbol{k}) = \sum_{n=1}^{\infty} a^n \delta^{(n)}(\boldsymbol{k})\,. \tag{1.94}$$

Focusing on the power spectrum, we can now write its definition as

$$\langle(\delta_1+\delta_2+\delta_3+\ldots)(\delta_1+\delta_2+\delta_3+\ldots)\rangle = (2\pi)^3 P_{\rm m}(k)\delta_D^{(3)}(\boldsymbol{k}-\boldsymbol{k}')\,. \tag{1.95}$$

So the power spectrum will now be given not only by the linear part, P_{11}, but also for higher-order contributions (P_{13}, P_{22}, ...), which introduce power from other scales, giving what we call mode coupling. These higher-order terms can be represented by Feynman diagrams. However, this approach is valid on large-scales, but it breaks down when approaching the non-linear regime. One option could be to sum up all the orders, but, depending on the slope of the power spectrum, different orders become equally important and it is no longer straightforward to cut the expansion. In Fig. 1.9 we can observe the results from Blas, Garny, and Konstandin, 2014, showing SPT up to three loops. The power spectrum is represented normalized to a power spectrum without wiggles for illustrative purposes. We can see in red the measurements from an N-body simulation, while in solid line there is the linear prediction, which starts to be biased quite early. In dashed line there is the 1-loop SPT prediction, which is able to stay closer to the simulation until slightly smaller scales. Going up to 2-loops in SPT improves the prediction (dotted-dashed line), but when 3-loops are considered (black diamonds) the prediction is completely off with respect to the simulations, showing that different orders become equally important.

Another theoretical approach to extend our predictions into the non-linear regime is the so-called renormalized perturbation theory (RPT) [Crocce and Scoccimarro, 2006]. This approach can also be represented by Feynman diagrams where the initial conditions correspond to the perturbation spectrum, the vertex represents the non-linearities, and the propagator describes the linear evolution. In this approach, each loop correction to the linear power spectrum can be classified into two classes: one corresponding to the coupling between

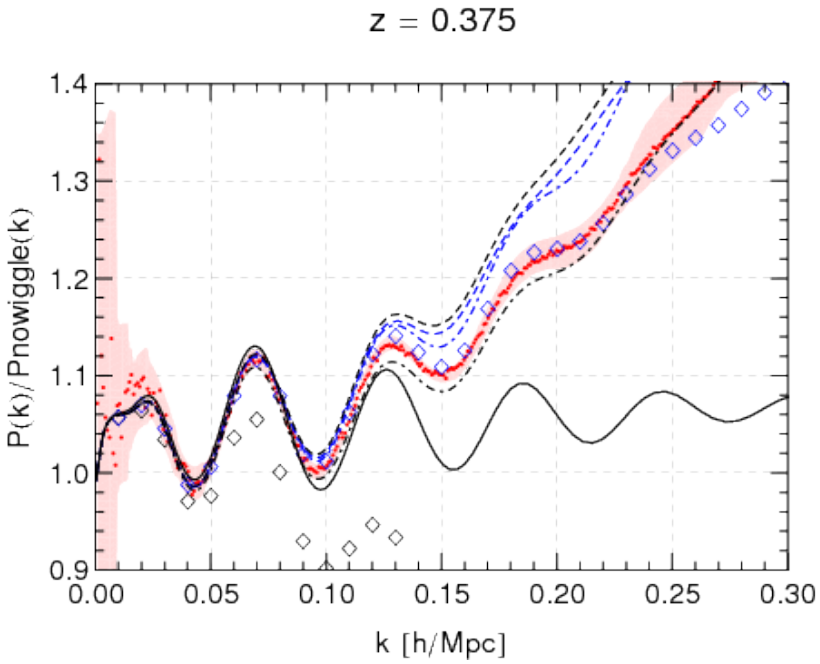

FIGURE 1.9: Original plot from Blas, Garny, and Konstandin, 2014: Comparison at redshift 0.375 of SPT up to 1-loop (black dashed line), 2-loops (black dot-dashed line), and 3-loops (black diamonds), with N-body results of the Horizon Run 2 [Kim et al., 2011]. The black solid line corresponds to the linear result. In blue the results of Padé resummation are shown, which is not discussed in this work.

modes, and another one concerning the renormalization of the propagator. The authors in Crocce and Scoccimarro, 2006, show that the latter class of diagrams can be resumed, implying that each term remaining in the mode-coupling class will dominate at some characteristic scale and will be subdominant otherwise. With this approach we can get rid of the main problem of SPT, where higher-order terms may be as important as lower-order ones. In Fig. 1.10 we can observe a comparison of RPT to N-body simulations from Crocce, Scoccimarro, and Bernardeau, 2012. The power spectrum (normalized to a smooth spectrum) is represented as a function of the wavelength for different cosmologies. The red dashed line corresponds to the linear prediction, while the blue line stands for RPT. We can observe that the RPT result is able to stay closer to the simulations down to smaller scales than the linear prediction.

However, RPT breaks Galilean invariance because it only resumes the unequal time propagator. There are more terms in the SPT expansion that need to be resumed in order to restore the Galilean invariance, which has led to some extensions, like TSPT [Blas et al., 2016]. Other recent approaches are the response functions [Nishimichi, Bernardeau, and Taruya, 2016], or the effective field theory [Baumann et al., 2012].

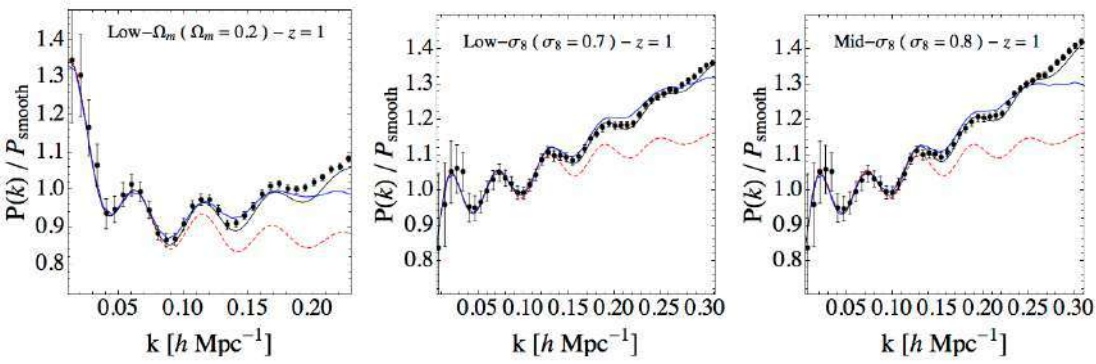

FIGURE 1.10: Original plot from Crocce, Scoccimarro, and Bernardeau, 2012: Comparison at redshift 1 of RPT (blue solid line) with simulation measurements (black dots). The red dashed line corresponds to the linear result. The results of halofit are also shown in black.

Just to summarize, in order to get an approximate idea, the best performance we can achieve nowadays is an agreement of 1-2% on the power spectrum down to $k \sim 0.25 - 0.4\,h/\mathrm{Mpc}$, depending on the redshift, and the theoretical approach used. This is enough for the modeling of the BAO peak (see Sec. 1.3), but it is still far from the small scales that weak lensing analyses probe.

Halofit

One of the first widely used prescriptions to model the non-linear part of the power spectrum (called `halofit`) was derived in 2003 by Smith et al., 2003. The authors measured the non-linear evolution of the matter power spectra from a large library of cosmological N-body simulations, using power-law initial spectra.

The `halofit` model is based on the halo model [Peacock and Smith, 2000; Seljak, 2000; Ma and Fry, 2000]. The basic approach suggested by the latter is to decompose the density field into a distribution of isolated haloes. The correlations in the field are then originated through the clustering of haloes with respect to each other (at large scales), and through the clustering of dark matter particles within the same halo (at small scales). The total non-linear power spectrum can then be decomposed into

$$P_{\mathrm{NL}}(k) = P_{\mathrm{Q}}(k) + P_{\mathrm{H}}(k)\,, \tag{1.96}$$

where $P_{\mathrm{Q}}(k)$ is the quasi-linear term related to the large-scale contribution to the spectrum, and $P_{\mathrm{H}}(k)$ describes the contribution from the self-correlation of haloes.

Let us first focus on the quasi-linear term. Seljak, 2000; Ma and Fry, 2000; Scoccimarro et al., 2001, proposed to use linear theory filtered by the effective window that corresponds to the distribution of halo masses, $n(M)$, convolved with their density profiles, $\tilde{\rho}(k, M)$, and a prescription for their bias with respect to the underlying mass field, $b(M)$. The quasi-linear term can then be expressed as

$$P_{\rm Q}(k) = P_{\rm L}(k) \left[\frac{1}{\bar{\rho}} \int {\rm d}M b(M) n(M) \tilde{\rho}(k, M) \right]^2 . \tag{1.97}$$

A simpler approach was made by Peacock and Smith, 2000. The authors assumed that the quasi-linear term corresponded to pure linear theory. However, quasi-linear effects must modify the relative correlations of haloes away from linear theory, irrespective of the allowance made for the finite size of the haloes (see Smith et al., 2003, and references therein). `halofit` takes then an empirical approach, allowing the quasi-linear term to depend on n, and truncating its effects at small scales. Removing the dimensions of the power spectrum by defining

$$\Delta^2(k) \equiv \frac{V}{(2\pi)^3} 4\pi k^3 P(k) \,, \tag{1.98}$$

where V is a normalization volume, the quasi-linear term in `halofit` is given by

$$\Delta^2_{\rm Q}(k) = \Delta^2_{\rm L}(k) \frac{[1 + \Delta^2_{\rm L}(k)]^{\beta_n}}{1 + \alpha_n \Delta^2_{\rm L}(k)} \, e^{-f(y)} \,, \tag{1.99}$$

where $y \equiv k/k_\sigma$, k_σ is a non-linear wavenumber related to the spherical collapse model [Press and Schechter, 1974; Sheth and Tormen, 1999; Jenkins et al., 2001], α_n and β_n are coefficients sensitive to the spectra, and $f(y) = y/4 + y^2/8$ governs the decay rate at small scales.

Let us now focus on the halo term of the power spectrum. In the halo model it is given by

$$P_{\rm H}(k) = \frac{1}{\bar{\rho}^2 (2\pi)^3} \int {\rm d}M n(M) |\tilde{\rho}(k, M)|^2 \,. \tag{1.100}$$

In order to model this we can use an expression looking like a shot-noise spectrum on large scales, but progressively reduced on small scales by the filtering effects of halo profiles and the mass function. A good candidate could be

$$\Delta^2_{\rm H}{}'(k) = \frac{a_n y^3}{1 + b_n y + c_n y^{3-\gamma_n}} \,, \tag{1.101}$$

where $(a_n, b_n, c_n, \gamma_n)$ are dimensionless numbers that depends on the spectrum. However, it has been shown [Cooray and Sheth, 2002] that with this expression the halo model fails to respect low-order perturbation theory in some cases. In order to solve this, `halofit` modifies Eq. (1.101) to obtain a spectrum steeper than Poisson on the largest scales

$$\Delta^2_{\rm H}(k) = \frac{\Delta^2_{\rm H}{}'(k)}{1 + \mu_n y^{-1} + \nu_n y^{-2}}\,, \tag{1.102}$$

where μ_n and ν_n are coefficients that depend on the spectrum. In Fig. 1.11 we show the original plot from Smith et al., 2003, where the full halo model calculation (thick solid lines) is compared to CDM simulations (points), and the `halofit` predictions (thin solid lines) are also shown. It is clear from the figure that `halofit` is able to reproduce the measurements from simulations more accurately, and down to smaller scales, than the halo model.

Halofit with Bird and Takahashi corrections

Although `halofit` seems to be able to correctly predict the non-linear matter power spectrum down to very small scales, all the coefficients depending on the spectrum have been determined in Smith et al., 2003, from a fit to CDM simulations. Therefore, if we want to test cosmologies with massive neutrinos, or go down to very small scales, where the impact of baryonic interactions is non-negligible, `halofit` may provide biased predictions.

In 2012, Bird, Viel, and Haehnelt, 2012, addressed the impact of massive neutrinos. The authors performed several N-body simulations of the matter power spectrum incorporating massive neutrinos with masses between 0.15 and 0.6 eV. They focused on non-linear scales below $10\,h/\mathrm{Mpc}$ at $z < 3$. The authors extended the `halofit` approximation to account for massive neutrinos, and they found that in the strongly non-linear regime `halofit` over-predicts the suppression due to the free-streaming of the neutrinos. More in detail, the asymptotic behavior of the non-linear term in `halofit` is given by $\Delta^2_{\rm H} \sim y^{\gamma_n}$, so the authors in Bird, Viel, and Haehnelt, 2012, altered γ_n fitting it to their ΛCDM with massive neutrinos simulations. Moreover, they modified the non-linear term with the ansatz

$$Q_\nu = \frac{l f_\nu}{1 + m k^3} \tag{1.103}$$

$$(\Delta^\nu_{\rm NL})^2 = \Delta^2_{\rm NL}(1 + Q_\nu)\,, \tag{1.104}$$

with l and m fitted to the simulations, which led to the modification of Eq. (1.99)

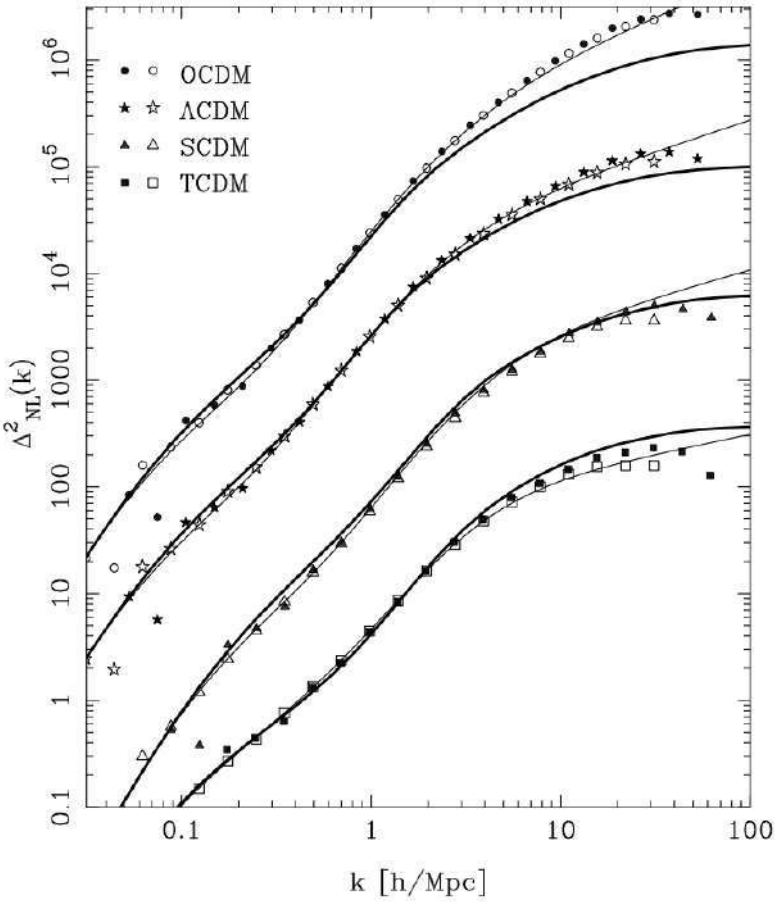

FIGURE 1.11: Original plot from Smith et al., 2003: comparison of the halo model calculation (thick solid lines), and the `halofit` predictions (thin solid line) to CDM data from N-body simulations (points). The four CDM models have been separated from each other by one order of magnitude in the y-direction for illustrative purposes.

$$\Delta^2_{\rm Q}(k) = \Delta^2_{\rm L}(k)\frac{[1+\tilde{\Delta}^2_{\rm L}(k)]^{\tilde{\beta}_n}}{1+\alpha_n\tilde{\Delta}^2_{\rm L}(k)}\,e^{-f(y)}\,, \tag{1.105}$$

with

$$\tilde{\Delta}^2_{\rm L} = \Delta^2_{\rm L}\left(1+\frac{pf_\nu k^2}{1+1.5k^2}\right) \tag{1.106}$$

$$\tilde{\beta}_n = \beta_n + f_\nu(r+sn^2)\,, \tag{1.107}$$

where p, r and s are fitted to the simulations. In Fig. 1.12 we show the original results from Bird, Viel, and Haehnelt, 2012, where the effect of massive neutrinos on the matter power spectrum is represented. We show only the case

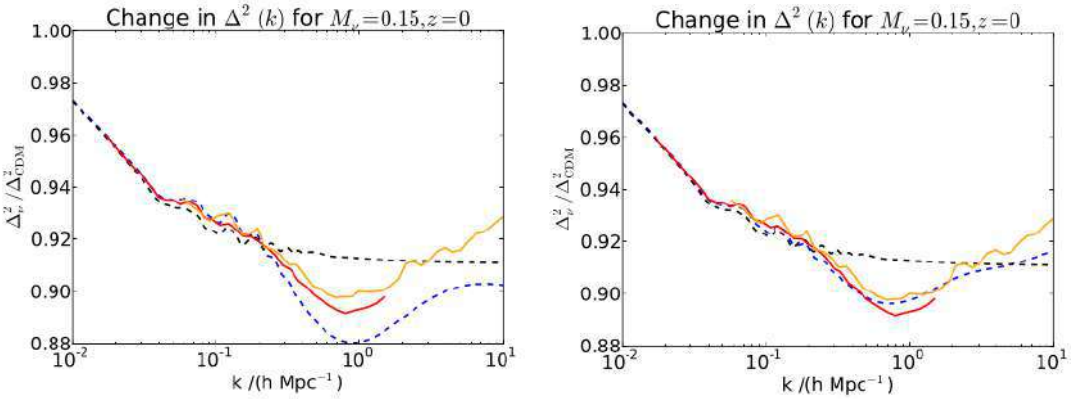

FIGURE 1.12: Original results from Bird, Viel, and Haehnelt, 2012: The effect of massive (0.15 eV) neutrinos on the matter power spectrum is shown at $z = 0$. Solid lines show the ratio between simulation with and without neutrinos for 512 Mpc/h (red) and 150 Mpc/h (orange) boxes. The blue dashed line shows the estimated ratio using the standard `halofit` correction (left panel) and the improved version accounting from massive neutrinos (right panel). The black dashed line represents the prediction from linear theory.

where the mass of the neutrinos equals 0.15 eV at $z = 0$. The solid red and orange lines show the measurements from N-body simulations, while the black dashed line stands for the linear prediction. In the left panel the blue dashed line shows the prediction from the standard `halofit` correction, while the same line in the right panel represents the corrected version taking into account the effect of massive neutrinos. We can observe that the latter is able to reproduce the results from the simulations with neutrinos down to smaller scales.

Another recent correction to `halofit` was also done in 2012 by Takahashi et al., 2012. The simulations used to calibrate `halofit` were already a decade old at that time and, given the need of correctly predicting smaller and smaller cases for future cosmological analyses, the authors of Takahashi et al., 2012, re-calibrated the parameters of `halofit` using high-resolution N-body simulations for 16 cosmological models around the WMAP best-fit cosmological parameters, including dark energy models with a constant equation of state. This revised version of `halofit` provides an accurate prediction of the non-linear matter power spectrum down to $k \sim 30\,h/\mathrm{Mpc}$ and up to $z \geq 3$. In Fig. 1.13 we show the original results from Takahashi et al., 2012, where the matter power spectra for the different WMAP models obtained from simulations (dots) are compared to the revised `halofit` prediction (red solid line), the standard `halofit` prediction (black solid line), and the linear results (black dashed line). We can clearly see that the revised version of `halofit` is able to recover the measurements from simulation down to much smaller scales.

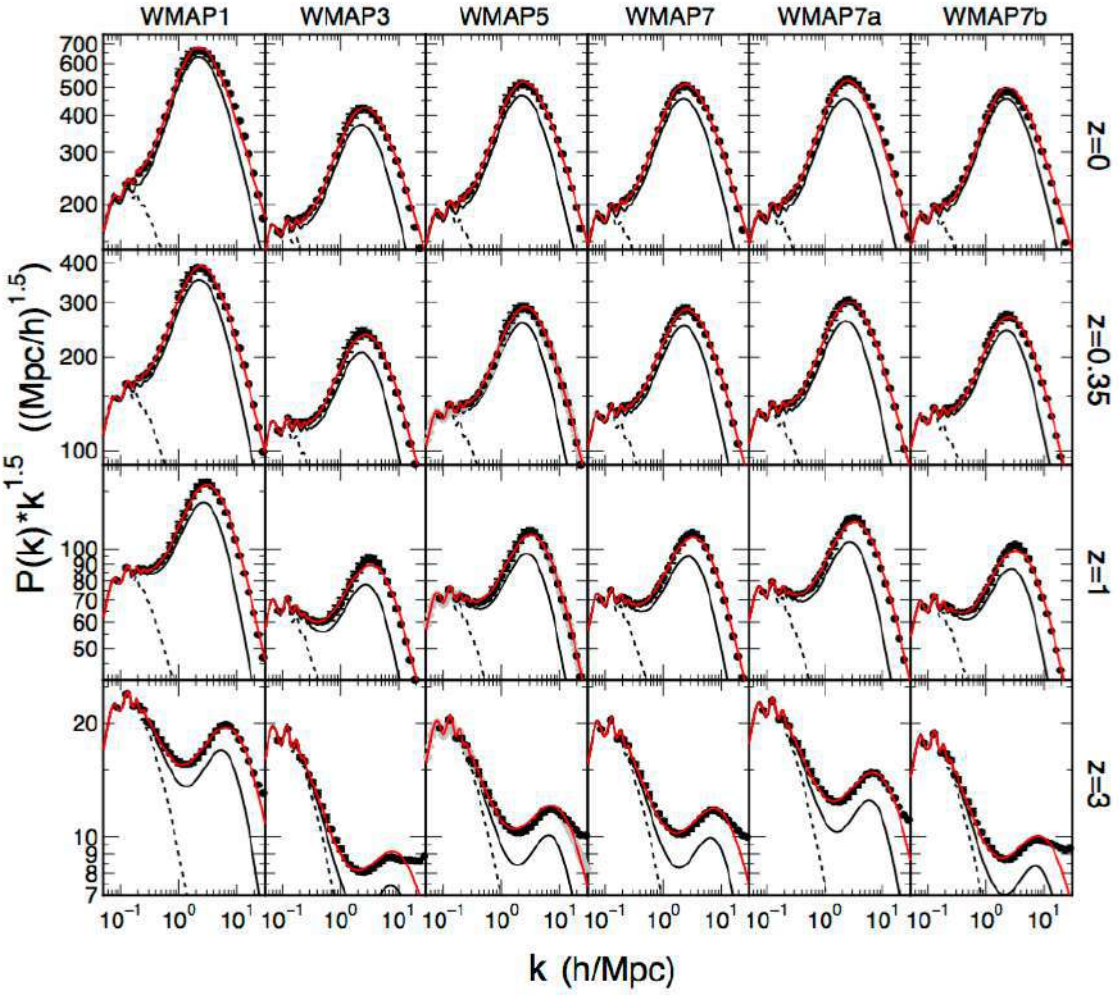

FIGURE 1.13: Original plot from Takahashi et al., 2012: matter power spectra for the WMAP cosmological models at $z = 0, 0.35, 1, 3$ measured from N-body simulations (black dots) compared to the revised version of the `halofit` prediction (red solid line), the standard `halofit` approximation (black solid line), and linear theory (black dashed line).

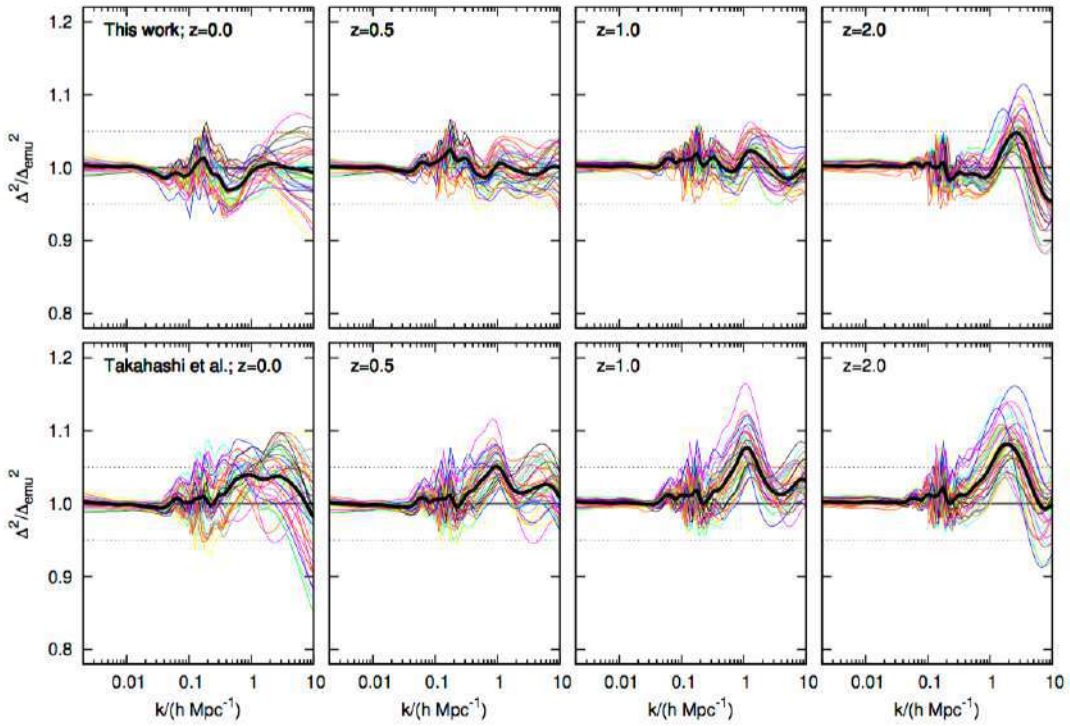

FIGURE 1.14: Original plot from Mead et al., 2015: `hmcode` and Takahashi revised version of `halofit` predictions compared to the Heitmann et al., 2014, emulator. Each line corresponds to one node of the emulator. The average fit is shown as the thick black line.

HaloModel and emulators

Another very recent recipe to predict the non-linear correction to the matter power spectrum was proposed in 2015 by Mead et al., 2015, and updated to take into account massive neutrinos and modified gravitational forces in 2016 [Mead et al., 2016], called `hmcode` (or `HaloModel`). The authors introduced physically motivated free parameters into the halo model formalism, instead of using empirical fitting functions, and fit these to high-resolution N-body simulations for a variety of ΛCDM and wCDM models. The main difference with respect to Takahashi or Bird corrections to `halofit` is that it can be adapted to account for the effects of baryonic feedback on the power spectrum, via fitting the halo model to hydrodynamical simulations with parameters that govern the halo internal structure.

Even another way to make predictions for the non-linear power spectrum is the so-called emulators (see e.g. Heitmann et al., 2014). The main idea is to run sets of high resolution simulations at key points in the cosmological parameter space (called nodes) in order to cover the space evenly. The emulator then

interpolates between the measured power spectra as a function of the cosmology, giving predictions for any set of parameters within the space.

In Fig. 1.14 we show the original plot from Mead et al., 2015, where both the `hmcode` and `halofit` (plus Takahashi and Bird corrections) predictions are compared to the emulators results for N-body simulations at different redshifts. For the cosmological models studied both `hmcode` and `halofit` perform similarly, although the `hmcode` performs slightly better.

1.2.4 The galaxy bias

The galaxy bias describes how the distribution of galaxies traces the underlying matter distribution. The study of the structures on large scales is a powerful cosmological probe, thanks to its dependence on the cosmological model. However, all our predictions are based on the dark matter field, and many of our observational techniques measure the light from galaxies, so even if the relation between the galaxy and matter distributions is often considered a nuisance parameter, it is a key ingredient to improve our cosmological knowledge.

The idea of galaxy bias first appeared when it was noticed that different galaxy populations have different clustering strengths [Davis and Geller, 1976; Dressler, 1980], showing that they cannot be linked to the matter distribution in the same way. A first physical mechanism was proposed by Kaiser, 1984; Bardeen et al., 1986, suggesting that galaxies would form in peaks of the matter distribution, being then more clustered than it. It was later shown that galaxy bias cannot be linear [Gaztañaga, 1992; Fry and Gaztañaga, 1993] and that it evolves with redshift, being larger at high-redshift as the first galaxies would have formed in the densest regions [Nusser and Davis, 1994; Fry, 1996; Tegmark and Peebles, 1998]. Moreover, we know that the galaxy bias depends on the scale, although this dependence is small on large scales [Mann, Peacock, and Heavens, 1998; Crocce et al., 2015]. In the following we present some models for the galaxy bias that are used in the literature.

Constant bias

This is the simplest model relating the mass and galaxy densities through a constant factor, b, at location $\boldsymbol{x}$ (see e.g. Peacock and Dodds, 1994)

$$\delta_{\rm g}(\boldsymbol{x}) = b\delta_{\rm m}(\boldsymbol{x})\,. \tag{1.108}$$

This linear, deterministic relation is know to be too simplistic, because it neglects the galaxy bias dependence on the scale and redshift, but it is usually considered in forecasts for its simplicity.

Linear redshift evolution

A simple linear dependence on the redshift has also been used in the literature (see e.g. Ferraro, Sherwin, and Spergel, 2015)

$$b(z) = b_0(1+z)\,. \tag{1.109}$$

It does not have any physical motivation either, but it encapsulates a dependence on the redshift.

Constant galaxy clustering

It is known from simulations [Kauffmann et al., 1999; Somerville and Primack, 1999] that the clustering of dark matter evolves and the clustering of galaxies is approximately constant (up to $z < 0.5$). Assuming a constant galaxy correlation function, since the matter correlation function grows with $D_1^2(z)$ in the linear regime, we can express the galaxy bias as

$$b(z) = \frac{b_0}{D_1(z)}\,. \tag{1.110}$$

Fry

Fry, 1996, proposed a simple model for the galaxy bias considering it after the point at which galaxies form, and assuming that they evolve then under gravity, without galaxy mergers. The expression for the bias is then given by

$$b(z) = 1 + \frac{b_0 - 1}{D_1(z)}\,. \tag{1.111}$$

Merging model

We know though that galaxies do merge. Matarrese et al., 1997, proposed a model, build on Fry's model, taking into account the merging of galaxies

$$b_{\rm eff}(z) = 0.41 + \frac{b_0 - 0.41}{D_1(z)^\alpha}\,, \tag{1.112}$$

where $b_{\rm eff}$ is an average of the bias over the mass range considered.

Tinker

Tinker et al., 2010, proposed a model for galaxy bias based on the halo model. Using a large set of N-body simulations, the authors calibrated the fitting function

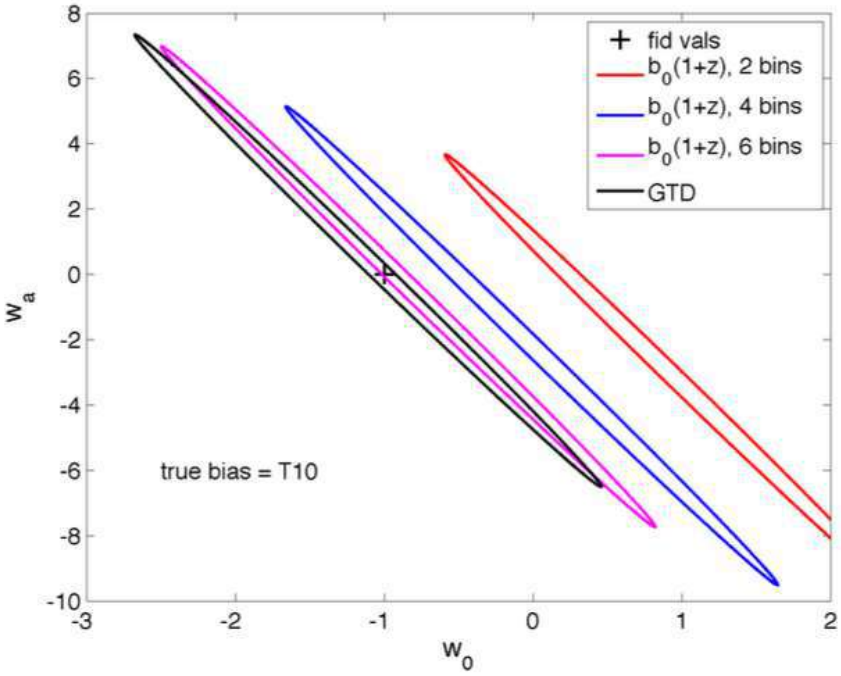

FIGURE 1.15: Original plot from Clerkin et al., 2015: shift in estimates of w_0, w_a introduced by modeling the galaxy bias with a binned linear evolution (one free parameter per bin), or the GTD model, while the true bias is given by the Tinker model. Fiducial values for w_0 and w_a are shown by the black cross.

$$b(\nu) = 1 - A\frac{\nu^\alpha}{\nu^\alpha + \delta_c^\alpha} + B\nu^\beta + C\nu^\gamma\,, \tag{1.113}$$

where

$$\nu(M,z) = \frac{\delta_c(z)}{D_1(z)\sigma(M)}\,, \tag{1.114}$$

with δ_c the critical density for collapse, $\sigma(M)$ the linear matter variance of the halo, and $A, \alpha, B, \beta, C, \gamma$ are constant obtained from the simulations. In order to recover the bias as a function of the redshift we use the redshift dependence of $\nu(M,z)$

$$\nu(z) = \frac{\nu_0}{D_1(z)}\,. \tag{1.115}$$

Croom

An empirically derived expression for the bias, often used for QSO, is given by [Croom et al., 2005]

$$b(z) = b_0[0.53 + 0.289(1+z)^2]\,. \tag{1.116}$$

Generalized time dependent bias

As a last model for the galaxy bias, we present here the generalized time dependent (GTD) model [Clerkin et al., 2015]. All of the previous presented models can be encapsulated into this generalized expression

$$b(z) = c + \frac{b_0 - c}{D_1(z)^\alpha}\,. \tag{1.117}$$

It is important to notice that the growth rate depends on the cosmological model, thus the galaxy bias will depend on the cosmological model too. When analyzing data, the bias should be determined together with the cosmological parameters, instead of using a fiducial cosmology to determine the bias.

The authors in Clerkin et al., 2015, compared their GTD model to a linear redshift evolution for the galaxy bias (see the original plot in Fig. 1.15). They showed that if the true galaxy bias model is the Tinker one, the fact of analyzing the data (forecast) with a GTD model (3 free parameters) for the galaxy bias does not give biased results, while if one assumes a linear evolution, 6 bins in redshift need to be added (6 free parameters) in order to get unbiased estimates.

Notice that the authors in Clerkin et al., 2015, use an extended Fisher matrix formalism [Cypriano et al., 2010; Shapiro et al., 2010] to predict the shift in cosmological parameters when an incorrect bias model is assumed.

1.3 Baryon acoustic oscillations and redshift-space distortions

1.3.1 BAO peak

Following the Big Bang model, the Universe was much smaller and hotter in the past. There was a time when the Universe was so hot that it was mainly composed of a plasma of photons and baryons, which were coupled via Thomson scattering. Due to gravity, baryons were exerting an inwards pressure, while the radiation pressure was exerting outwards. The corresponding competing forces generated oscillations in the plasma. If we consider a single, spherical density perturbation, it propagated outwards as an acoustic wave with speed c_s given by Eq. (1.150). Once the expansion rate of the Universe became larger than the interaction rate between baryons and photons, the photons were able to propagate freely (giving birth to the cosmic microwave background [see Sec. 1.5.2]) and the baryon waves froze. The characteristic radius of the spherical shell formed when

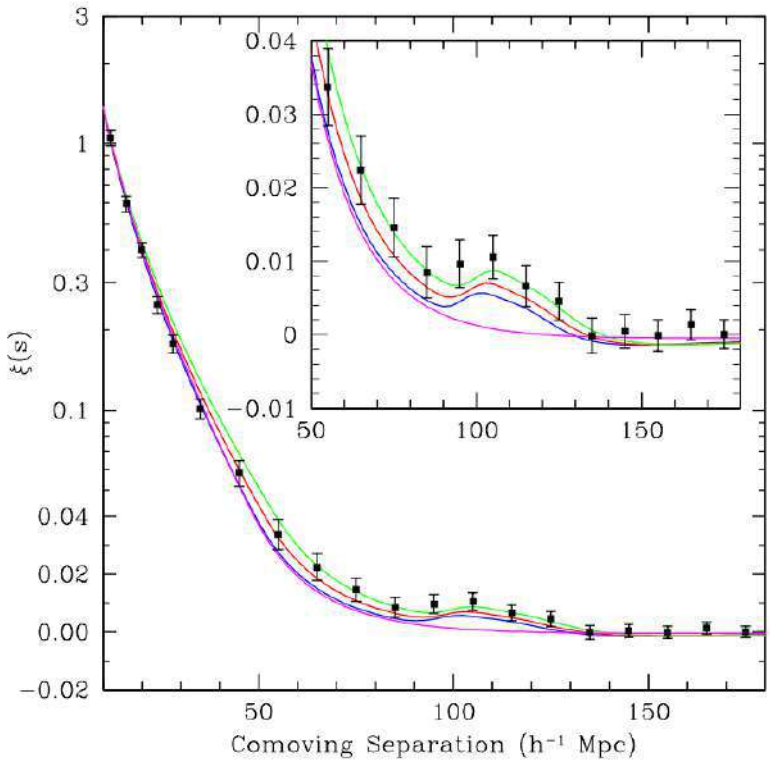

FIGURE 1.16: Original plot from Eisenstein et al., 2005: Redshift-space correlation function of the SDSS LRG sample compared to different cosmological models. The magenta line shows a pure CDM model without the acoustic peak. The BAO peak is statistically significant.

the waves froze is imprinted as an excess on the distribution of baryons. Since baryons and dark matter interact through gravity, the latter tends to cluster on this scale. Therefore, there is a larger probability that a galaxy forms in the higher density regions coming from the frozen baryon waves.

Let us consider a galaxy that formed at the center of an initial density perturbation. Then, because of the spherical shell from the baryon wave, there will be a bump in the 2PCF at the radius $r_{\rm d}$ of the spherical shell, showing that there is an excess of probability in finding two galaxies separated by this distance $r_{\rm d}$ (see Fig. 1.16). This quantity is known as the BAO standard ruler and is equal to the co-moving sound horizon at the redshift of the baryon drag epoch: $r_{\rm d} = r_{\rm s}(z_{\rm d})$ [see Eq. (1.149)], $z_{\rm d} \approx 1060$ [Eisenstein and White, 2004].

The main observable used in BAO measurements is the ratio of the BAO distance at low-redshift to this scale $r_{\rm d}$. The BAO are usually assumed to be isotropic. In this case the BAO distance scale is given by

$$D_V(z) \equiv \left(\chi^2(z)\frac{cz}{H(z)}\right)^{1/3} . \tag{1.118}$$

More recently it has also been possible to measure radial and transverse clustering separately, allowing for anisotropic BAO [Gaztañaga, Cabré, and Hui, 2009]. The BAO distance scales are then $\chi(z)$ and $c/H(z)$.

However, there is more cosmological information in the 2PCF (or higher order correlation functions) of galaxies than the BAO peak. In the following we present some other probes used in this work.

1.3.2 Redshift-space distortions

Galaxies follow the peculiar velocity field arising from the over-density field. But galaxy redshifts depend on the relative velocity of the galaxy with respect to us; therefore, they include both the Hubble recession and the peculiar velocities of the galaxies. This implies that if we only consider the Hubble recession when converting from redshift to distance, we recover a distorted field, with radial redshift-space distortions (RSD). Let us assume that the observed galaxies are sufficiently far away, so that their separations are small with respect to the distances between them (the so-called plane-parallel approximation). Assuming that the growth factor does not depend on the scale, and that the continuity equation holds, we can write (to linear order) the relation between the redshift-space galaxy power spectrum and the real-space matter power spectrum as [Kaiser, 1987; Hamilton, 1998]

$$P_{\rm g}^{\rm z-space}(k,\mu) = P_{\rm m}^{\rm r-space}(k)(b_\delta + b_\nu f\mu^2)^2\,, \tag{1.119}$$

where b_δ is the galaxy bias, b_ν is the bias between galaxy and matter velocity distributions (normally neglected), f the growth rate ($\mathrm{d}\ln D_1/\mathrm{d}\ln a$, with D_1 the growth factor), and μ the cosine of the angle to the line-of-sight.

Comparing to the definition of the galaxy bias in Sec. 1.2.4, we can observe that the RSDs introduce the μ^2-dependent term in the relation between the galaxy and the matter spectra. There are more accurate relations between $P_{\rm g}^{\rm z-space}$ and $P_{\rm m}^{\rm r-space}$ (see e.g. Percival et al., 2011, and references therein), but we limit here the description of this probe to the basics and provide the specific implementation used in this work in Sec. 6.1.2.

It is important to notice that the term introduced by the RSD signal in Eq. (1.119) depends on the cosmology. More precisely, on the growth rate, whose value depends on the theory of gravity used and it is well known that there are identical background evolutions with different growth rates [Piazza, Steigerwald, and Marinoni, 2014]. Therefore, using the RSD signal as cosmological probe offers an additional constraint on cosmological models.

Let us recall that the linear growth factor of matter perturbations, D_1, can be obtained by solving numerically Eq. (1.89). It is important to remind here

that this differential equation is only valid if we assume that dark energy cannot be perturbed and does not interact with dark matter, which is the case in this work. Once the growth factor has been obtained, we can compute the observable weighted growth rate, $f\sigma_8$, as

$$f\sigma_8(z) = f(z)\left(\sigma_8 \cdot \frac{D_1(z)}{D_1(0)}\right) . \tag{1.120}$$

Notice that if we want to use the derived value of σ_8 from Planck, for example, the normalization of the growth factor, $D_1(0)$, should be given by the Planck growth factor; i.e. the growth factor of the ΛCDM model with the corresponding Planck best-fit values for the parameters. The reason being that the inferred value of σ_8 from the CMB is obtained at $z \sim 1100$ and then extrapolated to $z = 0$.

As a last comment concerning RSDs, in this work we are also interested in using the angular clustering of galaxies as a cosmological probe (see Sec. 6.1.4). Since RSDs affect only inferred distances and not angles, we would not expect a large impact of the RSD signal on the angular clustering. However, RSDs still distort the projected angular clustering of galaxy samples that have been selected using redshift-dependent quantities. For instance, the edge of a window function that is straight in redshift space is distorted in real-space. There have been some works showing that we can use an estimator for the angular clustering independent of RSDs [Nock, Percival, and Ross, 2010], or that they can even be used as a probe selecting samples with photometric redshifts [Ross et al., 2011]. In this work, though, we will not consider the RSD signal when using the angular clustering of galaxies.

1.3.3 Fingers-of-God

The approach just described for RSDs is valid to linear order. However, on small scales non-linearities arise. The dominant non-linear contribution to RSDs is due to the virialized motion of galaxies within dark matter halos. These velocities can be large enough, such that if they are misinterpreted as being due to the Hubble flow, the clusters are stretched along the line-of-sight, causing what is known as Fingers-of-God (FoG). We provide an illustration of this effect in Fig. 1.17.

The impact of the FoG effect can be taken into account by reducing the power on small scales in Eq. (1.119) [Peacock and Dodds, 1996] introducing the exponential factor

$$F(k,\mu^2) = \frac{1}{1+(k\sigma_\nu\mu)^2} , \tag{1.121}$$

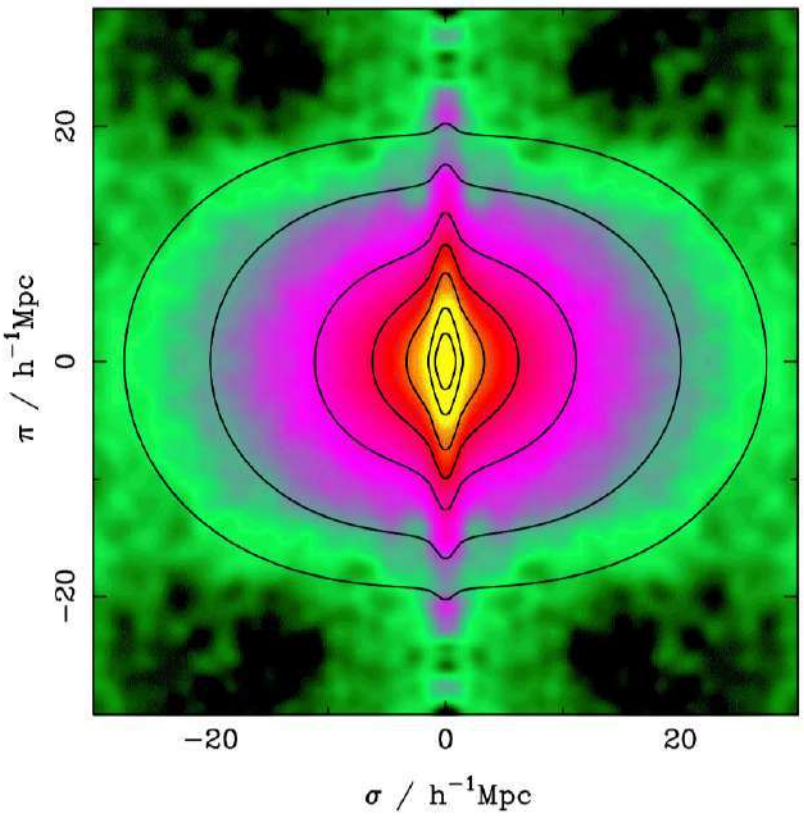

FIGURE 1.17: Original plot from Peacock et al., 2001: 2-dimensional redshift-space correlation function from 2dFGRS. The correlation function across (σ) and along (π) the line-of-sight is shown in the figure. Contours show lines of constant correlation function. The elongation along the line-of-sight caused by the FoG can be appreciated.

or the Gaussian factor

$$F(k,\mu^2) = \exp\left[-(k\sigma_\nu\mu)^2\right] . \tag{1.122}$$

Again, there are more complicated damping factors based on perturbation theory (see Percival et al., 2011, and references therein), but we provide here the basics on the FoG modeling and refer the reader to Sec. 6.1.2 for the specific implementation of the FoG effect in this work.

1.3.4 Alcock-Pacyznski effect

Redshift surveys measure the angular positions of galaxies on the sky and their redshifts. However, we need to translate these quantities to co-moving coordinates before measuring the galaxy clustering and compare with our predictions

from Eq. (1.119). If we assume a cosmological model to make this transformation which turns out not to be the real cosmology of our Universe, we can induce anisotropic distortions that are similar to the RSD signal [Ballinger, Peacock, and Heavens, 1996]. This is the so-called Alcock-Pacyznski effect (AP).

Let us assume that the angular and radial distances in our assumed cosmological model are different from the real ones by a factor $\alpha_\perp = R_A/\hat{R}_A$ and $\alpha_\parallel = R_r/\hat{R}_r$, respectively, where the hat denotes the true angular and radial distances. We can then rewrite Eq. (1.119) as [Ballinger, Peacock, and Heavens, 1996; Simpson and Peacock, 2010]

$$P_{\rm g}^{\rm z-space}(k,\mu) = \frac{1}{\alpha_\parallel \alpha_\perp^2} P_{\rm m}^{\rm r-space}\left(\frac{k}{\alpha_\perp}\sqrt{1+\mu^2(A^{-2}-1)}\right) \times \left[b_\delta + \frac{\mu^2 f}{A^2+\mu^2(1-A^2)}\right]^2 , \tag{1.123}$$

where $\mu = k_\parallel/k$, $A = \alpha_\parallel/\alpha_\perp$, and b_ν have been set to 1, for simplicity. As in the previous cases, we refer the reader to Sec. 6.1.2 for the details of the implementation used in this work.

1.4 Weak gravitational lensing

Measuring the formation of structures on large scales is a very useful cosmological probe, thanks to the effect of the cosmological model on the growth of these structures. However, many observational techniques observe galaxies (or other luminous tracers) while our predictions are with respect to the total matter distribution. As we have seen in the previous section, this implies that we need to know the bias between the galaxy and matter distributions, in order to extract cosmological information.

Another way to study the formation of structures is to look not only at the position of galaxies in the sky, but their shape. General Relativity tells us that photons follow geodesics of space-time. Therefore, light from distant objects will bend when passing close to foreground mass-energy concentrations, thus introducing distortions of distant galaxies due to foreground mass structures. This effect is called gravitational lensing, and we can immediately see that if we can measure distortions we might then be able to infer the mass distribution. This enables us to directly compare our predictions to observations, without the need of understanding the galaxy bias.

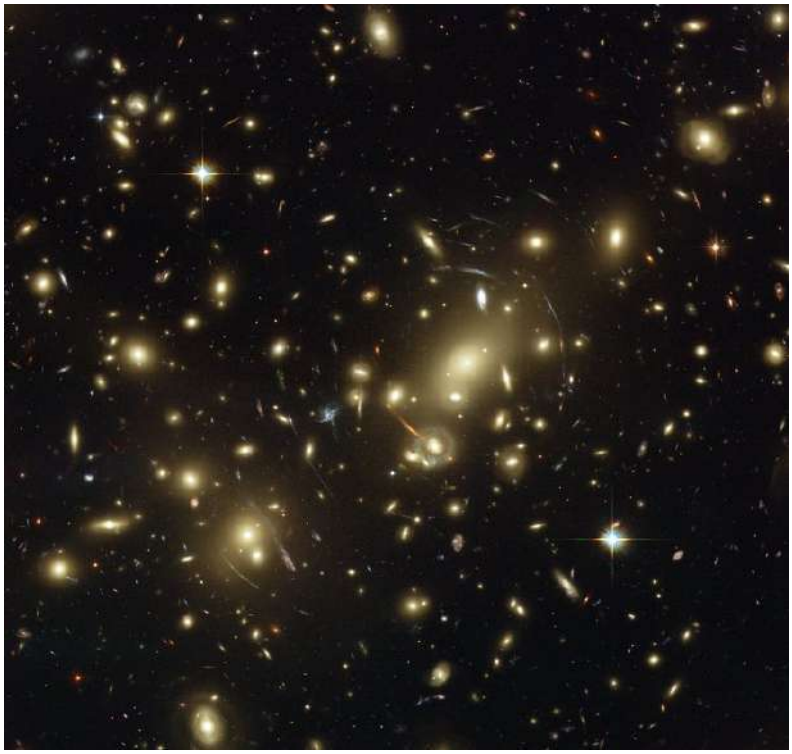

FIGURE 1.18: Full overview of the galaxy cluster Abell 2218 distorting the images of background galaxies. This image was taken by the Hubble Space Telescope. Credit: NASA, ESA, and Johan Richard (Caltech, USA).

1.4.1 Regimes of gravitational lensing

The distortion of distant images due to gravitational fields is a direct consequence of General Relativity, and it was the detection of this distortion that led to the acceptance of the theory. Dyson, Eddington, and Davidson, 1920, measured the deflection of starlight during a solar eclipse and the magnitude of it was in good agreement with the General Relativity prediction.

One of the most spectacular manifestations of gravitational field bending light paths is the so-called strong regime of gravitational lensing, or strong lensing. We enter this regime when there is a very massive foreground object bending the light paths of a background point source. Walsh, Carswell, and Weymann, 1979, observed a multiply imaged quasar. The light rays leaving the quasar in different directions are focused on us by a galaxy in between. The fraction of lensed quasars may depend on the background cosmology. Another example of strong lensing is shown in Fig. 1.18, where foreground galaxies within the Abell 2218 cluster distort the images of background galaxies. The distortion is so large than circular galaxies are observed as elliptical arcs.

There are other examples of gravitational lensing that can contain cosmological information. One of them is the so-called micro-lensing, where a lens

(foreground object) moves into the line connecting a source (background object) and us. When it does, the image of the source is magnified, so that we observe a variability in the distant source.

Another example is when we use background galaxies to infer the mass distribution of clusters. In general the images are not as spectacular as in Fig. 1.18, because the magnitude of distortions is smaller. However, we can compensate for this by the huge number of background galaxies. The idea is to statistically average small distortions, and we call it weak lensing.

Although the mass distribution for clusters of galaxies is important for cosmology, we focus here on weak lensing not by a single lens (like a cluster), but the large-scale structure in the Universe. We do not necessarily want to infer the distribution of matter in the sky, since measuring some statistics (like the power spectrum) can provide already very valuable cosmological information, as theory does not predict where the over-densities and under-densities of matter are in the sky, but their statistical properties. In the following we will thus focus on relating the distortion of galaxy images to the underlying mass power spectrum.

1.4.2 Geodesics and shear

Let us start the mathematical description of weak lensing with the illustration from Fig. 1.19 showing the sketch of a light ray of a source bended because of a lens plane between the observer and the source. Let us denote the position of the photon by $\boldsymbol{x}$, with the x_3 component equal to the radial distance χ and the transverse components equal to $\chi\vec{\theta}$. The observed intensity from the source is given by

$$I_{\rm obs}(\vec{\theta}) = I_{\rm true}(\vec{\theta}_s)\,, \tag{1.124}$$

where $\vec{\theta}$ and $\vec{\theta}_s$ are the apparent and actual position of the source, respectively.

Using the machinery from General Relativity, we can derive the geodesic equation for the transverse motion of photons

$$\frac{\mathrm{d}}{\mathrm{d}\chi}\left[\frac{1}{a^2}\frac{\mathrm{d}}{\mathrm{d}\chi}\left(\chi\theta^i\right)\right] = \frac{2}{a^2}\left[\Phi_{,i} + aH\frac{\mathrm{d}}{\mathrm{d}\chi}\left(\chi\theta^i\right)\right]\,. \tag{1.125}$$

Since the derivative on a^{-2} from the left hand side cancels the term proportional to aH on the right hand side, the equation for transverse displacement can be expressed by

$$\frac{\mathrm{d}^2}{\mathrm{d}\chi^2}\left(\chi\theta^i\right) = 2\Phi_{,i}\,. \tag{1.126}$$

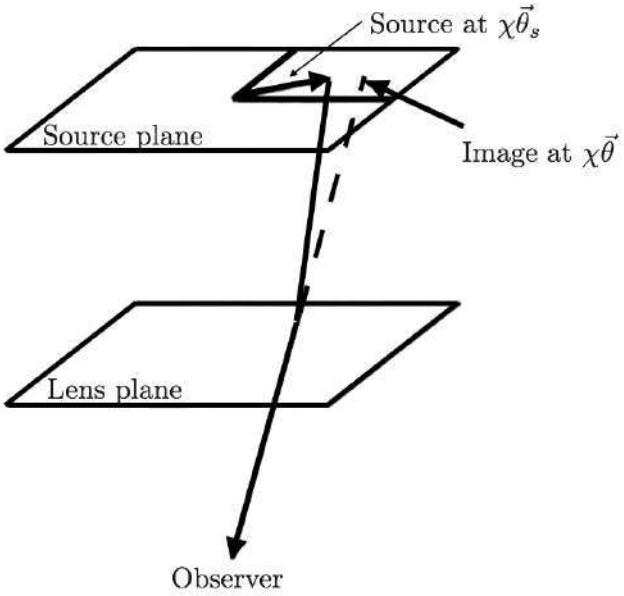

FIGURE 1.19: A light ray leaving a distance source is distorted when passing through an over-dense region (lens plane).

It tells us that a varying gravitational potential changes the angular direction, while a constant one keeps it constant. If we integrate twice this equation we can obtain the position of the image as a function of the source position

$$\theta_s^i = \theta^i + 2\int_0^\chi \mathrm{d}\chi' \Phi_{,i}(\boldsymbol{x}(\chi'))\left(1 - \frac{\chi'}{\chi}\right) . \tag{1.127}$$

To describe the change between the source and observed positions we usually define the two-dimensional symmetric matrix

$$A_{ij} \equiv \frac{\partial\theta_s^i}{\partial\theta^j} \equiv \begin{pmatrix} 1-\kappa-\gamma_1 & -\gamma_2 \\ -\gamma_2 & 1-\kappa+\gamma_1 \end{pmatrix} , \tag{1.128}$$

where κ is the so-called convergence, that describes the magnification of an image, and γ_1, γ_2 are the two components of the shear. Magnification is important for gravitational lensing analyses such as multiple images or micro-lensing, but the shear is the most important quantity for weak lensing studies [Dodelson, 2003].

Combining Eqs. (1.127) and (1.128) we can express the shear components as a function of the gravitational potential

$$A_{ij} - \delta_{ij} = \begin{pmatrix} -\kappa-\gamma_1 & -\gamma_2 \\ -\gamma_2 & -\kappa+\gamma_1 \end{pmatrix} = 2\int_0^\chi \mathrm{d}\chi' \Phi_{,ij}(\boldsymbol{x}(\chi'))\chi'\left(1 - \frac{\chi'}{\chi}\right) . \tag{1.129}$$

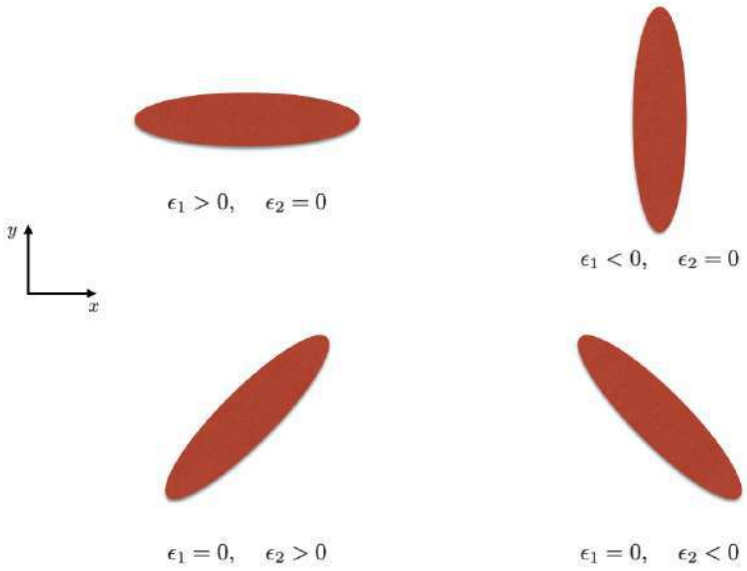

FIGURE 1.20: Shape of the images for different values of the ellipticities ϵ_1, ϵ_2.

1.4.3 Ellipticity as an estimator of shear

Gravitational lensing turns circular images into elliptical. In order to extract cosmological information from it we need to define how we can measure the ellipticity, and how we can relate it to the shear.

Let us first consider an image at the origin of the $\theta_x - \theta_y$ plane such that it has no dipole moment; i.e. the average over the intensity in each axis vanishes ($\langle\theta_x\rangle = \langle\theta_y\rangle = 0$). We can then define the quadrupole moments as

$$q_{ij} \equiv \int \mathrm{d}^2\theta I_{\mathrm{obs}}(\theta)\theta_i\theta_j \,. \tag{1.130}$$

A circular image has no quadrupole moments, so we can measure the ellipticity through

$$\epsilon_1 \equiv \frac{q_{xx} - q_{yy}}{q_{xx} + q_{yy}} \tag{1.131}$$

$$\epsilon_2 \equiv \frac{2q_{xy}}{q_{xx} + q_{yy}} \tag{1.132}$$

In Fig. 1.20 we can observe the different values for ϵ_1, ϵ_2 and the corresponding shapes for the images.

Let us now assume that the source is spherical. Using Eq. (1.124), ϵ_1 will then be given by

$$\epsilon_1 = \frac{\int \mathrm{d}^2\theta I_{\mathrm{true}}(\vec{\theta_s})[\theta_x\theta_x - \theta_y\theta_y]}{\int \mathrm{d}^2\theta I_{\mathrm{true}}(\vec{\theta_s})[\theta_x\theta_x + \theta_y\theta_y]} \,. \tag{1.133}$$

For small angles we can relate the angle of the source and the observed angle through $\theta_i = (A^{-1})_{ij}\theta_{s_j}$. This leads to

$$\begin{aligned}\epsilon_1 &= \frac{\sum_{ij}[(A^{-1})_{xi}(A^{-1})_{xj} - (A^{-1})_{yi}(A^{-1})_{yj}] \int \mathrm{d}^2\theta_s I_{\mathrm{true}}(\vec{\theta_s})\theta_{s_i}\theta_{s_j}}{\sum_{ij}[(A^{-1})_{xi}(A^{-1})_{xj} + (A^{-1})_{yi}(A^{-1})_{yj}] \int \mathrm{d}^2\theta_s I_{\mathrm{true}}(\vec{\theta_s})\theta_{s_i}\theta_{s_j}} = \\ &= \frac{(A^{-1}_{xx})^2 - (A^{-1}_{yy})^2}{(A^{-1}_{xx})^2 + (A^{-1}_{yy})^2 + 2(A^{-1}_{xy})^2} \,.\end{aligned} \tag{1.134}$$

Computing the inverse of A we can finally express the ellipticity in terms of the shear as

$$\epsilon_1 = \frac{4\gamma_1(1-\kappa)}{2(1-\kappa)^2 + 2\gamma_1^2 + 2\gamma_2^2} \approx 2\gamma_1 \,, \tag{1.135}$$

where the last equality holds if all the distortions are small. A similar equality is true for ϵ_2, showing that if we are able to measure ellipticities of background galaxies we can then get an estimate of the shear field, which contains information on the gravitational potential (Eq. 1.129).

It is important to mention here that not all the ellipticity of a galaxy has a lensing origin, since galaxies can have an intrinsic ellipticity due to tidal forces or other astrophysical effects. This is the main astrophysical systematic in weak lensing analyses and is called the intrinsic alignment (IA) of galaxies. In Sec. 6.1.3 we detail how we model this effect and how we include it in our analyses.

1.4.4 Weak lensing power spectrum

The simplest statistic that can be computed from the shear field is the power spectrum. Notice that if there are no inhomogeneities, the apparent angle θ is equal to the source angle θ_s, which implies that A is equal to the identity matrix. We can then define $\psi_{ij} \equiv A_{ij} - \delta_{ij}$ as the contribution of inhomogeneities to the distortion of the light path. This is the so-called distortion tensor. In general we do not consider a single galaxy, but rather a distribution of them. Let us denote it by $W(\chi)$ and assume it is normalized ($\int \mathrm{d}\chi W(\chi) = 1$). We can then express the distortion tensor as

$$\psi_{ij} = 2\int_0^{\chi_\infty} \mathrm{d}\chi W(\chi) \int_0^{\chi} \mathrm{d}\chi' \Phi_{,ij}(\boldsymbol{x}(\chi'))\chi' \left(1 - \frac{\chi'}{\chi}\right) = \\ = \int_0^{\infty} \mathrm{d}\chi \Phi_{,ij}(\boldsymbol{x}(\chi)) g(\chi)\,, \tag{1.136}$$

where

$$g(\chi) \equiv 2\chi \int_{\chi}^{\chi_\infty} \mathrm{d}\chi' \left(1 - \frac{\chi}{\chi'}\right) W(\chi')\,. \tag{1.137}$$

Applying Eq. (1.83), it leads to

$$\langle \tilde{\psi}_{ij}(\vec{\ell})\tilde{\psi}_{lm}(\vec{\ell}')\rangle = (2\pi)^2 \delta_D^2(\vec{\ell} - \vec{\ell}') C^{\psi}_{ijlm}(\vec{\ell})\,, \tag{1.138}$$

with the two-dimensional power spectrum

$$C^{\psi}_{ijlm}(\vec{\ell}) = \int_0^{\chi_\infty} \mathrm{d}\chi \frac{g^2(\chi)}{\chi^2} \frac{\ell_i \ell_j \ell_l \ell_m}{\chi^4} C_\Phi\left(\frac{\ell}{\chi}\right)\,. \tag{1.139}$$

Using Eq. (1.128), this power spectrum for the different components of the distortion tensor can be transformed into the power spectra for the convergence and the shear. Let us decompose the vector $\vec{\ell}$ into a radial, ℓ, and an angular, ϕ_ℓ, part. The convergence and shear power spectra can then be given by

$$C_\kappa(\ell) = \frac{\ell^4}{4} \int_0^{\chi_\infty} \mathrm{d}\chi \frac{g^2(\chi)}{\chi^6} C_\Phi\left(\frac{\ell}{\chi}\right) \tag{1.140}$$

$$C_{\gamma_1}(\ell, \phi_\ell) = \cos^2(2\phi_\ell) C_\kappa(\ell) \tag{1.141}$$

$$C_{\gamma_2}(\ell, \phi_\ell) = \sin^2(2\phi_\ell) C_\kappa(\ell)\,. \tag{1.142}$$

1.5 Background cosmological probes

In this last section of the chapter we present a brief description of the main background cosmological probes considered in this thesis. The cosmological probes sensitive to perturbations have already been presented in the previous sections.

1.5.1 Type Ia supernovae

There are two main observational groups of supernovae [Filippenko, 1997a]; those whose optical spectra show the presence of hydrogen (type II supernovae), and those without it (type I supernovae). We can further subdivide the latter by

their absorption lines. Type Ia supernovae are characterized by strong absorption attributed to Si II, while type Ib show He I lines, and type Ic have neither Si II nor He I lines. SNIa are believed to originate from the thermonuclear disruption of carbon-oxygen white dwarfs, while the other types come from core collapse in massive supergiant stars.

It is well known [Branch and Tammann, 1992; Branch, 1998] that SNIa may be used as distance indicators in cosmology for different reasons. In a first place, they are very luminous objects (some times brighter than the host galaxy itself) easy to spot at high redshifts. Also, they usually have a small dispersion among their peak absolute magnitudes, and our understanding of the progenitors and the explosion mechanism is on a reasonably firm physical basis. More in detail, although there is still some uncertainty on how these carbon-oxygen white dwarfs approach the Chandrasekhar mass limit, either by accretion from a non-degenerate companion or through tidal disruption followed by accretion of a degenerate companion, there has long been agreement on this model based on well-understood physics [Hoyle and Fowler, 1960; Arnett, 1969; Colgate and McKee, 1969]. The thermonuclear detonation of a carbon-oxygen white dwarf with the Chandrasekhar mass yields a mass of radioactive nickel whose energy matches that of a SNIa [Arnett, Branch, and Wheeler, 1985], and whose modeled nucleosynthesis coincides with its spectral elements [Nomoto, Thielemann, and Yokoi, 1984]. It has also been observed that the progenitor of a prototypical SNIa did not exceed a radius of 2% the solar one, fully consistent with the expected white dwarf [Nugent et al., 2011; Li et al., 2011; Bloom et al., 2012].

Until the mid-1990s, the standard approach when using SNIa as cosmological distance indicators was to assume that they are perfect standard candles, and to compare the observed peak brightness with that of SNIa in galaxies whose distance had been independently determined (using Cepheid stars for example). However, over the past two decades it has become clear that SNIa are not a perfectly homogeneous subclass [Filippenko, 1997b; Filippenko, 1997a]. Phillips, 1993, after several suggestions [Pskovskii, 1977; Pskovskii, 1984; Branch, 1981] found convincing evidence for a correlation between the shape of the light-curve and the luminosity at maximum brightness, so that brighter SNIa last longer. This correlation was later refined by Hamuy et al., 1995; Hamuy et al., 1996b; Tripp, 1997 [see also Perlmutter et al., 1997; Goldhaber et al., 2001; Riess, Press, and Kirshner, 1995]. In Figure 1.21 we can see how correcting for the stretch of different light curves provides standardized candles. By using light-curve shapes measured through several filters, Riess, Press, and Kirshner, 1996, were able to decrease the dispersion of SNIa even more. The standardization of SNIa correcting for the shape of the light-curve and the color at maximum

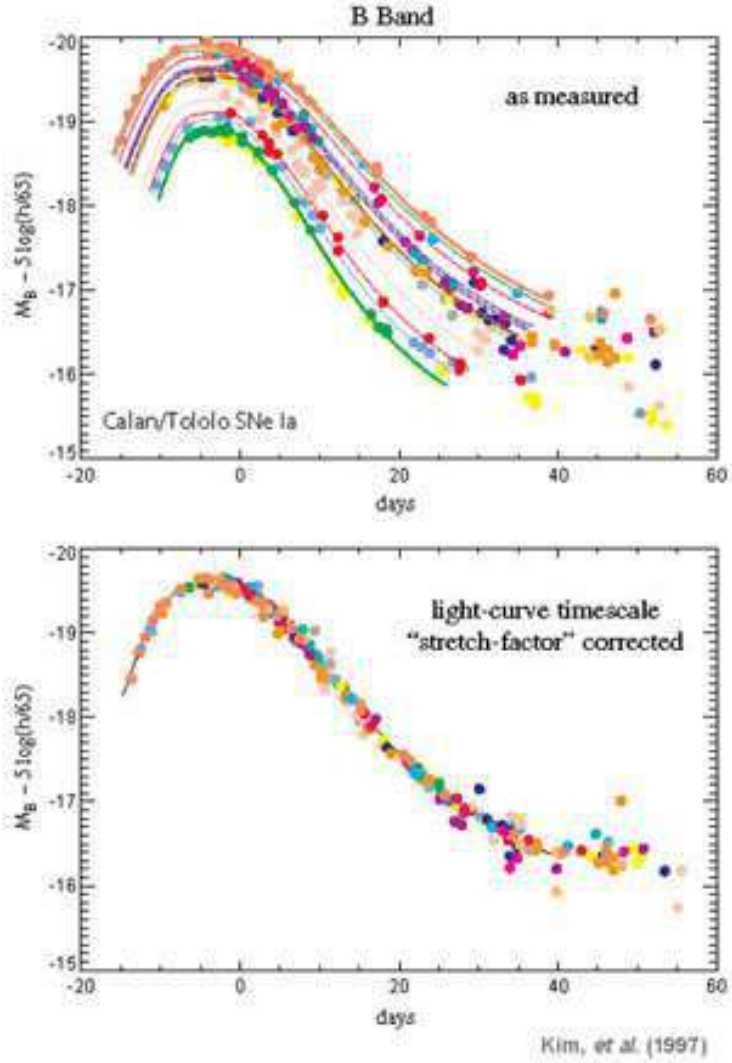

FIGURE 1.21: Seventeen light-curves of SNIa from the Calan-Tololo survey [Hamuy et al., 1996a] before and after correcting for the stretch of the light-curves. Figure from A. Kim [LBNL Report LBNL-56164 (2004)]

brightness is well described in Tripp, 1998.

Recent analyses of large samples of SNIa [Kelly et al., 2010; Lampeitl et al., 2010; Sullivan et al., 2010; Sullivan et al., 2011; Johansson et al., 2013] have shown a correlation between the SNIa luminosities and the stellar mass of their host galaxies, even after the shape and color corrections. The corrected luminosities are higher for SNIa in massive host galaxies. However, the mechanism generating this dependence is not yet fully understood. The common procedure to standardize the SNIa with respect to their dependence to the host stellar mass consists on adopting a step function of the latter; i.e. an offset on the absolute magnitude is added for the most massive galaxies, as it can be seen in Fig. 1.22.

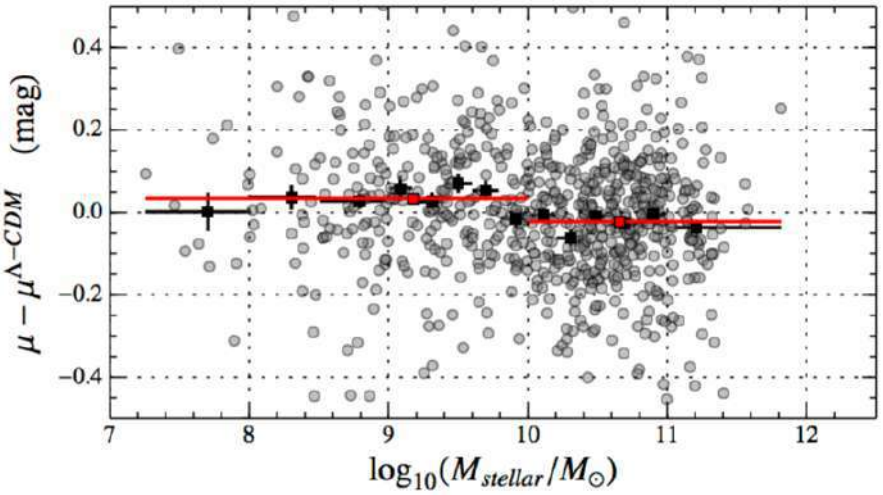

FIGURE 1.22: Original plot from Betoule et al., 2014: Residuals from the ΛCDM fit of the joint light-curve analysis Hubble diagram as a function of the host galaxy mass. Binned residuals are shown as black squares, while the red line shows the mass step correction, which has not been included in this fit.

Concerning cosmological analyses, SNIa are useful to measure cosmological distances and break degeneracies among the different parameters to achieve precise cosmological constraints. In the following we provide the standard treatment of SNIa data used in this work.

The main observable used in SNIa measurements is the so-called distance modulus,

$$\mu(z) = 5\log_{10}\left(\frac{H_0}{c}d_{\rm L}(z)\right), \tag{1.143}$$

where $d_{\rm L}(z) = (1+z)\chi(z)$ is the luminosity distance. Notice that we have defined the distance modulus in such a way that it is independent of the H_0 parameter, which is degenerate with the SNIa absolute magnitude.

In this work we use the joint light-curve analysis (JLA) for SNIa from Betoule et al., 2014. The authors assume that supernovae with identical color, shape and galactic environment have on average the same intrinsic luminosity for all redshifts. If we denote the time stretching of the light-curve by X_1 and the color of the SNIa at maximum brightness by C, we can express the observed distance modulus as

$$\mu_{\rm obs} = m_{\rm B}^{*} - (M_{\rm B} - \alpha \times X_1 + \beta \times C), \tag{1.144}$$

where $m_{\rm B}^{*}$ corresponds to the observed peak magnitude in the rest-frame B band and α and β are nuisance parameters in the distance estimate. The $M_{\rm B}$

nuisance parameter is given by the step function,

$$M_{\rm B} = \begin{cases} M_{\rm B}^1\,, & \text{if } M_{\rm stellar} < 10^{10} M_\odot\,, \\ M_{\rm B}^1 + \Delta_{\rm M}\,, & \text{otherwise}\,, \end{cases} \tag{1.145}$$

where $M_{\rm B}^1$ and $\Delta_{\rm M}$ are nuisance parameters, in order to take into account the dependence on host galaxy properties.

Concerning the errors and correlations on the measurements, we use the covariance matrix [1] provided by Betoule et al., 2014, where the authors consider the contribution from error propagation of light-curve fit uncertainties (statistical contribution) and the contribution of seven sources of systematic uncertainty: the calibration, the light-curve model, the bias correction, the mass step, the dust extinction, the peculiar velocities and the contamination of non-type Ia supernovae.

1.5.2 Cosmic microwave background

Coming back to the early Universe as described in Sec. 1.3, it was essentially composed of a baryon-photon plasma tightly coupled via Thomson scattering. The Universe was effectively opaque, since the mean free path of photons was very short. In these conditions, photons were in equilibrium, providing a blackbody spectral distribution. Since the Universe at that time was already expanding, there was a moment when the interaction rate between photons and baryons became smaller than the expansion rate; thus making the Universe transparent. The photons from the plasma were then free to propagate through the Universe, generating the radiation that we see now in all directions of the sky, and that we call the cosmic microwave background. It was first detected by Penzias and Wilson, 1965, when the authors detected an excess of temperature of about 3.5 K after accounting for possible noise in their observations. But it was not until the COBE satellite that we confirmed the nice agreement between the CMB and a blackbody spectrum [Fixsen et al., 1996].

Even if the agreement with a blackbody spectrum is extremely high, the CMB is not isotropic; i.e. if we look at different points in the sky there are anisotropies (after correcting for the motion of our galaxy with respect to the CMB rest frame) giving slightly different temperatures for the photons in those regions. Although these anisotropies are very small (at the order of 1 part in 10^5), they are caused by the density fluctuations in the early Universe, which eventually generated the large-scale structure we see today. Therefore, there is a lot of cosmological information imprinted in them and, more importantly, looking at these anisotropies we can extract cosmological information from the

[1] http://supernovae.in2p3.fr/sdss_snls_jla/

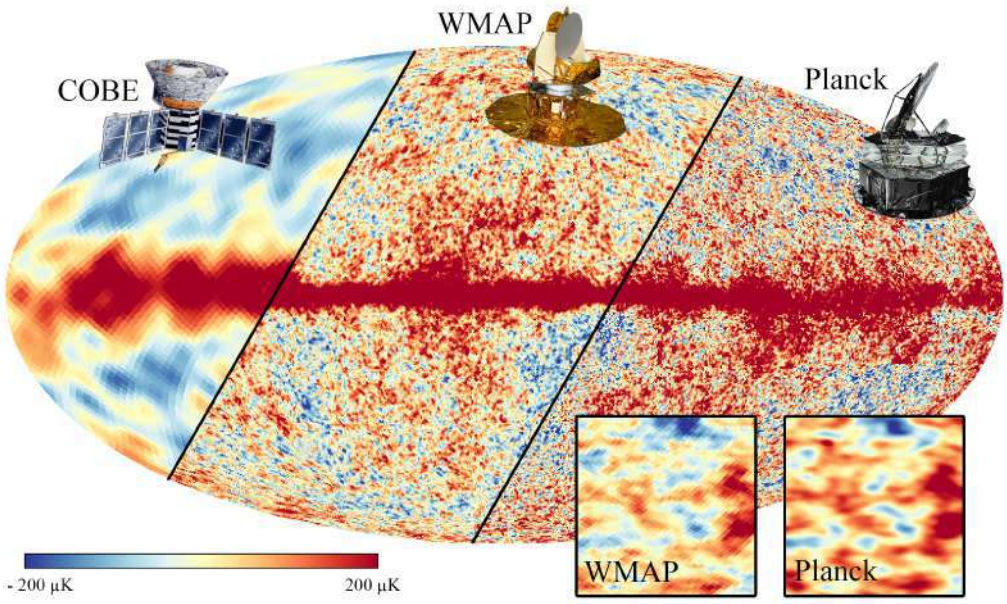

FIGURE 1.23: All-sky map of the temperature anisotropies of the CMB obtained with the COBE, WMAP, and Planck satellites. The image shows the improvement on the angular resolution over the years and technology [Credit: J. Gudmundsson].

early Universe, which is largely complementary to the information we can extract from low-redshift probes. Since the first all-sky map of the anisotropies by COBE (see Fig. 1.23), there has been a lot of effort in probing and understanding them with ground-based and satellite missions, like the South Pole Telescope [2], or the WMAP [3] or Planck [4] satellites.

The standard approach used when analyzing the CMB anisotropies consists in decomposing them in spherical harmonics, $Y_{\ell m}(\theta, \phi)$,

$$\frac{\Delta T(\theta, \phi)}{T_0} = \sum_{\ell=0}^{\infty} \sum_{m=-\ell}^{\ell} a_{\ell m} Y_{\ell m}(\theta, \phi) \,. \tag{1.146}$$

Using the $a_{\ell m}$ coefficients we can write the CMB angular power spectrum as

$$C_\ell = \frac{1}{2\ell + 1} \sum_{m=-\ell}^{\ell} |a_{\ell m}|^2 \,. \tag{1.147}$$

In Fig. 1.24 we show the great agreement between the measurements of the CMB angular power spectrum and its prediction. Notice also the wiggles in the

[2] https://pole.uchicago.edu/spt/
[3] https://map.gsfc.nasa.gov
[4] http://sci.esa.int/planck/

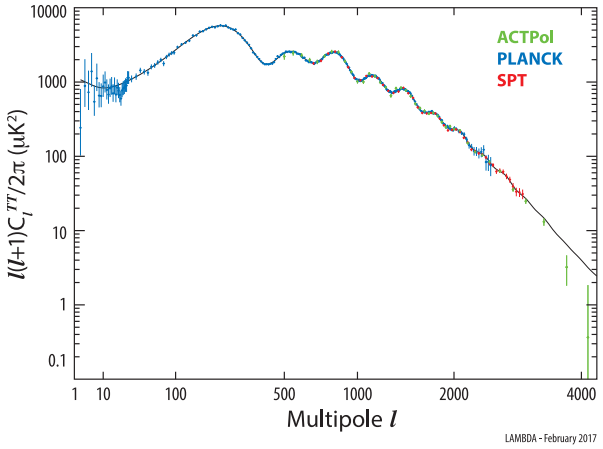

FIGURE 1.24: Comparison between measurements of the CMB angular power spectrum for the temperature anisotropies from Planck and ground-based telescopes, and the theoretical prediction for the concordance model of cosmology [Credit: LAMBDA/NASA].

spectrum, which are due to the baryon acoustic oscillations (see Sec. 1.3) and contain very important cosmological information.

Nowadays we have such precise measurements that we can not only use the temperature anisotropies, but also the anisotropies of the E-mode (and B-mode) polarization of the photons from the CMB. Also, we start to have enough precision to consider the lensing of the CMB photons by the matter field between us and the CMB when we constrain a cosmological model. However, this probe is not used in this work and we just refer here the reader to the extensive review from Lewis and Challinor, 2006.

When using CMB data we should use all the measurements of the different spectra (temperature and polarizations). However, it has been shown [Wang and Mukherjee, 2007] that a large fraction of the information contained in the CMB fluctuations of the angular power spectra can be captured into a few numbers, the so-called reduced parameters: the scaled distance to recombination R, the angular scale of the sound horizon at recombination ℓ_a, the reduced density parameter of baryons ω_b, and the spectral index n_s. For a flat universe their expressions are given by

$$\begin{aligned} R &\equiv \sqrt{\Omega_{\rm m} H_0^2} \int_0^{z_*} \frac{{\rm d}z}{H(z)} \,, \\ \ell_a &\equiv \frac{\pi c}{r_{\rm s}(z_*)} \int_0^{z_*} \frac{{\rm d}z}{H(z)} \,, \\ \omega_{\rm b} &\equiv \Omega_{\rm b} h^2 \,, \end{aligned} \tag{1.148}$$

where z_* stands for the redshift of the last scattering epoch, and the co-moving sound horizon at this redshift is given by

$$r_{\rm s}(z_*) = \int_{z_*}^{\infty} \frac{c_s(z)\,{\rm d}z}{H(z)}\,, \tag{1.149}$$

where

$$c_s(z) = \frac{c}{\sqrt{3(1+R_{\rm b}(z))}}, \qquad R_{\rm b}(z) = \frac{3\rho_{\rm b}}{4\rho_\gamma}\,, \tag{1.150}$$

with $\rho_{\rm b}$ being the baryon density and ρ_γ the photon density. Their ratio can be approximated [Eisenstein and Hu, 1998] by $R_{\rm b}(z) = 3.15\times10^4\Omega_{\rm b}h^2\Theta_{2.7}^{-4}(1+z)^{-1}$, with $\Theta_{2.7} = T_{\rm CMB}/2.7\,{\rm K}$.

In some sections of this work we will use the reduced parameters instead of the full measurements from Planck, for simplicity. However, in these cases we will not use n_s since it has no effect in our analyses using background cosmological probes. It is also important to notice that the values of the reduced parameters obtained from Planck data assume the concordance cosmological model; therefore, we should only use them for models that are close to ΛCDM.

1.5.3 The Hubble parameter

If we are interested in the background expansion of the Universe, one of the more direct observables is the Hubble parameter as a function of the redshift.

There are two main methods to measure the evolution of $H(z)$: the so-called differential age method [Jimenez and Loeb, 2002] and a direct measure of $H(z)$ using radial BAO information [Gaztañaga, Cabré, and Hui, 2009]. The former consists on spectroscopically measuring the age difference, Δt, between two passively-evolving galaxies that formed at the same time but are separated in redshift space by a small amount Δz. From the ratio of these quantities we can estimate the derivative ${\rm d}z/{\rm d}t$ and directly measure the Hubble parameter,

$$H(z) = -\frac{1}{(1+z)}\frac{{\rm d}z}{{\rm d}t}\,. \tag{1.151}$$

Notice that this model provides measurements on the expansion rate of the Universe without the need of specifying any cosmological model.

The direct measure of $H(z)$ from BAO is entirely based on the BAO feature around 110 Mpc/h. Using the peak location as a standard ruler, we can measure the radial distance (see Sec. 1.3). Notice that in this case we need to assume a fiducial cosmology to convert redshifts to distances.

A detailed discussion on the systematic uncertainties of both these methods can be found in Zhang and Ma, 2010. In this work, when we include the

measurements on $H(z)$, we use the compilation of independent measurements from Simon, Verde, and Jimenez, 2005; Stern et al., 2010; Moresco et al., 2012; Busca et al., 2013; Zhang et al., 2014; Blake et al., 2012; Chuang and Wang, 2013, provided in Farooq and Ratra, 2013.

1.5.4 The Hubble constant

The Hubble constant, H_0, is one of the most important parameters in modern cosmology, since it is used to construct time and distance cosmological scales. It was first measured by Hubble to be roughly 500 km/s/Mpc [Hubble, 1929]. Current data supports a value for H_0 close to 70 km/s/Mpc. However, nearly 100 years later there is still no consensus on its value. The main approach used nowadays consists on observing Cepheids in the host galaxies of recent, nearby SNIa, and link the geometric distance measurements to other SNIa at higher redshift. However, these local measurements already show some tension on the results depending on the calibration of SNIa distances [Riess et al., 2018a; Tammann and Reindl, 2013]. Moreover, there is also some tension between the direct measurement of H_0 and the value inferred from the CMB assuming a ΛCDM model [Planck Collaboration, 2016b]. There has been many attempts in the literature to solve this discrepancy both from an observational and a theoretical perspective [see Bernal, Verde, and Riess, 2016; Gómez-Valent and Amendola, 2018, and references therein for a detailed discussion on the trouble with H_0], but a consensus on the value of H_0 or the theoretical model that could explain the current differences has not yet been achieved.

Chapter 2

Cosmological parameter analysis

After the general overview of modern cosmology provided in the previous chapter, we focus here in the statistical methods used in cosmology. In particular, we focus on methods used to confront theoretical models to observational data. This chapter aims at giving the statistical basics in probability and information (Sec. 2.1), which are needed to discuss the different methods used to estimate the values of cosmological parameters, as well as their uncertainties in Sec. 2.2. We also give a brief review of how we can quantify the ability of a model to fit the data in Sec. 2.3. In Sec. 2.4 we present some methods to compare different theoretical models, beyond the mere ability to fit the data. We finish the chapter by discussing how we can predict the constraints on theoretical models with future data in Sec. 2.5.

When we start talking about statistics it is nearly mandatory to talk about philosophy. Statisticians do not agree on basic "philosophical" principles. There are mainly two different schools: Bayesian and frequentist statisticians. The name of the first group comes from the extended use of the Bayes theorem, while the second group corresponds to the classical statistics approach. The Bayesian approach is closer to everyday reasoning, where probability is interpreted as a degree of belief that something will happen, or, closer to cosmology, that a parameter will have a given value. The frequentist approach is closer to the scientific reasoning, where probability stands for the relative frequency of something happening. It is more objective, since it does not depend on the observer, but it can only be used for repeatable phenomena.

Concerning the estimation of parameters, numerical results tend to be the same for both approaches in the asymptotic regime, so when there are a lot of data, and when statistical uncertainties are small with respect to the physical boundaries. With respect to the ability of a model to fit the data (so no alternative method is proposed), it is essentially impossible to obtain any results in the Bayesian approach, so we use the frequentist approach in this case. On the contrary, when we compare two different models that are able to fit the data, because of its fundamentally subjective nature, we usually follow a Bayesian approach.

2.1 Basic concepts in probability and information

2.1.1 Definitions of probability

Mathematical probability

Let us denote Ω as the set of all possible elementary events X_i. Let us also assume that if the event X_i occurs none of the others do. We can then define the probability of the occurrence of X_i, $P(X_i)$, as any quantity obeying the Kolmogorov axioms

$$\begin{aligned} &P(X_i) \geq 0 \, \forall i \,, \\ &P(X_i \text{ or } X_j) = P(X_i) + P(X_j) \,, \\ &\sum_{\Omega} P(X_i) = 1 \,. \end{aligned} \tag{2.1}$$

Frequentist probability

Let us now consider an experiment for which we observe a series of events. Let us assume that some of these events are of a type X. Let us further assume that the total number of events is N, and that the number of events of type X is n. We can then define the frequentist probability that any event will be of type X as the empirical limit of the frequency ratio

$$P(X) = \lim_{N \to \infty} \frac{n}{N} \,. \tag{2.2}$$

There are some properties arising from this definition that are worth mentioning. In a first place, it may seem that an infinite number of experiments is required in order to know the probability, because of the limit in its definition. But as long as it is always possible to perform one more experiment, any accuracy can be achieved, and this is enough to define the concept. In a bit more detail, the bias on our estimation of the probability, as well as its uncertainty, converge to 0 as we increase the number of experiments. Another property that should be noticed is that we can only talk about frequentist probability when the experiment can be repeated (with the same conditions). This implies an important restriction. The conditions are never exactly the same when we repeat an experiment, but we should try to get the same relevant conditions, and correct for the unavoidable changes, in order to compute the frequentist probability.

Bayesian probability

The Bayesian probability is based on what we call degree of belief. The idea is to determine how strongly a person believes that X will occur by determining how much he would be willing to bet on it. Let us assume that he wins a fixed amount if X occurs and nothing if it does not. We can then define the Bayesian probability as the largest amount he would be willing to bet, divided by the amount he stands to win. Notice that this definition fulfills the Kolmogorov axions from Eq. (2.1) and is therefore a probability in the mathematical sense.

It is important to notice that this definition is as much a property of the observer as it is of the system being observed, so its value depends on the knowledge of the observer. There are other ways to define the Bayesian probability, but this one is one of the most amenable to measurement.

2.1.2 Bayes theorem

Let us now consider two different events A and B. We can define the conditional probability (in both schools), $P(A|B)$, as the probability that A occurs knowing that B has already occurred. It is given by

$$P(A \text{ and } B) = P(A|B)P(B) = P(B|A)P(A)\,. \tag{2.3}$$

We can now present the Bayes theorem [Bayes, 1958] which links $P(A|B)$ to $P(B|A)$ through

$$P(A|B) = \frac{P(B|A)\cdot P(A)}{P(B)}\,. \tag{2.4}$$

When A or B are no longer events, but hypotheses, the meaning of the Bayes theorem is less trivial and here is where the two schools start to differ. In the Bayesian approach, $P(\theta)$ is the degree of belief in hypothesis θ. In the frequentist approach, though, θ is not a random variable (see next subsection), so frequentist probabilities cannot be assigned and the Bayes theorem is not applicable. Therefore, when the Bayes theorem involves hypotheses it can only be applied in a Bayesian framework.

Let us denote by $\boldsymbol{X}^0$ the data observed. The Bayes theorem is then given by

$$P(\theta|\boldsymbol{X}^0) = \frac{P(\boldsymbol{X}^0|\theta)\cdot P(\theta)}{P(\boldsymbol{X}^0)}\,, \tag{2.5}$$

where $P(\theta|\boldsymbol{X}^0)$ is called the posterior probability for hypothesis θ, given that data $\boldsymbol{X}^0$ have been observed. $P(\boldsymbol{X}^0|\theta)$ is the probability of obtaining the observed measurements $\boldsymbol{X}^0$, given the hypothesis θ. $P(\theta)$ is the prior probability,

which represents the degree of belief in different hypotheses before the experiment was performed, and $P(\boldsymbol{X}^0)$ can be considered a normalization constant, since the sum of $P(\theta|\boldsymbol{X}^0)$ over all values of i must be equal to 1 (if the different hypotheses form a complete and exclusive set).

2.1.3 Random variables

A random event is defined as an event which has more than one possible outcome. We can associate a probability with each outcome. With a random event A we can associate a random variable X which can take different numerical values X_i corresponding to the different possible outcomes. The corresponding probabilities $P(X_i)$ form a probability distribution.

We can now generalize probabilities of events to probability distributions of random variables, and we can generalize from discrete to continuous random variables. Let us imagine an experiment with 2 discrete random variables X and Y. Let us denote by ΔX and ΔY the finite size of these variables. We can then define the joint probability density function of X and Y as

$$f(X,Y) = \lim_{\Delta X,\Delta Y\to 0} \frac{P(X_i \in [X, X+\Delta X] \text{ and } Y_i \in [Y, Y+\Delta Y])}{\Delta X \Delta Y} \,. \tag{2.6}$$

It is normalized such that the integral over all possible values for X and Y is equal to 1

$$\int\int_\Omega f(X,Y)\,\mathrm{d}X\,\mathrm{d}Y = 1\,. \tag{2.7}$$

We can also define the cumulative distribution, $F(X,Y)$, as the integrated probability density function

$$F(X,Y) = \int_{X_{\min}}^{X}\int_{Y_{\min}}^{Y} f(X',Y')\,\mathrm{d}Y'\,\mathrm{d}X'\,. \tag{2.8}$$

A section through a joint probability density function is called a conditional distribution. The normalized section through the probability density function $f(X,Y)$ at $X = X_0$ gives the conditional distribution of Y, given that $X = X_0$ (see Eq. 2.3)

$$f(Y|X_0) = \frac{f(X_0,Y)}{\int f(X_0,Y)\,\mathrm{d}Y} = \frac{f(X_0,Y)}{g(X_0)}\,, \tag{2.9}$$

where $g(X_0)$ is the marginal distribution of X at X_0

$$g(X = X_0) = \int_{Y_{\min}}^{Y_{\max}} f(X = X_0, Y)\,\mathrm{d}Y\,. \tag{2.10}$$

Bayes theorem revisited

Now that we have defined the continuous random variables and their probability density functions we can revisit the Bayes theorem. Let us consider the joint probability density function $f(X, Y)$ for two random variables X and Y with marginal distributions $g(X)$ and $h(Y)$, and conditional distributions $p(X|Y)$ and $q(Y|X)$. The Bayes theorem can then be written as

$$q(Y|X) = \frac{p(X|Y)h(Y)}{g(X)}\,. \tag{2.11}$$

Let us now focus on the Bayesian use of the Bayes theorem for continuous random variables. Let us denote a set of continuous random variables by $\boldsymbol{X}$, and $f_i(X_i|\theta)$ as the probability density function of the random variable number i, where θ represents the (continuous) value of a given parameter. The joint probability density function of the N random variables $\boldsymbol{X}$ is given by

$$p(\boldsymbol{X}|\theta) = \prod_{i=1}^{N} f_i(X_i|\theta)\,, \tag{2.12}$$

where we assume that the same parameter value θ holds for all variables X_i.

If we denote the probability density function of θ by $p(\theta)$, the Bayes theorem takes the form

$$p(\theta|\boldsymbol{X}) = \frac{p(\boldsymbol{X}|\theta)p(\theta)}{\int p(\boldsymbol{X}|\theta)p(\theta)\,\mathrm{d}\theta}\,. \tag{2.13}$$

When we substitute the random variable $\boldsymbol{X}$ by the actual measurements $\boldsymbol{X}^0$ we obtain the form of the Bayes theorem used in Bayesian parameter estimation. The probability density function $p(\theta|\boldsymbol{X}^0)$ is the posterior probability density for θ, while $p(\boldsymbol{X}^0|\theta)$ is the likelihood function (see next section). $p(\theta)$ is the so-called prior, and the denominator is just a normalization factor that can be determined from the fact that the integral of $p(\theta|\boldsymbol{X})$ over all θ must be equal to 1.

2.1.4 The likelihood function

Let us consider a set of N random variables $\boldsymbol{X}$ with probability density function $f(\boldsymbol{X}|\boldsymbol{\theta})$, where $\boldsymbol{\theta}$ is a set of parameters of our model. Let us denote the set of all allowed values of $\boldsymbol{X}$ by $\Omega_{\boldsymbol{\theta}}$, where the subscript shows that Ω may depend on the value of $\boldsymbol{\theta}$. Let us consider a set of N independent observations of $\boldsymbol{X}$: $X_1, \ldots, X_N$. The joint probability density function of $\boldsymbol{X}$ is then given by [according to Eq. (2.12)]

$$P(\boldsymbol{X}|\boldsymbol{\theta}) = P(X_1, \ldots, X_N|\boldsymbol{\theta}) = \prod_{i=1}^{N} f(X_i|\boldsymbol{\theta})\,. \tag{2.14}$$

Notice that we consider the same probability density function f for all X_i, since they are independent observations of $\boldsymbol{X}$.

When we replace the random variable $\boldsymbol{X}$ by the observed data $\boldsymbol{X}^0$, $P(\boldsymbol{X}^0|\boldsymbol{\theta})$ is no longer a probability density function, and we usually denote it by the likelihood function

$$L(\boldsymbol{\theta}) = P(\boldsymbol{X}^0|\boldsymbol{\theta})\,, \tag{2.15}$$

which only depends on θ.

2.2 Parameter and interval estimation

In this section we focus on estimating the values of our cosmological parameters, $\boldsymbol{\theta}$, and their confidence intervals from the likelihood of the data, $L(\boldsymbol{\theta})$. There are two main methods to do this: the Monte Carlo Markov Chain (MCMC) method and the profile-likelihood approach. The former is not intrinsically a Bayesian method, but using it from a Bayesian point-of-view allows to avoid the difficult calculation of high-dimensional integrals. It is the standard approach used in cosmology, and the method implemented in the mostly used cosmological parameter inference codes, like `Monte Python` [Audren et al., 2013] or `CosmoMC` [Lewis and Bridle, 2002].The profile-likelihood approach is essentially a frequentist method and, while it is largely used in particle physics, it is not so common in cosmology. However, some papers have appeared recently [Planck Collaboration, 2014b; Henrot-Versillé et al., 2015; Planck Collaboration, 2016a; Couchot et al., 2017] using this approach with the `CAMEL` code [Henrot-Versillé et al., 2016]. As it was said at the beginning of this chapter when comparing the two schools of statistics, if we have enough data to nicely constrain our model and we are not close to any physical boundary, both the MCMC and the profile-likelihood approach should give similar results. However, when we consider parameters like the sum of neutrino masses, with a physical boundary at zero, the two approaches can give different results (see e.g. Henrot-Versillé et al., 2016). In the following we present both approaches with a bit more of details.

2.2.1 Monte Carlo Markov chains

Looking back at Eq. (2.13) from a Bayesian perspective, the goal is to extract the posterior distribution of our parameters, $p(\boldsymbol{\theta}|\boldsymbol{X}^0)$, given the likelihood, $L(\boldsymbol{\theta})$,

and the prior, $p(\boldsymbol{\theta})$.

Monte Carlo integration

Let us first imagine we have some probability density function $\pi(x)$ and that we want to compute the following expectation value

$$E[f(x)] = \int f(x)\pi(x)\,\mathrm{d}x\,. \tag{2.16}$$

The brute force approach consists on numerically approximate the integral with an equally spaced grid. However, the Monte Carlo integration suggests to draw N identical and independent samples, $\{x_i\}_{i=1,\ldots,N}$, according to the probability distribution $\pi(x)$ and compute the expectation value as

$$E[f(x)] \approx \frac{1}{N}\sum_{i=1}^{N} f(x_i)\,. \tag{2.17}$$

With this approach we will have more points in the high probability region of $\pi(x)$, which is the most important region in the integral. In the following we describe how we can generate the sample according to the probability distribution, and how we can use it to sample a cosmological parameter space.

MCMC: basic concepts

The Monte Carlo Markov chain method provides a smarter way than an equally space grid to sample a high-dimensional distribution $\pi(\boldsymbol{x})$ using an ergodic Markov chain X. The main idea is to rewrite the high-dimensional version of Eq. (2.17) as

$$E[f(\boldsymbol{x})] \approx \bar{f}_N = \frac{1}{N}\sum_{i=1}^{N} f(X_i)\,, \tag{2.18}$$

where X_i is the element number i of the Markov chain, and the sum is an ergodic average. We now describe each one of these properties.

A Markov chain is a random process fulfilling the condition that each step only depends on the previous one. In terms of probability, if we denote by X_i the step number i of the Markov chain X, then

$$P(X_i \in X|X_0, X_1, \ldots, X_{i-1}) = P(X_i \in X|X_{i-1}),\,. \tag{2.19}$$

We can then define the transition probability to go from a point X_i to a point X_j by

$$P_{ij}(k) = P(X_k = X_j|X_0 = X_i)\,. \tag{2.20}$$

We say that the distribution of the chain X converges to a stationary distribution if it is irreducible, aperiodic, and positive recurrent. Step-by-step, a chain is called irreducible if

$$\forall\, i,\, j\, \exists\, k > 0 \text{ such that } P_{ij}(k) > 0\,, \tag{2.21}$$

which implies that we can always go from one point in the parameter space to another with a certain number of iterations. An irreducible chain is called aperiodic if the required number of iterations to move from one point to another is not a multiple of an integer, so that the chain does not oscillate between different states periodically. An irreducible chain is called recurrent if

$$P\left[\min(k > 0 : X_k = X_i | X_0 = X_i) < \infty\right] = 1\,, \tag{2.22}$$

which implies that a finite number of steps are needed in order to come back on a point in the parameter space. An irreducible recurrent chain is then called positive recurrent if

$$\forall\, j,\, k \geq 0\, \exists\, \pi(X) \text{ such that } \sum_i \pi(X_i) P_{ij}(k) = \pi(X_j)\,, \tag{2.23}$$

where $\pi(X)$ is the stationary distribution, and it implies that if X_0 is sampled from $\pi(X)$ then the following iterates will be distributed according to it. A chain is said to be reversible if

$$\pi(X_i) P_{ij} = \pi(X_j) P_{ji}\,. \tag{2.24}$$

In this case the stationary distribution $\pi(X)$ is unique. If X is positive recurrent and aperiodic we call it ergodic and the following conditions are fulfilled

$$\lim_{k\to\infty} P_{ij}(k) = \pi(X_j)\, \forall\, i,\, j\,, \tag{2.25}$$

$$E[|f(X)|] < \infty \Rightarrow P(\bar{f}_N \to E[f(X)]) = 1\,. \tag{2.26}$$

This latter condition is the point validating the MCMC methods according to Eq. (2.18). However, it is very difficult to theoretically know how long we should run our chain until its iterations are distributed according to $\pi(X)$, and we do not have any estimation on the error of $\bar{f}_N$. In the following we will present, though, a diagnostic to know if our chain have converged to the stationary distribution.

Metropolis-Hastings algorithm

One of the most used algorithms for MCMC is the Metropolis-Hastings [Metropolis and Ulam, 1949; Metropolis et al., 1953; Hastings, 1970], since it is powerful and easy to implement. According to it, the transition probability from a point X_i to a point X_j is given by

$$P_{ij} = q(X_i|X_j) \times \alpha(X_i|X_j) \text{ with } \alpha(X_i|X_j) = \min\left[1, \frac{\pi(X_j)q(X_i|X_j)}{\pi(X_i)q(X_j|X_i)}\right], \tag{2.27}$$

where $q(X_i|X_j)$ is an auxiliary function such that $q(X|X_j)$ is the probability density for each X_j. The Metropolis-Hastings algorithm is given by

1. Choose a starting point of the chain X_0 and set the index $i = 0$.
2. Generate a candidate for the new point in the parameter space X_j from a proposal density $q(X_j|X_i)$.
3. Compute the value of $\alpha(X_i|X_j)$.
4. Generate a random number u uniformly distributed between 0 and 1, both included.
5. If $u \leq \alpha(X_i|X_j)$ set $X_{i+1} = X_j$; else, $X_{i+1} = X_i$.
6. Set $i = i + 1$ and go back to step number 2.

With this algorithm we can run some MCMC to obtain the posterior distribution $p(\boldsymbol{\theta}|\boldsymbol{X}^0)$ in Eq. (2.13). However, it is a joint distribution of all cosmological parameters, and we are also interested in the posterior distribution of each parameter alone. In principle, we should compute the marginalized distribution integrating as in Eq. (2.10), but if we compute the histogram of the values of the chain for a specific parameter we directly obtain its marginalized distribution.

The main question that arise after presenting the Metropolis-Hastings algorithm is how we should choose the proposal distribution $q(X_j|X_i)$. If the steps from a given point X_i to a candidate X_j are too small, the difference between $\pi(X_j)$ and $\pi(X_i)$ is in general small, which will imply a too high acceptance rate; i.e. the number of accepted points with respect to the total number of candidates will be too high. On the contrary, if the trial steps are too large, the chain will remain stuck at one point before accepting a step, giving a too low acceptance rate. In both cases we explore the parameter space too slow and inaccurately. The correct choice of the proposal distribution is not straightforward. In practice, we use a multivariate Gaussian distribution centered at the

previous accepted point X_i. Even in this simple scenario, we do not usually know a priori which should be the covariance of the Gaussian proposal distribution. As a general rule of thumb, the acceptance rate when both the proposal and the target distributions are Gaussian is given by [Gelman, Roberts, and Gilks, 1996]

$$\frac{\sigma_{\text{prop}}}{\sigma_{\text{target}}} = \frac{2.4}{\sqrt{d}}, \tag{2.28}$$

where σ_i is the square root of the diagonal elements of the proposal or target covariance matrix, and d the dimension of the parameter space. For the number of parameters that we usually deal with in cosmological analyses, the acceptance rate should be close to 0.25. According to this expression, a good proposal distribution is given by our knowledge on the target covariance matrix. However, if it is our fist analysis we may not have a clear idea of the errors that we are expecting, and it may be even worse for the correlations between the parameters. The standard approach here is to run a chain with a diagonal matrix build from a first guess of the errors of the parameters. After some time, we compute the covariance matrix of the chain, and we then use it as proposal distribution for a new run. This method may require an important fine tuning until we find a good proposal distribution. Some methods have been developed to extend the Metropolis-Hastings into an adaptive algorithm, noticeably reducing the time needed for this fine tuning (see M. Spinelli's thesis for a detailed explanation on one of this methods and its application [Spinelli, 2015]).

Other algorithms

Despite the Metropolis-Hastings popularity, there are other algorithms used in cosmology and that may be best suited to specific problems. One of them is the Nested sampling [Skilling, 2004; Skilling, 2006], where there is a first quick exploration of the entire volume in the parameter space, and it then over-samples the most likely regions. The samples are finally re-weighted accordingly. This method is usually used to compute the Bayesian evidence and choose the best model between several candidates [Bassett and Kunz, 2004]. Another example of alternative algorithms is the affine-invariant ensemble sampler [Goodman and Weare, 2010], whose main characteristic is the fact of being invariant under linear transformations of the parameter space. It is specially powerful on highly skewed distributions (see Spinelli, 2015, and references therein for a detailed description of these and other algorithms used in the literature).

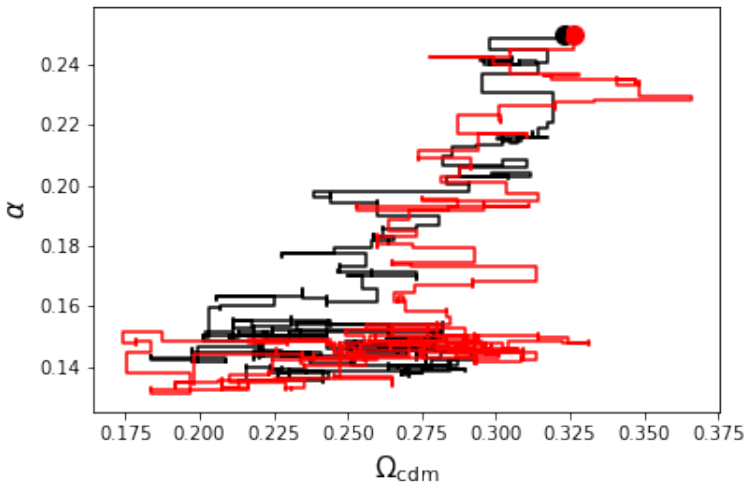

FIGURE 2.1: Two MCMC chains obtained with the Metropolig-Hastings algorithm, using the JLA SNIa likelihood, for $\Omega_{\rm cdm}$ and the SNIa stretch nuisance parameter α. The black and red large dots show the starting point of the chains. We can see the burn-in period until the chains reach the relevant zone.

Chain convergence

In order for a chain to be useful we need to be sure that Eq. (2.18) is fulfilled. We can intuitively guess that the longer our chain runs, the closer we are to fulfill it. However, in practice we want to know when we can stop our chain and use it for our cosmological analysis. The first thing that is usually done is discard the first points of the chain, which are close to the starting point. In this way, we consider only the points sampling the region around the maximum of the distribution. This is the burn-in period. The quantity of points that should be removed as burn-in cannot be predicted, so in general we discard around 30% of the total number of accepted points, but if we start closer or further from the maximum of the distribution this quantity can significantly change. See Fig. 2.1 for a graphic example of the burn-in period.

Once we have rejected the first points, we still want to know if we have enough points to perform our analysis or we should run longer. In practice we use not only one chain, but several of them, because thanks to this we can use the Gelman-Rubin test [Gelman and Rubin, 1992] to check if our chains have converged (see e.g. Spinelli, 2015, for some other tests of convergence). The main idea of this test is to compare several sequences of points drawn from different starting points and check if we can distinguish them. Also, this test provides us with an idea of how much the estimate of the distribution is going to improve if we run longer. Let us assume that we run m chains of $2n$ elements each. Let us reject as burn-in 50% of these points; thus keeping the points X_i^j

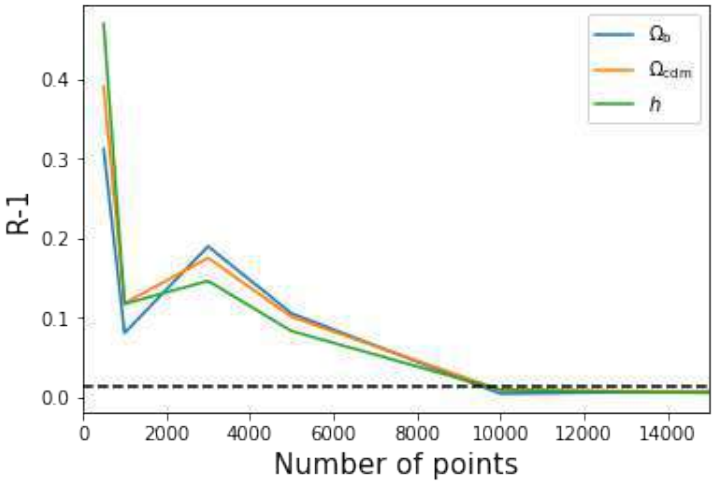

FIGURE 2.2: Evolution of the Gelman-Rubin $R-1$ value as a function of the length of two MCMC chains. They have been obtained with the Metropolig-Hastings algorithm, using the CMB, SNIa, and BAO likelihoods discussed in Chapter 7. We show only the values for the cosmological parameters $\Omega_{\rm b}$, $\Omega_{\rm cdm}$, and h. The threshold $R-1=0.015$ is shown with a dashed line.

with $i=1,\dots,n$ and $j=1,\dots,m$ (X_i^j is the ith element of the jth chain). We can then define

- the mean of the chain $\overline{X}^j \equiv \frac{1}{n}\sum_{i=1}^{n} X_i^j$,
- the mean of the distribution $\overline{X} \equiv \frac{1}{nm}\sum_{i,j} X_i^j$,
- the variance between the different chains $B \equiv \frac{n}{m-1}\sum_{j=1}^{m}(\overline{X}^j-\overline{X})^2$,
- and the variance within a chain $W \equiv \frac{1}{m(n-1)}\sum_{i,j}(X_i^j-\overline{X}^j)^2$.

Using these quantities we can define the factor

$$R \equiv \frac{\frac{n-1}{n}W+\frac{B}{n}\left(\frac{m+1}{m}\right)}{W}\,, \tag{2.29}$$

where the numerator is an unbiased estimate of the variance if we sample from the stationary distribution, while it is an overestimation otherwise. The denominator is an underestimation of the variance of the target distribution if the single chain has not yet converged. If R is high this implies that either we have not yet reached the stationary distribution, or that we have not reached convergence yet (the chains have not yet explored the entire target distribution), or even both. If $R\sim 1$ we can stop our chains and consider them as converged. The standard cut used in current cosmological analyses (see e.g. Thomas, Kopp, and Skordis, 2016) is $R-1<0.03$ for all parameters. In all the MCMC used

in this work, we decided to be slightly more conservative and we consider that the chains have converged once $R-1 < 0.015$ for all parameters. In Fig. 2.2 we show the evolution of the $R-1$ value as a function of the length of two MCMC chains, using the combination of CMB, SNIa, and BAO from Chapter 7, for 3 cosmological parameters: $\Omega_{\rm b}$, $\Omega_{\rm cdm}$, and h.

2.2.2 Profile-likelihood

As it was explained at the beginning of the section, the profile-likelihood is an intrinsically frequentist approach, and essentially different from the MCMC technique previously presented. Unlike the Bayesian approach, the frequentist school does not have any priors and, by definition, the quantities we want to measure (cosmological parameters in our case) have a true fixed value, so they cannot be assigned a distribution. Estimating the value for the parameters and finding the confidence interval is a two-step process. In a first place we need to find the maximum of our likelihood. This is usually done numerically maximizing the likelihood or, equivalently, minimizing the $\chi^2 = -2\ln L$ [1]. The main problem resides on the complicated numerical calculations that have to be performed if we want to estimate the maximum of our likelihood with high precision. There are plenty of minimization softwares in the market, but not all of them are able to extract the maximum with the required level of accuracy for our cosmological analyses. One of the most used codes to do it is the `minuit` software [James and Roos, 1975]. It has been largely used in particle physics since the 70's, and it has been continuously improved. `minuit` contains several tools for minimizing a function and study the shape of the function around the minimum, but here we focus only on the minimization part, which is done by the `migrad` algorithm. It is based on the "switching" algorithm from Fletcher, 1970, and it belongs to the variable metric methods, which provide the expected distance to the minimum to help quantify the level of convergence.

Once we have the values for our parameters that lead to the maximum of the likelihood (the best-fit values), we want to estimate the confidence interval for each parameter. The idea behind the profile-likelihood technique is to fix the value of one of the parameters, $\theta = \theta_1$, and minimize the χ^2 function varying all the remaining parameters. Once we obtain the point $(\theta_1, \chi^2(\theta_1))$, we fix the same parameter to a different value $\theta = \theta_2$ and perform the minimization varying all the remaining parameters again. This will give us a second point $(\theta_2, \chi^2(\theta_2))$. After we have done this for a certain amount of points in the neighborhood of the best-fit value for θ, the profile-likelihood for θ is given by the curve $\{(\theta_i, \chi^2(\theta_i))\}$. We can then compute the likelihood ratio statistic,

[1] Not to be confused with the square of the co-moving distance

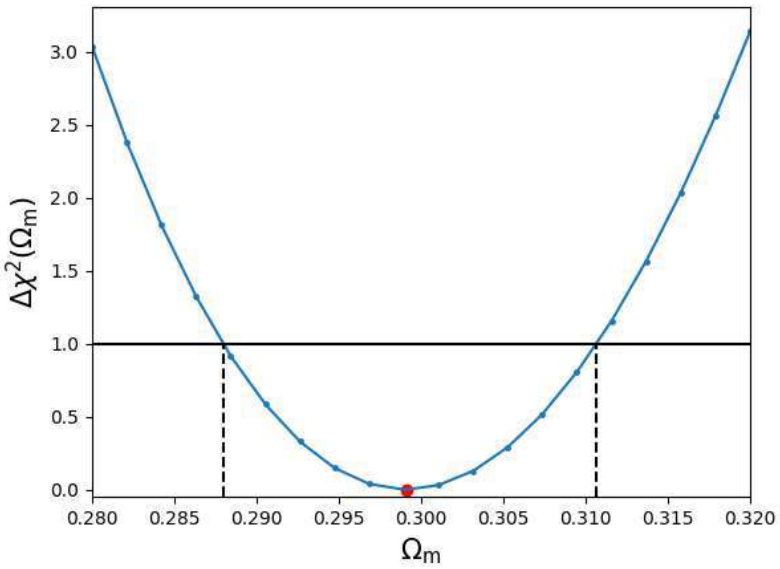

FIGURE 2.3: Profile-likelihood (minus $\chi^2_{\rm min}$) on $\Omega_{\rm m}$ using the CMB, SNIa, and BAO likelihoods from Chapter 7. The specific points used to derive the profile-likelihood are superimposed as blue dots. The red dot correspond to $\chi^2_{\rm min}$. The confidence interval at 68% confidence level is represented with the black vertical dashed lines. The black horizontal solid line stands for the cut at $\Delta\chi^2 = 1$ needed to obtain the confidence interval at 68% confidence level.

$\Delta\chi^2(\theta) = \chi^2(\theta) - \chi^2_{\rm min}$, and obtain the confidence interval by selecting the θ values that fulfill $\Delta\chi^2(\theta) \leq \chi^2_1(\alpha)$, where $\chi^2_1(\alpha)$ is the $1-\alpha$ quantile of the χ^2 distribution with 1 degree of freedom. So, if we want to obtain the 1σ confidence interval (68% confidence level) we only need to cut the likelihood ratio statistic at 1 (see an example in Fig. 2.3). Notice that this approach can immediately be extrapolated to two-dimensions to give the two-dimensional contours, as it is the case in Sec. 7.4.

2.3 Goodness-of-fit

Once we fit our model to the data, either running some MCMC or using a profile-likelihood technique, we are interested into knowing if our model is able to correctly fit the data. There is a large statistical literature addressing this issue (see e.g. James, 2006). In this section, though, we only present the approach used in the following.

Once we have the minimum value of our χ^2 function, we can compute the probability that a larger value for the χ^2 could occur for a fit with $\nu = N - k$

degrees of freedom, where N is the number of data points and k is the number of free parameters of the model,

$$P(\chi^2, \nu) = \frac{\Gamma\left(\frac{\nu}{2}, \frac{\chi^2}{2}\right)}{\Gamma\left(\frac{\nu}{2}\right)}, \tag{2.30}$$

with $\Gamma(t, x)$ being the upper incomplete gamma function and $\Gamma(t) = \Gamma(t, 0)$ the complete gamma function.

Obtaining a probability close to 1 implies that it is very likely to get larger χ^2 values, meaning that the model fits correctly (possibly too well) the data. On the other hand, obtaining a small probability indicates that the model does not provide a good fit to the data. It is important to add that Eq. (2.30) is valid (strictly speaking) when the N data points come from N independent random variables with Gaussian distributions (see Sec. 4.3, Sec. 5.1.3, and Sec. 5.2.4 for more detail concerning this independence).

2.4 Model comparison

As it was the case in the previous section, finding criteria to compare different models and choose the best of them is an entire field of research, and there is not a unique way to do it (see also James, 2006, and references therein, for a nice review on different methods). In this section we follow the previous approach and present only the model comparison criteria used in the following.

We focus on two widely used model comparison criteria: the Akaike information criterion (AIC) [Akaike, 1973] and the Bayesian information criterion (BIC) [Schwarz, 1978]. Both account for the fact that a model with fewer parameters is generally preferable to a more complex model if both of them fit the data equally well.

The AIC is built from information theory. Rather than having a simple measure of the direct distance between two models (Kullback-Leibler distance [2]), the AIC provides us with an estimate of the expected, relative distance between the fitted model and the unknown true mechanism that actually generated the observed data. We must be aware that the AIC is useful in selecting the best model in the set of tested models; however, if all the models are very poor, the AIC still gives us the best model, which would actually be the least bad. This is why it is important to previously check the goodness-of-fit of a model [see Eq. (2.30)]. Given the minimum of the χ^2 and the number of free parameters of the model k, the AIC is given by

[2] The Kullback-Leibler information between models f and g denotes the information lost when g is used to approximate f. As a heuristic interpretation, the Kullback-Leibler information is the distance from g to f.

$$\mathrm{AIC} = \chi^2_{\mathrm{min}} + 2k\,. \tag{2.31}$$

The AIC may perform poorly if there are too many parameters compared to the size of the sample [Sugiura, 1978; Sakamoto, Ishiguro, and Kitagawa, 1986]. In this case, a second-order variant of the AIC can be used, the so-called AICc [Hurvich and Tsai, 1989],

$$\mathrm{AICc} = \mathrm{AIC} + \frac{2k(k+1)}{N-k-1}\,, \tag{2.32}$$

where N is the number of data points. An extensive presentation and discussion of the AIC and its variations can be found in Burnham and Anderson, 2002.

The BIC is one of the most used criterion from the so-called dimension-consistent criteria (see Bozdogan, 1987, for a review of many of these criteria). It was derived in a Bayesian context with equal prior probability on each model and minimal priors on the parameters, given the model. It is given by

$$\mathrm{BIC} = \chi^2_{\mathrm{min}} + k\ln(N)\,. \tag{2.33}$$

Both the AICc and the BIC strongly depend on the size of the sample. In order to compare different models we use the exponential of the differences ΔAICc/2 (ΔBIC/2), where ΔAICc=AICc$_{\mathrm{ref}}$-AICc (Id. for the BIC) and ref stands for the reference model, since the exponential can be interpreted as the relative probability that the corresponding model minimizes the estimated information loss with respect to the reference model.

Given that the AIC (AICc) and the BIC can both be derived as either frequentist or Bayesian procedures, what fundamentally distinguishes them is their different philosophy, including the nature of their target models. Thus, the choice of the criterion depends on their performance under realistic conditions. A comparison of these two criteria is outside the scope of this work (see Burnham and Anderson, 2004, for an extended and detailed comparison). In general, though, the BIC penalizes extra parameters more severely than the AIC.

It is important to notice that when comparing two models with the same data sample and the same number of parameters, ΔAIC and ΔBIC basically reduce to $\Delta\chi^2_{\mathrm{min}} = \chi^2_{\mathrm{ref}} - \chi^2$.

For the sake of completeness, it is important to mention that another method to compare different models largely used in the literature is the Bayesian model comparison (usually through the computation of the Bayesian evidence). Contrary to the model criteria presented here, it takes into account the full shape of the likelihood, instead of only considering its maximum, but it is usually more expensive from a computational point-of-view, and it is inherently a Bayesian approach. However, since it is not used in this work, we just refer the reader

to Knuth et al., 2015, for a detailed review, and to Efstathiou, 2008; Kilbinger et al., 2010; Kunz, Trotta, and Parkinson, 2006, for some applications in cosmology.

2.5 The Fisher matrix formalism

In the previous sections we have provided the basic ingredients to fit a model to some observations, quantify the ability of the model to correctly fit the data, and choose the best model among several candidates. However, we may be interested in quantifying the ability of a future survey, like Euclid, to constrain our preferred model. Since we do not have the observations yet, we need statistical tools to predict what will be the accuracy on the parameters of our model. One option consists on generating mock data for our future survey and run some MCMC (or apply the profile-likelihood technique) to predict the precision on the parameters of the model. However, this can be very time consuming, and not relevant to rapidly test a bunch of theoretical models beyond ΛCDM. One of the most used methods to compute future forecasts is the Fisher matrix technique.

The Fisher matrix is defined as the expectation value of the second derivative of the logarithm of the likelihood [3]

$$F_{\alpha\beta} = \left\langle \frac{-\partial^2(\ln L)}{\partial\theta_\alpha \partial\theta_\beta} \right\rangle , \tag{2.34}$$

where θ_α and θ_β are the parameters of interest. If the likelihood is Gaussian it can be computed analytically

$$F_{\alpha\beta} = \frac{1}{2}\,\mathrm{Tr}\left[\frac{\partial \boldsymbol{C}}{\partial\theta_\alpha}\boldsymbol{C}^{-1}\frac{\partial \boldsymbol{C}}{\partial\theta_\beta}\boldsymbol{C}^{-1}\right] + \sum_{p,q}\frac{\partial\mu_p}{\partial\theta_\alpha}(\boldsymbol{C}^{-1})_{pq}\frac{\partial\mu_q}{\partial\theta_\beta}\,, \tag{2.35}$$

where $\boldsymbol{\mu}$ is the mean of the data vector, $\boldsymbol{C}$ is the expected covariance of the data, and $\boldsymbol{\theta}$ is the vector of parameters. Tr stands for the trace. We can interpret this Fisher matrix as the curvature of the logarithm of the likelihood, which tells us how fast the likelihood falls around its maximum. In general, if we assume that the data is distributed according to a Gaussian function with mean $\boldsymbol{\mu}$ and covariance $\boldsymbol{C}$, either the mean is zero, or the covariance does not depend on the parameters of the model. In both cases, one of the terms does not vanish. In cosmological analyses we generally assume that the covariance is parameter-independent; therefore, we just consider the second term in Eq. (2.35). This is the approach that we will follow in this work. Notice that, since we want to use

[3] This is the standard definition of the Fisher matrix from a frequentist approach. It can be shown (see e.g. Sellentin, Quartin, and Amendola, 2014) that it is equivalent to the Bayesian definition of the Fisher matrix when doing a forecast.

the Fisher matrix formalism for forecasting, our data vector will be the vector of the observables with our fiducial cosmological model, and the covariance matrix will be a theoretical covariance of the observables based on our fiducial cosmology, too.

Once we have the Fisher matrix, an estimate of the covariance matrix of our parameters is given by [4]

$$C_{\alpha\beta} = (\boldsymbol{F}^{-1})_{\alpha\beta} \,. \tag{2.36}$$

The diagonal elements of the parameter covariance matrix correspond to the square of the 1σ marginalized uncertainties on each parameter

$$\sigma_\alpha = \sqrt{C_{\alpha\alpha}} \,, \tag{2.37}$$

while the un-marginalized constraints (i.e. fixing all the remaining parameters) are given by

$$\sigma_{\alpha,\,\text{un-marg}} = \frac{1}{\sqrt{F_{\alpha\alpha}}} \,. \tag{2.38}$$

We can define the correlation coefficient between the constraints on the parameters, ρ, as

$$C_{\alpha\beta} = \rho_{\alpha\beta}\sigma_\alpha\sigma_\beta \,. \tag{2.39}$$

We might also be interested into marginalizing over some parameters (nuisance) but not the others (cosmology). This can easily be achieved by removing the rows and columns of the covariance matrix corresponding to the parameters we want to marginalize over, and re-invert to obtain a marginalized Fisher matrix.

2.5.1 Visualizing the confidence regions

With the Fisher matrix formalism we can easily plot the marginalized joint posterior probability of two parameters, θ_α and θ_β, assuming it is a Gaussian distribution. The ellipses posteriors are fully specified by the semi-minor and semi-major axes, a and b, which correspond to the larger and smaller eigenvalue of the covariance matrix. We also need to specify the angle of the ellipse, ϕ, which is given by the ratio between the y-component and the x-component of the eigenvector with the largest eigenvalue

[4] More in detail, the Cramer-Rao inequality tells us that the variance of a given parameter cannot be smaller than the one given by the inverse of the Fisher matrix.

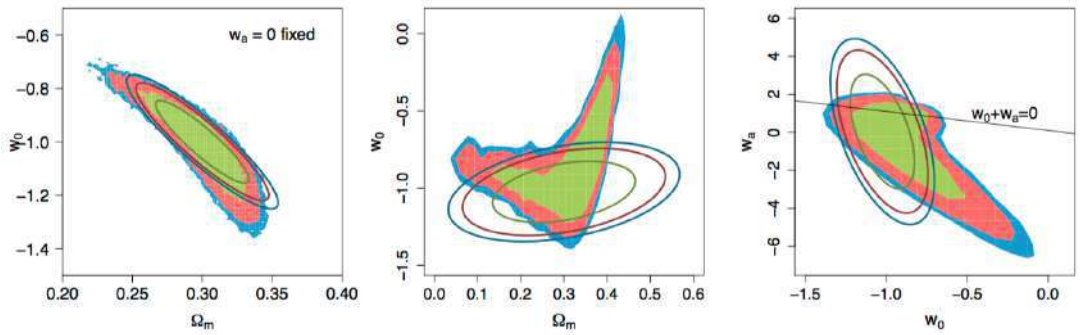

FIGURE 2.4: Original plot from Wolz et al., 2012: 1σ, 2σ, and 3σ contours for a supernovae survey. The filled contours correspond to the posterior distributions obtained with MCMC, while the solid lines show the results from a Fisher matrix analysis.

$$a = A\sqrt{\frac{1}{2}(\sigma_\alpha^2 + \sigma_\beta^2) + \sqrt{\frac{1}{4}(\sigma_\alpha^2 - \sigma_\beta^2)^2 + \sigma_{\alpha\beta}^4}}\,, \tag{2.40}$$

$$b = A\sqrt{\frac{1}{2}(\sigma_\alpha^2 + \sigma_\beta^2) - \sqrt{\frac{1}{4}(\sigma_\alpha^2 - \sigma_\beta^2)^2 + \sigma_{\alpha\beta}^4}}\,, \tag{2.41}$$

$$\phi = \frac{1}{2}\text{atan}\left(\frac{2\sigma_{\alpha\beta}^2}{\sigma_\alpha^2 - \sigma_\beta^2}\right)\,, \tag{2.42}$$

where A is a constant factor equal to $\sqrt{2.3}$, $\sqrt{6.17}$, $\sqrt{11.8}$ for two-parameter contours at 1σ, 2σ, and 3σ confidence level, respectively.

Some times we might build a Fisher matrix using a given set of parameters, $\boldsymbol{\theta}$, but be also interested in a derived set of parameters, $\boldsymbol{p}(\boldsymbol{\theta})$. We can project the primary Fisher matrix, $\boldsymbol{F}$, into a derived Fisher matrix, $\boldsymbol{S}$, using a Jacobian transformation

$$S_{mn} = \sum_{i,j} \frac{\partial\theta_i}{\partial p_m} F_{ij} \frac{\partial\theta_j}{\partial p_n}\,. \tag{2.43}$$

2.5.2 Limits of the formalism

The Fisher matrix formalism is largely used in the literature to predict the accuracy of future surveys thanks to its simplicity and its speed, compared to MCMC techniques, for example. However, the assumption of dealing with Gaussian posteriors is quite strong and it is not true for specific cosmological data sets and parameters. In Wolz et al., 2012, the authors performed a rigorous comparison between Fisher matrix and MCMC forecasting techniques for SNIa, BAO, and WL data. They found that if the posterior distributions show

highly non-elliptical shapes, the Fisher matrix technique is not able to recover the expected constraints, as it can be seen in Fig. 2.4, and it underestimates the marginalized errors between 30% and 70% for purely background probes. On the contrary, when the authors consider WL data, their Fisher matrix forecast agrees with the MCMC predictions at a 5% level, since the posterior distributions are closer to a Gaussian. Moreover, the Fisher matrix technique may provide constraints that enter physically forbidden regions (like $\Omega_{\rm m} < 0$), and it may suffer from numerical instabilities when computing the derivatives of the observables with respect to the parameters. This requires a high level of accuracy when computing the observables. However, there exist some codes in the literature that extend the Fisher matrix formalism in order to recover the degeneracies in the posterior distributions without the need of running time consuming MCMC (like DALI [Sellentin, Quartin, and Amendola, 2014; Sellentin, 2015; Sellentin and Schäfer, 2016]).

Chapter 3

The Euclid mission

As we have seen in Sec. 1.5, in order to extract cosmological information from our observations we need large data sets of galaxies containing not only their positions on the sky, but also their redshift. The so-called galaxy redshift surveys are projects aiming at surveying large volumes and detect the galaxies (or other objects like quasars), in order to probe the large-scale structure of the Universe and extract the cosmological information from it. There have been several galaxy redshift surveys in the past. The Center for Astrophysics Redshift Survey (CfA) [Tonry and Davis, 1979] was the first systematic redshift survey which observed roughly 2,200 galaxies between 1977 and 1982. It was later extended to the CfA2, with 15,000 galaxies, completed in the early 1990s. These early surveys were limited in size because the redshift of galaxies could only be measured for one galaxy at a time. More recently, technological developments enabled the measurement of several redshifts simultaneously, and it led to larger surveys like the 2-degree Field Galaxy Redshift Survey (2dFGRS [1]), with 221,000 redshifts, completed in 2002, and the Sloan Digital Sky Survey (SDSS [2]), with roughly 1 million redshifts by 2007, which have shown that galaxy redshift surveys can successfully probe the large-scale structure of the Universe and improve our cosmological knowledge.

In this chapter we focus our attention to describe the future Euclid mission [3], which is the main future source of cosmological information used in this work. We first present, in Sec. 3.1, the two main approaches that can be used when measuring redshifts in a galaxy redshift survey: spectroscopic and photometric. We then describe the mission and the satellite in Sec. 3.2. In Sec. 3.3 we present the structure of the Euclid Consortium, the single team having the scientific responsibility of the mission, the data production, and of the scientific instruments. Finally, in Sec. 3.4, we present the group responsible for producing the official Fisher matrix forecasts for the consortium. A very large part of the

[1] http://www.2dfgrs.net
[2] http://www.sdss.org
[3] https://www.euclid-ec.org

work done in this thesis (presented in Chapter 6) has been realized within this group.

3.1 Spectroscopic and photometric redshift surveys

In this first section of the chapter we give a brief overview of the two main methods to determine the distance of distant objects in galaxy redshift surveys.

In order to probe the large-scale structure of the Universe we look for the three-dimensional position of the objects. The angular position of the objects on the sky can be measured directly, but it is very difficult to infer the distance to them (see the different definitions for distance given in Sec. 1.1.2). Because of this, we use the redshift of the objects to obtain the radial information, but even this quantity is not straightforward to extract. The standard way to measure the redshift of an object is by using the flux distribution of the source in wavelength space; the so-called spectrum $S(\lambda)$. If we can measure the spectrum of a distant object at redshift z, $S'(\lambda', z)$, and compare it to the spectrum in the rest frame, $S(\lambda)$, we can then extract the redshift as

$$S(\lambda) \to S'(\lambda', z) = \frac{S(\lambda = \lambda'/(1+z))}{(1+z)^2}\,, \tag{3.1}$$

where the wavelength transformation comes from the definition of the redshift, $z \equiv (\lambda' - \lambda)/\lambda$. The extra $(1+z)^{-2}$ factor can be derived from a dimensional analysis. Indeed, the spectrum has dimensions of energy divided by surface, time, and wavelength. Since the energy of a photon is proportional to λ^{-1}, the energy will be given by $E' = E/(1+z)$, giving one of the factors in Eq. (3.1). The second factor comes from the fact that in an expanding Universe the time between two consecutive photons is given by $\tau' = (1+z)\tau$. It is important to say that most detectors used nowadays are Charge Coupled Devices (CCDs), and they are not sensitive to the energy of the detected photons, but only to the number of photon counts. If we define the spectra in number of counts instead of energy, we should remove one of the $(1+z)^{-1}$ factors in Eq. (3.1).

The galaxy redshift surveys can be mainly classified into spectroscopic and photometric surveys, depending on how they observe the galaxies and measure their redshifts. The spectroscopic technique uses a spectrograph to measure redshifts with high accuracy, but it requires a large amount of time to collect enough photons from distant objects, as well as previous knowledge of the angular position of the galaxies (galaxy targeting). The photometric technique

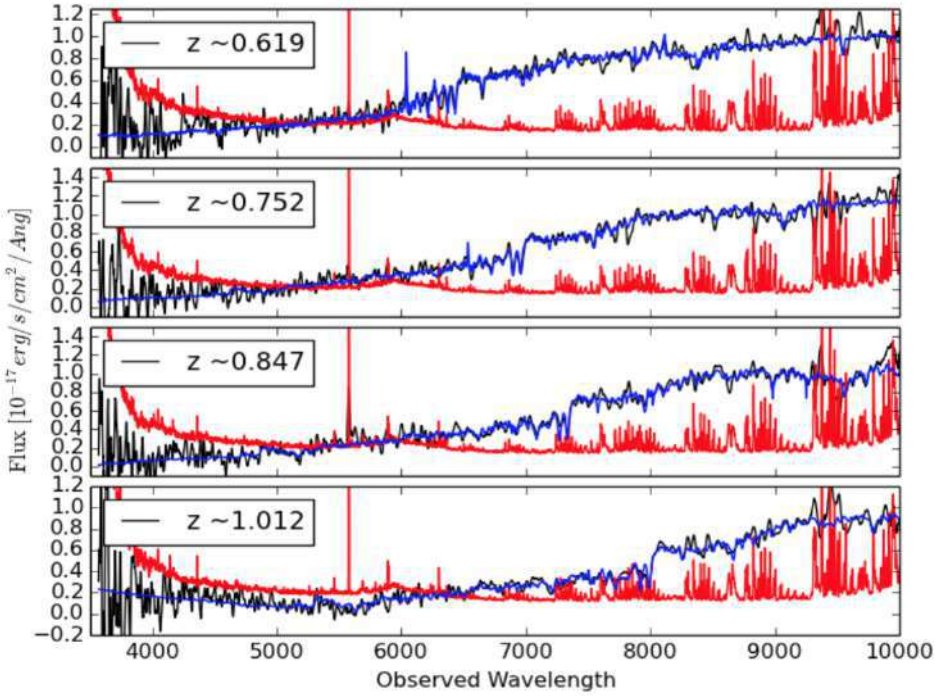

FIGURE 3.1: Original plot from Prakash et al., 2016: Representative spectra of Luminous Red Galaxies of eBOSS. Flux errors are plotted in red, while the template model fits are in blue, and black shows the observed spectra.

provides less accurate estimates of redshifts, but requires less time and can provide an estimate of the redshift for all the objects in the field of view, without a previous targeting.

3.1.1 Spectroscopic technique

The main idea behind this technique is first to measure the spectrum of the source, as the different spectra shown in Fig. 3.1. In order to do this, the light coming from the object is separated into several narrow bins (a few Å) through dispersion, so this implies a large amount of time to detect enough photons in each bin. Once we have measured the spectrum of the source, we compare it to a known spectrum of an object of the same class at rest and look for the shift of a characteristic feature. For example, we know that Luminous Red Galaxies (LRGs) spectra show a characteristic feature at roughly 4000 Å, known as the 4000 Å break in LRGs, which consists on a significant increase of the flux. The spectra shown in Fig. 3.1 correspond to LRGs at different redshifts. If we take, for example, the last panel of the figure we can observe that the 4000 Å break is located at roughly 8000 Å. Using the definition of the redshift, we can infer

a value $z \approx (8000 - 4000)/4000 = 1$. We can do the exact same thing for the third panel and infer a redshift $z \approx (7400 - 4000)/4000 = 0.85$.

3.1.2 Photometric technique

The main idea of this alternative method is to use imaging instead of spectroscopy. The photometry of distant objects is converted into low-resolution spectra, and we then infer the redshifts by comparing the spectra to red-shifted template galaxy spectra for the given class of objects, or to low-resolution spectra for which we already have spectroscopy. One clear advantage with respect to the spectroscopic method is the speed of the method. Instead of dispersing the light of the sources we use different filters which integrate all the light within a broad ($\sim 100\,\mathrm{nm}$) wavelength band. Let us assume that each filter i has a response function that depends on the wavelength, $R_i(\lambda)$ (see for example the filter responses of SDSS in Fig. 3.2). Then, the fluxes of the object in each filter will be given by

$$F_i \propto \int_0^\infty S(\lambda, z) R_i(\lambda) \lambda \, \mathrm{d}\lambda \,. \tag{3.2}$$

Since filters are much wider than the bins used in the spectroscopic technique, a short exposure time is enough to get enough photons to reach a high signal-to-noise ratio. Moreover, imaging detectors usually cover a larger area of the sky than spectrographs, thus giving the redshift for many more objects, and without targeting them a priori. The problem of this method is the accuracy of the redshift estimation. Since we have a low-resolution spectra, the mean uncertainty on the redshift is larger than with the spectroscopic technique.

Because of the low-resolution spectra, the redshift cannot be inferred from a characteristic feature. There are two main ways to extract the redshift once we have the low-resolution spectrum. One option is to use a set of theoretical spectra for different types of objects, called templates, and integrate them using the response functions of our filters, while red-shifting the templates. This provides us with a set of fluxes for each band that depend on the redshift. We then compare our fluxes with the redshifted ones from the templates and look for the redshift that minimizes the differences. This is the so-called template-based technique. The other option is what we call the training-based technique. In this case we start with a set of objects for which we have both photometry and spectroscopy, called training sample. The method consists in finding a mapping function between the fluxes and redshift space, and then apply this function to all the objects for which we do not have spectroscopy, called testing sample. This mapping is usually found using machine-learning techniques, like artificial neural networks, or random forests. See Sánchez et al., 2014, and

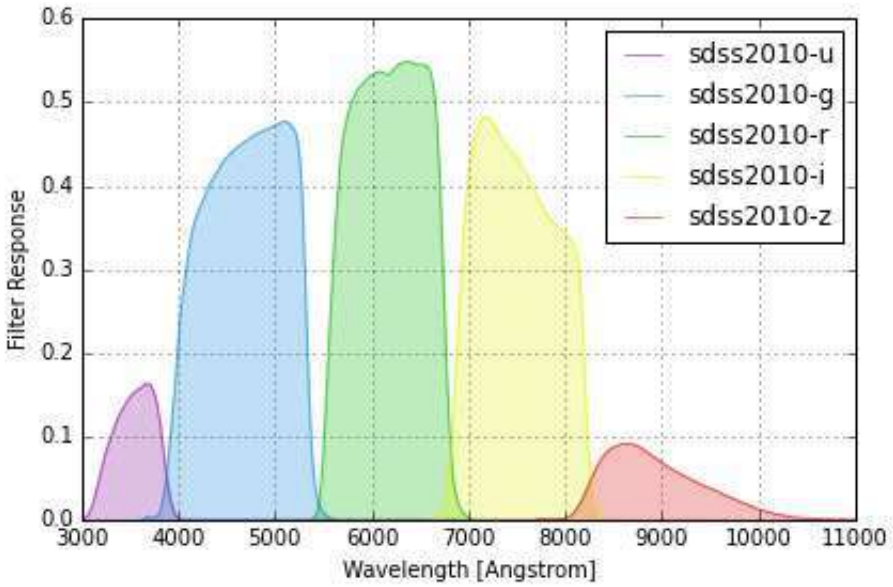

FIGURE 3.2: SDSS filter responses taken from Table 4 of Doi et al., 2010 [Original plot from the `speclite` documentation].

references therein, for several examples of template-based and machine-learning techniques.

3.2 The Euclid satellite

In this section we present the Euclid mission, as well as the satellite (see an artist view in Fig. 3.3) with the different instruments that will be onboard. The structure of the consortium to exploit the future data will be presented in the following sections.

Euclid is a medium class astronomy and astrophysics space mission of the European Space Agency (ESA). It was selected in October 2011 and its launch is planned for 2021. Euclid will try to understand the nature and properties of dark energy, dark matter, and gravity by exploring the past 10 billion years. It will also provide useful information on the early Universe physics and the initial conditions of cosmic structures. Euclid will be launched by a Soyuz ST-2.1B rocket and it will then travel to the L2 Sun-Earth Lagrangian point, where it will operate for 6 years. In Fig. 3.4 we present the Euclid mission summary as shown in the Euclid study definition report (Red-book) [Laureijs et al., 2011], and we detail the different aspects of it in the following subsections. Notice that some technical specifications in this summary may have changed during the building phase and might also slightly evolve before launch.

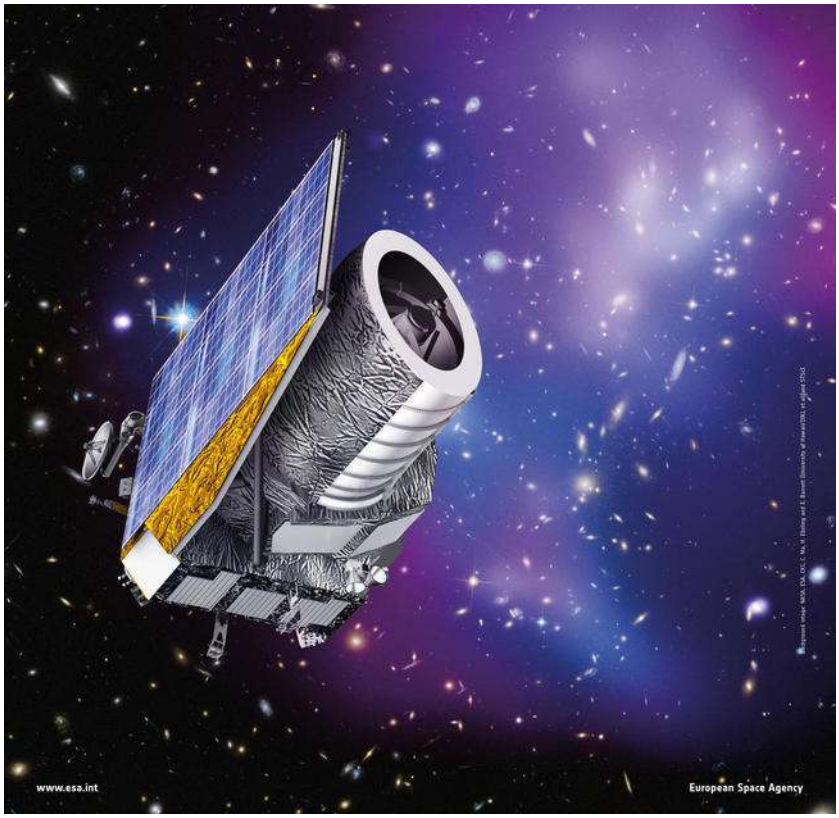

FIGURE 3.3: Artist view of the Euclid satellite [Credit: ESA].

3.2.1 Primary and secondary science

Euclid is primarily a cosmological mission focused on understanding what dark matter and dark energy are, the initial conditions which seed the formation of cosmic structure, and the future of our Universe, as well as understanding the validity range of General Relativity. In order to reach these objectives, Euclid will probe the expansion rate of the Universe and the growth of cosmic structures using two complementary probes: weak gravitational lensing (WL) and galaxy clustering through baryon acoustic oscillations and redshift-space distortions (see Sec. 1.4 and Sec. 1.3, respectively). BAO provide a distance-redshift probe sensitive to the expansion of the Universe, while WL probes all matter (baryonic and dark) but combines angular distances (sensitive to the expansion rate) and the mass density contrast (sensitive to the growth rate of structures and gravity). The RSD are also sensitive to the growth rate of structures and gravity. Therefore, by combining all these probes Euclid will be able to put strong constraints on our models for the dark sector.

Even if Euclid is mainly a cosmological mission, it will detect several billion galaxies that will allow us to consider other complementary probes to galaxy clustering and weak lensing, like clusters of galaxies, strong lensing, supernovae and transients, or exo-planets, for example.

Main Scientific Objectives

Understand the nature of Dark Energy and Dark Matter by:

- Reach a dark energy *FoM* > 400 using only weak lensing and galaxy clustering; this roughly corresponds to 1 sigma errors on w_p and w_a of 0.02 and 0.1, respectively.
- Measure γ, the exponent of the growth factor, with a 1 sigma precision of < 0.02, sufficient to distinguish General Relativity and a wide range of modified-gravity theories
- Test the Cold Dark Matter paradigm for hierarchical structure formation, and measure the sum of the neutrino masses with a 1 sigma precision better than 0.03eV.
- Constrain n_s, the spectral index of primordial power spectrum, to percent accuracy when combined with Planck, and to probe inflation models by measuring the non-Gaussianity of initial conditions parameterised by f_{NL} to a 1 sigma precision of ~2.

SURVEYS

	Area (deg2)	Description
Wide Survey	15,000 (required) 20,000 (goal)	Step and stare with 4 dither pointings per step.
Deep Survey	40	In at least 2 patches of > 10 deg^2 2 magnitudes deeper than wide survey

PAYLOAD

Telescope	1.2 m Korsch, 3 mirror anastigmat, f=24.5 m				
Instrument	VIS	NISP			
Field-of-View	0.787×0.709 deg^2	0.763×0.722 deg^2			
Capability	Visual Imaging	NIR Imaging Photometry			NIR Spectroscopy
Wavelength range	550– 900 nm	Y (920-1146nm),	J (1146-1372 nm)	H (1372-2000nm)	1100-2000 nm
Sensitivity	24.5 mag 10σ extended source	24 mag 5σ point source	24 mag 5σ point source	24 mag 5σ point source	3 10^{-16} erg cm-2 s-1 3.5σ unresolved line flux
Detector Technology	36 arrays 4k×4k CCD	16 arrays 2k×2k NIR sensitive HgCdTe detectors			
Pixel Size Spectral resolution	0.1 arcsec	0.3 arcsec			0.3 arcsec R=250

SPACECRAFT

Launcher	Soyuz ST-2.1 B from Kourou
Orbit	Large Sun-Earth Lagrange point 2 (SEL2), free insertion orbit
Pointing	25 mas relative pointing error over one dither duration 30 arcsec absolute pointing error
Observation mode	Step and stare, 4 dither frames per field, VIS and NISP common FoV = 0.54 deg^2
Lifetime	7 years
Operations	4 hours per day contact, more than one ground station to cope with seasonal visibility variations;
Communications	maximum science data rate of 850 Gbit/day downlink in K band (26GHz), steerable HGA

Budgets and Performance

	Mass (kg)		*Nominal Power (W)*	
industry	TAS	Astrium	TAS	Astrium
Payload Module	897	696	410	496
Service Module	786	835	647	692
Propellant	148	232		
Adapter mass/ Harness and PDCU losses power	70	90	65	108
Total (including margin)	**2160**		**1368**	**1690**

FIGURE 3.4: Euclid mission summary from the Euclid study definition report (Red-book) [Laureijs et al., 2011].

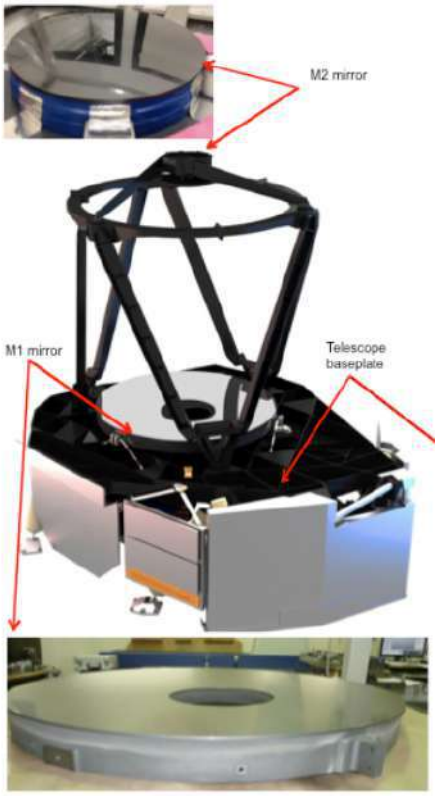

FIGURE 3.5: Detailed view of the telescope on the PLM baseplate [Credit: Airbus Defence and Space, and ESA].

3.2.2 Satellite, service module and payload module

ESA has selected Thales Alenia Space for the construction of the satellite and its service module (SVM), and Airbus (Defence and Space) for the payload module (PLM). The SVM includes several sub-systems, like the sunshield, the solar panel, the electric power system, the star trackers, the slews control systems (with hydrazine and cold gas tanks), the thermal regulation system, or the downlink communication system. The PLM comprises the telescope, the PLM thermal control system, the Fine Guidance Sensor, the scientific instruments VIS and NISP (delivered by the Euclid Consortium), and the detectors (delivered by ESA).

The Euclid telescope will be a 1.2 m on axis 3-mirror Korsch cold telescope, that will provide a field of view of $1.25 \times 0.727\,\mathrm{deg}^2$. The primary mirror M1 (see Fig. 3.5) will be kept below 130 K with a thermal stability better than 50 mK. All the mirrors and structures will be made in Silicon Carbide. The design of the telescope allows for a 3 degree-of-freedom mechanism for the secondary mirror M2 focus and tilt correction, that will enable to reach the requirements on the image quality for WL science.

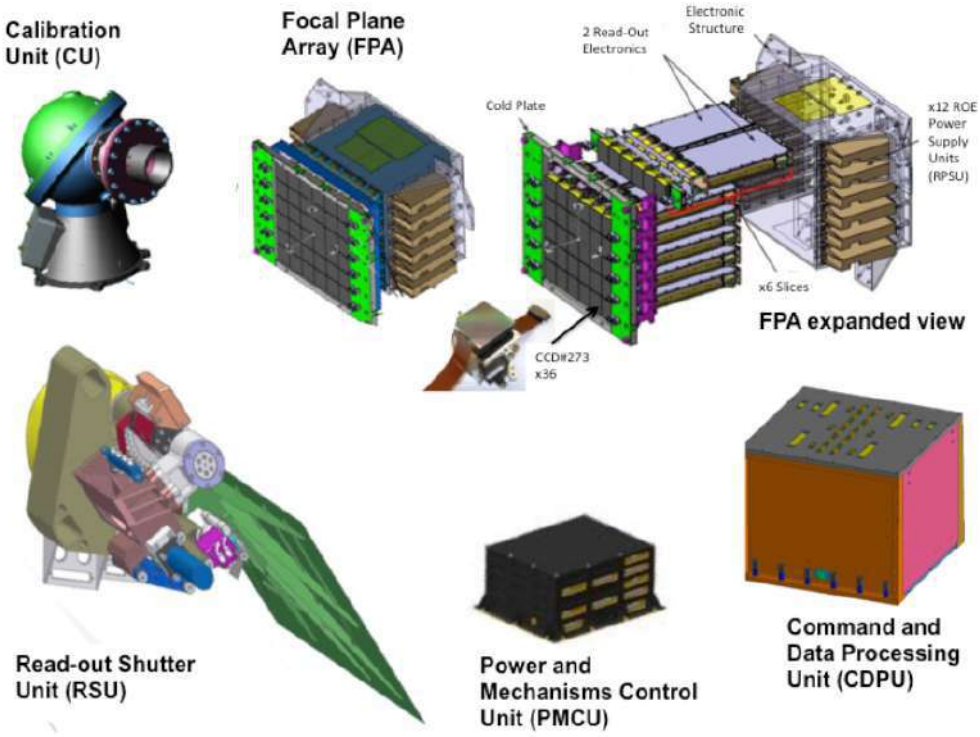

FIGURE 3.6: Overview of the different VIS subsystems [Credit: Euclid Consortium/VIS team].

3.2.3 VIS and NISP instruments

There will be 2 instruments onboard the satellite: the VIS and NISP instruments, built by the Euclid Consortium. VIS will be a high quality panoramic visible imager, while NISP will have a near infrared 3-filter (Y, J, and H) photometer (NISP-P) and a slit-less spectrograph (NISP-S).

The VIS instrument will be used to measure the shape of galaxies in order to perform the WL analyses. It will be composed of the different subsystems shown in Fig. 3.6. The VIS focal plane will consist of a 6×6 matrix of 12-micron CCDs with a resolution of 4096×4132 pixels, and it will cover a field of view of 0.57 $\deg^2$ with 0.1 arc-second pixels. The VIS instrument will be equipped with one single broad band filter covering the wavelength range from 550 nm to 900 nm with a mean image quality of $\sim$ 0.23 arc-seconds.

The NISP instrument will provide near infrared (between 900 nm and 2000 nm) photometry for all the galaxies observed with VIS, and near infrared low-resolution spectra of millions of galaxies. The near infrared photometry will be combined with VIS data to derive the photometric redshift of the VIS galaxies. The near infrared spectra will be used to determine the spectroscopic redshifts of millions of galaxies in order to perform the galaxy clustering analyses. The NISP focal plane will be composed of a 4×4 matrix of 18-micron detectors with a

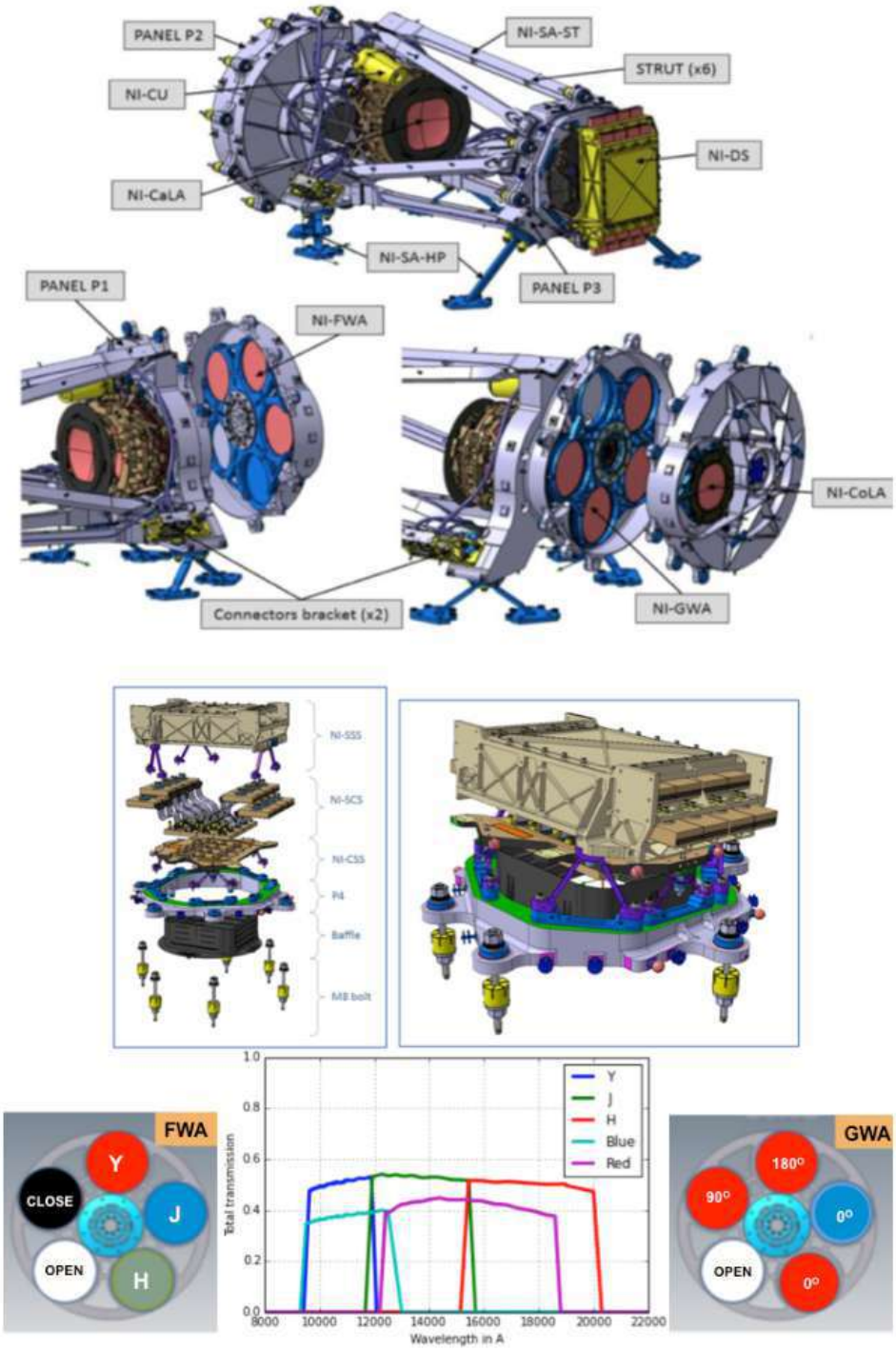

FIGURE 3.7: Overview of the different NISP subsystems. The top panel shows the calibration unit (NI-CU), the camera lens assembly (NI-CaLA), the structure assembly (NI-SA-ST, NI-SA-HP), the corrector lens assembly (NI-CoLA), the detector system (NI-DS), the filter wheel assembly (NI-FWA), and the grism wheel assembly (NI-GWA). The central panel shows the NISP focal plane with the elements of the NISP detector system. The bottom panel shows the filter positions, the transmission curves of the Y, J, and H filters, and the blue and red grisms, as well as the grism positions. [Credit: Euclid Consortium/NISP team].

resolution of 2040×2040 pixels, and it will cover a field of view of 0.53 $\deg^2$ with 0.3 arc-second pixels. The photometric channel will have 3 broad band filters: Y [900-1192] nm, J [1192-1544] nm, and H [1544-2000] nm, with a mean image quality delivering 50% encircled energy within 0.3 arc-seconds and 80% encircled energy within 0.7 arc-seconds. The spectroscopic channel will be equipped with 4 low-resolution grisms (3 red [1250-1850] nm with different orientations and 1 blue [920-1250] nm). The different NISP subsystems are shown in Fig. 3.7.

3.2.4 Ground segment

As we saw in the previous section, Euclid photometry will include the near infrared bands Y, J, and H, and only one optical band from VIS. The remaining bands in the optical domain, g, r, i ,z (see Fig. 3.2) that are required to estimate accurate photometric redshifts will be obtained from ground-based surveys. Therefore, in addition to the large data volume that Euclid will provide, there is the challenge to process, analyze, and mix heterogeneous data sets coming from different space and ground-based surveys, with different depth and resolution.

The Science Ground Segment (SGS) of Euclid is composed of the Science Operation Center (SOC) and the Euclid Consortium Science Ground Segment (EC SGS). The SOC is in charge of the survey planning, managing the downlinked data and providing the Euclid Consortium with the data to perform further processing of the science data. The scientific processing of the data down to the production of the scientific results will be done in the EC SGS. The processing of the data will take place in the Science Data Centers (SDCs). Two of these SDCs will monitor the instruments performance, while others will be responsible for providing large external data sets from ground-based surveys.

3.2.5 Surveys

Once Euclid reaches the L2 Sun-Earth Lagrangian position, it will start two different surveys that will take 6 years to be completed. One of these surveys is called the Euclid Wide Survey, and it will cover 15,000 $\deg^2$ of the sky down to a magnitude of 24.5 for VIS and 24 for NISP (see Fig. 3.4). It is nearly all the sky once the contamination from our Galaxy and our Solar System has been removed. This will be the core of the mission where most of the weak lensing and galaxy clustering signal will come from. The other survey will consist on 3 Euclid Deep Fields about 2 magnitudes deeper than the wide survey. They will cover in total around 40 $\deg^2$. These surveys will be basically used to calibrate the wide survey data, and observe high-redshift galaxies, quasars, and Active Galactic Nuclei (AGNs). In Fig. 3.8 we show a survey model for the mission.

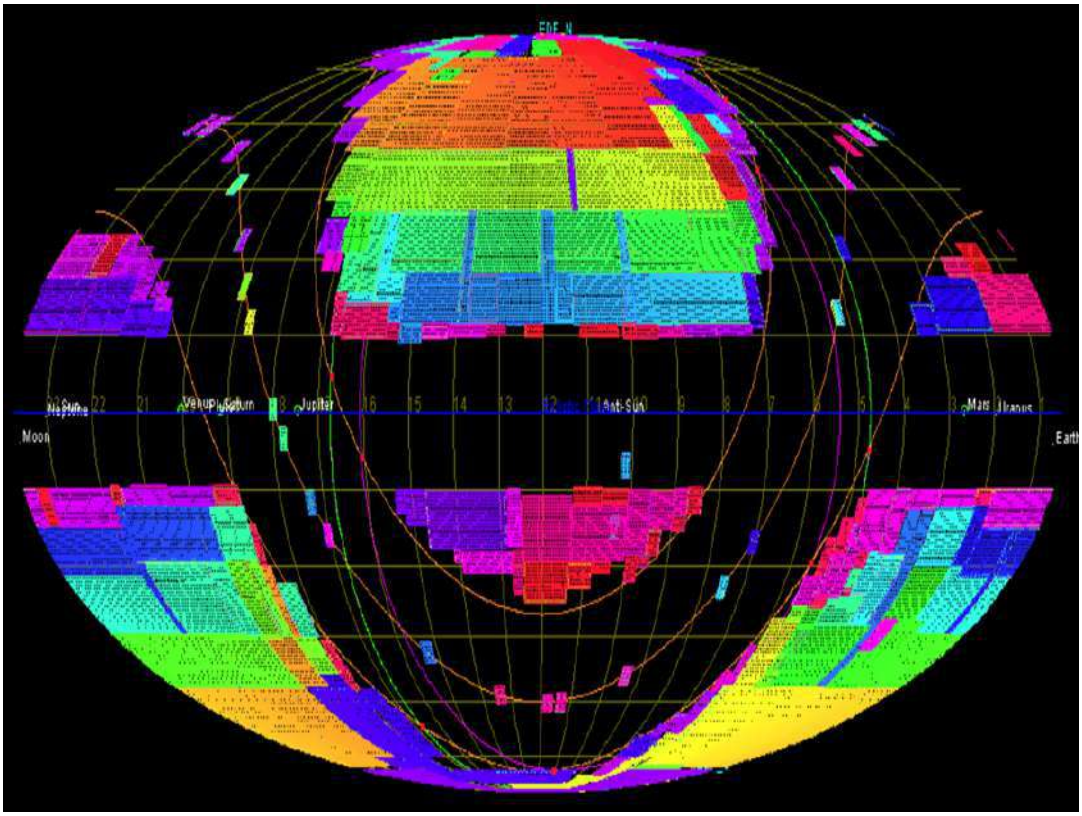

FIGURE 3.8: Portion of the sky covered by Euclid after 6 years of observations in ecliptic coordinates. [Credit: Euclid Consortium/ESA/Science Survey Working Group].

The colored areas of the sky correspond to the observed field (one color per year of observations). Each patch correspond to a $0.54\,\mathrm{deg}^2$ field of view (VIS and NISP shared field of view). The isolated patches over the galactic plane correspond to calibration fields. The methodology of observation will consist on waiting for both VIS and NISP observations in a field before moving to the following one. According to this, Euclid will be able to observe a strip of about $\sim 15\,\mathrm{deg}$ long per day, which will imply patches of $\sim 400\,\mathrm{deg}^2$ per month. Every 6 months the telescope will be pointed toward the opposite direction to survey the other hemisphere. After the 6 years of observations, Euclid will provide the shape and photometric redshifts of about 1.5×10^9 galaxies (photometric Euclid survey), and the spectroscopic redshift of about 5×10^7 galaxies (spectroscopic Euclid survey).

3.3 The Euclid Consortium

The Euclid Consortium (EC) is the single official scientific consortium (selected by ESA in June 2012) with the responsibility of the scientific instruments, the

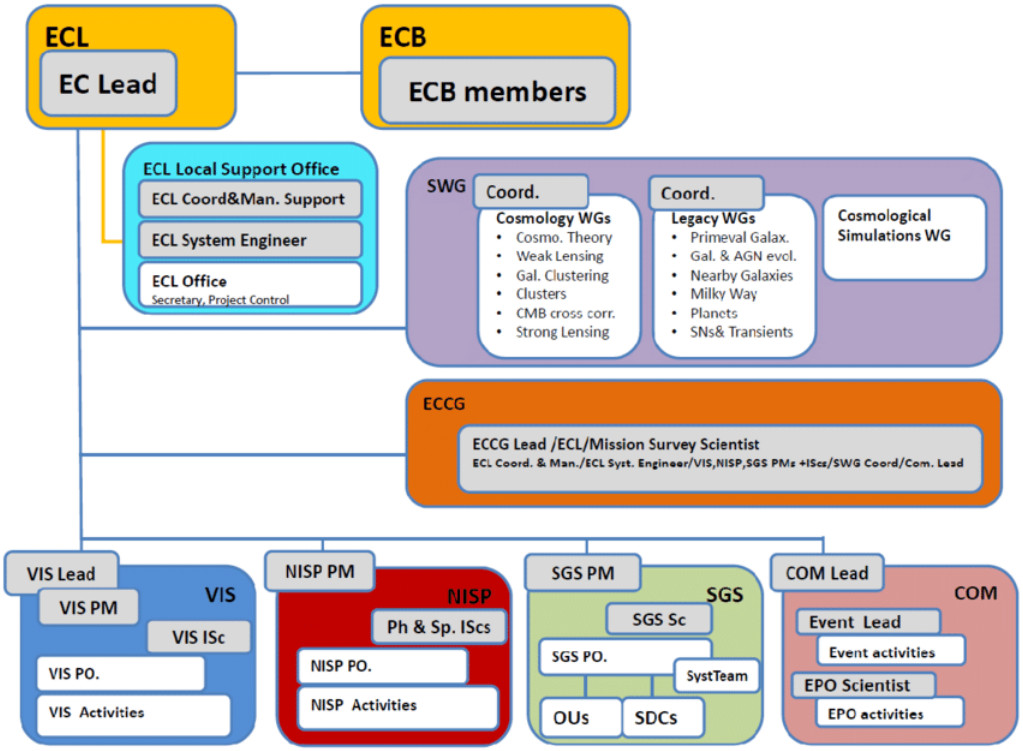

FIGURE 3.9: Top level organization of the EC from the Euclid Red-book [Laureijs et al., 2011].

production of the scientific data, and its scientific exploitation during all the duration of the mission. Because of this, it comprises researchers in theoretical physics, particle physics, astrophysics and space astronomy, as well as engineers, technicians, management, and administrative staff. In total there are around 1500 members in the EC. To date, in the EC there are national space agencies, national research organizations and research laboratories from 14 European countries (Austria, Belgium, Denmark, Finland, France, Germany, Italy, the Netherlands, Norway, Portugal, Romania, Spain, Switzerland, and the United Kingdom), Canada, and the USA (through NASA and a few US laboratories).

More in detail, the EC is responsible for the definition of the scientific goals, the mission concept, the science requirements, and the survey. It is also the responsibility of the EC to design, build, test, integrate, and deliver the VIS and NISP instruments to ESA (blue and red panels, respectively, in Fig. 3.9). The EC SGS (green panel in Fig. 3.9) is the group within the EC responsible for the design, test, integration and operation of the data processing tools, pipelines and SDCs. It comprises different Organizational Units (OUs), each one dedicated to a specific task, like providing the photometric redshifts, or measurements of the spectral features. The EC Science Working Groups (SWGs) (purple panel in Fig. 3.9), together with the EC SGS, have the responsibility of the

scientific production and delivery of Euclid data releases, and essentially their scientific exploitation. There are 3 types of SWGs: the cosmology SWGs (like weak lensing, galaxy clustering, or clusters of galaxies), the legacy SWGs (like planets, or the Milky Way), and the cosmological simulations SWG. The EC is led by the Euclid Consortium Lead (ECL) and a Euclid Consortium Board (ECB) (yellow panels in Fig. 3.9), which are also the primary contact points between the EC members and ESA.

3.4 The Inter-Science Taskforce for Forecasting

The Inter-Science Taskforce for Forecasting (IST) is an inter-SWG of the EC that was created to respond to the general need of a common forecasting pipeline. Before the IST, each SWG was producing their own forecasts, but it became clear that in order to have official, validated, and combined forecasts, a specific task-force between the different SWGs was needed. The IST started in February 2015, and its aim is to provide the official Fisher matrix forecasts for Euclid, after a detailed procedure of validation. The IST will end before the end of 2018 because its goal has been achieved (see Chapter 6), and it will lead to the creation of 2 new ISTs. One of them is the IST: Likelihood, with the responsibility of building the common likelihood for Euclid and prepare the pipeline for the future data, as well as providing more realistic forecasts than those using a Fisher matrix technique. The other one is the IST: Non-linear, with the responsibility of providing the non-linear recipe that should be used to correct for non-linearities in our predictions.

The IST is basically composed of 3 groups: the spectroscopic galaxy clustering (GCs) group, which focus on the galaxy clustering probe from the spectroscopic Euclid survey, the weak lensing group, and the cross-correlations (XC) group, which is responsible for the galaxy clustering of the photometric Euclid survey and the combination of all the probes taking into account their cross-correlations. Each group is then divided into 2 subgroups called recipe and baseline. The former is responsible for establishing the recipe that should be used when computing a Fisher matrix forecast for the specific probe, while the latter is responsible for the implementation of the recipe into several independent codes, and performing the code comparison to validate the results. A detailed description of the recipe and the code comparison for the different probes is presented in Chapter 6.

Chapter 4

$R_\mathrm{h} = ct$ and power law cosmologies confronted to CMB data

In this chapter we focus our interest on the so-called $R_\mathrm{h} = ct$ model, where the Universe is expanding without acceleration, and more general power law cosmologies, where the expansion of the Universe is given by a power law; i.e. we consider cosmologies in which the scale radius of the Universe evolves as a power law of cosmic time, $R(t) \propto t^n$. This kind of models, even if not being widely recognized in the community, have been proposed as an alternative to the standard cosmological model. It has even been claimed that they can fit the low-redshift observations better than the cosmological concordance model, ΛCDM (see next section). We examine here these models, introducing, for the first time, information coming from the cosmic microwave background, in addition to low-redshift data. In order to be as conservative as possible, we also allow for a redshift dependence of type Ia supernovae intrinsic luminosity. All the results presented in this chapter have been published in Tutusaus et al., 2016b.

4.1 Context

The cosmological concordance model framework offers a simple description of the properties of our Universe, but, since the dark contents of the Universe remain unidentified, alternative models still deserve to be investigated. A notable alternative to the ΛCDM model is the so-called power law cosmology, where the scale factor $a(t)$ evolves proportionally to a power of the cosmic time: $a(t) \propto t^n$. This class of models may for instance emerge when classical fields couple to spacetime curvature [Dolgov, 1997]. Predicted abundances by primordial nucleosynthesis seem problematic [Kaplinghat et al., 1999; Kaplinghat, Steigman, and Walker, 2000], but the confrontation to low-redshift data,

type Ia supernovae and the baryon acoustic oscillations may not be as problematic [Dolgov, Halenka, and Tkachev, 2014], although there is some controversy in the literature concerning the ability of the power law cosmology to fit these data [Shafer, 2015; Rani et al., 2015]. It seems therefore interesting to compare the performance of the standard ΛCDM model to those of power law models taking into account all standard cosmological probes.

Among these power law models stands the so-called $R_h = ct$ cosmology [Melia and Shevchuk, 2012], where $R_h = c/H(t)$ is the Hubble radius and $H(t)$ the Hubble parameter. This model, which is characterized by a total equation of state $\rho + 3p = 0$ (that is to say a total zero gravitational mass), turns out to be a particular case of the power law cosmology with exponent $n = 1$. From a theoretical point of view, there is some controversy on the motivation for such models [Melia, 2016b; Kim, Lasenby, and Hobson, 2016; Melia, 2017; Lewis, 2013; Lewis, Barnes, and Kaushik, 2016]. As in the general power law case, some studies claimed that this model is ruled out by observations [Bilicki and Seikel, 2012; Shafer, 2015], while some others claimed that $R_h = ct$ is able to fit the data even better than ΛCDM [Wei, 2015], and that it can explain a large amount of physics like the epoch of re-ionization [Melia and Fatuzzo, 2016], the high-redshift quasars [Melia, 2013], the CMB multipole alignment [Melia, 2015a] or the constancy of the cluster gas mass fraction [Melia, 2016a]. Again, as it is the case on the power law cosmologies, even if there is some controversy about this model and its ability to fit the observations, it is interesting to study it including new probes, and to test the concordance model against it.

In the following, we examine how the flat ΛCDM and power law models compare to the main cosmological probes, using robust model selection criteria. In this work, contrary to previous studies in the literature, we also allow for some SNIa intrinsic luminosity dependence with the redshift. Moreover, we consider the implication of the CMB properties, which certainly represents the most impressive success of the standard model, and use it in combination with the above-mentioned low-redshift probes.

4.2 Models

In this section we present the models studied in this chapter: the power law and the $R_h = ct$ cosmologies. We recall that the standard equations for the background expansion in the flat ΛCDM model have been given in Sec. 1.1.5. Let us just mention that we fix[1] $N_{\rm eff} = 3.04$ [Planck Collaboration, 2016b], the effective number of neutrino-like relativistic degrees of freedom, $H_0 = 67.74\,{\rm km\,s^{-1}Mpc^{-1}}$ [Planck Collaboration, 2016b] and $T_{\rm CMB} = 2.725$ [Fixsen,

[1] We have checked that small variations on these parameters do not affect the results.

2009], the temperature of the CMB today. Notice that we only fix H_0 for the radiation contribution. It is left free in the rest of the chapter.

The main assumption in power law cosmologies is that the scale factor evolves as a power of the cosmic time,

$$a(t) = \left(\frac{t}{t_0}\right)^n , \tag{4.1}$$

where n is the power of the model and $a(t_0) = 1$. This provides us with the Hubble parameter,

$$H(z) = H_0(1+z)^{1/n} , \tag{4.2}$$

which leads to the co-moving distance,

$$\chi(z) = \frac{c}{H_0} \times \begin{cases} \frac{(1+z)^{1-1/n}-1}{1-1/n} , & n \neq 1 , \\ \ln(1+z) , & n = 1 . \end{cases} \tag{4.3}$$

Notice that an expanding Universe requires $0 < n < \infty$. If $n > 1$, the expansion is accelerated, while it decelerates if $0 < n < 1$. The special case $n = 1$ corresponds to the $R_\mathrm{h} = ct$ cosmology. Indeed, this model states that the Hubble radius $R_\mathrm{h} = c/H(t)$ is proportional to time, so we can write $H(t) = t^{-1}$, and therefore $a(t) \propto t$, for this model.

Figure 4.1 shows the variation with redshift of the Hubble parameter $H(z)$ for these three models. The matter and radiation contributions have been fixed to 0.3 and 8×10^{-5}, respectively, while the Hubble constant has been fixed to $68\,\mathrm{km\,s^{-1}Mpc^{-1}}$, for illustrative purposes.

4.3 Method

In this section we review the statistical tools used to quantify the goodness-of-fit and to compare the models under study.

4.3.1 Goodness-of-fit and effect of correlations

To quantify the capacity of a model to fit the data we minimize the common χ^2 function,

$$\chi^2 = (\boldsymbol{u} - \boldsymbol{u}_\mathrm{data})^T C^{-1} (\boldsymbol{u} - \boldsymbol{u}_\mathrm{data}) , \tag{4.4}$$

using the `migrad` application from the `iminuit` Python package [2], designed for finding the minimum value of a multi-parameter function and analyzing the

[2] https://github.com/iminuit/iminuit

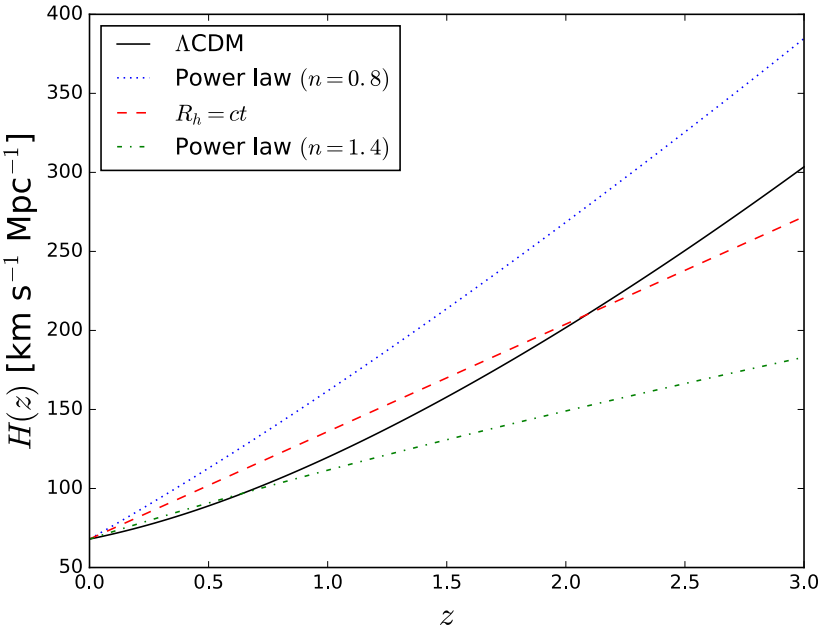

FIGURE 4.1: Hubble parameter as a function of the redshift for ΛCDM, $R_h = ct$ cosmology and two different power law cosmologies. Ω_m, Ω_r and H_0 have been fixed to 0.3, 8×10^{-5} and $68\,\mathrm{km\,s^{-1}Mpc^{-1}}$, respectively, for illustrative purposes.

shape of the function around the minimum. This code is the Python implementation of the former `minuit` Fortran code [James and Roos, 1975] (see Sec. 2.2.2 for a more detailed description of `minuit`). In Eq. (4.4), $\boldsymbol{u}$ stands for the model prediction, while $\boldsymbol{u}_{\rm data}$ and C^{-1} hold for the observables and their inverse covariance matrix, respectively. We then compute the probability, $P(\chi^2, \nu)$, that a larger value for the χ^2 could occur for a fit with $\nu = N - k$ degrees of freedom, where N is the number of data points and k is the number of free parameters of the model [Eq. (2.30)]. When combining different probes, we minimize the χ^2 function given by the sum of the individual χ^2's, i.e., we assume that the probes are statistically independent.

It is important to notice that Eq. (2.30) is only valid when we work with N data points coming from N independent random variables with Gaussian distributions. However, in this work we consider the correlation within probes; i.e. we take into account the correlations between SNIa measurements, as well as the correlations between BAO measurements. Thus, the data points come from non-independent Gaussian random variables, even if we neglect the correlations between different probes. In order to check the impact of correlations on this probability we compute the histogram of χ^2 through Monte Carlo simulations with and without correlations. First of all, we generate a vector $\boldsymbol{v} = \boldsymbol{u} -$

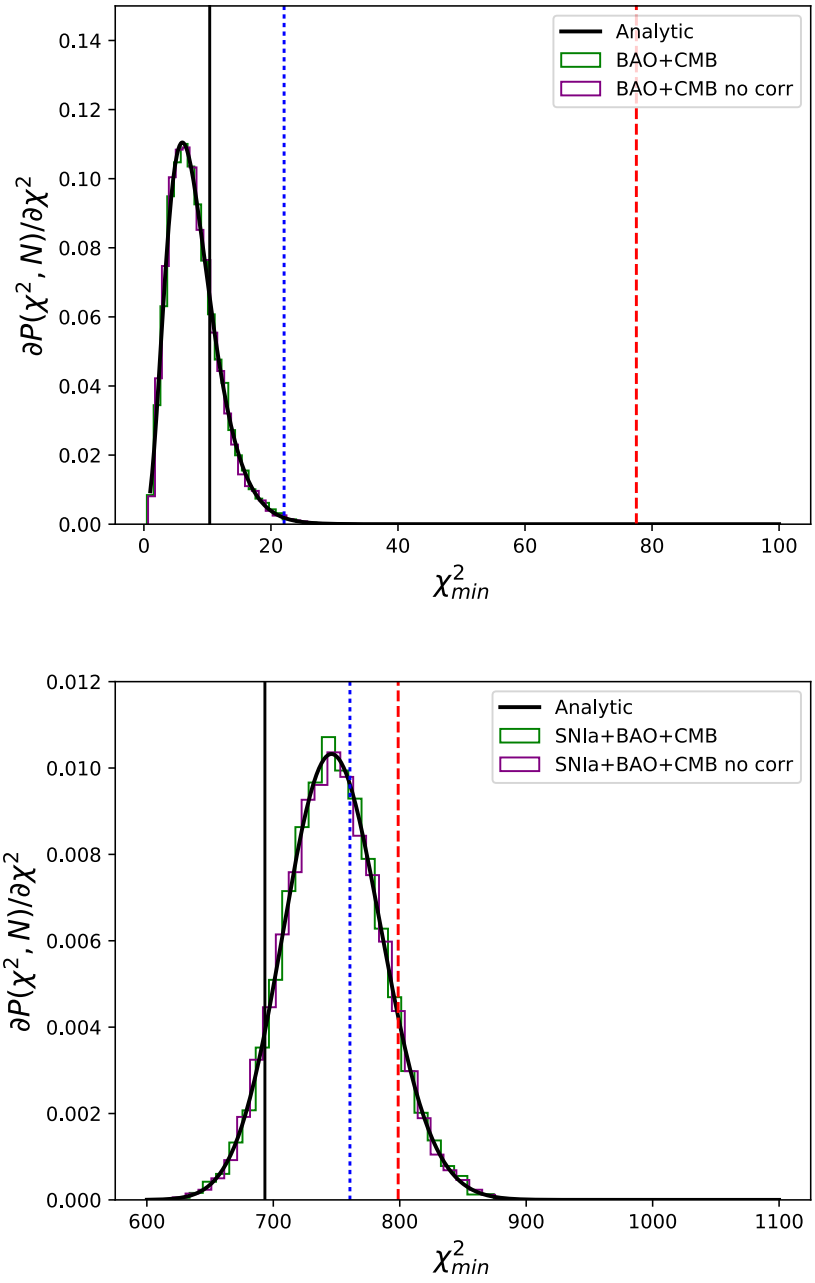

FIGURE 4.2: Histograms of χ^2 for Monte Carlo simulations [to study the impact of correlations in Eq. (2.30)] using correlations (green) and neglecting them (purple). The analytic distribution is also represented for further comparison (thick black solid line). The compatibility of the three distributions in each plot shows that Eq. (2.30) can be used in this work. The measured values of the minimum of the χ^2 are also represented, only for illustrative purposes, for each model and each combination of probes used (see Table 4.2. Black solid line, ΛCDM; blue dotted line, power law cosmology; red dashed line, $R_h = ct$ cosmology). *Top plot*: BAO+CMB covariance matrix with M=10000 iterations. *Bottom plot*: SNIa+BAO+CMB covariance matrix with M=10000 iterations.

$\boldsymbol{u}_{\rm data}$ from an N-dimensional Gaussian distribution centered at $\mathbf{0}$ and with the corresponding covariance matrix C for the probes used. Notice that we save computation time by directly generating the difference $\boldsymbol{u} - \boldsymbol{u}_{\rm data}$, since we do not need then to fit a specific model each time we compute a χ^2. Notice also that there are no parameters in this case; thus, $k = 0$ and $\nu = N$. We then compute the χ^2 using Eq. (4.4) and we repeat M times to obtain the histograms shown in Fig. 4.2. When neglecting correlations, we consider only the diagonal terms of C both when generating the $\boldsymbol{u} - \boldsymbol{u}_{\rm data}$ vector and when computing the χ^2 value.

In the top plot we use the covariance matrix for BAO and CMB data. We can clearly observe that the histogram obtained with correlations (green) is completely consistent with the histogram obtained neglecting any correlation (purple). Moreover, both of them are consistent with the analytic distribution (thick black solid line), which is given by the derivative of Eq. (2.30) with respect to χ^2. Notice that we have neglected here the number of free parameters of the model because we are directly generating several realizations of the vector $\boldsymbol{v} = \boldsymbol{u} - \boldsymbol{u}_{\rm data}$. The fact that the three distributions are essentially the same implies that the correlations in the BAO+CMB covariance matrix do not affect Eq. (2.30) and we can safely use it. In the bottom plot of Fig. 4.2 we have the equivalent results using the covariance matrix for SNIa, BAO and CMB. As before, the three distributions are completely consistent, implying that we can use Eq. (2.30) with these correlations. A particularity in this case is that the covariance matrix is not completely independent of the cosmology: as discussed in the following sections, the covariance matrix depends on two SNIa nuisance parameters. In order to correctly predict the effect of these correlations, we need to consider these nuisance parameters and determine them when fitting each model under study to the M mock data samples. However, we keep the approach of generating realizations of $\boldsymbol{u} - \boldsymbol{u}_{\rm data}$, due to the fact that the two SNIa nuisance parameters remain very close to $\alpha = 0.14$ and $\beta = 3.1$, as can be seen in Table 4.1.

In Fig. 4.3 we show, for completeness, the correlation matrices for SNIa and BAO measurements. We can see for the former probe that even if some SNIa are correlated ($\sim 30\,\%$), the mean correlation (after removing the diagonal is of only $\sim 6\,\%$. We can also observe that only two pairs of data points are correlated for BAO, with a percentage close to $50\,\%$.

4.3.2 Model comparison

In this section we consider the two widely used criteria to compare the models under study presented in Sec. 2.4: the Akaike information criterion [Akaike, 1973] and the Bayesian information criterion [Schwarz, 1978].

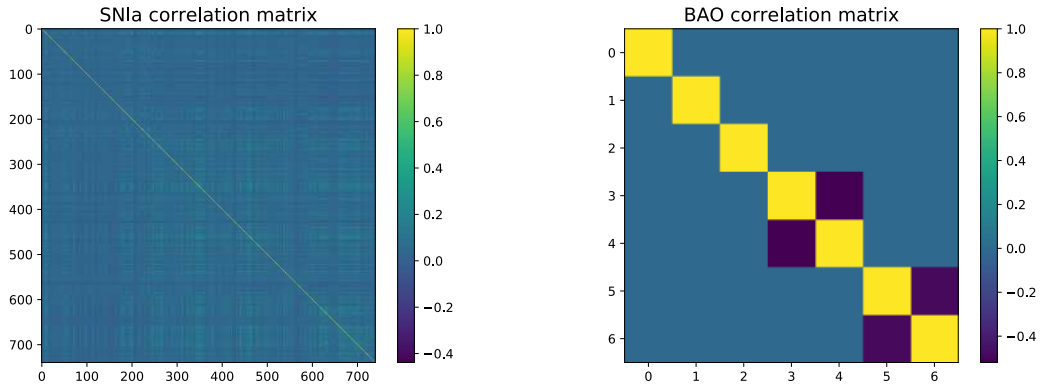

FIGURE 4.3: Correlation matrices for the cosmological measurements used in this chapter. *Left panel*: 740 SNIa measurements ranging from 0 to 739, with the SNIa nuisance parameters α and β fixed to 0.14 and 3.1, respectively. *Right panel*: 7 BAO measurements ranging from 0 to 6, increasing the redshift. The last two pairs of data points are the only ones showing some correlation.

Let us recall that the second-order AIC (AICc) and the BIC strongly depend on the size of the sample. Therefore, in order to compare different models we use the exponential of the differences ΔAICc/2 (ΔBIC/2), where ΔAICc=AICc$_{\Lambda\text{CDM}}$-AICc (Id. for the BIC), which can be interpreted as the relative probability of preference of one model with respect to ΛCDM. Let us also point out that if we compare two models with the same data sample and the same number of parameters, as it is the case for ΛCDM and power law with SNIa data ($N = 740$, $k = 5$), ΔAIC and ΔBIC basically reduce to $\Delta\chi^2_{\text{min}} = \chi^2_{\Lambda\text{CDM}} - \chi^2$. This leads to the same numerical values for $\exp(\Delta\text{AICc}/2)$ and $\exp(\Delta\text{BIC}/2)$ for ΛCDM and power law models in Table 4.2.

4.4 Cosmological probes

In this section we describe the cosmological probes and the corresponding data sets used to compare the different models presented. We only describe the specificities concerning this chapter. The general description of the different probes has already been provided in Sec. 1.5.

4.4.1 Type Ia supernovae

In this work we use the joint light-curve analysis for SNIa from Betoule et al., 2014. It is important to stress that the covariance matrix provided by

the authors depends on the stretch and color nuisance parameters, α and β respectively, so we recompute the covariance matrix at each step of the χ^2 minimization with the corresponding values for these parameters.

In some specific cases during this chapter, we relax the redshift independence assumption made in Betoule et al., 2014. In order to account for a possible SNIa luminosity dependence (SNIa+ev) with redshift (caused by some astrophysical procedures, for example) we add an extra nuisance parameter ϵ to the distance modulus estimate [see Eq. (1.144)],

$$\mu_{\rm obs} = m_{\rm B}^{*} - (M_{\rm B} - \alpha \times X_1 + \beta \times C - \epsilon \times z)\,. \tag{4.5}$$

A much more detailed study concerning SNIa intrinsic luminosity dependence on the redshift is presented in the next chapter.

When using SNIa data, we consider the following set of nuisance parameters: $\{\alpha,\ \beta,\ M_{\rm B}^1,\ \Delta_{\rm M},\ \epsilon\}$ (see Sec. 1.5.1). For ΛCDM and the power law cosmology we consider the matter energy density, $\Omega_{\rm m}$, and n, respectively, as cosmological parameters. Notice that there is no free cosmological parameter when using SNIa data with the $R_h = ct$ cosmology.

4.4.2 Baryon acoustic oscillations

In the ΛCDM model, the BAO come from the sound waves propagating in the early Universe and the standard ruler $r_{\rm d}$ is equal to the co-moving sound horizon at the redshift of the baryon drag epoch: $r_{\rm d} = r_{\rm s}(z_{\rm d})$, $z_{\rm d} \approx 1060$. For models differing from the ΛCDM model, $r_{\rm d}$ does not need to coincide with $r_{\rm s}(z_{\rm d})$ [Verde et al., 2017b]. In order to be as general as possible, we do not delve into the physics governing the sound horizon $r_{\rm d}$, so we consider $r_{\rm d}$ as a free parameter.

In this chapter, we follow Aubourg et al., 2015, in combining the measurements of 6dFGS [Beutler et al., 2011], SDSS [Main Galaxy Sample (MGS)] [Ross et al., 2015], BOSS (CMASS and LOWZ samples - Data Release 11) [Tojeiro et al., 2014; Anderson et al., 2014] and BOSS Lyman-α forest (Data Release 11) [Delubac, T. et al., 2015; Font-Ribera et al., 2014]. As in Shafer, 2015, we assume that all the measurements are independent, apart from the CMASS anisotropic measurements (correlated with coefficient -0.52) and the Lyman-α forest measurements (correlated with coefficient -0.48).

According to Bassett and Afshordi, 2010, when we want to constrain parameters to a high confidence level or when we want to claim that a model is a poor fit to the data, we should take into account that BAO observable likelihoods are not Gaussian far from the peak. In this work we follow the same approach

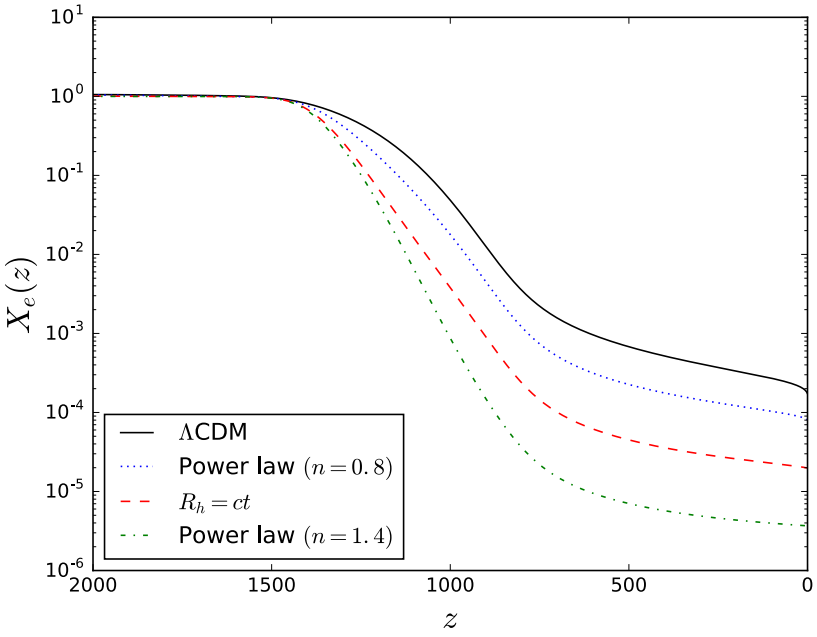

FIGURE 4.4: Free electron function X_e as a function of the redshift for ΛCDM, $R_\mathrm{h} = ct$ cosmology and two different power law cosmologies. The parameters relevant for re-ionization have been fixed to the Planck 2015 values for illustrative purposes [Planck Collaboration, 2016b] (helium mass fraction, CMB temperature at $z = 0$, Ω_m, Ω_b, Ω_K, h and N_eff).

and account for this effect by replacing the usual expression for a Gaussian likelihood observable, $\Delta\chi^2_\mathrm{G} = -2\ln\mathcal{L}_\mathrm{G}$, by

$$\Delta\chi^2 = \frac{\Delta\chi^2_\mathrm{G}}{\sqrt{1 + \Delta\chi^4_\mathrm{G}\left(\frac{S}{N}\right)^{-4}}}\,, \tag{4.6}$$

where S/N is the corresponding detection significance, in units of σ, of the BAO feature. Following Shafer, 2015, we consider a detection significance of 2.4σ for 6dFGS, 2σ for SDSS MGS, 4σ for BOSS LOWZ, 6σ for BOSS CMASS and 4σ for BOSS Lyman-α forest.

When using BAO data, we consider the following set of cosmological parameters: $\{r_\mathrm{d} \times H_0/c,\, \Omega_\mathrm{m},\, n\}$. The latter two only apply for ΛCDM and power law cosmology, respectively. We do not consider any nuisance parameter.

4.4.3 Cosmic microwave background

In this section we present the high-redshift probe used, the cosmic microwave background, and the approach we follow in order to consider this probe in our study, including power law models.

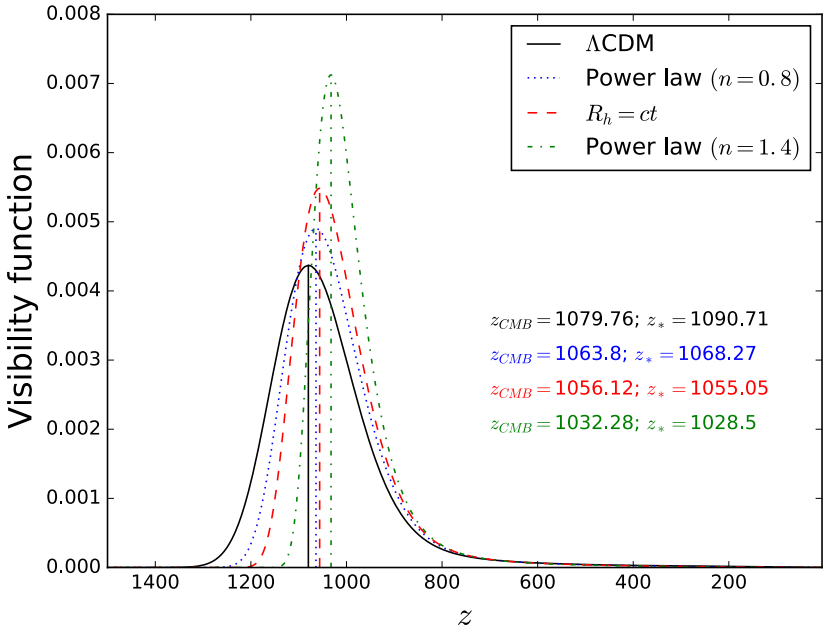

FIGURE 4.5: Visibility function as a function of the redshift for ΛCDM (black), $R_{\rm h} = ct$ cosmology (red) and $n = 0.8$, 1.4 power law cosmologies (blue and green, respectively). We show the redshift of the CMB computed with two different definitions (see the text for details).

In standard cosmology, the physics governing the sound horizon at the early Universe is that of a baryon-photon plasma in an expanding Universe. The observed angular scale of the sound horizon at recombination, ℓ_a [Eq. (1.148)], then depends on the angular distance to the CMB, a physical quantity sensitive to the expansion history up to the redshift of the last scattering, and thereby to the background history of models [Blanchard, 1984]. Notice that ℓ_a roughly corresponds to the position of the first peak of the temperature angular power spectrum of the CMB. Although this is only one parameter, it is well known that reduced parameters capture a large fraction of the information contained in the CMB fluctuations of the angular power spectra [Wang and Mukherjee, 2007]. We use the value provided by the Planck Collaboration [Planck Collaboration, 2016c]: $\ell_a = 301.63 \pm 0.15$ and, in the following of this chapter, we refer to this information as CMB data. It has been obtained from Planck temperature and low-ℓ polarization data [3]. Marginalization over the amplitude of the lensing power spectrum has been performed, since it leads to a more conservative approach.

[3] Although ℓ_a is one of the reduced parameters of the CMB and therefore its value from Planck data has been obtained assuming the ΛCDM model, it is the most model independent reduced parameter.

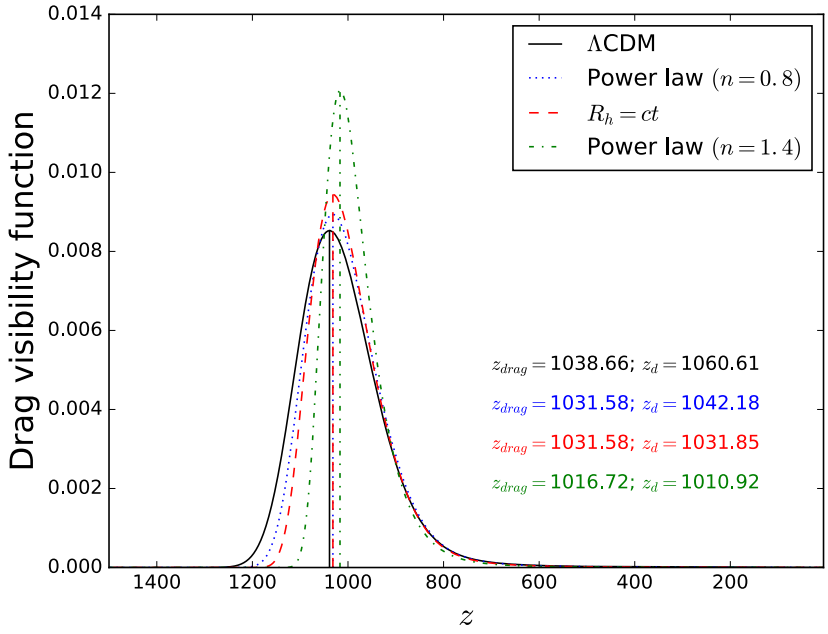

FIGURE 4.6: Drag visibility function as a function of the redshift for ΛCDM (black), $R_\mathrm{h} = ct$ cosmology (red) and $n = 0.8$, 1.4 power law cosmologies (blue and green, respectively). The redshift of the drag epoch computed with two different definitions is presented (see the text for details).

Although the computation of ℓ_a is simple in the concordance model (see Sec. 1.5.2), it can be not straightforward for exotic models significantly differing from ΛCDM. In the following we present in detail how we compute this quantity, and how we add add it into the analysis.

According to Melia, 2015b, the $R_\mathrm{h} = ct$ universe assumes the presence of dark energy and radiation in addition to baryonic and dark matter. The only requirement of this model is to constrain the total equation of state by requiring $\rho + 3p = 0$. Following this definition, and extending the idea to the power law cosmology, we infer that the physics governing the sound horizon at the early Universe is the same as for ΛCDM, since we are again essentially dealing with a baryon-photon plasma in an expanding universe. This assumption has already been made in the literature. In Benoit-Lévy and Chardin, 2012, for example, the authors considered the Dirac-Milne universe (a matter-antimatter symmetric cosmology) and kept the same expression for the co-moving sound horizon at the last scattering redshift, $r_\mathrm{s}(z_*)$ [see Eq. (1.149)], as in the ΛCDM case.

Starting with ΛCDM, in order to compute ℓ_a we first need to obtain $r_\mathrm{s}(z_*)$, which requires the baryon density in the Universe. We use the value provided

in Planck Collaboration, 2016b, for $\Omega_\mathrm{b}h^2 = 0.02230$ and we use Eq. (1.65) for the radiation contribution.

For a power law cosmology,

$$r_\mathrm{s}(z_*) \propto \int_{z_*}^{\infty} \frac{(1+z)^{1/2}}{(1+z)^{1/n}}\,\mathrm{d}z \tag{4.7}$$

converges only for $n < 2/3$; therefore, there is already a fundamental problem in these theories when describing the early Universe. This divergence also exists for the sound horizon $r_\mathrm{s}(z_\mathrm{d})$ in the BAO. Given that the Big Bang nucleosynthesis already suffers from a problem in the early Universe in this model [Lewis, Barnes, and Kaushik, 2016], one might imagine that the physics of the early Universe allows us to solve this issue, essentially by restoring the standard model in the very early Universe, keeping the sound horizon finite. In other words, we might assume that the standard ruler r_d is finite and a free parameter of our model. Since it is now an unknown quantity, we have to obtain its value by fitting it to the data. We can then develop $r_\mathrm{s}(z_*)$ as

$$r_\mathrm{s}(z_*) = \int_{z_*}^{\infty} \frac{c_\mathrm{s}(z)\,\mathrm{d}z}{H(z)} = r_\mathrm{d} - \int_{z_\mathrm{d}}^{z_*} \frac{c_\mathrm{s}(z)\,\mathrm{d}z}{H(z)}\,, \tag{4.8}$$

where the sound speed, $c_\mathrm{s}(z)$, is given by Eq. (1.150).

In Benoit-Lévy and Chardin, 2012, the authors also had to deal with this divergence near the initial singularity. They opted for putting upper and lower bounds to the integral on physically motivated grounds, while we allow the data to determine r_d and avoid the divergence.

We now need to determine z_d and z_* for all the models. A common definition of the redshift of the CMB is given by the maximum of the visibility function [Hu and Sugiyama, 1996],

$$g(z) = \dot{\tau}(z)e^{-\tau(z)}\,, \tag{4.9}$$

where $\tau(z)$ is the optical depth [Liu et al., 2016a],

$$\tau(z) = \sigma_\mathrm{T} \int_0^z n_e(z') \frac{c}{(1+z')H(z')}\,\mathrm{d}z'\,, \tag{4.10}$$

with σ_T being the Thomson cross section and n_e the free electron number density. This definition is well motivated because the visibility function can be understood as the probability of the last photons of the CMB to scatter; thus, the maximum provides us with the most probable redshift of this last scattering. In order to obtain n_e we need to calculate the free electron fraction X_e and further multiply it by the hydrogen number density,

TABLE 4.1: Best-fit values for the cosmological and nuisance parameters of the studied models (ΛCDM, power law, and $R_h = ct$ cosmologies) with the different cosmological probes considered [SNIa(+ev), BAO, and CMB].

		Ω_m	n	$r_d \times H_0/c$	α	β	M_B^1	Δ_M	ϵ
ΛCDM	SNIa	0.295 ± 0.034	-	-	0.1412 ± 0.0066	3.101 ± 0.081	24.110 ± 0.023	-0.070 ± 0.023	-
	BAO	0.289 ± 0.021	-	0.03377 ± 0.00057	-	-	-	-	-
	SNIa+BAO	0.291 ± 0.018	-	0.03373 ± 0.00050	0.1413 ± 0.0066	3.103 ± 0.080	24.110 ± 0.019	-0.070 ± 0.023	-
	SNIa+ev	0.49 ± 0.17	-	-	0.1410 ± 0.0066	3.100 ± 0.081	24.120 ± 0.025	-0.070 ± 0.023	-0.23 ± 0.19
	SNIa+ev+BAO	0.291 ± 0.021	-	0.03373 ± 0.00057	0.1413 ± 0.0066	3.103 ± 0.081	24.110 ± 0.022	-0.070 ± 0.023	-0.001 ± 0.055
	BAO+CMB	0.307 ± 0.011	-	0.03348 ± 0.00049	-	-	-	-	-
	SNIa+BAO+CMB	0.306 ± 0.010	-	0.03353 ± 0.00045	0.1411 ± 0.0066	3.098 ± 0.080	24.110 ± 0.018	-0.070 ± 0.023	-
	SNIa+ev+BAO+CMB	0.308 ± 0.011	-	0.03345 ± 0.00049	0.1413 ± 0.0066	3.103 ± 0.081	24.110 ± 0.022	-0.070 ± 0.023	-0.024 ± 0.049
Power law	SNIa	-	1.55 ± 0.13	-	0.1408 ± 0.0066	3.100 ± 0.081	24.130 ± 0.023	-0.071 ± 0.023	-
	BAO	-	0.908 ± 0.019	0.02963 ± 0.00040	-	-	-	-	-
	SNIa+BAO	-	1.46 ± 0.11	0.03313 ± 0.00059	0.1404 ± 0.0066	3.094 ± 0.080	24.140 ± 0.023	-0.072 ± 0.023	-
	SNIa+ev	-	3.7 ± 5.1	-	0.1410 ± 0.0066	3.100 ± 0.081	24.120 ± 0.024	-0.071 ± 0.023	0.31 ± 0.32
	SNIa+ev+BAO	-	0.910 ± 0.019	0.02967 ± 0.00040	0.1404 ± 0.0066	3.100 ± 0.081	24.150 ± 0.022	-0.072 ± 0.023	-0.354 ± 0.049
	BAO+CMB	-	0.7345 ± 0.0025	0.02758 ± 0.00029	-	-	-	-	-
	SNIa+BAO+CMB	-	1.545 ± 0.067	0.402 ± 0.054	0.1408 ± 0.0066	3.100 ± 0.080	24.130 ± 0.019	-0.071 ± 0.023	-
	SNIa+ev+BAO+CMB	-	3.330 ± 0.089	1.019 ± 0.068	0.1409 ± 0.0066	3.100 ± 0.081	24.120 ± 0.022	-0.071 ± 0.023	0.292 ± 0.047
$R_h = ct$	SNIa	-	-	-	0.1382 ± 0.0066	3.073 ± 0.080	24.230 ± 0.017	-0.077 ± 0.023	-
	BAO	-	-	0.03045 ± 0.00031	-	-	-	-	-
	SNIa+BAO	-	-	0.03045 ± 0.00031	0.1382 ± 0.0066	3.073 ± 0.080	24.230 ± 0.017	-0.077 ± 0.023	-
	SNIa+ev	-	-	-	0.1405 ± 0.0066	3.100 ± 0.081	24.140 ± 0.022	-0.072 ± 0.023	-0.277 ± 0.046
	SNIa+ev+BAO	-	-	0.03045 ± 0.00031	0.1405 ± 0.0066	3.100 ± 0.081	24.140 ± 0.022	-0.072 ± 0.023	-0.277 ± 0.046
	BAO+CMB	-	-	0.083770 ± 0.000036	-	-	-	-	-
	SNIa+BAO+CMB	-	-	0.083770 ± 0.000036	0.1382 ± 0.0066	3.073 ± 0.080	24.230 ± 0.017	-0.077 ± 0.023	-
	SNIa+ev+BAO+CMB	-	-	0.083770 ± 0.000036	0.1405 ± 0.0066	3.100 ± 0.081	24.140 ± 0.022	-0.072 ± 0.023	-0.277 ± 0.046

TABLE 4.2: Goodness-of-fit and model comparison between the models studied (ΛCDM, power law, and $R_h = ct$ cosmologies) with the different cosmological probes considered [SNIa(+ev), BAO, and CMB]. The last two columns for ΛCDM and power law cosmology are combined because $\exp(\Delta\text{AICc}/2) = \exp(\Delta\text{BIC}/2)$ in these cases (see the text for details).

		k	N	χ^2_{min}	$P(\chi^2, \nu)$	$\exp(\Delta\text{AICc}/2)$	$\exp(\Delta\text{BIC}/2)$
ΛCDM	SNIa	5	740	682.89	0.915	1	
	BAO	2	7	9.57	0.088	1	
	SNIa+BAO	6	747	692.49	0.898	1	
	SNIa+ev	6	740	681.90	0.916	1	
	SNIa+ev+BAO	7	747	692.48	0.893	1	
	BAO+CMB	2	8	10.36	0.110	1	
	SNIa+BAO+CMB	6	748	693.36	0.899	1	
	SNIa+ev+BAO+CMB	7	748	693.13	0.895	1	
Power law	SNIa	5	740	682.90	0.915	0.998	
	BAO	2	7	4.13	0.531	15.198	
	SNIa+BAO	6	747	703.71	0.833	0.0036	
	SNIa+ev	6	740	682.20	0.914	0.860	
	SNIa+ev+BAO	7	747	690.03	0.905	3.421	
	BAO+CMB	2	8	22.07	0.0012	0.0029	
	SNIa+BAO+CMB	6	748	760.61	0.310	2.501×10^{-15}	
	SNIa+ev+BAO+CMB	7	748	759.93	0.307	3.127×10^{-15}	
$R_h = ct$	SNIa	4	740	721.22	0.644	1.308×10^{-8}	1.291×10^{-7}
	BAO	1	7	15.68	0.016	0.385	0.125
	SNIa+BAO	5	747	736.90	0.546	6.251×10^{-10}	6.184×10^{-9}
	SNIa+ev	5	740	685.00	0.906	0.588	5.793
	SNIa+ev+BAO	6	747	700.67	0.853	0.046	0.455
	BAO+CMB	1	8	77.53	4.39×10^{-14}	1.680×10^{-14}	7.349×10^{-15}
	SNIa+BAO+CMB	5	748	798.75	0.077	3.598×10^{-23}	3.562×10^{-22}
	SNIa+ev+BAO+CMB	6	748	762.52	0.293	2.363×10^{-15}	2.332×10^{-14}

$$n_e(z) = X_e(z) \left[\frac{3H_0^2 \Omega_\mathrm{b}}{8\pi G m_\mathrm{H} \mu} (1+z)^3 \right] , \tag{4.11}$$

where m_H is the mass of the hydrogen atom and $\mu = 1/(1-Y)$ with Y being the helium mass fraction.

The free electron fraction, or ionization history, $X_e(z)$ depends on the expansion rate. In order to obtain it we use the `Recfast++` [Chluba and Thomas, 2011] code [4], based on the C version of `Recfast` [Seager, Sasselov, and Scott, 1999], adapting the expansion history to the corresponding one for each model. This new version includes recombination corrections [Chluba and Thomas, 2011; Rubiño-Martín et al., 2010] and allows us to run a dark matter annihilation module [Chluba, 2010]. It also includes a new ordinary differential equations solver [Chluba, Vasil, and Dursi, 2010]. More details about this code can be found in Switzer and Hirata, 2008; Grin and Hirata, 2010; Ali-Haïmoud and Hirata, 2010. Figure 4.4 provides a comparison between X_e for the different power law cosmologies and ΛCDM. We have neglected the recombination corrections and dark matter annihilations because this level of precision in the X_e determination is not needed for our purposes.

Another definition for the redshift of the CMB is the one adopted by the Planck Collaboration [Planck Collaboration, 2016b] by determining the redshift when the optical depth equals 1. We denote z_CMB the redshift obtained with the first definition [Eq. (4.9)] and z_* the redshift obtained with the Planck Collaboration convention. Although we use z_* for consistency with Planck when performing our analyses, we have defined z_CMB for illustrative and comparative purposes.

In Fig. 4.5 we show the visibility functions for ΛCDM, $R_\mathrm{h} = ct$ cosmology and two power law cosmologies ($n = 0.8$ and $n = 1.4$). In this case we have fixed the cosmological parameters to ΛCDM present-day values: $Y = 0.249$, $\Omega_\mathrm{m} = 0.3089$, $\Omega_\mathrm{b} = 0.0485976$, $N_\mathrm{eff} = 3.04$ and $H_0 = 67.74\,\mathrm{km\,s^{-1}Mpc^{-1}}$ [Planck Collaboration, 2016b]. However, we have checked that any variation of 25% in one of these parameters has a negligible impact on the redshift of the CMB (less than 0.6%) for a fixed model and that it has no influence in our study. Even if the redshift of the CMB does not change significantly with the parameters, it does change with the model; therefore we fix $z_* = 1090.71$ for ΛCDM and $z_* = 1055.05$ for the $R_\mathrm{h} = ct$ cosmology. Concerning the power law cosmology, since the redshift changes significantly with n, we interpolate z_* as a function of n.

The redshift of the baryon drag epoch can be defined in two analogous

[4] http://www.cita.utoronto.ca/~jchluba/Science_Jens/Recombination/Recfast++.html

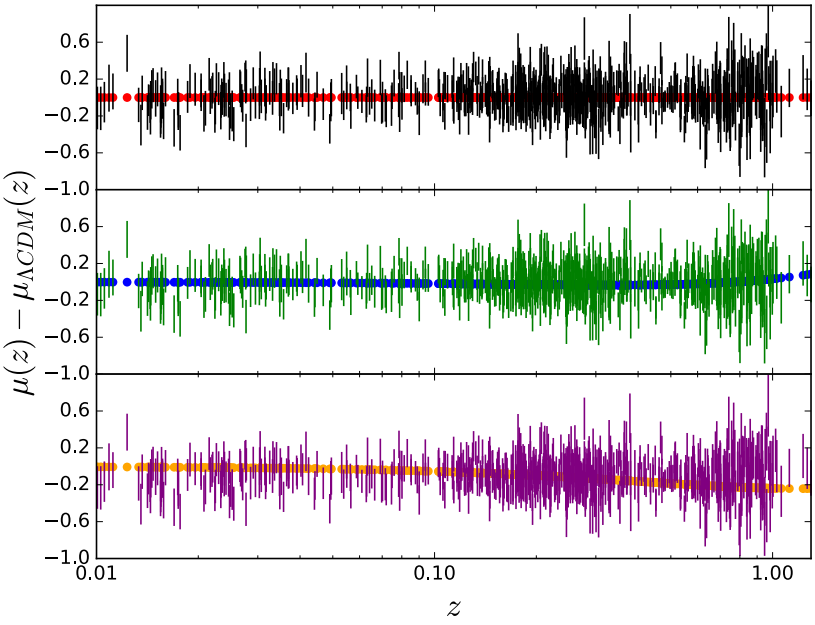

FIGURE 4.7: Fit from the three models under study to the SNIa data. All the plots show the residuals with respect to the prediction from ΛCDM with the best-fit values. *Top panel*: SNIa measurements standardized to ΛCDM (black) and ΛCDM prediction (red) as a function of the redshift. *Central panel*: SNIa measurements standardized to power law cosmology (green) and power law cosmology prediction (blue) as a function of the redshift. *Bottom panel*: SNIa measurements standardized to $R_h = ct$ cosmology (purple) and $R_h = ct$ cosmology prediction (orange) as a function of the redshift. For each model we marginalize over the nuisance parameters.

ways. We first consider the definition given by a drag visibility function [Hu and Sugiyama, 1996],

$$g_d(z) = \dot{\tau}_d(z) e^{-\tau_d(z)}\,, \tag{4.12}$$

where the drag optical depth is given by,

$$\tau_d(z) = \int_0^z \frac{\dot{\tau}(z')}{R_b(z')}\,dz'\,, \tag{4.13}$$

with R_b defined in Eq. (1.150). We denote the maximum of this drag visibility function z_{drag}. The second definition (the one adopted by the Planck Collaboration [Planck Collaboration, 2016b]) is given by the redshift at which the drag optical depth equals 1. We denote it z_d. As before, we use z_d to be consistent with Planck, but we keep both definitions for illustrative and comparative

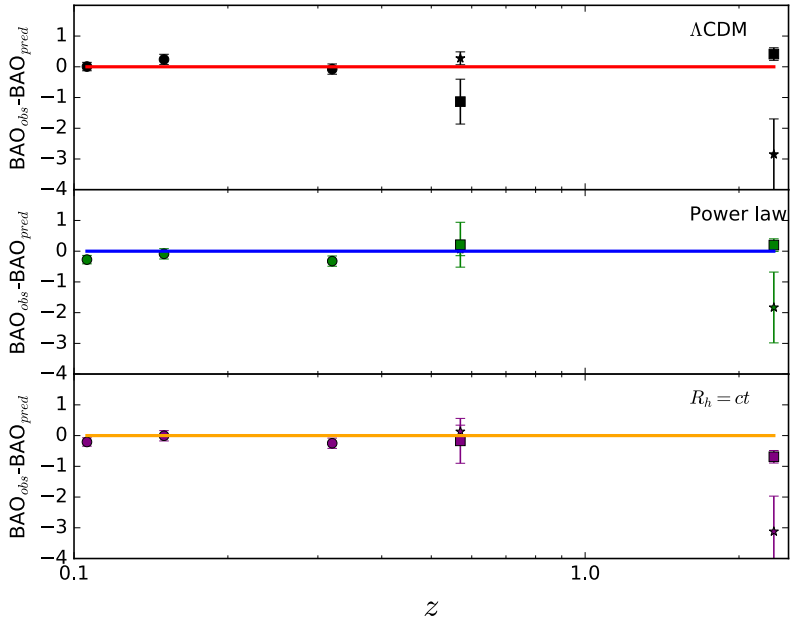

FIGURE 4.8: Fit from the three models under study to the BAO data. Each plot shows the residuals with respect to the corresponding model. The isotropic measurements of the BAO are represented with a circle and their observable is $D_{\rm V}(z)/r_{\rm d}$, while the stars stand for the radial measurements with observable $\chi(z)/r_{\rm d}$ and the squares stand for the transverse measurements with observable $c/(H(z)r_{\rm d})$. *Top panel*: BAO measurements (black) and ΛCDM prediction (red) as a function of the redshift. *Central panel*: BAO measurements (green) and power law cosmology prediction (blue) as a function of the redshift. *Bottom panel*: BAO measurements (purple) and $R_{\rm h} = ct$ cosmology prediction (orange) as a function of the redshift.

purposes.

In Fig. 4.6 we show the drag visibility functions for the same models that appear in Fig. 4.5. The cosmological parameters are fixed to the same present-day values [Planck Collaboration, 2016b] and we have also checked that any variation of 25% in one of the parameters does not lead to significant changes in our results. Therefore, we fix $z_{\rm d} = 1060.61$ for ΛCDM and $z_{\rm d} = 1031.85$ for the $R_{\rm h} = ct$ cosmology. As for z_*, we observe that $z_{\rm d}$ changes significantly with the exponent of the power law cosmology; thus, we interpolate $z_{\rm d}$ as a function of n.

No extra cosmological or nuisance parameters are considered when including the CMB data.

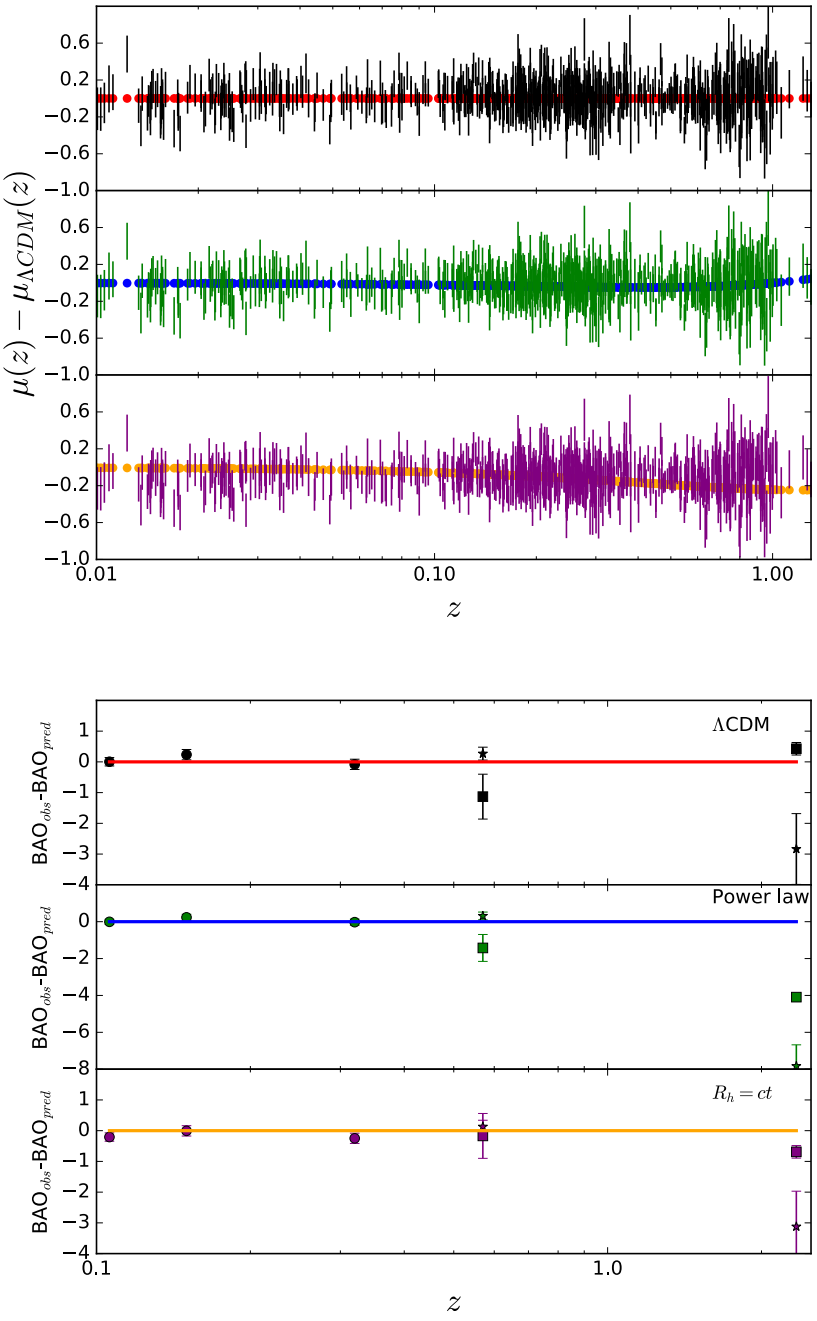

FIGURE 4.9: Fit from the three models under study to the SNIa and BAO data; i.e. the parameter values of the models are the best-fit values from SNIa+BAO data. *Top plot*: SNIa residuals with respect to the prediction from ΛCDM with the best-fit values, for the three models under study (see Fig. 4.7). *Bottom plot*: BAO residuals with respect to the model under study (see Fig. 4.8).

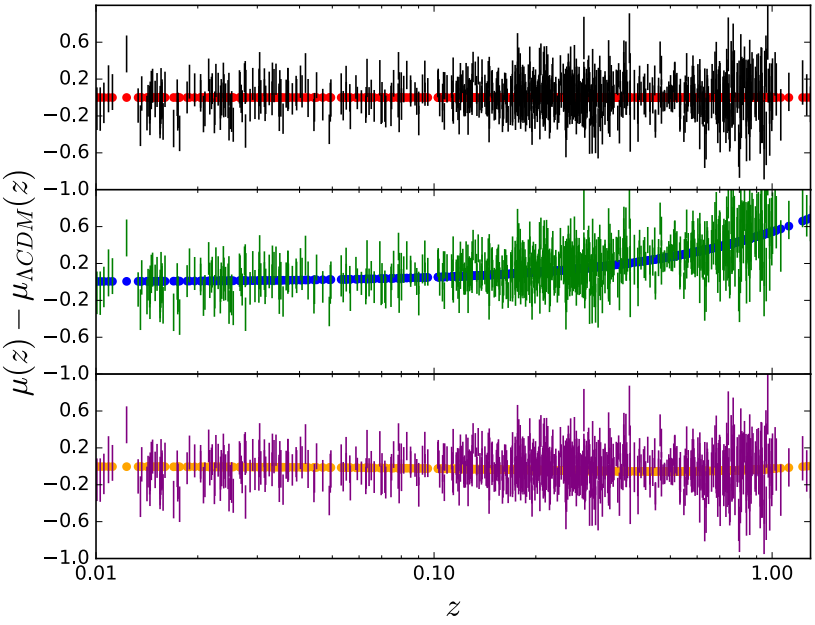

FIGURE 4.10: Fit from the three models under study to the SNIa data allowing for some evolution with the redshift. All the plots show the residuals with respect to the prediction from ΛCDM with the best-fit values (see Fig. 4.7). The introduction of some evolution with the redshift modifies the observed $\mu(z)$ giving a good fit for all the models.

4.5 Results

After having presented the different cosmological probes used in this analysis (distance modulus for SNIa, isotropic and anisotropic BAO measurements, and ℓ_a for the CMB), we focus here on the results obtained. In Table 4.1 we present the best-fit values obtained for the different cosmological and nuisance parameters of the models studied with the different probes used. In Table 4.2 we show the results of the goodness-of-fit and model comparisons. More specifically, we report the number of parameters of the model, the number of data points used, the minimum value for the χ^2 function, the goodness-of-fit statistic and the exponential of the differences $\Delta\text{AICc}/2$ and $\Delta\text{BIC}/2$.

Focusing first on SNIa alone, Fig. 4.7 provides the residuals to the best-fit (normalized to the ΛCDM model) for each model. ΛCDM provides a very good fit to the data ($P(\chi^2, \nu) = 0.915$), as well as the power law cosmology ($P(\chi^2, \nu) = 0.915$, with $n = 1.55 \pm 0.13$). Although the $R_\text{h} = ct$ cosmology provides a slightly worse fit ($P(\chi^2, \nu) = 0.644$), it is still acceptable. However, it is highly disfavored when considering the model comparison statistics ($\exp(\Delta\text{AICc}/2) = 1.308 \times 10^{-8}$ and $\exp(\Delta\text{BIC}/2) = 1.291 \times 10^{-7}$). Despite

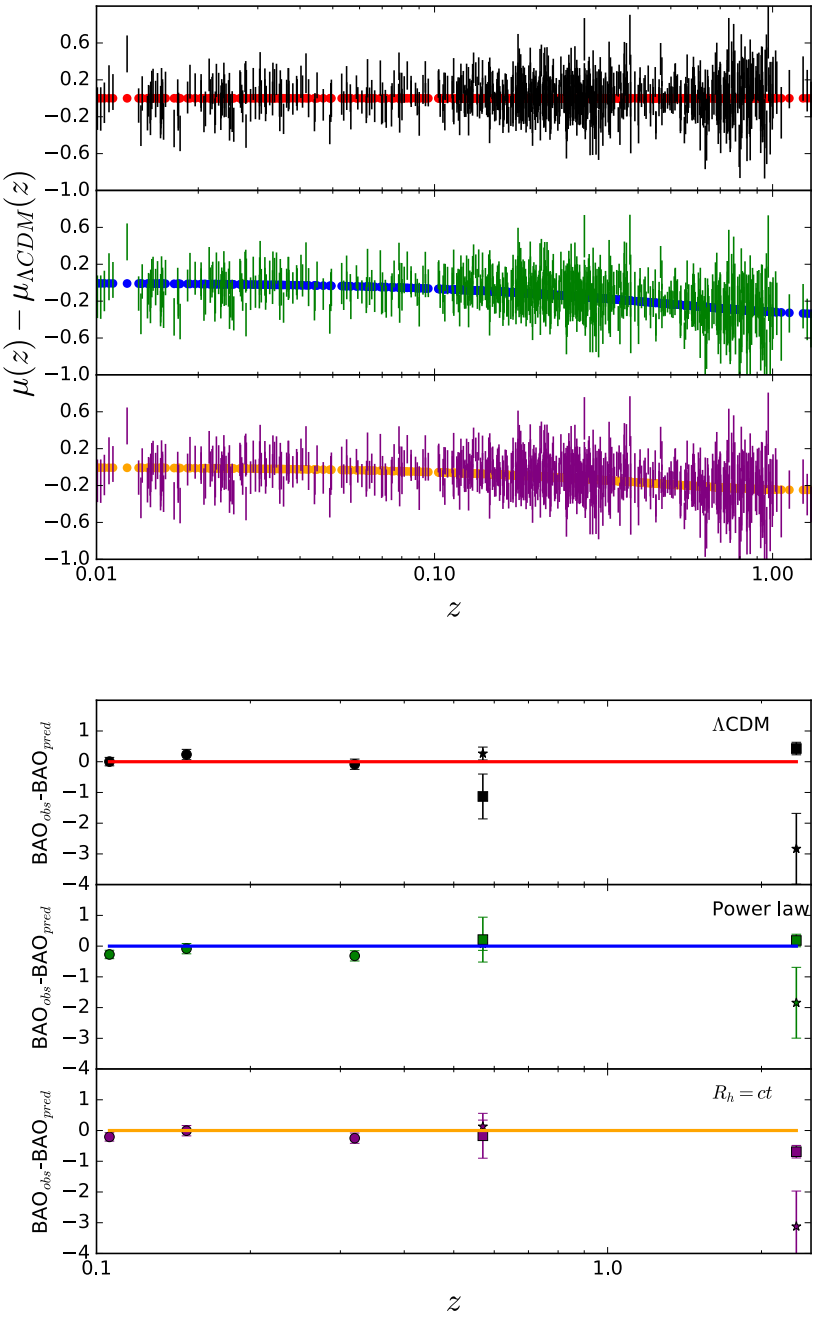

FIGURE 4.11: Fit from the three models under study to the SNIa and BAO data allowing for redshift evolution for the SNIa; i.e. the parameter values of the models are the best-fit values from SNIa+evolution+BAO data. *Top plot*: SNIa residuals with respect to the prediction from ΛCDM with the best-fit values (see Fig. 4.7). *Bottom plot*: BAO residuals with respect to the model under study (see Fig. 4.8). Allowing for some redshift evolution for SNIa provides a good fit for the three models to both SNIa and BAO data.

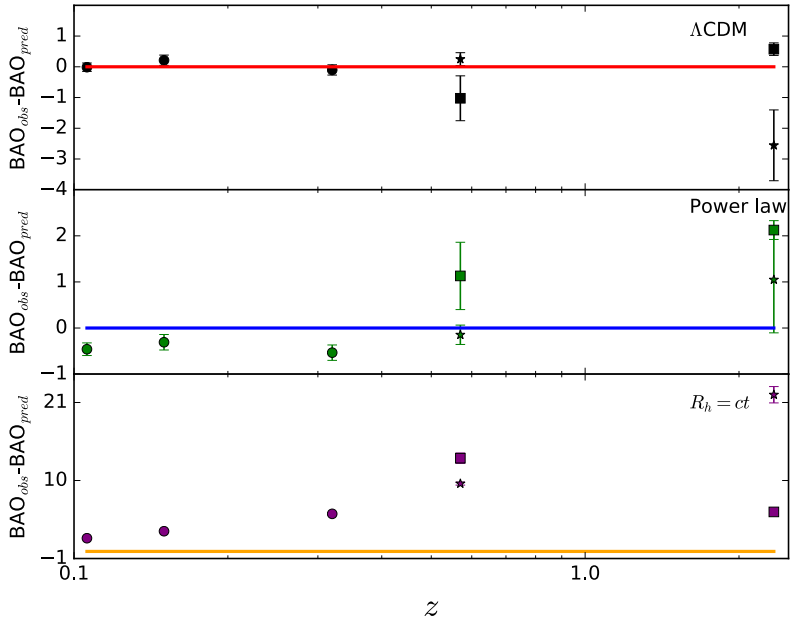

FIGURE 4.12: Fit from the three models under study to the BAO and CMB data. All the plots show the BAO residuals with respect to the model under study (see Fig. 4.8). The introduction of the CMB data strongly degrades (notice the increase in the Y-axis limits and the small size of the error bars) the fit to BAO data for the power law and the $R_{\rm h} = ct$ cosmologies.

the fact that the $R_{\rm h} = ct$ model has fewer parameters than ΛCDM, the χ^2 difference is large enough ($\Delta\chi^2 = 38.33$) to compensate for the preference of the $R_{\rm h} = ct$ model coming from the Occam factor of the AIC and the BIC. By Occam factor we mean here the non-χ^2 term in Eqs. (2.32) and (2.33).

In Fig. 4.8 we present the residuals of the fit to the BAO data alone from the three models under study. From the top panel we immediately see that ΛCDM is not a good fit to BAO data ($P(\chi^2, \nu) = 0.088$). This tension has already been noted in the literature [Aubourg et al., 2015; Shafer, 2015] and is due to the anisotropic Lyman-α forest BAO measurements at high redshift ($z = 2.34$). Since SNIa and BAO prefer similar values of $\Omega_{\rm m}$, no extra tension appears when combining these probes. The power law cosmology provides a better fit to BAO data than ΛCDM ($P(\chi^2, \nu) = 0.531$) implying preference of the power law cosmology over ΛCDM from the model comparison statistics ($\exp(\Delta{\rm AICc}/2)$ =$\exp(\Delta{\rm BIC}/2) = 15.198$). Regarding the $R_{\rm h} = ct$ model, the fit is worse than for ΛCDM ($P(\chi^2, \nu) = 0.016$), but the difference of χ^2 with respect to ΛCDM is nearly compensated by the Occam factor, so that the model has commensurate values of the AICc and the BIC: $\exp(\Delta{\rm AICc}/2) = 0.385$ and $\exp(\Delta{\rm BIC}/2) = 0.125$, respectively.

TABLE 4.3: Value of ℓ_a for the different models under study (ΛCDM, power law, and $R_h = ct$ cosmologies), with the best-fit values coming from the different combinations of data sets used. The Planck 2015 value has been added for comparison.

	ℓ_a Planck 2015	ℓ_a ΛCDM	ℓ_a Power law	ℓ_a $R_h = ct$
BAO+CMB	301.63 ± 0.15	301.651	301.677	301.649
SNIa+BAO+CMB	301.63 ± 0.15	301.591	301.856	301.649
SNIa+ev+BAO+CMB	301.63 ± 0.15	301.529	301.415	301.649

In Fig. 4.9 we show the results from fitting the three models to SNIa and BAO data simultaneously. In the top plot we present the fits from the models to SNIa data using the best-fit values obtained from both SNIa and BAO data. These results are very similar to the ones obtained for SNIa alone (Fig. 4.7), showing that adding the BAO does not affect the SNIa-related parameters. In the bottom plot of Fig. 4.9 we show the fit from the models to BAO data, using the SNIa+BAO best-fit values for the parameters. We notice that the power law cosmology provides a slightly worse fit than when considering BAO data alone (Fig. 4.8). Looking at the goodness-of-fit for SNIa and BAO data, we find that the power law cosmology provides a slightly worse fit ($P(\chi^2, \nu) = 0.833$) than ΛCDM ($P(\chi^2, \nu) = 0.898$), which is also the case for the $R_h = ct$ cosmology ($P(\chi^2, \nu) = 0.546$). Despite the small difference between the power law cosmology and the ΛCDM fits, the model comparison statistics tell us that the latter is preferred ($\exp(\Delta\text{AICc}/2)$ =$\exp(\Delta\text{BIC}/2) = 0.0036$). The $R_h = ct$ cosmology is even more strongly disfavored with respect to ΛCDM than when considering SNIa data alone ($\exp(\Delta\text{AICc}/2) = 6.251 \times 10^{-10}$ and $\exp(\Delta\text{BIC}/2) = 6.184 \times 10^{-9}$).

From these results (the best-fit values are nearly all consistent with Shafer, 2015, within 1σ) we deduce that $R_h = ct$ is very disfavored with respect to ΛCDM, while the power law cosmology is slightly disfavored with respect to ΛCDM.

We now present the results when allowing for some SNIa evolution with the redshift [Eq. (4.5)]. In Fig. 4.10 we have the results for SNIa data. We can observe that now all the models provide a very good fit to the data. Interestingly, the evolution nuisance parameter is nearly consistent with 0 for ΛCDM and the power law cosmology, while it is clearly non-null for the $R_h = ct$ cosmology. This is completely consistent since the ΛCDM and the power law cosmology were already able to provide a good fit without evolution, while the $R_h = ct$ needed this nuisance term in order to correctly fit the data. From the model

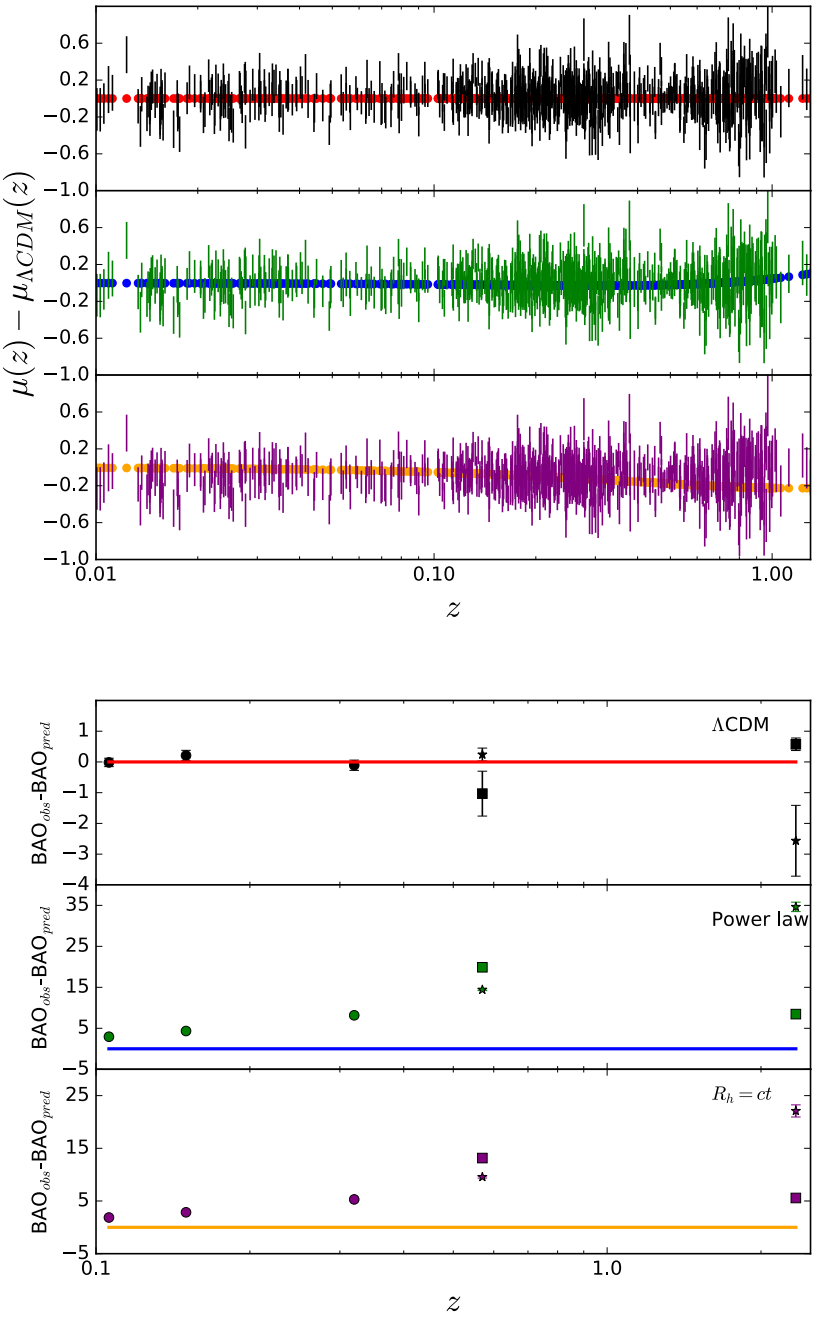

FIGURE 4.13: Fit from the three models under study to the SNIa, BAO and CMB data; i.e. the parameter values of the models are the best-fit values from SNIa+BAO+CMB data. *Top plot*: SNIa residuals with respect to the prediction from ΛCDM with the best-fit values (see Fig. 4.7). *Bottom plot*: BAO residuals with respect to the model under study (see Fig. 4.8).

comparison statistics we can deduce that there is no clear preference for one model over another.

Now we can combine the SNIa data (allowing for evolution) with the BAO data. The results are shown in Fig. 4.11. Contrary to what we have seen in Fig. 4.9, adding the BAO does modify the SNIa-related parameter values, but we still obtain a very good fit to SNIa data using the best-fit values obtained from SNIa+BAO data and allowing for evolution. Concerning the fit to BAO data, using this combination of data to determine the best-fit values, we recover the results obtained with BAO data alone (Fig. 4.8). This shows that when we relax the redshift independence for SNIa, the power in model selection from the combination of SNIa and BAO weakens. As the power law cosmology was slightly preferred over ΛCDM when considering BAO data alone, it is not surprising that it is also the case here ($\exp(\Delta\mathrm{AICc}/2) = \exp(\Delta\mathrm{BIC}/2) = 3.421$). Concerning the $R_h = ct$ cosmology, the Occam factor is nearly as important as the χ^2 difference and it leads to only a marginal preference for ΛCDM ($\exp(\Delta\mathrm{AICc}/2) = 0.046$ and $\exp(\Delta\mathrm{BIC}/2) = 0.455$).

From these results we can deduce that adding a redshift evolution in SNIa as a nuisance parameter leads to no clear preference of one model over another.

We now consider the addition of CMB data. Let us recall that these high-redshift data are very complementary to low-redshift observations like SNIa or BAO and, thanks to their high precision, adding the CMB can provide extra important information when comparing different cosmological models (see Sec. 1.5.2). Notice that in this work we cannot combine CMB and SNIa data, since we rely on the BAO scale to introduce the CMB scale (see Sec. 4.4.3); therefore we always need to consider BAO data when including the CMB. The results for BAO and CMB data are shown in Fig. 4.12 and in Table 4.3. In the plot we have the results for BAO data with the best-fit values obtained with BAO and CMB data. In the table we present the value of ℓ_a for each model with the BAO and CMB data best-fit values. We can see that there is no evolution in the ΛCDM BAO fit when we add the CMB information to determine the best-fit values, as expected. However, adding the CMB information is crucial for the power law and the $R_h = ct$ cosmologies, since the fit to the BAO data is strongly degraded [$P(\chi^2, \nu) = 1.2 \times 10^{-3}$ and $P(\chi^2, \nu) = 4.4 \times 10^{-14}$, respectively]. From the model comparison point of view, the power law cosmology is disfavored ($\exp(\Delta\mathrm{AICc}/2) = \exp(\Delta\mathrm{BIC}/2) = 0.0029$) and the $R_h = ct$ cosmology is strongly disfavored ($\exp(\Delta\mathrm{AICc}/2) = 1.680 \times 10^{-14}$ and $\exp(\Delta\mathrm{BIC}/2) = 7.349 \times 10^{-15}$) with respect to ΛCDM.

We can now combine the information from the three probes: SNIa, BAO and CMB. The results are presented in Fig. 4.13 and in Table 4.3. From the top plot we can see that adding the CMB information does not affect the fit to SNIa (see

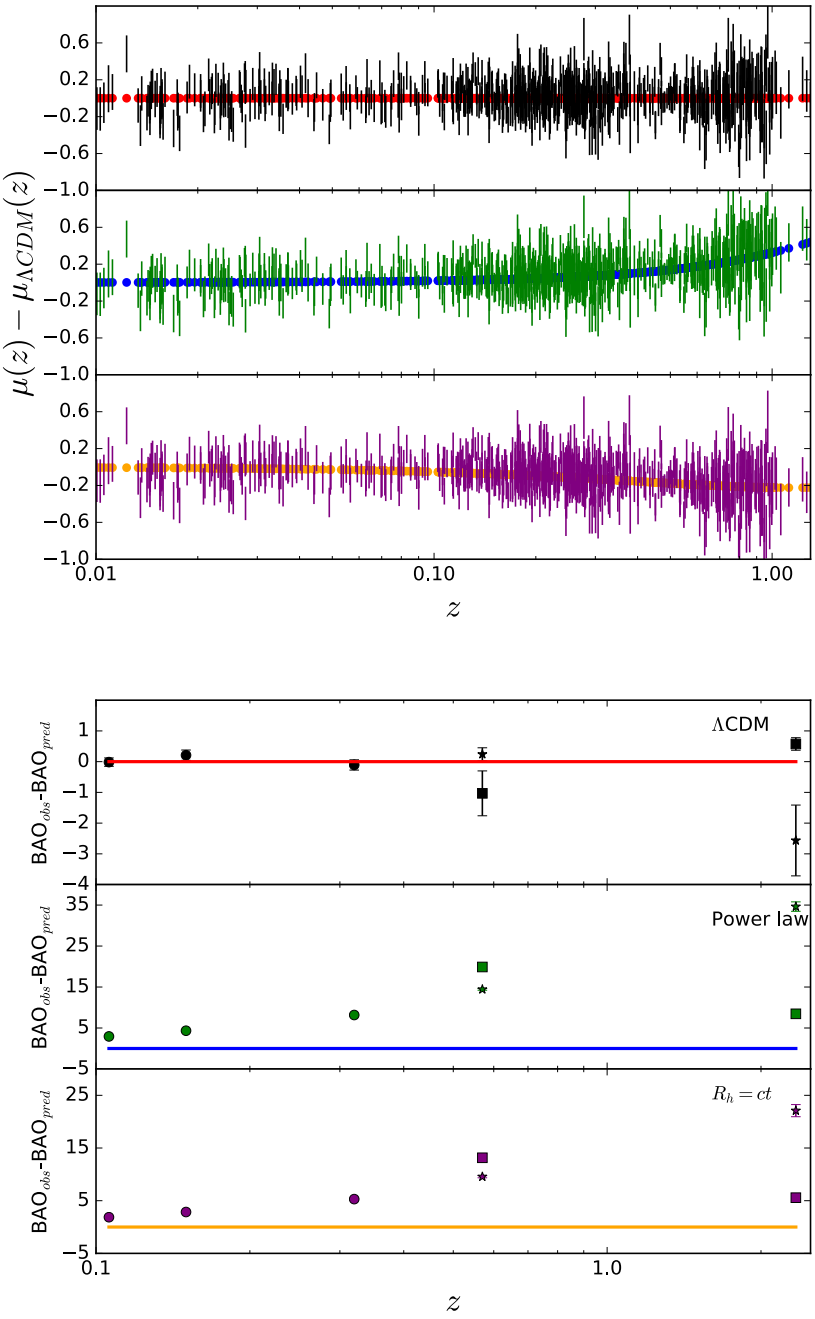

FIGURE 4.14: Fit from the three models under study to the SNIa, BAO and CMB data and allowing for redshift evolution for SNIa; i.e. the parameter values of the models are the best-fit values from SNIa+ ev +BAO+CMB data. *Top plot*: SNIa residuals with respect to the prediction from ΛCDM with the best-fit values (see Fig. 4.7). *Bottom plot*: BAO residuals with respect to the model under study (see Fig. 4.8). Allowing for some redshift evolution for SNIa is not sufficient to compensate for the effect of the CMB, and we remain with a poor fit for the power law and $R_h = ct$ cosmologies.

the top panel of Fig. 4.11). However, it completely degrades the fit to the BAO data for the power law and the $R_h = ct$ cosmologies (see the bottom panel of Fig. 4.11 and Fig. 4.12). In terms of model comparison, the power law cosmology is very disfavored ($\exp(\Delta\text{AICc}/2)$ =$\exp(\Delta\text{BIC}/2) = 2.501 \times 10^{-15}$) and the $R_h = ct$ cosmology is extremely disfavored ($\exp(\Delta\text{AICc}/2) = 3.598 \times 10^{-23}$ and $\exp(\Delta\text{BIC}/2) = 3.562 \times 10^{-22}$) with respect to ΛCDM. It is important to notice here that the χ^2 and the $P(\chi^2, \nu)$ obtained for the $R_h = ct$ and the power law cosmologies are acceptable, but the model criteria tell us that these models are highly disfavored. This is due to the introduction of SNIa data. Both models provide an acceptable fit to these data; so, when including so many data points, the global fit is still acceptable. However, the model criteria are essentially sensitive to the exponential of the difference of χ^2, so they can distinguish between different models approximately fitting the data. It is a clear example between the difference of correctly fitting the data and being better than another model.

We finally present the results when we also allow for some redshift evolution of SNIa intrinsic luminosity in Fig. 4.14 and in Table 4.3. From the top plot we notice that adding the evolution leads to very good fits to SNIa data. However, from the bottom plot we can see that the redshift evolution in SNIa is not sufficient to compensate for the effect of the CMB; thus the power law and $R_h = ct$ cosmologies are not able to correctly fit the BAO data. The results from the model comparison still remain clear, showing that ΛCDM is very strongly preferred over the power law ($\exp(\Delta\text{AICc}/2)$ =$\exp(\Delta\text{BIC}/2) = 3.127 \times 10^{-15}$) and the $R_h = ct$ ($\exp(\Delta\text{AICc}/2) = 2.363 \times 10^{-15}$ and $\exp(\Delta\text{BIC}/2) = 2.332 \times 10^{-14}$) cosmologies.

4.6 Summary

In this chapter we have studied the ability of three different models, ΛCDM, power law cosmology and $R_h = ct$ cosmology, to fit cosmological data and we have compared these models using two different model comparison statistics: the Akaike information criterion and the Bayesian information criterion. We have seen that all three models are able to fit SNIa data, but $R_h = ct$ is disfavored with respect to ΛCDM and the power law cosmology, from a model comparison point of view. Considering BAO data alone, we have observed that ΛCDM does not provide a good fit to data, due to the anisotropic measurement of the Lyman-α forest, and we have seen that the power law cosmology is slightly preferred over ΛCDM (and significantly preferred over the $R_h = ct$ cosmology). However, when combining SNIa and BAO data, the ΛCDM is preferred over the other models. We have then considered a possible redshift evolution in SNIa.

This has led to an excellent fit to SNIa for all the models and, even when adding the BAO data, there is no clearly preferred model. We have finally considered the scale information coming from the CMB. In order to use this information we have made one assumption: the physics driving the co-moving sound horizon at the early Universe in the $R_{\rm h} = ct$ and power law cosmologies is the same as in the ΛCDM model. This assumption is justified by the existence of radiation and baryon components in the power law and $R_{\rm h} = ct$ cosmologies, which should lead to an early universe photon-baryon plasma similar to the one predicted by ΛCDM. When adding the scale information from the CMB to BAO and SNIa data we have observed that the goodness-of-fit remains the same for ΛCDM, but it is completely degraded for the other models. Even accounting for some evolution of SNIa intrinsic luminosity, we have seen that it is not sufficient to compensate for the effect of the CMB. This degradation shows the tension present in the power law and $R_{\rm h} = ct$ cosmologies between the BAO scale and the CMB scale, coming from the first peak of the temperature angular power spectrum.

In conclusion, even accounting for some SNIa intrinsic luminosity evolution as a function of the redshift, the addition of CMB data shows that ΛCDM is statistically very strongly preferred over power law and $R_{\rm h} = ct$ cosmologies. Therefore, these models are essentially ruled out by current observations.

Chapter 5

Cosmic acceleration and SNIa luminosity-redshift dependence

In this chapter we focus our interest on the expansion of the Universe and its accelerated nature. In particular, we pay special attention to the role of type Ia supernovae in the final conclusions that can be drawn with respect to the nature of the late-time expansion, and we study if a non-accelerated expanding universe can fit the main cosmological observations.

The evidence for an accelerated expansion, coming from the SNIa Hubble diagram [Riess et al., 1998; Perlmutter et al., 1999], was key to consider ΛCDM as the cosmological concordance model. But there has recently been a debate in the literature wondering whether SNIa data alone, or combined with other low-redshift cosmological probes, can prove the accelerated expansion of the Universe [Nielsen, Guffanti, and Sarkar, 2016; Shariff et al., 2016; Rubin and Hayden, 2016; Ringermacher and Mead, 2016; Dam, Heinesen, and Wiltshire, 2017; Lonappan et al., 2017; Haridasu et al., 2017; Lin, Li, and Sang, 2017; Luković, Haridasu, and Vittorio, 2018]. For instance, the authors in Nielsen, Guffanti, and Sarkar, 2016, claim that, allowing for the varying shape of the light curve and extinction by dust, they find that SNIa data are still quite consistent with a constant rate of expansion, while the authors in Rubin and Hayden, 2016, claim, redoing this analysis, a 11.2σ confidence level for acceleration with SNIa data alone in a flat universe.

It is commonly assumed that two SNIa in two different galaxies at different redshifts, with the same color, stretch of the light-curve, and host stellar mass, have in average the same intrinsic luminosity (see Sec. 1.5.1). Although there are theoretical models for the mechanism of SNIa detonation that are nicely compatible with the observations, the difficulty of observing the system before becoming a SNIa leaves enough uncertainty to wonder whether considering a luminosity dependence with the redshift may have an effect on the cosmological conclusions we can extract from them [Riess et al., 2018b]. A varying gravitational constant, a fine structure constant variation, or any redshift-dependent

astrophysical systematic could generate such luminosity dependence on the redshift, but our approach here is just to relax the redshift independence hypothesis and consider phenomenological models to explore the degeneracy of SNIa distance-dependent effects with the cosmological information.

We divide this chapter into two sections corresponding to the results of the articles Tutusaus et al., 2017, and Tutusaus, Lamine, and Blanchard, 2018b, respectively.

In the first section, we only consider low-redshift data in order to focus on the era of cosmic acceleration, and study luminosity-redshift dependence models in the redshift range where we actually have SNIa data. We consider a flat, non-accelerated power law expansion of the Universe, $R(t) \propto t^n$ with $n \leq 1$. Notice that this corresponds to the power law cosmology discussed in the previous chapter. Although we have proven that these models are completely ruled out if we extend them up to the cosmic microwave background era, there is nothing preventing us to use them as a null test for cosmic acceleration at low-redshift, since the behavior of our cosmology at high-redshift is irrelevant for the cosmological probes considered.

In the second section, we extend the previous analysis by including the CMB data, and, instead of testing a specific model for the expansion, we perform a model-independent reconstruction of the expansion rate of the Universe through a cubic spline interpolation. Again, we assess the impact that any dependence between the SNIa intrinsic luminosity and the redshift may have on the conclusions we extract concerning the accelerated nature of the expansion of the Universe.

5.1 Non-accelerated expansion at low-redshift

5.1.1 Context

In this section we examine whether the accelerated nature of the expansion can be firmly established based not only on SNIa data, but also on the other low-redshift cosmological probes: the baryon acoustic oscillations, the Hubble parameter as a function of the redshift ($H(z)$), and measurements of the growth of structures ($f\sigma_8(z)$). We relax the SNIa luminosity-redshift independence hypothesis by considering a large variety of luminosity evolution models, in order to be as general as possible. Relaxing this assumption has also been considered in other analyses [Wright, 2002; Drell, Loredo, and Wasserman, 2000; Nordin, Goobar, and Jönsson, 2008; Ferramacho, Blanchard, and Zolnierowski, 2009; Linden, Virey, and Tilquin, 2009]. We discard for the moment high-redshift data, such as the CMB, because the goal in this section is to assess whether

measurements of the local Universe are sufficient to prove the accelerated expansion of the Universe, which, at least in the standard cosmological model, appears at low-redshift (see next section for the inclusion of the CMB). In order to do this, we consider a simple model behaving as a non-accelerated power law cosmology at low-redshift. We denote it by NALPL (non-accelerated local power law). Let us stress again that NALPL should not be confused with the standard power law model, since it behaves like it at low-redshift, but can significantly differ from a power law at high-redshift.

The models considered in this section, as well as the methodology used to fit the data have been already described in Sec. 4.2 and Sec. 4.3.

5.1.2 Cosmological probes

In this subsection we present the low-redshift probes and the specific data samples used in this section, specifying the differences with respect to the general introduction presented in Sec. 1.5. The treatment and data used for BAO and $H(z)$ is exactly the same as what has been presented in Sec. 4.4.2 and Sec. 1.5.3, respectively [1].

Type Ia supernovae

In this chapter we also use the joint light-curve analysis for SNIa from Betoule et al., 2014, including their covariance matrix for the observations. We relax the assumption that the intrinsic luminosity of SNIa is independent of the redshift, as in the previous chapter [see Eq. (4.5)], by considering an extra nuisance term, $\Delta m_{\rm evo}(z)$, accounting for a possible evolution of the supernovae luminosity with the redshift,

$$\mu_{\rm obs} = m_{\rm B}^{*} - (M_{\rm B} - \alpha X_1 + \beta C + \Delta m_{\rm evo}(z)) \,. \tag{5.1}$$

However, this time the function $\Delta m_{\rm evo}(z)$ is more general than the linear model used in the previous chapter.

Different phenomenological models for $\Delta m_{\rm evo}(z)$ can be found in the literature [see for example Drell, Loredo, and Wasserman, 2000; Linder, 2006; Nordin, Goobar, and Jönsson, 2008; Ferramacho, Blanchard, and Zolnierowski, 2009; Linden, Virey, and Tilquin, 2009]. In the absence of any clear physics governing this evolution, one stays at a phenomenological level and considers a

[1] Notice that some of the $H(z)$ measurements have been obtained with anisotropic BAO analyses. Therefore, there could be some correlations between the BAO and the $H(z)$ data sets used in this section that has not been taken into account. A more detailed analysis including the correct correlations or discarding the $H(z)$ measurements obtained from the BAO should be done. However, given the precision of the current measurements of $H(z)$ we do not expect any significant change in the conclusions of this section.

TABLE 5.1: Different luminosity evolution models considered for SNIa. All models have two different parameters, ϵ and δ.

Model	$\Delta m_{\rm evo}(z)$	Reference
A	$\epsilon\left[(1+z)^{\delta}-1\right]$	-
B	ϵz^{δ}	Linden, Virey, and Tilquin, 2009
C	$\epsilon\left[\ln(1+z)\right]^{\delta}$	Linden, Virey, and Tilquin, 2009
D	$\epsilon\left(\frac{t_0-t(z)}{t_0-t(1)}\right)^{\delta}$	Ferramacho, Blanchard, and Zolnierowski, 2009

bunch of different models. We can embed all the models studied in this section into four categories, which are summarized in table 5.1. These categories all possess two parameters, ϵ and δ.

Model B is equivalent to model 2 in Linden, Virey, and Tilquin, 2009, while model C is a generalization of model 1 in Linden, Virey, and Tilquin, 2009. Model D is a generalization of Ferramacho, Blanchard, and Zolnierowski, 2009. Models C and D were initially motivated from a parameterization of the intrinsic luminosity $\mathcal{L} \to \mathcal{L}(1+z)^{-\epsilon}$ [Drell, Loredo, and Wasserman, 2000], while models A and B are more general to study the contribution of powers in z to the results.

Let us observe that when $\delta \to 0$, $\Delta m_{\rm evo}(z)$ becomes strongly degenerate with $M_{\rm B}^1$. Therefore, to avoid this kind of parameter degeneracies, we consider three sub-models fixing $\delta = 0.3$, 0.5, and 1. We denote these sub-models A1, A2, A3, B1, B2, B3, and so on (notice that the model used in the previous chapter corresponds to B3). If δ is small, the luminosity evolution is more prominent at low redshift, while a higher δ leads to a luminosity evolution dominating at high redshift.

When SNIa data are taken into account, the set of nuisance parameters considered is $\{\alpha,\ \beta,\ M_{\rm B}^1,\ \Delta_{\rm M}, \epsilon\}$. We consider the matter energy density, $\Omega_{\rm m}$, and n as cosmological parameters for the ΛCDM and the NALPL model, respectively.

Growth rate

Let us recall (see Sec. 1.3) that the observable weighted growth rate, $f\sigma_8$, can be expressed as

$$f\sigma_8(z) = f(z)\left(\sigma_8 \cdot \frac{D_1(z)}{D_1(0)}\right), \tag{5.2}$$

where D_1 stands for the growth factor and σ_8 accounts for the root mean square mass fluctuation amplitude on scales of $8h^{-1}$Mpc at redshift $z = 0$. We do not use the value for σ_8 deduced from the CMB since it requires some assumptions about the early Universe physics (the value derived from the CMB is determined

at $z \sim 1100$ and then extrapolated at $z = 0$). Instead, we let the low-redshift observations choose the preferred value for the $\sigma_8 / D_1(0)$ ratio.

In this section we use the measurements of $f\sigma_8(z)$ from Beutler et al., 2012; Samushia, Percival, and Raccanelli, 2012; Tojeiro et al., 2012; Blake et al., 2012; de la Torre et al., 2013, provided in Macaulay, Wehus, and Eriksen, 2013, together with their correlations. When using these measurements we add the $K \equiv \sigma_8 / D_1(0)$ parameter to our set of parameters under consideration. Notice that we also need to add the $\Omega_{\rm m}$ parameter for the NALPL model, since we need to specify the quantity of matter in the Universe to compute the growth factor. In other words, when we add the measurements of $f\sigma_8(z)$ into our analysis, we allow for the existence of some matter, $\Omega_{\rm m}$, and we consider that the uncoupled and non-perturbed dark energy fluid evolves to provide the required power law expansion at low-redshift.

5.1.3 Goodness-of-fit and effect of correlations

Although in this section we follow the methodology described in Sec. 4.3, some of the data sets used here are different than the ones used in the previous chapter. Therefore, we test again whether the impact of correlations within each probe is negligible when we compute the probability, $P(\chi^2, \nu)$, that a larger χ^2 value could occur for a fit with $\nu = N - k$ degrees of freedom, with N the number of data points and k the number of free parameters [Eq. (2.30)]. We recall that Eq. (2.30) can, in principle, only be used when the data points come from independent random variables with Gaussian distributions, so we need to assess whether we can still use this equation in our case.

In the left panel of Fig. 5.1 we present the χ^2 histograms of the Monte Carlo simulations computed with (green) and without (purple) correlations when we use all the probes of this section (see Sec. 4.3 for the details of the simulations). As it was the case in the previous chapter, the distributions are completely equivalent and compatible with the theoretical prediction. Therefore, we can safely use Eq. (2.30) in this section, too. For completeness, we present the correlation matrix of the $f\sigma_8(z)$ measurements in the right panel of Fig. 5.1. We can see that most of the points are uncorrelated, and only three of them show a correlation of $\sim 50\,\%$. The correlation matrices for the other probes (SNIa and BAO) were already provided in Fig. 4.3, and the $H(z)$ measurements are uncorrelated.

5.1.4 Results

We present the results of this section in two different steps. In the first place we focus on low-redshift background probes, namely SNIa, BAO, and $H(z)$, and in

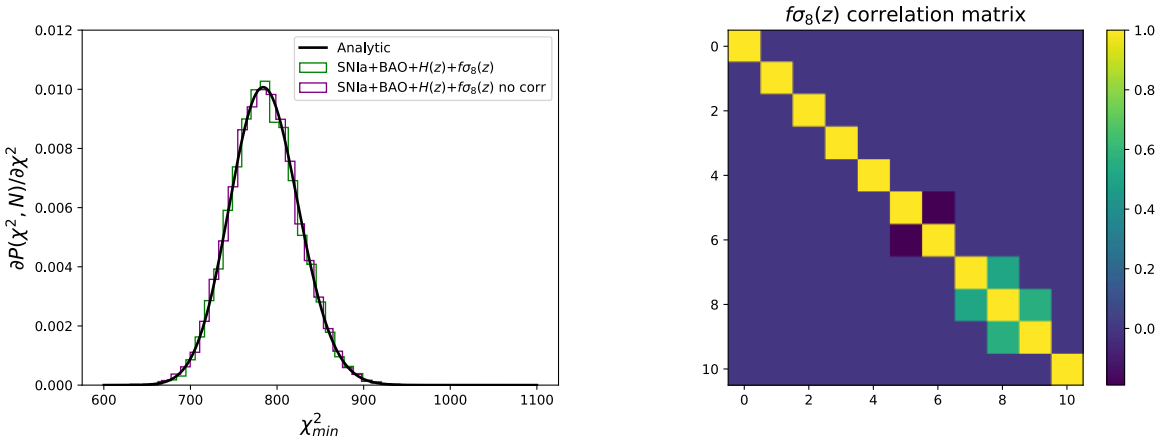

FIGURE 5.1: *Left plot*: histograms (with 10000 iterations) of χ^2 for Monte Carlo simulations using correlations (green) and neglecting them (purple). The analytic distribution is represented with a thick black solid line. *Right plot*: correlation matrix of the $f\sigma_8$(z) measurements (ranging from 0 to 10) used in this section.

the second step we add the measurements of the growth of matter perturbations.

Background probes

The results obtained from low-redshift background probes only are presented in Fig. 5.2. In the top panel we show the best-fit values obtained for the $\Omega_{\rm m}$, n, $r_{\rm d} \times H_0/c$ and H_0 cosmological parameters, as well as the ϵ nuisance parameter for the different cosmological and luminosity evolution models under study. The blue region of the left panel corresponds to the value, and the error, obtained for $\Omega_{\rm m}$ in the standard ΛCDM case, i.e., with no luminosity evolution. We can observe that all the obtained values for $\Omega_{\rm m}$ are completely compatible with the standard ΛCDM value.

In the second panel we plot the exponent n of NALPL for each model, together with a colored band corresponding to the allowed values when no evolution is imposed. We can observe that all the obtained values are compatible with a slightly lower value than in the no evolution case.

In the third panel we present the nuisance parameter associated with the luminosity evolution for all the models under consideration. As expected, all the ΛCDM models are perfectly compatible with 0. On the contrary, the NALPL models clearly need some positive luminosity evolution to fit the data, which implies that the luminosity decreases with the redshift.

Concerning the $r_{\rm d} \times H_0/c$ cosmological parameter, we can observe that the

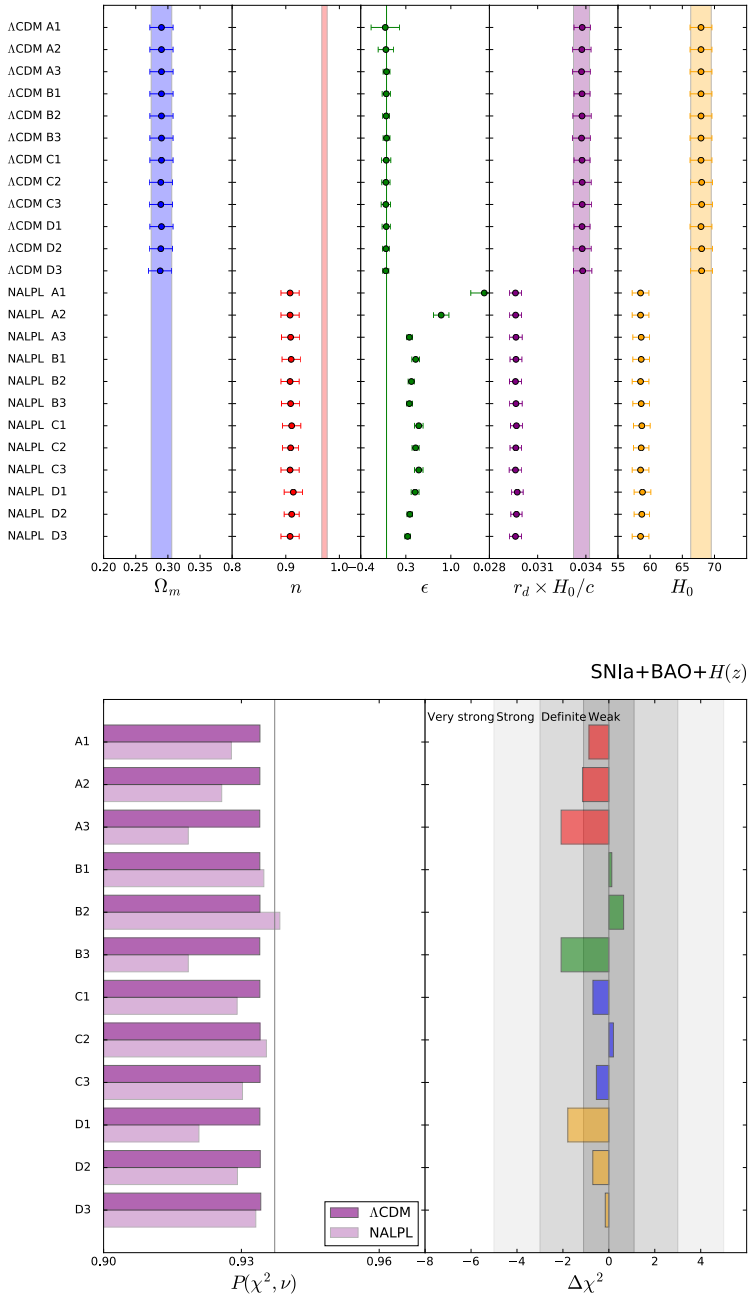

FIGURE 5.2: Results obtained from low-redshift background probes. *Top panel*: best-fit values for $\Omega_{\rm m}$, n, ϵ, $r_{\rm d} \times H_0/c$, and H_0 parameters for all the cosmological and luminosity evolution models under consideration. The values for these parameters when no luminosity evolution is allowed are represented with bands as a reference. *Bottom panel*: goodness-of-fit statistics and difference of the χ^2 values, $\Delta\chi^2 = \chi^2_{\Lambda\rm CDM} - \chi^2_{\rm NALPL}$, for the luminosity evolution models under study. The vertical solid line in the left plot illustrates the goodness-of-fit statistics for the standard ΛCDM imposing no luminosity evolution. The various gray bands in the right plot show the strength of $\Delta\chi^2$ given by the Jeffrey scale (see the text for details).

ΛCDM values are compatible with the no evolution case, while the values obtained for the NALPL models are compatible with a lower value. This is also the case for the H_0 parameter, as we can see in the last panel.

Focusing on the ability of these models to fit the data, all of them provide a very good fit to the data with a goodness-of-fit statistic value of $P(\chi^2, \nu) > 0.9$, as we can see in the left plot of the bottom panel of Fig. 5.2. We present the difference of χ^2 values given by $\Delta\chi^2 = \chi^2_{\Lambda\text{CDM}} - \chi^2_{\text{NALPL}}$ in the right plot of Fig. 5.2 bottom panel. Let us mention that in this case, $\Delta\chi^2$ is equal to the difference of widely used standard model comparison criteria, such as the Akaike information criterion [Akaike, 1973] or the Bayesian information criterion [Schwarz, 1978], because both ΛCDM and NALPL have the same number of free parameters and we are using the same data for the fits. However, we are only interested in the ability of NALPL to fit the data, and we are not in search of performing a model comparison against ΛCDM. In the plot we also show the standard Jeffrey scale [following Nesseris and García-Bellido, 2013] to provide a qualitative idea of the strength of the $\Delta\chi^2$ variation. We consider $0 \leq \Delta\chi^2 < 1.1$ as a weak variation (thus compatible χ^2 values), $1.1 \leq \Delta\chi^2 < 3$ as a definite variation, $3 \leq \Delta\chi^2 < 5$ as a strong variation, and $5 \leq \Delta\chi^2$ as a very strong variation.

From these results, we can observe that most NALPL models (A1, B1, B2, C1, C2, C3, D2, and D3) are not only able to fit the data with a very high goodness-of-fit statistic, but their χ^2 value is also compatible with that obtained for ΛCDM. We can conclude that a non-accelerated model is perfectly able to fit the main low-redshift background cosmological probes if SNIa intrinsic luminosity depends on the redshift.

Background probes and growth rate of matter perturbations

We now consider the results when adding the measurements of the growth of matter perturbations to the analysis. As described in Sec. 1.3, when we use the redshift-space distortions as a cosmological probe we need to assume a cosmology in order to translate from redshift to co-moving coordinates, which introduces the Alcock-Pacyznski effect. Nowadays, the majority of the $f\sigma_8$ measurements have been obtained by marginalizing over this effect, in order to be as cosmology independent as possible. Even if the $f\sigma_8$ measurements may still rely on simulations (that depend on the cosmology), they can account for variations with respect to the concordance model. In this work we use the measurements of the growth rate without any further treatment with respect to the cosmological model.

In Fig. 5.3 we present the results obtained when adding the measurements of the growth of matter perturbations to the low-redshift background probes.

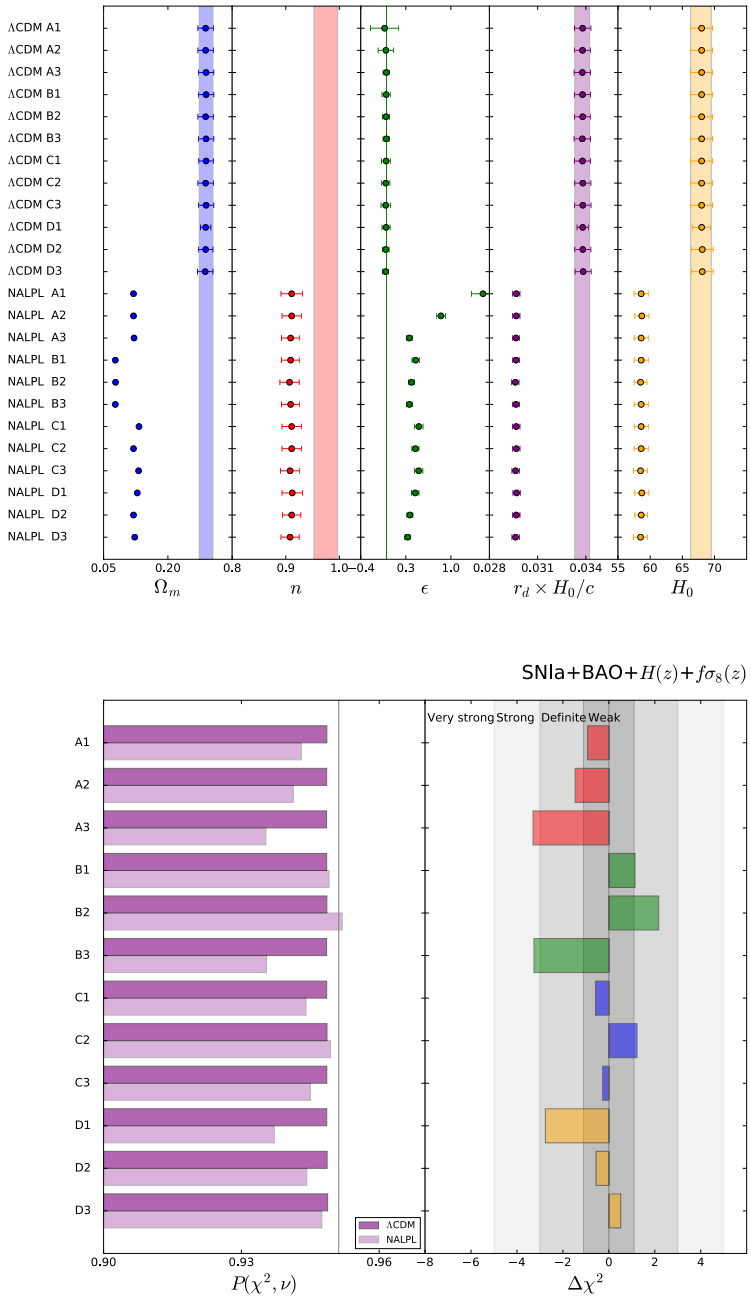

FIGURE 5.3: Results obtained from low-redshift background probes combined with measurements of the growth of matter perturbations. *Top panel*: best-fit values for Ω_m, n, ϵ, $r_\mathrm{d} \times H_0/c$, and H_0 parameters for all the cosmological and luminosity evolution models under consideration. The values for these parameters when no luminosity evolution is allowed are represented with bands as a reference. *Bottom panel*: goodness-of-fit and $\Delta\chi^2 = \chi^2_{\Lambda\mathrm{CDM}} - \chi^2_{\mathrm{NALPL}}$ values for the luminosity evolution models under study (see Fig. 5.2).

In the top panel we show the best-fit values for the cosmological and nuisance parameters. The obtained values for the ΛCDM models are completely compatible with the no luminosity evolution case, as in the previous case (Fig. 5.2). The only difference here are slightly smaller error bars due to the introduction of more data points. Concerning the NALPL models, we have an extra cosmological parameter, $\Omega_{\rm m}$ (see Sec. 5.1.2), which is very well constrained, but the other parameters remain qualitatively compatible with the results from Fig. 5.2: the cosmological parameters n, $r_{\rm d} \times H_0/c$ and H_0 are compatible with lower values than those obtained when no luminosity evolution is allowed, while ϵ is clearly not compatible with 0.

In the bottom panel of Fig. 5.3 we provide the results for the goodness-of-fit statistic and the variation of the χ^2 values. In the first plot we can observe that all models provide a very good fit to the data ($P(\chi^2, \nu) > 0.93$), while in the second panel we show that most NALPL models (A1, B1, B2, C1, C2, C3, D2, and D3) have a χ^2 value compatible with (or slightly better than) those provided by ΛCDM. From a model criteria point of view it is clear that NALPL is slightly disfavored because of the introduction of the extra $\Omega_{\rm m}$ parameter. However, the importance of the Occam factor depends on the model criteria used and, as discussed before, our goal is not to test the NALPL model against ΛCDM, but simply to show that it can fit the observational data extremely well.

It is important to stress that the best-fit values of both $\Omega_{\rm m}$ and H_0 are significantly smaller than the concordance ΛCDM values. Although this is not a problem to fit the low-redshift probes (as shown in the bottom panel of Fig. 5.3), this could be a problem when trying to fit the CMB, given the discrepancy with the concordance values. In Sec. 5.2.5 we discuss in more detail how variations on these parameters can still reproduce the CMB measurements, but we just recall here that the extrapolation of the power law model to the CMB era was already ruled out in the previous chapter. Therefore, it is not surprising that we find values not compatible with the concordance ones that reproduce the CMB measurements. Since the goal of this section was to focus on low-redshift data, we leave the discussion on the CMB for the following section.

In Fig. 5.4, just for completeness and illustrative purposes, we present the prediction for all probes using the best low-redshift power law model (B2), ΛCDM B2, and ΛCDM imposing no luminosity evolution. We used the global best-fit values for the cosmological and nuisance parameters. It is clear that all three models are able to reproduce the observations extremely well.

To conclude, taking all the low-redshift probes into account (SNIa, BAO, $H(z)$, and $f\sigma_8(z)$), a NALPL model is perfectly compatible with the data for several luminosity evolution models. This points to the fact that low-redshift

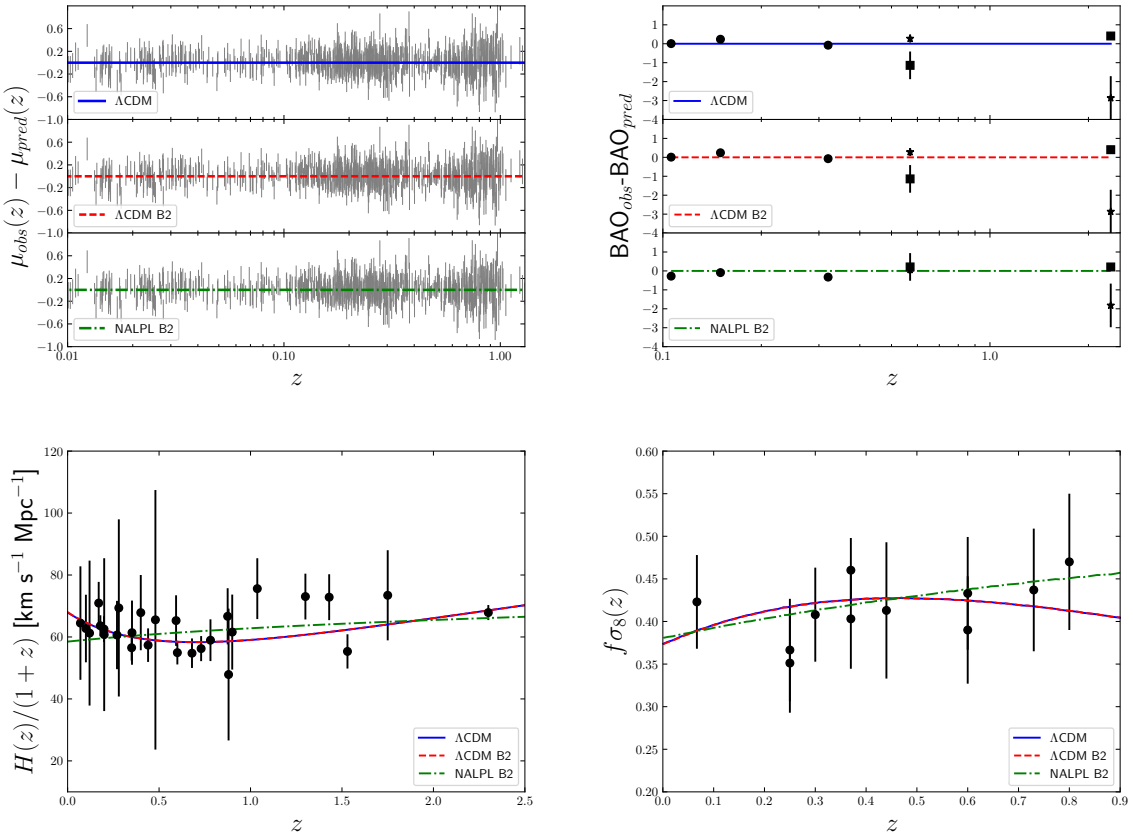

FIGURE 5.4: Model predictions vs. observations for the best luminosity evolution model, ΛCDM B2 and NALPL B2 (together with the standard ΛCDM prediction, for illustrative purposes) for all the cosmological probes considered. In each prediction, we used the best-fit values obtained from the global fit. *Top left*: residuals of SNIa data with respect to the corresponding model. *Top right*: residuals of BAO data with respect to the corresponding model. The isotropic measurements of the BAO are represented with a circle and their observable is $D_{\rm V}(z)/r_{\rm d}$, while the stars stand for the radial measurements with observable $\chi(z)/r_{\rm d}$ and the squares stand for the transverse measurements with observable $c/(H(z)r_{\rm d})$. *Bottom left*: measurements of $H(z)/(1+z)$ together with the model predictions. *Bottom right*: measurements of $f\sigma_8(z)$ and the different model predictions.

probes do not definitively prove the acceleration of the Universe, if we relax the luminosity-redshift independence assumption, and that we need more precise low-redshift measurements to claim this acceleration firmly.

5.1.5 Summary

In this section we have examined the ability of the low-redshift probes (SNIa, BAO, $H(z)$, and $f\sigma_8(z)$) to prove the accelerated expansion of the Universe. More precisely, we have considered a non-accelerating low-redshift power law cosmology and checked its ability to fit these cosmological data. Using only the low-redshift background probes, and not imposing the SNIa intrinsic luminosity to be redshift independent (accounting for several luminosity evolution models), we find that a non-accelerated low-redshift power law cosmology is able to fit very well all the observations, for all the luminosity evolution models considered. Moreover, most of the NALPL models provide a value for the χ^2 perfectly compatible with that obtained for ΛCDM.

When we add the measurements of the growth of matter perturbations, a non-accelerated low-redshift power law cosmology is still able to fit all the data extremely well for all the luminosity evolution models considered. As in the previous case, most of the NALPL models provide χ^2 values that are perfectly compatible (or even slightly better) than those coming from ΛCDM.

The main conclusion of this section is that if we do not impose the SNIa intrinsic luminosity to be independent of the redshift, the combination of low-redshift probes is not sufficient to firmly prove the accelerated expansion of the Universe.

5.2 Model-independent reconstruction of the expansion rate

5.2.1 Context

In this section we follow the approach of the previous one; we relax the assumption of SNIa luminosity-redshift independence by allowing SNIa to have different intrinsic luminosities as a function of the redshift. In the previous section it was shown that a non-accelerated power law cosmology was able to fit the main low-redshift cosmological probes: SNIa, BAO, $H(z)$, and $f\sigma_8(z)$, when some intrinsic luminosity redshift dependence is allowed. Nevertheless, this specific power-law model is excluded if we extend it up to the CMB era, as

it was shown in the previous chapter, or if we consider the latest SNIa observations at $z > 1$ [Riess et al., 2018b], even when accounting for some luminosity evolution.

In this section we extend our previous study with a model-independent analysis, and we include the latest BAO observations as well as the complementary high-redshift CMB data, with the assumption of a matter and radiation dominated early universe. In order to be as model-independent as possible, we follow the approach of Bernal, Verde, and Riess, 2016, and reconstruct the expansion rate at late times through a cubic spline interpolation. Notice that this approach introduces many more free parameters than a specific power law model, for example, so any reconstruction will be obviously disfavored with respect to the concordance model. However, our goal is to let the data choose the preferred expansion and study the impact of luminosity-redshift dependence on cosmic acceleration; not to propose a cosmological model to confront ΛCDM.

5.2.2 Cosmological probes

In this subsection we present the different cosmological probes considered in the analysis, as well as the specific data sets used, paying special attention to the differences with respect to the general introduction in Sec. 1.5.

Type Ia supernovae

In this section we consider again the joint light-curve analysis for SNIa from Betoule et al., 2014. With respect to the SNIa luminosity dependence on the redshift, we only consider here Model B from the previous section, that has also been used in Riess et al., 2018b, where $\Delta m_{\rm evo}(z) = \epsilon z^{\delta}$. We recall that a lower δ value models a luminosity evolution dominant at low-redshift, while a higher δ value leads to a luminosity evolution dominating at high-redshift. In this section we consider not only ϵ but also δ as free parameters. Since δ must be greater than 0, in order not to be degenerate with $M_{\rm B}^1$, we restrict ourselves to $\delta \in [0.2, 2]$ when sampling the parameter space.

Baryon acoustic oscillations

As already said in Sec. 4.4.2, models differing from the standard ΛCDM framework may have a value for the BAO standard ruler, $r_{\rm d}$, that is not compatible with the co-moving sound horizon at the redshift of the baryon drag epoch, $r_{\rm s}(z_{\rm d})$ [Verde et al., 2017b]. It has also been shown that the computed value of $r_{\rm d}$ may depend on the physics of the early Universe, and that adding dark radiation at early times could alleviate the tension between the local measurement and the CMB-derived value of H_0 [Bernal, Verde, and Riess, 2016]. Moreover,

there has recently been some analyses computing $r_{\rm d}$ without any dependence on late-time Universe assumptions, thanks to the fact that late-time physics only affect the CMB through projection effects from real space to harmonic space, the late integrated Sachs-Wolfe effect [2], and re-ionization (see Verde et al., 2017a, and references therein for all the details). Because of all this, in this section we consider three different methods to include BAO data:

1. compute $r_{\rm d}$ with Eq. (1.149) replacing z_* by $z_{\rm d}$,
2. let $r_{\rm d}$ free,
3. include the prior $r_{\rm d} = 147.4 \pm 0.7\,{\rm Mpc}$ from Verde et al., 2017a.

However, we only compute $r_{\rm d}$ when we consider SNIa, BAO, and CMB data together, since it is the only case for which we specify the expansion rate of the Universe up to very high redshift (see next subsection).

In this section we use the isotropic measurements provided by 6dFGS at $z = 0.106$ [Beutler et al., 2011] and by SDSS - MGS at $z = 0.15$ [Ross et al., 2015], as well as the results from WiggleZ at $z = 0.44, 0.6, 0.73$ [Kazin et al., 2014]. We also consider the anisotropic final results of BOSS DR12 at $z = 0.38, 0.51, 0.61$ [Alam et al., 2017], and the new anisotropic measurements from the eBOSS DR14 quasar sample [Gil-Marín et al., 2018] at $z = 1.19, 1.50, 1.83$. These results have been obtained by measuring the redshift-space distortions using the power spectrum monopole, quadrupole and hexadecapole. The authors in Gil-Marín et al., 2018, have shown that their results are completely consistent with different methods used for analyzing the same data [Hou et al., 2018; Zarrouk et al., 2018]. We finally consider the latest results from the combination of the Ly-α forest auto-correlation function [Bautista, J. E. et al., 2017] and the Lyα-quasar cross-correlation function [du Mas des Bourboux, H. et al., 2017] from the complete BOSS survey at $z = 2.4$. We take into account the covariance matrix provided for the measurements of WiggleZ, BOSS DR12, eBOSS DR14, we consider a correlation coefficient of -0.38 for the Ly-α forest measurements, and we assume measurements of different surveys to be uncorrelated [3]. In order to take into account the non-Gaussianity of the BAO observable likelihoods far from the peak, we follow the approach presented in Bassett and Afshordi, 2010, and already used in the previous chapter. We consider a detection significance (S/N) of 2.4σ for 6dFGS, 2σ for SDSS-MGS and WiggleZ, 9σ for BOSS DR12, 4σ for eBOSS DR14, and 5σ for the Ly-α forest. Some of these values are slightly lower than the quoted ones by the different collaborations in order to

[2] The large-scale gravitational potential energy wells and hills are modified due to a dark energy dominated expansion, which changes the energy of the CMB photons passing through them.

[3] In particular, we neglect any correlation between the WiggleZ and BOSS measurements.

follow a conservative approach, and in case the likelihood becomes non-Gaussian at these high confidence levels.

Cosmic microwave background

In this section we include the CMB data through the reduced parameters: the scaled distance to recombination R, the angular scale of the sound horizon at recombination ℓ_a, and the reduced density parameter of baryons $\omega_{\rm b}$ [Eq. (1.148)]. We consider the data obtained from the Planck 2015 data release [Planck Collaboration, 2016c], where the compressed likelihood parameters are obtained from the Planck temperature-temperature plus the low-ℓ Planck temperature-polarization likelihoods. We specifically consider the reduced parameters obtained when marginalizing over the amplitude of the lensing power spectrum for the lower values, since it leads to a more conservative approach, together with their covariance matrix.

It is important to recall that the reduced parameters can only be used for models close to ΛCDM, since this is the model assumed to derive the values of the reduced parameters from Planck data. In the previous chapter we considered a very exotic model for which the reduced parameters could not be used. Therefore, we limited ourselves to the use of ℓ_a, which is the most model independent parameter. In this section we allow for a general expansion rate at low-redshift, but we consider a concordance early universe dominated by matter and radiation (as will be explained in the following); therefore, although not being perfectly model independent, we consider here all the reduced parameters of the CMB.

5.2.3 Expansion rate reconstruction method

In this subsection we first present the reconstruction method used to obtain the expansion rate as a function of the redshift, and we then give a detailed explanation of how we introduce each cosmological probe in the analysis. The ΛCDM model (used as a reference) and the method used to determine the best-fit values of the parameters have already been described in Sec. 1.1.5 and Sec. 4.3, respectively.

We want our reconstruction to be as model-independent as possible, and we impose a smooth and continuous expansion rate. Several model-independent reconstruction methods have been used in the literature to reconstruct the dark energy equation of state parameter, or even the Hubble parameter. Among them let us mention the principal component analysis [Huterer and Starkman, 2003; Crittenden, Pogosian, and Zhao, 2009; Liu et al., 2016b; Said et al., 2013; Qin et al., 2015], the Gaussian processes [Clarkson and Zunckel,

TABLE 5.2: Summary of the cosmological probes and parameters present in the different cases considered. The i-index on E_i goes from 1 to 5 for SNIa data alone, while it goes up to 6 when BAO data is included. When working with coasting reconstructions we only consider the last two knots E_i.

Case	Cosmological probes	Cosmological parameters	Nuisance parameters
SNIa	SNIa	E_i	$\alpha, \beta, M_{\rm B}^1, \Delta_{\rm M}$
SNIa+BAO free $H_0 r_{\rm d}$	SNIa+BAO	$E_i, H_0 r_{\rm d}$	$\alpha, \beta, M_{\rm B}^1, \Delta_{\rm M}$
SNIa+ev+BAO free $H_0 r_{\rm d}$	SNIa+BAO	$E_i, H_0 r_{\rm d}$	$\alpha, \beta, M_{\rm B}^1, \Delta_{\rm M}, \epsilon, \delta$
SNIa+BAO prior $r_{\rm d}$	SNIa+BAO	$E_i, H_0, r_{\rm d}$	$\alpha, \beta, M_{\rm B}^1, \Delta_{\rm M}$
SNIa+ev+BAO prior $r_{\rm d}$	SNIa+BAO	$E_i, H_0, r_{\rm d}$	$\alpha, \beta, M_{\rm B}^1, \Delta_{\rm M}, \epsilon, \delta$
SNIa+BAO free $r_{\rm d}$+CMB	SNIa+BAO+CMB	$E_i, H_0, r_{\rm d}, \Omega_{\rm m}, \omega_{\rm b}$	$\alpha, \beta, M_{\rm B}^1, \Delta_{\rm M}, z_*$
SNIa+ev+BAO free $r_{\rm d}$+CMB	SNIa+BAO+CMB	$E_i, H_0, r_{\rm d}, \Omega_{\rm m}, \omega_{\rm b}$	$\alpha, \beta, M_{\rm B}^1, \Delta_{\rm M}, z_*, \epsilon, \delta$
SNIa+BAO prior $r_{\rm d}$+CMB	SNIa+BAO+CMB	$E_i, H_0, r_{\rm d}, \Omega_{\rm m}, \omega_{\rm b}$	$\alpha, \beta, M_{\rm B}^1, \Delta_{\rm M}, z_*$
SNIa+ev+BAO prior $r_{\rm d}$+CMB	SNIa+BAO+CMB	$E_i, H_0, r_{\rm d}, \Omega_{\rm m}, \omega_{\rm b}$	$\alpha, \beta, M_{\rm B}^1, \Delta_{\rm M}, z_*, \epsilon, \delta$
SNIa+BAO compute $r_{\rm d}$+CMB	SNIa+BAO+CMB	$E_i, H_0, \Omega_{\rm m}, \omega_{\rm b}$	$\alpha, \beta, M_{\rm B}^1, \Delta_{\rm M}, z_*, z_{\rm d}$
SNIa+ev+BAO compute $r_{\rm d}$+CMB	SNIa+BAO+CMB	$E_i, H_0, \Omega_{\rm m}, \omega_{\rm b}$	$\alpha, \beta, M_{\rm B}^1, \Delta_{\rm M}, z_*, z_{\rm d}, \epsilon, \delta$

2010; Holsclaw et al., 2010; Seikel, Clarkson, and Smith, 2012; Yu, Ratra, and Wang, 2017; Busti, Clarkson, and Seikel, 2014; Wang and Meng, 2017], or, very recently, the Weighted Polynomial Regression method [Gómez-Valent and Amendola, 2018]. In this work we follow the approach from Bernal, Verde, and Riess, 2016, reconstructing the late-time expansion history by expressing $E(z) \equiv H(z)/H_0$ in piece-wise natural cubic splines. When we consider SNIa data alone, $E(z)$ is specified by its value at 5 different "knots" in redshift: $z = 0.1, 0.25, 0.57, 0.8, 1.3$ [4]. Therefore, our reconstruction when analyzing SNIa data considers the following set of parameters $\{E_i, \alpha, \beta, M_{\rm B}^1, \Delta_{\rm M}, \epsilon, \delta\}$ with E_i for $i \in [1, 5]$ being the 5 knots in redshift, $\alpha, \beta, M_{\rm B}^1, \Delta_{\rm M}$ the standard SNIa nuisance parameters, and ϵ, δ the SNIa intrinsic luminosity evolution parameters.

When BAO data is added into the analysis we consider an extra knot in our reconstruction at $z = 2.4$ [5]. We follow two different approaches to include the BAO measurements: first we consider the product $H_0 r_{\rm d}$ as a free parameter, and secondly we add information coming from the early Universe through the prior on $r_{\rm d}$ from Verde et al., 2017a, $r_{\rm d} = 147.4 \pm 0.7\,{\rm Mpc}$. In the first case, the set of parameters considered in our reconstruction of $E(z)$ is $\{E_i, \alpha, \beta, M_{\rm B}^1, \Delta_{\rm M}, H_0 r_{\rm d}, \epsilon, \delta\}$ with E_i for $i \in [1, 6]$ being the 6 knots in redshift,

[4] These values have been chosen such that the expansion rate has a significant amount of freedom at low-redshift, and because this is the interval for which SNIa data are available. A more detailed analysis on the number of knots and their position is left for future work.

[5] It corresponds to the redshift of the Ly-α forest measurements.

while in the second case we consider H_0 and r_d separately $\{E_i, \alpha, \beta, M_\mathrm{B}^1, \Delta_\mathrm{M}, H_0, r_\mathrm{d}, \epsilon, \delta\}$. It is important to comment here that our statistical approach in this chapter is frequentist (see Sec. 4.3); therefore, by prior we mean here that we add a Gaussian likelihood centered at the corresponding value (of r_d in this case) with the corresponding 1σ error to our full likelihood before minimizing the χ^2 function. Rigorously, we are modifying the likelihood, from a frequentist approach.

When we finally add the reduced parameters for the CMB we need to specify $E(z)$ up to early-times. In order to do this we add the seventh knot at $z = 2.7$ computed according to a matter dominated model (with flat Robertson-Walker metric and Friedmann-Lemaître dynamics) with free H_0 and Ω_m parameters [see Eq. (1.63)], and we extend the model up to very high-redshift. The main idea in this reconstruction is to start at early-times following a matter dominated model (plus radiation and a negligible contribution of dark energy through a cosmological constant) and, when we start to have late Universe data and a cosmological constant is still negligible with respect to the quantity of matter present in the Universe, we reconstruct $E(z)$ through a cubic spline interpolation; in this way we give our reconstruction the freedom to choose the preferred expansion without specifying a particular model for dark energy. When analyzing the data we consider three different cases, depending on the way of introducing the BAO measurements. First, we consider r_d as a free parameter, while, in a second place, we add the prior on r_d from Verde et al., 2017a ($r_\mathrm{d} = 147.4 \pm 0.7\,\mathrm{Mpc}$). In both cases, the set of parameters that enters into the reconstruction is given by $\{E_i, \alpha, \beta, M_\mathrm{B}^1, \Delta_\mathrm{M}, H_0, r_\mathrm{d}, \Omega_\mathrm{m}, z_*, \omega_\mathrm{b}, \epsilon, \delta\}$, and we add the prior on the last scattering redshift $z_* = 1089.90 \pm 0.23$ [Planck Collaboration, 2016b]. As a last case we compute the value of r_d using Eq. (1.149) with z_d . In this case the set of parameters is given by $\{E_i, \alpha, \beta, M_\mathrm{B}^1, \Delta_\mathrm{M}, H_0, \Omega_\mathrm{m}, z_*, \omega_\mathrm{b}, z_\mathrm{d}, \epsilon, \delta\}$, and we add the prior on $z_\mathrm{d} = 1059.68 \pm 0.29$ [Planck Collaboration, 2016b].

In order to test the degeneracy between a SNIa intrinsic luminosity evolution and cosmic acceleration, we consider different cases with and without luminosity redshift dependence, so ϵ and δ can be removed from the analysis. Finally, we also consider the so-called coasting reconstructions, in which the universe has a late-time constant expansion rate. More specifically, we fix the first 4 knots [6] (since it is roughly the region where the expansion is accelerated in the concordance model) such that $E(z)$ is equal to $(1 + z)$ at these points. Let us recall that $E(z) \propto H(z) \equiv \dot{a}/a$; therefore,

[6] When using SNIa data alone we only fix the first 3 knots because there is not a lot of data beyond $z \sim 0.8$, but we have checked that fixing the first 4 knots leads to equivalent conclusions.

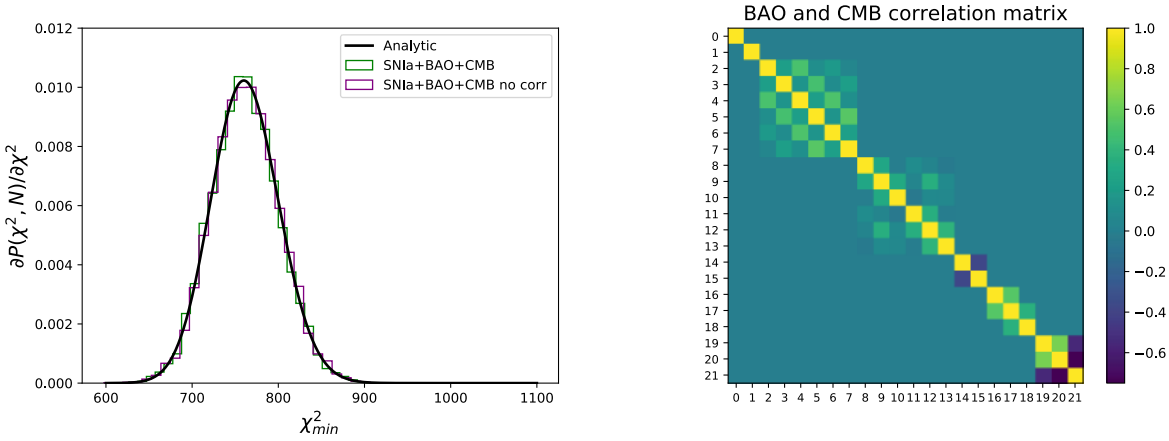

FIGURE 5.5: *Left plot*: histograms (with 10000 iterations) of χ^2 for Monte Carlo simulations using correlations (green) and neglecting them (purple). The analytic distribution is represented with a thick black solid line. *Right plot*: correlation matrix of the BAO measurements (ranging from 0 to 18) and CMB measurements (ranging from 19 to 21) used in this section.

$$E(z) = (1+z) \Rightarrow \frac{\dot{a}}{a} \propto (1+z) = \frac{1}{a}\,, \tag{5.3}$$

which implies that $\dot{a}$ is a constant, giving a coasting universe. See Table 5.2 for a summary of the different cases considered and the cosmological and nuisance parameters present in them.

5.2.4 Goodness-of-fit and effect of correlations

As it was the case in Sec. 5.1.3, we follow the methodology of Sec. 4.3 to determine the goodness-of-fit, but we use different data sets, so we test again the impact of the correlations within probes when we compute $P(\chi^2, \nu)$ [Eq. (2.30)].

In the left panel of Fig. 5.5 we present the χ^2 histograms obtained from the Monte Carlo simulations with the correlations within probes (green) and neglecting them (purple) for the cosmological data sets used in this section. Both distributions are equivalent and compatible with the analytic prediction. Therefore, we can still use Eq. (2.30) to compute $P(\chi^2, \nu)$. We also show, for completeness, the correlation matrix of the BAO and CMB measurements in the right panel of Fig. 5.5. We can observe that some BAO points show correlations of the order $\sim 50\,\%$, but the majority of them are only slightly correlated or uncorrelated. However, we can also observe that the CMB reduced parameters are significantly correlated (between $55\,\%$ and $75\,\%$). The SNIa correlation matrix was already provided in Fig. 4.3.

TABLE 5.3: Best-fit values with the corresponding 1σ error bars for the cosmological and nuisance parameters of the first case: SNIa data. The values in parentheses show the fixed knots. The values of ΛCDM are added as a reference. The reduced χ^2 and the probability $P(\chi^2, \nu)$ are also provided for the different models.

Case	SNIa		
Model	ΛCDM	Splines	CS (3 knots)
E_1	–	1.041 ± 0.022	(1.10)
E_2	–	1.141 ± 0.023	(1.25)
E_3	–	1.344 ± 0.071	(1.57)
E_4	–	1.46 ± 0.13	1.69 ± 0.15
E_5	–	1.90 ± 0.90	1.27 ± 0.58
$\Omega_{\rm m}$	0.295 ± 0.034	–	–
α	0.1412 ± 0.0066	0.1414 ± 0.0066	0.1385 ± 0.0066
β	3.101 ± 0.081	3.106 ± 0.082	3.075 ± 0.081
$M_{\rm B}^1$	24.110 ± 0.023	24.110 ± 0.032	24.230 ± 0.017
$\Delta_{\rm M}$	-0.070 ± 0.023	-0.070 ± 0.023	-0.077 ± 0.023
χ^2/d.o.f	682.89/735	681.38/731	717.60/734
$P(\chi^2, \nu)$	0.915	0.905	0.661

5.2.5 Results

In this subsection we present the results of the reconstruction of the expansion rate of the Universe as a function of the redshift for different sets of cosmological probes: SNIa, SNIa combined with BAO, and SNIa combined with both BAO and CMB data. We also comment on the linear growth of structures measurements, and the importance of the value of the Hubble constant, H_0, to draw conclusions on the accelerated nature of the expansion of the Universe.

Case 1: SNIa

We first start considering only SNIa data without any luminosity evolution as a function of the redshift. We present this case as an illustration of the reconstruction method used for $E(z) \equiv H(z)/H_0$. The best-fit values for the cosmological and nuisance parameters are presented in Table 5.3 together with the 1σ error bars, and the reconstructions are shown in Fig. 5.6. We show three different models in this case: the reconstruction through cubic splines (red), the reconstruction for a coasting universe (labelled CS) at low-redshift (fixing

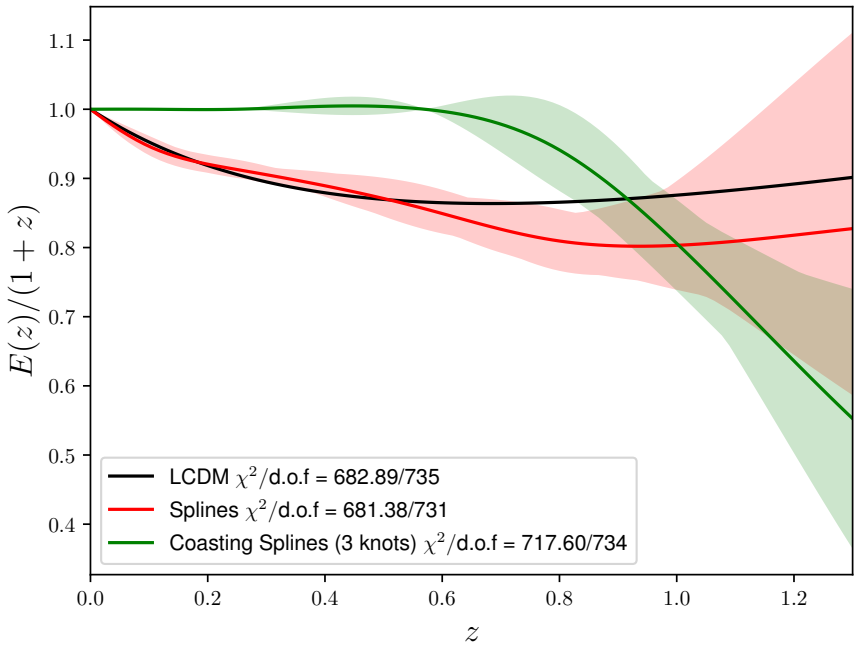

FIGURE 5.6: Reconstruction of the expansion rate, $E(z)/(1+z)$, as a function of the redshift using SNIa data alone. The black line represents the ΛCDM model, while the red band shows the reconstruction with $\Delta\chi^2 \leq 1$ with respect to the best reconstruction (red line). The green band stands for the reconstruction of a coasting universe at low-redshift. See the text for the details of the reconstruction.

the first 3 knots - green), and ΛCDM as a reference (black). In Table 5.3 we also provide the reader with the ratio of the χ^2 over the number of degrees of freedom, and the probability $P(\chi^2, \nu)$ from Eq. (2.30). In order to obtain the bands for the reconstructions we generate 500 splines from an N-dimensional Gaussian centered at the best-fit values and with the covariance matrix obtained from the fit to the data. We further require each spline to have a $\Delta\chi^2$ value smaller or equal than 1 with respect to the best-fit reconstruction. We recall that the derivative of $E(z)/(1+z)$ is proportional to $\ddot{a}$; therefore, a decreasing $E(z)/(1+z)$ as a function of the redshift implies acceleration, while an increasing one implies deceleration.

In Table 5.3 we can clearly see that all the SNIa nuisance parameters values $(\alpha, \beta, M_{\rm B}^1, \Delta_{\rm M})$ are compatible for the three models, and that a coasting universe shows a lower expansion rate when we increase the redshift with respect to the standard spline reconstruction. This is confirmed from Fig. 5.6 where we see that the expansion rate drops above $z \approx 0.8$. We can also observe in this figure that the bands increase when we increase the redshift, as expected, since there are

less data points in this region. Comparing the three models, we observe that the spline reconstruction provides a slightly smaller χ^2 value (681.38) than ΛCDM (682.89), but the former has many more parameters in the model, so the ability of these models to fit the data is roughly the same, being slightly better for ΛCDM ($P(\chi^2, \nu) = 0.915$) than the spline reconstruction ($P(\chi^2, \nu) = 0.905$, see also the reduced χ^2 values in Fig. 5.6). However, the χ^2 value obtained for the coasting reconstruction (717.60) is much larger than the previous values, which also implies that this model is less able to nicely fit the data ($P(\chi^2, \nu) = 0.661$). A detailed model comparison is beyond the scope of this work, since we are interested in studying the accelerated expansion of the Universe and the relation it may have with SNIa luminosity, not in proposing a new cosmological model to confront against ΛCDM. However, the coasting reconstruction has a relative probability of $\exp(-\Delta\chi^2/2) \approx 1.4 \times 10^{-6}\,\%$, showing that a coasting universe at low-redshift is highly disfavored ($> 5\,\sigma$)[7], even using SNIa data alone, when SNIa intrinsic luminosity is assumed to be redshift independent (see also the previous chapter). Notice also that, even if we ask the reconstruction to be non-accelerated at low-redshift by fixing the first knots, the data prefers to add some acceleration (decreasing $E(z)/(1+z)$) at earlier times (above $z \approx 0.8$) than just having a constant velocity expansion.

Case 2: SNIa+BAO

After having shown how the reconstruction method works, and having applied it to SNIa data alone, we focus on the combination of SNIa and BAO data. As it is shown in Table 5.2, we consider two different ways to combine these data sets: we either let the product $H_0 r_\mathrm{d}$ free, or we add a prior on r_d. Since we consider the models with and without SNIa intrinsic luminosity evolution, and we always add ΛCDM into the analysis as a reference, we finally have 4 different sub-cases with the corresponding three models per sub-case. The best-fit values and errors of the parameters for all these cases are shown in Table 5.4.

Let us first focus on the case where $H_0 r_\mathrm{d}$ is treated as a free parameter. As it was the case with SNIa data alone, all the SNIa nuisance parameters $(\alpha, \beta, M_\mathrm{B}^1, \Delta_\mathrm{M})$ have compatible values for the different models considered. However, the coasting reconstruction now does not show a reduced expansion rate at high-redshift (adding or not SNIa luminosity evolution), due to the addition of the BAO data points above $z \sim 0.8$. We can also see that the value of

[7] Notice that we do find more than a 5σ preference for cosmic acceleration (when SNIa luminosity does not evolve with the redshift), contrary to the results of Nielsen, Guffanti, and Sarkar, 2016, because we consider the standard SNIa systematics, instead of the extra systematics proposed by these authors. However, we are still far from the 11.2σ detection from Rubin and Hayden, 2016, because we use a model-independent reconstruction with many more degrees-of-freedom than a fixed non-accelerated model.

TABLE 5.4: Best-fit values with the corresponding 1σ error bars for the cosmological and nuisance parameters of the second case of: SNIa and BAO data. The values in parentheses show the fixed knots. The values of ΛCDM are added as a reference. The reduced χ^2 and the probability $P(\chi^2, \nu)$ are also provided for the different models. H_0 is expressed in km/s/Mpc, $r_{\rm d}$ in Mpc, and their product $H_0 r_{\rm d}$ in km/s.

Case	SNIa+BAO free $H_0 r_{\rm d}$			SNIa+ev+BAO free $H_0 r_{\rm d}$			SNIa+BAO prior $r_{\rm d}$			SNIa+ev+BAO prior $r_{\rm d}$		
Model	ΛCDM	Splines	CS (4 knots)	ΛCDM	Splines	CS (4 knots)	ΛCDM	Splines	CS (4 knots)	ΛCDM	Splines	CS (4 knots)
E_1	–	1.050 ± 0.020	(1.10)	–	1.118 ± 0.044	(1.10)	–	1.050 ± 0.020	(1.10)	–	1.048 ± 0.021	(1.10)
E_2	–	1.133 ± 0.020	(1.25)	–	1.241 ± 0.065	(1.25)	–	1.133 ± 0.019	(1.25)	–	1.149 ± 0.023	(1.25)
E_3	–	1.385 ± 0.035	(1.57)	–	1.510 ± 0.078	(1.57)	–	1.385 ± 0.032	(1.57)	–	1.410 ± 0.039	(1.57)
E_4	–	1.591 ± 0.074	(1.80)	–	1.77 ± 0.13	(1.80)	–	1.591 ± 0.073	(1.80)	–	1.671 ± 0.095	(1.80)
E_5	–	2.15 ± 0.14	2.33 ± 0.15	–	2.34 ± 0.18	2.38 ± 0.15	–	2.15 ± 0.14	2.33 ± 0.15	–	2.20 ± 0.15	2.38 ± 0.16
E_6	–	3.43 ± 0.10	3.768 ± 0.098	–	3.70 ± 0.19	3.760 ± 0.090	–	3.43 ± 0.10	3.768 ± 0.098	–	3.46 ± 0.11	3.759 ± 0.097
$H_0 r_{\rm d}$	10120 ± 126	10040 ± 174	9144 ± 69	10120 ± 137	9286 ± 420	9140 ± 64	–	–	–	–	–	–
H_0	–	–	–	–	–	–	68.66 ± 0.91	68.1 ± 1.2	62.04 ± 0.55	68.48 ± 0.97	67.3 ± 1.3	62.01 ± 0.55
$r_{\rm d}$	–	–	–	–	–	–	147.40 ± 0.70	147.40 ± 0.70	147.40 ± 0.70	147.40 ± 0.70	147.40 ± 0.70	147.40 ± 0.70
$\Omega_{\rm m}$	0.292 ± 0.017	–	–	0.292 ± 0.019	–	–	0.292 ± 0.017	–	–	0.296 ± 0.019	–	–
α	0.1413 ± 0.0066	0.1410 ± 0.0066	0.1382 ± 0.0066	0.1413 ± 0.0066	0.1414 ± 0.0066	0.1416 ± 0.0064	0.1413 ± 0.0066	0.1411 ± 0.0066	0.1382 ± 0.0066	0.1414 ± 0.0066	0.1413 ± 0.0066	0.1416 ± 0.0066
β	3.102 ± 0.080	3.099 ± 0.081	3.073 ± 0.080	3.103 ± 0.080	3.101 ± 0.081	3.104 ± 0.081	3.103 ± 0.080	3.099 ± 0.081	3.073 ± 0.080	3.105 ± 0.081	3.101 ± 0.081	3.104 ± 0.081
$M_{\rm B}^1$	24.110 ± 0.019	24.120 ± 0.030	24.230 ± 0.017	24.110 ± 0.058	23.94 ± 0.11	24.050 ± 0.081	24.110 ± 0.019	24.120 ± 0.029	24.230 ± 0.017	24.110 ± 0.020	24.110 ± 0.031	24.050 ± 0.094
$\Delta_{\rm M}$	-0.070 ± 0.023	-0.070 ± 0.023	-0.077 ± 0.023	-0.070 ± 0.023	-0.070 ± 0.023	-0.070 ± 0.022	-0.070 ± 0.023	-0.070 ± 0.023	-0.077 ± 0.023	-0.070 ± 0.023	-0.070 ± 0.023	-0.070 ± 0.023
ϵ	–	–	–	0.001 ± 0.080	0.39 ± 0.22	0.322 ± 0.075	–	–	–	0.029 ± 0.052	0.094 ± 0.065	0.322 ± 0.078
δ	–	–	–	0.20 ± 0.19	0.20 ± 0.16	0.41 ± 0.20	–	–	–	2.0 ± 1.7	2.0 ± 1.5	0.41 ± 0.24
χ^2/d.o.f	698.64/753	696.46/748	739.91/752	698.64/751	694.21/746	698.95/750	698.64/753	696.46/748	739.91/752	698.35/751	694.37/746	698.95/750
$P(\chi^2, \nu)$	0.922	0.911	0.616	0.914	0.912	0.909	0.922	0.911	0.616	0.915	0.912	0.909

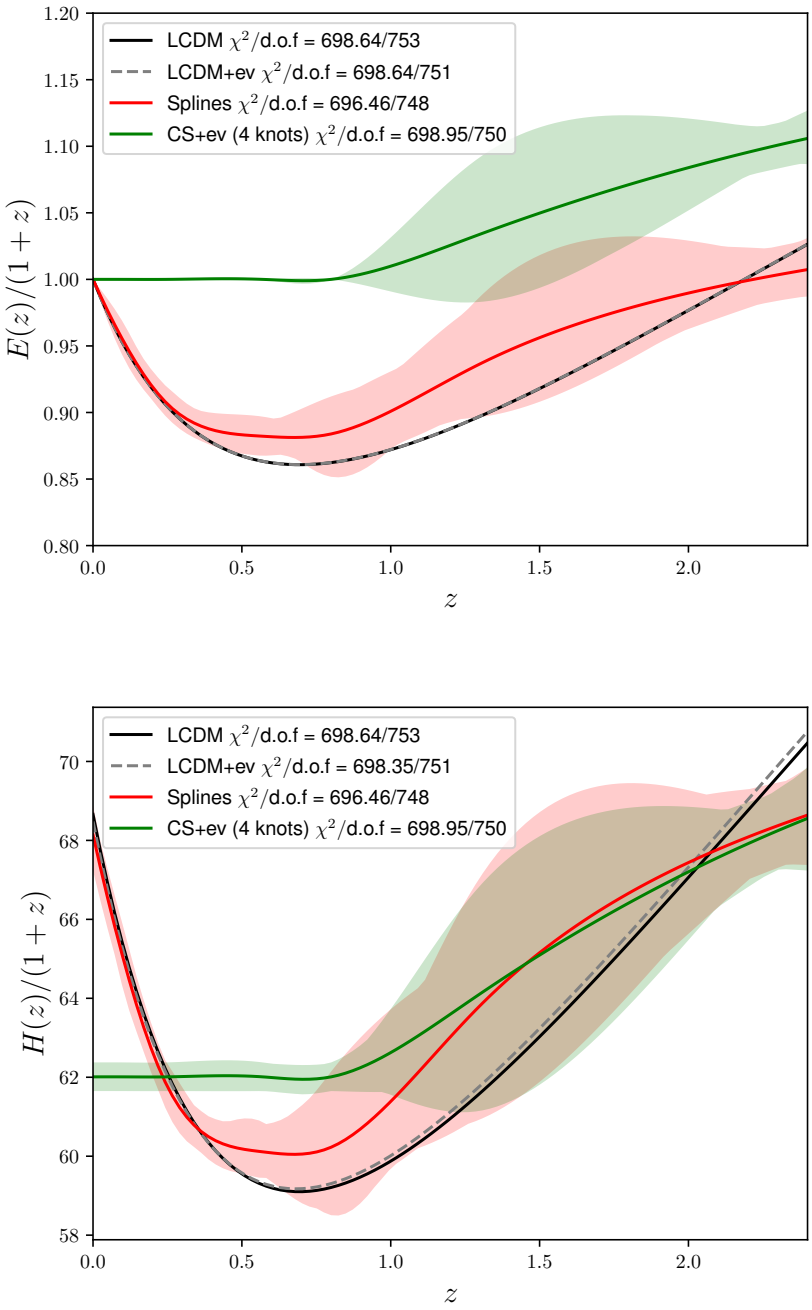

FIGURE 5.7: Reconstruction of the expansion rate, $E(z)/(1+z)$ (top) and $H(z)/(1+z)$ (bottom), as a function of the redshift using the combination of SNIa and BAO data. In the top panel the data sets have been combined considering $H_0 r_\mathrm{d}$ a free parameter, while in the bottom panel a prior on r_d has been added. In both panels the black and grey lines represent the ΛCDM model (without and with SNIa luminosity evolution, respectively), while the red band shows the reconstruction with $\Delta\chi^2 \leq 1$ with respect to the best reconstruction (red line). The green band stands for the reconstruction of a coasting universe at low-redshift when SNIa intrinsic luminosity is allowed to vary as a function of the redshift.

$H_0 r_\mathrm{d}$ obtained from the spline reconstruction is more or less compatible with the one obtained with ΛCDM, but it is lower for the coasting reconstruction, adding SNIa intrinsic luminosity or not. Concerning the ability of the models to fit the data, the χ^2 of the spline reconstruction is always slightly smaller than the ΛCDM one (696.46 against 698.64, and 694.21 against 698.64 when we allow the SNIa luminosity to vary). But as it was the case before, the probability of providing a good fit is roughly the same for both models, being slightly better for ΛCDM (0.911 against 0.922, and 0.912 against 0.914 when we account for evolution). It is also what can be seen in the reconstruction plot on the top panel of Fig. 5.7. With respect to the coasting reconstruction, we can see in Table 5.4 that, when SNIa intrinsic luminosity is allowed to vary, we obtain a χ^2 value very close to the ΛCDM one, thus giving also a good probability to correctly fit the data (0.909 against 0.912, for the standard reconstruction, and 0.914, for ΛCDM).

Let us now focus on the combination of SNIa and BAO data with a prior on r_d (last columns of Table 5.4 and the bottom panel of Fig. 5.7). It allows us to obtain a constraint on H_0, so we represent in this case the expansion rate by $H(z)/(1+z)$. All the best-fit values of the parameters are very close to the previous case, with nearly the same χ^2 values and the same probabilities, since we have only added one data point and one parameter in the analysis. As before, a coasting universe provides a good fit to the data with a probability of 0.909 against 0.912, for the standard spline reconstruction, and 0.915 for ΛCDM, when SNIa luminosity is allowed to vary. The interesting result from these cases is that the value found for H_0 for the spline reconstruction is always smaller than the one obtained for ΛCDM, but still compatible ($67.3 \pm 1.3\,\mathrm{km/s/Mpc}$ compared to $68.48 \pm 0.97\,\mathrm{km/s/Mpc}$, when SNIa luminosity is allowed to vary); nevertheless, it is significantly smaller for the coasting reconstruction, as it can be seen in the bottom plot of Fig. 5.7 ($62.01 \pm 0.55\,\mathrm{km/s/Mpc}$ compared to $68.48 \pm 0.97\,\mathrm{km/s/Mpc}$, when SNIa luminosity is allowed to vary). This is consistent with the lower value found for $H_0 r_\mathrm{d}$ in the previous cases for the coasting reconstruction.

Case 3: SNIa+BAO+CMB

Let us recall that the addition of CMB data is a key ingredient when studying cosmological models thanks to its complementarity with low-redshift cosmological probes. An example of the constraining power of the CMB was provided in Chapter 4, where only one reduced parameter of the CMB was enough to rule out power law cosmologies. Therefore, as a last case in this section we consider the combination of the three main background expansion cosmological probes: SNIa, BAO, and CMB.

We have already presented two different ways to combine SNIa and BAO data, so when we add CMB data (the reduced parameters ℓ_a, R, and $\omega_{\rm b}$) we keep this approach and, since we now include the physics of the early Universe, we add a third way consisting on computing the explicit value of $r_{\rm d}$ (see Sec. 5.2.2). The best-fit values, with the 1σ errors, of the parameters for these three sub-cases are presented in Table 5.5, and the corresponding reconstruction in Fig. 5.8. Let us mention that even if z_* and $z_{\rm d}$ in Table 5.5 seem to be fixed, both of them have been fitted each time adding the Planck priors, as explained in Sec. 5.2.3; however, the best-fit values are very stable and they are identical in the table given the number of decimals presented.

Let us start with the combination considering $r_{\rm d}$ a free parameter. Both assuming the SNIa intrinsic luminosity to be redshift independent or allowing it to vary, the three models provide compatible values for all the parameters except H_0, which is significantly smaller for the coasting reconstruction, as it was already shown in the combination of SNIa and BAO data, and which is compensated by a larger $\Omega_{\rm m}$. Notice that the CMB is sensitive to the physical matter energy density $\Omega_{\rm m}h^2$, which is roughly equal to 0.14 for all models. So even if the value of H_0 is smaller than in the concordance model, if the value of $\Omega_{\rm m}$ is large enough, the coasting reconstruction can perfectly fit the CMB too. When SNIa luminosity is allowed to vary, a coasting reconstruction provides roughly the same χ^2 (699.44) as ΛCDM (698.66) with a slightly smaller probability (0.906 against 0.918), showing that a non-accelerated expanding universe can fit the three main background probes when SNIa intrinsic luminosity is allowed to vary.

In a second place we add a prior on $r_{\rm d}$ [Verde et al., 2017a] obtained without assumptions on the late-time Universe (see Sec. 5.2.2). All the best-fit values are compatible between the different models as before, except for H_0 and $\Omega_{\rm m}$, which are smaller and larger for a coasting reconstruction, respectively, accounting for SNIa luminosity evolution or not. The obtained χ^2 values are very similar, leading to very similar $P(\chi^2, \nu)$, and they show that a coasting reconstruction can correctly fit the data when SNIa luminosity evolution is accounted for. In the last place we compute $r_{\rm d}$ using Eq. (1.149) with $z_{\rm d}$. All the best-fit values are compatible with the previous results, and compatible between the different models, except for H_0 and $\Omega_{\rm m}$. It is also the case for the χ^2 values and the corresponding probabilities.

We conclude that, if we account for a redshift dependence in the intrinsic luminosity of SNIa, the main cosmological probes cannot firmly prove the accelerated nature of the expansion of the Universe in a model-independent way, since a non-accelerated reconstruction can correctly fit the observations.

For completeness, we present in Fig. 5.9 the residuals to SNIa and BAO

TABLE 5.5: Best-fit values with the corresponding 1σ error bars for the cosmological and nuisance parameters of the third case of: SNIa, BAO, and CMB data. The values in parentheses show the fixed knots. The values of ΛCDM are added as a reference. The reduced χ^2 and the probability $P(\chi^2, \nu)$ are also provided for the different models. H_0 is expressed in km/s/Mpc, and $r_{\rm d}$ in Mpc.

Case	SNIa+BAO free $r_{\rm d}$+CMB			SNIa+ev+BAO free $r_{\rm d}$+CMB			SNIa+BAO prior $r_{\rm d}$+CMB			SNIa+ev+BAO prior $r_{\rm d}$+CMB			SNIa+BAO compute $r_{\rm d}$+CMB			SNIa+ev+BAO compute $r_{\rm d}$+CMB		
Model	ΛCDM	Splines	CS (4 knots)	ΛCDM	Splines	CS (4 knots)	ΛCDM	Splines	CS (4 knots)	ΛCDM	Splines	CS (4 knots)	ΛCDM	Splines	CS (4 knots)	ΛCDM	Splines	CS (4 knots)
E_1	–	1.050 ± 0.020	(1.10)	–	1.049 ± 0.021	(1.10)	–	1.050 ± 0.020	(1.10)	–	1.049 ± 0.021	(1.10)	–	1.050 ± 0.020	(1.10)	–	1.049 ± 0.020	(1.10)
E_2	–	1.133 ± 0.020	(1.25)	–	1.149 ± 0.023	(1.25)	–	1.133 ± 0.020	(1.25)	–	1.149 ± 0.023	(1.25)	–	1.133 ± 0.020	(1.25)	–	1.149 ± 0.023	(1.25)
E_3	–	1.386 ± 0.034	(1.57)	–	1.410 ± 0.039	(1.57)	–	1.385 ± 0.034	(1.57)	–	1.410 ± 0.038	(1.57)	–	1.385 ± 0.034	(1.57)	–	1.410 ± 0.039	(1.57)
E_4	–	1.592 ± 0.075	(1.80)	–	1.671 ± 0.094	(1.80)	–	1.595 ± 0.074	(1.80)	–	1.670 ± 0.092	(1.80)	–	1.595 ± 0.074	(1.80)	–	1.671 ± 0.090	(1.80)
E_5	–	2.14 ± 0.15	2.29 ± 0.16	–	2.18 ± 0.16	2.36 ± 0.17	–	2.166 ± 0.096	2.355 ± 0.089	–	2.175 ± 0.096	2.374 ± 0.090	–	2.171 ± 0.096	2.362 ± 0.087	–	2.180 ± 0.096	2.380 ± 0.091
E_6	–	3.45 ± 0.10	3.795 ± 0.096	–	3.48 ± 0.10	3.783 ± 0.095	–	3.45 ± 0.10	3.792 ± 0.095	–	3.48 ± 0.10	3.782 ± 0.094	–	3.45 ± 0.10	3.792 ± 0.094	–	3.48 ± 0.10	3.782 ± 0.094
H_0	69.14 ± 0.93	68.4 ± 1.5	62.5 ± 1.1	69.11 ± 0.97	67.3 ± 1.7	62.2 ± 1.1	68.69 ± 0.72	68.2 ± 1.2	62.09 ± 0.53	68.65 ± 0.75	67.3 ± 1.3	62.02 ± 0.53	68.55 ± 0.59	68.1 ± 1.2	62.04 ± 0.47	68.51 ± 0.60	67.3 ± 1.3	61.98 ± 0.50
$r_{\rm d}$	146.2 ± 1.4	146.7 ± 2.5	146.2 ± 2.5	146.2 ± 1.4	147.5 ± 2.6	147.1 ± 2.6	147.20 ± 0.63	147.40 ± 0.68	147.30 ± 0.67	147.20 ± 0.63	147.40 ± 0.68	147.40 ± 0.67	–	–	–	–	–	–
$\Omega_{\rm m}$	0.293 ± 0.011	0.300 ± 0.015	0.359 ± 0.014	0.294 ± 0.012	0.310 ± 0.017	0.364 ± 0.015	0.2986 ± 0.0090	0.302 ± 0.011	0.3644 ± 0.0085	0.2991 ± 0.0093	0.310 ± 0.013	0.3650 ± 0.0085	0.3006 ± 0.0071	0.303 ± 0.011	0.3655 ± 0.0063	0.3010 ± 0.0073	0.310 ± 0.012	0.3657 ± 0.0065
$10^2\omega_{\rm b}$	2.264 ± 0.025	2.263 ± 0.029	2.264 ± 0.029	2.264 ± 0.025	2.263 ± 0.029	2.263 ± 0.029	2.255 ± 0.021	2.262 ± 0.028	2.261 ± 0.028	2.254 ± 0.022	2.264 ± 0.028	2.263 ± 0.028	2.254 ± 0.022	2.261 ± 0.028	2.260 ± 0.027	2.253 ± 0.022	2.263 ± 0.028	2.262 ± 0.028
α	0.1412 ± 0.0066	0.1410 ± 0.0066	0.1382 ± 0.0066	0.1413 ± 0.0066	0.1413 ± 0.0066	0.1416 ± 0.0066	0.1412 ± 0.0066	0.1410 ± 0.0066	0.1382 ± 0.0066	0.1413 ± 0.0066	0.1413 ± 0.0066	0.1416 ± 0.0066	0.1411 ± 0.0066	0.1410 ± 0.0066	0.1382 ± 0.0065	0.1413 ± 0.0066	0.1413 ± 0.0066	0.1416 ± 0.0066
β	3.102 ± 0.080	3.099 ± 0.081	3.073 ± 0.080	3.103 ± 0.081	3.101 ± 0.081	3.104 ± 0.081	3.101 ± 0.080	3.099 ± 0.081	3.073 ± 0.080	3.102 ± 0.081	3.101 ± 0.081	3.104 ± 0.081	3.100 ± 0.080	3.099 ± 0.081	3.073 ± 0.078	3.103 ± 0.081	3.101 ± 0.081	3.104 ± 0.081
$M_{\rm B}^1$	24.110 ± 0.018	24.120 ± 0.030	24.230 ± 0.017	24.110 ± 0.056	24.110 ± 0.031	24.050 ± 0.089	24.110 ± 0.018	24.120 ± 0.030	24.230 ± 0.017	24.100 ± 0.056	24.110 ± 0.030	24.050 ± 0.095	24.110 ± 0.018	24.120 ± 0.030	24.230 ± 0.017	24.100 ± 0.056	24.110 ± 0.030	24.050 ± 0.095
$\Delta_{\rm M}$	-0.070 ± 0.023	-0.070 ± 0.023	-0.077 ± 0.023	-0.070 ± 0.023	-0.070 ± 0.023	-0.070 ± 0.023	-0.070 ± 0.023	-0.070 ± 0.023	-0.077 ± 0.023	-0.070 ± 0.023	-0.070 ± 0.023	-0.070 ± 0.023	-0.070 ± 0.023	-0.070 ± 0.023	-0.077 ± 0.023	-0.070 ± 0.023	-0.070 ± 0.023	-0.070 ± 0.023
z_*	1090.00 ± 0.23	1090.00 ± 0.23	1090.00 ± 0.23	1090.00 ± 0.23	1090.00 ± 0.23	1090.00 ± 0.23	1090.00 ± 0.23	1090.00 ± 0.23	1090.00 ± 0.23	1090.00 ± 0.23	1090.00 ± 0.23	1090.00 ± 0.23	1090.00 ± 0.23	1090.00 ± 0.23	1090.00 ± 0.22	1090.00 ± 0.23	1090.00 ± 0.22	1090.00 ± 0.23
$z_{\rm d}$	–	–	–	–	–	–	–	–	–	–	–	–	1060.00 ± 0.29	1060.00 ± 0.29	1060.00 ± 0.29	1060.00 ± 0.29	1060.00 ± 0.29	1060.00 ± 0.29
ϵ	–	–	–	0.005 ± 0.075	0.094 ± 0.064	0.322 ± 0.074	–	–	–	0.015 ± 0.073	0.094 ± 0.063	0.322 ± 0.079	–	–	–	0.019 ± 0.073	0.094 ± 0.063	0.322 ± 0.078
δ	–	–	–	0.20 ± 0.99	2.0 ± 1.6	0.41 ± 0.24	–	–	–	0.2 ± 1.7	2.0 ± 1.6	0.41 ± 0.25	–	–	–	0.2 ± 1.8	2.0 ± 1.4	0.41 ± 0.25
χ^2/d.o.f	698.67/754	697.01/748	740.32/752	698.66/752	694.93/746	699.44/750	699.21/755	697.07/749	740.51/753	699.17/753	694.93/747	699.46/751	699.31/755	697.09/749	740.55/753	699.24/753	694.93/747	699.47/751
$P(\chi^2, \nu)$	0.926	0.909	0.612	0.918	0.909	0.906	0.927	0.913	0.620	0.920	0.913	0.911	0.927	0.912	0.620	0.920	0.913	0.911

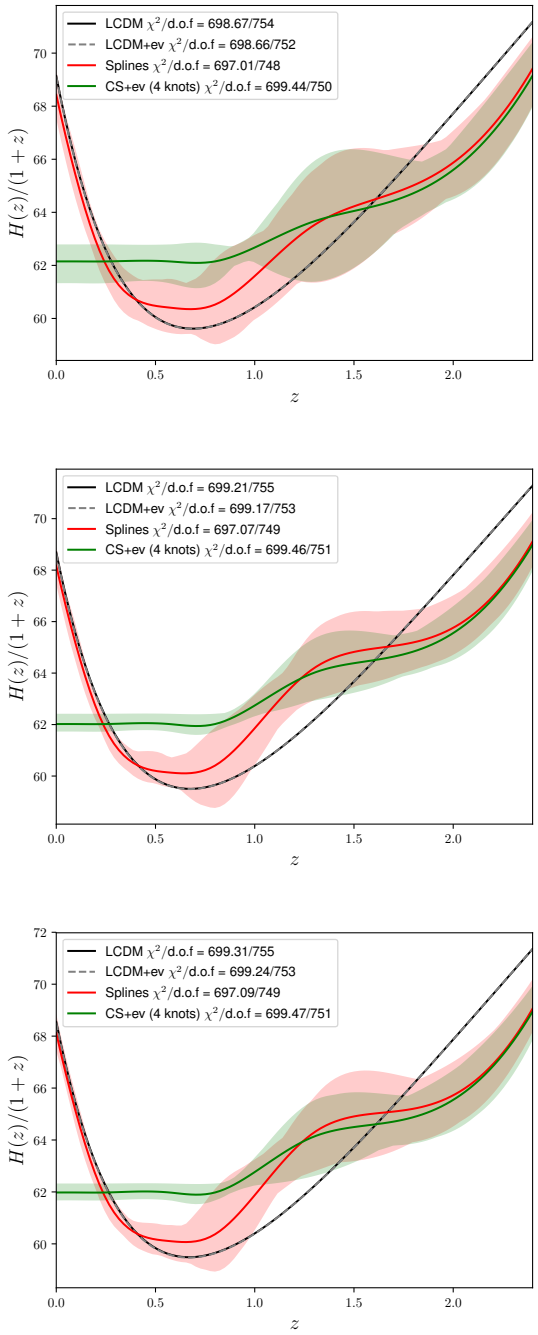

FIGURE 5.8: Reconstruction of the expansion rate, $H(z)/(1+z)$, as a function of the redshift using the combination of SNIa, BAO, and CMB data. In the top panel the data sets have been combined considering $r_{\rm d}$ a free parameter, while in the central panel a prior on $r_{\rm d}$ has been used, and it has been explicitly computed in the bottom panel. In all panels the black and grey lines represent the ΛCDM model (without and with SNIa luminosity evolution, respectively), while the red band shows the reconstruction with $\Delta\chi^2 \leq 1$ with respect to the best reconstruction (red line). The green band stands for the reconstruction of a coasting universe at low-redshift when SNIa intrinsic luminosity is allowed to vary as a function of the redshift.

TABLE 5.6: Prediction of the different models for the CMB quantities R, ℓ_a, $\omega_{\rm b}$, for the combination of SNIa, BAO, and CMB data computing $r_{\rm d}$ explicitly, and accounting for SNIa intrinsic luminosity evolution as a function of the redshift when dealing with a coasting reconstruction. The measured values are added as a reference.

Parameter	Measured value	ΛCDM	Splines	CS (4 knots)+ev
R	1.7382 ± 0.0088	1.7414	1.7385	1.7382
ℓ_a	301.63 ± 0.15	301.68	301.67	301.65
$10^2\omega_{\rm b}$	2.262 ± 0.029	2.254	2.261	2.262

observations for three different models: ΛCDM (black), the reconstruction through cubic splines (red), and the non-accelerated model using a coasting reconstruction (green) taking into account SNIa intrinsic luminosity evolution. We also provide the predictions for the CMB quantities R, ℓ_a, and $\omega_{\rm b}$ in Table 5.6. All these predictions have been computed using the best-fit values of the parameters obtained from the global fit to the combination of SNIa, BAO, and CMB data, computing explicitly the value of $r_{\rm d}$ using Eq. (1.149) with $z_{\rm d}$. From these results (Fig. 5.9 and Table 5.6) we can graphically see that all three models are perfectly able to fit the data; including the coasting reconstruction with SNIa luminosity evolution. As it can be seen in Table 5.5, a different approach when combining SNIa, BAO, and CMB data (free $r_{\rm d}$ or prior on $r_{\rm d}$) gives nearly the same values for the parameters of the reconstruction, which leads to nearly the same predictions for the observables.

Growth rate

Let us first recall (see Sec. 1.3) that we can express the observable weighted growth rate $f\sigma_8$ as

$$f\sigma_8(z) = f(z) \cdot \left(\sigma_{8_{\rm Planck}} \frac{D(z)}{D_{\rm Planck}(0)} \right) , \tag{5.4}$$

where $\sigma_{8_{\rm Planck}}$ stands for the ΛCDM observed value (with Planck) of σ_8 (fixed to 0.8159 in this section [Planck Collaboration, 2016b]), and $D_{\rm Planck}$ represents the ΛCDM Planck growth factor [Planck Collaboration, 2016b]. In this section we consider the measurements of the weighted growth rate from the 6dFGS survey [Beutler et al., 2012], the WiggleZ survey [Blake et al., 2012], and the VIPERS survey [de la Torre et al., 2013], as well as the different SDSS projects: SDSS-II MGS DR7 [Howlett et al., 2015] (with the main galaxy sample of the seventh

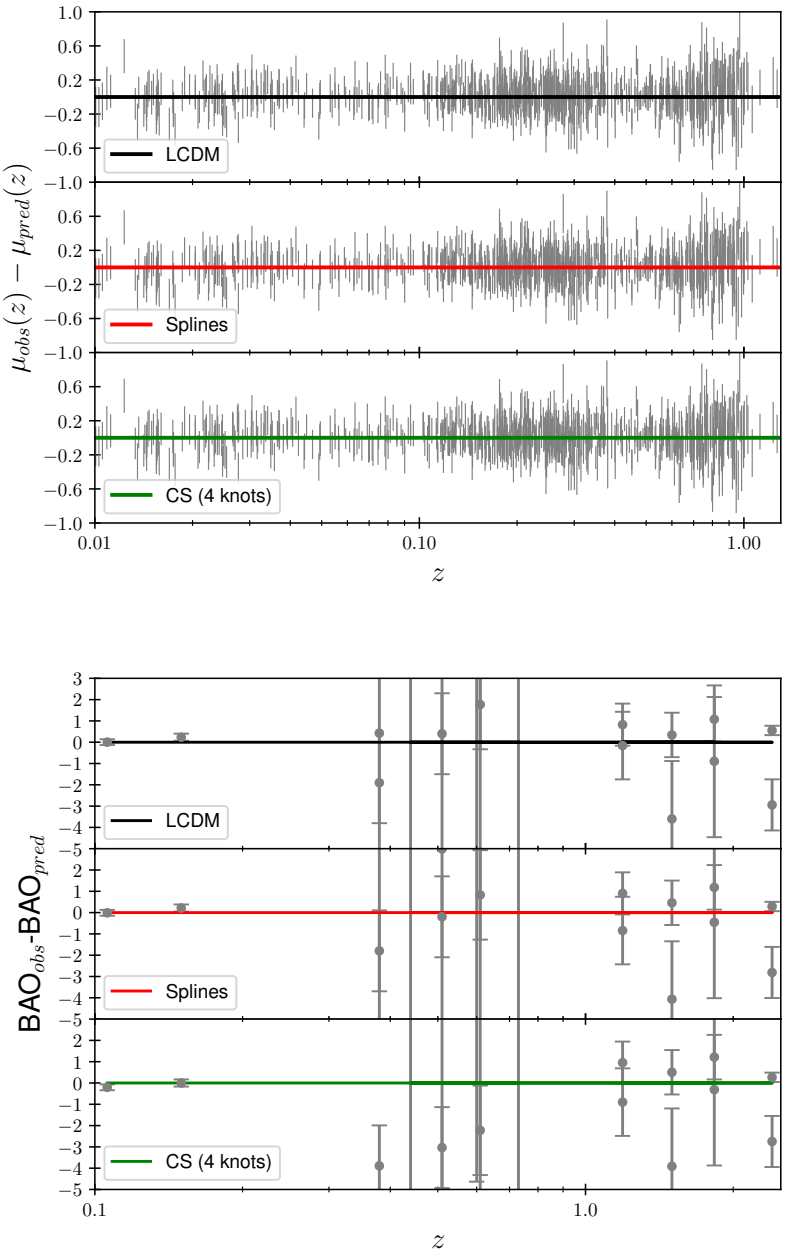

FIGURE 5.9: Residuals between the observations and the prediction of the different models, ΛCDM, spline reconstruction, and coasting reconstruction with SNIa intrinsic luminosity evolution, for the SNIa and BAO observables. The predictions have been computed using the best-fit values for the parameters obtained from the fit of the combination SNIa+BAO+CMB computing $r_{\rm d}$ explicitly. *Top plot:* residuals of the SNIa distance modulus for the three different models: ΛCDM (black top panel), spline reconstruction (red central panel), and coasting reconstruction (green bottom panel). The residuals have been normalized with respect to the prediction for each model. *Bottom plot:* residuals of the BAO measurements following the same color convention as in the top plot. The residuals have been normalized with respect to the prediction for each model.

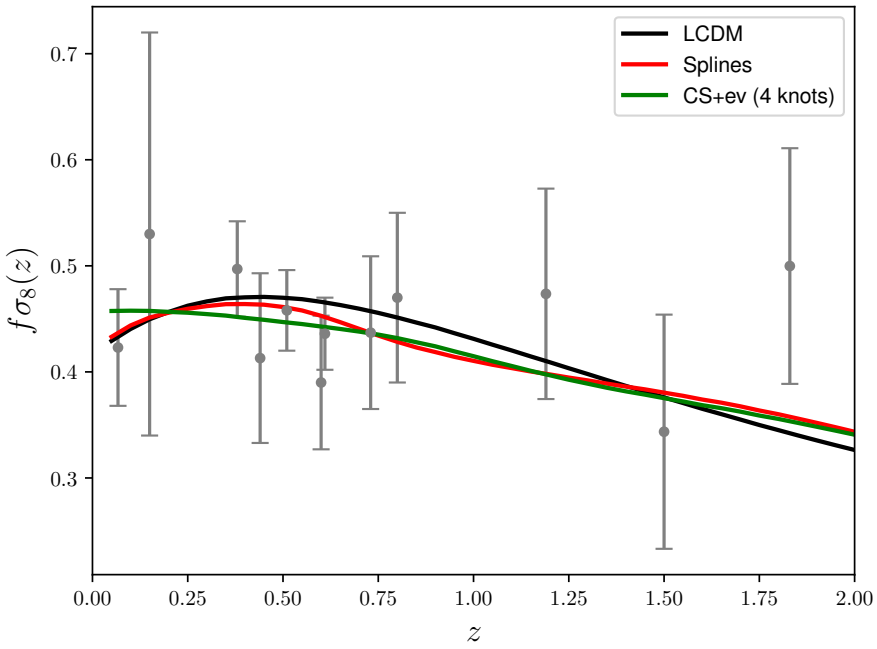

FIGURE 5.10: Prediction of the different models, ΛCDM, spline reconstruction, and coasting reconstruction with SNIa intrinsic luminosity evolution, for the growth of matter perturbations $f\sigma_8$ observable. The predictions have been computed using the best-fit values for the parameters obtained from the fit of the combination SNIa+BAO+CMB computing r_d explicitly. Therefore, it is not a fit to the $f\sigma_8$ measurements. We follow the same color legend as in the previous figures: black for ΛCDM, red for the spline reconstruction, and green for the coasting reconstruction.

data release), SDSS-III BOSS DR12 [Alam et al., 2017] (with the LRGs from the 12th BOSS data release), and SDSS-IV DR14Q [Gil-Marín et al., 2018] (with the latest quasar sample of eBOSS). We follow the approach of the previous section in not modifying the $f\sigma_8$ values provided by the different papers, since they have already been obtained marginalizing over the cosmological model (see Sec. 5.1.4).

We have not included this data set in our fitting analysis for simplicity, but we show in Fig. 5.10 that, using the best-fit values for the parameters from the SNIa+BAO+CMB fit, the prediction for the three models considered (ΛCDM, spline reconstruction, and coasting reconstruction with SNIa luminosity evolution) is in very good agreement with the observations. Notice that the values for the parameters used in Fig. 5.10 have been obtained computing the value of r_d, but the results are equivalent using the other approaches for the combination of our three main data sets.

The Hubble constant

We conclude this section by considering two very recent model independent measurements of H_0 in order to check its effect on the conclusions we can draw concerning cosmic acceleration. We first consider the value obtained from the Hubble Space Telescope observations in Riess et al., 2018a (R18 in the following), $H_0 = 73.45 \pm 1.66$ km/s/Mpc. We then consider the value obtained with Gaussian Processes using SNIa data, and constraints on $H(z)$ from cosmic chronometers in Gómez-Valent and Amendola, 2018 (GVA18 in the following), $H_0 = 67.06 \pm 1.68$ km/s/Mpc. This last value is closer to the one derived with an "inverse distance ladder" approach in Aubourg et al., 2015, $H_0 = 67.3 \pm 1.1$ km/s/Mpc, where the measurement assumes standard pre-recombination physics but is insensitive to dark energy or space curvature assumptions. It is also closer to the value derived from the CMB observations using a flat ΛCDM model, $H_0 = 67.51 \pm 0.64$ km/s/Mpc [Planck Collaboration, 2016b].

In Fig. 5.11 we represent the profile likelihood (minus $\chi^2_{\rm min}$ and assuming Gaussian likelihoods) for both the observed values of H_0, R18 (black) and GVA18 (blue), and the values derived from the non-accelerated reconstruction for the combination SNIa+BAO+CMB taking into account the SNIa intrinsic luminosity evolution. We present the three values obtained for the three approaches followed when combining the data sets: consider $r_{\rm d}$ a free parameter (green), add a prior on it (yellow), or compute it explicitly (purple). From the figure alone it is clear that the H_0 value for the non-accelerated reconstruction is in tension with R18 at more than 5σ, independently of the approach used when combining the data sets. More precisely, a non-accelerated reconstruction is ruled out if we consider the R18 measurement at 5.65σ (free $r_{\rm d}$, $H_0 = 62.2 \pm 1.1$ km/s/Mpc), 6.56σ (prior $r_{\rm d}$, $H_0 = 62.02 \pm 0.53$ km/s/Mpc), or 6.62σ (compute $r_{\rm d}$, $H_0 = 61.98 \pm 0.50$ km/s/Mpc), showing that, with the R18 measurement, cosmic acceleration is proven even if some astrophysical systematics evolving with the redshift modify the intrinsic luminosity of SNIa. However, we can also see from the figure that if we consider the measured value from the Gaussian Processes, a non-accelerated reconstruction shows a bit less than a 3σ tension. More precisely, there is a tension of 2.42σ (free $r_{\rm d}$), 2.86σ (prior $r_{\rm d}$), or 2.90σ (compute $r_{\rm d}$). In this case, the measured value of H_0 points towards ruling out these reconstructions, but the tension is still far from the usually recognized 5σ threshold.

5.2.6 Summary

The impact of SNIa luminosity evolution on our cosmological knowledge has already been addressed before [Wright, 2002; Drell, Loredo, and Wasserman,

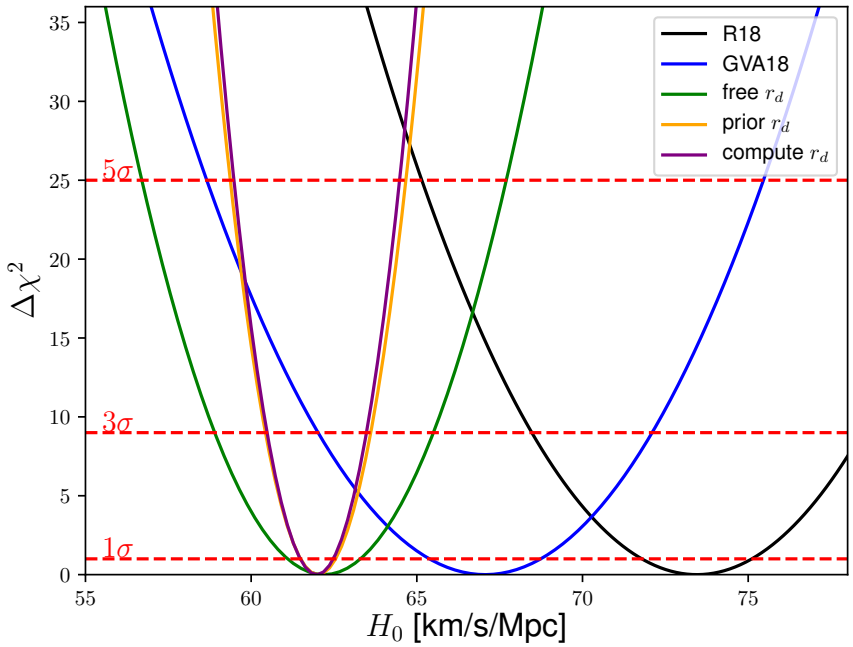

FIGURE 5.11: Profile likelihood (minus $\chi^2_{\rm min}$ and assuming Gaussian likelihoods) of different values for the Hubble constant. The black line corresponds to the value measured from the HST (R18), while the blue one stands for the measured value from SNIa and $H(z)$ data using Gaussian Processes (GVA18). The other three profiles represent the predicted value from a non-accelerated reconstruction (with SNIa intrinsic luminosity evolution) with different approaches to combine the three main data sets of this work (SNIa, BAO, and CMB): consider $r_{\rm d}$ a free parameter (green), add a prior on it (yellow), or compute it explicitly (purple). The 1σ, 3σ, and 5σ lines are represented as a reference.

2000; Linden, Virey, and Tilquin, 2009; Nordin, Goobar, and Jönsson, 2008; Ferramacho, Blanchard, and Zolnierowski, 2009], but in this section we have extended the analysis by including the physics of the early Universe ($z \approx 1100$), and thus considering the main background cosmological probes: SNIa, BAO, and the CMB. In order to be as general as possible, we have not imposed a cosmological model, but we have reconstructed the expansion rate of the Universe using a cubic spline interpolation.

We have first applied, as an illustration of the method, the reconstruction to SNIa data alone with the standard SNIa luminosity-redshift independence assumption. We have shown that with this assumption cosmic acceleration is definitely preferred against a local non-accelerated universe. However, in the previous section of this chapter we showed that if SNIa intrinsic luminosity does

evolve, a non-accelerated universe can perfectly fit the data.

In a second step we have added the latest BAO data to our analysis. We have considered two different ways to combine it with SNIa data: either we have considered $H_0 r_\mathrm{d}$ as a free parameter, or we have added a prior on r_d coming from CMB observations, without any dependence on late-time Universe assumptions. In both cases we have seen that a non-accelerated universe is able to fit the data nearly as nicely as ΛCDM, when we allow the SNIa intrinsic luminosity to vary as a function of the redshift.

Next, we have extended the data sets in the analysis by adding the information coming from the CMB through the reduced parameters. In order to deal with this information we have been forced to specify the model up to very high redshifts. We have decided to follow a matter-radiation dominated model from the early Universe down to $z \approx 3$, where we start to have low-redshift data. We have then coupled the model to our spline reconstruction. In other words, we consider a matter-radiation dominated model at the early Universe and, when we enter the redshift range where we have low-redshift data and a cosmological constant is still negligible, we allow the expansion rate to vary freely without specifying any dark energy model. When adding the CMB data we follow three different approaches: treat r_d as a free parameter, add a prior on it, or compute it assuming that the BAO and the CMB share the same physics. For simplicity we have not added the $f\sigma_8$ measurements of the growth rate of matter perturbations, but we have checked that using the best-fit values from the global fit SNIa+BAO+CMB we are able to correctly predict the latest $f\sigma_8$ measurements.

In all three cases considered we have seen that a non-accelerated model is able to nicely fit the data, when SNIa intrinsic luminosity is allowed to vary, including the information on the early Universe coming from the CMB. This shows that a non-accelerated expanding universe can fit all the main background cosmological probes, and even be compatible with the growth of matter perturbations, if SNIa intrinsic luminosity depends on the redshift.

After this conclusion, we focus on the impact that the Hubble constant may have on this question. We have considered two different model independent recent measurements of H_0: 73.45 ± 1.66 km/s/Mpc (R18) from Riess et al., 2018a, and 67.06 ± 1.68 km/s/Mpc (GVA18) from Gómez-Valent and Amendola, 2018. We have shown that if we consider the R18 value, cosmic acceleration is proven at more than 5.65σ for a general expansion rate reconstruction [for which we get $H_0 = 62.2 \pm 1.1$ km/s/Mpc (free r_d), $H_0 = 62.02 \pm 0.53$ km/s/Mpc (prior r_d), and $H_0 = 61.98 \pm 0.50$ km/s/Mpc (compute r_d)], even if SNIa intrinsic luminosity varies as a function of the redshift due to any astrophysical unknown systematic. It is important to say, though, that if we consider

the GVA18 value, a non-accelerated reconstruction for the expansion rate is at a 3σ tension with the measurement, but still below the 5σ detection.

In conclusion, if SNIa intrinsic luminosity varies as a function of the redshift, a non-accelerated universe is able to correctly fit all the main background probes. However, the value of H_0 turns out to be a key ingredient in the conclusions we can draw concerning cosmic acceleration. If we take it into account we are close to claim an accelerated expansion of the Universe using an approach very independent of the cosmological model assumed, and even if SNIa intrinsic luminosity varies. A final consensus on a direct measurement of H_0 and its precision will be decisive to finally prove the cosmic acceleration independently of the cosmological model and any redshift dependent astrophysical systematic that may remain in the SNIa analysis.

Chapter 6

Euclid forecasts: large-scale structure probe combination

In this chapter we focus on the results of the Inter-Science Taskforce for Forecasting of the Euclid Consortium presented in Sec. 3.4. Its main objective is to provide rigorously validated Fisher matrix forecasts for the different cosmological probes of Euclid, as well as their combination. Since the Euclid forecast presented in the Red-book [Laureijs et al., 2011], there have been many interesting works computing Euclid forecasts for ΛCDM or models beyond it (see e.g. Amendola et al., 2013; Hamann, Hannestad, and Wong, 2012; Di Porto, Amendola, and Branchini, 2012; Majerotto et al., 2012; Wang, 2012; de Putter, Doré, and Takada, 2013; Casas et al., 2017). The main difference of this work with respect to these previous forecasts is the detailed code comparison performed before providing the final results, and the fact that all the required details to reproduce the forecasts are provided. Moreover, if we compare this work to the results presented in the Red-book, there are significant changes in several aspects of the survey specifications or the modeling, like the target population for the spectroscopic galaxy clustering, the non-linear prescription, or the treatment of weak lensing intrinsic alignments. However, we do not include systematic effects due to the instrument design (instrumental effects), foreground contamination, or the data reduction pipeline. Just to give some examples, we do not consider the impact of the mask on the final results: holes or shallower regions in the observed area could lead to a non-isotropic galaxy distribution as a function of the redshift, and it could change the shot-noise that we are considering. Also, we do not take into account the systematics related to the measurement of the shape of galaxies (like the point spread function quantifying how a point source is spread due to the instrument optics), neither the quality cuts that need to be applied to the galaxy catalogs for GCp and WL, which could lead to different galaxy distributions for the different probes. We do not take into account the foreground contamination by stars, zodiacal light, or even our own galaxy. The Euclid footprint will be optimized to minimize these effects (see Chapter 3) but they could still have a significant effect in Euclid data.

As a last example, we assume we perfectly know the galaxy distribution and the photometric redshifts performance, so we do not consider any systematic related to the heterogeneity of the ground based data sets that will be used for the Euclid photometric redshifts (see Chapter 3). All the results presented here should be updated in the future taking into account all these effects, in order to obtain the best predictions (as realistic as possible). However, some of these systematics will not be known until the satellite is fully build. The results presented here are therefore the best case realistic Euclid forecasts, while the forecasts including the different systematics are left for future work.

As described in Chapter 3, Euclid will conduct a spectroscopic survey and a photometric survey. The former will enable us to study the large-scale structure of the Universe with the spectroscopic galaxy clustering probe, while the latter will give us the opportunity to use the weak lensing probe. However, since the latter will provide the position and photometric redshifts of more than a billion of galaxies, we can also consider the photometric galaxy clustering probe (GCp). In this chapter we present the Euclid forecast for each one of these probes.

One of the most powerful ways to constrain a cosmological model is to combine several observations coming from different cosmological probes, because different probes are, in general, sensitive to different aspects of how gravity acts in the cosmos. For instance, WL is used to probe the total matter distribution (visible and dark) via the deflection of the light-rays, while GC quantifies the distribution and peculiar velocities of galaxies in the cosmic web. Combining both probes we can remove degeneracies, and it can provide us with significantly better constraints on the cosmological parameters under study (see e.g. Laureijs et al., 2011), not only for ΛCDM but especially for cosmological models going beyond it.

The power of combining different probes has already been shown in the last years (see e.g. Simpson et al., 2013), but in these analyses we usually assume that the different probes are statistically uncorrelated. This may be an acceptable assumption when combining data coming from the cosmic microwave background (without lensing) and low-redshift data (like type Ia supernovae), since we are looking at different epochs of the Universe history. However, the combination of GC and WL data may be using the same volume of the Universe (as it will be the case for GCp and WL in Euclid). Adding the correlations between these probes may provide us with extra information leading to even better constraints on the cosmological parameters, and better knowledge of the Universe. The effect of these correlations on state-of-the-art observations is already non-negligible [Blake et al., 2016; DES Collaboration, 2017b; Reyes et al., 2010; Zhang et al., 2007], but it is mandatory for the upcoming surveys, like Euclid, to determine the effect of correlations in order to extract all the

available information from the future precise observations. Therefore, we will pay special attention in this chapter to the effect of cross-correlations when we combine the different cosmological probes for Euclid.

This chapter is structured as follows: in the first section (Sec. 6.1) we present the recipe used to compute the Fisher matrix forecast for GCs, WL, and GCp, as well as the recipe for the combination of all probes. In Sec. 6.2 we present the `CosmoSIS`[1] code [Zuntz et al., 2015] used for computing the predictions. We then show the results and the validation of the forecasting code in Sec. 6.3 and Sec. 6.4 for WL and GCp, and Sec. 6.5 and Sec. 6.6 for the combination of all probes.

The baseline results presented here will appear in Euclid Collaboration, in prep. It is important to mention that all the results of the IST have been obtained thanks to the contribution of 11 different codes and many people. Therefore, we will describe all the probes for completeness, but we will spend most of the time on WL, GCp and their cross-correlations, since it is where I have been strongly involved. More in detail, we will show the results obtained with the `CosmoSIS` code, for which I have been the contact person within the IST. Concerning the GCs probe, we will present the results obtained with the `SpecSAF` code, where I have been partially involved (it is the improved version of the forecasting code used in Sec. 7.4), in order to eventually combine all Euclid probes. Notice that the majority of results presented in this chapter beyond the baseline cases will not appear in Euclid Collaboration, in prep. but they have been obtained with the validated `CosmoSIS` code.

6.1 Forecasting recipe

In this section we first present some general ingredients common to all probes, like the fiducial cosmology chosen, and we then describe the recipe used to compute the Fisher matrix forecast for the different probes.

6.1.1 General ingredients

Cosmological context

We start by briefly presenting the cosmological context and the different models under consideration in this chapter. Let us remind that using Einstein's field equations of General Relativity (Eq. 1.11) together with the Robertson-Walker metric (Eq. 1.10) we can obtain the Friedmann-Lemaître equation

[1] `https://bitbucket.org/joezuntz/cosmosis/wiki/Home`

$$(H_0 E(z))^2 \equiv H^2 \equiv \left(\frac{\dot{a}}{a}\right)^2 = \frac{8\pi G}{3}\rho - \frac{K}{a^2}\,, \tag{6.1}$$

where a is the scale factor, K the curvature parameter, and ρ the total energy density. This chapter is focused on predicting the accuracy of Euclid to constrain the parameters of the standard cosmological model, as well as the alternative scenario where dark energy evolves dynamically and is parametrized using the fluid description. We consider here the standard CPL (see Sec. 1.1.4) parametrization of the equation of state parameter for dark energy given by

$$w(z) = w_0 + w_a \frac{z}{1+z}\,. \tag{6.2}$$

Therefore, the Hubble parameter is given by

$$H(z) = H_0\sqrt{\Omega_{\rm m}(1+z)^3 + \Omega_{\rm r}(1+z)^4 + \Omega_{\rm de} f_{\rm de}(z) + \Omega_{\rm K}(1+z)^2}\,, \tag{6.3}$$

where we already express the density of the different components as density parameter, the curvature term fulfills the closure relation $\Omega_{\rm K} = 1 - \Omega_{\rm m} - \Omega_{\rm r} - \Omega_{\rm de}$, and finally

$$f_{\rm de}(z) = \begin{cases} 1 & \text{if de} = \Lambda\,, \\ (1+z)^{3(1+w_0+w_a)} e^{-3w_a\frac{z}{1+z}} & \text{if de} = \text{dynamical}\,. \end{cases}$$

Another important quantity for the computation of the forecasts is the angular diameter distance (see Sec. 1.1.2)

$$d_{\rm A}(z) = \begin{cases} \frac{1}{1+z}\frac{c}{H_0\sqrt{|\Omega_{\rm K}|}} \sin\left(\sqrt{|\Omega_{\rm K}|}\int_0^z \frac{{\rm d}z'}{E(z')}\right)\,, & \text{if } \Omega_{\rm K} < 0\,, \\ \frac{1}{1+z}\frac{c}{H_0}\int_0^z \frac{{\rm d}z'}{E(z')}\,, & \text{if } \Omega_{\rm K} = 0\,, \\ \frac{1}{1+z}\frac{c}{H_0\sqrt{\Omega_{\rm K}}} \sinh\left(\sqrt{\Omega_{\rm K}}\int_0^z \frac{{\rm d}z'}{E(z')}\right)\,, & \text{if } \Omega_{\rm K} > 0\,, \end{cases} \tag{6.4}$$

which enables us to compute the proper volume of a survey bin as

$$V_{\rm proper}(z_i, z_j) = \Omega \int_{z_i}^{z_j} d_{\rm A}^2(z) \frac{{\rm d}z}{(1+z)H(z)}\,, \tag{6.5}$$

where Ω is the solid angle in steradian. Since the co-moving volume is related to the proper volume through ${\rm d}V_{\text{co-moving}} = (1+z)^3\,{\rm d}V_{\rm proper}$, the co-moving volume of a shell is given by

$$V_{\text{co-moving}}(z_i, z_j) = \Omega \int_{z_i}^{z_j} d_{\rm A}^2(z)(1+z)^2 \frac{{\rm d}z}{H(z)}\,. \tag{6.6}$$

Until now we have provided a few details concerning the background cosmological context, but Euclid will also probe the growth of structures with GC and WL. Therefore, we also present the context of linear perturbations used in this chapter.

First of all, when we consider a dynamically evolving dark energy, we need to specify how it evolves at the level of perturbations. We follow the standard approach of using a minimally-coupled scalar field, called quintessence (see Sec. 1.1.4), with a sound speed equal to the speed of light, and no anisotropic stress. This implies that we can neglect the fluctuations related to the dark energy fluid in our analysis. Moreover, we allow for the equation of state of dark energy to cross -1. In practice, we use the PPF prescription [Hu and Sawicki, 2007; Fang, Hu, and Lewis, 2008] to do this.

Let us also recall (see Sec. 1.2.1) that given the density contrast of a generic species

$$\delta_i(\boldsymbol{x}, z) \equiv \frac{\rho_i(\boldsymbol{x}, z)}{\bar{\rho}_i(z)} - 1\,, \tag{6.7}$$

we can define the power spectrum by

$$\left\langle \tilde{\delta}_i(\boldsymbol{k}, z)\tilde{\delta}_i(\boldsymbol{k}', z)\right\rangle = (2\pi)^3\delta_{\rm D}^{(3)}(\boldsymbol{k}+\boldsymbol{k}')P_{\delta_i\delta_i}(k, z)\,. \tag{6.8}$$

Concerning the growth rate of matter perturbations, we recall that it is given by

$$f(a) = \frac{\mathrm{d}\ln D_1(a)}{\mathrm{d}\ln a}\,, \tag{6.9}$$

where $D_1(a)$ stands for the growth factor (Eq. 1.92). In presence of massive neutrinos, the linear growth rate depends not only on redshift, but also on the scale, k. However, this dependence is small and we will neglect it in the following.

Fiducial cosmology and main survey specifications

Since we want to compute forecasts, we need to specify the fiducial cosmological model [2]. We consider the baryon and total matter critical densities ($\Omega_{\rm b}$ and $\Omega_{\rm m}$, respectively), the w_0 and w_a parameters of the dark energy equation of state, the reduced Hubble constant, h, the spectral index of the primordial density

[2] Let us recall that the standard Fisher matrix approach only allows us to get an estimate of the constraints on the parameters. A generalized version of the Fisher matrix method can also quantify the bias on the parameters if the fiducial has been obtained with a given cosmology and the analysis is performed assuming a different cosmology [Cypriano et al., 2010; Shapiro et al., 2010]. In this work we focus on estimating the constraints on the different cosmological parameters, while the study of their biases is left for future work.

power spectrum, n_s, and the root mean square of the density fluctuations in spheres of $8h^{-1}$ Mpc, σ_8, as primary parameters with the following values

$$\begin{aligned} \boldsymbol{p} &= \{\Omega_{\rm m},\, \Omega_{\rm b},\, w_0,\, w_a,\, h,\, n_s,\, \sigma_8\} \\ &= \{0.32,\, 0.05,\, -1.0,\, 0.0,\, 0.67,\, 0.96,\, 0.816\}\,. \end{aligned} \tag{6.10}$$

We fix the re-ionization optical depth $\tau = 0.058$, because Euclid is not sensitive to it [3]. Moreover, we fix the sum of neutrino masses to $\sum m_\nu = 0.06\,\mathrm{eV}$, and check the impact of massless neutrinos on the final results. In some cases we also consider non-flat universes by allowing $\Omega_{\rm K} \neq 0$, which is equivalent to allowing $\Omega_{\rm de} \neq 0.68$ in our fiducial cosmology. All these fiducial values correspond to those of Planck 2015 [Planck Collaboration, 2016b].

We also summarize here the main specifications for the photometric and spectroscopic Euclid surveys. In both cases they will cover 15000 square degrees of the sky. The spectroscopic survey will have a spectroscopic redshift precision of $\sigma_z = 0.001(1+z)$, while the photometric redshift precision will be of $\sigma_z = 0.05(1+z)$. The spectroscopic survey will have 9 redshift bins of width 0.1 from $z = 0.9$ up to $z = 1.8$, while the photometric survey will consist on 10 equi-populated redshift bins from $z = 0.001$ up to $z = 2.5$. The photometric survey will detect 30 galaxies per arcmin^2, and the galaxy distribution, as well as the galaxy bias fiducial for the spectroscopic survey are presented in Table A.1.

Figure of Merit

When interpreting the results of the forecasts we can look at each parameter constraint, and their two-dimensional contours. But sometimes we want to have a single number quantifying the constraining power of a future survey. This quantity is usually represented by the Figure of Merit (FoM) [Albrecht et al., 2006]. In our case, we define it as the inverse of the area of the 2σ contour in the marginalized parameter plane for two parameters α and β (assuming that both likelihoods are Gaussian),

$$\mathrm{FoM}_{\alpha\beta} = \sqrt{\det\left(\tilde{F}_{\alpha\beta}\right)}\,, \tag{6.11}$$

where $\tilde{F}_{\alpha\beta}$ is the Fisher matrix for α and β once we have marginalized over all the remaining parameters. In the following, when we refer to the FoM it will concern the case $\alpha = w_0$ and $\beta = w_a$, providing the dark energy equation of state FoM.

[3] We have checked that changing its value by more than 50 % has no effect on the final results.

6.1.2 Spectroscopic galaxy clustering recipe

When considering the spectroscopic galaxy clustering probe, the main observable is the full, anisotropic, and redshift-dependent galaxy power spectrum. In order to provide a Fisher matrix for the baseline parameters from Eq. (6.10) we follow a two-step process by first computing a Fisher matrix on the following parameters

- power spectrum broadband (shape-parameters): $\{\omega_\mathrm{b},\, \omega_\mathrm{m},\, h,\, n_s\}$,
- non-linear nuisance parameters: $\{\sigma_\mathrm{p},\, \sigma_\mathrm{v}\}$,
- redshift-dependent parameters:
  $\{\ln d_\mathrm{A}(z_i),\, \ln H(z_i),\, \ln f\sigma_8(z_i),\, \ln b\sigma_8(z_i),\, P_s(z_i)\}$,

and then converting it to a baseline parameters Fisher matrix using a Jacobian projection (see Sec. 2.5).

The first set of parameters, given by the physical densities of baryons and total matter ($\omega_\mathrm{b} = \Omega_\mathrm{b}h^2$ and $\omega_\mathrm{m} = \Omega_\mathrm{m}h^2$, respectively), h, and n_s, determines the shape of the linear matter power spectrum, while the second takes into account the uncertainty in our non-linear correction, which cause the fingers-of-God effect of redshift-space distortions (see Sec. 1.3). Anisotropies around the line-of-sight in the power spectrum can be parametrized by the angular diameter distance and the Hubble parameter (to quantify the Alcock-Pazcynski effect), and the linear growth rate of structures (to quantify the RSD). See also Sec. 1.3. These three parameters are considered in the third set of parameters. We consider however the product of the linear growth rate and $\sigma_8(z)$ as a parameter, since we do not expect to break their degeneracy with GCs alone. We also consider the galaxy bias b (see Sec. 1.2.4), and the residual shot-noise P_s as parameters. Notice that all the parameters in the third set depend on the redshift, so we will have one parameter per redshift bin. In the following we detail how we take into account the different effects, and what is the role of the different nuisance parameters.

Observable

The main observable of the GCs probe is the galaxy power spectrum $P(k, \mu; z)$, where k is the modulus of the wave mode in Fourier space, μ is the cosine between the wave mode and the line-of-sight vector, and z stands for the effective redshift of each bin. In order to correctly model the power spectrum we need to take many observational effects into account. We first need to consider the galaxy bias, which corresponds to the bias of Hα-emitting galaxies for GCs. We also need to take into account the spectroscopic redshift uncertainty, and

the residual shot-noise that remains after the Poisson sampling noise by galaxy targeting has been removed. Moreover, we need to consider the anisotropy effects due to the AP effect and RSD.

Concerning the galaxy bias, we use a linear model where the galaxy power spectrum is given by the matter power spectrum, $P_{\rm m}(k;z)$, times b^2. Also, the redshift uncertainty introduces a smearing of the galaxy density field that can be modeled by adding an exponential factor [Seo and Eisenstein, 2003]

$$F_z(k,\mu;z) = \exp\left(-\frac{k^2\mu^2\sigma_0 c(1+z)}{H(z)}\right), \tag{6.12}$$

where $\sigma_0 = 0.001$ is the spectroscopic redshift accuracy at $z = 0$.

If we also take into account the shot-noise, we can express the galaxy linear power spectrum as

$$P_{\rm g,\,lin}(k,\mu;z) = b^2(z)P_{\rm m}(k;z)F_z(k,\mu;z) + P_s(z)\,. \tag{6.13}$$

We consider a fiducial of $P_s(z) = 0$ for all the redshift bins.

We can express the angle to the line-of-sight as

$$\mu^2 = \frac{k_\parallel^2}{k_\perp^2 + k_\parallel^2}\,, \tag{6.14}$$

where $k_\perp$ and $k_\parallel$ are the wave-numbers perpendicular and along the line-of-sight, respectively. With respect to the AP effects, assuming an incorrect cosmology when converting redshifts to distances leads to a rescaling of these components

$$k_\perp = \frac{d_{\rm A,\,ref}(z)}{d_{\rm A}(z)}k_{\perp,\,\rm ref} \qquad \text{and} \qquad k_\parallel = \frac{H(z)}{H_{\rm ref}(z)}k_{\parallel,\,\rm ref}\,. \tag{6.15}$$

With these expressions we can model the (future) observed real-space power spectrum in terms of the assumed geometry, $k_{\rm ref}$, $\mu_{\rm ref}$, and the spectroscopically measured redshift z. The matter power spectrum from Eq. (6.13) will then be given by

$$P_{\rm m,\,AP}(k_{\rm ref},\mu_{\rm ref};z) = \frac{H(z)d_{\rm A,\,ref}^2(z)}{H_{\rm ref}(z)d_{\rm A}^2(z)}P_{\rm m}(k(k_{\rm ref},\mu_{\rm ref});z)\,. \tag{6.16}$$

Finally, concerning the anisotropy due to RSD, the peculiar velocity displacements of galaxies are proportional to the growth rate $f(z)$, so we modify the real-space galaxy power spectrum by (see Sec. 1.3)

$$P_{\rm g,\,lin,\,RSD}(k,\mu;z) = (b(z)\sigma_8(z) + f(z)\sigma_8(z)\mu^2)^2\frac{P_{\rm m}(k;z)}{\sigma_8^2(z)}\,. \tag{6.17}$$

Combining all the previous modeling of observational effects, we can write the full linear observed power spectrum for our galaxies as

$$P_{\rm obs}(k_{\rm ref},\mu_{\rm ref};z) = \frac{H(z)d^2_{\rm A,\,ref}(z)}{H_{\rm ref}(z)d^2_{\rm A}(z)}\times \\ \times (b\sigma_8(z)+f\sigma_8(z)\mu^2)^2\frac{P_{\rm m}(k;z)}{\sigma^2_8(z)}F_z(k,\mu;z)+P_s(z)\,, \tag{6.18}$$

where all $k = k(k_{\rm ref},\mu_{\rm ref})$ and $\mu = \mu(k_{\rm ref},\mu_{\rm ref})$.

In order to add the non-linear effects into our analysis, we follow the phenomenological approach used in Wang, Chuang, and Hirata, 2013. The first implication of non-linearities is that the RSD factor gains an extra line-of-sight factor that accounts for the FoG effect. We model it with the factor $[1+(f(z)k\mu\sigma_{\rm p}(z))^2]^{-1}$, where $\sigma_{\rm p}$ is a new nuisance parameter. The second effect due to non-linearities is a damping of the BAO feature. We account for this with an extra exponential damping factor. Therefore, we can rewrite Eq. (6.17) as

$$P_{\rm g,\,non\text{-}lin,\,RSD}(k,\mu;z) = \left[\frac{1}{1+(f(z)k\mu\sigma_{\rm p}(z))^2}\right]\times \\ \times (b(z)\sigma_8(z)+f(z)\sigma_8(z)\mu^2)^2\frac{P_{\rm dw}(k,\mu;z)}{\sigma^2_8(z)}\,, \tag{6.19}$$

where the "de-wiggled" power spectrum, $P_{\rm dw}(k,\mu;z)$ is given by

$$P_{\rm dw}(k,\mu;z) = P_{\rm m}(k;z)e^{-g_\mu k^2}+P_{\rm nw}(k,\mu;z)\left[1-e^{-g_\mu k^2}\right]\,, \tag{6.20}$$

with

$$g_\mu(k,\mu;z) = \sigma^2_{\rm v}(z)[1-\mu^2+\mu^2(1+f(z))^2]\,, \tag{6.21}$$

and $P_{\rm nw}$ stands for the power spectrum without wiggles; i.e. with only cold dark matter (no BAO or RSD effects). We have introduced $\sigma_{\rm v}$ as another nuisance parameter.

So we can finally write the full non-linear observed power spectrum for our galaxies as

$$P_{\rm obs}(k_{\rm ref},\mu_{\rm ref};z) = \frac{H(z)d^2_{\rm A,\,ref}(z)}{H_{\rm ref}(z)d^2_{\rm A}(z)}\left[\frac{1}{1+(f(z)k\mu\sigma_{\rm p}(z))^2}\right]\times \\ \times\,(b\sigma_8(z)+f\sigma_8(z)\mu^2)^2\frac{P_{\rm dw}(k,\mu;z)}{\sigma_8^2(z)}F_z(k,\mu;z)+P_s(z)\,. \tag{6.22}$$

Observable covariance matrix

The statistical errors on the observable can be estimated with the number of galaxies that will be observed, as well as the volume of the survey. In this chapter we use the expected differential number density of galaxies given in Table A.1. We can directly obtain the number density per bin (shown in Fig. 6.1) as

$$n(z) = \frac{{\rm d}n}{{\rm d}V_{{\rm d}z}}{\rm d}z\,, \tag{6.23}$$

where ${\rm d}z = z_{\rm max} - z_{\rm min}$ for each bin, and the volume of each bin is given by

$${\rm d}V_{{\rm d}z} = \frac{\frac{4\pi}{3}\left[(1+z_{\rm max})^3 d_{\rm A}(z_{\rm max})^3 - (1+z_{\rm min})^3 d_{\rm A}(z_{\rm min})^3\right]}{4\pi\left(\frac{180}{\pi}\right)^2}\,. \tag{6.24}$$

We can then define the effective volume of the survey, $V_{\rm eff}$, as

$$V_{\rm eff}(k_{\rm ref},\mu_{\rm ref};z) = V_{\text{co-moving}}\left[\frac{nP_{\rm obs}(k_{\rm ref},\mu_{\rm ref};z)}{nP_{\rm obs}(k_{\rm ref},\mu_{\rm ref};z)+1}\right]^2\,, \tag{6.25}$$

where $V_{\text{co-moving}}$ [Eq. (6.6)] is the co-moving volume of the survey. In the Fisher formalism, as we will see in the following, the effective volume of the survey plays the role of the inverse of the covariance matrix (for the logarithm of the power spectrum). Notice that the redshift error contributes to the covariance via the exponential damping $F_z(k,\mu;z)$. The covariance matrix is evaluated at the fiducial cosmology. It is important to recall that no systematics errors are considered here. The impact of errors in the number density, for example, on the final FoM is definitely of interest, but left for future work.

Fisher matrix

The Fisher matrix for the observed power spectrum in redshift bins can be written as [Tegmark, 1997; Seo and Eisenstein, 2003]

$$F^{\rm bin}_{\alpha\beta}(z_i) = \frac{1}{8\pi^2}\int_{-1}^{1} {\rm d}\mu \int_{k_{\rm min}}^{k_{\rm max}} k^2\,{\rm d}k \frac{\partial \ln P_{\rm obs}(k_{\rm ref},\mu_{\rm ref};z_i)}{\partial p_\alpha} \times \\ \times \frac{\partial \ln P_{\rm obs}(k_{\rm ref},\mu_{\rm ref};z_i)}{\partial p_\beta} V_{\rm eff}(k_{\rm ref},\mu_{\rm ref};z_i)\,, \tag{6.26}$$

where p_α and p_β run over the cosmological (and nuisance) parameters. The total Fisher matrix is then calculated as the sum of the Fisher matrices for each bin

$$F_{\alpha\beta} = \sum_{i=1}^{N_{\rm bin}} F^{\rm bin}_{\alpha\beta}(z_i)\,. \tag{6.27}$$

For the redshift-dependent parameters, we assume that different redshift bins are independent.

6.1.3 Weak lensing recipe

When considering the weak lensing probe, the distortions induced in the images of galaxies can be decomposed into convergence and shear, γ. In this work we focus on the coherent correlation of galaxy shapes, which corresponds to the cosmic shear. Its information can be obtained working in real space (with two-point correlation functions), or in Fourier space (with the angular power spectrum). In this work we consider the latter space and split the volume of the survey in redshift slices (tomographic cosmic shear) in order to extract some information about the three-dimensional shear field. Contrary to GCs, we directly use the baseline parameters of Eq. (6.10) as primary parameters, so we do not use any Jacobian projection.

Observable

The main observable used in this analysis is the tomographic cosmic shear angular power spectrum. In order to correctly obtain the observable, we need to model several observational effects beyond the linear matter power spectrum. In a first place we need to obtain the power spectrum corresponding to the cosmic shear, as well as the power spectrum related to the main astrophysical systematic effect: the intrinsic alignment of galaxies. Moreover, WL probes very small scales, so we need to correct our predictions for the non-linearities arising at these scales. Also, we need to take into account the photometric redshift accuracy, and the shot-noise due to Poisson sampling by galaxy positions of the shear field.

Let us start with the cosmic shear power spectrum. Although its computation is far from being straightforward [Taylor et al., 2018], we can use the properties of spherical Bessel functions under the flat-sky [4] and Limber approximations (it is expected to be valid at angular scales $\ell > 100$) [Kitching et al., 2017; Kilbinger et al., 2017; Lemos, Challinor, and Efstathiou, 2017] to get the simple form (for a pair of redshift bins i and j)

$$C_{ij}^{\gamma\gamma}(\ell) = \frac{c}{H_0}\int \mathrm{d}z \frac{W_i^{\gamma}(z)W_j^{\gamma}(z)}{E(z)\chi^2(z)} P_{\delta\delta}\left(\frac{\ell+1/2}{\chi(z)}; z\right), \tag{6.28}$$

where $\chi(z)$ is the co-moving distance, $P_{\delta\delta}(k,z)$ is the matter power spectrum evaluated at $k = (\ell+1/2)/\chi(z)$ due to the Limber approximation, and $W^{\gamma}(z)$ is the window function given by

$$W_i^{\gamma}(z) = \frac{3}{2}\frac{H_0}{c}\Omega_{\mathrm{m}}(1+z)\tilde{\chi}(z)\int_z^{z_{\mathrm{max}}} \mathrm{d}z'\, n_i(z')\left(1-\frac{\tilde{\chi}(z)}{\tilde{\chi}(z')}\right), \tag{6.29}$$

where z_{max} is the maximum redshift of the survey, and $\tilde{\chi}(z) = \chi(z)/(H_0/c)$, showing that the window function only depends on the Hubble constant through the multiplicative factor H_0/c.

Let us now focus on the IA power spectrum. The change on the observed ellipticity of a galaxy can be expressed as

$$\epsilon = \gamma + \epsilon^I, \tag{6.30}$$

where γ corresponds to the cosmic shear just presented, and ϵ^I is the intrinsic (un-lensed) ellipticity of the galaxy. This intrinsic ellipticity may be induced from tidal processes during the formation of galaxies, and it cannot be completely removed by observational strategies; therefore, we need to take it into account when we model the total observed ellipticity. If we take the two-point correlation function of Eq. (6.30) we obtain

$$C_{ij}^{\epsilon\epsilon}(\ell) = C_{ij}^{\gamma\gamma}(\ell) + C_{ij}^{\mathrm{I}\gamma}(\ell) + C_{ij}^{\gamma\mathrm{I}}(\ell) + C_{ij}^{\mathrm{II}}(\ell). \tag{6.31}$$

Since we do not expect a foreground shear to be very correlated with a background ellipticity, we remove $C_{ij}^{\gamma\mathrm{I}}(\ell)$ from Eq. (6.31) and include this small contribution into the dominant cross-correlation $C_{ij}^{\mathrm{I}\gamma}$. So the IA power spectrum consists then of two terms: the auto-correlation (II) and the cross-correlation with the shear (Iγ). Following the so-called linear-alignment model [Catelan,

[4] It consists on replacing the expansion in spherical harmonics by an expansion in Fourier modes. This approximation is valid when we work with distant objects in a patch of the sky.

Kamionkowski, and Blandford, 2001; Hirata and Seljak, 2004], we can write these terms analogously to the cosmic shear angular power spectrum as

$$C_{ij}^{\mathrm{I}\gamma}(\ell) = \frac{c}{H_0}\int \mathrm{d}z \frac{W_i^{\gamma}(z)W_j^{\mathrm{IA}}(z) + W_i^{\mathrm{IA}}(z)W_j^{\gamma}(z)}{E(z)\chi^2(z)} P_{\delta\mathrm{I}}\left(\frac{\ell+1/2}{\chi(z)}; z\right), \quad (6.32)$$

$$C_{ij}^{\mathrm{II}}(\ell) = \frac{c}{H_0}\int \mathrm{d}z \frac{W_i^{\mathrm{IA}}(z)W_j^{\mathrm{IA}}(z)}{E(z)\chi^2(z)} P_{\mathrm{II}}\left(\frac{\ell+1/2}{\chi(z)}; z\right), \quad (6.33)$$

$$(6.34)$$

where the IA window function is given by

$$W_i^{\mathrm{IA}}(z) = \frac{H_0}{c} n_i(z) E(z)\,, \quad (6.35)$$

and $P_{\delta\mathrm{I}}$ and P_{II} stand for the IA power spectra. There are many models to relate these spectra to the matter power spectrum, $P_{\delta\delta}$, but we follow here a simple, observationally motivated model

$$P_{\delta\mathrm{I}}(k,z) = -\mathcal{A}_{\mathrm{IA}}\mathcal{C}_{\mathrm{IA}}\Omega_{\mathrm{m}}\frac{\mathcal{F}_{\mathrm{IA}}(z)}{D_1(z)} P_{\delta\delta}(k,z)\,, \quad (6.36)$$

$$P_{\mathrm{II}}(k,z) = \left(-\mathcal{A}_{\mathrm{IA}}\mathcal{C}_{\mathrm{IA}}\Omega_{\mathrm{m}}\frac{\mathcal{F}_{\mathrm{IA}}(z)}{D_1(z)}\right)^2 P_{\delta\delta}(k,z)\,, \quad (6.37)$$

with $\mathcal{C}_{\mathrm{IA}}$ and $\mathcal{A}_{\mathrm{IA}}$ being parameters of the IA model, and

$$\mathcal{F}_{\mathrm{IA}}(z) = \begin{cases} 1 & \text{if NLA}\,, \\ (1+z)^{\eta_{\mathrm{IA}}} & \text{if dNLA}\,, \\ (1+z)^{\eta_{\mathrm{IA}}}\left[\frac{\langle L\rangle(z)}{L_*(z)}\right]^{\beta_{\mathrm{IA}}} & \text{if eNLA}\,, \end{cases} \quad (6.38)$$

where η_{IA} and β_{IA} are two extra parameters of the IA model.

The first case, NLA, corresponds to the so-called non-linear alignment model for IA [Blazek, Vlah, and Seljak, 2015], while the second model, dNLA, is the one used in the recent DES analysis [Baxter et al., 2018], where they model the dependence on the redshift through a power law. The third model, eNLA, is our baseline, where we extend the previous approaches by including the luminosity dependence of the IA hinted by low-redshift studies and hydrodynamical simulations. $\langle L\rangle(z)$ and $L_*(z)$ stand for the redshift-dependent mean and the characteristic luminosity of source galaxies, respectively. We use the interpolation of the values for this ratio present in Table A.2, and the following values as fiducial for the different parameters

$$\{\mathcal{C}_{\mathrm{IA}}, \mathcal{A}_{\mathrm{IA}}, \eta_{\mathrm{IA}}, \beta_{\mathrm{IA}}\} = \{0.0134, 1.72, -0.41, 2.17\}\,. \quad (6.39)$$

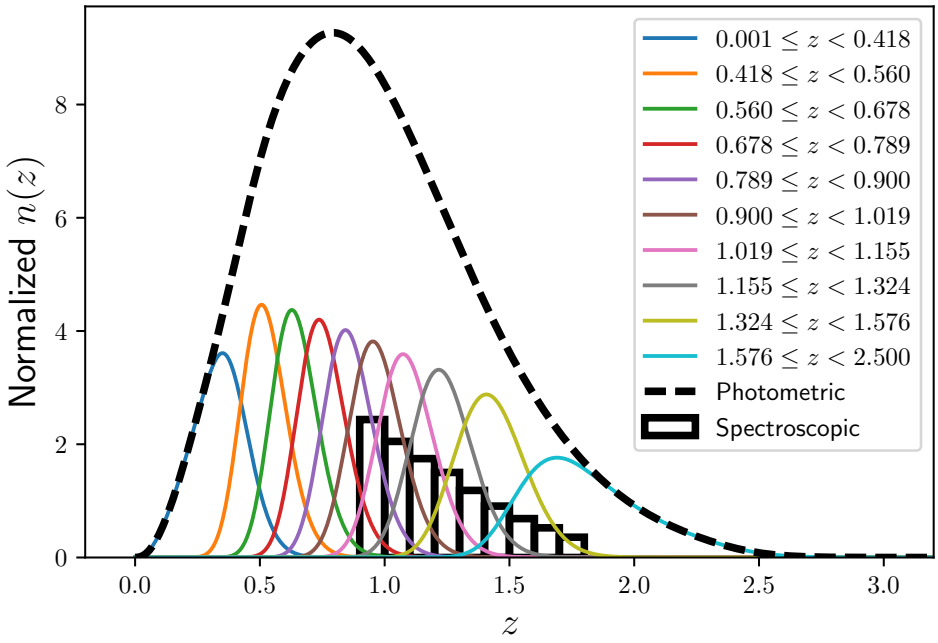

FIGURE 6.1: Number of galaxies as a function of the redshift for the spectroscopic sample (black thick solid histogram) and the photometric sample. The $n(z)$ for each bin in the photometric sample is represented in a different color. All these distributions have been normalized such that their integral over the redshift range is equal to 1. The addition of the photometric $n(z)$ distributions is shown with a black thick dashed line.

However, only $\mathcal{A}_{\rm IA}, \eta_{\rm IA}, \beta_{\rm IA}$ are allowed to vary. Indeed, $\mathcal{C}_{\rm IA}$ could be absorbed into $\mathcal{A}_{\rm IA}$, but we keep it only for historical reasons.

Let us now consider the photometric redshift accuracy and the number density of galaxies. The number density in a redshift bin i, in the presence of photometric redshifts, can be written as

$$n_i(z) = \frac{\int_{z_i^-}^{z_i^+} \mathrm{d}z_{\rm p}\, n(z)\, p_{\rm ph}(z_{\rm p}|z)}{\int_{z_{\rm min}}^{z_{\rm max}} \mathrm{d}z \int_{z_i^-}^{z_i^+} \mathrm{d}z_{\rm p}\, n(z)\, p_{\rm ph}(z_{\rm p}|z)}\,, \tag{6.40}$$

where z_i^- and z_i^+ stand for the lower and higher edges of the ith redshift bin, respectively. Notice that the underlying true distribution of sources, $n(z)$, is convolved with the probability density function, $p_{\rm ph}(z_{\rm p}|z)$, describing the probability that a galaxy with true redshift z has an estimated photometric redshift $z_{\rm p}$. In order to be very accurate we should parametrize this probability density

function using simulations adapted to the future Euclid specifications. However, we limit ourselves here to a general analytical parametrization, where this distribution is assumed to be

$$p_{\rm ph}(z_{\rm p}|z) = \frac{1-f_{\rm out}}{\sqrt{2\pi}\sigma_{\rm b}(1+z)} e^{-\frac{1}{2}\left(\frac{z-c_{\rm b}z_{\rm p}-z_{\rm b}}{\sigma_{\rm b}(1+z)}\right)^2} + \frac{f_{\rm out}}{\sqrt{2\pi}\sigma_{\rm o}(1+z)} e^{-\frac{1}{2}\left(\frac{z-c_{\rm o}z_{\rm p}-z_{\rm o}}{\sigma_{\rm o}(1+z)}\right)^2} . \tag{6.41}$$

This parametrization allows us to include a multiplicative and an additive bias in the photometric estimation of a fraction of sources $1-f_{\rm out}$ with reasonably well estimated redshifts, while we consider a fraction, $f_{\rm out}$, of catastrophic outliers, for which the estimation of the redshift is far from the true value. We fix the following values for the parameters specifying the photometric probability density function

$$\{c_{\rm b}, z_{\rm b}, \sigma_{\rm b}, c_{\rm o}, z_{\rm o}, \sigma_{\rm o}, f_{\rm out}\} = \{1.0, 0.0, 0.05, 1.0, 0.1, 0.05, 0.1\} . \tag{6.42}$$

Looking back at Eq. (6.40), in order to have the number density of galaxies in each redshift bin we also need the true redshift distribution. Following the Red-book [Laureijs et al., 2011] we use

$$n(z) \propto \left(\frac{z}{z_0}\right)^2 \exp\left[-\left(\frac{z}{z_0}\right)^{3/2}\right] , \tag{6.43}$$

where $z_0 = z_{\rm m}/\sqrt{2}$ being the median redshift ($z_{\rm m} = 0.9$). The surface density of galaxies, according to the Red-book, is 30 galaxies per square arc-minute; therefore, we can split the redshift range of the Euclid photometric survey into 10 equi-populated redshift bins, with edges

$$z_{\rm edges} = \{0.001, 0.418, 0.560, 0.678, 0.789, 0.900, 1.019, 1.155, 1.324, 1.576, 2.500\} . \tag{6.44}$$

We represent the number density $n_i(z)$ for all these bins, as well as the global photometric distribution in Fig. 6.1.

Concerning the shot-noise modeling, the uncorrelated part of the un-lensed ellipticity field adds a shot-noise term in the observed power spectrum. It vanishes for cross-correlations between different redshift bins, since the un-lensed ellipticities of different galaxies are uncorrelated. However, it is important for the auto-correlations within a redshift bin. It can be expressed as

$$N_{ij}^{\epsilon}(\ell) = \frac{\sigma_\epsilon^2}{\bar{n}_{\rm g}/10}\delta_{ij}^{\rm K}\,, \tag{6.45}$$

where the galaxy surface density per bin, $\bar{n}_{\rm g}/10$, has to be expressed in inverse steradians, $\delta_{ij}^{\rm K}$ is the Kronecker delta, and σ_ϵ^2 is the variance of the observed ellipticities, which we fix at $\sigma_\epsilon^2 = 0.3^2$.

Finally, the full cosmic shear tomographic angular power spectrum (using the flat-sky and Limber approximations) is given by

$$C_{ij}^{\epsilon\epsilon}(\ell) = C_{ij}^{\gamma\gamma}(\ell) + C_{ij}^{\rm II}(\ell) + C_{ij}^{\rm I\gamma}(\ell) + N_{ij}^{\epsilon}(\ell)\,, \tag{6.46}$$

which can be expanded into

$$\begin{aligned} C_{ij}^{\epsilon\epsilon}(\ell) =& \frac{c}{H_0}\int {\rm d}z \frac{W_i^{\gamma}(z)W_j^{\gamma}(z)}{E(z)\chi^2(z)} P_{\delta\delta}\left(\frac{\ell+1/2}{\chi(z)};z\right) + \\ & \frac{c}{H_0}\int {\rm d}z \frac{W_i^{\gamma}(z)W_j^{\rm IA}(z) + W_i^{\rm IA}(z)W_j^{\gamma}(z)}{E(z)\chi^2(z)} P_{\delta{\rm I}}\left(\frac{\ell+1/2}{\chi(z)};z\right) + \\ & \frac{c}{H_0}\int {\rm d}z \frac{W_i^{\rm IA}(z)W_j^{\rm IA}(z)}{E(z)\chi^2(z)} P_{\rm II}\left(\frac{\ell+1/2}{\chi(z)};z\right) + N_{ij}^{\epsilon}(\ell)\,. \end{aligned} \tag{6.47}$$

Notice that the integrals should go up to the redshift of the horizon, but there is no contribution beyond $z_{\rm max}$, so we limit the integrals up to $z_{\rm max} = 3.7$.

Looking back at the beginning of the section, we can see that there is only one effect missing that we should take into account: the non-linear correction at small scales. WL probes very small scales, deeply entering into the non-linear regime. In order to correct our predictions for this effect, we follow the standard approach of modeling the non-linear matter power spectrum as a correction on top of the linear matter power spectrum. As we saw in Sec. 1.2.3, theoretical corrections allow us to extend our predictions beyond linear scales, but we need to extend them deep into the non-linear scales for WL. Therefore, we need corrections obtained from simulations. In this chapter we consider the `halofit` prescription with the Takahashi and Bird corrections, as well as the `HaloModel` prescription (see Sec. 1.2.3 for a description of both approaches).

Observable covariance matrix

The error on the observed tomographic cosmic shear angular power spectrum can be expressed as

$$\Delta C_{ij}^{\epsilon\epsilon}(\ell) = \sqrt{\frac{2}{(2\ell+1)\Delta\ell f_{\rm sky}}} C_{ij}^{\epsilon\epsilon}(\ell)\,, \tag{6.48}$$

where $f_{\rm sky}$ stands for the fraction of the sky of the survey, and $\Delta\ell$ is the multipole bandwidth. The last term of Eq. (6.47) stands for the Poisson noise, while the first three terms correspond to the cosmic variance contribution to the errors. The factor in front the $C_{ij}^{\epsilon\epsilon}(\ell)$ in Eq. (6.48) accounts for the limited number of available independent modes, and the observed fraction of the sky.

It is important to notice that Eq. (6.48) correspond to a Gaussian covariance. However, because of the small scales probed in WL, non-Gaussian terms in the covariance may also be important. Their contribution is not straightforward to compute and, although an approximated analytical approach can be given by the halo model formalism [Kayo, Takada, and Jain, 2013], we decide here not to implement them and perform a conservative cut to remove the smallest scales from the analysis. We use $\ell_{\rm max} = 1500$ and $\ell_{\rm min} = 10$ as baseline.

Fisher matrix

The Fisher matrix for tomographic cosmic shear angular power spectrum can be written as

$$F_{\alpha\beta} = f_{\rm sky} \sum_{\ell=\ell_{\rm min}}^{\ell_{\rm max}} \left(\ell + \frac{1}{2}\right) \Delta\ell \frac{\partial(C_{ij}^{\epsilon\epsilon}(\ell) - N_{ij}^{\epsilon}(\ell))}{\partial p_\alpha} \left[\boldsymbol{C}^{\epsilon\epsilon}(\ell)^{-1}\right]_{jm} \times \\ \times \frac{\partial(C_{mn}^{\epsilon\epsilon}(\ell) - N_{mn}^{\epsilon}(\ell))}{\partial p_\beta} \left[\boldsymbol{C}^{\epsilon\epsilon}(\ell)^{-1}\right]_{ni} , \tag{6.49}$$

where summation over repeated indices is assumed (the indices run over all unique pairs of tomographic bins). Notice that different ℓ modes are uncorrelated, which is true under the Gaussian covariance assumption.

6.1.4 Photometric galaxy clustering recipe

We focus now on the galaxy clustering probe using the Euclid photometric survey. Since we do not have very accurate estimates of the redshift, as it is the case in GCs, we do not use a three-dimensional analysis, but rather a tomographic one with the angular galaxy clustering power spectrum. Also, since we will be using the same galaxies as in WL, we use the same tomographic bins, with the exact same number density in each redshift bin, n_i, given by Eq. (6.40) (and Fig. 6.1), and the angular galaxy density, $\bar{n}_i$, given by the integral of n_i over the redshift. It is important to say that in practice the catalogs that will be used for GCp and WL will not be exactly the same, since there are several quality cuts that needs to be applied (concerning the shape of galaxies, for instance) when using galaxies for WL or GCp analyses. However, we assume here that both catalogs are the same. The GCp window function can be expressed as

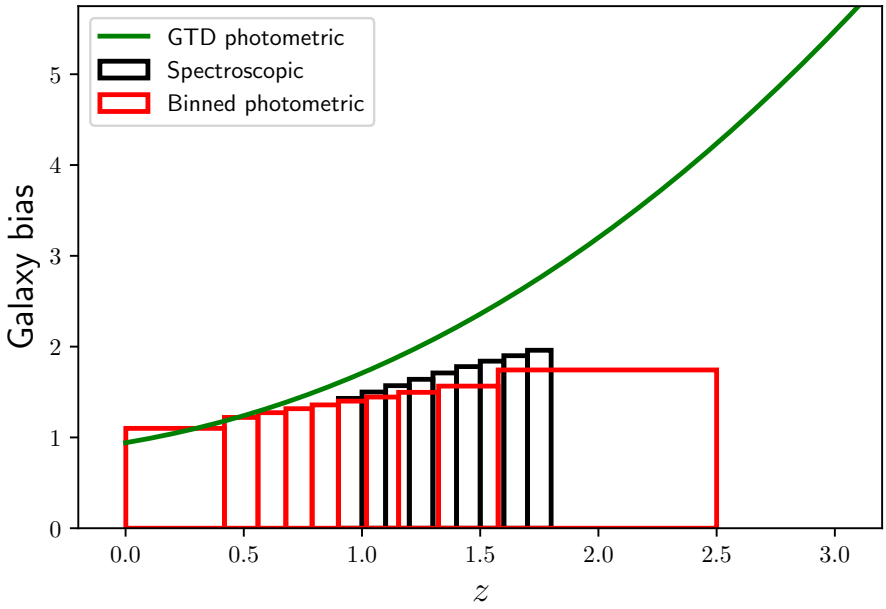

FIGURE 6.2: Fiducial galaxy bias as a function of the redshift for GCs (black histogram), the binned galaxy bias model for GCp (red histogram), and the GTD galaxy bias model for GCp (green line).

$$W_i^{\delta_{\rm g}}(k;\chi) = b_i(k, z(\chi))\frac{n_i(z(\chi))}{\bar{n}_i}\frac{{\rm d}z}{{\rm d}\chi}\,, \tag{6.50}$$

where $\delta_{\rm g}$ denotes the angular density contrast of galaxies, and b_i is the galaxy bias in the tomographic bin i. We assume a constant galaxy bias per redshift bin, leading to 10 nuisance parameters. Its fiducial is given by

$$b_i(z) = \sqrt{1+\bar{z}}\,, \tag{6.51}$$

where $\bar{z}$ stands for the mean redshift of each bin. We represent the fiducial galaxy bias in Fig. 6.2.

Using the Limber approximation, we can express the galaxy clustering tomographic angular power spectrum as

$$C_{ij}^{\delta_{\rm g}\delta_{\rm g}}(\ell) = \int {\rm d}\chi \frac{W_i^{\delta_{\rm g}}\left(\frac{\ell+1/2}{\chi},\chi\right) W_j^{\delta_{\rm g}}\left(\frac{\ell+1/2}{\chi},\chi\right)}{\chi^2} P_{\delta\delta}\left(\frac{\ell+1/2}{\chi}; z(\chi)\right)\,. \tag{6.52}$$

Concerning the correction for the non-linear scales, we follow the exact same approach as in WL, by using the `halofit` (with the Takahashi and Bird corrections) and `HaloModel` prescriptions.

With respect to the error on the observable, we use the Gaussian expression analogous to the one used for WL

$$\Delta C_{ij}^{\delta_{\rm g}\delta_{\rm g}}(\ell) = \sqrt{\frac{2}{(2\ell+1)\Delta\ell f_{\rm sky}}} \left(C_{ij}^{\delta_{\rm g}\delta_{\rm g}}(\ell) + N_{ij}^{\delta_{\rm g}}(\ell)\right) , \tag{6.53}$$

where the shot-noise is given by

$$N_{ij}^{\delta_{\rm g}}(\ell) = \frac{\delta_{ij}^{\rm K}}{\bar{n}_{\rm g}/10} . \tag{6.54}$$

As it was the case for WL, we consider a Gaussian covariance matrix, but non-Gaussian terms could have an impact on the final results. Following the previous approach, we consider not to implement these non-Gaussian terms which are difficult to model, and instead discard the smallest scales from the analysis. However, we expect GCp to be more sensitive to non-Gaussian terms than WL due to the fact of sampling high-density regions instead of total matter, and because shot-noise is subdominant for GCp, while it is not the case on WL. Therefore, we consider an even more conservative approach than in WL and we discard the scales beyond $\ell_{\rm max} = 750$ as baseline.

Finally, we can express the Fisher matrix for GCp by analogy to Eq. (6.49)

$$\begin{aligned} F_{\alpha\beta} =& f_{\rm sky} \sum_{\ell=\ell_{\rm min}}^{\ell_{\rm max}} \left(\ell + \frac{1}{2}\right) \Delta\ell \frac{\partial C_{ij}^{\delta_{\rm g}\delta_{\rm g}}(\ell)}{\partial p_\alpha} \left[\left(\boldsymbol{C}^{\delta_{\rm g}\delta_{\rm g}}(\ell) + \boldsymbol{N}^{\delta_{\rm g}}(\ell)\right)^{-1}\right]_{jm} \times \\ & \times \frac{\partial C_{mn}^{\delta_{\rm g}\delta_{\rm g}}(\ell)}{\partial p_\beta} \left[\left(\boldsymbol{C}^{\delta_{\rm g}\delta_{\rm g}}(\ell) + \boldsymbol{N}^{\delta_{\rm g}}(\ell)\right)^{-1}\right]_{ni} , \end{aligned} \tag{6.55}$$

where again the indices run over all unique pairs of tomographic bins.

6.1.5 Probe combination

We now focus on the combination of the different probes. In this work we only consider the three main probes of Euclid: GCs, GCp, and WL. Starting with the last ones, since we use the same approach to model the observables, we can combine the probes taking into account their cross-correlations in a simple, coherent way. The idea is to model the angular power spectra for WL, GCp, and their cross-correlations with $\boldsymbol{C}^{\rm AB}(\ell)$, where A and B run over WL and GCp observables. This provides us with a data vector composed of three sets of observables. We include then the covariance between these three sets as fourth-order correlations, $\mathrm{Cov}(\boldsymbol{C}^{\rm AB}(\ell), \boldsymbol{C}^{\rm A'B'}(\ell'))$.

Let us redefine the noise-less cosmic shear tomographic angular power spectrum, $C_{ij}^{\epsilon\epsilon}(\ell) - N_{ij}^{\epsilon}(\ell)$, as

$$C_{ij}^{\gamma\gamma}(\ell) = \int \mathrm{d}\chi\, \mathcal{W}_i^{\gamma}(\chi)\mathcal{W}_j^{\gamma}(\chi)\, P_{\delta\delta}\left(\frac{\ell+1/2}{\chi}; z(\chi)\right), \tag{6.56}$$

where we already include the IA effects through

$$\mathcal{W}_i^{\gamma} = \frac{W_i^{\gamma}(\chi)}{\chi} - \frac{\mathcal{A}_{\rm IA}\mathcal{C}_{\rm IA}\Omega_{\rm m}\mathcal{F}_{\rm IA}(\chi)}{D_1(z)}\frac{W_i^{\rm IA}(\chi)}{\chi}. \tag{6.57}$$

So in the following, when we refer to cosmic shear γ we will assume that all the intrinsic alignments are already included in the analysis.

Redefining the GCp window function as

$$\mathcal{W}_i^{\delta_{\rm g}} = \frac{W_i^{\delta_{\rm g}}\left(\frac{\ell+1/2}{\chi}, \chi\right)}{\chi}, \tag{6.58}$$

we can rewrite the GCp observable, given in Eq. (6.52), as

$$C_{ij}^{\delta_{\rm g}\delta_{\rm g}}(\ell) = \int \mathrm{d}\chi\, \mathcal{W}_i^{\delta_{\rm g}}\left(\frac{\ell+1/2}{\chi}, \chi\right)\mathcal{W}_j^{\delta_{\rm g}}\left(\frac{\ell+1/2}{\chi}, \chi\right) P_{\delta\delta}\left(\frac{\ell+1/2}{\chi}; z(\chi)\right). \tag{6.59}$$

The three observables will then be given by Eq. (6.56) (for WL), Eq. (6.59) (for GCp), and their cross-correlations

$$C_{ij}^{\delta_{\rm g}\gamma}(\ell) = \int \mathrm{d}\chi\, \mathcal{W}_i^{\delta_{\rm g}}\left(\frac{\ell+1/2}{\chi}, \chi\right)\mathcal{W}_j^{\gamma}(\chi)\, P_{\delta\delta}\left(\frac{\ell+1/2}{\chi}; z(\chi)\right). \tag{6.60}$$

Notice that we do not specify the cross-correlations $C_{ij}^{\gamma\delta_{\rm g}}(\ell)$ because their contribution is already included if we compute $C_{ij}^{\delta_{\rm g}\gamma}(\ell)$ for all the redshift pairs ij, and not only for unique pairs of tomographic bins.

In order to be consistent, we correct (in the three observables) for the non-linearities using the `halofit` (plus Takahashi and Bird corrections) and `HaloModel` prescriptions.

In order to take into account the covariance between the three probes, we use the expression

$$\begin{aligned}\mathrm{Cov}(C_{ij}^{\rm AB}(\ell), C_{kl}^{\rm A'B'}(\ell')) =& \frac{\delta_{\ell\ell'}^{\rm K}}{(2\ell+1)f_{\rm sky}\Delta\ell}\times \\ &\times\Big[\Big(C_{ik}^{\rm AA'}(\ell)+N_{ik}^{\rm AA'}(\ell)\Big)\cdot\Big(C_{jl}^{\rm BB'}(\ell)+N_{jl}^{\rm BB'}(\ell)\Big) \\ &+\Big(C_{il}^{\rm AB'}(\ell)+N_{il}^{\rm AB'}(\ell)\Big)\cdot\Big(C_{jk}^{\rm BA'}(\ell)+N_{jk}^{\rm BA'}(\ell)\Big)\Big]\end{aligned} \tag{6.61}$$

where A, B, A′, and B′ run over γ, $\delta_{\rm g}$; i, j, k, l run over the redshift bins (unique pairs of tomographic bins for GCp and WL, and all pairs for their cross-correlations), and the shot-noise is given by

$$N_{ij}^{\rm AB}(\ell) = \begin{cases} \frac{\delta_{ij}^{\rm K}\sigma_\epsilon^2}{\bar{n}_{\rm g}/10} & \text{if A=B=}\gamma\,, \\ \frac{\delta_{ij}^{\rm K}}{\bar{n}_{\rm g}/10} & \text{if A=B=}\delta_{\rm g}\,, \\ 0 & \text{if A} \neq \text{B}\,. \end{cases} \tag{6.62}$$

Notice that we assume that the shot-noise of cosmic shear and galaxy clustering are uncorrelated. This is true as long as there are no systematic effects contributing to the error of both probes.

The combined Fisher matrix for GCp, WL, and their cross-correlations is then given by

$$F_{\alpha\beta} = \sum_{\ell=\ell_{\rm min}}^{\ell_{\rm max}} \frac{\partial \boldsymbol{C}^{\rm AB}(\ell)}{\partial p_\alpha} \left[{\rm Cov}(\boldsymbol{C}^{\rm AB}(\ell), \boldsymbol{C}^{\rm A'B'}(\ell'))\right]^{-1} \frac{\partial \boldsymbol{C}^{\rm A'B'}(\ell')}{\partial p_\beta}\,, \tag{6.63}$$

where we recall that p_α and p_β run over the cosmological (and nuisance) parameters of the analysis.

In addition to the combination of GCp and WL, we want to combine with GCs. The computation of the cross-correlations in this case is far from being straightforward, since we combine two-dimensional with three-dimensional data. However, the spectroscopic Euclid survey will probe galaxies at redshift $z > 0.9$, having a small overlap with the lensing kernel. Therefore, we expect the cross-correlations between GCs and WL to be small, and we will neglect them in the following. Concerning the cross-correlations between GCs and GCp, they might still be important, because there will be many galaxies from the photometric catalog that will be used for clustering and will enter into the spectroscopic redshift range. Therefore, as conservative baseline, when we combine GCs and GCp we only select galaxies for the latter below $z = 0.9$. Neglecting the scatter from high-redshift galaxies due to the photometric redshifts, these two probes are then uncorrelated. Finally, the Fisher matrix for the combination of all probes will be given by the sum of the GCs matrix and the matrix coming from Eq. (6.63). In Sec. 6.6 we provide more details on how we combine all Euclid primary probes.

6.2 Forecasting in practice: the CosmoSIS code

In this section we briefly review the code used in this work to compute the Fisher matrix forecasts for Euclid, and we explain the different modifications performed with respect to the public version.

CosmoSIS is a cosmological parameter estimation code, whose modular structure eases re-usability, debugging, verifiability, and code sharing. Thanks to this modularity, CosmoSIS enables the use of existing codes for observable predictions, and different experimental likelihoods, written in different languages, like Fortran90, Python, or C/C++. The public version of CosmoSIS provides a standard library with different modules for the Boltzmann solver (like CAMB [Lewis, Challinor, and Lasenby, 2000; Howlett et al., 2012], CLASS [Lesgourgues, 2011a; Blas, Lesgourgues, and Tram, 2011; Lesgourgues, 2011b; Lesgourgues and Tram, 2011], or MGCAMB [Zhao et al., 2009; Hojjati, Pogosian, and Zhao, 2011]), the background quantities, or nuisance parameters (like the galaxy bias, and the intrinsic alignments), among many others. CosmoSIS also provides several experimental likelihoods (like for CMB, type Ia supernovae, and baryonic acoustic oscillations data), as well as different samplers, like the classic Metropolis-Hastings sampling [Metropolis et al., 1953], the ensemble walker sampling [Foreman-Mackey et al., 2013], or the MPI-aware maxlike sampler from the ROOT package [James and Roos, 1975], most of them in a fully parallelized way with MPI and OpenMP. More importantly for us, it also contains a sampler that computes Fisher matrices. CosmoSIS has been largely used in the literature to analyze real data [see e.g. DES Collaboration, 2017b; DES Collaboration, 2017a; Baxter et al., 2018], and to compute forecasts [see e.g. DES Collaboration, 2016; Harrison et al., 2016; Olivari et al., 2018].

Because of the modularity of CosmoSIS, it runs using a pipeline. The main idea is that each module of the pipeline takes some input from the core of the code, the **datablock**, performs the computation that it is supposed to do, and saves the output to the **datablock** again, such that the next module will be able to load the needed inputs from the **datablock** and proceed with the global computation.

We present the baseline pipeline used in this work in Fig. 6.3. The large light brown box corresponds to the main part of the pipeline, which is composed of 9 different modules. The first of them, **Consistency**, deduces missing cosmological parameters and check the consistency of the provided values, so it enables the user to consider derived cosmological parameters as the primary set,

$$\boldsymbol{p} = \{\Omega_{\rm m},\, \Omega_{\rm b},\, w_0,\, w_a,\, h,\, n_s,\, \sigma_8\}\,. \tag{6.64}$$

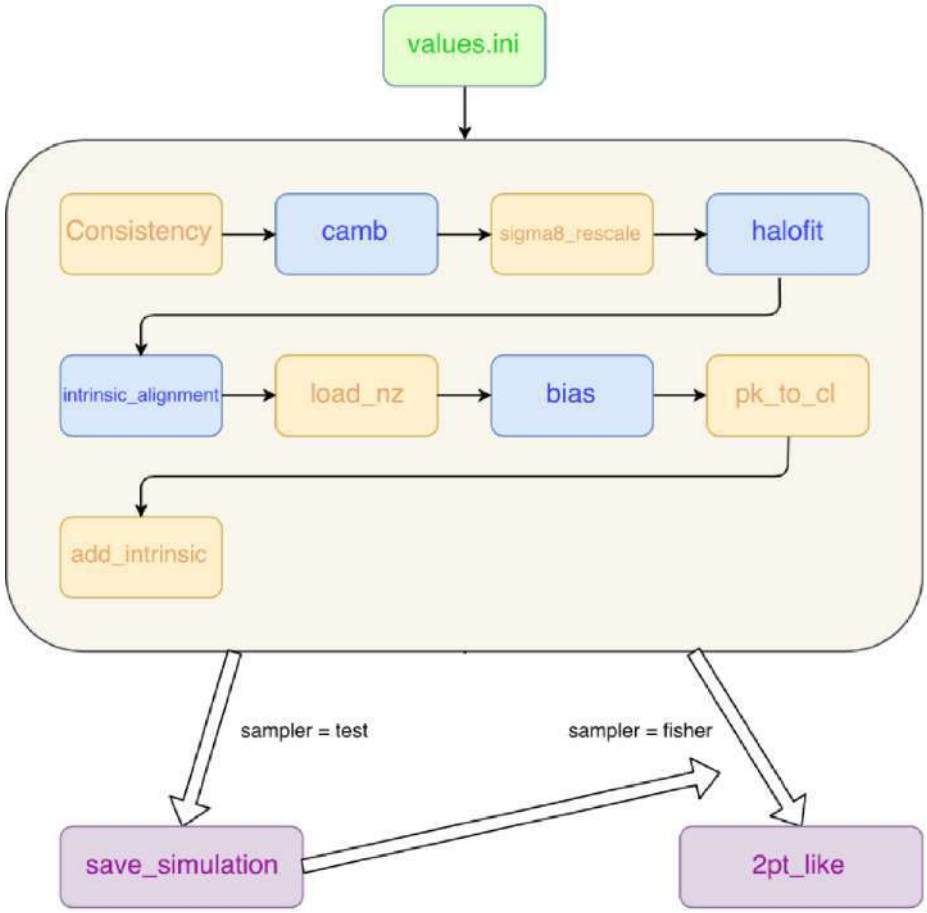

FIGURE 6.3: Schema of the modular pipeline used in CosmoSIS. The blue modules have been modified with respect to the public version.

The second module, **camb**, calls the Boltzmann solver to obtain the linear matter power spectrum using the output of the first module. Our baseline Boltzmann solver is CAMB, but it can easily be replaced by CLASS, or modified versions of them.

Since the Boltzmann solvers use A_s instead of σ_8 to normalize the matter power spectrum, we fix A_s to a dummy value and we add a third module into the pipeline, **sigma8_rescale**, to rescale the matter power spectrum to the desired value of σ_8.

We then add the fourth module, **halofit**, to take into account the non-linear correction to the matter power spectrum. As it was the case for the Boltzmann solver module, we can use different non-linear corrections. Our baseline is halofit with the Takahashi and Bird corrections, but we can easily replace it by HaloModel. Notice that we add the non-linear correction in a second step, so we can simply rescale the linear matter power spectrum.

We add a fifth module, **intrinsic_alignment**, to consider the intrinsic

alignments of galaxies. There are different models for the IA effects, and we can choose among them within this module.

We then add two modules, **load_nz** and **bias**, to load the distribution of galaxies, $n(z)$, and take into account the galaxy bias model when computing the galaxy power spectrum, respectively.

We finally perform the projection from power spectra to angular power spectra for each of the considered observables in **pk_to_cl**, and we add the last module, **add_intrinsic**, to add the IA angular power spectra to the cosmic shear angular power spectra (and to the cross-correlations angular power spectra).

All the modules colored in blue in Fig. 6.3 have been modified with respect to the public `CosmoSIS` version. We have modified **camb** to include the latest version of the code, and **halofit** to include the latest version of both `halofit` (plus Takahashi and Bird corrections) and `HaloModel`. We have implemented the eNLA model for IA used in this work into **intrinsic_alignment**, and we have implemented the binned galaxy bias model in **bias**.

Once having described the main modules of the pipeline, we present how it should be run. First of all, we generate a **values.ini** file with the values of the cosmological and nuisance parameters. Then, we run the pipeline adding the **save_simulation** module at the end using the **test** sampler. The **save_simulation** module is responsible for computing the covariance matrix of the observables (angular power spectra), as well as saving all the output, like the cosmological parameters, the observables, the galaxy distributions, or the covariance matrix of the observables. Since we run the pipeline with the **test** sampler, all the output will be based on our fiducial cosmology.

In a second step, we replace the **save_simulation** module by the **2pt_like** module, which consists on a two-point likelihood, and we run the pipeline again using the **fisher** sampler. This sampler calls the pipeline iteratively for all the variations of the parameters required to compute the numerical derivatives, and finally, it provides us with the Fisher matrix for the required parameters. Two derivative methods are available (3-point stencil, 5-point stencil) with a user-defined step-size per parameter.

In the following sections we present the results for the different probes. Given the number of contour-plots obtained in each section we limit them here to the minimum and refer the reader to Appendix A for the majority of the plots.

6.3 Weak lensing

In this section we focus on the results corresponding to WL. We start by presenting the baseline results, as well as the validation of `CosmoSIS` with the other

TABLE 6.1: Absolute 1σ (marginalized) forecasted constraints of the cosmological parameters for the WL Euclid probe with different specifications. The FoM for each case is shown for completeness.

Case	Ω_m	Ω_b	w_0	w_a	h	n_s	σ_8	FoM
ΛCDM baseline (Fig. A.1)	0.00571	0.0243	–	–	0.142	0.0336	0.00726	–
wCDM baseline (Fig. A.2)	0.00682	0.0243	0.0733	–	0.142	0.0361	0.00727	–
w_0w_aCDM baseline (Fig. 6.4)	0.0144	0.0243	0.163	0.591	0.143	0.0363	0.0157	23.1
w_0w_aCDM no IA (Fig. A.3)	0.0136	0.0267	0.148	0.551	0.155	0.0382	0.0154	26.9
w_0w_aCDM $\sum m_\nu = 0$ (Fig. A.4)	0.0141	0.0240	0.167	0.607	0.138	0.0338	0.0158	22.5
w_0w_aCDM `HaloModel` (Fig. A.5)	0.0226	0.0240	0.203	0.737	0.202	0.0975	0.0256	15.2
w_0w_aCDM $\ell_\mathrm{max} = 5000$ (Fig. A.6)	0.0114	0.0236	0.139	0.465	0.139	0.0310	0.0114	44.1
w_0w_aCDM $\Omega_\mathrm{K} \neq 0$ (Fig. A.7)	0.0172	0.0248	0.439	1.30	0.147	0.0465	0.0174	8.4
w_0w_aCDM 5-point (Fig. A.8)	0.0146	0.0245	0.165	0.594	0.144	0.0364	0.0159	23.0
w_0w_aCDM `halofit` 1 % (Fig. A.9)	0.0148	0.0237	0.167	0.606	0.147	0.0406	0.0177	22.7
w_0w_aCDM `HaloModel` 0.1 % (Fig. A.10)	0.0223	0.0239	0.201	0.722	0.195	0.0935	0.0208	15.6
ΛCDM `CLASS` (Fig. A.11)	0.00572	0.0242	–	–	0.142	0.0332	0.00767	–

codes used in the IST. We then study how the forecast change if we perform several variations to our baseline. For example, we study the impact of neglecting the IA nuisance parameters or the mass of neutrinos, as well as using a different non-linear correction or a different cut to discard the smallest scales.

6.3.1 Baseline results

Let us start by the baseline results. As described in Sec. 6.1, the baseline cosmological model is flat w_0w_aCDM, where the equation of state for dark energy is parametrized by w_0 and w_a. We model the IA with the eNLA model, and we account for 1 massive neutrino of mass 0.06 eV and 2 massless neutrinos. We model the non-linear scales with `halofit` including the Takahashi and Bird corrections, and we discard all the multipoles beyond $\ell_\mathrm{max} = 1500$. Our baseline considers `CAMB` as Boltzmann solver, and we use a 3-point stencil method with a 4 % step-size for the numerical derivatives.

The WL baseline forecast is shown in Table 6.1 and Fig. 6.4. We can clearly see that the best constraints are obtained for Ω_m (4.5 %), n_s (3.8 %) and σ_8 (1.9 %), while the other parameters are less constrained (48.6 % for Ω_b, 16.3 % for w_0 and 21.3 % for h)[5]. It is important to mention that parametrizing the

[5]Notice that we do not provide the percentage error on w_a because its fiducial is equal to 0.

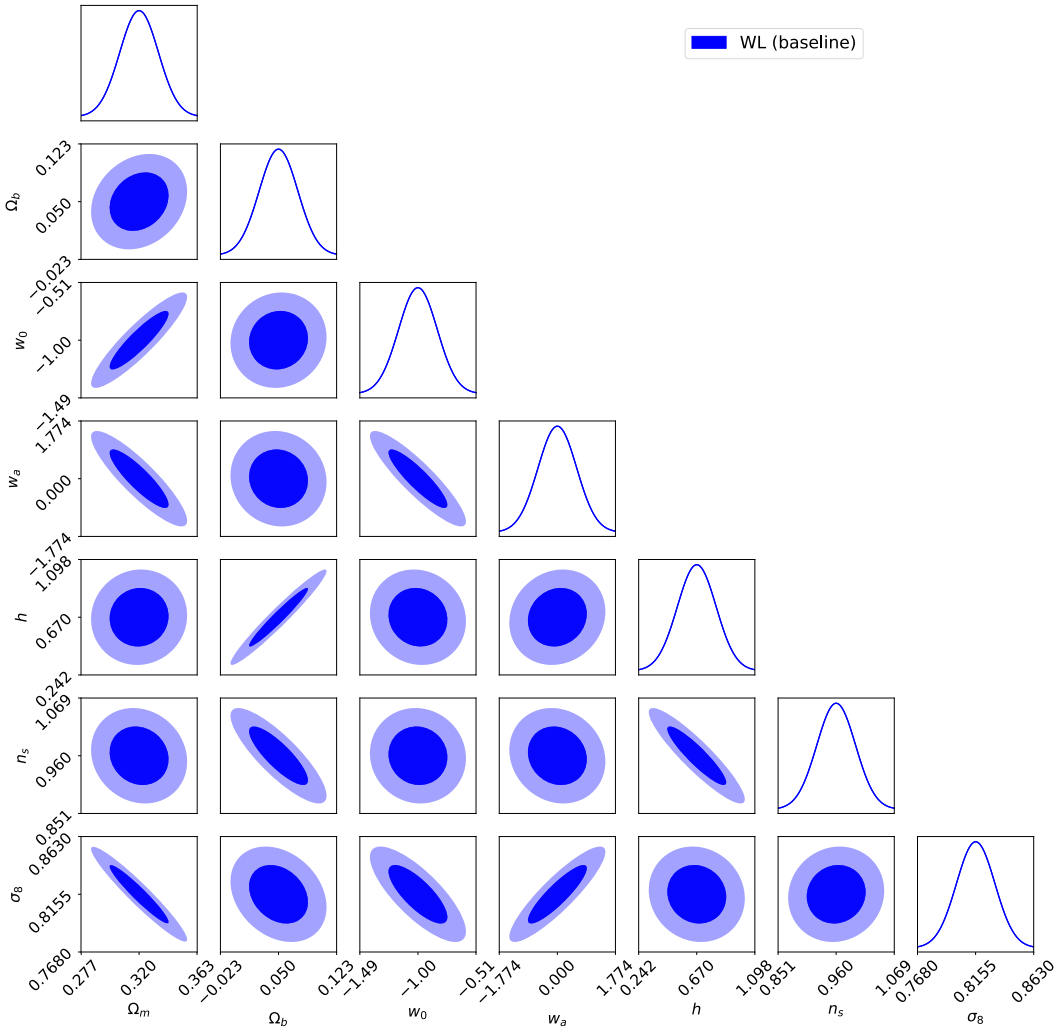

FIGURE 6.4: 1σ and 2σ marginalized Fisher contours for the parameters of the baseline w_0w_aCDM model (see the text for details).

dark energy equation of state with two parameters degrades some of the constraints. As we can see in Table 6.1, comparing the w_0w_aCDM baseline results with the wCDM baseline ones, we obtain worse constraints on $\Omega_{\rm m}$, w_0 and σ_8 by a factor 2.2. However, the constraints on $\Omega_{\rm b}$, h and n_s remain essentially the same. If we compare the w_0w_aCDM results to ΛCDM we degrade the constraints on $\Omega_{\rm m}$ by a factor 2.5, and on σ_8 by a factor 2.2, while the other constraints remain basically the same. We refer the reader to Fig. A.1 and Fig. A.2 for the contour-plots of the ΛCDM baseline and the wCDM baseline, respectively. As was discussed at the beginning of the section, one way to compress all the information into a single value is the Figure of Merit. Our baseline FoM is equal to 23.1, as can be seen in Table 6.1. It is also worth mentioning that, although they do not appear in the plot for readability, we have checked that the IA nuisance parameters are not significantly correlated with any cosmological parameter.

Once having presented the baseline results with `CosmoSIS`, it is an important task to check the validity of the code. In Fig. 6.5 we present the comparison of the different WL codes used in the IST, namely `CosmoSIS`, `CosmicFish`[6] [Raveri et al., 2016a; Raveri et al., 2016b], `FisherMathica`, `CCCP` and `STAFF`. All these codes use the same recipe presented in the previous sections, but use different implementations and different languages (see Euclid Collaboration, in prep. for a detailed description of each code). In more details, for each one of the cosmological parameters of the w_0w_aCDM baseline we present the marginalized (dots) and un-marginalized (solid lines) percentage differences with respect to the median of all codes. We can immediately see that all codes agree at a level better than 10 %, which is the accepted threshold for validity in the IST. Notice that `CosmoSIS` and `CosmicFish` are the two codes differing most. The reason being that they compute the input matter power spectra themselves, while the other codes use the exact same input for both the matter power spectra and their derivatives.

As said before, WL alone is not able to put strong constraints on all parameters, since some of them are quite degenerate (like $\Omega_{\rm b}$ or h). In Fig. 6.6 we present again the percentage difference with respect to the median of all codes but including a prior on $\Omega_{\rm m}$, $\Omega_{\rm b}$, h and n_s which roughly correspond to the constraints on these parameters obtained from GCs alone (2.5 %, 5 %, 1.5 % and 2 %, respectively). We can observe that the agreement of all codes is now much better (below $\sim$4 %). This points to the fact that combining probes will remove discrepancies between different implementations of the same forecasting recipe.

[6] `https://cosmicfish.github.io`

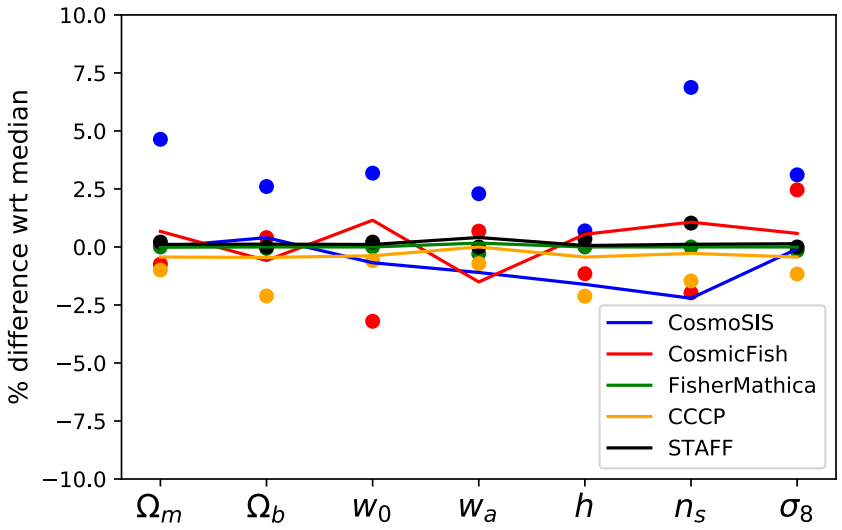

FIGURE 6.5: Percentage difference with respect to the median of all codes for the different cosmological parameters of the baseline model w_0w_aCDM, and the different WL codes used in the IST: `CosmoSIS` (blue, this work), `CosmicFish` (red), `FisherMathica` (green), `CCCP` (yellow), and `STAFF` (black). The dots stand for the differences using the marginalized errors, while the solid lines show the differences considering the un-marginalized errors.

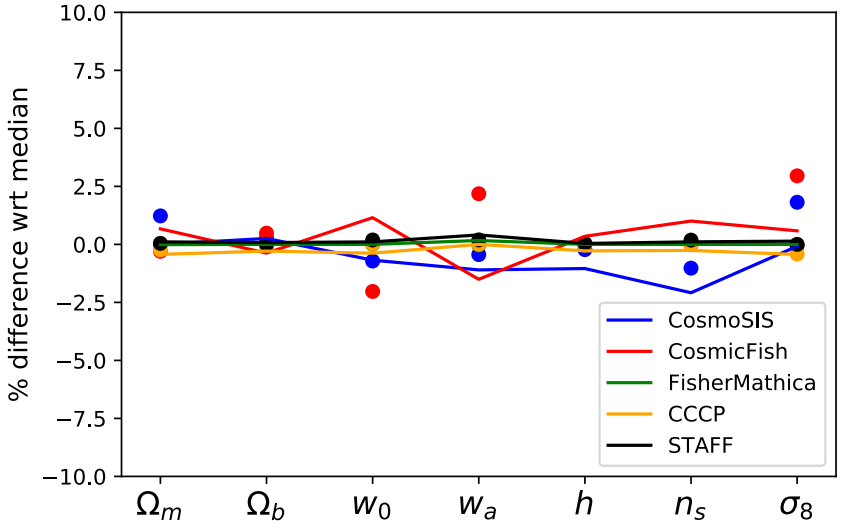

FIGURE 6.6: Same as in Fig. 6.5 adding priors on $\Omega_{\rm m}$, $\Omega_{\rm b}$, h, n_s of 2.5 %, 5 %, 1.5 %, 2 %, respectively, which roughly correspond to the constraints coming from GCs alone.

6.3.2 Impact of intrinsic alignments

Let us now start modifying the specifications of our forecast to check their impact on our baseline predictions. First, we consider the impact of neglecting the intrinsic alignment of galaxies. We present the results in Table 6.1 and the comparison with the baseline forecast in Fig. A.3. We can observe that even if the w_0-w_a contour is smaller when we neglect the IA (the FoM improves by 16 %), as well as some constraints (like $\Omega_{\rm m}$, w_0, w_a, n_s), the general results are roughly compatible with the baseline forecast.

6.3.3 Impact of massive neutrinos

Let us now focus on the impact of massive neutrinos. In Table 6.1 we present the results when we consider 3 massless neutrinos, and we show the comparison to our baseline predictions in Fig. A.4. We can observe that accounting for massive neutrinos or not does not significantly change the results. The constraint on some parameters is slightly better for massless neutrinos ($\Omega_{\rm m}$, $\Omega_{\rm b}$, h, n_s), while it is slightly worse for the other parameters (w_0, w_a, σ_8), but the differences are negligible (the FoM only decreases by 2.6 %). Notice that we do not consider the sum of neutrino masses as a free parameter; therefore, we did not expect a large difference between the massive and the massless case. However, allowing the sum of neutrinos masses to vary could significantly degrade the constraints. This test is left for future work.

6.3.4 Non-linear correction and cut at non-linear scales

Our baseline non-linear prescription is `halofit` with the Takahashi and Bird corrections. However, as discussed in Sec. 1.2.3, there are different non-linear recipes in the literature. We study here the impact of using `HaloModel` instead of `halofit`. The forecasted constraints for this case are also shown in Table 6.1, and we present the comparison between the two non-linear recipes in Fig. A.5. Notice that we use a step-size of 1 % for the numerical derivatives of the `HaloModel` forecast, as will be motivated in the following subsections.

It is completely clear from the figure that the choice of the non-linear prescription is very important for the final constraints. Not only the constraints are worse for `HaloModel` [by a factor ranging between 1.0 (for $\Omega_{\rm b}$) and 2.7 (for n_s)], but also the area of the two-dimensional contours is larger and sometimes with different orientation. Summarizing, the FoM decreases by 34 %, showing the importance of the non-linear correction in WL forecasts.

We focus now on the cut performed to discard the largest multipoles from the predictions. Our baseline is $\ell_{\rm max} = 1500$. We show the results for a cut

at $\ell_{\rm max} = 5000$ in Table 6.1, and their comparison with respect to the baseline predictions in Fig. A.6.

From the contour-plot we can easily see that most of the constraints improve (by a factor ranging between 1.0 and 1.4), but the main difference comes from the area of the contours, which decreases significantly thanks to the addition of small-scale information. The FoM in this case improves by 91 %. We have focused here on our `halofit` baseline but, given the importance of the non-linear recipe we have just seen, it is clear that going down to these small scales makes our predictions strongly sensitive to the non-linear prescription used, and that the improvement of the FoM should be taken with caution. Also, we recall that we do not include non-Gaussian terms in the covariance matrix of the observable, so going down to these small scales can probably be too optimistic.

6.3.5 Non-flat universe

We relax now the flatness assumption of the Universe by allowing the sum of the energy densities for the different components (including $\Omega_{\rm de}$) to be different than 1. In other words, we allow for $\Omega_{\rm K}$ to be different from 0. We show the results for this case in Table 6.1 and in Fig. A.7. We can see that allowing for some curvature degrades all constraints, especially those on w_0 and w_a (by a factor ranging between 2.7 and 2.2). This is automatically translated into a FoM smaller by 64 %. We can extract that allowing for some curvature basically degrades our knowledge of the dark energy equation of state.

6.3.6 Method and step of the numerical derivatives

Until now we have used the 3-point stencil method for the numerical derivatives. However, `CosmoSIS` also allows for the use of the 5-point stencil method. Although this method is more time consuming, it should be more precise than the 3-point method. In Table 6.1 and in Fig. A.8 we present the comparison between these two approaches.

We can observe both from the table and the plot that there is no difference between the 3-point and the 5-point stencil method for the numerical derivatives.

Another numerical issue concerning the derivatives is the step-size used for the parameters. Let us start with the `halofit` non-linear prescription. In the left panel of Fig. 6.7 we present the value of the FoM as a function of the step-size used for the parameters (same step-size for all of them). The red dot stands for the baseline (4 %), while the horizontal dashed lines show +10 % and −10 % of the baseline FoM. It is clear from the plot that the value of the FoM is stable using a step-size ranging from 0.5 % up to 5 %, while it largely oscillates when

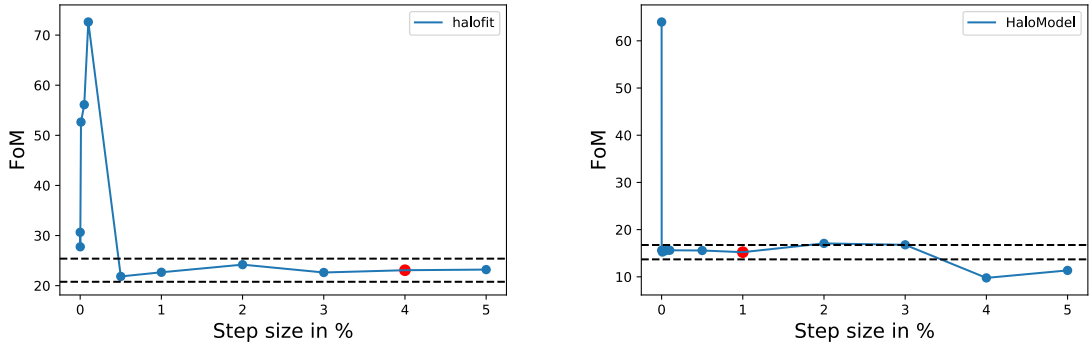

FIGURE 6.7: Figure of Merit as a function of the step-size used for the numerical derivatives. *Left panel:* `halofit` with Takahashi and Bird corrections. *Right panel:* `HaloModel`. The red dot stands for the baseline step used in all the results, while the black dashed lines show the band within +10 % and −10 % of the baseline FoM.

using smaller steps. For completeness, we show the comparison of the contours when using the baseline step of 4 % and a step of 1 % in Fig A.9 and in Table 6.1. We observe that not only the FoM is compatible (1.7 % variation), but also the constraints and the contours.

Let us now focus on the stability of the `HaloModel` results. In the right panel of Fig. 6.7 we observe that the FoM value is stable from considerably small steps (below 0.1 %) up to roughly 3 %. As before, the red dot stands for the baseline when using the `HaloModel` prescription. Notice that in this case, contrary to what happens with `halofit`, the FoM is no longer stable once we use large steps for the numerical derivatives. We also show, for completeness, the comparison between the `HaloModel` baseline step of 1 % and a step of 0.1 % in Fig. A.10 and in Table 6.1. As before, we do not observe any significant variation on the FoM, the constraints, or the contours. The largest difference concerns σ_8 with a factor of 1.2.

6.3.7 Boltzmann solver

As a last test on our baseline predictions, we study the impact of the Boltzmann solver on the results. For all the previous plots we have used the `CAMB` code. In Fig. A.11 and in Table 6.1 we present the comparison for the ΛCDM model between both Boltzmann solvers (`CAMB` and `CLASS`). We can observe that there is no significant difference in the results and the largest difference comes from σ_8 with a 1.06 factor of difference. We can extract from these results that the Boltzmann code used does not have any impact on the final results.

6.3.8 Summary

In this first section of results of this chapter we have focused on the WL probe. We have first presented the baseline results for ΛCDM, wCDM and w_0w_aCDM with

- eNLA model for IA,
- 1 massive neutrino of mass 0.06 eV and 2 massless neutrinos,
- `halofit` with the Takahashi and Bird corrections,
- cut at $\ell_{\rm max} = 1500$,
- flat universe,
- 3-point stencil method with a 4 % step for the numerical derivatives,
- and `CAMB` as Boltzmann solver.

We have seen that WL alone is able to nicely constrain some parameters (especially $\Omega_{\rm m}$ and σ_8), but there are important degeneracies among the others. The baseline FoM obtained is equal to 23.1. We have validated the results from `CosmoSIS` with the other WL forecasting codes used in the IST, and we have checked that adding priors on some of the degenerate parameters improve the agreement between the different codes.

After that, we have focused on studying the impact of the different baseline assumptions on the final results. In a first place, we have seen that neglecting IA improves the FoM, but the constraints on the parameters remain roughly the same. Concerning the massive neutrinos, we have seen that neglecting their mass does not change the results. Note, nevertheless, that we have not considered the sum of neutrino masses as a free parameter. We have also seen that the cut to discard the smallest scales can largely change the FoM, but this result should be taken with caution since we enter deeply into the non-linear regime and the non-linear correction can strongly modify the results. With respect to the flatness assumption of the Universe, we have seen that it essentially degrades the constraints on the dark energy equation of state, leading to a significant smaller value for the FoM.

Concerning numerical assumptions, we have seen that changing from a 3-point to a 5-point stencil method does not modify the results. However, the step-size that should be used is not known a priori. We have identified a region of step-size values for which the FoM is stable, and we have checked that within this range using a different step does not significantly change the constraints or the contours. As a last test, we have checked the impact of the Boltzmann

TABLE 6.2: Absolute 1σ (marginalized) forecasted constraints of the cosmological parameters for the GCp Euclid probe with different specifications. The FoM for each case is shown for completeness.

Case	$\Omega_{\rm m}$	$\Omega_{\rm b}$	w_0	w_a	h	n_s	σ_8	FoM
ΛCDM baseline (Fig. A.12)	0.00761	0.00301	–	–	0.0280	0.0287	0.0117	–
wCDM baseline (Fig. A.13)	0.0209	0.00392	0.131	–	0.0494	0.0384	0.0329	–
w_0w_aCDM baseline (Fig. 6.8)	0.0359	0.00647	0.417	1.37	0.0530	0.0401	0.0378	5.6
w_0w_aCDM fixed bias (Fig. A.14)	0.00863	0.00267	0.0788	0.193	0.0295	0.0153	0.00695	280.0
w_0w_aCDM GTD bias (Fig. A.15)	0.0117	0.00314	0.164	0.728	0.0390	0.0375	0.0226	19.7
w_0w_aCDM $\sum m_\nu = 0$ (Fig. A.16)	0.0383	0.00713	0.415	1.33	0.0495	0.0419	0.0365	5.8
w_0w_aCDM `HaloModel` (Fig. A.17)	0.0312	0.00691	0.365	1.33	0.0612	0.0624	0.0260	7.8
w_0w_aCDM $\ell_{\rm max} = 2000$ (Fig. A.18)	0.0145	0.00332	0.160	0.569	0.0244	0.00761	0.00943	39.2
w_0w_aCDM $\Omega_{\rm K} \neq 0$ (Fig. A.19)	0.0367	0.00703	0.512	1.57	0.0554	0.0493	0.0373	4.3
w_0w_aCDM 5-point (Fig. A.20)	0.0317	0.00558	0.356	1.17	0.0527	0.0390	0.0357	6.5
w_0w_aCDM `halofit` 2 % (Fig. A.21)	0.0373	0.00646	0.403	1.29	0.0537	0.0413	0.0363	5.8
w_0w_aCDM `HaloModel` 5 % (Fig. A.22)	0.0298	0.00690	0.365	1.34	0.0637	0.0641	0.0274	7.7
ΛCDM `CLASS` (Fig. A.23)	0.00763	0.00236	–	–	0.0211	0.0216	0.0105	–

solver, showing that our results are largely independent of the specific solver used.

In conclusion, the baseline results presented in Fig. 6.4 are stable with respect to numerical decisions and quite general in terms of cosmology. Of course allowing for some curvature degrades the constraining power of the WL probe of Euclid, but, what is more important is that the main sensitivity on the results comes from the non-linear recipe used, even if we discard the smallest scales.

6.4 Photometric galaxy clustering

In this section we present the results of the photometric galaxy clustering forecasts. We will follow the approach presented in the previous section by first showing the baseline results, and then testing the impact of different assumptions on the final results. The only difference is that the intrinsic alignment of galaxies are no longer relevant in this section, but we need to take into account the galaxy bias as nuisance parameter.

6.4.1 Baseline results

Let us start by presenting the baseline results for w_0w_aCDM. We recall that our baseline model for galaxy bias, given in the GCp recipe of Sec. 6.1.4, is given by a constant galaxy bias per bin (binned model), whose fiducial follows $\sqrt{1+\bar{z}}$,

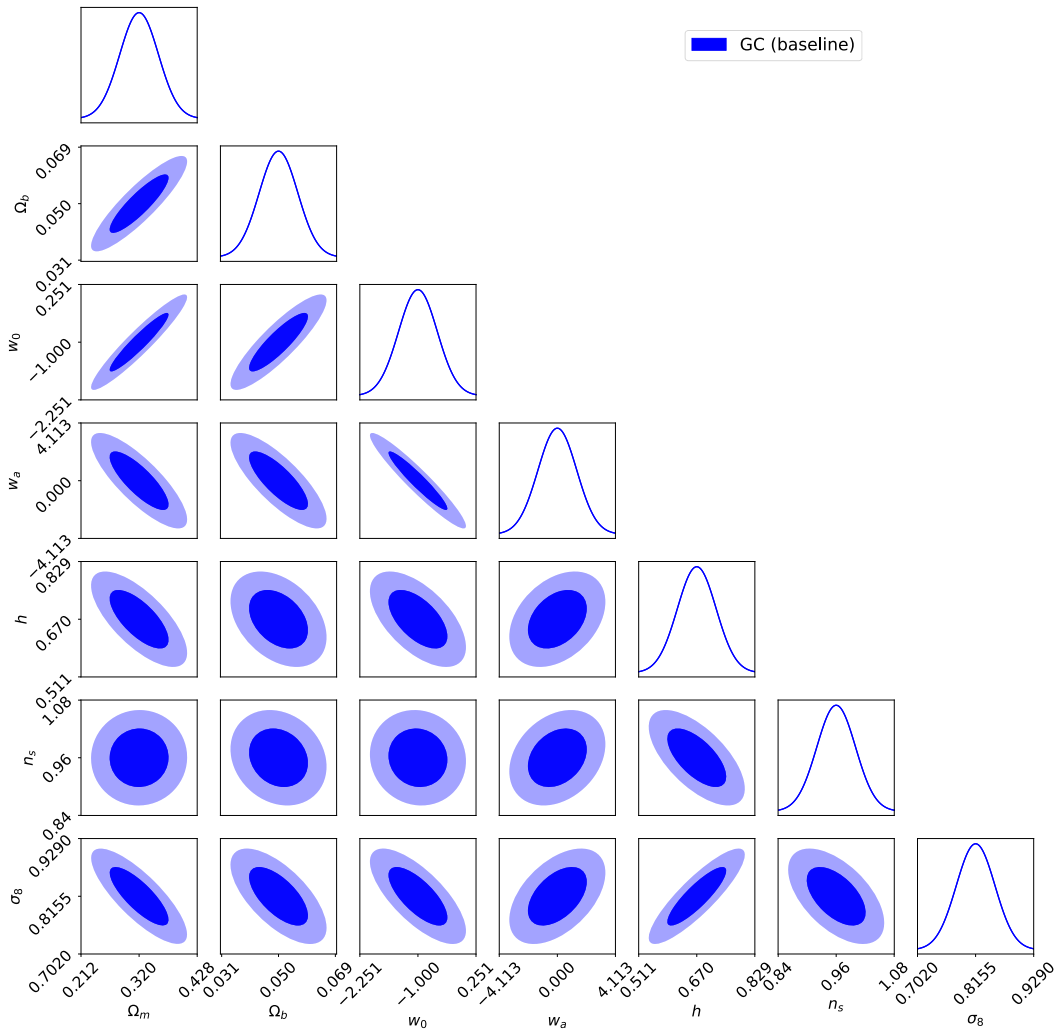

FIGURE 6.8: 1σ and 2σ marginalized Fisher contours for the parameters of the baseline w_0w_aCDM model (see the text for details).

where $\bar{z}$ is the mean redshift of each bin. We present the results for this case in Table 6.2 and in Fig. 6.8.

We can observe that the constraining power on the dark energy equation of state is smaller than it is for WL, since we obtain now a FoM of 5.6 instead of 23.1. However, GCp is able to constrain some parameters better than WL alone, like Ω_b (12.9 %) and h (7.9 %), pointing to the fact that combining both probes we will break some degeneracies between the parameters and lead to much better constraints (see next section). As before, we do not show the nuisance parameters in the plot, for readability, but we have checked that all the galaxy bias nuisance parameters are correlated with n_s, and anti-correlated with h and σ_8. Therefore, it is important to master these nuisance parameters in order not to bias the derived cosmology from the future data; especially concerning the cosmological parameters with whom they are correlated.

As it was the case before, the fact of parametrizing the dark energy equation of state with two parameters degrades the constraints on most of the parameters. In Table 6.2 and in Figs. A.12 and A.13 we present the forecasted constraints for the ΛCDM and wCDM baseline models, respectively. Going from one parameter w to two parameters w_0 and w_a degrades the constraints by a factor ranging from 1.0 (for n_s) to 3.2 (for w). If we compare the w_0w_aCDM results to ΛCDM, we degrade the constraints by a factor ranging between 1.4 (for n_s) and 4.7 (for Ω_m). Just as a comment, notice that the orientation for some contours in the ΛCDM case has changed with respect to what we expect. For instance, Ω_m and σ_8 are correlated instead of anti-correlated. However, this is just due to the marginalization, since we have checked that fixing the other parameters we recover the expected anti-correlation on Ω_m and σ_8. Another example of this change of orientations due to marginalization is discussed in Sec. 7.4.

After having presented the baseline forecast, we focus on the validation of `CosmoSIS` with the other forecasting code for GCp used in the IST: `CosmicFish`. As we did for WL, we present the percentage difference with respect to the median of the two codes in Fig. 6.9, where blue stands for `CosmoSIS` and red for `CosmicFish`. We can observe that for all cosmological parameters both codes show a difference below 10 % with respect to the median, being thus below the IST threshold for validation.

Looking back at Fig. 6.8 we can observe that some parameters are largely degenerate with GCp alone, as it was the case with WL alone. In Fig. 6.10 we present the percentage differences with respect to the median for all cosmological parameters but adding in this case a prior on Ω_m, w_0 and σ_8 roughly corresponding to the constraints from WL alone. As it was the case in Fig. 6.6, we can see that the agreement of both codes improves, pointing again to the

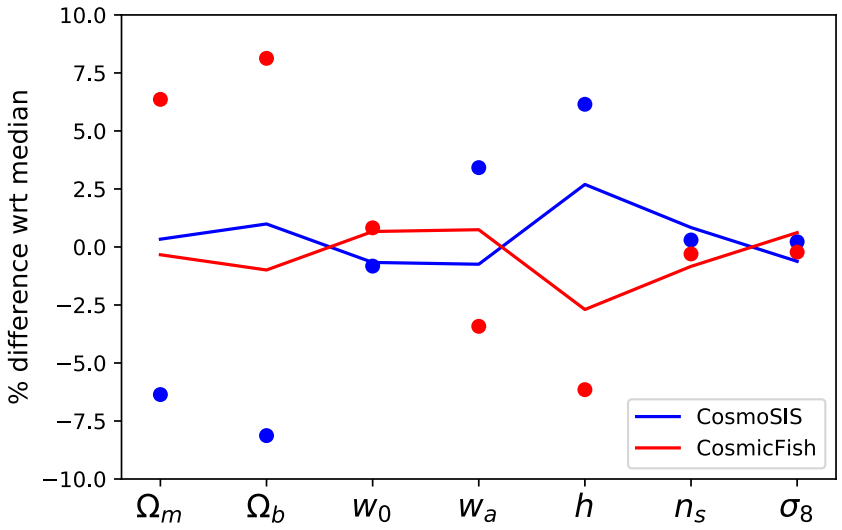

FIGURE 6.9: Percentage difference with respect to the median of all codes for the different cosmological parameters of the baseline model w_0w_aCDM, and the different GCp codes used in the IST: `CosmoSIS` (blue, this work) and `CosmicFish` (red). The dots stand for the differences using the marginalized errors, while the solid lines show the differences considering the un-marginalized errors.

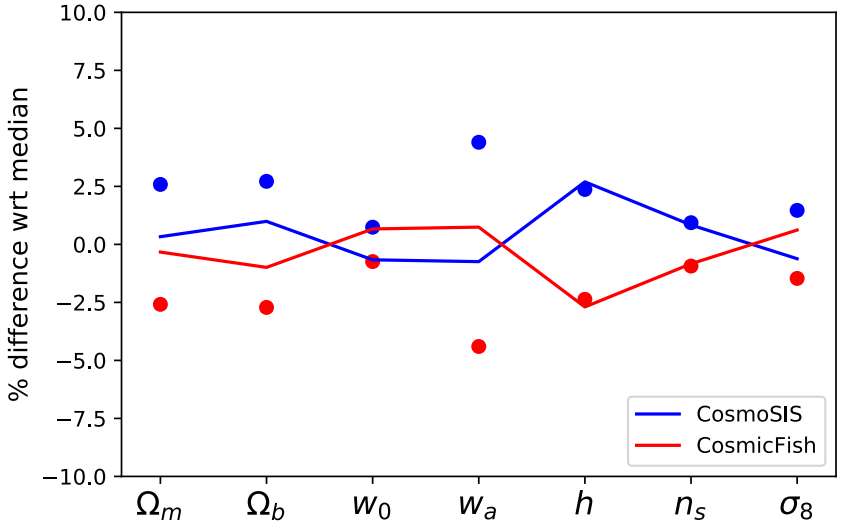

FIGURE 6.10: Same as in Fig. 6.9 adding priors on $\Omega_{\rm m}$, w_0, σ_8 of 4 %, 15 %, 2 %, respectively, which roughly correspond to the constraints coming from WL alone.

fact that combining probes may reduce the discrepancies between different implementations of the same recipe.

6.4.2 Impact of galaxy bias

Let us now start studying the impact of different assumptions on our baseline computations. First of all, we consider the main nuisance parameter of GCp: the galaxy bias. In Fig. A.14 we show the comparison between the baseline and the same binned galaxy bias model but with fixed parameters; i.e. we consider the same fiducial for the galaxy bias in each tomographic bin but we do not allow it to vary. It is clear from the figure that if we improve our knowledge of the galaxy bias we strongly reduce our GCp constraints. This improvement can be quantified with the results in Table 6.2. Fixing the galaxy bias improves the constraints on the different parameters by a factor ranging between 1.8 (for h) and 7.1 (for w_a). However, what is astonishing is the improvement on the FoM by 4900 %. Of course we will never fully know the galaxy bias, so these results are over-optimistic, but we still show them to emphasize the importance of improving our knowledge of the galaxy bias to extract the maximum of information from GCp.

In Fig. A.15 we provide the comparison between the baseline and a less conservative model for galaxy bias: the Generalized Time Dependent bias (see Sec. 1.2.4), which has 3 free parameters. We follow Clerkin et al., 2015, in using the fiducial values

$$c = 0.57, \quad b_0 = 0.79, \quad \alpha = 2.23\,. \tag{6.65}$$

We recall that the GTD model uses the growth factor to compute the dependence of the galaxy bias on the redshift. Therefore, we need to add the **growth_factor** module after the **Consistency** module in the `CosmoSIS` pipeline.

From the figure we can observe that we obtain smaller constraints using this less conservative, but still realistic, galaxy bias model. Looking at Table 6.2, we improve by a factor between 1.1 (for n_s) and 3.1 (for $\Omega_{\rm m}$), and the FoM improves by 252 %, showing again the importance of the knowledge of the galaxy bias.

6.4.3 Impact of massive neutrinos

Let us now consider the mass of neutrinos. In Fig. A.16 we show the comparison between the baseline (1 massive neutrinos of mass 0.06 eV and 2 massless neutrinos) and 3 massless neutrinos. Although we are able to distinguish two ellipses in some combination of parameters, the contours are roughly the same,

as it is also the case for the different constraints on the parameters. Quantitatively (see Table 6.2), the largest difference appears on $\Omega_{\rm b}$ with a factor of 1.1, and the FoM improves by 3.6 % when all neutrinos are massless.

6.4.4 Non-linear correction and cut at non-linear scales

As it was the case for WL, the correct modeling of non-linear scales is of vital importance for GCp. In Fig. A.17 we show the comparison between the baseline (`halofit` with Takahashi and Bird corrections) and the `HaloModel` prescription. We can observe that there are clear discrepancies between the contours obtained using one non-linear correction or the other. Not only they differ in size but also in orientation, in some cases. However, the constraints on the cosmological parameters are not as different as they were in Fig. A.5 for WL. The constraint on n_s and σ_8 differ by a factor of 1.6 and 1.5, respectively (see Table 6.2), but all the others agree by less than a factor 1.2. The FoM in this case improves by 39 %, showing that even if the constraints on the parameters are not completely different, the difference on the contours is significant. This shows again that even using a cut to discard all multipoles where non-Gaussian terms start to be important, the way we model non-linearities is of major importance to the final results.

We recall that we use a step-size of 1 % for the numerical derivatives when using `HaloModel`.

Still focusing on the non-linear scales, we study the impact of the $\ell_{\rm max}$ value when using the baseline `halofit` correction. In Fig. A.18 we show the comparison between the baseline $\ell_{\rm max} = 750$ value and the $\ell_{\rm max} = 2000$ value. As expected, all the constraints improve significantly, thanks to the addition of small-scale data. Quantitatively (see Table 6.2), they improve between a factor 1.9 (for $\Omega_{\rm b}$) and 5.3 (for n_s), while the FoM improves by 600 %. This shows that even with a conservative model for galaxy bias, if we can manage to use very small scales in our analyses, we can strongly improve our constraints obtained from GCp alone. However, as we have just seen, this relies on our non-linear correction and at ℓ values much below 2000 we already obtain different results depending on the non-linear recipe used.

6.4.5 Non-flat universe

In the previous section we saw that allowing for some curvature in the Universe strongly degrades the constraints on w_0 and w_a, and therefore it degrades the WL FoM. In Fig. A.19 (and Table 6.2) we show the GCp results concerning a non-flat universe. In this case the constraints are less affected by the fact of allowing for some curvature (the largest difference comes from n_s by a factor

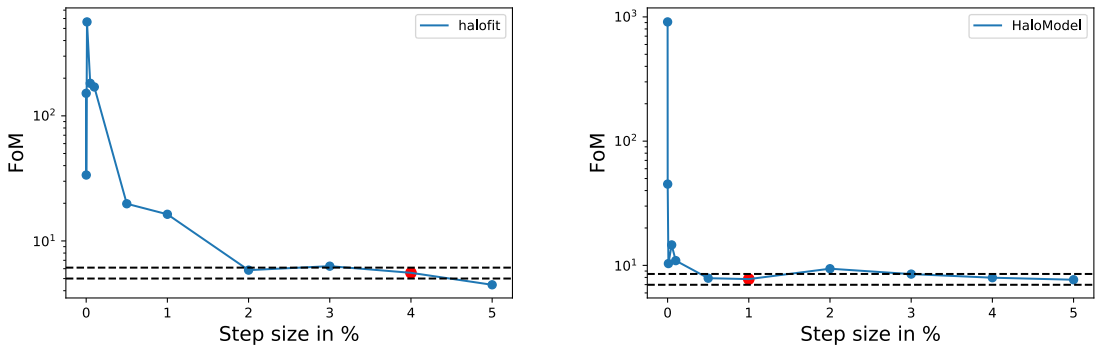

FIGURE 6.11: Figure of Merit as a function of the step-size used for the numerical derivatives. *Left panel:* `halofit` with Takahashi and Bird corrections. *Right panel:* `HaloModel`. The red dot stands for the baseline step used in all the results, while the black dashed lines show the band within +10 % and −10 % of the baseline FoM.

1.2), but the FoM is still degraded by 23 % (although significantly less than it was for WL - 64 %).

6.4.6 Method and step of the numerical derivatives

After having studied the impact of different cosmological assumptions of our baseline on the final results, we consider numerical aspects. Let us start with the method of the numerical derivative used. In Fig. A.20 and in Table 6.2 we present the comparison between the 3-point and 5-point stencil method. We can see that both methods give approximately the same results, but we are still able to distinguish the ellipses while they were perfectly overlapping for WL (Fig. A.8). This may be due to the fact that the WL angular spectra are quite smooth, while the BAO oscillations are present in the GCp angular spectra. Being less smooth could create a larger dependency on the numerical method used to compute the derivatives. Quantitatively, the constraints differ up to a factor 1.2, and the FoM changes by 16 %.

Let us now consider again the baseline 3-point stencil method, and focus on the step-size used for the numerical derivatives. In Fig. 6.11 we provide the value of the FoM as a function of the step-size for both `halofit` (with Takahashi and Bird corrections) and `HaloModel`. If we look at the `halofit` results we can immediately see that there is nearly no region of stability either at small or large step-size. However, since we use a 4 % step-size for WL we have decided to keep it in order to eventually combine both probes. In Fig. A.21 we provide the comparison between a step-size of 4 % and 2 %. Although the results are

roughly the same, the FoM improves by 3.6 % when we reduce the step-size (see Table 6.2).

We can now consider the change of step-size using `HaloModel`. Contrary to what was obtained for WL (Fig. 6.7), the value of the FoM is not very sensitive to the step-size and we can use from quite small steps (0.5 %) to large steps (5 %) without significantly modifying it. For completeness, we show in Fig. A.22 the comparison between using a step-size of 1 % (the baseline with `HaloModel`) and a step of 5 %. The results are nicely compatible, with a smaller FoM by only 1.3 % (see Table 6.2).

From these results it is clear that a more detailed analysis on the stability of the constraints as a function of the step-size is required. This is left for future work.

6.4.7 Boltzmann solver

Last, but not least, we study the impact of using a different Boltzmann solver on the final results. In Fig. A.23 and in Table 6.2 we present the comparison between the results using `CAMB` and `CLASS` for the ΛCDM model. From the figure it is clear that there are some differences, while the results were much more in agreement for WL (see Fig. A.11). This may be due to the fact that the oscillations of the power spectrum are present on the tomographic galaxy angular power spectra, while the cosmic shear angular power spectra are smoother. Therefore, a difference in the wiggles appearing in the spectra because of the Boltzmann code may have a larger effect on GCp than on WL. A more detailed comparison modifying the precision parameters of both Boltzmann solvers is left for future work. However, with the standard configuration (see Sec. A.5 for the precision parameters used for both codes in this work) we obtain differences on the cosmological parameters constraints by a factor ranging between 1.0 (for $\Omega_{\rm m}$) and 1.3 (for n_s).

6.4.8 Summary

In this second section of results of the chapter we have considered the GCp probe of Euclid. We have followed the approach of the previous section by presenting the baseline results for ΛCDM, wCDM and w_0w_aCDM, and then studying the impact of different cosmological or numerical assumptions on the final results. We recall that the only difference on the GCp baseline recipe with respect to the WL one is the nuisance parameters. The IA are no longer relevant for GCp, while the galaxy bias needs to be taken into account now.

From the baseline results we have seen that GCp alone is able to constrain some parameters better than WL (like $\Omega_{\rm b}$ and h), while the others show strong

degeneracies between them. This points already to the fact that both probes are quite orthogonal, and that their combination can significantly improve the constraints on all parameters (see next section). Concerning the dark energy equation of state, GCp is less able to constrain it than WL, giving a FoM of 5.6 (compared to 23.1 for WL). In this section we have also validated the `CosmoSIS` baseline results with the other GCp code used in the IST: `CosmicFish`. Also, we have shown that adding priors on some of the most degenerate parameters significantly reduces the disagreement between both codes.

After presenting the baseline results, we have studied the impact of different cosmological assumptions. First of all, we have shown that our knowledge on galaxy bias is critical to extract the maximum of information from GCp. For instance, if we perfectly knew the galaxy bias we would obtain a FoM of 280.0 (instead of 5.6). Of course, this is not realistic. However, using a more realistic galaxy bias model (the GTD model), less conservative than the binned baseline model, we improve the FoM from 5.6 to 19.7. In a second step we have addressed the impact of massive neutrinos, showing that the results obtained with 1 massive and 2 massless neutrinos, or 3 massless neutrinos are comparable, as it was the case for WL in the previous section. We have then focused on the non-linear recipe. As it was also the case for WL, we have noticed that the results are very sensitive to the non-linear recipe used, and that using smaller scales in the analyses can really improve our constraints. As a last check on the cosmological side, we have studied the constraints for a non-flat universe. The constraints and the FoM are degraded with respect to the flat case, but the decrease of constraining power is significantly smaller than it was for WL.

After studying different cosmological variations to the baseline used, we have focused on numerical aspects. In a first place, we have seen that while there was no difference between a 3-point and a 5-point stencil method for numerical derivatives in WL, there are some small differences in GCp. Also, even if the FoM obtained with `HaloModel` is quite stable with respect to the step-size used for the derivatives, there is nearly no stable region of the FoM when we use `halofit` as non-linear correction. Finally, we have seen that changing the Boltzmann solver does create some differences in the results, while they were largely independent of the Boltzmann solver for WL. These differences could be explained by the fact that the oscillations in the matter power spectrum disappear in the cosmic shear angular power spectra (they are smoothed out), but they are still visible in the galaxy angular power spectra. Therefore, the required numerical accuracy in determining these wiggles and the derivatives of the spectra in this region may be higher, leading to more sensitivity of GCp with respect to numerical decisions.

In conclusion, the baseline results presented in Fig. 6.8 are quite general in

terms of cosmology (although the galaxy bias is very important), and quite stable with respect to numerical assumptions (although a bit less stable than the WL results). We should still keep in mind that the non-linear recipe plays an important role, even if we discard the smallest scales.

6.5 Probe combination: photometric galaxy clustering and weak lensing

After having presented the baseline results for WL and GCp alone, and studied how different cosmological or numerical assumptions may impact the final constraints, we focus in this section on combining both probes. As explained in the beginning of the chapter, we usually combine different cosmological probes assuming they are statistically independent, which, in Fisher matrix terms, corresponds to summing the different Fisher matrices. While this might be true in some cases, it is not true in general, since different probes may sample the same distribution of galaxies. In our case, although WL and GCp are complementary, they probe the same large-scale structure; therefore, we expect the correlation between these probes to be non-negligible. In the following, we combine GCp and WL with and without their cross-correlations to assess the importance of the later. Also, as in the previous sections, we study the impact of different cosmological and numerical assumptions in the final results. In this section we focus only on the photometric Euclid survey. The combination of all Euclid primary probes, including GCs, is left for the next section.

6.5.1 Baseline results

Let us start with the baseline results. In Fig. 6.12 we show the constraints for the different cosmological parameters of the w_0w_aCDM model with and without cross-correlations. It is clear from Table 6.3 that the combination of WL and GCp (even neglecting their cross-correlations) is able to break some degeneracies between the parameters and provide very good constraints on all parameters at the same time. We can quantify this claim with the FoM, which increases from 23.1 (for WL) and 5.6 (for GCp) to 61.5 (neglecting cross-correlations). However, what is even more important is that adding the cross-correlations into the analysis boosts the constraining power by nearly 390 %, leading to a final baseline FoM of 299.2.

It is also important to notice that cross-correlations are not only able to noticeably improve the constraints on the cosmological parameters, but also on the nuisance ones. In Fig. A.26 and Fig. A.27 we show the improvement on the IA and galaxy bias nuisance parameters, respectively, when we include the

TABLE 6.3: Absolute 1σ (marginalized) forecasted constraints of the cosmological parameters for the combination of GCp and WL Euclid probes with and without cross-correlations, and with different specifications. The FoM for each case is shown for completeness.

Case	Ω_m	Ω_b	w_0	w_a	h	n_s	σ_8	FoM
ΛCDM baseline (Fig. A.24)	0.00309	0.00262	–	–	0.0206	0.00984	0.00370	–
ΛCDM baseline + XC (Fig. A.24)	0.00271	0.00257	–	–	0.0182	0.00819	0.00322	–
wCDM baseline (Fig. A.25)	0.00561	0.00297	0.0338	–	0.0208	0.0109	0.00501	–
wCDM baseline + XC (Fig. A.25)	0.00311	0.00277	0.0185	–	0.0195	0.00973	0.00326	–
w_0w_aCDM baseline (Fig. 6.12)	0.0119	0.00346	0.148	0.482	0.0229	0.0109	0.0111	61.5
w_0w_aCDM baseline + XC (Fig. 6.12)	0.00427	0.00277	0.0471	0.180	0.0210	0.0103	0.00452	299.2
w_0w_aCDM no IA (Fig. A.28)	0.0109	0.00336	0.135	0.438	0.0226	0.0109	0.0103	75.8
w_0w_aCDM no IA + XC (Fig. A.28)	0.00360	0.00274	0.0421	0.172	0.0210	0.0103	0.00409	348.8
w_0w_aCDM fixed bias (Fig. A.31)	0.00552	0.00261	0.0572	0.155	0.0196	0.00835	0.00495	637.7
w_0w_aCDM fixed bias + XC (Fig. A.31)	0.00287	0.00256	0.0306	0.0922	0.0172	0.00709	0.00260	1673.3
w_0w_aCDM GTD bias (Fig. A.34)	0.00831	0.00287	0.106	0.375	0.0218	0.0102	0.00802	94.3
w_0w_aCDM GTD bias + XC (Fig. A.34)	0.00389	0.00262	0.0414	0.162	0.0198	0.00957	0.00425	386.3
w_0w_aCDM $\sum m_\nu = 0$ (Fig. A.38)	0.0116	0.00353	0.147	0.485	0.0216	0.0108	0.0110	61.5
w_0w_aCDM $\sum m_\nu = 0$ + XC (Fig. A.38)	0.00427	0.00276	0.0488	0.188	0.0203	0.00991	0.00458	288.1
w_0w_aCDM `HaloModel` (Fig. A.41)	0.0145	0.00360	0.157	0.449	0.0334	0.0164	0.0130	66.0
w_0w_aCDM `HaloModel` + XC (Fig. A.41)	0.00493	0.00296	0.0498	0.166	0.0286	0.0161	0.00501	358.0
w_0w_aCDM $\ell_\mathrm{max} = 2000, 5000$ (Fig. A.44)	0.00737	0.00281	0.0941	0.302	0.0149	0.00557	0.00651	138.4
w_0w_aCDM $\ell_\mathrm{max} = 2000, 5000$ + XC (Fig. A.44)	0.00280	0.00240	0.0348	0.126	0.0143	0.00471	0.00263	636.2
w_0w_aCDM $\Omega_\mathrm{K} \neq 0$ (Fig. A.47)	0.0126	0.00391	0.238	0.758	0.0251	0.0136	0.0120	38.1
w_0w_aCDM $\Omega_\mathrm{K} \neq 0$ + XC (Fig. A.47)	0.00440	0.00287	0.0947	0.309	0.0218	0.0110	0.00466	143.5
w_0w_aCDM 5-point (Fig. A.48)	0.0118	0.00343	0.145	0.473	0.0232	0.0109	0.0110	62.3
w_0w_aCDM 5-point + XC (Fig. A.48)	0.00429	0.00279	0.0471	0.180	0.0211	0.0102	0.00453	297.5
w_0w_aCDM `halofit` 2 % (Fig. A.51)	0.0103	0.00332	0.135	0.451	0.0222	0.0110	0.00968	67.0
w_0w_aCDM `halofit` 2 % + XC (Fig. A.51)	0.00406	0.00277	0.0462	0.179	0.0209	0.0103	0.00435	303.6
ΛCDM `CLASS` (Fig. A.54)	0.00316	0.00233	–	–	0.0174	0.00863	0.00382	–
ΛCDM `CLASS` + XC (Fig. A.54)	0.00276	0.00232	–	–	0.0157	0.00725	0.00328	–

cross-correlations into the analysis. While the constraints on the IA nuisance parameters are largely reduced, we do not gain that much on galaxy bias. This might be explained by the fact that we use a general approach to model the galaxy bias, using many nuisance parameters. Concerning the correlations between cosmological and nuisance parameters, although they are not shown in the plot for readability, we have checked that only n_s is correlated with the bias parameters and h is anti-correlated with them, while all the other parameters are not significantly correlated (adding XC or not). It is also important to mention that adding XC reduces the area of the two-dimensional 1σ contours between cosmological and nuisance parameters in most of the cases, showing again the importance of including XC in the analysis.

As a last point, it is interesting to notice from Fig. 6.12 that cross-correlations

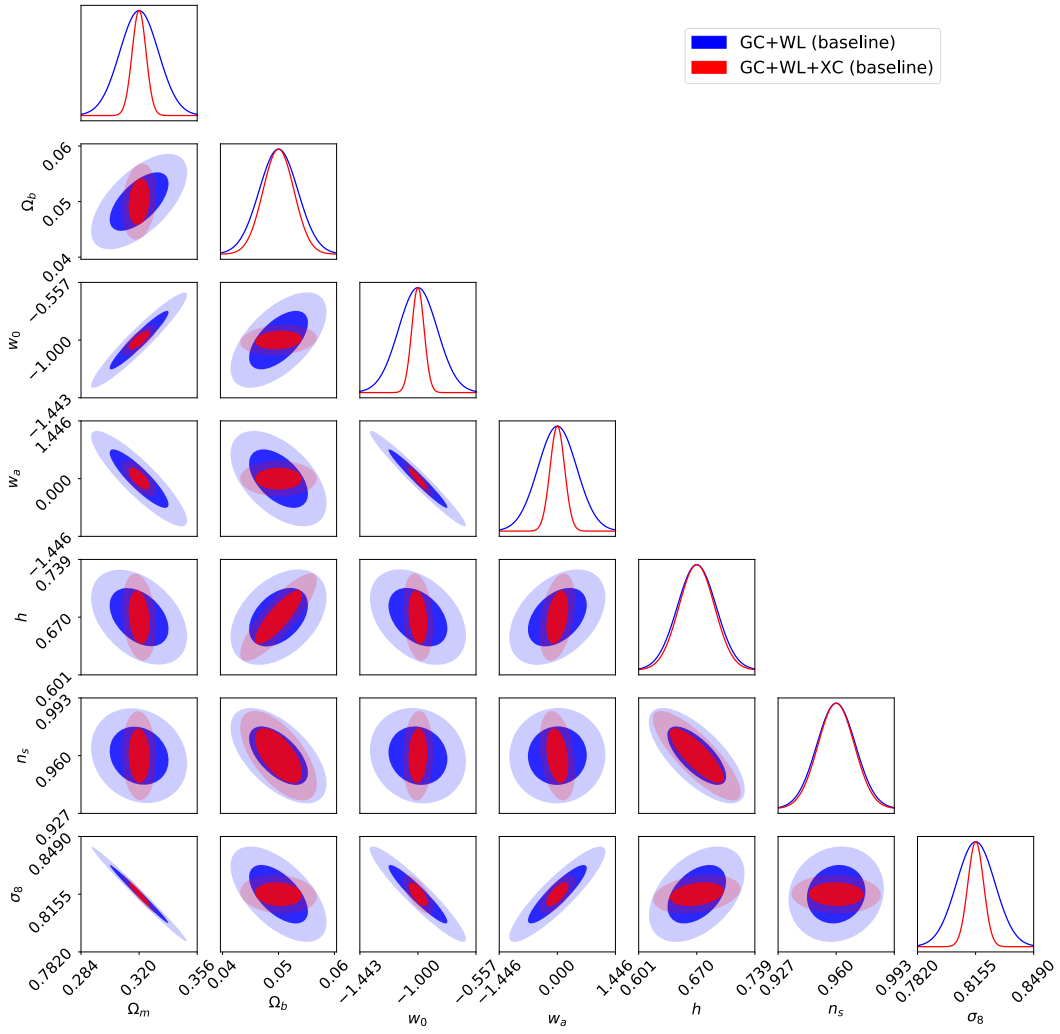

FIGURE 6.12: Comparison of probe combination with (red) and without (blue) cross-correlations on the 1σ and 2σ marginalized Fisher contours for the parameters of the baseline $w_0 w_a$CDM model (see the text for details).

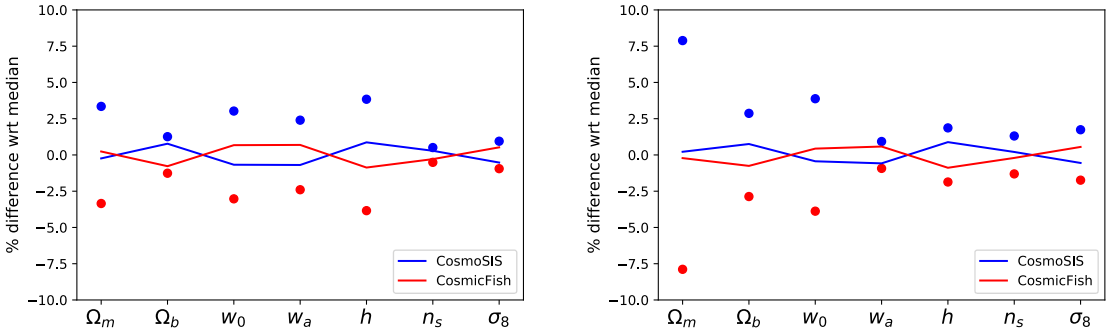

FIGURE 6.13: Percentage difference with respect to the median of all codes for the different cosmological parameters of the baseline model w_0w_aCDM, and the different codes for probe combination used in the IST: `CosmoSIS` (blue, this work) and `CosmicFish` (red). We show the combination without (left panel) cross-correlations and with (right panel) cross-correlations. The dots stand for the differences using the marginalized errors, while the solid lines show the differences considering the un-marginalized errors.

are not very helpful in constraining $\Omega_{\rm b}$, h, and n_s, since the constraint on these parameters is essentially the same with or without XC. The reason being that WL (and XC) is not very sensitive to these parameters; therefore, the constraints basically come from GCp alone. In the next section we will see that when we add GCs into the analysis the largest modifications concern these parameters.

In the previous sections we saw that parametrizing the dark energy fluid with one or two parameters instead of a cosmological constant degrades the constraints on the different parameters. Since we are now combining the results of the previous sections we see the same behavior. If we take into account the cross-correlations, comparing w_0w_aCDM to wCDM we degrade the constraints by a factor between 1.0 (for $\Omega_{\rm b}$) and 2.5 (for w_0). When we compare w_0w_aCDM to ΛCDM results we observe a decrease between a factor 1.1 (for $\Omega_{\rm b}$) and 1.6 (for $\Omega_{\rm m}$). If we now consider the combination GCp+WL and compare w_0w_aCDM to wCDM we degrade the constraints between a factor 1.0 (for n_s) and 4.4 (for w_0). If we compare w_0w_aCDM to ΛCDM the factors become 1.1 (for n_s) and 3.9 (for $\Omega_{\rm m}$). Notice that the degradation of constraints is stronger for the GCp+WL case, since when we add XC into the analysis all parameters are better constrained. The impact of cross-correlations on the contours for the ΛCDM and wCDM models is shown in Table 6.3, and in Fig. A.24 and Fig. A.25, respectively.

Before showing the results of varying different assumptions, we focus on the

validation of `CosmoSIS` for probe combination. As it was the case for GCp, the other code used in the IST for probe combination is `CosmicFish`. In Fig. 6.13 we show the percentage difference with respect to the median of the two codes for each cosmological parameter. In the left panel we show the combination GCp+WL, while we add the XC in the right panel. In both cases the difference with respect to the median is below 10 %, as required to validate the codes in the IST.

6.5.2 Impact of intrinsic alignments

Let us now consider the IA impact on our results. In Fig. A.29 and Fig. A.30 we show the comparison between the baseline probe combination and the probe combination when we neglect IA for GCp+WL+XC and GCp+WL, respectively. We can observe that neglecting IA reduces the contours, as expected, but the difference is not large. Quantitatively, the largest difference appears in $\Omega_{\rm m}$ by a factor 1.2 for GCp+WL+XC, and in w_a by a factor 1.1 for GCp+WL (see Table 6.3). However, even if the constraints and the contours are roughly the same, we can appreciate an improvement on the FoM by 17 % (with XC) and 23 % (without XC). We show for completeness the impact of cross-correlations on probe combination when we neglect the IA in Fig. A.28. We can see that the impact of XC is qualitatively the same than it is in our baseline.

6.5.3 Impact of galaxy bias

Concerning the galaxy bias, in the previous section we have considered the over-optimistic case of fixing the bias; i.e. assume it is fully known, and use the GTD model which is still realistic but less conservative than the baseline binned galaxy bias model. Let us start with the fixed bias case. In Fig. A.31 we show the impact of cross-correlations when we perfectly know the galaxy bias. We can see that the constraints are better when we include XC, but the improvement is not as large as it was in the baseline case. More specifically, the FoM improves by 162 % while it improved by 387 % in the baseline model. The reason being that part of the XC contribution consists in better determining the galaxy bias, which propagates to better constraints on all parameters. If the bias is perfectly known, the addition of XC is not so important. However, as was said in the previous section, this is a sadly unrealistic case which gives too over-optimistic constraints, as we can see in Table 6.3, and in Fig. A.32 and Fig. A.33, where we show the impact of fixing the bias when we combine the different probes.

Let us now focus on the GTD model for galaxy bias. We show the impact of cross-correlations for this case in Fig. A.34. We can see that the effect of cross-correlations is qualitatively the same as in the baseline model for galaxy bias. However, concerning the galaxy bias nuisance parameters shown in Fig. A.35, we can see that the addition of cross-correlations help in reducing the contours. Although the improvement is less impressive than for the IA nuisance parameters of Fig. A.26, it is still larger than the improvement for the general binned galaxy bias model. In Fig. A.36 and Fig. A.37 we show the impact of GTD on probe combination with and without XC, respectively. Although the differences are smaller when we include the XC into the analysis (the parameters are better constrained), using the GTD model for galaxy bias improves the FoM by 29 %, showing again the importance of understanding the galaxy bias.

6.5.4 Impact of massive neutrinos

Concerning the neutrinos, in Fig. A.39 and Fig. A.40 we show the impact of massless neutrinos compared to the baseline neutrinos for probe combination with and without XC, respectively. The results are roughly the same, as expected, since we are combining GCp and WL, and the impact of neutrinos was not very significant in these cases. Also, in Fig. A.38 we can see the impact of XC for probe combination when we only consider massless neutrinos. The plot is indistinguishable from the baseline one. More quantitatively, the FoM decreases when we consider massless neutrinos (compared to the baseline) by less than 4 % if we include XC, and remains the same when we do not include XC.

6.5.5 Non-linear correction and cut at non-linear scales

With respect to the non-linear recipe used to correct our predictions, we have already seen in the previous sections that the results are sensitive to the recipe used. In Fig. A.42 and Fig. A.43 we show the comparison of probe combination using `HaloModel` or `halofit` with and without XC, respectively. We can observe that the contours are more similar now than they were for WL or GCp alone. This may be due to the fact that there are less degeneracies between the parameters now, and they are better constrained. However, there are still significant differences for h and n_s. More quantitatively, when we compare `HaloModel` with `halofit` the FoM increases by 20 % if we include XC, and increases by 7 % when we do not include them. Concerning the impact of cross-correlations using only `HaloModel`, we can see in Fig. A.41 that they are still very important, boosting the FoM by 442 %. Notice that XC are slightly more important here than when we use `halofit` as non-linear correction.

Let us now focus on the small-scales used in the analysis. In Fig. A.45 and Fig. A.46 we show the impact of using more small-scales ($\ell_{\rm max} = 2000$ for GCp, XC, and $\ell_{\rm max} = 5000$ for WL) when we combine GCp and WL with and without XC, respectively. As it was the case for the single probes, the fact of using smaller scales adds extra information and allows us to reduce the constraints. The FoM increases by 113 % when we include XC, and by 125 % when we do not. However, it is important to notice that the impact of XC is still very important even if we go down to these small scales, as we can see in Fig. A.44. Quantitatively, the FoM increases by 360 % when we add XC with a higher ℓ cut.

6.5.6 Non-flat universe

As a last cosmological modification to our baseline, let us focus on the curvature of the Universe. In Fig. A.47 we show the impact of XC for probe combination in a non-flat universe. As always, the addition of XC helps in significantly reducing the contours and the constraints on the parameters. Quantitatively, the FoM increases by 277 % when we add the XC. We should note, though, that this extra information is not enough to compensate for the loss due to allowing for some curvature, and we finally get a lower FoM (compared to the flat case) by 52 %, which is in between the decrease from WL (64 %) and GCp (23 %) alone.

6.5.7 Method and step of the numerical derivatives

We now consider the implications of different numerical assumptions done in our baseline. In a first place, we consider the use of the 5-point stencil method for the numerical derivatives. The comparison between the 3-point and 5-point stencil methods for probe combination is shown in Fig. A.49 and Fig. A.50 with and without XC, respectively. We also show the impact of XC when we consider the 5-point stencil method in Fig. A.48. In all cases we clearly see that there are no significant differences between the 3-point and the 5-point stencil methods. Let us recall that this is also the result we obtained for WL alone, but we were able to detect some differences for GCp. Since we are here combining both probes, it is reasonable to be somewhere in between WL and GCp, which leads to quite small differences between the 3-point and 5-point methods. Just for completeness, the FoM between both methods differs by less than 0.6 % (with XC) and less than 1.3 % (without XC).

Concerning the stability of our results with respect to the step-size used for the numerical derivatives, we present the value of the FoM as a function

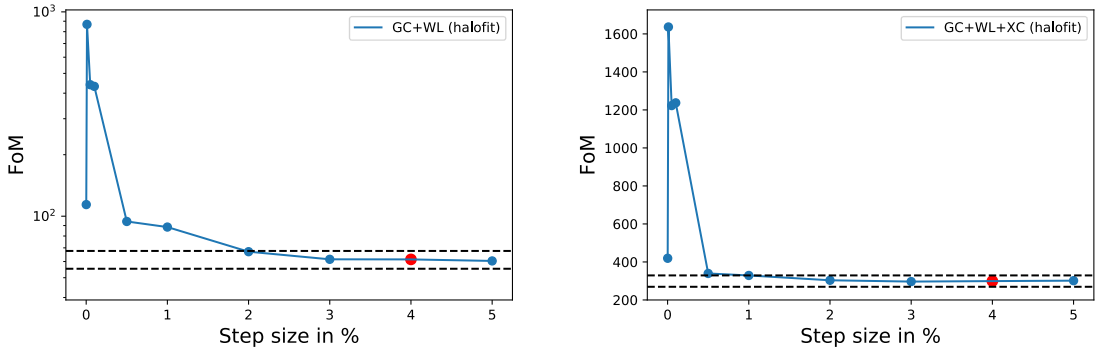

FIGURE 6.14: Figure of Merit as a function of the step-size used for the numerical derivatives. *Left panel:* baseline GCp+WL. *Right panel:* baseline GCp+WL+XC. The red dot stands for the baseline step used in all the results, while the black dashed lines show the band within +10 % and −10 % of the baseline FoM.

of the step-size used in Fig. 6.14 [7]. In the left panel we show the combination of GCp and WL without the cross-correlations, while we include them in the right panel. We can see that the results are more stable than GCp alone (see Fig. 6.11) but less stable than WL alone (see Fig. 6.7). Also, the combination of probes is more stable when we add XC into the analysis. For completeness, we show the comparison between the 2 % and the baseline 4 % steps not only for the FoM but also for the different contours in Fig. A.52 and Fig. A.53 with and without XC, respectively. We can clearly see that all contours look the same for the GCp+WL+XC case and, even if we can slightly distinguish the ellipses for the GCp+WL case, the results are nicely compatible. We also show the impact of XC when we use a 2 % step in Fig. A.51, which is hardly distinguishable from the baseline result in Fig. 6.12.

6.5.8 Boltzmann solver

As a last case to study, we consider again a different Boltzmann solver in our analysis. We show the impact of using `CLASS` instead of `CAMB` for probe combination in Fig. A.55 and Fig. A.56 with and without XC, respectively. As it was the case in Figs. A.49, A.50, we are in between WL and GCp alone; i.e the agreement between `CLASS` and `CAMB` was very good for WL alone, while it was worse for GCp. Since we are combining both probes we find a better agreement than for GCp alone but still worse than the one obtained for WL. In any case, even if we can distinguish the `CLASS` and `CAMB` contours, the largest difference comes from h with a factor of 1.2, both with and without XC. We also show

[7] We limit here ourselves to the baseline `halofit` non-linear recipe, for simplicity.

the impact of XC when we combine GCp and WL with `CLASS` in Fig. A.54. It is qualitatively equivalent to the `CAMB` results from Fig. A.24.

6.5.9 Summary

In this third section of results we have combined the GCp and WL probes. In a first place we have produced the baseline results of the combination with and without the cross-correlations between these probes. We have seen that they are quite complementary and the fact of combining them, even without XC, breaks some degeneracies between the parameters leading to very good constraints. The improvement is particularly important concerning the dark energy equation of state, where the FoM improves from 23.1 (for WL) and 5.6 (for GCp) to 61.5, when we neglect the cross-correlations, and to 299.2 when we take them into account. Therefore, it is also clear from these baseline results that the impact of cross-correlations is very important and it should be taken into account, since it largely helps to improve our constraints on the cosmological parameters. Also, we have seen that the addition of XC is important not only for the cosmological parameters, but also for the constraints on the nuisance parameters, particularly for those of IA.

After presenting the baseline results and, following the approach from the single probes sections, we have perturbed several assumptions of our baseline approach to address the impact of each one of them on the final results. In general, the results are quite consistent with what we have found for the single probes and, in most cases, the impact of each assumption is somewhere in between the impact for each one of the probes.

For IA, for instance, we have seen that the FoM increases by 17 %-23 % when we neglect them, but the constraints remain roughly the same, as it was the case for WL alone. Also, as it was the case for GCp alone, we have seen that our knowledge of the galaxy bias is very important to extract the maximum of information from our analysis, leading to sadly unrealistic high values for the FoM if we assume a perfect knowledge of the galaxy bias. We have also looked at massless neutrinos, but the results are perfectly compatible with the baseline, as it was the case before. Let us just recall here that we fix the neutrino mass. Allowing it to vary would probably have a larger impact in our analysis. This extension is left for future work.

We have then considered the impact of the non-linear correction used in the analysis. We have shown that the differences between `halofit` and `HaloModel` are now smaller than in the single probe cases. This could be due to the fact that there are less degeneracies and the parameters are better constrained now, giving distributions closer to a Gaussian and a more robust Fisher matrix result. Following on the non-linearities, we have considered the cut to neglect

the smallest scales, showing that allowing smaller scales into the analysis can significantly improve the constraints on the parameters. Even if we go down to smaller scales, the XC are still very important. As a last cosmological variation, we have considered a non-flat universe and we have seen that even combining both probes it is not enough to compensate for the extra curvature parameter, giving a significantly smaller FoM. However, the improvement coming from XC is still very important.

With respect to the numerical baseline assumptions, we have seen that there are no significant differences between the 3-point and 5-point stencil methods for the numerical derivatives, but the step-size used is still very important. We have shown that our results are stable using a step between 2 % and 5 %, while the FoM diverges for smaller steps. This range is essentially limited by the stability of GCp, which is less stable than WL. We have finally considered `CLASS` as Boltzmann solver and we have seen that the differences are larger than for WL alone, but smaller than for GCp. At the end, the results are not very dependent on the Boltzmann code used. We recall here that we are using the default precision parameters in `CLASS`. A more detailed comparison could be done by fine-tuning the precision parameters of both codes to reach a better agreement, but this is left for future work.

In conclusion, we have shown that combining different probes is crucial to improve the constraints on the cosmological parameters, but also, adding XC is extremely important to boost our knowledge and extract the maximum of information from the future data.

6.6 Probe combination: Euclid primary probes

In this last section, acting as main result of this chapter, we present the final forecasts for the combination of all Euclid primary probes: GCs, GCp, and WL, together with their cross-correlations.

There are essentially 3 cross-correlations that we need to take into account. The first one is between GCp and WL, which has already been considered in the previous section and denoted by XC. The second and third ones correspond to the cross-correlation between GCs and WL, and between GCs and GCp. As briefly mentioned at the beginning of the chapter, it is not straightforward to combine three-dimensional (GCs) and two-dimensional data (GCp, WL) together with their cross-correlations. Several papers in the literature address this issue [Asorey et al., 2012; Passaglia, Manzotti, and Dodelson, 2017], but it is still not trivial to perform this combination. Concerning the cross-correlation between GCs and WL, we may assume it is small and therefore neglect it, since the spectroscopic sample starts at $z = 0.9$ and the WL kernel peaks at lower

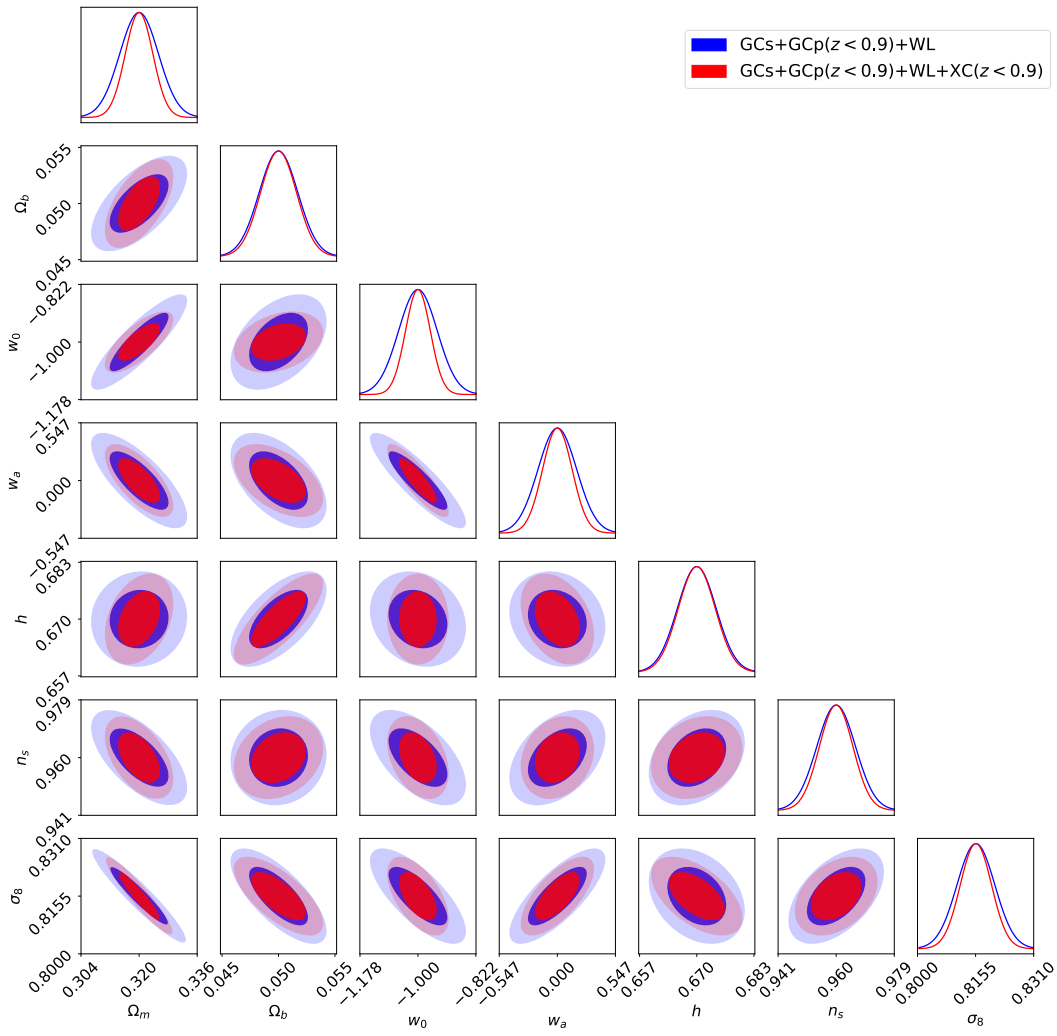

FIGURE 6.15: Comparison of probe combination for all Euclid primary probes with (red) and without (blue) cross-correlations on the 1σ and 2σ marginalized Fisher contours for the parameters of the baseline $w_0 w_a$CDM model, when we cut the z- range for GCp and XC at $z = 0.9$ (see the text for details).

TABLE 6.4: Absolute 1σ (marginalized) forecasted constraints of the cosmological parameters for the combination of all Euclid primary probes: GCs, GCp and WL with and without cross-correlations, and with different ways to combine them. The FoM for each case is shown for completeness.

Case	$\Omega_{\rm m}$	$\Omega_{\rm b}$	w_0	w_a	h	n_s	σ_8	FoM
GCs+GCp($z<0.9$)+WL (Fig. 6.15)	0.00521	0.00171	0.0595	0.182	0.00440	0.00630	0.00506	192.4
GCs+GCp($z<0.9$)+WL+XC($z<0.9$) (Fig. 6.15)	0.00371	0.00160	0.0381	0.139	0.00419	0.00546	0.00418	373.6
GCs+GCp+WL (Fig. 6.16)	0.00509	0.00151	0.0573	0.179	0.00319	0.00575	0.00482	244.8
GCs+GCp+WL+XC (Fig. 6.16)	0.00348	0.00128	0.0363	0.124	0.00315	0.00501	0.00364	521.6
GCs+GCp+WL high $\ell_{\rm max}$ (Fig. 6.17)	0.00434	0.00130	0.0515	0.162	0.00265	0.00339	0.00387	352.7
GCs+GCp+WL+XC high $\ell_{\rm max}$ (Fig. 6.17)	0.00249	0.000987	0.0293	0.102	0.00264	0.00266	0.00233	840.4

redshift. However, GCp and GCs are effectively sampling the same distribution of galaxies, even if we have more photometric galaxies than spectroscopic ones in the spectroscopic redshift range. Therefore, we have decided to take a pessimistic and an optimistic approach, such that the real FoM will be somewhere in between the two values provided. In the pessimistic case we discard all photometric galaxies above $z = 0.9$ when computing GCp and XC. In this way, if the photo-zs are well behaved (good precision, without bias, and few outliers) we will not overlap in redshift space with GCs, thus removing any possible cross-correlation. However, this approach discards a lot of information from GCp and XC, so we also present a second optimistic approach by just combining GCs and GCp neglecting any cross-correlation.

In this section we use the GCs Fisher matrix obtained with `SpecSAF` for the baseline cosmology with the non-linear correction for GCs and a cut on small-scales at $k = 0.25\,h/\mathrm{Mpc}$ [Euclid Collaboration, in prep.].

We provide the final results for the pessimistic case in Fig. 6.15, where we also show the impact of XC on the contours. Notice that the effect of XC is slightly less impressive than in the previous section, because the combination with GCs already provides smaller constraints. If we compare these results (Table 6.4) with the baseline GCp+WL+XC results from the previous section, we can see that all constraints improve, especially those on $\Omega_{\rm b}$, h, and n_s by a factor 1.7, 5.0, and 1.9, respectively, as expected, since these parameters are the worst constrained from the photometric probes alone. Notice that the FoM increases by 25 %, reaching up to 373.6.

If we now consider the optimistic case shown in Fig. 6.16, and compare the results to the baseline GCp+WL+XC from the previous section, we can see that all constraints improve by a factor ranging between 1.2 (for $\Omega_{\rm m}$) to 6.7 (for h). As before, the largest improvement concerns $\Omega_{\rm b}$, h, and n_s. With respect to

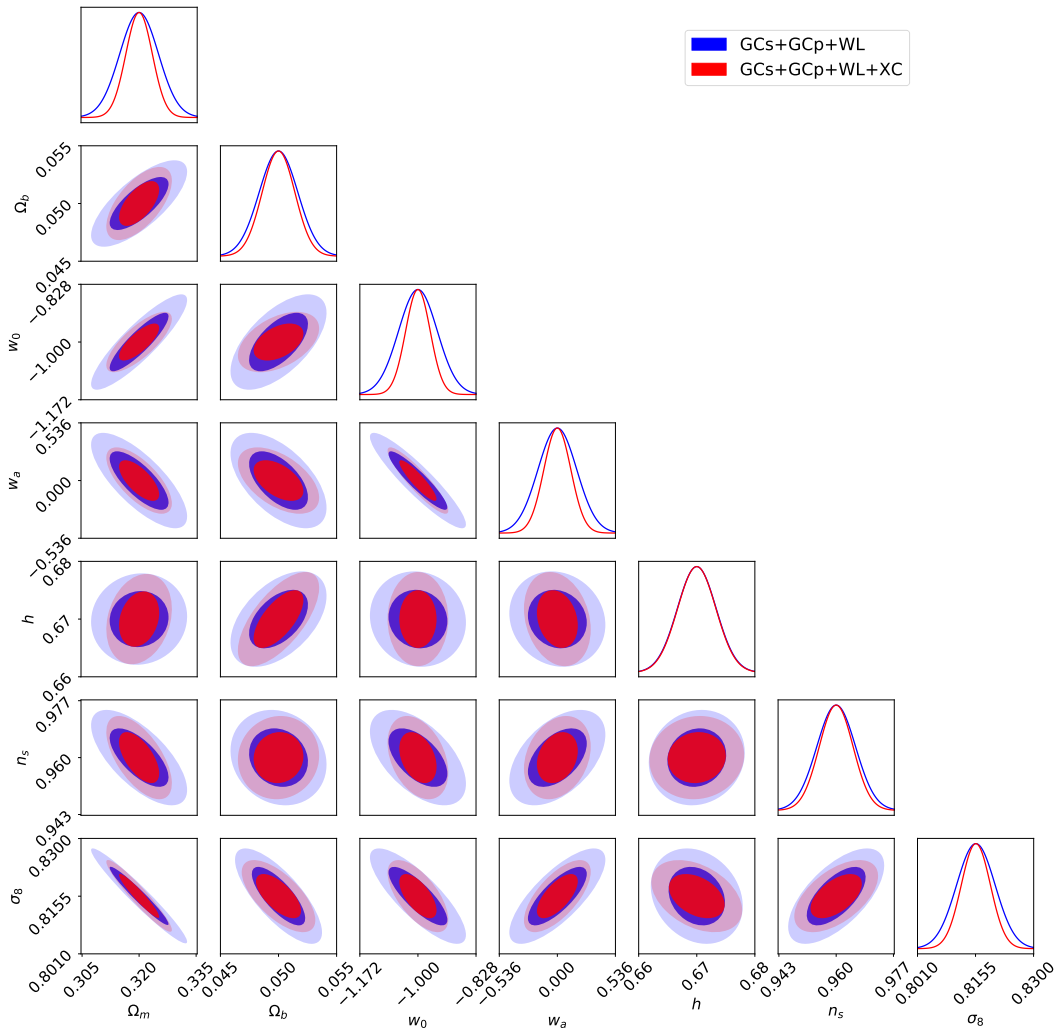

FIGURE 6.16: Comparison of probe combination for all Euclid primary probes with (red) and without (blue) cross-correlations on the 1σ and 2σ marginalized Fisher contours for the parameters of the baseline w_0w_aCDM model, when we use the full redshift range for GCp and XC (see the text for details).

the FoM, it improves by 74 % leading to a value of 521.6.

In conclusion, using a pessimistic approach we obtain a FoM of 374, while using an optimistic approach its value goes up to 522. The realistic FoM should be in between these values, but further work is required in order to correctly model the cross-correlations between three-dimensional and two-dimensional data.

It is important to mention that the initial forecasts for Euclid provided in Laureijs et al., 2011, used an $\ell_{\rm max}$ cut at 5000 for GCp, WL, and XC. In Fig. 6.17 we provide the results for an even less conservative approach, where we neglect the cross-correlations between GCs and GCp, and limit $\ell_{\rm max} = 2000$ for GCp and XC, and $\ell_{\rm max} = 5000$ for WL. As it can be seen in Table 6.4, the FoM in this case goes up to 840.4. Notice that we cannot directly compare to the values in Laureijs et al., 2011, since the approach used here is significantly different, but the FoM values obtained in this work point to the fact that Euclid will give exquisite constraints on the cosmological parameters and it will be largely able to meet the scientific requirements that we expect from it; in particular, thanks to the cross-correlations.

As a last comment, in the following years we will also have other surveys probing the large-scale structure of the Universe, which will be able to constrain the concordance cosmological model with high precision, like the ground-based spectroscopic survey DESI [8] or the ground-based photometric survey LSST [9]. Although the goal of this work is to determine the constraining power of the Euclid survey, we have computed, just for completeness, the forecast for LSST using our baseline with 5.5 galaxies/arcmin^2 (instead of 3 for Euclid), and 18000 sq. deg (instead of 15000). Notice that we have assumed several specifications (like the $n(z)$, the photometric redshifts precision, or the accuracy of the shape measurements [10]) to be exactly the same as Euclid. Therefore, this is not intended to be an accurate LSST forecast but just a first computation to provide an order of magnitude. According to our forecast for both surveys, LSST will provide better constraints for all parameters by a factor ranging between 1.2 (for $\Omega_{\rm b}$) and 1.5 (for w_0), if we consider only the photometric Euclid survey (GCp, WL, and XC). This result was expected, since LSST will detect more galaxies in a larger area of the sky; therefore, using the same cosmological probes (and the same galaxy distribution) we expect LSST to perform better

[8] https://www.desi.lbl.gov

[9] https://www.lsst.org

[10] Notice that Euclid alone will probably provide more accurate measurements of the shape of galaxies than LSST alone, since Euclid will have a very broad filter in the optical band (the VIS instrument) without the contamination from the atmosphere. However, we assume here the same value of σ_ϵ^2 for simplicity.

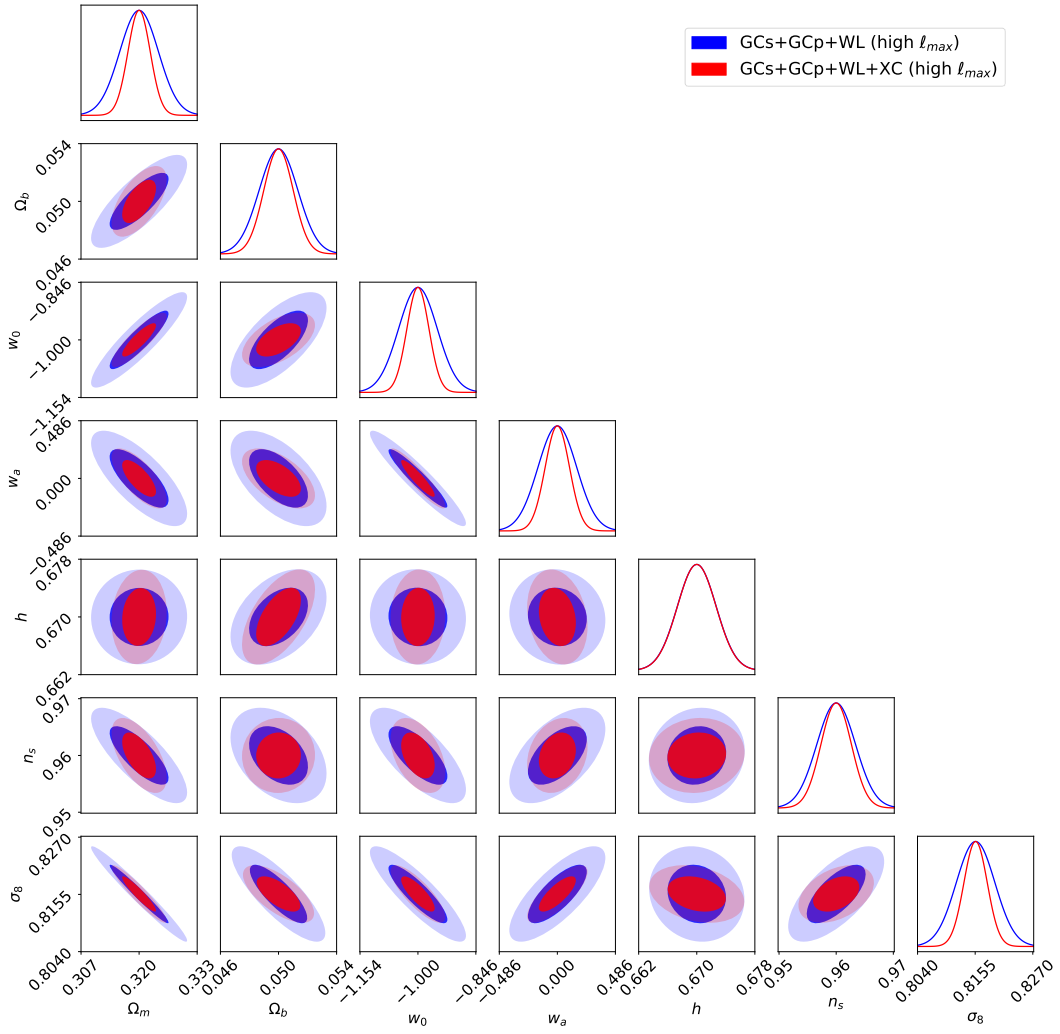

FIGURE 6.17: Comparison of probe combination for all Euclid primary probes with (red) and without (blue) cross-correlations on the 1σ and 2σ marginalized Fisher contours for the parameters of the baseline w_0w_aCDM model. We use the full redshift range for GCp and XC, and we perform less conservative cuts with $\ell_{\rm max} = 2000$ for GCp and XC, and $\ell_{\rm max} = 5000$ for WL (see the text for details).

than Euclid. However, if we compare LSST to the full Euclid survey, including the spectroscopic galaxy clustering, Euclid will better constrain $\Omega_{\rm b}$, w_a, h, and n_s by a factor ranging from 1.1 (for w_a) up to 5.6 (for h), while LSST will better constrain the remaining parameters ($\Omega_{\rm m}$, w_0, and σ_8) by a factor roughly equal to 1.2. As before, this result was expected because LSST lacks the spectroscopic galaxy clustering probe which is much more sensitive to $\Omega_{\rm b}$, h, and n_s than the photometric galaxy clustering or weak lensing probes. It is important to add here that the constraints coming from both surveys are quite complementary. Therefore, it will be very important to combine the future data from both surveys in order to extract the best possible constraints on all parameters. Concerning the spectroscopic survey DESI, the redshift range of Euclid GCs has been chosen to be more sensitive than DESI in this region. Therefore, the three future surveys, Euclid, LSST, and DESI, will be quite complementary and their combination with all cross-correlations will be crucial to extract the largest amount of information from the observations.

Chapter 7

Generalized dark matter

The concordance model in cosmology, ΛCDM, is mainly characterized by its dark sector, composed of non-interacting cold dark matter (CDM) and a cosmological constant Λ. In particular, these components are usually considered as perfect fluids and modeled with no pressure (for cold dark matter) and an equation of state parameter $w = -1$ for the cosmological constant. Many physically motivated particles have been proposed as candidates for dark matter [Bertone, Hooper, and Silk, 2005], but in most cases we assume that they behave as a pressure-less fluid. Thus, we cannot distinguish them only through their gravitational interaction, and all can be modeled as a CDM fluid. This simple modeling is able to fit all the cosmological observations, but there has not been any detection of dark matter in direct or indirect searches yet [Aprile et al., 2012; Aprile et al., 2014; Buckley et al., 2013; CRESST Collaboration, 2015; Akerib et al., 2016]. See also Boveia and Doglioni, 2018, for a recent detailed review of the dark matter searches at the Large Hadron Collider, with a discussion on the importance of collider searches within the broader field of dark matter searches.

There are also some dark matter candidates for which the assumption of vanishing pressure does not hold. One example are massive neutrinos as warm dark matter [Dodelson and Widrow, 1994; Colombi, Dodelson, and Widrow, 1996; Shi and Fuller, 1999], which can be modeled as an imperfect fluid with some pressure and viscosity [Lesgourgues and Tram, 2011]. Even CDM is better described as an imperfect fluid due to unresolved small-scale nonlinearities (according to the effective field theory of large-scale structure [Baumann et al., 2012; Carrasco, Hertzberg, and Senatore, 2012; Carroll, Leichenauer, and Pollack, 2014; Foreman and Senatore, 2016; Blas et al., 2015; Blas et al., 2016]). Although CDM is able to nicely fit the main cosmological observations, some observations on halo properties [Moore, 1994; Jee et al., 2014; Boylan-Kolchin, Bullock, and Kaplinghat, 2011; Papastergis, E. et al., 2015; Klypin et al., 2015] deviate from the predictions of ΛCDM. This may point towards a more complicated dark matter fluid than just standard CDM.

There are two different approaches that can be followed when trying to

detect signatures beyond the concordance model, which are either fundamental or phenomenological. The former consists on a specific model where every observable can be derived (in principle) from fundamental principles, like axions [Hlozek et al., 2015], collision-less massive neutrinos [Lesgourgues and Tram, 2011; Shoji and Komatsu, 2010], or dark matter coupled to dark radiation [Cyr-Racine and Sigurdson, 2013; Diamanti et al., 2013]. This approach enables us to deeply understand the model under study, but each model needs to be studied separately. The phenomenological approach consists on parametrizing some modifications to the concordance model, which correspond to physical properties shared by several models. We end up with many more degrees of freedom, but we can study families of models at the same time. The most famous example of such a phenomenological test of General Relativity is the so-called Parametrized Post Newtonian (PPN) formalism, used in Solar System tests of General Relativity. The PPF formalism used in the previous chapter is based on it.

In this chapter we focus mainly on the dark matter component of the Universe and we follow a phenomenological approach. In particular, we use the generalized dark matter (GDM) model, first proposed by Hu, 1998, to constrain dark matter properties in the linear regime. We first present the theoretical framework of the GDM model in Sec. 7.1. We then show the constraints on this model using current observations in Sec. 7.2, as well as the expected precision of the Euclid survey on the GDM model parameters in Sec. 7.3. The results shown in these two sections will appear in Tutusaus et al., in prep.(a), and in Tutusaus et al., in prep.(b), respectively. Part of them have already been presented in Tutusaus, Lamine, and Blanchard, 2018a. In Sec. 7.4 we discuss the degeneracy between GDM and dark energy presented in Tutusaus et al., 2016a, and Tutusaus, Lamine, and Blanchard, 2016.

7.1 Theoretical framework

In this section we present a brief overview of the generalized dark matter model, and its implementation in our analysis. We refer to Kopp, Skordis, and Thomas, 2016, for a detailed description of it. We assume that dark matter is only coupled to the visible sector through gravitational interaction, so we assume that the dark matter energy-momentum tensor is conserved (see Yang, 2015, for constraints on dark matter properties when it is metastable or interacts with radiation). This implies that all kind of dark matter components can be covered by the standard conservation equations for a general matter source [Ma and Bertschinger, 1995]. At the background level, the dark matter energy density ρ evolves as [see Eq. (1.23)]

$$\dot{\rho} + 3H(1+w)\rho = 0\,, \tag{7.1}$$

where the over-dot stands for the derivative with respect to cosmic time. In this work we focus on the scalar modes, neglecting vector and tensor perturbations. Therefore, according to Ma and Bertschinger, 1995, a conserved energy-momentum tensor must satisfy (at a linear level of perturbations)

$$\dot{\delta} + (1+w)\left(\theta + \frac{\dot{h}}{2}\right) + 3H\left(\frac{\delta p}{\delta \rho} - w\right) = 0\,, \tag{7.2}$$

$$\dot{\theta} + H(1-3w)\theta + \frac{\dot{w}}{1+w}\theta - \frac{\delta p/\delta\rho}{1+w}k^2\delta + k^2\sigma = 0\,, \tag{7.3}$$

where w, δ, and θ stand for the fluid equation of state parameter, its density fluctuation and the divergence of its velocity, respectively. δp represents the pressure perturbation, and σ corresponds to the anisotropic stress (see Ma and Bertschinger, 1995, for the derivation of these equations from the perturbed part of the energy-momentum conservation equations). Notice that we have presented the equations in the synchronous gauge.

Provided Eqs. (7.2-7.3), the GDM model is specified by the dark matter equation of state parameter w [1], and relations between the pressure perturbations δp and scalar anisotropic stress σ to the dynamically evolving variables δ, θ; i.e. $\delta p(\delta, \theta)$ and $\sigma(\delta, \theta)$. Dark matter particles interact very rarely compared to the time scale of cosmological evolution. Therefore, thermodynamical equilibrium cannot be established and these relations must be obtained by solving the Boltzmann equation with the corresponding particle distribution (usually using a multipole moment decomposition). It has been shown [Kunz, Nesseris, and Sawicki, 2016] that each higher moment is suppressed with respect to the previous one by the ratio of the kinetic energy to the particle mass. Therefore, if dark matter is relativistic we need to solve the full set of coupled moment equations, while the moment expansion can be truncated when dark matter is non-relativistic.

Since non-relativistic dark matter can allow for the formation of galaxies, a common multipole expansion truncation is the so-called $c_{\rm vis}$ parametrization [Hu, 1998; Hu and Eisenstein, 1999], where the pressure perturbation is related to δ and θ by the following relation:

$$\delta p = c_s^2\delta\rho - \dot{\rho}(c_s^2 - c_a^2)\theta/k^2\,, \tag{7.4}$$

[1] Notice that w stands for the dark matter equation of state parameter here, not for the dark energy one, as it is usually seen in the literature.

where c_s is the so-called rest-frame sound speed, and the adiabatic sound speed is defined by $c_a^2 \equiv (w\rho)^{\cdot}/\dot{\rho}$. In this parametrization, the anisotropic stress σ evolves according to

$$\dot{\sigma} + 3H\frac{c_a^2}{w}\sigma = \frac{4}{3}\frac{c_{\rm vis}^2}{1+w}(2\theta + \dot{h} + 6\dot{\eta})\,, \tag{7.5}$$

where $c_{\rm vis}^2$ is a new viscosity parameter, and h and η are the synchronous metric perturbations. As discussed in Oldengott, Rampf, and Wong, 2015, this truncation is not realistic when considering relativistic species since we neglect the contribution from higher multipoles. However, in Thomas, Kopp, and Skordis, 2016; Kunz, Nesseris, and Sawicki, 2016, the authors used $c_{\rm vis}^2$ as a proxy for the size of the higher multipoles. In both cases the authors found that $c_{\rm vis}^2 \ll c_s^2$, pointing to the fact that a more precise investigation of higher moments is not necessary for dark matter. Extending this truncation, and due to the small value for $c_{\rm vis}^2$ found in Thomas, Kopp, and Skordis, 2016; Kunz, Nesseris, and Sawicki, 2016, we fix this value equal to 0 and we consider only the equation of state parameter w and the sound velocity c_s^2 as parameters for the GDM model.

In principle, the GDM parameters can depend on both time and space. In this chapter we follow the approach of Thomas, Kopp, and Skordis, 2016; Kunz, Nesseris, and Sawicki, 2016, and consider constant parameterizations, i.e. we take w and c_s^2 to be constant with respect to time and space. This approximation provides us with an idea of the maximum values that these parameters are allowed to take.

In addition to the evolution equations, the appropriate initial conditions must be chosen for the evolution of the modes. However, as shown in Kunz, Nesseris, and Sawicki, 2016, the observables are not sensitive to initial conditions for the parameter values allowed by the data; thus, the posterior distribution is also insensitive to the choice of initial conditions.

7.2 Current constraints

In this section we confront the GDM model to current observations from different cosmological probes. In the first subsection we present the methodology; in the second subsection we discuss the data used for our analysis, and in the third subsection we determine the constraints on the cosmological parameters using only background cosmological probes. We then discuss in Sec. 7.2.4 the tension on the value of H_0 between direct measurements and derived values from the ΛCDM and ΛGDM models. In Sec. 7.2.5 we focus on the non-linear scales and, finally, we present the results obtained when adding weak lensing data in Sec. 7.2.6.

7.2.1 Method

We first need a Boltzmann code to compute the power spectrum for the GDM model. In this chapter we follow the approach of Thomas, Kopp, and Skordis, 2016, by using the `CLASS` code [Lesgourgues, 2011a; Blas, Lesgourgues, and Tram, 2011; Lesgourgues, 2011b; Lesgourgues and Tram, 2011]. It solves the Boltzmann equation for each component coupled to Einstein equations and it computes the cosmic microwave background and matter power spectra for a given set of cosmological parameters. `CLASS` already includes a parametrization for the dark energy fluid with a constant equation of state parameter and a constant sound velocity [Lesgourgues and Tram, 2011]. We use this parametrization as GDM, we keep a cosmological constant for the dark energy contribution, and we remove the cold dark matter component [2]. In the default version of `CLASS` this fluid is supposed to behave as dark energy. However, since we want to use it as dark matter, we have modified the code to include the perturbations of this fluid when we ask for the total matter perturbations. We have validated our modified version of `CLASS` with the one used in Thomas, Kopp, and Skordis, 2016; Kopp et al., 2018, reaching an agreement of 0.1% in all $C(\ell)$ (lensed and non-lensed), of 0.01% in the matter power spectra at $z = 0$ and $z = 1$, and of 0.6% in the matter power spectrum at $z = 1000$.

We then investigate the constraints on the cosmological parameters using a Markov chain Monte Carlo approach, with the Metropolis-Hastings algorithm, implemented in the parameter inference `Monte Python` code [Audren et al., 2013]. We use the Gelman-Rubin test [Gelman and Rubin, 1992], requiring $1 - R < 0.015$ for all parameters, to claim that the chains have converged (see Sec. 2.2.1).

For ΛCDM we consider the standard six parameters: the baryon density $\Omega_{\rm b}$, the dark matter density $\Omega_{\rm dm}$, the reduced Hubble constant h, the amplitude of scalar perturbations through $\ln(10^{10}A_s)$, the spectral index of scalar perturbations n_s, and the optical depth at the re-ionization era τ. We also consider the root mean square matter density fluctuation σ_8, the Hubble constant H_0, and the total matter density $\Omega_{\rm m}$ as derived parameters.

When considering ΛGDM, we add the equation of state parameter of dark matter, w, and its sound velocity, c_s^2. We use flat priors for all the parameters, and we restrict c_s^2 to be positive (or equal to 0) and τ to be larger than 0.04.

The spatial curvature is fixed to zero by choosing the cosmological constant density, Ω_Λ, to fulfill the closure relation [see Eq. (1.63)]. We compute the value of the primordial helium fraction with the Big Bang nucleosynthesis module from `CLASS` with the corresponding value for the baryon density parameter.

[2] Since we work in the synchronous gauge we cannot completely remove the cold dark matter component, so we just keep a negligible fraction of it.

TABLE 7.1: Mean values with the $\pm 1\,\sigma$ constraints of the primary cosmological parameters for both ΛCDM and ΛGDM fitted to the different combinations of cosmological probes. The likelihood $-\ln \mathcal{L}_{\rm min}$ is also shown for each model and each combination of cosmological probes, for completeness. Notice that it has been obtained as the maximum of the MCMC histogram, not through maximization; therefore, its value should only be taken as an approximation.

Model	Parameters	CMB	CMB+SNIa+BAO	CMB+SNIa+BAO+H_0	CMB+SNIa+BAO+WL	CMB+SNIa+BAO+WL (halofit)
ΛCDM	$10^2 \times \Omega_{\rm b}$	$4.884^{+0.071}_{-0.07}$	$4.834^{+0.053}_{-0.054}$	$4.811^{+0.051}_{-0.053}$	$4.819^{+0.052}_{-0.05}$	$4.815^{+0.049}_{-0.053}$
	$\Omega_{\rm dm}$	$0.2621^{+0.0079}_{-0.0081}$	$0.2562^{+0.0058}_{-0.006}$	$0.2535^{+0.0056}_{-0.0058}$	$0.2544^{+0.0057}_{-0.0056}$	$0.2539^{+0.0057}_{-0.0055}$
	h	$0.675^{+0.0062}_{-0.0065}$	$0.6797^{+0.0048}_{-0.0049}$	$0.682^{+0.0047}_{-0.0048}$	$0.6811^{+0.0046}_{-0.0048}$	$0.6816^{+0.0045}_{-0.0048}$
	$\ln(10^{10} A_s)$	$3.065^{+0.022}_{-0.026}$	$3.075^{+0.023}_{-0.024}$	$3.08^{+0.023}_{-0.023}$	$3.074^{+0.023}_{-0.023}$	$3.067^{+0.023}_{-0.024}$
	n_s	$0.9648^{+0.0047}_{-0.0049}$	$0.9674^{+0.0042}_{-0.0043}$	$0.9687^{+0.0041}_{-0.0042}$	$0.9681^{+0.004}_{-0.0042}$	$0.9686^{+0.0043}_{-0.0039}$
	$10 \times \tau$	$0.6628^{+0.12}_{-0.14}$	$0.724^{+0.12}_{-0.13}$	$0.7535^{+0.12}_{-0.12}$	$0.7215^{+0.12}_{-0.12}$	$0.6849^{+0.12}_{-0.13}$
	$-\ln \mathcal{L}_{\rm min}$	6475.02	6818.60	6821.46	6834.87	6834.50
ΛGDM	$10^2 \times \Omega_{\rm b}$	$4.879^{+0.54}_{-0.75}$	$4.705^{+0.12}_{-0.12}$	$4.633^{+0.11}_{-0.12}$	$4.684^{+0.11}_{-0.11}$	$4.691^{+0.11}_{-0.12}$
	$\Omega_{\rm dm}$	$0.2633^{+0.039}_{-0.058}$	$0.2491^{+0.0082}_{-0.0087}$	$0.244^{+0.0075}_{-0.0082}$	$0.2477^{+0.0082}_{-0.008}$	$0.2458^{+0.0075}_{-0.0088}$
	$10^2 \times w$	$0.02733^{+0.22}_{-0.22}$	$0.06585^{+0.054}_{-0.054}$	$0.09337^{+0.052}_{-0.052}$	$0.07381^{+0.051}_{-0.054}$	$0.0545^{+0.053}_{-0.053}$
	$10^6 \times c_s^2$	< 0.8196	< 0.7768	< 0.7826	< 1.0389	< 0.0103
	h	$0.6792^{+0.044}_{-0.046}$	$0.6873^{+0.0082}_{-0.0082}$	$0.6924^{+0.0078}_{-0.0077}$	$0.6887^{+0.0076}_{-0.0083}$	$0.6898^{+0.0079}_{-0.0082}$
	$\ln(10^{10} A_s)$	$3.078^{+0.027}_{-0.03}$	$3.08^{+0.024}_{-0.027}$	$3.081^{+0.025}_{-0.027}$	$3.08^{+0.026}_{-0.027}$	$3.048^{+0.017}_{-0.027}$
	n_s	$0.9646^{+0.0069}_{-0.0069}$	$0.9656^{+0.0043}_{-0.0044}$	$0.9659^{+0.0043}_{-0.0045}$	$0.9656^{+0.0043}_{-0.0044}$	$0.9682^{+0.0041}_{-0.0042}$
	$10 \times \tau$	$0.7179^{+0.14}_{-0.16}$	$0.7301^{+0.13}_{-0.15}$	$0.7299^{+0.13}_{-0.14}$	$0.7302^{+0.13}_{-0.15}$	$0.5843^{+0.067}_{-0.16}$
	$-\ln \mathcal{L}_{\rm min}$	6475.69	6819.03	6820.92	6833.27	6835.23

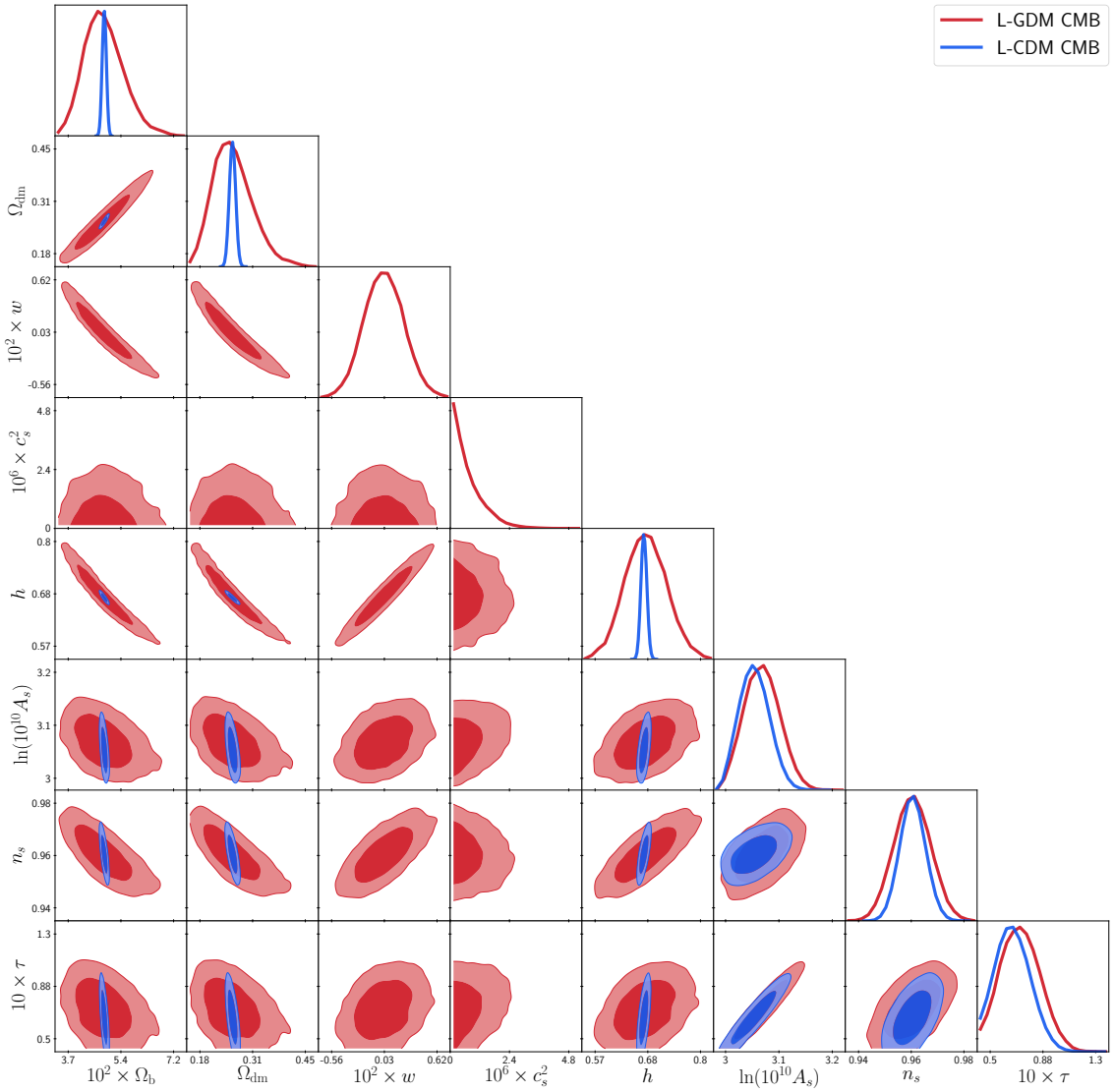

FIGURE 7.1: Primary cosmological parameter constraints for ΛCDM (blue) and ΛGDM (red) using only information coming from the cosmic microwave background. The contours correspond to the 1σ and 2σ confidence level.

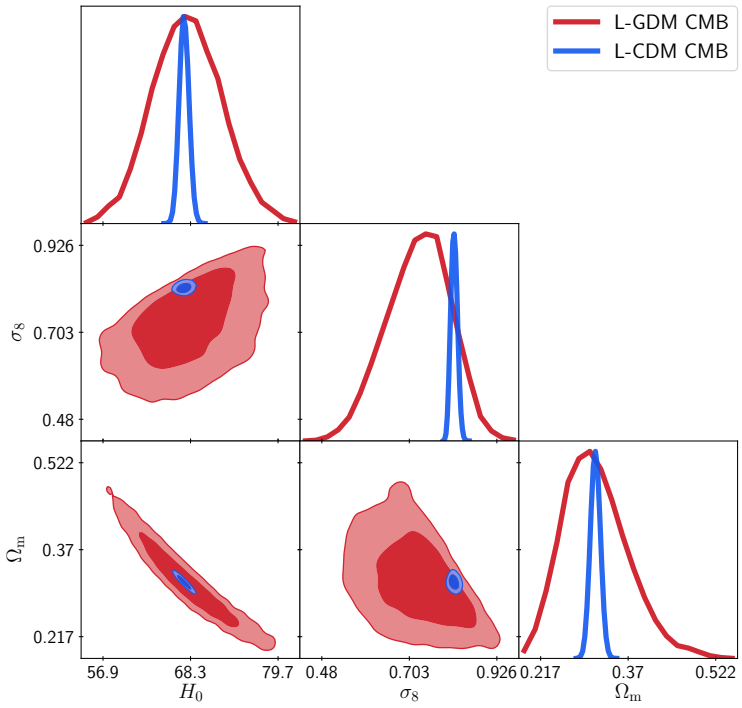

FIGURE 7.2: Derived cosmological parameter constraints for ΛCDM (blue) and ΛGDM (red) using only CMB information. The contours correspond to the 1σ and 2σ confidence level.

Moreover, we use two massless neutrinos and a massive one with mass 0.06 eV, keeping the value of the effective number of neutrino-like relativistic degrees of freedom $N_{\rm eff} = 3.046$. More in detail, we fix the number of ultra-relativistic species to $N_{\rm ur} = 2.0328$ such that the ratio of the neutrino mass over their critical energy density is equal to 93.14 eV. The values of the rest of `CLASS` precision parameters used here are specified in Sec. A.5 [3].

7.2.2 Data sets

The constraints on the parameters are obtained by using several current data sets at both high and low-redshift. Concerning high-redshift data, we use the 2015 Planck CMB likelihoods [Planck Collaboration, 2016a; Planck Collaboration, 2016d]. More specifically, the low-ℓ likelihood, the high-ℓ likelihood of the TT, TE, EE (for temperature and polarization) spectra, and the lensing likelihood. We include all the nuisance parameters with the recommended priors by the Planck Collaboration and in the way they are implemented in `Monte Python`.

[3] Notice that in this chapter we use $N_{\rm ur} = 2.0328$ instead of $N_{\rm ur} = 2.046$, as it was the case in the previous chapter.

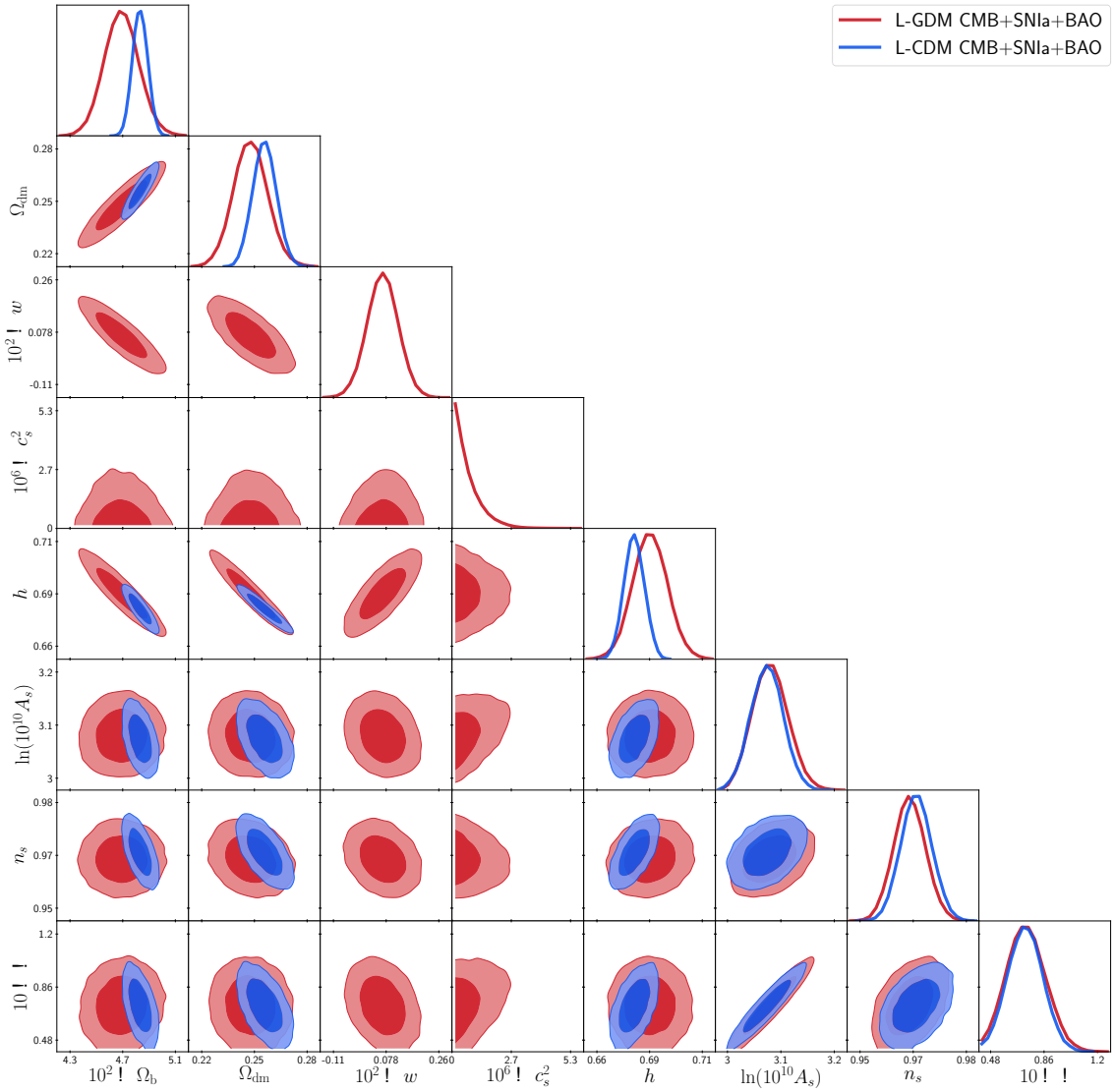

FIGURE 7.3: Primary cosmological parameter constraints for ΛCDM (blue) and ΛGDM (red) using the combination of CMB and low-redshift data (SNIa and BAO). The contours correspond to the 1σ and 2σ confidence level.

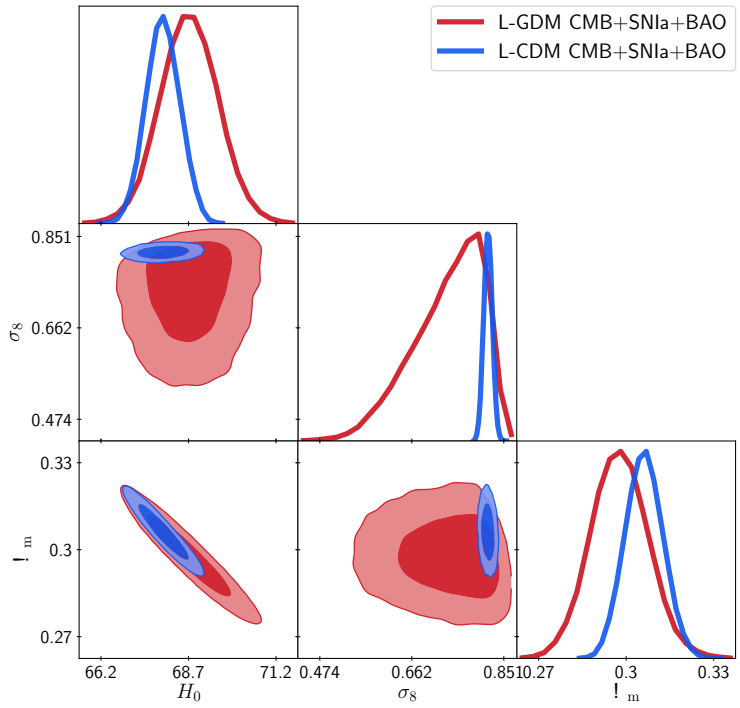

FIGURE 7.4: Derived cosmological parameter constraints for ΛCDM (blue) and ΛGDM (red) using the combination of CMB and low-redshift data (SNIa and BAO). The contours correspond to the 1σ and 2σ confidence level.

With respect to low-redshift data, we consider the baryon acoustic oscillations measurements from BOSS (CMASS and LOWZ) [Anderson et al., 2014], 6dFGS [Beutler et al., 2011], and the main galaxy sample of SDSS DR7 [Ross et al., 2015]. We also consider the luminosity distance-redshift relation coming from the joint light-curve analysis for type Ia supernovae [Betoule et al., 2014] with all the nuisance parameters and recommended priors as implemented in `Monte Python`. For some runs we include the HST measurement of the Hubble constant [Riess et al., 2011], and measurements on the galaxy weak lensing shear from the CFHTLenS survey [Heymans et al., 2013]. It has been shown [Planck Collaboration, 2016b] that these measurements are slightly in tension with Planck data within a ΛCDM cosmology. However, we include them here to assess their compatibility in a ΛGDM model.

It is important to add that, whereas the ΛGDM linear prediction (for the matter spectrum, for instance) is well understood, there are no prescriptions on how we should correct the predictions at non-linear scales, yet. Because of it, we use linear theory in all the analyses including background cosmological probes, and we discuss the non-linearities in the last two subsections, when we add weak lensing data.

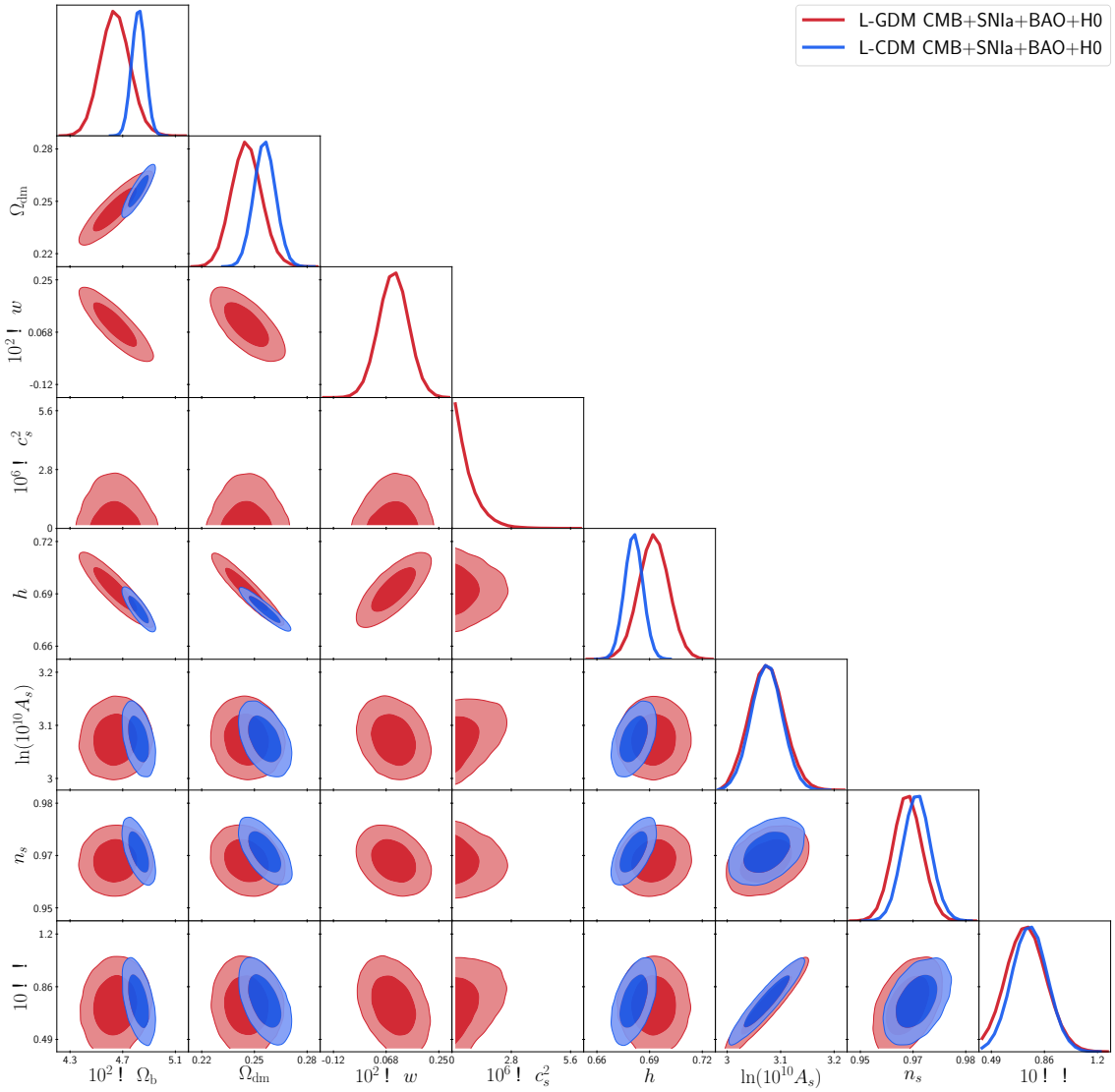

FIGURE 7.5: Primary cosmological parameter constraints for ΛCDM (blue) and ΛGDM (red) using the combination of CMB and low-redshift data (SNIa and BAO) with the HST prior on H_0. The contours correspond to the 1σ and 2σ confidence level.

7.2.3 Constraints from background cosmological probes

We first focus on the cosmological parameter constraints obtained when we consider only background probes.

Constraints from CMB alone

In Fig. 7.1 we show the 1σ and 2σ contours for the baseline cosmological parameters, both for ΛCDM (blue) and ΛGDM (red), when we only consider CMB data. The numerical values for the constraints are shown in Table 7.1. Focusing first on the cosmological parameters common to both models, we can see that they are always less constrained in ΛGDM than in ΛCDM, as expected, since we are adding two degrees of freedom into the analysis. What is interesting, though, is that the constraints on some parameters ($\ln(10^{10}A_s)$, n_s, τ) remain roughly the same, while for the others ($\Omega_{\rm b}$, $\Omega_{\rm dm}$, h) the constraints are much smaller in ΛCDM. Notice also that all the mean values are compatible (within 1σ) between the two models.

Concerning the parameters specific to GDM, w and c_s^2, we can observe from Fig. 7.1 that the CMB alone is able to put good constraints on the equation of state parameter, $w = 0.0003 \pm 0.0022$, and the sound speed, $c_s^2 < 8.2 \times 10^{-7}$; nevertheless, these values are large enough to increase the contours of the other cosmological parameters in Fig. 7.1.

It is also important to notice from Fig. 7.1 that allowing for a generalized dark matter enables a larger value for h, and we can also decrease the quantity of matter without modifying too much A_s. This motivates the contours shown in Fig. 7.2, where we focus on the derived parameters $\Omega_{\rm m}$, σ_8, H_0. In this figure we can clearly see that GDM may alleviate the tension between the high (direct measurements) and low (indirect measurements) value of H_0 (see Sec. 7.2.4), and the tension between the low (weak lensing analyses) and high (CMB analyses) value of σ_8 (see Sec. 7.2.6), when ΛCDM is assumed.

Although the nuisance parameters are not shown in the figures for readability, we have checked that there are no significant correlations between the cosmological and nuisance parameters.

Constraints from all background probes

We now consider the constraints on the cosmological parameters when the SNIa and BAO data are added on top of the CMB. We present them in Fig. 7.3 and Table 7.1. As it was the case for CMB data alone, the constraints are weaker when we consider ΛGDM, as expected. However, the difference is not as large as before thanks to the constraining power from low-redshift data. All the parameters are compatible within 1σ for the two models, but now the

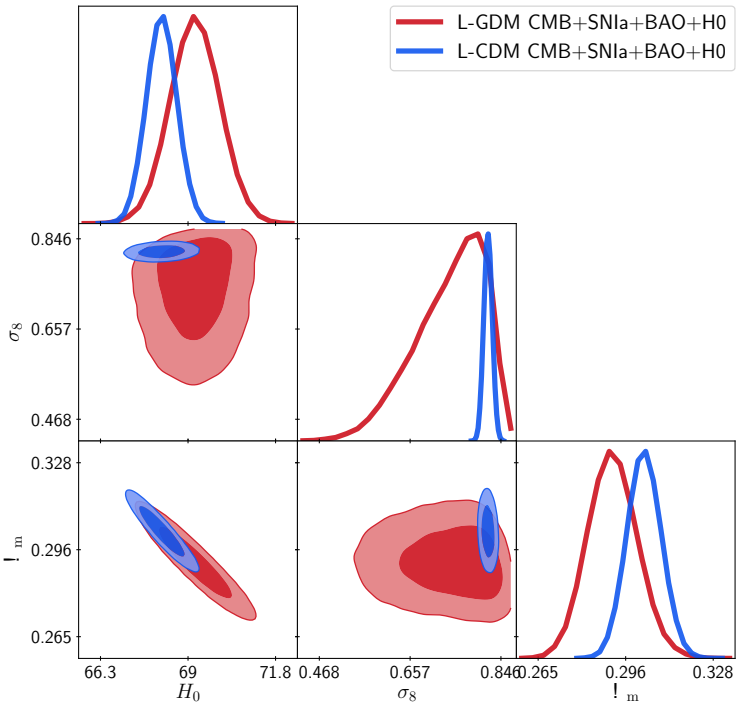

FIGURE 7.6: Derived cosmological parameter constraints for ΛCDM (blue) and ΛGDM (red) using the combination of CMB and low-redshift data (SNIa and BAO) with the HST prior on H_0. The contours correspond to the 1σ and 2σ confidence level.

constraints on the GDM parameters are given by $w = 0.00066 \pm 0.00054$ and $c_s^2 < 7.8 \times 10^{-7}$. The addition of low-redshift data has decreased the constraint on the equation of state parameter by a factor 4, but has left nearly unchanged the constraint on the sound speed, showing that low-redshift data is sensitive to w but have little effect on the c_s^2 constraint. This is completely consistent with the fact that w affects the expansion history (thus the background probes are sensitive to it), but c_s^2 affects the growth of structures, implying that the constraint comes basically from the lensing likelihood of the CMB (see Thomas, Kopp, and Skordis, 2016; Kopp, Skordis, and Thomas, 2016, for a detailed discussion on how these two parameters affect differently the CMB). Notice that after the addition of low-redshift data, the constraints on $\ln(10^{10} A_s)$, n_s, and τ are nearly the same for both models. But a smaller value of $\Omega_{\rm b}$ and $\Omega_{\rm dm}$, and a larger value of h are still allowed when considering ΛGDM. In Fig. 7.4 we present the contours for the derived parameters showing that ΛGDM may still alleviate the H_0 and σ_8 tensions.

Concerning the nuisance parameters, in this case (and the following ones of this section) only the $M_{\rm B}^1$ SNIa absolute magnitude nuisance parameter is correlated with the cosmological parameters. Since it is quite degenerate with h,

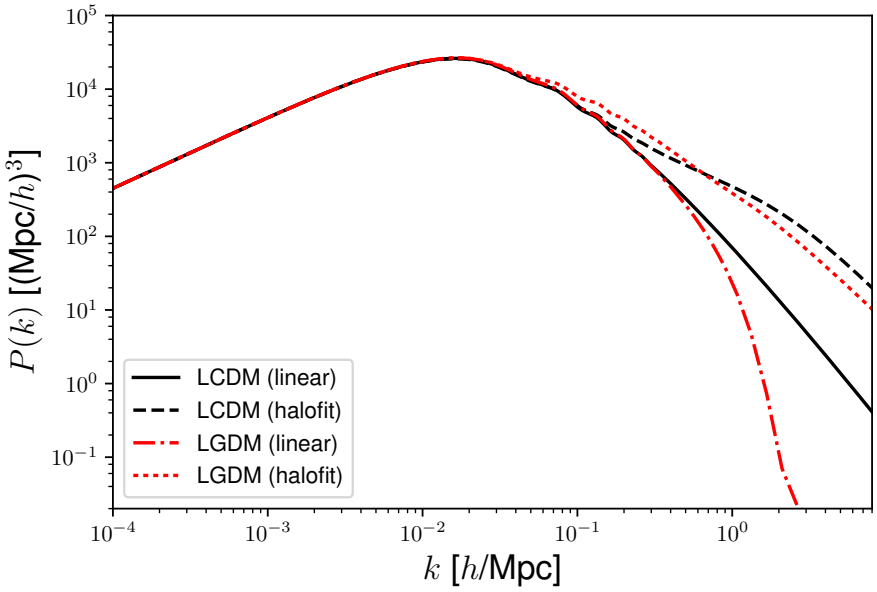

FIGURE 7.7: Linear and non-linear matter power spectra for ΛCDM and ΛGDM at redshift $z = 0$. The cosmological parameters have been fixed to the values obtained from the fit to CMB+SNIa+BAO data (fourth column in Table 7.1) using a ΛCDM model. We further consider $w = 10^{-3}$ and $c_s^2 = 10^{-7}$ for the ΛGDM model. The black solid line and the red dot-dashed line stand for the linear predictions for ΛCDM and ΛGDM, respectively. The dashed black line and the dotted red line stand for the non-linear predictions for ΛCDM and ΛGDM, respectively.

both parameters show roughly the same contours with the remaining cosmological parameters. There are no significant correlations between the cosmological and the other nuisance parameters.

7.2.4 Tension with H_0

We focus now on the tension concerning the direct measurement of H_0 and the derived measurement assuming a ΛCDM cosmology. The value of the former is significantly larger than the latter, as already discussed in Sec. 1.5.4 and Sec. 5.2.5. In this section we add a Gaussian prior on H_0 around 73.8 ± 2.4, according to the Hubble Space Telescope measurement from Riess et al., 2011, and check if the tension is alleviated when considering ΛGDM.

In Fig. 7.5 and Table 7.1 we present the constraints on the parameters when we add the prior on H_0 on top of SNIa, BAO, and CMB data. We can see that qualitatively the constraints do not change much, since we are only adding one data point. Also, we see that a higher value of h, and a smaller one for

$\Omega_{\rm b}$ and $\Omega_{\rm dm}$ are still allowed when considering ΛGDM. What is interesting in this case is that the equation of state parameter is only compatible with 0 at nearly 2σ, $w = 0.00093 \pm 0.00052$. However, as we can see in Fig. 7.6, although a positive equation of state parameter allows for a larger value of H_0, it is not enough to completely remove the tension between the H_0 measurements (a tension slightly below 2σ still remains). The reason being that the combination of BAO and CMB data forces H_0 to be lower than the preferred value for the HST measurement (see Thomas, Kopp, and Skordis, 2016, for constraints using only the CMB and the HST measurement. They find a larger value for H_0, which is able to remove the tension between the HST measurement and the CMB derived value for H_0). From the same figure we can observe that ΛGDM may still alleviate the tension on the σ_8 value (see Sec. 7.2.6).

7.2.5 Non-linear regime

In Fig. 7.7 we show the linear matter power spectra at $z = 0$, for both ΛCDM (black solid line) and ΛGDM (dot-dashed red line), using the values of the cosmological parameters obtained from the fit of ΛCDM to CMB+SNIa+BAO data (fourth column in Table 7.1). For ΛGDM we consider here an equation of state parameter equal to $w = 10^{-3}$ and a sound speed of $c_s^2 = 10^{-7}$. Notice that even if these values are perfectly compatible within 1σ with the constraints obtained from CMB+SNIa+BAO data, the linear prediction of the matter power spectrum behaves significantly different for ΛCDM and ΛGDM at small scales (above $k \gtrsim 0.3\,h/\text{Mpc}$). This effect is basically due to the introduction of the sound speed, which suppresses the formation of structures at small scales. From this figure it is clear that including cosmological probes sensitive to small scales could be the key to strongly improve the constraints on the GDM parameters. However, as was mentioned at the beginning of this section, the GDM model is only well understood at the linear level, and there are no prescriptions of how we should correct the predictions when we enter into the non-linear regime, yet. One option could be to use the standard `halofit` approach (see Sec. 1.2.3), assuming that the constraints on the GDM parameters are good enough to remain close to CDM. In Fig. 7.7 we show the non-linear matter power spectrum (`halofit` with Takahashi and Bird corrections) for both ΛCDM (dashed black line) and ΛGDM (dotted red line). Notice that now we can already appreciate some differences at $k \gtrsim 0.03\,h/\text{Mpc}$. But, more importantly, we can observe that a sound speed of 10^{-7} is large enough to change significantly the prediction with respect to ΛCDM. Therefore, the conservative conclusion that we can draw from these results is that, given the lack of a GDM-based non-linear recipe for the non-linear scales, we should not use the smallest scales in our analyses, and we should treat the results coming from the `halofit` correction with caution.

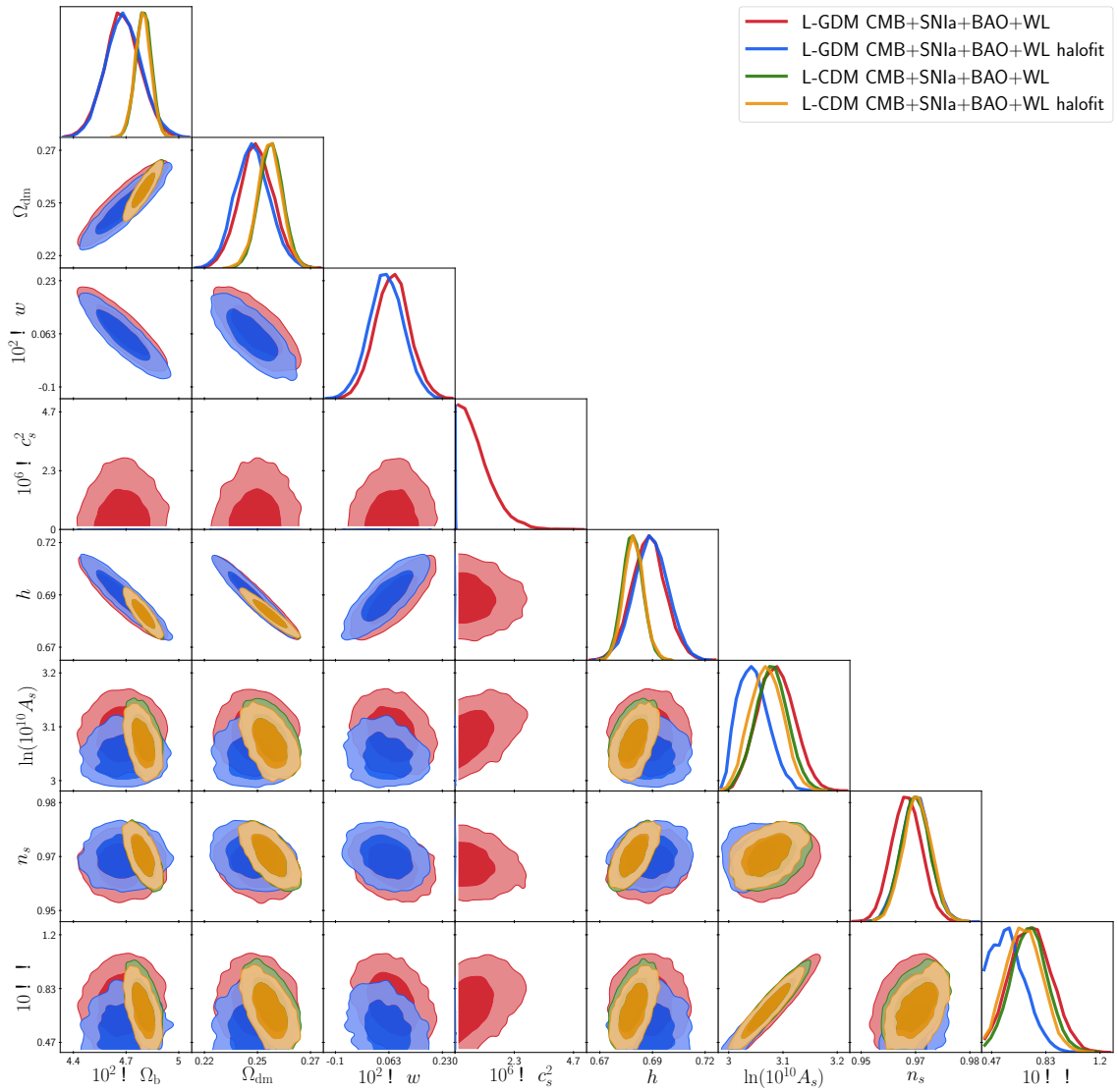

FIGURE 7.8: Primary cosmological parameter constraints for ΛCDM and ΛGDM using the combination of CMB, SNIa, BAO, and WL data. We show the results using the linear predictions for ΛCDM (green) and ΛGDM (red), as well as the results using the Takahashi+Bird `halofit` non-linear correction for ΛCDM (yellow) and ΛGDM (blue). Notice that the constraint on c_s^2 when using `halofit` is so small, with respect to the linear prediction, that it is not visible from the plot. The contours correspond to the 1σ and 2σ confidence level.

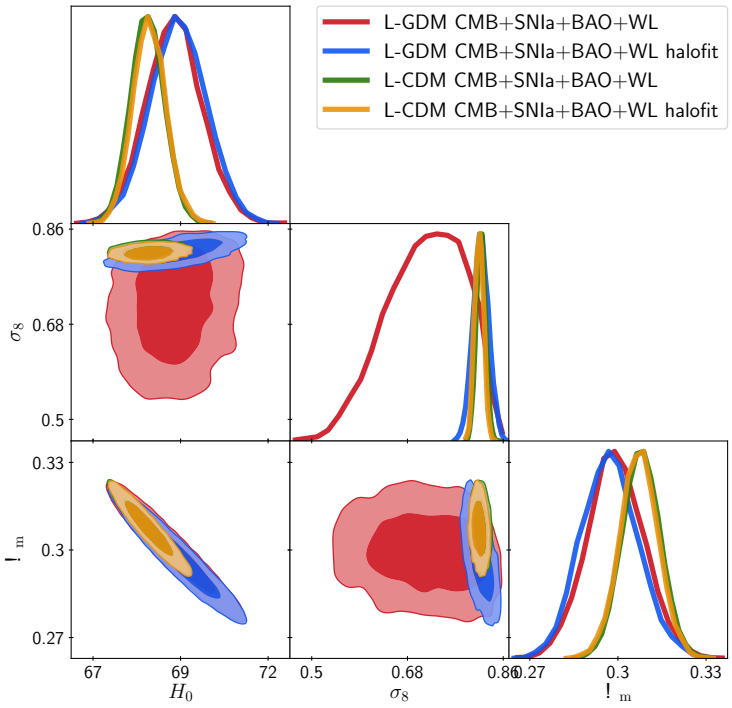

FIGURE 7.9: Derived cosmological parameter constraints for ΛCDM and ΛGDM using the combination of CMB, SNIa, BAO, and WL data. We show the results using the linear predictions for ΛCDM (green) and ΛGDM (red), as well as the results using the Takahashi+Bird `halofit` non-linear correction for ΛCDM (yellow) and ΛGDM (blue). The contours correspond to the 1σ and 2σ confidence level.

In the following we focus on adding weak lensing data into the analysis, since it is very sensitive to small scales, and we turn on and off the Takahashi+Bird `halofit` non-linear correction to study its impact on the final parameter constraints.

7.2.6 Tension with weak lensing data

Let us now focus on the addition of weak lensing data. Before presenting the results, let us just recall that there is currently a 2-3σ tension between CFHTLenS WL measurements and Planck CMB data [Planck Collaboration, 2016b]. More in detail, weak lensing is especially powerful in measuring the amplitude of matter fluctuations, σ_8, at low-redshifts. With CFHTLenS data alone [Heymans et al., 2013] we constrain the combination $\sigma_8(\Omega_{\rm m}/0.27)^{\alpha}$ to be equal to $0.774^{+0.032}_{-0.041}$ with $\alpha = 0.46 \pm 0.02$, which gives $\sigma_8 \sim 0.78$. On the contrary, CMB data can constrain σ_8 at the redshift of the CMB. Planck provides the constraint $\sigma_8 = 0.831 \pm 0.013$ [Planck Collaboration, 2016b], which clearly shows some tension between the low-redshift and high-redshift measurements

of σ_8. It has been argued that this difference may arise from the small scales that WL probe (compared to the large scales probed by the CMB), and the effect of baryons at these scales; since WL and CMB results are in agreement if we only use the largest scales for WL, while they disagree once we include the small scales into the analysis [Kitching et al., 2014; Heymans et al., 2013; Kilbinger et al., 2013; Fu et al., 2014; MacCrann et al., 2015]. Also, the latest results from the DES Collaboration [DES Collaboration, 2017b] do not show any tension between the WL and CMB measurements of σ_8 and $\Omega_{\rm m}$. However, the debate on this tension is still open and there is an ongoing effort in the community trying to better understand if there are remaining systematics that need to be taken into account, or if it is just a statistical fluctuation, or if it may really point towards new physics.

Concerning our results obtained from the addition of weak lensing data into the analysis, they are essentially shown in Figs. 7.8 and 7.9, and Table 7.1. We show the results for ΛGDM with (blue) and without (red) the `halofit` correction, as well as the results for ΛCDM with (yellow) and without (green) the `halofit` correction. It is important to say that given the lack of a non-linear recipe for ΛGDM, and the large difference that we expect at small scales (as it is shown in Fig. 7.7), we follow the recommendation from Heymans et al., 2013, and use an ultra-conservative cut to remove the smallest scales from the analysis.

Let us first consider the results without the `halofit` correction. In Fig. 7.8 we can observe that the contours for the ΛGDM parameters (red) are in general larger than the ones for the ΛCDM parameters (green), as before, due to the introduction of two extra degrees of freedom. However, we can still see that the constraint for some parameters $(\ln(10^{10}A_s), n_s, \tau)$ is nearly the same in both models, while a smaller quantity of baryons and dark matter, as well as a larger value of h, are allowed when considering ΛGDM. If we look at Table 7.1 we can see that all the constraints remain basically unchanged when we add weak lensing data. The reason being that we have discarded most of the information when performing the ultra-conservative cut. Concerning the specific GDM parameters, we constrain the equation of state parameter as $w = 0.00074 \pm 0.00054$ and the sound speed $c_s^2 < 1.0 \times 10^{-6}$. Notice that the constraint on the sound speed is slightly worse than when we do not add weak lensing data, but this may be due to the tension between weak lensing and CMB data that prefers a slightly larger value of the sound speed (see the mean values of c_s^2 in Table 7.1). Concerning the derived parameters in Fig. 7.9 we can see that the tension between the weak lensing measurement of σ_8 and the CMB one disappears if we consider the ΛGDM model.

Let us now focus on the results obtained when we switch on the `halofit`

correction. In Fig. 7.8 we observe that the constraints on the ΛCDM parameters (yellow) are equivalent to the ones obtained without `halofit` (green). This is due to the fact that we are only using the largest scales of the CFTHLenS data, and there is not a large difference between the linear and non-linear prediction for ΛCDM at these scales (see Fig. 7.7). However, if we look now at the ΛGDM contours (blue), it is clear that some of them have been shifted with respect to the analysis without `halofit` (red). And, more surprisingly, we are not even able to see the constrain on c_s^2 because it has improved by two orders of magnitude $c_s^2 < 1.0 \times 10^{-8}$. These results can be justified by looking again at Fig. 7.7. Even if we remove the small scales from the WL data, there is a large difference between the linear prediction and the non-linear one for ΛGDM. The latter gives a larger spectrum by several orders of magnitude, putting much more severe constraints on the sound speed. However, we recall that the `halofit` correction is only valid for ΛCDM, so the constraint on c_s^2 may probably be too optimistic. We can also see this effect in the derived parameters in Fig. 7.9. The (probably) over-estimated spectrum at small scales for ΛGDM gives very good constraints on σ_8, showing that ΛGDM may no longer be able to remove the tension between WL and CMB measurements. As a final remark, we notice that the addition of the `halofit` correction does not significantly change the constraints for the remaining parameters of ΛGDM, which is consistent with the fact that they are sensitive to the expansion of the Universe and large scales.

7.2.7 Summary

In this section we have studied the ΛGDM model using current cosmological observations. In a first place we have focused on the background expansion of the Universe, using SNIa, BAO, and CMB data. Using CMB data alone we have seen that the constraints on the ΛGDM parameters are worse than the ones on the ΛCDM parameters, due to the addition of two extra degrees of freedom: the equation of state parameter w, and the sound speed c_s^2. Already in this first case we have seen that ΛGDM allows for a smaller value of the matter density, a smaller value of σ_8, and a larger value of H_0, that could help alleviate the current tensions between low-redshift and high-redshift measurements of these quantities.

We have then added other background probes, SNIa and BAO, and we have observed that the constraints become smaller; although a smaller value of $\Omega_{\rm m}$ and σ_8, and a larger one for H_0, are still allowed when considering ΛGDM. However, after adding the direct measurement of H_0 from Riess et al., 2011, into the analysis, we have seen that even if ΛGDM allows for a larger value of H_0, it is not enough to completely remove the tension between the direct measurement of it and the one derived from CMB data. It is important to

notice that we have added the H_0 measurement on top of CMB and BAO data, which already constrain H_0. It was shown in Thomas, Kopp, and Skordis, 2016, that using only CMB data with a prior on the direct H_0 measurement completely removes the tension on its value.

Finally, we have added WL data into the analysis to study the tension on the σ_8 value. WL data probe small scales, so we enter the non-linear regime and we need to correct for it when using our predictions. The problem is that there are no non-linear recipes for ΛGDM yet. Because of it we have added the WL data with an ultra-conservative cut keeping only the largest scales, and we have switched on and off the non-linear correction to study its effect on the final parameter constraints. We have observed that there is no improvement on the ΛGDM constraints using the linear prediction when we add WL data. When using the non-linear correction we have seen that some contours for the ΛGDM parameters are slightly shifted but, more importantly, we obtain an exquisite constraint on the sound speed thanks to the larger non-linear spectrum at small scales. It is no longer clear whether ΛGDM is then able to completely remove the tension on the σ_8 value, while it was the case with a linear prediction. In conclusion, we have seen that adding a non-linear recipe strongly improves the constraints on the GDM parameters (especially the sound speed) and, therefore, it strongly improves our knowledge of the nature of dark matter. However, we need cosmological simulations to extract the correct non-linear correction and constrain the GDM parameters without biasing our results.

As a last remark, we have added the value of $-\ln \mathcal{L}_{\min}$ for each model and each combination of cosmological probes in Table 7.1, for completeness. We can see from these values that ΛGDM fits the data as well as ΛCDM, as expected, since GDM includes CDM as a special case. From a model comparison point of view ΛCDM would still be preferred since it has two parameters less, but the idea here was not to propose a model that performs better than ΛCDM to rule it out, but to understand the nature of dark matter. And let us recall that GDM is a phenomenological model, therefore having much more freedom to account for different types of dark matter models. Also, it is important to keep in mind that the values of $-\ln \mathcal{L}_{\min}$ for the different models have been obtained from the maximum of the MCMC histogram, instead of a direct maximization of the likelihood; therefore, they should be interpreted only as an approximation, and not used for accurate model comparisons.

TABLE 7.2: Absolute 1σ error bars for the ΛGDM cosmological parameters for different combinations of Euclid probes and current observations. GC and WL stand for photometric galaxy clustering and weak lensing, respectively. A plus sign represents the addition of the two probes assuming they are independent, while the star takes into account their cross-correlations. CD stands for the combination of CMB, SNIa, and BAO current observations. Lin and NL describe the linear or Takahashi+Bird `halofit` prediction used in the forecast. The fiducial model is the one obtained from the fit of ΛGDM to the combination of CMB, SNIa, and BAO data (fourth column in Table 7.1).

Parameters	CD	GC+WL (Lin)	GC*WL (Lin)	CD+GC*WL (Lin)	GC+WL (NL)	GC*WL (NL)	CD+GC*WL (NL)
$10^2 \times \Omega_{\rm b}$	0.12	0.185	0.183	0.0758	0.101	0.0793	0.0536
$\Omega_{\rm dm}$	0.0087	0.0209	0.0140	0.00517	0.0132	0.00931	0.00425
$10^2 \times w$	0.054	0.271	0.197	0.0346	0.121	0.0979	0.0250
$10^6 \times c_s^2$	< 0.7768	0.00213	0.00207	0.00134	0.000803	0.000790	0.000504
h	0.0082	0.0261	0.0212	0.00512	0.0165	0.0142	0.00404
$\ln(10^{10} A_s)$	0.027	0.190	0.152	0.0145	0.0684	0.0581	0.0134
n_s	0.0044	0.0294	0.0253	0.00389	0.0240	0.0234	0.00388

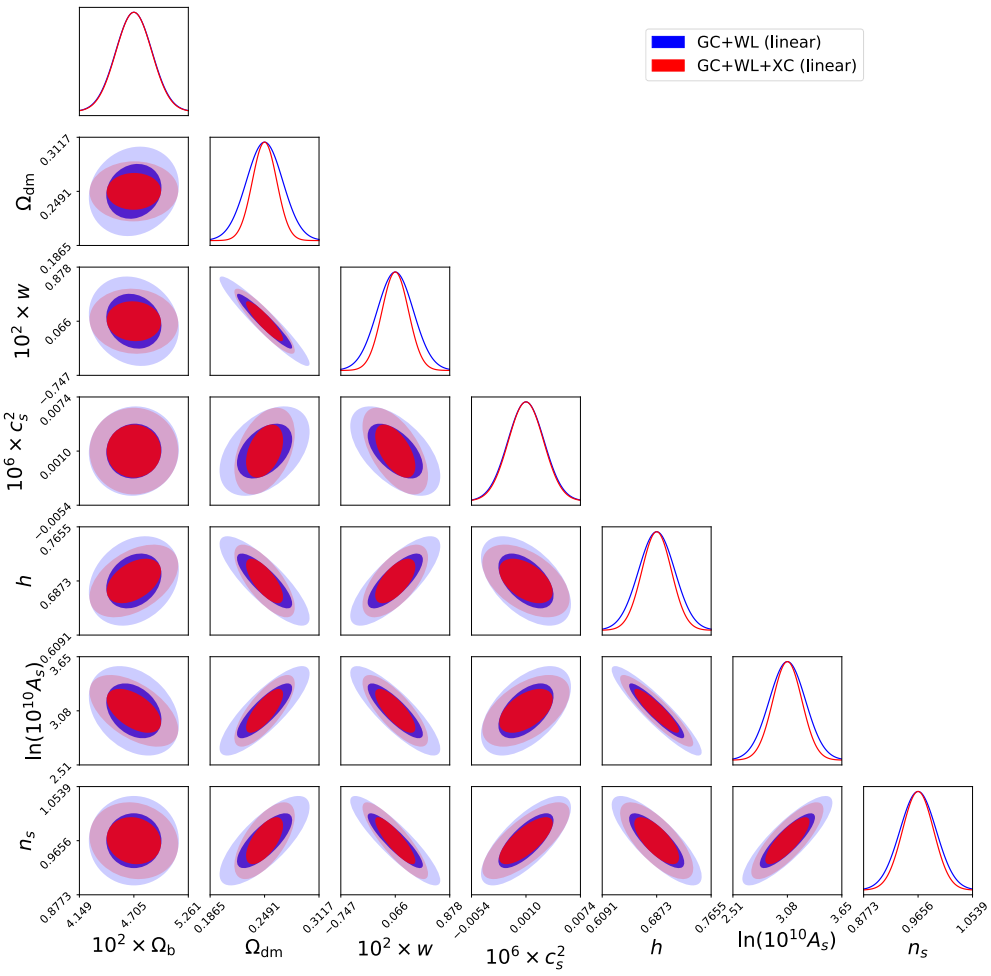

FIGURE 7.10: Fisher matrix forecast contours of the ΛGDM cosmological parameters for the photometric galaxy clustering and weak lensing probes of the Euclid satellite with a linear prediction. In blue we represent the addition of these two probes assuming they are statistically independent, while in red we take into account their cross-correlations.

7.3 Euclid forecast

In this section we focus our attention to the ΛGDM model in the context of the future Euclid satellite (see Chapter 3) [4]. We use the `CosmoSIS` pipeline described in the previous chapter (Chapter 6) to compute a forecast for the photometric Euclid survey. In particular, for the photometric galaxy clustering, the weak lensing, and their cross-correlations. More precisely, we replace (in the `CosmoSIS` pipeline) the Boltzmann code used in Chapter 6, `CAMB`, by our GDM modified version of `CLASS` used in the previous section, and we marginalize over the galaxy bias and intrinsic alignments nuisance parameters as described in Chapter 6. Since weak lensing data probe very small scales, and because there is no prescription for the GDM corrections at this regime, we follow the approach from the previous section by turning on and off the `halofit` non-linear prescription with the Takahashi and Bird corrections. Although the baseline cut on small scales from Chapter 6 ($\ell_{\rm max} = 750$ for GC and XC, and $\ell_{\rm max} = 1500$ for WL) has been chosen to avoid the scales where non-Gaussian contributions in the covariance matrix start to be important, we use here a more conservative approach by keeping only the largest scales for WL, so we use $\ell_{\rm max} = 750$ for all probes.

Concerning the fiducial cosmological model for the forecast, we use the values obtained from the fit of ΛGDM to the combination of CMB, SNIa, and BAO data from the previous section (fourth column of table 7.1), including the treatment of massive neutrinos and the value of τ, which are fixed in the forecast. In this way we are able to easily combine the Euclid forecast with the data of the three main background probes. We use $c_s^2 = 10^{-9}$ instead of 0 because of the Fisher matrix technique. Indeed, in order to use $c_s^2 = 0$ as fiducial we should modify the numerical derivative method by using one-sided derivatives for c_s^2. This modification is left for future work. Notice that we neglect any correlation between the BAO data (at low-redshift) and the Euclid forecast. Although this might not be entirely true, the main signal of BAO from Euclid will come from the spectroscopic survey (starting at $z = 0.9$), so we expect the correlation between Euclid and the BAO data used in this section to be negligible.

7.3.1 Linear prediction

Let us first consider the linear prediction for the matter power spectrum. We show the 1σ and 2σ contours obtained with the Fisher matrix forecast in Fig. 7.10. The 1σ error bars are shown in Table 7.2. In blue we can see the

[4] Part of this work has been done within the Theory Science Working Group of the Euclid Consortium.

combination of GC and WL assuming they are statistically independent, while in red we show their combination taking into account the cross-correlations. It is clear from the figure that the role of cross-correlations is important when we look at the area and orientation of the ellipses. Although it is slightly less important when we look at the constraints on the parameters, we can see (looking at Table 7.2) that we improve the constraints by a factor 1.5 (for $\Omega_{\rm dm}$) when we add the cross-correlations.

Focusing now on the constraints themselves, most of the parameters are slightly worse constrained by Euclid alone than the combination of CMB, SNIa, and BAO current data. This can be explained by the lack of high-redshift data, since Euclid only probes up to $z \sim 2.5$, while CMB information is important to put a good constraint on w and to break the remaining degeneracies. However, it is important to notice that Euclid alone is able to put nice constraints on all parameters (that are nearly of the same order of magnitude than CMB, SNIa, and BAO data), while low-redshift data alone (SNIa and BAO) are only marginally able to constrain ΛGDM, as it is shown in the next section. Moreover, thanks to the addition of information at mildly non-linear scales, Euclid is able to reduce the constraint on the sound speed by more than two orders of magnitude.

With respect to the IA and galaxy bias nuisance parameters (not shown in the figure), we have checked that the former are not significantly correlated with the cosmological parameters. However, $\Omega_{\rm b}$, w, and h are correlated with the galaxy biases, while $\Omega_{\rm dm}$, c_s^2, A_s, and n_s are anti-correlated. This points again to the importance of well knowing the galaxy biases in order not to bias our constraints on the cosmological parameters.

7.3.2 Non-linear prediction

Let us now consider the case where we correct for the non-linearities in our predictions with `halofit`, including the Takahashi and Bird corrections. The 1σ and 2σ contours are shown in Fig. 7.11 for the combination of GC and WL with (red) and without (blue) their cross-correlations. We can see that the addition of cross-correlations has a slightly smaller impact on the results than for the linear case of Fig. 7.10, as we can check in Table 7.2.

Although the addition of cross-correlations is not extremely important in this particular case, the use of the non-linear recipe for our predictions provides nice constraints for all parameters. Comparing with the combination of CMB, SNIa, and BAO current data, Euclid provides a better constraint for $\Omega_{\rm b}$, and slightly worse constraints for the other parameters ($\Omega_{\rm dm}$, w, h, A_s, n_s), but all are of the same order of magnitude (let us recall that we are comparing Euclid to a combination of low-redshift and CMB data). What is surprising

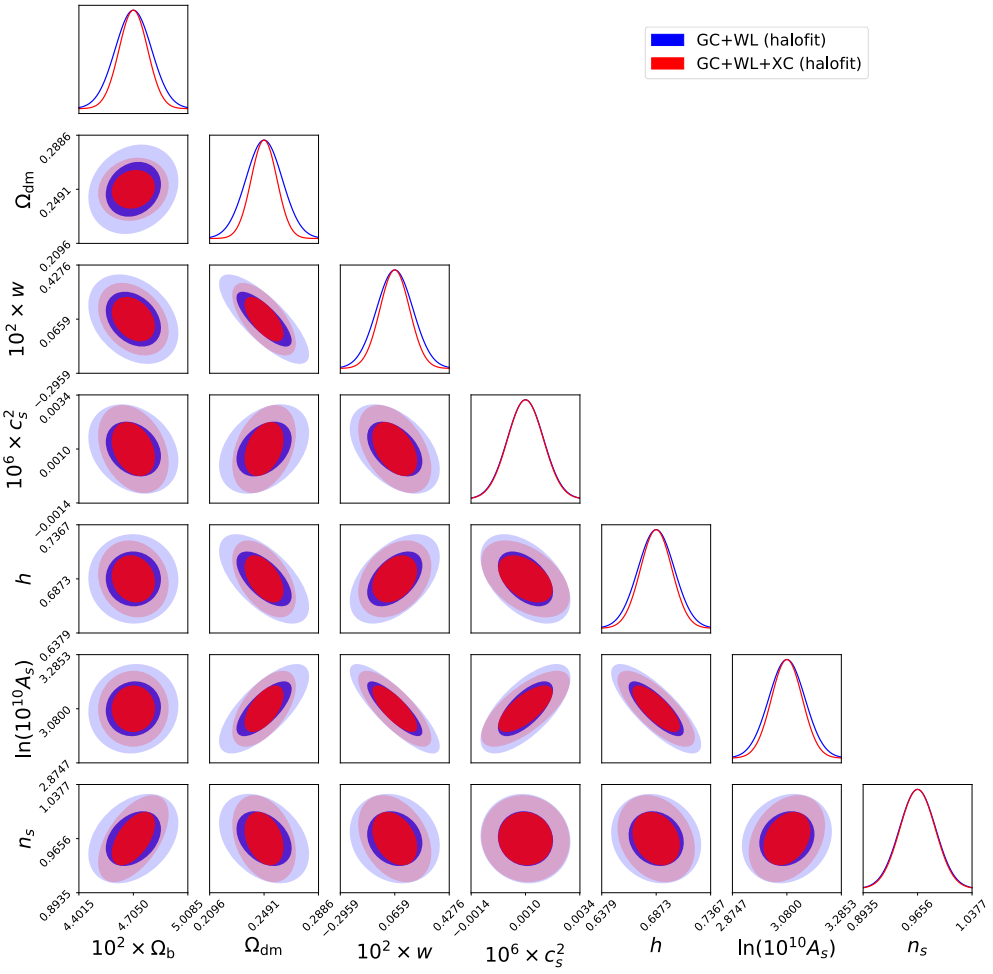

FIGURE 7.11: Fisher matrix forecast contours of the ΛGDM cosmological parameters for the photometric galaxy clustering and weak lensing probes of the Euclid satellite with a non-linear prediction (Takahashi+Bird `halofit`). In blue we represent the addition of these two probes assuming they are statistically independent, while in red we take into account their cross-correlations.

is the constraint on c_s^2, which improves by nearly 3 orders of magnitude. If we compare with Euclid itself using the linear prediction, all the constraints improve by a factor between 1.1 (for n_s) and 2.6 (for c_s^2). This improvement on the constraints on all parameters with the non-linear recipe is consistent with the results of the previous section. Even if we only consider the largest scales, the non-linear matter power spectrum for ΛGDM is larger than the linear one, giving better constraints on the parameters. However, it is important to recall that we should treat these forecasted constraints with caution, since we know that the `halofit` correction has not been adapted to GDM. It is also worth mentioning that we have checked the impact of our fiducial model on the results. More precisely, we have seen that the more our fiducial GDM parameters differ with respect to the standard CDM values ($w = c_s^2 = 0$), the more all our forecasted constraints with `halofit` are better, while it is not the case for the linear prediction. This can be justified by the fact that the more w and c_s^2 evolve, the more our matter power spectrum differs from the standard ΛCDM one, and the less our `halofit` correction is accurate anymore.

Concerning the nuisance parameters, the IA nuisance parameters are not correlated with the cosmological ones, while $\Omega_{\rm b}$, w, h, and n_s are correlated with the galaxy biases, and $\Omega_{\rm dm}$, c_s^2, and A_s are anti-correlated. Notice that the sign of the correlation between n_s and the galaxy biases is the only difference with respect to the linear case.

7.3.3 Combination with real data

Now that the ΛGDM forecast for Euclid has been computed, it is interesting to combine it with observed data. Especially with the CMB, since it provides a good constraint on w that helps to break some degeneracies that may remain between the parameters using only low-redshift information. In Fig. 7.12 we show the 1σ and 2σ contours for the full photometric Euclid survey (GCp, WL, and XC) with the linear prediction (blue), and its combination with CMB, SNIa, and BAO current data (red) using the covariance matrix obtained in the previous section (i.e. we add the Euclid Fisher matrix with the inverse covariance matrix of the parameters obtained in the previous section). It is clear from the figure that all the constraints improve noticeably with the addition of current data. Looking at Table 7.2 we can see the constraints improve by a factor ranging between 1.5 (for c_s^2) and 10.5 [for $\ln(10^{10}A_s)$]. Notice that the smallest improvement concerns c_s^2, as expected, since the main constraining power on this parameter comes from Euclid.

If we now combine the current data with the Euclid forecast using the non-linear prediction, the constraints improve by a factor ranging between 1.5 (for

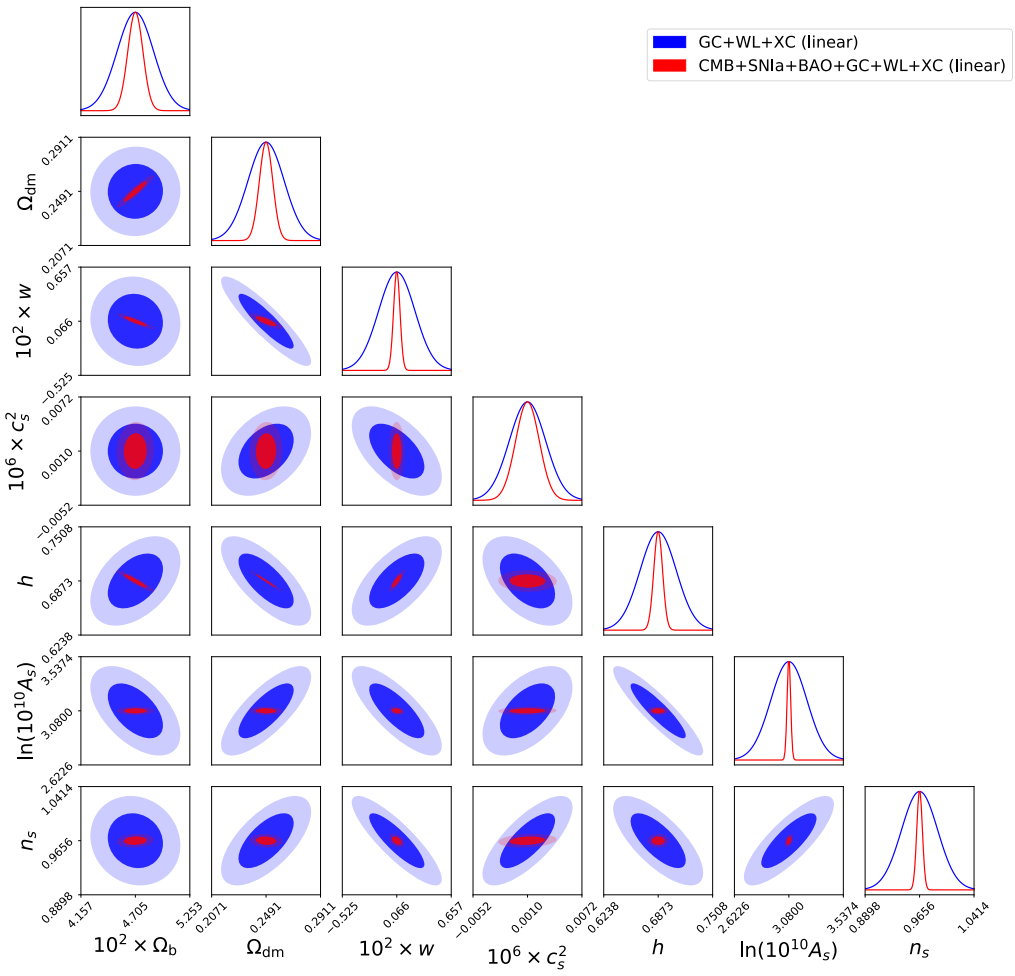

FIGURE 7.12: Fisher matrix forecast contours of the ΛGDM cosmological parameters. In blue we show the results for the photometric galaxy clustering and weak lensing probes of the Euclid satellite together with their cross-correlations, while in red we add the information from current CMB, SNIa, and BAO observations (see the text for details).

$\Omega_{\rm b}$) and 6.0 (for n_s). Again, c_s^2 is one of the parameters with the smallest improvement (by a factor 1.6).

7.3.4 Summary

In this section we have focused on the ability of the future Euclid satellite to put constraints on the GDM model. More precisely, we have studied the ability of the photometric Euclid survey (GCp and WL) to constrain the GDM parameters, and the impact of their cross-correlations on the final constraints. We have used the `CosmoSIS` pipeline described in Chapter 6, replacing the Boltzmann code by the modified version of `CLASS` used in the previous section. We have chosen the fiducial cosmology corresponding to the values obtained from the fit of ΛGDM to the combination of CMB, SNIa, and BAO data from the previous section (plus $c_s^2 = 10^{-9}$), in order to be able to easily combine the current results with the Euclid forecast. We have considered a more conservative approach than the baseline cut to discard the smallest scales in the analysis: $\ell_{\rm max} = 750$ for all probes.

In a first place we have computed the constraints for Euclid alone using the linear prediction. We have immediately seen that cross-correlations significantly reduce the area of the ellipses (as well as changing some orientations), although they are slightly less important for the constraints on the parameters than they were on the previous chapter. Concerning the value of the constraints on the parameters, they are slightly worse than using the full combination of CMB, SNIa, and BAO data, because of the lack of information beyond $z \sim 2.5$, which is important to constrain w and to break degeneracies. However, Euclid alone is already able to place nice constraints (of nearly the same order of magnitude) and, more importantly, it can constrain the sound speed much better (by two orders of magnitude) than current background probes, thanks to the addition of mildly non-linear scales.

We have then computed the forecast again using the non-linear prediction. In this case, all constraints are of the same order of magnitude than the current ones, although slightly better for $\Omega_{\rm b}$. Compared to the linear prediction, using the `halofit` correction improves the constraints roughly by a factor 2. This improvement is justified by the larger non-linear matter power spectrum (with respect to the linear one). As it was said before, we need to treat these forecasted constraints (especially on c_s^2) with caution, since the `halofit` correction is not adapted to GDM.

We have finally combined the Euclid forecast with the current constraints. It noticeably improves the constraints on all parameters thanks to the high-redshift data from the CMB. However, it is important to notice that the constraint on c_s^2 is roughly the same, since the constraining power for this parameter

comes essentially from Euclid.

One thing to take into account is that we have used a Fisher matrix formalism in this section, which should only be used when the posterior of the parameters are close to a Gaussian distribution, which is not the case for the sound speed here. Moreover, we have seen that the improvement coming from the `halofit` correction depends on the fiducial model and how far we are from standard cold dark matter. Improving on these aspects, as well as adding the spectroscopic Euclid survey in the analysis (which will certainly improve the constraints), are left for future studies.

In conclusion, Euclid will be able to put strong constraints on the GDM parameters and allow us to increase our knowledge on the nature of dark matter, but it is crucial to have a non-linear correction adapted to GDM to be able to explore the small scales that Euclid will probe, and extract the maximum of information of it.

7.4 Degeneracy with dark energy

7.4.1 Context

The dark sector of the Universe is composed, in the concordance model, of dark matter (discussed in the previous sections), but also contains a cosmological constant, Λ. The theoretical basis of this cosmological constant is not clearly established, especially with respect to the issue of gravitational effects of quantum vacuum energy (the cosmological constant problem −see Martin, 2012, for an extensive review). In this context, a large variety of explanations have been proposed beyond a simple Einstein cosmological constant (see Sec. 1.1.4): scalar field domination known as quintessence [Caldwell, Dave, and Steinhardt, 1998], generalized gravity theory beyond general relativity [Nojiri and Odintsov, 2011] or even inhomogeneous cosmological models [Buchert and Räsänen, 2012]. In addition, even the separation of the dark sector in physically independent components such as a dark matter component and a dark energy may not be relevant with cosmological observations alone [Kunz, 2009].

In this section, we extend our previous analysis and add a dark energy fluid that goes beyond a simple cosmological constant, with the idea of studying the dark degeneracy from Kunz, 2009. More precisely, we examine the consequences of considering the simplest version of GDM (w constant and $c_s^2 = c_{\rm vis}^2 = 0$) when constraining the dark energy sector, with present-day observations and in the context of the future Euclid survey mission. We also focus on the simplest model for the dark energy (DE) sector too. In summary, we assume a constant equation of state for both sectors.

7.4.2 Dark content(s) of the Universe

In a first place, we use current observations from SNIa, BAO, and the CMB to constrain the equation of state for both GDM and DE. We pay special attention to correlations between both sectors.

Method and data samples

In the following, we assume a flat Robertson-Walker metric and Friedmann-Lemaître dynamics. We further assume that the GDM and the dark energy fluid do not interact, and that their equations of state are parametrized by the constants $w_{\rm dm}$ and $w_{\rm de}$, respectively. The Friedmann-Lemaître equation is then given by

$$\begin{aligned}\frac{H^2(z)}{H_0^2} =&\Omega_{\rm r}(1+z)^4+\Omega_{\rm b}(1+z)^3+\\ &(\Omega_{\rm m}-\Omega_{\rm b})(1+z)^{3(1+w_{\rm dm})}+\\ &(1-\Omega_{\rm r}-\Omega_{\rm m})(1+z)^{3(1+w_{\rm de})}\,,\end{aligned} \tag{7.6}$$

where the radiation density parameter is given by [Komatsu et al., 2011] [5]

$$\Omega_{\rm r}=\Omega_\gamma(1+0.2271N_{\rm eff}f)\,, \tag{7.7}$$

with $N_{\rm eff}=3.046$, $\Omega_\gamma=2.469\times10^{-5}h^{-2}$ and

$$f=\left\{1+\left[0.3173\cdot187\times10^3\left(\frac{m_\nu}{94\,\mathrm{eV}}\right)\left(\frac{1}{1+z}\right)\right]^{1.83}\right\}^{1/1.83}\,, \tag{7.8}$$

where m_ν is the sum of the mass of three neutrino families, which we have approximated to be equal to 0.

In order to determine the constraints on the different parameters, we follow the approach from the previous chapters and minimize the χ^2 function,

$$\chi^2=(\boldsymbol{u}-\boldsymbol{u}_{\rm data})^T C^{-1}(\boldsymbol{u}-\boldsymbol{u}_{\rm data})\,, \tag{7.9}$$

where $\boldsymbol{u}_{\rm data}$ is the data vector, $\boldsymbol{u}$ is the compressed likelihood parameters representation of the data in the models under investigation and C is the covariance matrix of the data. As we combine essentially independent probes, we obtain the total χ^2 function as the sum of each of them.

[5] Notice that it slightly differs from the approach presented in Chapter 1 and used in the main part of this thesis, but it has no impact on the final results.

The SNIa sample: For the SNIa data we use the compressed form [6] of the likelihood of the JLA sample [Betoule et al., 2014]. The χ^2 for the SNIa probe then reads

$$\chi^2 = \boldsymbol{r} C_b^{-1} \boldsymbol{r}^T \,, \tag{7.10}$$

with

$$\boldsymbol{r} = \boldsymbol{\mu}_b - M - 5\log_{10} d_{\rm L}(\boldsymbol{z}_b) \,, \tag{7.11}$$

where $\boldsymbol{\mu}_b$ is the vector of distance modulus at redshift $\boldsymbol{z}_b$ (binned redshifts), M is a free normalization parameter, C_b is the covariance matrix of $\boldsymbol{\mu}_b$ and $d_{\rm L}$ is the luminosity distance (see Betoule et al., 2014, for detailed explanations). It is important to note that the normalization parameter M must be left free in the fit and marginalized over when deriving uncertainties, in order to avoid introducing artificial constraints on the Hubble constant H_0.

Baryon acoustic oscillations: In this section, we use the isotropic BAO measurements at $z = 0.106$ [Beutler et al., 2011], $z = 0.35$ [Padmanabhan et al., 2012] and $z = 0.57$ [Anderson et al., 2012], following Planck Collaboration XVI [Planck Collaboration, 2014a], which consists in the data vector $d_{\rm z} = (0.336, 0.1126, 0.07315)$ and the inverse of the covariance matrix $C^{-1} = {\rm diag}(4444, 215156, 721487)$. We use the fitting formulas from Eisenstein and Hu, 1998, to compute the redshift of the baryon drag epoch, $z_{\rm d}$.

Cosmic microwave background: In this section we include CMB data into the analysis with the reduced parameters as in Chapter 5. We use the fitting formulas from Hu and Sugiyama, 1996, to compute the redshift of the last scattering epoch, z_*.

Models

We now present the different models considered in this section and the specific treatment of the CMB compressed likelihood.

wCDM model: We first study a reference model with standard cold dark matter and a dark energy component with constant equation of state parameter: $w_{\rm dm} = 0$ and $w_{\rm de} = w$ in Eq. (7.6). We denote this model wCDM (see for example Cheng and Huang, 2014, for a previous study of this model). Notice that w now stands for dark energy, as usual, and not as dark matter, as it was the case in the previous sections of this chapter.

[6] Notice that we do not use the full JLA likelihood in this section, as it is the case in the rest of the work. Since we are considering models close to the concordance one, the information inside the compressed likelihood is enough for our purposes.

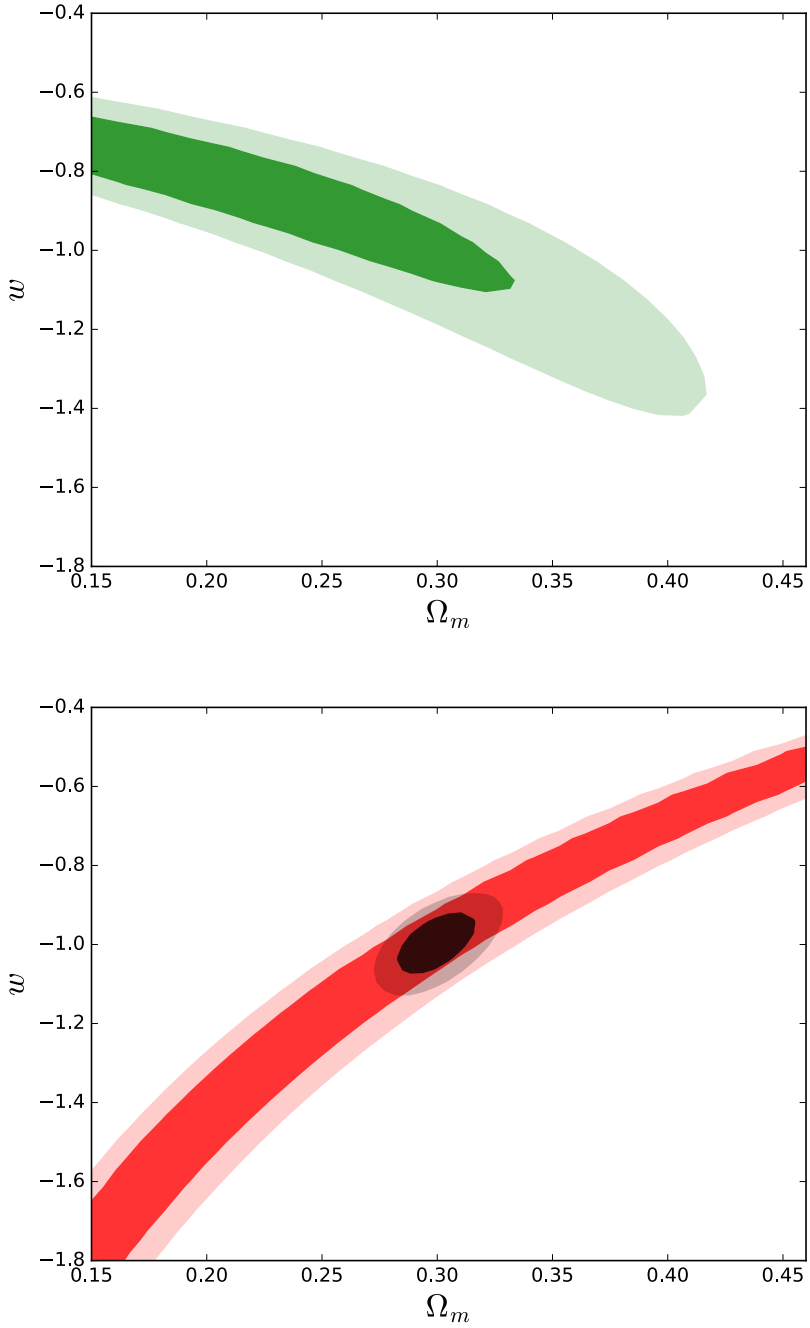

FIGURE 7.13: Confidence contours at 68% and 95% ($\Delta\chi^2 = 2.30$ and $\Delta\chi^2 = 6.17$, respectively) for the $\Omega_{\rm m}$ and w cosmological parameters of the wCDM model. *Top panel*: contours obtained using the SNIa and the BAO cosmological probes with $\omega_{\rm b} = 0.02262$ fixed. *Bottom panel*: the red contours correspond to the CMB probe while the black contours account for the combination of the three probes: SNIa, BAO and CMB.

TABLE 7.3: Cosmological parameter constraints for the different models and the different probes considered (Euclid GC stands for the spectroscopic galaxy clustering probe of the Euclid survey). The errors are given at the 1σ confidence level on one parameter ($\Delta\chi^2 = 1$). The ΛCDM model is included for comparison. The stars in some reduced baryon densities stand for fixed values. The dash in the ϵwCDM model using SNIa+BAO data stands for the extreme degeneracies which do not allow us to obtain significant constraints on the cosmological parameters.

		SNIa+BAO	Euclid GC	SNIa+BAO+CMB	Euclid GC + CMB
ΛCDM	$\Omega_{\rm m}$	$0.288^{+0.032}_{-0.031}$	$0.2984^{+0.0015}_{-0.0015}$	$0.2984^{+0.0096}_{-0.0092}$	$0.2984^{+0.0015}_{-0.0015}$
	H_0	$67.6^{+2.7}_{-2.4}$	$68.80^{+0.10}_{-0.10}$	$68.80^{+0.75}_{-0.74}$	$68.80^{+0.10}_{-0.10}$
	$\omega_{\rm b}$	0.02262^*	0.02257^*	$0.02257^{+0.00024}_{-0.00024}$	$0.022574^{+0.000098}_{-0.000098}$
wCDM	$\Omega_{\rm m}$	≤ 0.28	$0.299^{+0.022}_{-0.022}$	$0.299^{+0.012}_{-0.011}$	$0.2990^{+0.0021}_{-0.0021}$
	w	$-0.72^{+0.18}_{-0.25}$	$-0.995^{+0.026}_{-0.026}$	$-0.995^{+0.052}_{-0.054}$	$-0.994^{+0.022}_{-0.022}$
	H_0	$53.0^{+13.3}_{-5.5}$	$68.70^{+0.45}_{-0.45}$	$68.7^{+1.3}_{-1.3}$	$68.68^{+0.39}_{-0.40}$
	$\omega_{\rm b}$	0.02262^*	0.02259^*	$0.02259^{+0.00026}_{-0.00026}$	$0.022581^{+0.000098}_{-0.000098}$
ϵCDM	$\Omega_{\rm m}$	≥ 0.31	$0.301^{+0.010}_{-0.010}$	$0.301^{+0.014}_{-0.013}$	$0.3001^{+0.0030}_{-0.0030}$
	ϵ	$-0.49^{+0.44}_{-0.20}$	$-0.0003^{+0.0092}_{-0.0092}$	$-0.0003^{+0.0011}_{-0.0011}$	$-0.00024^{+0.00065}_{-0.00066}$
	H_0	$50.00^{+3.83}_{-0.90}$	$68.60^{+0.27}_{-0.27}$	$68.6^{+1.2}_{-1.2}$	$68.62^{+0.12}_{-0.12}$
	$\omega_{\rm b}$	0.02262^*	0.02262^*	$0.02262^{+0.00029}_{-0.00029}$	$0.02262^{+0.00029}_{-0.00029}$
ϵwCDM	$\Omega_{\rm m}$	–	$0.301^{+0.041}_{-0.041}$	$0.301^{+0.014}_{-0.013}$	$0.3011^{+0.0038}_{-0.0037}$
	w		$-1.01^{+0.13}_{-0.13}$	$-1.010^{+0.075}_{-0.077}$	$-1.010^{+0.023}_{-0.023}$
	ϵ		$0.000^{+0.046}_{-0.046}$	$-0.0004^{+0.0016}_{-0.0016}$	$-0.00045^{+0.00065}_{-0.00066}$
	H_0		$68.6^{+1.0}_{-1.0}$	$68.6^{+1.3}_{-1.3}$	$68.60^{+0.44}_{-0.43}$
	$\omega_{\rm b}$		0.02262^*	$0.02262^{+0.00029}_{-0.00029}$	$0.02262^{+0.00029}_{-0.00029}$

ϵCDM model: We define the ϵCDM model by assigning $w_{\rm dm} = 0 + \epsilon$ and $w_{\rm de} = -1$. This is the simplest version of ΛGDM. Since in this ϵCDM model we are modifying the matter component in the Universe and it has an extremely important role in the CMB era we must adapt the computation of z_* and $z_{\rm d}$ by changing $(\Omega_{\rm m} - \Omega_{\rm b})$ by $(\Omega_{\rm m} - \Omega_{\rm b})(1 + z_*)^{3\epsilon} \approx (\Omega_{\rm m} - \Omega_{\rm b})(10^3)^{3\epsilon}$ and compute the reduced parameter R as

$$R = \sqrt{(\Omega_{\rm b} + (\Omega_{\rm m} - \Omega_{\rm b})(1 + z_*)^{3\epsilon})H_0^2} \int_0^{z_*} \frac{{\rm d}z}{H(z)} \,. \tag{7.12}$$

This comes from the fact that we change $\Omega_{\rm dm}(z) = \Omega_{\rm m}(z) - \Omega_{\rm b}(z) = \Omega_{\rm dm}(1 + z)^3$ by $\Omega_{\rm dm}(z) = \Omega_{\rm dm}(1 + z)^{3(1+\epsilon)}$; therefore, the effective $\Omega_{\rm dm}$ that

should appear in the CMB era is given by

$$\Omega_{\rm dm}^{\rm eff} = \Omega_{\rm dm}\frac{(1+z_*)^{3(1+\epsilon)}}{(1+z_*)^3} = \Omega_{\rm dm}(1+z_*)^{3\epsilon}\,. \tag{7.13}$$

ϵwCDM model: Finally, we consider an extended version of the ϵCDM model allowing for variations in the dark matter and the dark energy sectors at the same time. We denote such a model as the ϵwCDM model, having two parameters for the dark sector, $w_{\rm dm} = \epsilon$ and $w_{\rm de} = w$. Notice that for this model we must keep the previous modifications on z_*, $z_{\rm d}$, and R since we modify the matter component.

Results

In order to perform the χ^2 minimization described in Sec. 7.4.2, we use the `migrad` application from the `minuit` tool [James and Roos, 1975]. To compute the contours and the errors on the parameters we use the profile-likelihood method described in Sec. 2.2.2.

In Fig. 7.13 we show the result of our analysis for the wCDM model, with the 1σ and 2σ contours obtained for the $\Omega_{\rm m}$ and w cosmological parameters. In the top panel only the information coming from the SNIa and the BAO probes has been used (fixing the reduced baryon density parameter to $\omega_{\rm b} = 0.02262$ [Planck Collaboration, 2016c]), while in the bottom panel the red contours correspond to the CMB probe and the black ones correspond to the combination of the three probes: SNIa+BAO+CMB. In these cases we have not fixed the baryon density as this quantity is well constrained by the CMB probe. We have marginalized over H_0 in both panels. The constraints obtained for the different models are summarized in Table 7.3. For the wCDM model, our constraints are (logically) very similar to those of Betoule et al., 2014, whose authors used the BAO, SNIa and CMB through temperature fluctuations from Planck 2013 and polarization fluctuations from WMAP.

In Fig. 7.14 the 1σ and 2σ contours for the $\Omega_{\rm m}$ and ϵ parameters of the ϵCDM model are represented. As in Fig. 7.13, the top panel corresponds to the result using only SNIa+BAO (fixing $\omega_{\rm b} = 0.02262$), while the bottom panel shows the CMB contours and the combination of the three probes, with marginalization over the baryon density. We have marginalized over H_0 in all cases. The specific constraints we have obtained are $\Omega_{\rm m} = 0.301^{+0.014}_{-0.013}$ and $\epsilon = -0.0003 \pm 0.0011$ (errors at 1σ on one parameter), which clearly differ from the result in Avelino, Cruz, and Nucamendi, 2012, where they provide $\epsilon = 0.009 \pm 0.002$ at the 3σ confidence level. This difference can be due to the use of different cosmological probes. However, our results are compatible with Thomas, Kopp, and Skordis,

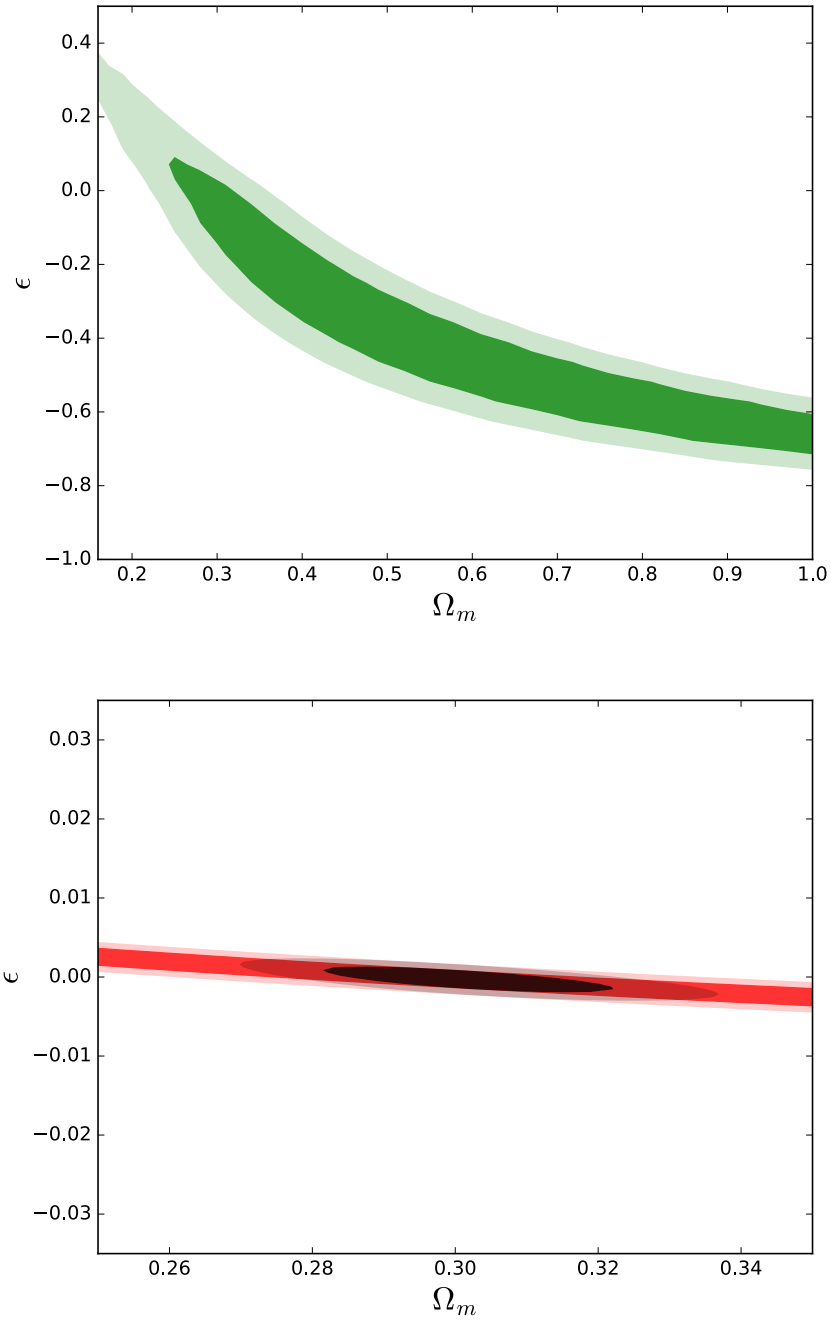

FIGURE 7.14: Confidence contours at 68% and 95% ($\Delta\chi^2 = 2.30$ and $\Delta\chi^2 = 6.17$, respectively) for the $\Omega_{\rm m}$ and ϵ cosmological parameters of the ϵCDM model. *Top panel*: contours obtained using the SNIa and the BAO cosmological probes with $\omega_{\rm b} = 0.02262$ fixed. *Bottom panel*: the red contours correspond to the CMB probe while the black contours account for the combination of the three probes: SNIa, BAO and CMB.

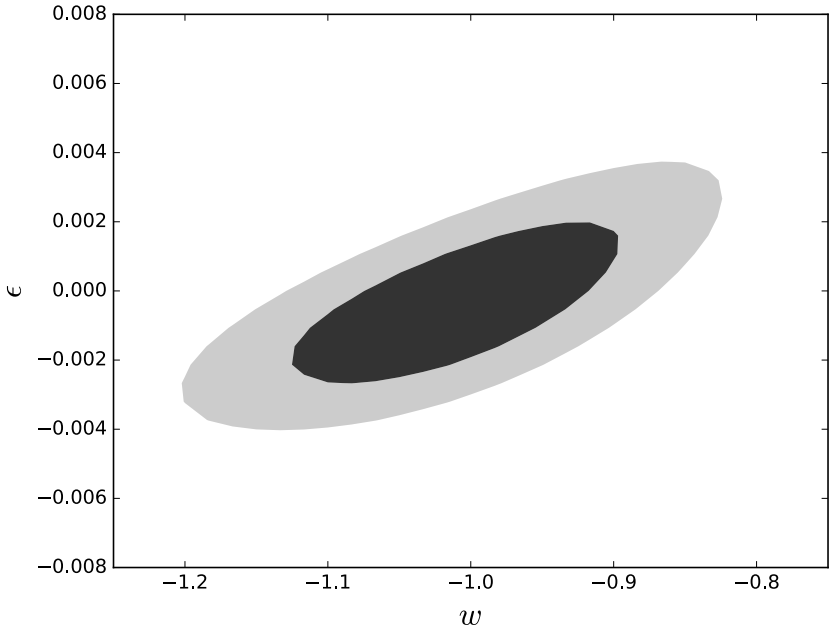

FIGURE 7.15: Confidence contours at 68% and 95% ($\Delta\chi^2 = 2.30$ and $\Delta\chi^2 = 6.17$, respectively) for the w and ϵ cosmological parameters of the ϵwCDM model. The combination of the three probes SNIa, BAO and CMB has been used.

2016, where the authors provide $\epsilon = 0.00063^{+0.00108}_{-0.00112}$ at the 2σ confidence level, using Planck data plus lensing information and the BAO probe.

Finally, in Fig. 7.15 the 1σ and 2σ contours for the w and ϵ cosmological parameters of the ϵwCDM model are provided. In this case only the combination of the three probes is represented, since the contours coming only from SNIa+BAO or only from the CMB are highly degenerate. We have marginalized over H_0 and ω_b. The specific constraints obtained are $w = -1.010^{+0.075}_{-0.077}$ and $\epsilon = -0.0004 \pm 0.0016$ (errors at 1σ on one parameter), which are slightly worse than for the wCDM and ϵCDM models due to the introduction of a new degree of freedom. Also, the sign of the correlation between ϵ and w may be surprising. We come back to this correlation at the end of this section.

As a conclusion, all the constraints we have obtained are compatible with the standard ΛCDM model. However, it is important to stress two points here: first of all, we have seen the strong role of the CMB probe (SNIa+BAO alone cannot provide us with good constraints for the cosmological parameters) and, secondly, we have seen that the constraints on dark matter and dark energy are not completely independent (see Fig. 7.15). This implies that all the assumptions made in one of the sectors may influence the constraints obtained in the other one.

7.4.3 Dark content(s) of the Universe: a Euclid forecast

We now focus on deriving the expected precision achievable on the previous models using the spectroscopic galaxy power spectrum Euclid survey in the linear regime. This probe is not included in the `CosmoSIS` pipeline described in Chapter 6. Merging it with the `CosmoSIS` pipeline is left for future work.

Notice that a recipe for spectroscopic galaxy clustering was already provided in Chapter 6. However, the approach used here is simpler and we provide again all the details in order to make this section self-consistent and reproducible.

Method

The forecast is based on a Fisher matrix formalism in a parametrized cosmological model considering the Hubble parameter and the angular-diameter distance as observables. We rely on the following matter power spectrum [Amendola et al., 2013]:

$$P_{\rm m}(k,z) = \frac{8\pi^2 c^4 k_0 \Delta^2_{\rm R}(k_0)}{25 H_0^4 \Omega_{\rm m}^2} T^2(k) \cdot \left[\frac{D_1(z)}{D_1(z=0)}\right]^2 \left(\frac{k}{k_0}\right)^{n_s} , \tag{7.14}$$

where $D_1(z)$ is the growth factor, $T(k)$ is the transfer function [Hu and Sugiyama, 1996; Eisenstein and Hu, 1999; Eisenstein and Hu, 1998], $k_0 = 0.002$ Mpc^{-1}, $\Delta^2_{\rm R}(k_0) = 2.45 \times 10^{-9}$ [Amendola et al., 2013] and $n_s = 0.96$ [Planck Collaboration, 2016b] is the spectral index. Notice that the matter power spectrum used in the GCs recipe from Chapter 6 is obtained from a Boltzmann solver, which is more accurate than the analytical formula used here.

The observed galaxy power spectrum is different from the matter power spectrum because of the biasing of galaxies and their velocity field. It can be related to $P_{\rm m}$ by [Seo and Eisenstein, 2003]

$$P_{\rm obs}(k_\perp, k_\parallel, z) = \frac{d_{\rm A}(z)^2_{\rm ref} H(z)}{d_{\rm A}(z)^2 H(z)_{\rm ref}} P_{\rm g}(k_\perp, k_\parallel, z) + P_s \,, \tag{7.15}$$

with

$$P_{\rm g}(k_\perp, k_\parallel, z) = b(z)^2 \left[1 + \beta(z) \frac{k_\parallel^2}{k_\parallel^2 + k_\perp^2}\right] P_{\rm m}(k,z) \,, \tag{7.16}$$

where $b(z)$ is the bias factor between the galaxy and matter distributions, $\beta(z) = f(z)/b(z) \approx \Omega_{\rm m}^{0.6}/b(z)$ [Seo and Eisenstein, 2007] and $k_\parallel$, $k_\perp$ stand for the parallel and transverse components of $\boldsymbol{k}$. P_s is an unknown residual noise which we neglect, since it is expected to introduce negligible error [Samushia et al., 2011]. The ref subscript stands for the reference cosmology.

For a given redshift interval, the Fisher matrix is given by [Tegmark, 1997]

$$F_{ij} = \int_{-1}^{1} \int_{k_{\rm min}}^{k_{\rm max}} \frac{\partial \ln P_{\rm obs}(k,\mu)}{\partial p_i} \frac{\partial \ln P_{\rm obs}(k,\mu)}{\partial p_j} \cdot \\ \cdot V_{\rm eff}(k,\mu) \frac{2\pi k^2 \, {\rm d}k \, {\rm d}\mu}{2(2\pi)^3} \,, \tag{7.17}$$

where we have changed $k_\parallel$, $k_\perp$ by k and μ (the modulus of $\boldsymbol{k}$ and the cosine of the angle between $\boldsymbol{k}$ and the line-of-sight, respectively). According to Seo and Eisenstein, 2003, the maximum scale of the survey $k_{\rm min}^{-1}$ has almost no effect on the results; therefore we adopt $k_{\rm min} = 0$. The minimum scale $k_{\rm max}^{-1}$ is used to exclude scales affected by the nonlinear regime, where our linear power spectra would be inaccurate. We interpolate the values given in Seo and Eisenstein, 2003, for $k_{\rm max}$. The effective volume of the survey is given by

$$V_{\rm eff}(k,\mu) = \int \left[\frac{n(\boldsymbol{r}) P(k,\mu)}{n(\boldsymbol{r}) P(k,\mu) + 1} \right]^2 {\rm d}\boldsymbol{r} \\ = \left[\frac{nP(k,\mu)}{nP(k,\mu)+1} \right]^2 V_{\text{co-moving}} \,. \tag{7.18}$$

The last equality holds for a uniform density of galaxies. The co-moving volume of the survey $V_{\text{co-moving}}$ is given by Eq. (6.6). According to Seo and Eisenstein, 2003, we multiply the integrand of the Fisher matrix by an exponential suppression $e^{-k^2\mu^2\sigma_r^2}$, with $\sigma_r = c\sigma_z / H(z)$, in order to take into account the redshift error σ_z of the galaxy survey. Once we have obtained the Fisher matrix for the observables $H(z)$ and $d_{\rm A}(z)$ we can propagate it to the Fisher matrix for the parameters using a Jacobian transformation [see e.g. Wang et al., 2010]

$$F_{\alpha\alpha'} = \sum_{ij} \frac{\partial p_i}{\partial q_\alpha} F_{ij} \frac{\partial p_j}{\partial q_{\alpha'}} \,, \tag{7.19}$$

where p_i stand for the observables $H(z)$ or $d_{\rm A}(z)$, and q_α for the parameters under study. The Fisher matrix for all the redshift range of the survey is given by the sum of the Fisher matrices for each redshift bin. The inverse of the resulting Fisher matrix gives us the uncertainties and correlations of all the parameters studied in the forecast.

If we compare the recipe presented in this section with the GCs recipe provided in Chapter 6, we can see that we also include here the same effects: Alcock-Pacyznski effect, redshift-space distortions, shot-noise, and the uncertainty of the spectroscopic redshifts. However, this approach is simpler because we do not consider any non-linearities (like the Fingers-of-God effect), we fix the shape parameters of the power spectrum (which is analytical in this case), we assume

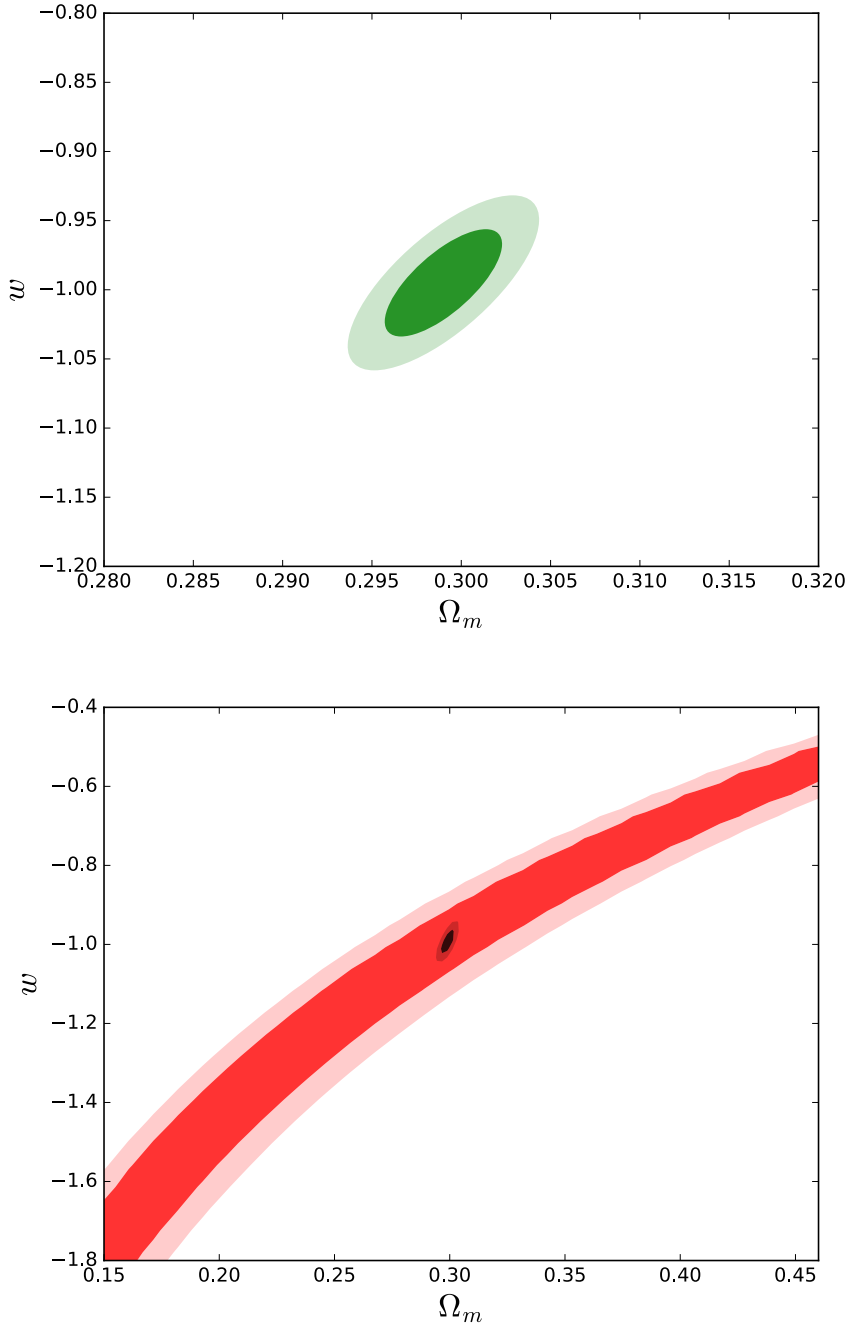

FIGURE 7.16: Confidence contours at 68% and 95% ($\Delta\chi^2 = 2.30$ and $\Delta\chi^2 = 6.17$, respectively) for the $\Omega_{\rm m}$ and w cosmological parameters of the wCDM model. *Top panel*: contours obtained using the Euclid spectroscopic galaxy clustering forecast with $\omega_{\rm b} = 0.02262$ fixed. *Bottom panel*: the red contours correspond to the CMB probe while the black contours account for the combination of the CMB and the Euclid spectroscopic galaxy clustering forecast.

that our fiducial cosmology is the true one (removing any AP effect), and we fix the remaining nuisance parameters [like the galaxy bias (detailed in the following) or the shot-noise]. Although this approach is simpler than the previously presented one, it is sufficient for our purposes in this section.

Euclid spectroscopic survey

In this section, we restrict ourselves to the spectroscopic galaxy clustering probe of the Euclid mission. In order to adapt our forecast to it, we only need five parameters, whose values are taken from the Euclid Red-book [Laureijs et al., 2011]: the minimum and maximum redshift, $z_{\rm min} = 0.7$, $z_{\rm max} = 2.1$; the area, 15000 square degrees; the number of galaxies, 50×10^6; and the precision of the redshift estimation, $\sigma_z/(1+z) \leq 0.1\%$. We adopt the galaxy bias given in Amendola et al., 2013: $b(z) = \sqrt{1+z}$. We split the redshift range of the survey into bins of width 0.1 in redshift. Narrower bins only marginally increase the precision while requiring more computational time. Finally, the reference cosmology is the one obtained in Sec. 7.4.2 and it is summarized in the fifth column of Table 7.3. Notice that only the area of the survey is common to the more robust approach presented in Chapter 6.

In this section we limit ourselves to the spectroscopic survey on linear scales. We have checked that the photometric galaxy clustering only marginally improves the constraints on the parameters, while including weakly nonlinear scales noticeably improves these constraints. Combination with the weak lensing probe would obviously lead to even better constraints [Majerotto et al., 2012]. A quantitative evaluation of these improvements is left for future work.

Results

The results for the wCDM model are represented in Fig. 7.16. In the top panel the 1σ and 2σ contours for the $\Omega_{\rm m}$ and w cosmological parameters are computed using the Euclid spectroscopic galaxy power spectrum forecast and fixing the reduced baryon density parameter to its reference value $\omega_{\rm b} = 0.02257$. In the bottom panel the red contours correspond to the CMB probe and the black contours stand for the combination of the CMB and the forecast assuming a Gaussian likelihood for the latter. More precisely, when minimizing the χ^2 function as presented in Eq. (7.9), we minimize the sum of the χ^2 corresponding to the CMB plus a χ^2 function associated to the forecast where the covariance matrix is directly the one provided by the forecast. We have marginalized over H_0 in all the figures. The results of the forecast are the following constraints: $\Omega_{\rm m} = 0.299 \pm 0.022$ and $w = -0.995 \pm 0.026$ (errors at 1σ on one parameter), which are much better than the degeneracy obtained

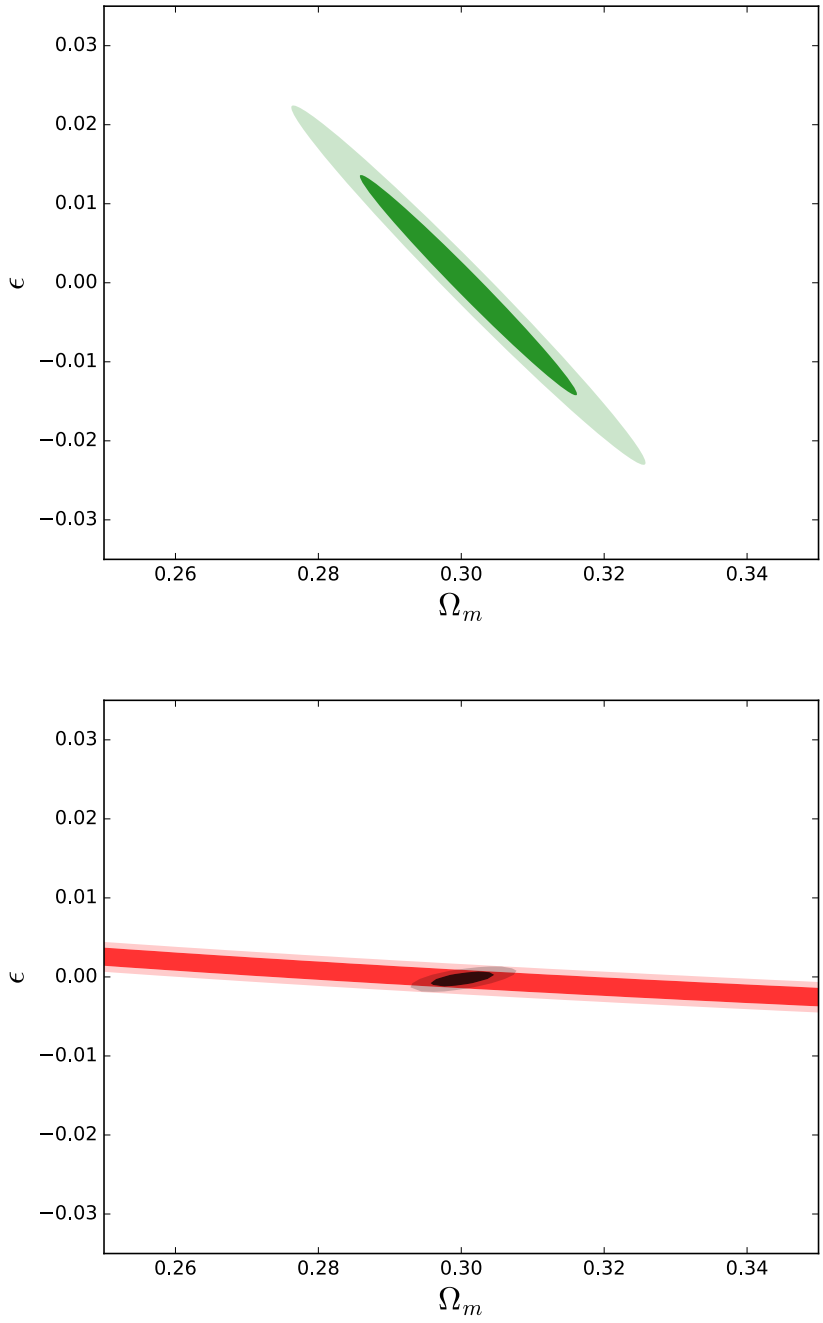

FIGURE 7.17: Confidence contours at 68% and 95% ($\Delta\chi^2 = 2.30$ and $\Delta\chi^2 = 6.17$, respectively) for the $\Omega_{\rm m}$ and ϵ cosmological parameters of the ϵCDM model. *Top panel*: contours obtained using the Euclid spectroscopic galaxy clustering forecast with $\omega_{\rm b} = 0.02262$ fixed. *Bottom panel*: the red contours correspond to the CMB probe while the black contours account for the combination of the CMB and the Euclid spectroscopic galaxy clustering forecast.

with SNIa+BAO present-day data (Fig. 7.13, top panel). Combination with the CMB gives $\Omega_{\rm m} = 0.2990 \pm 0.0021$ and $w = -0.994 \pm 0.022$ (errors at 1σ on one parameter), which are between a factor 2 and 6 better than SNIa+BAO+CMB present-day data constraints (Fig. 7.13, bottom panel).

The 1σ and 2σ contours for the $\Omega_{\rm m}$ and ϵ cosmological parameters of the ϵCDM model are represented in Fig. 7.17. As in Fig. 7.16, the top panel corresponds to the Euclid spectroscopic galaxy power spectrum forecast with fixed baryon density, while the bottom panel corresponds to the CMB (red) and the combination of the forecast and the CMB (black) contours. We have also marginalized over H_0 in all the figures. The specific constraints given by the forecast are $\Omega_{\rm m} = 0.301 \pm 0.010$ and $\epsilon = -0.0003 \pm 0.0092$ (errors at 1σ on one parameter), which again have greatly improved compared to the degeneracy found with SNIa+BAO present-day data (Fig. 7.14, top panel). Adding the CMB we obtain the constraints, $\Omega_{\rm m} = 0.3001 \pm 0.0030$ and $\epsilon = -0.00024^{+0.00065}_{-0.00066}$ (errors at 1σ on one parameter), which are between a factor 2 and 5 better than present-day SNIa+BAO+CMB constraints (Fig. 7.14, bottom panel).

Let us recall that all the results shown here are only for the spectroscopic galaxy clustering probe restricted to the linear scales, so we can expect significantly better constraints from the full exploitation of the future Euclid survey data.

Figure 7.18 provides the 1σ and 2σ contours for the w and ϵ cosmological parameters of the ϵwCDM model. The top panel corresponds to the forecast with fixed baryon density, while the bottom panel shows, in addition, the combination of the forecast with the CMB. We have marginalized over H_0 in both cases. The specific constraints we have obtained using the forecast are $w = -1.01 \pm 0.13$ and $\epsilon = 0.000 \pm 0.046$ (errors at 1σ on one parameter), which are much better than present-day SNIa+BAO degeneracies that do not provide any significant constraint (see the absence of constraints in the third column of Table 7.3). This is a remarkable result illustrating that Euclid can break this degeneracy in the dark sector at low-redshift.

It is worth noticing, apart from the better constraints expected from the Euclid survey, that we still find[7] a significant correlation between the ϵ and w cosmological parameters from the Euclid survey (Fig. 7.18, top panel, green contour) illustrating the fact that the dark matter and the dark energy sectors are not completely uncoupled and cannot be constrained independently from each other. However, the sign of this correlation may be somewhat surprising:

[7] We have checked that changing (by a 20% difference) the fixed value for the reduced baryon density parameter negligibly affects the $\epsilon - w$ contours.

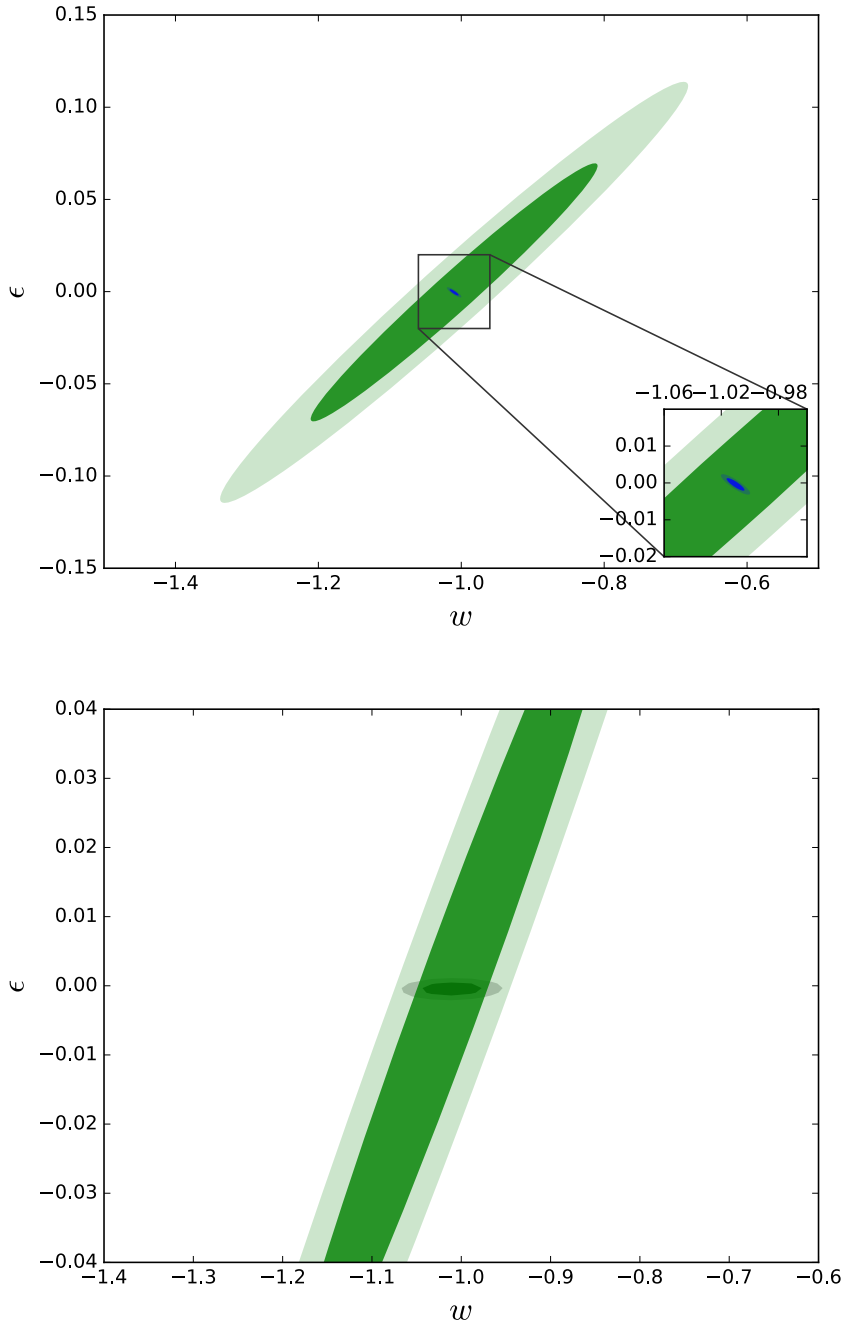

FIGURE 7.18: Confidence contours at 68% and 95% ($\Delta\chi^2 = 2.30$ and $\Delta\chi^2 = 6.17$, respectively) for the ϵ and w cosmological parameters of the ϵwCDM model. *Top panel*: contours obtained using the Euclid spectroscopic galaxy clustering forecast with $\omega_\mathrm{b} = 0.02262$ fixed. In the small box on the lower right corner, the equivalent contours when fixing $H_0 = 68.6\ \mathrm{km\,s^{-1}\,Mpc^{-1}}$ and $\Omega_\mathrm{m} = 0.301$ are represented. *Bottom panel*: the green contours correspond to the forecast while the black contours account for the combination with the CMB, marginalizing over the baryon density.

if the total density were to be constant we would expect w and ϵ to be anti-correlated. We have checked that this is indeed the case, when all the other parameters are kept fixed (see the small box in Fig. 7.18, left panel). When marginalizing over H_0 and $\Omega_{\rm m}$ the correlation changes and leads to weak constraints on the dark energy equation of state parameter, $w = -1.01 \pm 0.13$ ($w = -1.01$ being the fiducial value that corresponds to our best estimate in view of present-day constraints), and on the equation of state of dark matter $\epsilon = 0 \pm 0.046$.

Adding the CMB constraint to the forecast results in much more stringent limits on the parameters describing the dark sector, $w = -1.010 \pm 0.023$ and $\epsilon = -0.00045^{+0.00065}_{-0.00066}$ (errors at 1σ on one parameter), which are similar to the obtained constraints on the wCDM and the ϵCDM model parameters (Figs. 7.16 and 7.17, respectively). This fact highlights again the strong role of the CMB in breaking degeneracies thanks to the strong constraint on the dark matter equation of state parameter.

7.4.4 Summary

We have investigated in this section the degeneracy between GDM and dark energy. We restricted ourselves to the simple case of constant equation of state parameter for both dark sectors. Even if not fully theoretically motivated, these simple models allow us to ascertain the maximum values that the equation of state parameters are allowed to take [Kunz, Nesseris, and Sawicki, 2016]. We have found that cosmological constraints from present-day SNIa and BAO data are strongly degraded, revealing a complete degeneracy between the equations of state of dark matter and dark energy. The constraints are essentially restored by the inclusion of CMB data thanks to its leverage. We have then studied the anticipated accuracy from the Euclid spectroscopic redshift galaxy survey. We have found that Euclid is expected to break the above degeneracy between dark matter and dark energy, but the high accuracy on the dark energy equation of state parameter is lost. Combining with the CMB allows us to restore constraints at a similar level to the $w_{\rm dm} = 0$ forecast in the specific model we investigated. We expect even better performance from the full exploitation of the future Euclid survey data, but the remaining correlation between dark matter and dark energy equation of state parameter deserves further investigation.

As a last remark, it would be also interesting to extend this analysis not only using the full Euclid survey, but also allowing the equation of state parameters to vary as a function of the redshift. There has recently been an analysis [Kopp et al., 2018] addressing this question for GDM alone by binning the equation of state parameter for GDM as a function of the redshift. The authors of this paper have observed strong degeneracies between the cosmological parameters,

especially at low-redshift. Extending our analysis to a binned equation of state parameter for both dark sectors, and check if Euclid would be able to break the degeneracies, is also left for future work.

Conclusions

[English version]

The main objective of this thesis was to forecast the constraining power of the future Euclid satellite for the concordance ΛCDM model, and simple extensions beyond it. Our goal was not only to estimate the constraining power from the different cosmological probes [galaxy clustering (GC) and weak lensing (WL)], but especially to combine them taking into account their cross-correlations, in order to quantify their impact for future cosmological analyses. A second objective of this work was to study phenomenological models for the dark components of the Universe beyond the standard approach both with current observations, and with the future Euclid data. In the following we present the main conclusions from this thesis. We show the different topics in the same order of appearance in the thesis.

Let us start with the exotic phenomenological model for dark energy, where the expansion rate of the Universe is given by a power law (Chapter 4). We have fitted the concordance ΛCDM model, the power law model, and the specific case $R_{\rm h} = ct$ to current data from background cosmological probes both at low-redshift [type Ia supernovae (SNIa) and baryon acoustic oscillations (BAO)] and at high-redshift [cosmic microwave background (CMB)]. And we have then compared the different models with robust model selection criteria. Starting with low-redshift probes, we have seen that all models are able to provide a good fit to the data, but the $R_{\rm h} = ct$ model is disfavored with respect to the others from a model comparison point-of-view, even if it has less parameters. However, if we add information coming from the CMB, both the general power law model and the $R_{\rm h} = ct$ model are completely ruled out, since they cannot fit at the same time the BAO scale and the CMB scale. This shows that these exotic models can fit the low-redshift data, but they are completely excluded if we extrapolate them up to the redshift of the CMB.

Let us now consider the study of the impact of SNIa luminosity-redshift dependence on the conclusions we can draw on the accelerated nature of the expansion of the Universe (Chapter 5). It is important to mention that, even if there are no evidences supporting such dependence, the difficulty of perfectly modeling SNIa leaves enough uncertainty to consider it. And, more importantly, it is important to know if there are degeneracies between redshift-dependent

astrophysical systematics in SNIa analyses and the cosmological conclusions we obtain from them. In a first step, we have considered only low-redshift data to focus on the region where cosmic acceleration starts. We have considered a non-accelerated power law model and tested it against the observations when we allow SNIa intrinsic luminosity to evolve as a function of the redshift. Notice that even if we ruled out the power law model in Chapter 4 when we extrapolate it up to the redshift of the CMB, there is nothing preventing us from considering it at low-redshift as a null test, since we do not specify the evolution of the model at high-redshift. We have considered a bunch of SNIa luminosity evolution models to be as general as possible, and we have shown that, even adding measurements from the growth of structures, a non-accelerated power law model can perfectly fit the main low-redshift cosmological observations if SNIa intrinsic luminosity is allowed to vary as a function of the redshift. In a second step we have performed a much more robust analysis including also CMB data and reconstructing the expansion rate of the Universe with a model-independent approach. We have shown that a non-accelerated expansion of the Universe can nicely fit not only the low-redshift probes, but also the CMB when SNIa intrinsic luminosity is allowed to vary as a function of the redshift. However, we have also shown that the value of H_0 for these reconstructions is significantly smaller than current measurements. Quantitatively, a non-accelerated reconstruction is in $3\,\sigma$-$6\,\sigma$ tension with H_0, depending on the method used to measure it. We can conclude that a consensus on the value of H_0 and its precision will be decisive to finally prove cosmic acceleration independently of any cosmological model and redshift dependent astrophysical systematic that may remain in SNIa analyses.

Focusing now on the core of the thesis (Chapter 6), we present the main conclusions on our predictions for Euclid. In a first step, we have presented the baseline results for WL alone, where we have considered the w_0w_aCDM cosmological model, with the eNLA model for intrinsic alignments (IA), 1 massive neutrino of mass 0.06 eV and 2 massless neutrinos, the `halofit` recipe to correct for the non-linearities, a cut to discard scales smaller than $\ell_{\rm max} = 1500$, a flat universe, the 3-point stencil method for the numerical derivatives (with a step of 4 % on the parameters), and `CAMB` as Boltzmann solver. We have shown that WL alone will be able to put strong constraints on some parameters (like $\Omega_{\rm m}$ and σ_8), while the others will be significantly degenerate. We claim a baseline Figure of Merit (FoM) of 23.1. After that, we have quantitatively assessed the impact of each one of our baseline assumptions on the final results. We have seen that neglecting IA improves the FoM, but the constraints on the parameters remain roughly the same, while massless neutrinos do not significantly change any conclusion, as it is the case for the method used for the numerical derivatives, or the Boltzmann solver used. However, we have detected a

strong dependence on the non-linear recipe, even after discarding the smallest scales from the analysis. Our baseline FoM is stable with respect to numerical choices, and quite general in terms of cosmology. However, our knowledge of the non-linear scales is very important to trust our results.

In a second step, we have presented our forecast for the photometric GC (GCp) alone. The only difference in the baseline used is that we now consider the galaxy bias, instead of the IA. We have seen that GCp alone is less constraining than WL with a FoM of 5.6, but it is able to constrain some parameters (like $\Omega_{\rm b}$ and h) better than WL. As before, we have assessed the effect of each one of our baseline assumptions, and we have seen that our knowledge on galaxy bias is vital to improve the constraints from GCp. In general, GCp is slightly more sensitive to numerical choices than WL, due to the need of better sampling the wiggles from the spectra; nevertheless, our baseline results are again quite general in terms of cosmology and numerical assumptions. The most important common factor with WL is that the non-linear recipe used plays an important role, even after neglecting the smallest scales.

In a third step, we have combined GCp and WL with and without their cross-correlations for our baseline, and we have modified all the baseline assumptions to check their impact on the final results. We have shown that the basic combination of GCp and WL neglecting their cross-correlations already improves the FoM up to 61.5, but, more importantly, when we add the cross-correlations its value is boosted up to 299.2. It clearly shows that not only the cross-correlations cannot be neglected in the future Euclid data, but also that they significantly help in improving our constraints. Also, cross-correlations are not only able to reduce the constraints on the cosmological parameters, but also on the nuisance ones. In particular, they help in improving our knowledge of intrinsic alignments. Concerning the different assumptions of the baseline, we find conclusions in between those of WL and GCp alone, showing that our results are again quite general in terms of cosmology, and quite stable with respect to numerical assumptions.

As a last point from Chapter 6, we have combined the main Euclid probes [GCp, WL, and spectroscopic GC (GCs)] together with their cross-correlations. Since it is not straightforward to combine three-dimensional and two-dimensional data without loosing information, we have considered a very conservative case, an optimistic one, and a very optimistic one. The final Euclid FoM varies from 373.6 to 521.6 and 840.4. The realistic FoM should be in between these values, but a more robust modeling of the cross-correlations between three and two-dimensional data, as well as a better model for non-linearities and non-Gaussianities is required. All these aspects define new perspectives for future work. In any case, with the approach presented in this work it is out of doubt

that Euclid will be able to provide us with exquisite constraints on the cosmological parameters, and that it will perfectly reach all our expectations.

In the last chapter of the thesis (Chapter 7), we have considered a phenomenological model for dark matter beyond the standard approach; the so-called generalized dark matter model, where we allow dark matter to have some pressure and some sound speed. In a first step we have studied this model with state-of-the-art observations both from low and high-redshift, and at the background and perturbations level. We have shown that current observations are able to put very strong constraints on dark matter (always compatible with the standard cold dark matter), but the allowed values are still large enough to be able to reduce the tension on H_0 and σ_8 between low and high-redshift data. Since we do not have any recipe to correct for the non-linearities in our predictions for this model, we have considered a conservative approach by just keeping the largest scales and turning on and off the standard `halofit` recipe. We have seen that the addition of WL data can strongly reduce the constraints on dark matter, and significantly improve our knowledge of this dark fluid. However, an adequate non-linear recipe is needed to use smaller scales and improve even more our knowledge. In a second step we have forecasted the constraints from the future Euclid data (using only the photometric survey in this case). We have shown that the photometric part of Euclid alone will be able to provide exquisite constraints on dark matter but it is even more important than before to obtain an appropriate non-linear recipe, in order to be able to use all the precise future Euclid data. In the last section of the chapter, we have considered a very basic phenomenological extension of both dark matter and dark energy beyond ΛCDM. We have shown that current low-redshift data are not able to place any constraints because of the degeneracies between both fluids. However, GCs from Euclid alone will able to place nice constraints on both components at the same time, and these constraints will become extremely precise once we combine with CMB data.

In order to conclude the conclusions, in this thesis we have shown that Euclid will be able to provide exquisite constraints on the cosmological parameters, not only for ΛCDM and simple extensions beyond it, but also for more elaborated dark matter models. We have provided enough details to claim that cross-correlations between galaxy clustering and weak lensing cannot be neglected in future surveys like Euclid, and, more importantly, they can largely help in improving our knowledge of the dark sector of the Universe. However, it is clear that we need to better understand the non-linear scales, and the non-Gaussianities that may arise in the observables covariances or the likelihood, as well as the cross-correlations between three-dimensional and two-dimensional data to properly analyze all the future available Euclid data and extract the

maximum of information from it. These aspects, together with the inclusion of systematic and foreground effects in the forecasts, more detailed studies about the stability of numerical derivatives or the Boltzmann solver used, forecasts for Euclid power in constraining the mass of neutrinos, or forecasts beyond the Fisher approximation, establish new perspectives for future work.

[Version française]

L'objectif principal de cette thèse était de prévoir la puissance de contrainte du futur satellite Euclid pour le modèle de concordance ΛCDM et des extensions simples au-delà. Notre objectif n'était pas seulement d'estimer le pouvoir contraignant des différentes sondes cosmologiques [groupement de galaxies (GC) et lentilles faibles (WL)], mais de les combiner en tenant compte de leurs corrélations croisées, afin de quantifier leur impact pour les analyses cosmologiques futures. Un deuxième objectif de ce travail était d'étudier les modèles phénoménologiques pour les composantes sombres de l'Univers au-delà de l'approche standard à la fois avec les observations actuelles et avec les données futures d'Euclid. Nous présentons ci-après les principales conclusions de cette thèse. Nous montrons les différents sujets dans le même ordre d'apparition que celui du manuscrit.

Commençons par le modèle phénoménologique exotique pour l'énergie sombre, où le taux d'expansion de l'Univers est donné par une loi de puissance (chapitre 4). Nous avons ajusté le modèle de concordance ΛCDM, le modèle de loi de puissance et le cas spécifique $R_\mathrm{h} = ct$ aux données actuelles des sondes cosmologiques de fond à la fois à faible redshift [supernovae de type Ia (SNIa) et oscillations acoustiques baryoniques (BAO)] et à haut redshift [fond diffus cosmologique (CMB)]. Nous avons ensuite comparé les différents modèles avec des critères de sélection de modèles robustes. En partant des données à bas redshift, nous avons vu que tous les modèles sont en mesure de s'adapter aux données, mais le modèle $R_\mathrm{h} = ct$ est défavorisé par rapport aux autres du point de vue de la comparaison de modèles, bien qu'il ait moins de paramètres. Si nous ajoutons des informations provenant du CMB, le modèle général de loi de puissance et le modèle $R_\mathrm{h} = ct$ sont complètement exclus, puisqu'ils ne peuvent pas s'adapter en même temps à l'échelle BAO et à l'échelle CMB. Cela montre que ces modèles exotiques peuvent s'adapter aux données de bas redshift, mais ils sont complètement exclus si on les extrapole jusqu'au redshift du CMB.

Considérons maintenant l'étude de l'impact de la dépendance de la luminosité des SNIa avec le redshift sur les conclusions que nous pouvons tirer de la nature accélérée de l'expansion de l'Univers (chapitre 5). Il est important de mentionner que, même s'il n'y a pas de preuves à l'appui de cette dépendance, la difficulté de parfaitement modéliser les SNIa laisse suffisamment d'incertitude pour la considérer. Et, plus important encore, il est nécessaire de déterminer s'il existe des dégénérescences entre des systématiques astrophysiques qui dépendent du redshift dans les analyses SNIa et les conclusions cosmologiques que nous tirons de celles-ci. Dans une première étape, nous n'avons considéré que les données à bas redshift pour se concentrer sur la région où l'accélération cosmique commence. Nous avons considéré un modèle en loi de puissance non

accélérée et l'avons testé par rapport aux observations lorsque nous permettons à la luminosité intrinsèque des SNIa d'évoluer en fonction du redshift. Notez que même si nous avons exclu le modèle de loi de puissance au chapitre 4 quand nous l'extrapolons jusqu'au redshift du CMB, rien ne nous empêche de le considérer comme un test d'hypothèse nulle à bas redshift, puisque nous ne spécifions pas l'évolution du modèle à haut redshift. Nous avons considéré plusieurs modèles d'évolution de la luminosité des SNIa pour être aussi général que possible et nous avons montré que même en ajoutant des mesures de croissance de structures, un modèle de loi de puissance non accélérée peut parfaitement correspondre aux observations cosmologiques si la luminosité intrinsèque varie en fonction du redshift. Dans une deuxième étape, nous avons effectué une analyse beaucoup plus robuste incluant également des données CMB et reconstruisant le taux d'expansion de l'Univers avec une approche indépendante du modèle. Nous avons montré qu'une expansion non accélérée de l'Univers peut parfaitement s'adapter non seulement aux sondes à bas redshift, mais aussi au CMB lorsque la luminosité intrinsèque de la SNIa peut varier en fonction du redshift. Cependant, nous avons également montré que la valeur de H_0 pour ces reconstructions est significativement plus petite que les mesures actuelles. Quantitativement, une reconstruction non accélérée est en tension de $3\,\sigma$-$6\,\sigma$ avec H_0, selon la méthode utilisée pour la mesurer. Nous pouvons conclure qu'un consensus sur la valeur de H_0 et sa précision sera décisif pour finalement démontrer l'accélération cosmique indépendamment de tout modèle cosmologique et de toute systématique astrophysique dépendante du redshift qui pourrait subsister dans les analyses des SNIa.

En nous concentrant maintenant sur le noyau de la thèse (chapitre 6), nous présentons les principales conclusions sur nos prédictions pour Euclid. Dans un premier temps, nous avons présenté les résultats de référence pour WL seul, où nous avons considéré le modèle cosmologique w_0w_aCDM, avec le modèle eNLA pour les alignements intrinsèques (IA), 1 neutrino massif de masse 0.06 eV et 2 neutrinos sans masse, la méthode `halofit` pour corriger les non-linéarités, une coupure pour écarter des échelles inférieures à $\ell_{\rm max} = 1500$, un univers plat, des dérivées numériques centrées à 3 points (avec un pas de 4 % sur les paramètres) et `CAMB` comme solveur de Boltzmann. Nous avons montré que WL seul sera capable de mettre de fortes contraintes sur certains paramètres (comme $\Omega_{\rm m}$ et σ_8), alors que les autres seront significativement dégénérés. Nous obtenons une figure de mérite (FoM) de référence de 23,1. Après cela, nous avons modifié chacune des hypothèses faites dans notre base de référence pour vérifier leur impact sur les résultats finaux. Nous avons vu que négliger les IA améliore la FoM, mais les contraintes sur les paramètres restent à peu près les mêmes, alors que les neutrinos sans masse ne changent pas de façon significative, comme

c'est le cas pour la méthode utilisée pour les dérivées numériques ou le solveur de Boltzmann utilisé. Cependant, nous avons détecté une forte dépendance à la correction non linéaire, même après avoir écarté les plus petites échelles de l'analyse. Notre FoM de référence est stable par rapport aux choix numériques et assez générale en termes de cosmologie. Cependant, notre connaissance des échelles non linéaires est très importante pour faire confiance à nos résultats.

Dans un deuxième temps, nous avons présenté nos prévisions pour le GC photométrique (GCp) seul. La seule différence dans la base de référence utilisée est que nous considérons maintenant le biais des galaxies au lieu des IA. Nous avons vu que GCp seul est moins contraignant que WL avec une FoM de 5,6, mais il est capable de contraindre certains paramètres (comme $\Omega_{\rm b}$ et h) mieux que WL. Comme précédemment, nous avons modifié chacune des hypothèses faites dans la base de référence et nous avons vu que nos connaissances sur le biais des galaxies sont essentielles pour améliorer les contraintes obtenues avec GCp. En général, GCp est légèrement plus sensible aux choix numériques que WL, en raison du besoin de mieux échantillonner les oscillations des spectres, mais nos résultats de base sont à nouveau assez généraux en termes de cosmologie et d'hypothèses numériques. Le facteur commun le plus important avec WL est que la méthode non linéaire utilisée joue un rôle important, même après avoir négligé les plus petites échelles.

Dans une troisième étape, nous avons combiné GCp et WL avec et sans leurs corrélations croisées pour notre base de référence et nous avons modifié toutes les hypothèses de base pour vérifier leur impact sur les résultats finaux. Nous avons montré que la combinaison basique de GCp et WL en négligeant leurs corrélations croisées améliore déjà la FoM jusqu'à 61,5, mais, plus important encore, lorsque nous ajoutons les corrélations croisées, sa valeur est augmentée jusqu'à 299,2. Cela montre clairement que non seulement les corrélations croisées ne peuvent pas être négligées dans les futures données Euclid, mais qu'elles contribuent également de manière significative à l'amélioration de nos contraintes. De plus, les corrélations croisées sont non seulement capables de réduire les incertitudes sur les paramètres cosmologiques, mais aussi sur les paramètres de nuisance. En particulier, ils aident à améliorer nos connaissances sur les alignements intrinsèques. En ce qui concerne les différentes hypothèses de la ligne de base, nous trouvons des conclusions entre celles de WL et GCp seuls, montrant que nos résultats sont encore assez généraux en termes de cosmologie et assez stables par rapport aux hypothèses numériques.

Comme dernier point du chapitre 6, nous avons combiné les principales sondes d'Euclid [GCp, WL et GC spectroscopique (GCs)] avec leurs corrélations croisées. Comme il n'est pas simple de combiner des données tridimensionnelles et bidimensionnelles sans perdre d'informations, nous avons considéré un cas

très conservateur, un cas optimiste et un cas très optimiste. La FoM finale d'Euclid varie de 373,6 à 521,6 et 840,4. La FoM réaliste devrait se situer entre ces valeurs, mais une modélisation plus robuste des corrélations croisées entre les données tridimensionnelles et bidimensionnelles, ainsi qu'un meilleur modèle pour les non-linéarités et les non-gaussianités est nécessaire. Tous ces aspects sont laissés pour un travail futur. En tout cas, avec l'approche présentée dans ce travail, il n'y a aucun doute qu'Euclid pourra nous fournir des contraintes excellentes sur les paramètres cosmologiques et qu'il atteindra parfaitement tous ses objectifs.

Dans le dernier chapitre de la thèse (chapitre 7), nous avons considéré un modèle phénoménologique de la matière noire au-delà de l'approche standard; le modèle dit de matière noire généralisée, où nous permettons à la matière noire d'avoir une certaine pression et une certaine vitesse sonore. Dans un premier temps, nous avons étudié ce modèle avec des observations actuelles à la fois à bas et haut redshift, du fond et au niveau de perturbations. Nous avons montré que les observations actuelles sont capables de mettre de très fortes contraintes sur la matière noire (toujours compatible avec la matière noire froide standard), mais les valeurs permises sont encore assez importantes pour réduire la tension sur H_0 et σ_8 entre des données de bas et haut redshift. Comme nous n'avons aucune méthode pour corriger les non linéarités de nos prédictions pour ce modèle, nous avons considéré une approche conservatrice en gardant les plus grandes échelles et en activant et désactivant la recette `halofit` standard. Nous avons vu que l'ajout de données WL peut fortement réduire les contraintes sur la matière noire et améliorer significativement notre connaissance de ce fluide sombre. Cependant, une recette non linéaire adéquate est nécessaire pour utiliser des échelles plus petites et améliorer encore plus nos connaissances. Dans un deuxième temps, nous avons prédit les contraintes des futures données d'Euclid (en utilisant seulement l'étude photométrique dans ce cas). Nous avons montré que la partie photométrique d'Euclid seule sera capable de fournir des contraintes excellentes sur la matière noire mais il est encore plus important qu'auparavant d'obtenir une recette non linéaire appropriée, afin de pouvoir utiliser toutes les futures données précises d'Euclid. Dans la dernière section du chapitre, nous avons considéré une extension phénoménologique très basique de la matière noire et de l'énergie noire au-delà de ΛCDM. Nous avons montré que les données actuelles de bas redshift ne sont pas capables de placer des contraintes en raison des dégénérescences entre les deux fluides. Cependant, le GCs d'Euclid sera capable de placer de bonnes contraintes sur les deux composantes en même temps et ces contraintes deviendront extrêmement précises une fois combinées avec les données CMB.

En guise de conclusion, nous avons montré dans cette thèse qu'Euclid sera

capable de fournir des contraintes excellentes sur les paramètres cosmologiques, non seulement pour ΛCDM et des extensions simples au-delà, mais aussi pour des modèles de matière noire plus élaborés. Nous avons fourni suffisamment de détails pour affirmer que les corrélations croisées entre le groupement de galaxies et les lentilles faibles ne peuvent pas être négligées dans les futures sondages comme Euclid et, plus important encore, elles peuvent largement aider à améliorer nos connaissances sur le secteur sombre de l'Univers. Cependant, il est clair que nous devons mieux comprendre les échelles non linéaires et les non gaussianités qui peuvent apparaître dans les covariances des observables ou la vraisemblance, ainsi que les corrélations croisées entre les données tridimensionnelles et bidimensionnelles pour analyser correctement toutes les futures données Euclid et en extraire le maximum d'information. Ces aspects, ainsi que l'inclusion d'effets systématiques et de premier plan dans les prédictions, des études plus détaillées sur la stabilité des dérivées numériques ou le solveur de Boltzmann, des prévisions de la puissance d'Euclid pour contraindre la masse des neutrinos, ou des prévisions au-delà de l'approximation de Fisher, établissent de nouvelles perspectives pour les travaux futurs.

Appendix A

Triangular plots of the Euclid forecasts

A.1 Additional ingredients to compute the forecasts

TABLE A.1: Fractional number density of galaxies for the spectroscopic survey, $\mathrm{d}n(z_c)$, in each redshift bin given by the $z_{\min}$ and $z_{\max}$ bin edges. z_c stands for the central redshift in each bin. $\sigma(\mathrm{d}n)$ corresponds to the uncertainty on $\mathrm{d}n$ (not used in this work), and $b(z_c)$ stands for the galaxy bias in each bin [Euclid Collaboration, in prep.].

$z_{\min}$	$z_{\max}$	$\mathrm{d}n(z_c)$	$\sigma(\mathrm{d}n)$	$b(z_c)$
0.90	1.00	2492	738	1.43
1.00	1.10	2287	666	1.50
1.10	1.20	2090	598	1.57
1.20	1.30	1904	534	1.64
1.30	1.40	1574	456	1.71
1.40	1.50	1253	373	1.78
1.50	1.60	977	286	1.84
1.60	1.70	764	222	1.90
1.70	1.80	533	220	1.96

TABLE A.2: Ratio of the mean luminosity over the characteristic luminosity of source galaxies as a function of the redshift used in the eNLA model for intrinsic alignments of Chapter 6. [Cardone, V. F., private communication]

z	$\langle L \rangle (z) / L_*(z)$
0.00	0.025554264544469851
0.01	0.04226248404816618
0.02	0.05897070355186251
0.03	0.07255577739983624
0.04	0.08467091946888433
0.05	0.09593189812230896
0.06	0.10664712177770144
0.07	0.11699521627347793
0.08	0.1270992083277226
0.09	0.13705390990899569
0.10	0.14690642344508484
0.11	0.1566888676060969
0.12	0.16643375391606047
0.13	0.1724344869254337
0.14	0.17433109194333457
0.15	0.1757473541945655
0.16	0.17672440753252677
0.17	0.17732443933359154
0.18	0.17755095992312336
0.19	0.1774276546632702
0.20	0.17697607537146498
0.21	0.17618116399835188
0.22	0.17510010444807342
0.23	0.17375659038677757
0.24	0.17217320673196346
0.25	0.17037819143823982
0.26	0.16838260293214272
0.27	0.1662032558802489
0.28	0.16385607109506392
0.29	0.16135993200888227
0.30	0.1268395609585578
0.31	0.12907985938692612
0.32	0.1313227497577787
0.33	0.16665609703505335
0.34	0.16929584470712533

0.35	0.1719423915586864
0.36	0.17459946931642292
0.37	0.17727797307571466
0.38	0.17997288336398
0.39	0.18268574301584492
0.40	0.18541814245604074
0.41	0.18818176471197284
0.42	0.190964732695651
0.43	0.19376426348974152
0.44	0.19657718620587164
0.45	0.19937968574624748
0.46	0.20219534900647373
0.47	0.20502891585161717
0.48	0.20788554744423796
0.49	0.21080261127285052
0.50	0.21374283204553862
0.51	0.22350952406511845
0.52	0.2336035324541177
0.53	0.2439433943684961
0.54	0.2545993321891511
0.55	0.26558444157656447
0.56	0.2769130418135315
0.57	0.28860077466932055
0.58	0.30066471185279176
0.59	0.3131234720767489
0.60	0.3259973488810591
0.61	0.33936970696490565
0.62	0.35320269038374674
0.63	0.3675156939533921
0.64	0.3820640469548151
0.65	0.3971047212579667
0.66	0.41265847319232857
0.67	0.4287472836218983
0.68	0.4453944366382141
0.69	0.4626721820724299
0.70	0.48055840217251805
0.71	0.4813775205236058
0.72	0.4820990176914395
0.73	0.4827218884910109
0.74	0.4832451175572389

0.75	0.48366768480479383
0.76	0.4839885708985562
0.77	0.4841368641336053
0.78	0.4841878684606975
0.79	0.48414736914298007
0.80	0.48402119744976757
0.81	0.4838152191357108
0.82	0.4835353237347566
0.83	0.4831874146768369
0.84	0.4827774002305864
0.85	0.4823350742681689
0.86	0.48183983064015856
0.87	0.4812953425368187
0.88	0.48070533434551505
0.89	0.48007358032718883
0.90	0.47940390358588325
0.91	0.4847907664243074
0.92	0.49020822444684875
0.93	0.49598618363962366
0.94	0.5018098125480869
0.95	0.5076776814645202
0.96	0.5135882040113844
0.97	0.5195396322991797
0.98	0.5255300520416227
0.99	0.5315573776464875
1.00	0.537619347301646
1.01	0.5436823166591477
1.02	0.5497745609123192
1.03	0.5558956713828336
1.04	0.5620452094653283
1.05	0.5682227073154881
1.06	0.5744276686130143
1.07	0.580659569403094
1.08	0.5869178590201877
1.09	0.5932019610980112
1.10	0.5995112746688078
1.11	0.605891692836351
1.12	0.6127211449556171
1.13	0.6195815964160508
1.14	0.6264690132765793

1.15	0.6333791356086362
1.16	0.644813608686229
1.17	0.6564103462269469
1.18	0.6681668054966379
1.19	0.6800800703828802
1.20	0.6921468339496962
1.21	0.7043546542935721
1.22	0.7167082491038208
1.23	0.7292036132655302
1.24	0.7418363336503534
1.25	0.7546015742255656
1.26	0.7674940613716712
1.27	0.7805080694832518
1.28	0.7936374069306319
1.29	0.8068754024659347
1.30	0.8202148921613625
1.31	0.8337637971242551
1.32	0.847394650378998
1.33	0.8610911971470123
1.34	0.8748362234293243
1.35	0.8886115570378099
1.36	0.9023980749858372
1.37	0.9161757177724361
1.38	0.9299235110792485
1.39	0.9436195953733806
1.40	0.9572412638757712
1.41	0.9698852603074248
1.42	0.9824404018717212
1.43	0.9949389839085061
1.44	1.0074149202606668
1.45	1.019903669573896
1.46	1.0324421889327275
1.47	1.045068917613638
1.48	1.0578237936784805
1.49	1.0707483061522391
1.50	1.0838855856394694
1.51	1.0986678244882293
1.52	1.1137037049200518
1.53	1.1289549385532192
1.54	1.1443810380961028

1.55	1.1599391827034355
1.56	1.176494387537008
1.57	1.1931280204897803
1.58	1.209790321333468
1.59	1.226427998092991
1.60	1.2429841895869798
1.61	1.2581986866237946
1.62	1.2732430767753842
1.63	1.2881294450409944
1.64	1 1.3028712522663541
1.65	1.3174833143954974
1.66	1.3276787813562607
1.67	1.3376872391682864
1.68	1.3475286979667724
1.69	1.3572241570940484
1.70	1.3667955737010224
1.71	1.3767642588366098
1.72	1.3866336031210778
1.73	1.3963967417141472
1.74	1.4060467090179107
1.75	1.4155764438525145
1.76	1.424978794984031
1.77	1.4342465270084865
1.78	1.443372326594829
1.79	1.45234880908668
1.80	1.4611685254655216
1.81	1.4695713514818438
1.82	1.477814548391021
1.83	1.4859064046013324
1.84	1.4938555371769204
1.85	1.5016708809854848
1.86	1.5093616783194161
1.87	1.516937469049639
1.88	1.5244080813671905
1.89	1.5317836231678212
1.90	1.5390744741300817
1.91	1.546612225274048
1.92	1.5540708365244194
1.93	1.5614414292077905
1.94	1.568714954415731

1.95	1.5758821983567408
1.96	1.5829337884348316
1.97	1.589860200075993
1.98	1.5966517643186025
1.99	1.6032986761878085
2.00	1.6097910038667198
2.01	1.6154226950405541
2.02	1.6208957389150478
2.03	1.6262205109290262
2.04	1.6314076067227155
2.05	1.6364678303116396
2.06	1.641412183049919
2.07	1.6462518534222426
2.08	1.6509982077032226
2.09	1.6556627815164082
2.10	1.6602572723268954
2.11	1.6650448308014139
2.12	1.6697724515473982
2.13	1.6744367914067166
2.14	1.6790344687262646
2.15	1.6835620646116296
2.16	1.6880161242737217
2.17	1.6923931584658716
2.18	1.6966896450160363
2.19	1.7009020304535918
2.20	1.705026731733588
2.21	1.7090759252716083
4.1	2.4743735039574171

A.2 Weak lensing

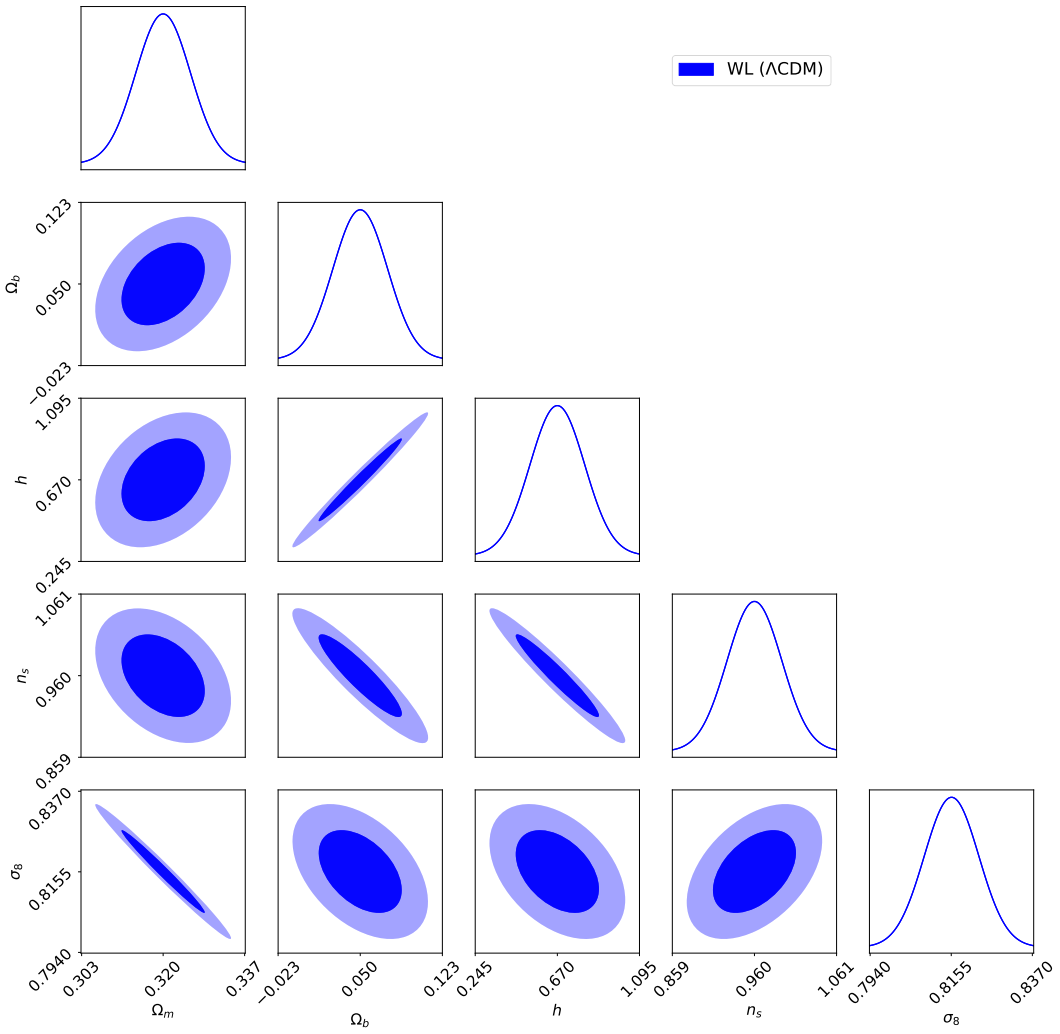

FIGURE A.1: 1σ and 2σ marginalized Fisher contours for the parameters of the baseline ΛCDM model (see Sec. 6.3.1 for details).

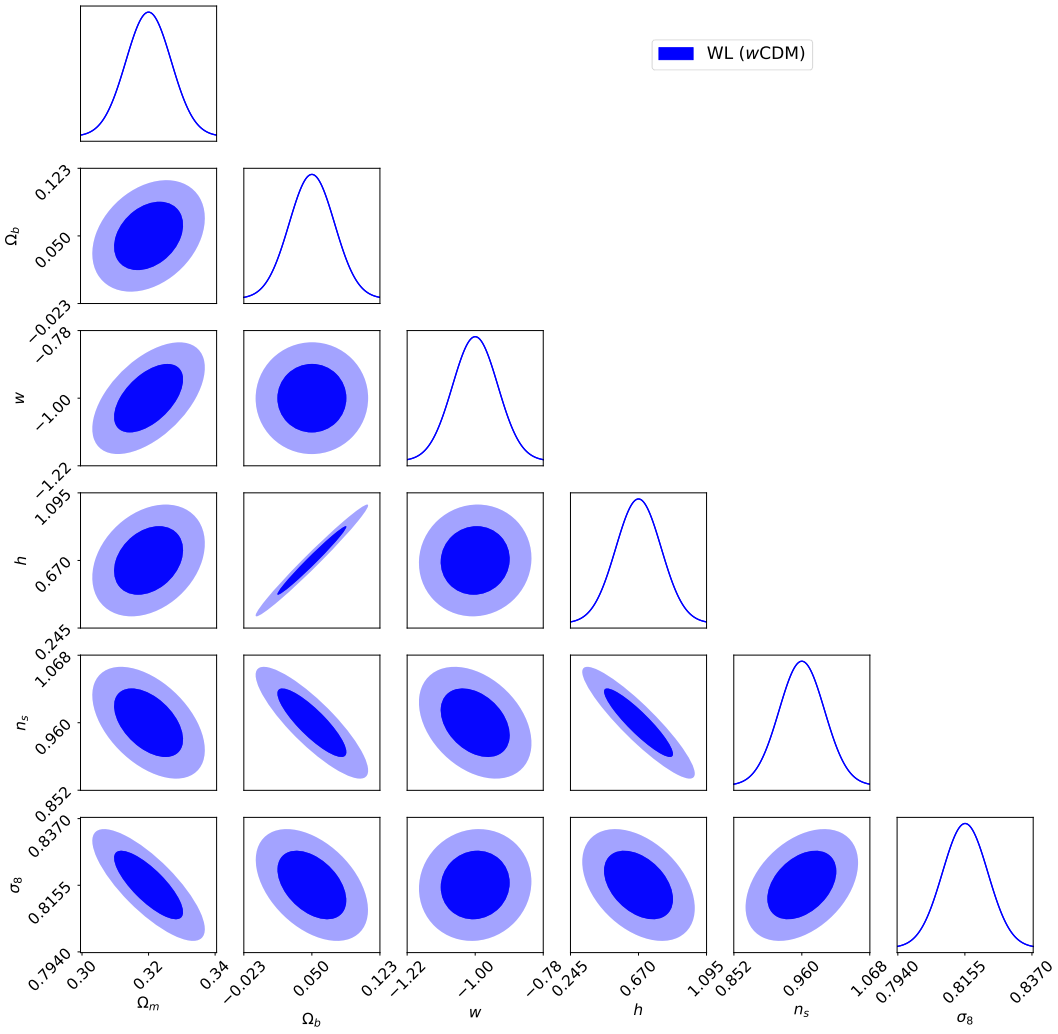

FIGURE A.2: 1σ and 2σ marginalized Fisher contours for the parameters of the baseline wCDM model (see Sec. 6.3.1 for details).

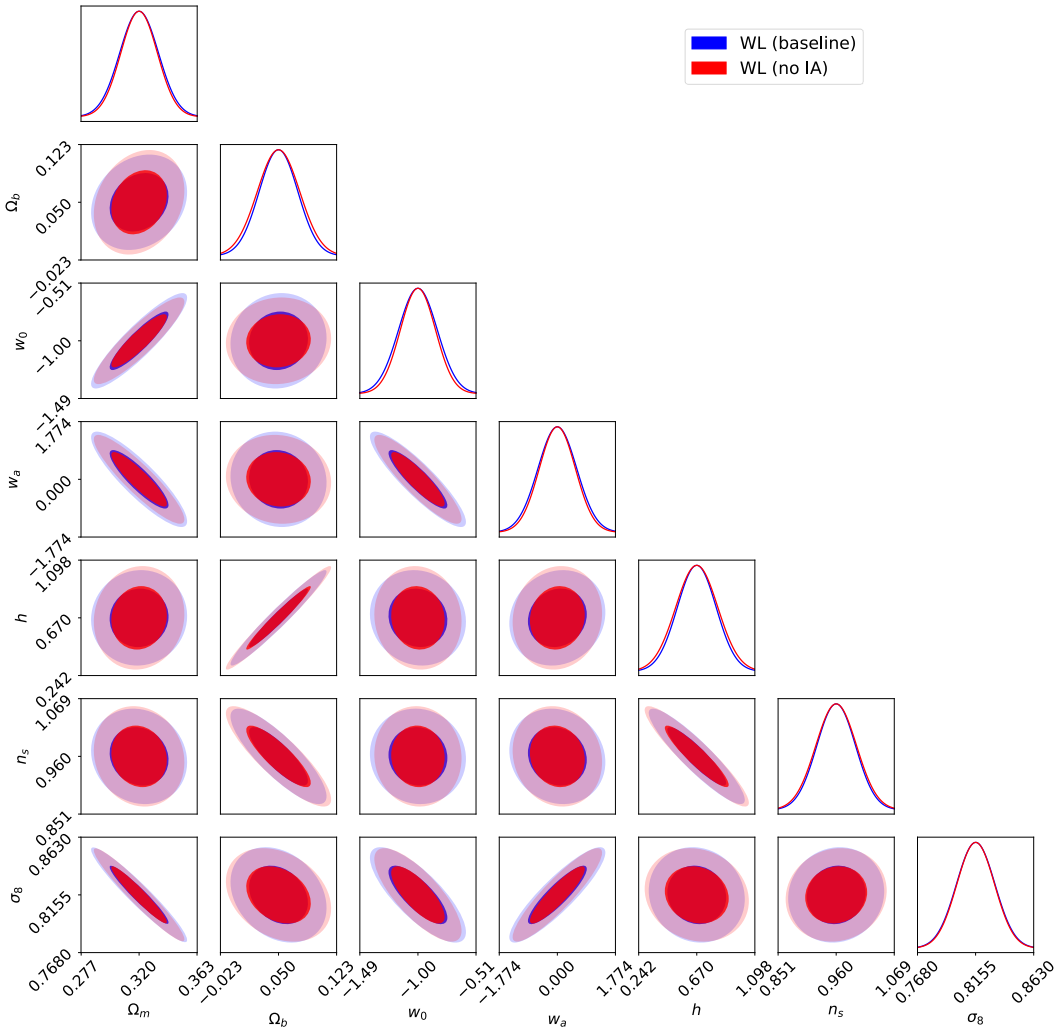

FIGURE A.3: 1σ and 2σ marginalized Fisher contours for the parameters of the w_0w_aCDM model with (blue) and without (red) intrinsic alignments.

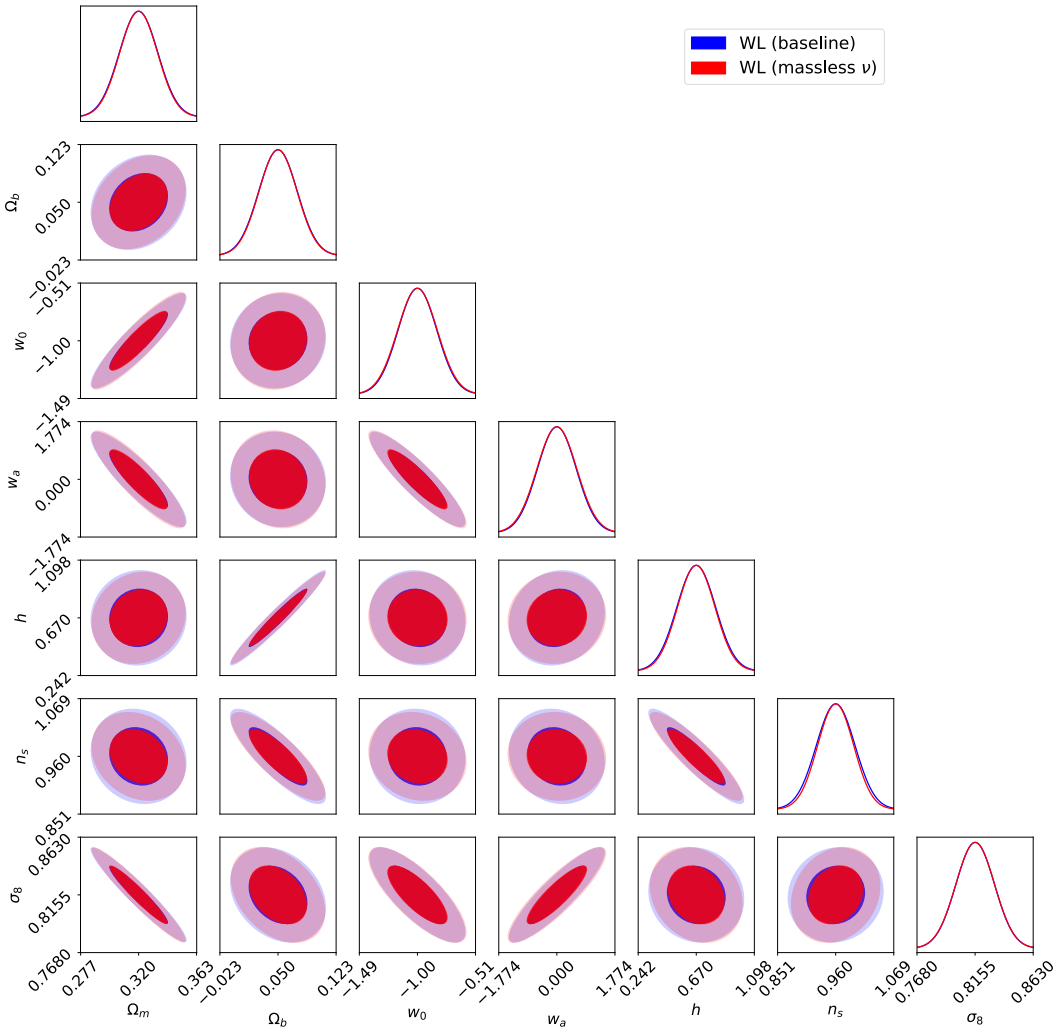

FIGURE A.4: 1σ and 2σ marginalized Fisher contours for the parameters of the w_0w_aCDM model with 1 massive neutrino of mass 0.06 eV and 2 massless neutrinos (blue), and with 3 massless neutrinos (red).

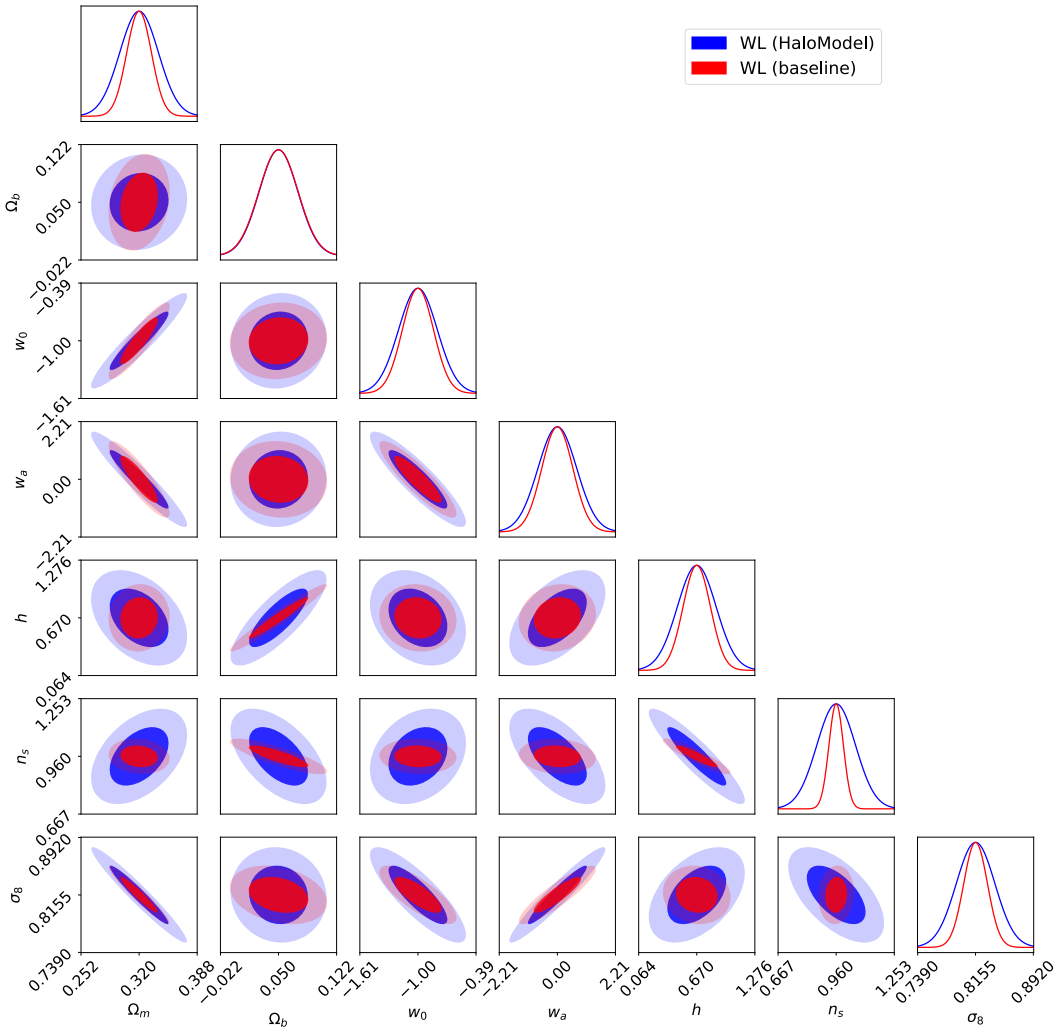

FIGURE A.5: 1σ and 2σ marginalized Fisher contours for the parameters of the w_0w_aCDM model with the `HaloModel` non-linear recipe (blue) and the `halofit` (plus Takahashi and Bird corrections) non-linear recipe (red).

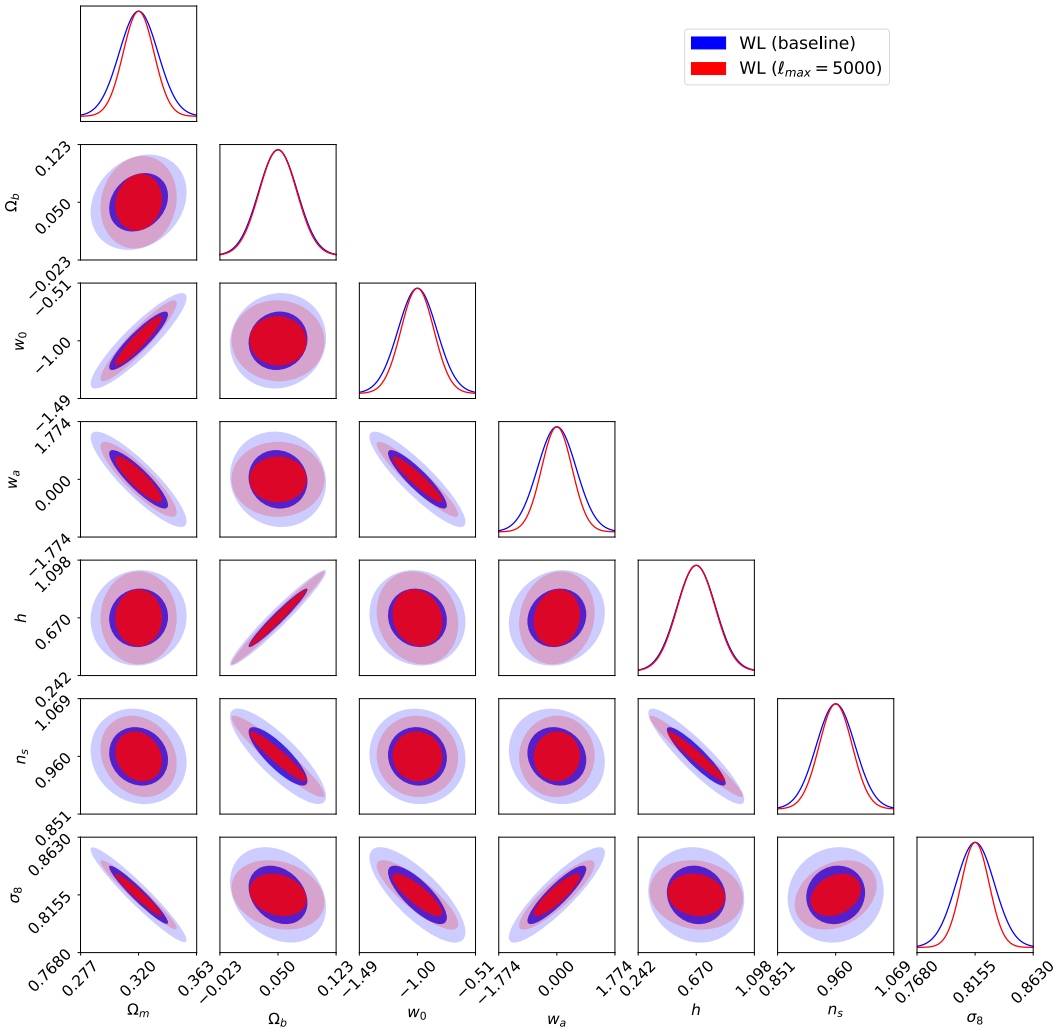

FIGURE A.6: 1σ and 2σ marginalized Fisher contours for the parameters of the $w_0 w_a$CDM model with $\ell_{\max} = 1500$ (blue) and $\ell_{\max} = 5000$ (red).

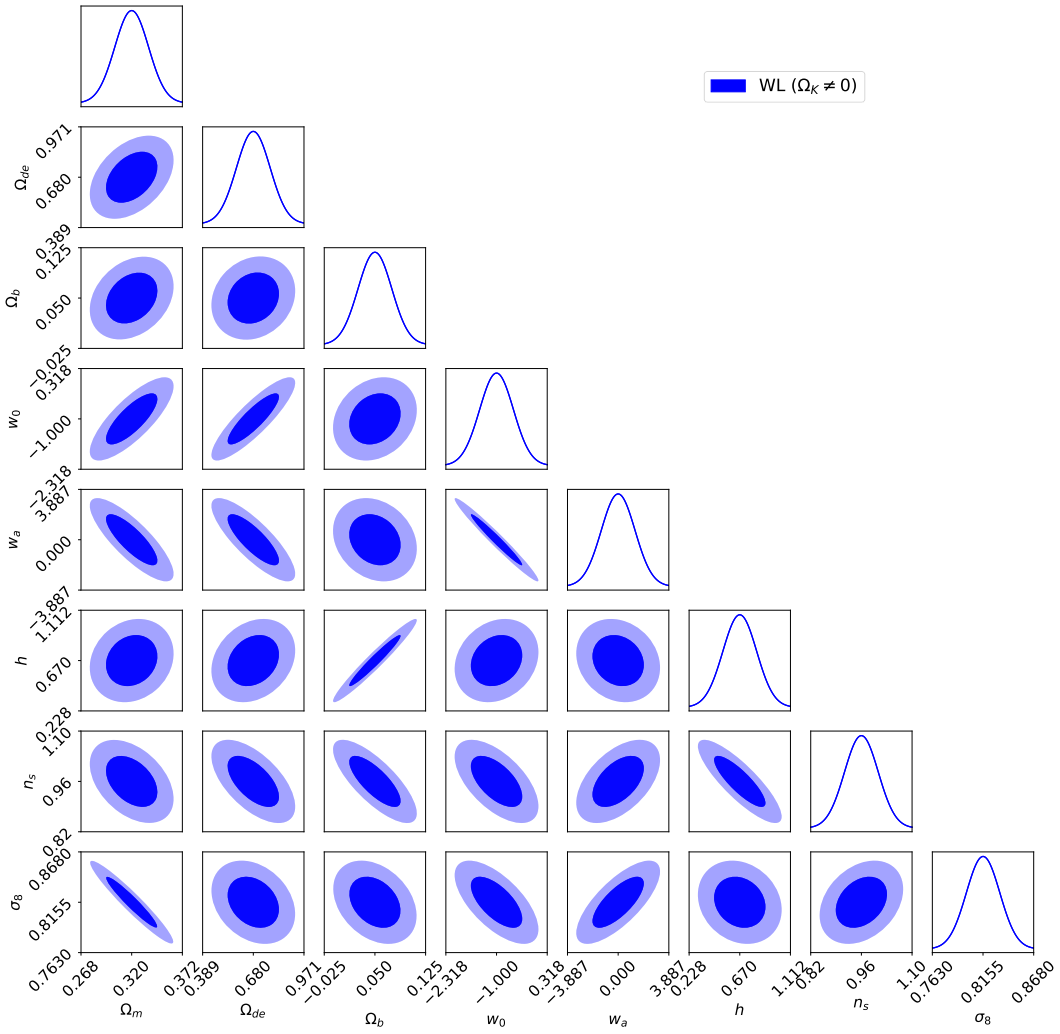

FIGURE A.7: 1σ and 2σ marginalized Fisher contours for the parameters of the w_0w_aCDM model when we allow for some curvature.

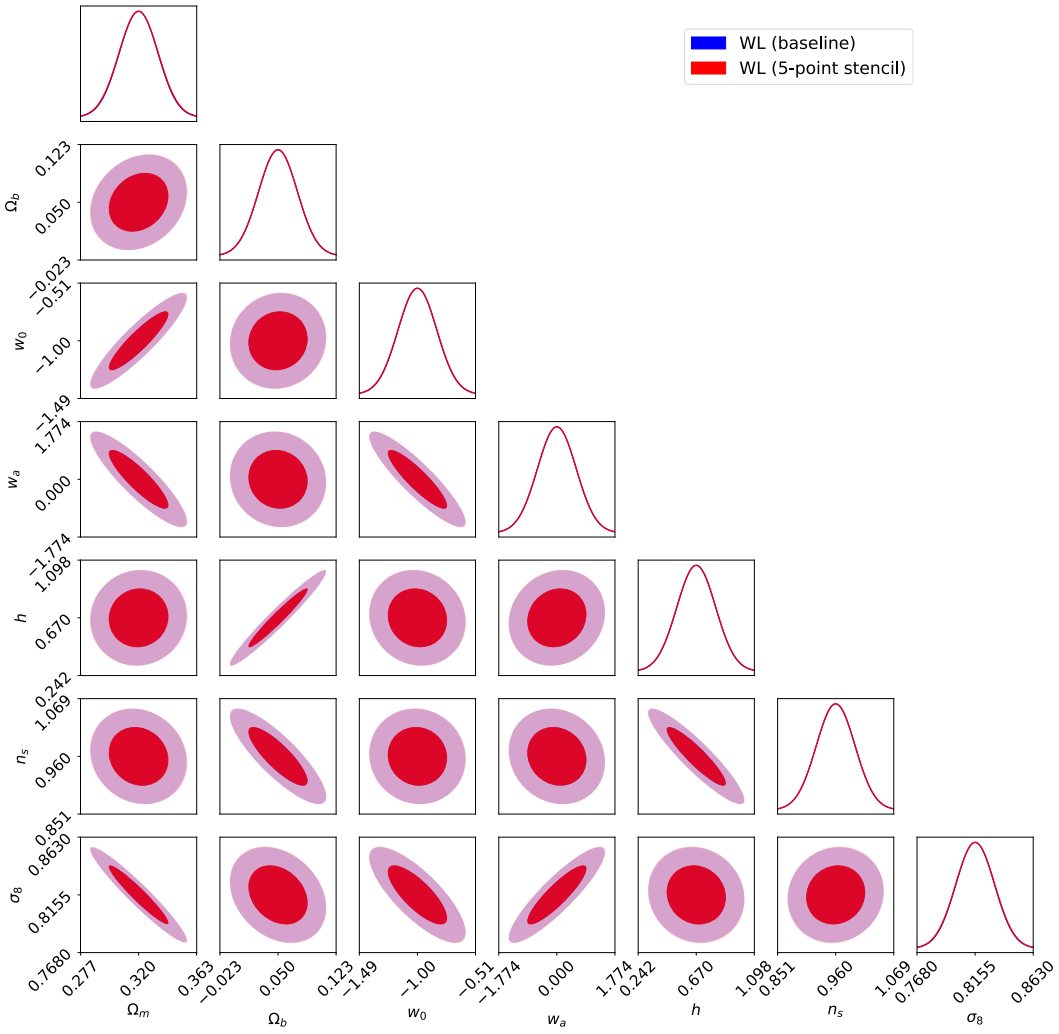

FIGURE A.8: 1σ and 2σ marginalized Fisher contours for the parameters of the w_0w_aCDM model using the 3-point stencil method (blue) and the 5-point stencil method (red) for the numerical derivatives.

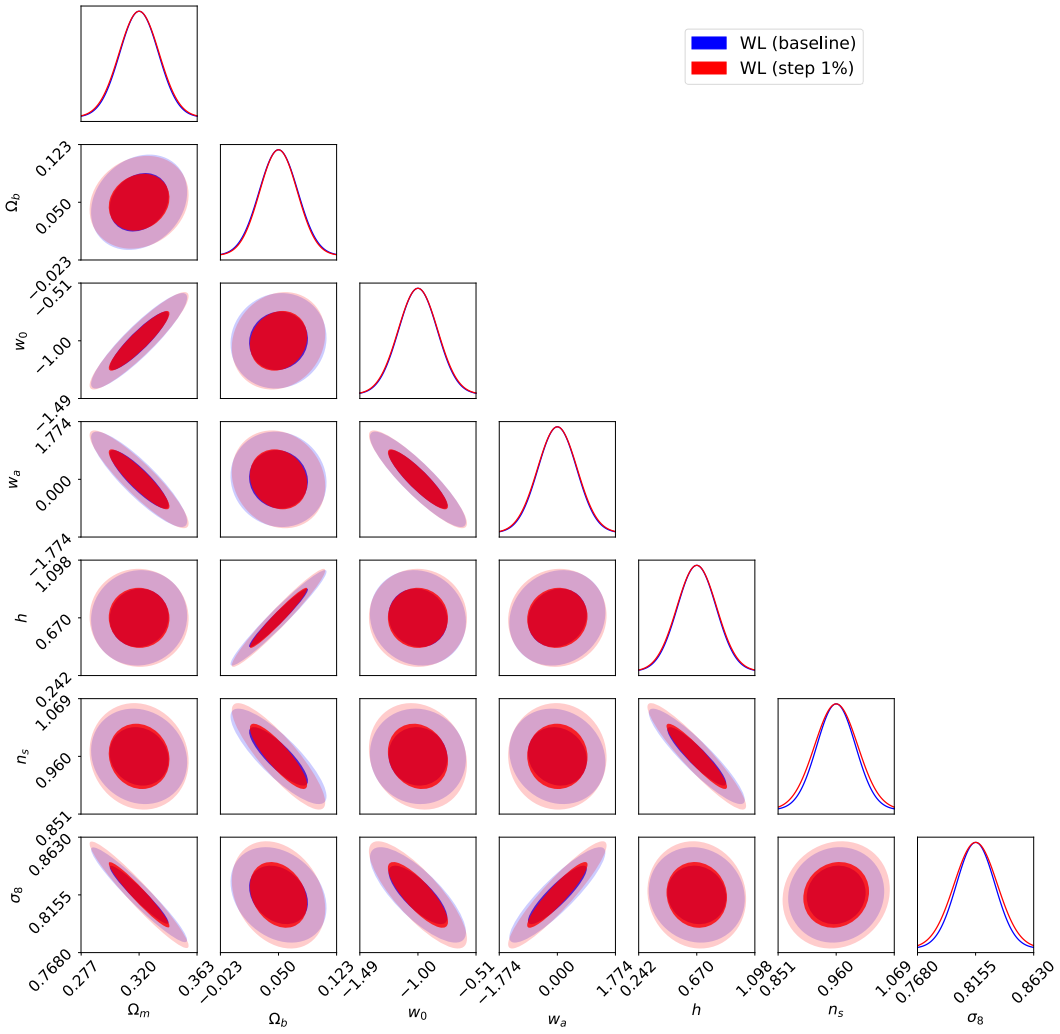

FIGURE A.9: 1σ and 2σ marginalized Fisher contours for the parameters of the w_0w_aCDM model using the baseline step of 4 % (blue) and a step of 1 % (red) for the numerical derivatives with the `halofit` non-linear recipe.

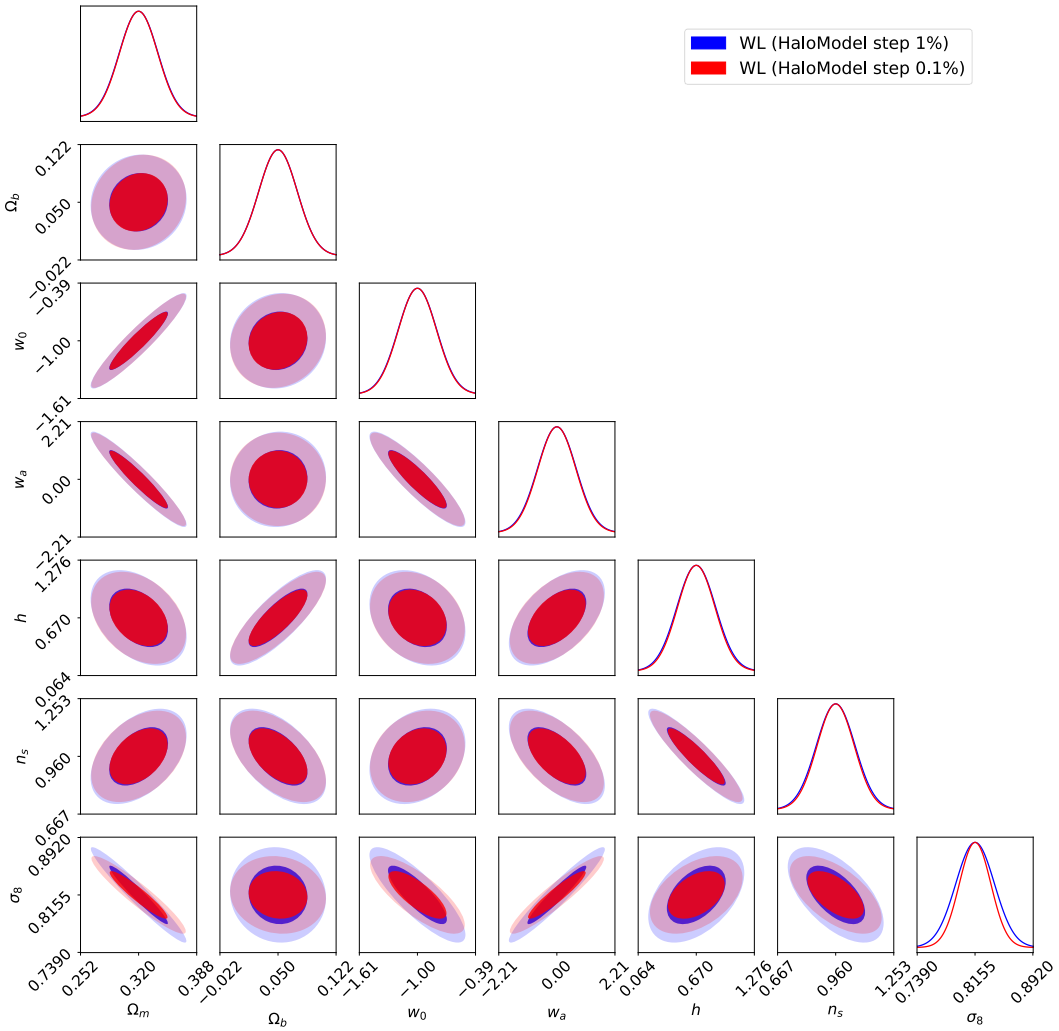

FIGURE A.10: 1σ and 2σ marginalized Fisher contours for the parameters of the w_0w_aCDM model using the baseline step of 1 % (blue) and a step of 0.1 % (red) for the numerical derivatives with the `HaloModel` non-linear recipe.

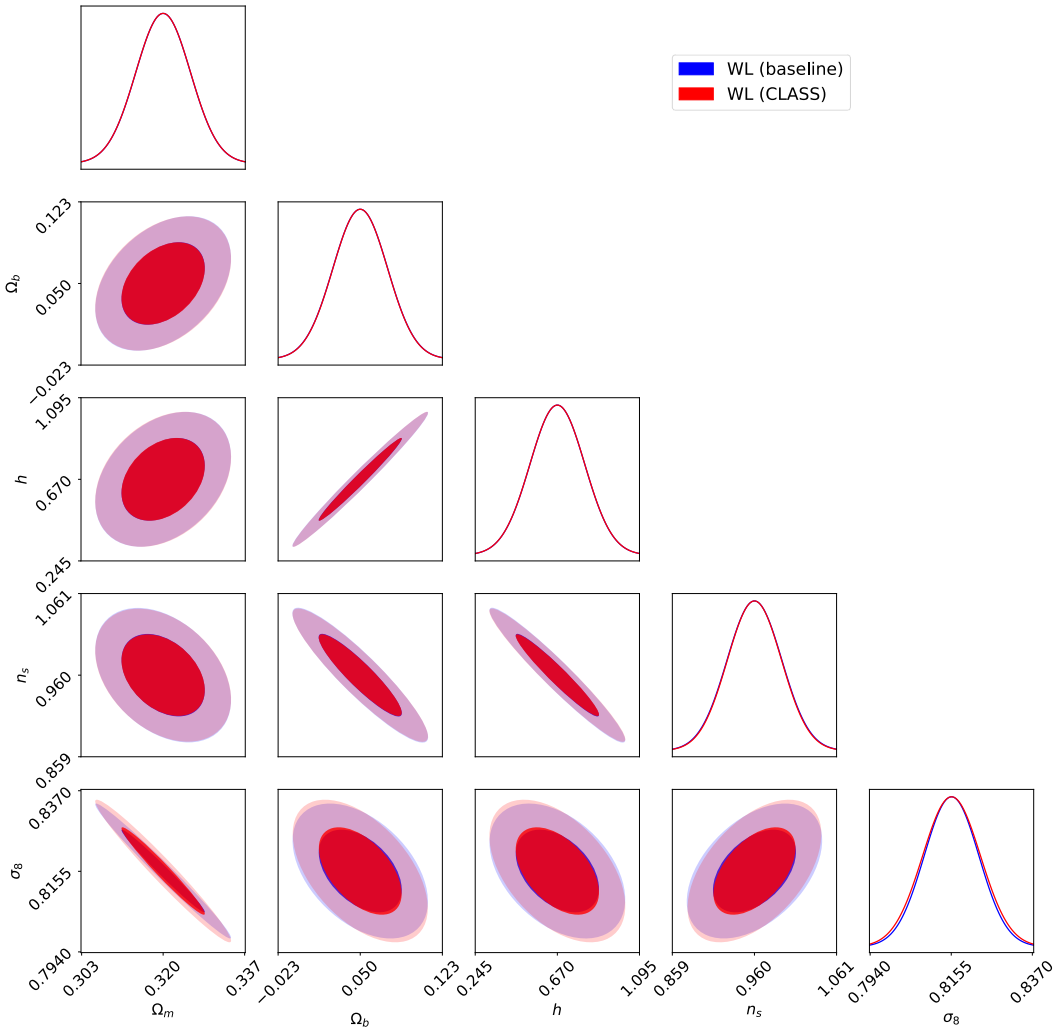

FIGURE A.11: 1σ and 2σ marginalized Fisher contours for the parameters of the ΛCDM baseline model using `CLASS` (red) and `CAMB` (blue) as Boltzmann solver.

A.3 Photometric galaxy clustering

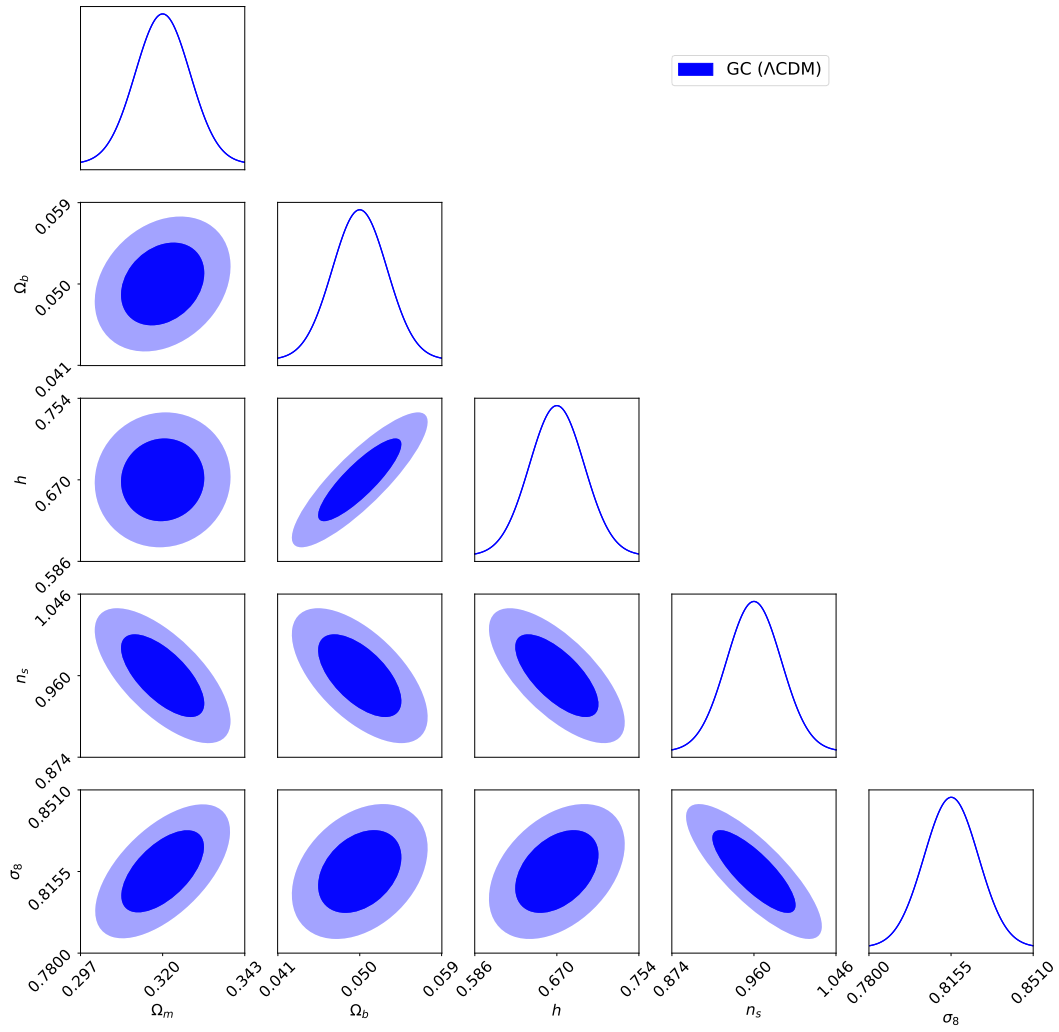

FIGURE A.12: 1σ and 2σ marginalized Fisher contours for the parameters of the baseline ΛCDM model (see Sec. 6.4.1 for details).

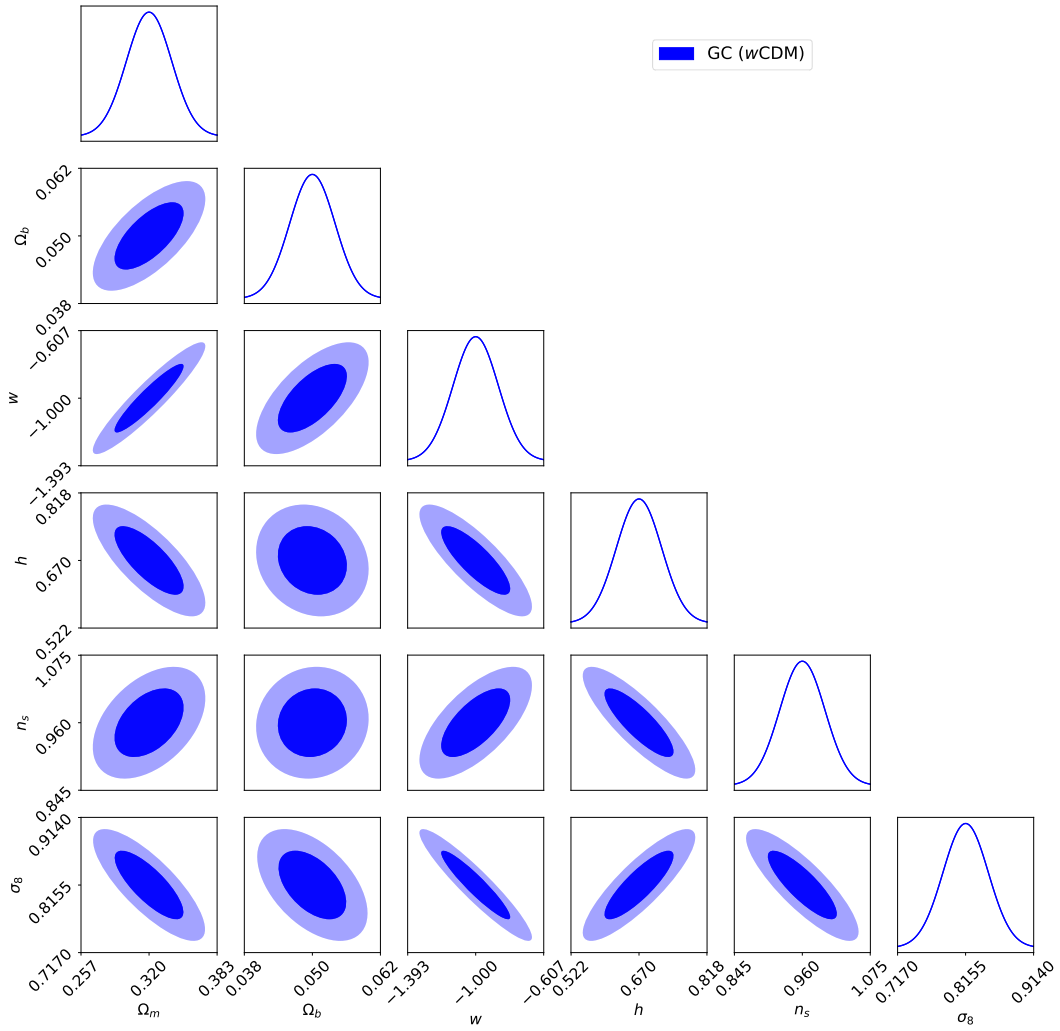

FIGURE A.13: 1σ and 2σ marginalized Fisher contours for the parameters of the baseline wCDM model (see Sec. 6.4.1 for details).

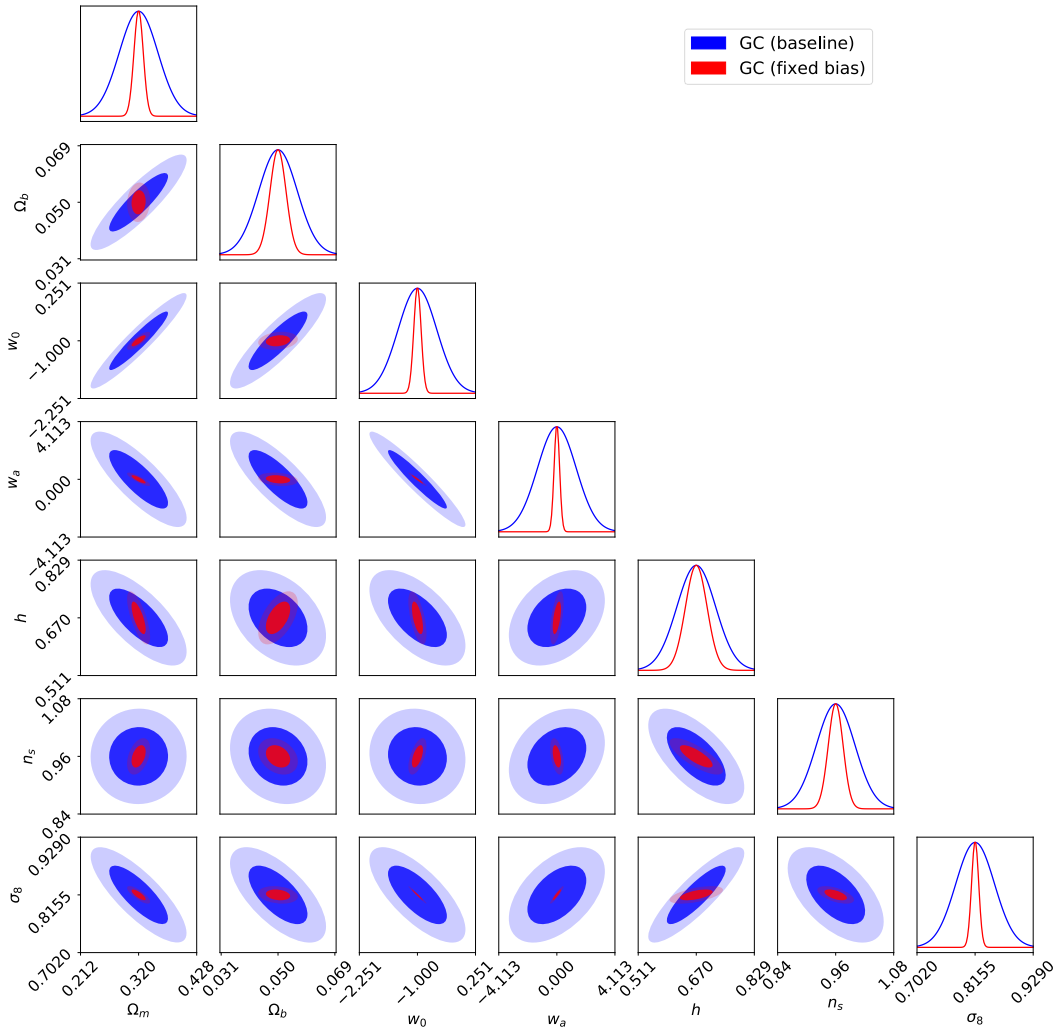

FIGURE A.14: 1σ and 2σ marginalized Fisher contours for the parameters of the w_0w_aCDM model with free (blue) and with fixed (red) binned galaxy bias.

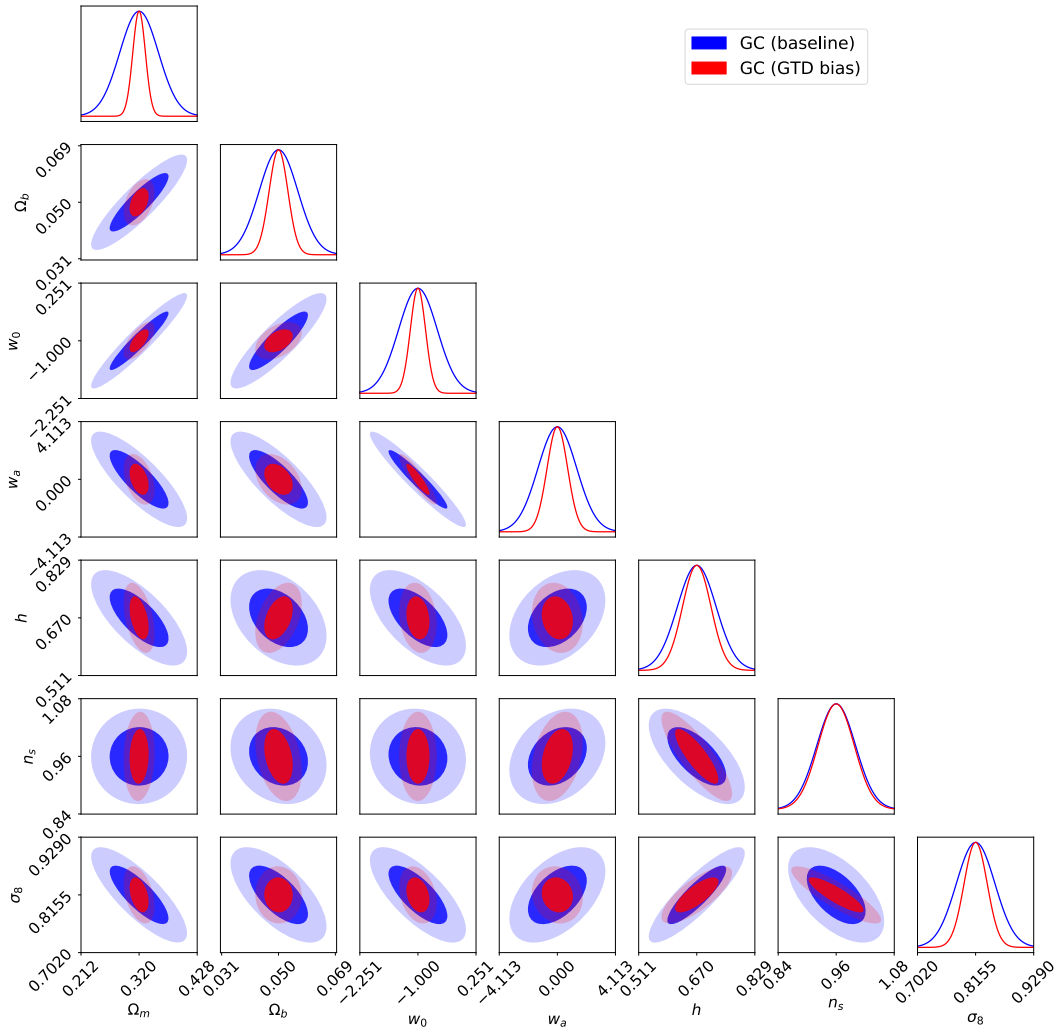

FIGURE A.15: 1σ and 2σ marginalized Fisher contours for the parameters of the w_0w_aCDM model with free binned galaxy bias (blue) and the GTD model for galaxy bias (red).

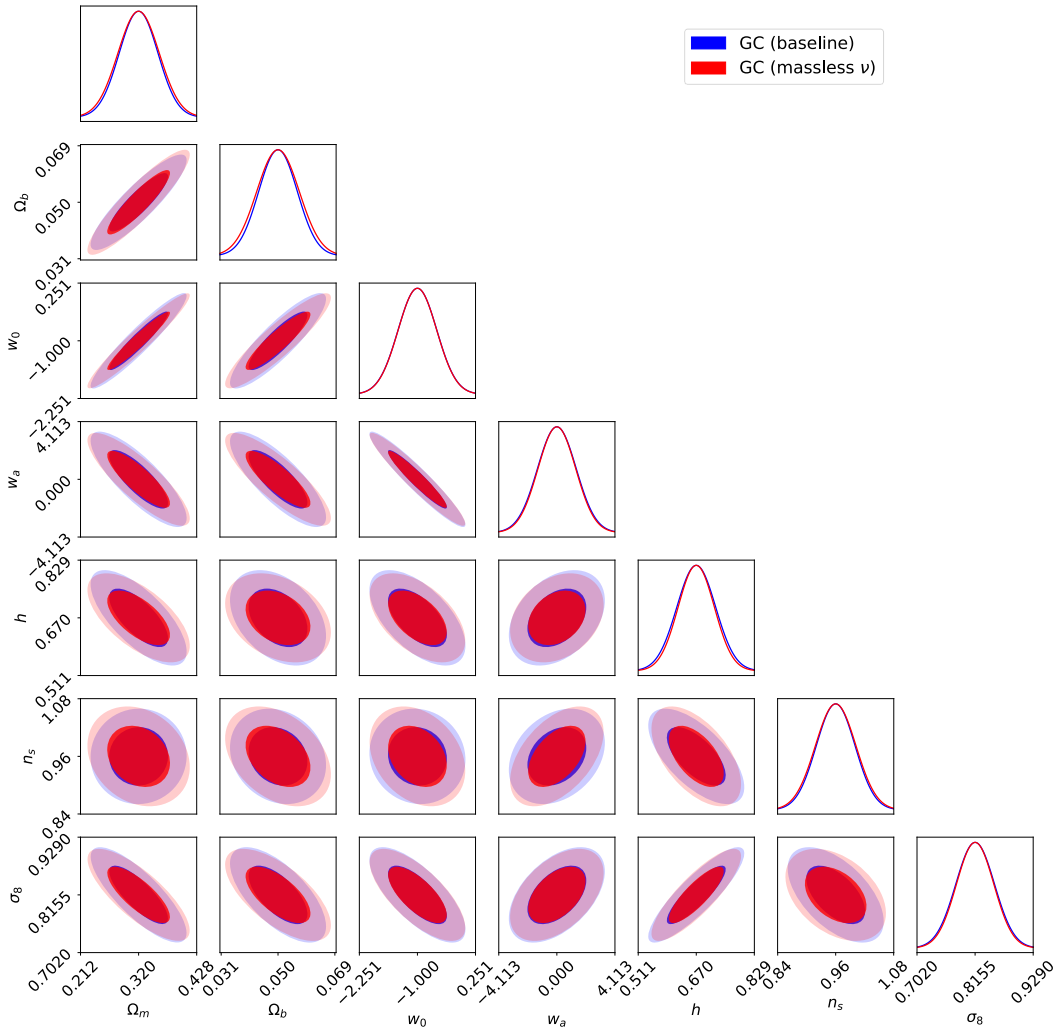

FIGURE A.16: 1σ and 2σ marginalized Fisher contours for the parameters of the w_0w_aCDM model with 1 massive neutrino of mass 0.06 eV and 2 massless neutrinos (blue), and with 3 massless neutrinos (red).

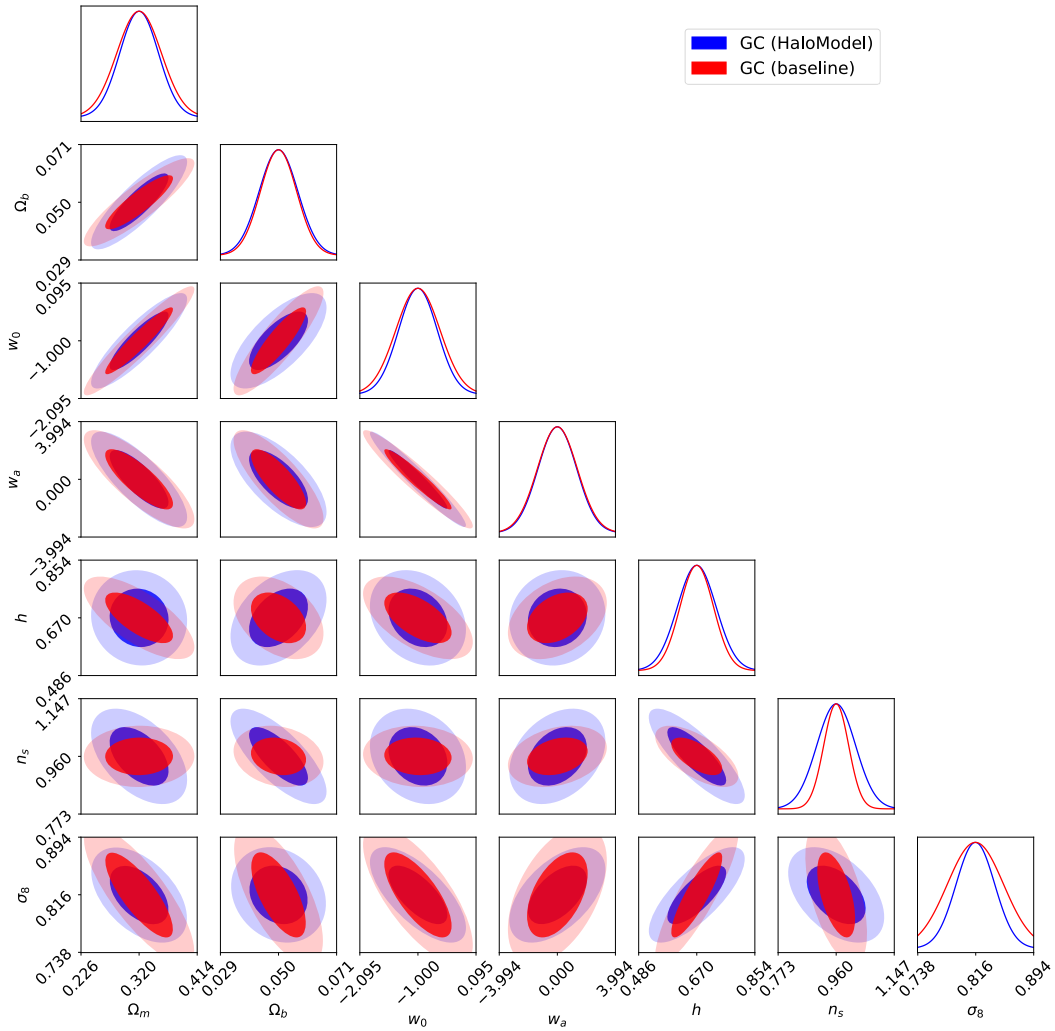

FIGURE A.17: 1σ and 2σ marginalized Fisher contours for the parameters of the w_0w_aCDM model with the `HaloModel` non-linear recipe (blue) and the `halofit` (plus Takahashi and Bird corrections) non-linear recipe (red).

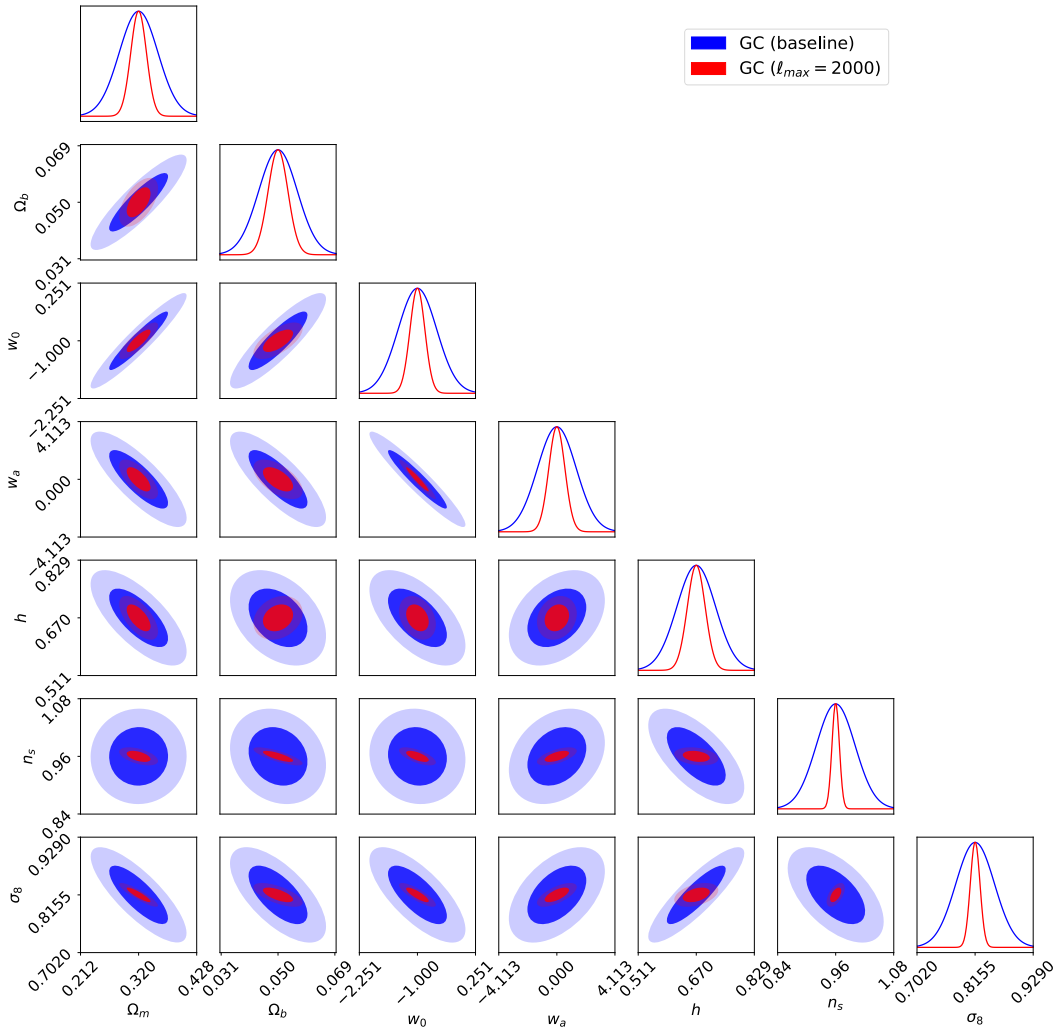

FIGURE A.18: 1σ and 2σ marginalized Fisher contours for the parameters of the $w_0 w_a$CDM model with $\ell_{\max} = 750$ (blue) and $\ell_{\max} = 2000$ (red).

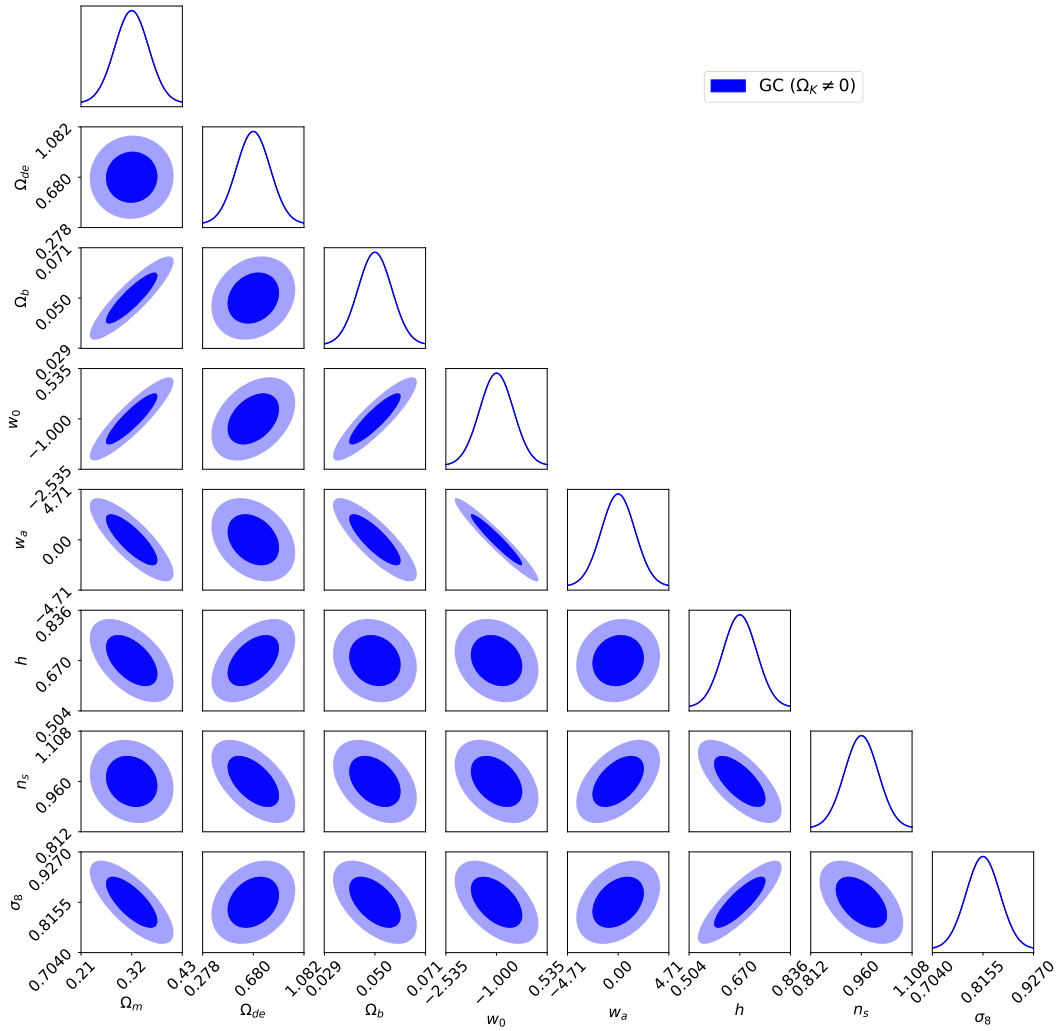

FIGURE A.19: 1σ and 2σ marginalized Fisher contours for the parameters of the w_0w_aCDM model when we allow for some curvature.

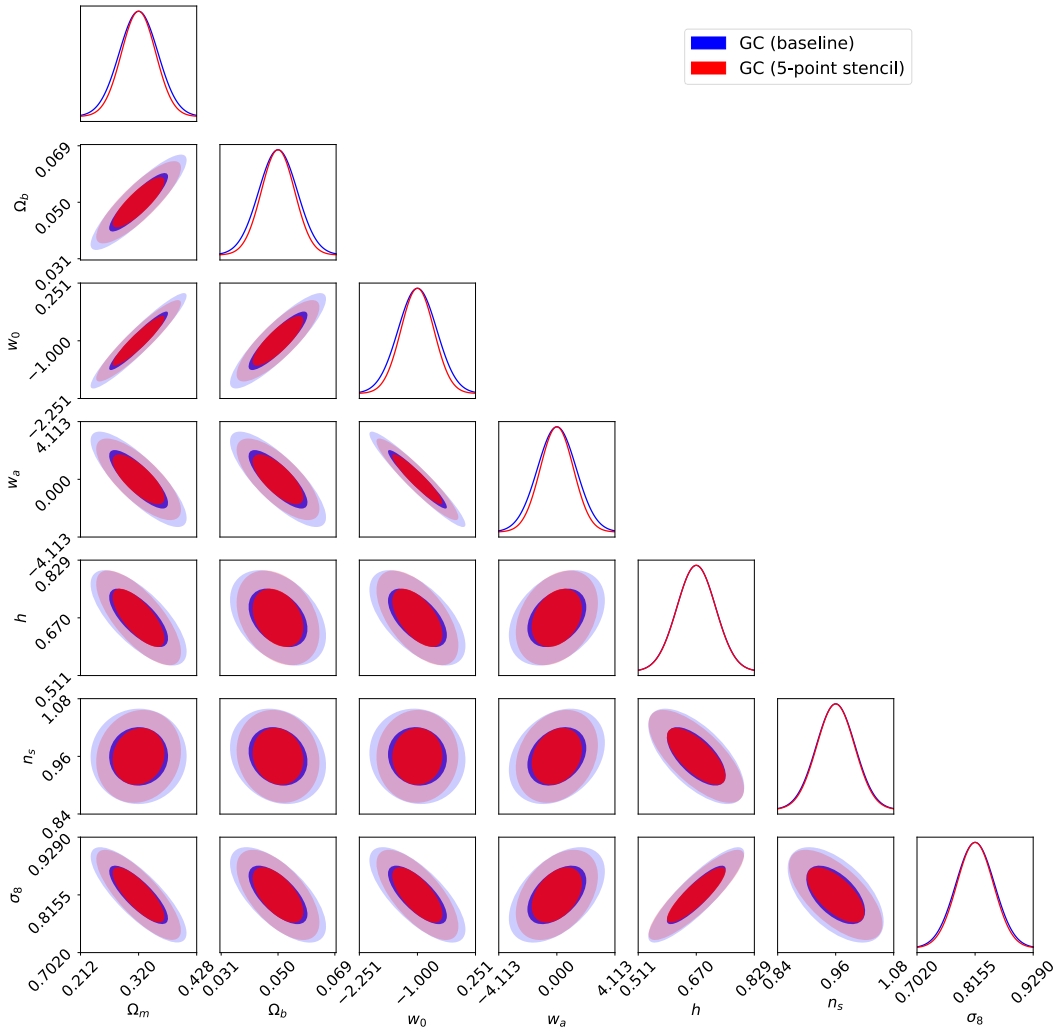

FIGURE A.20: 1σ and 2σ marginalized Fisher contours for the parameters of the w_0w_aCDM model using the 3-point stencil method (blue) and the 5-point stencil method (red) for the numerical derivatives.

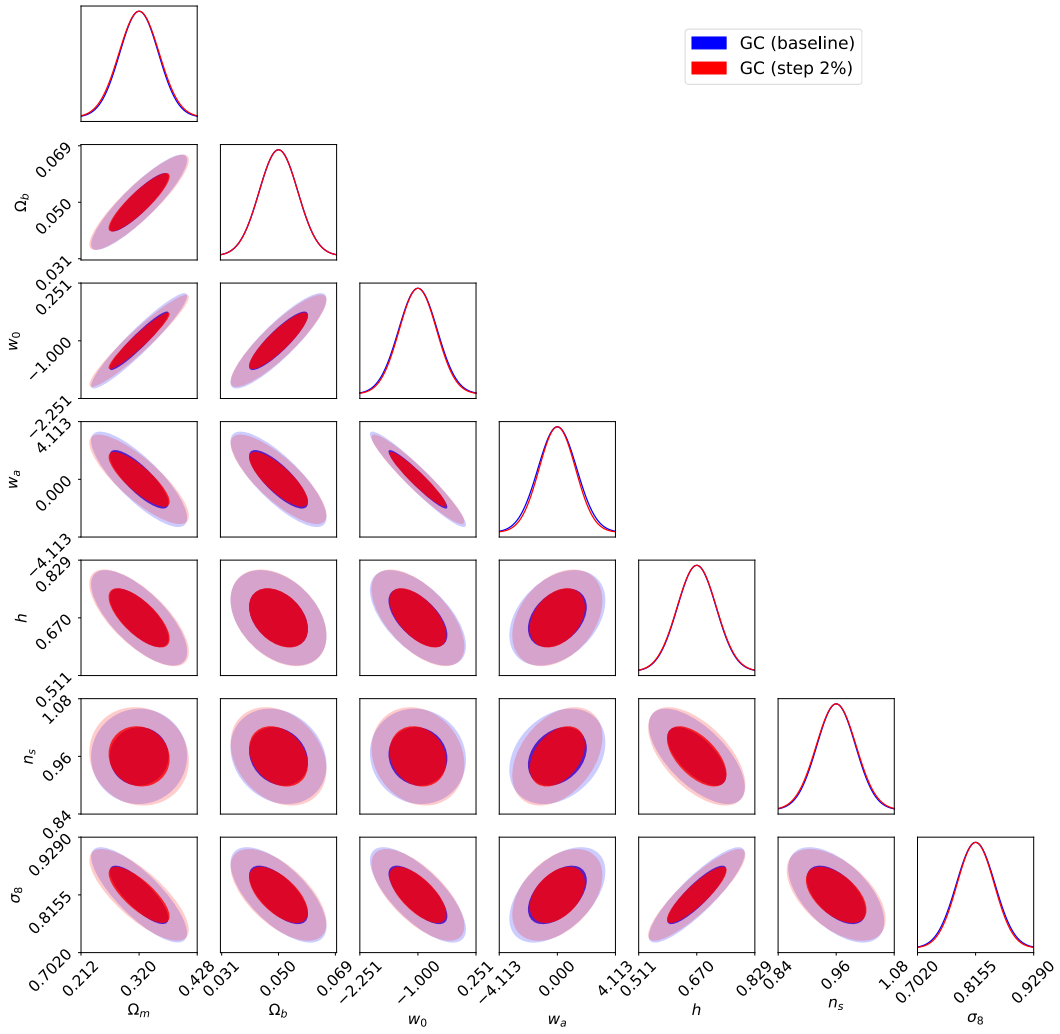

FIGURE A.21: 1σ and 2σ marginalized Fisher contours for the parameters of the w_0w_aCDM model using the baseline step of 4 % (blue) and a step of 2 % (red) for the numerical derivatives with the `halofit` non-linear recipe.

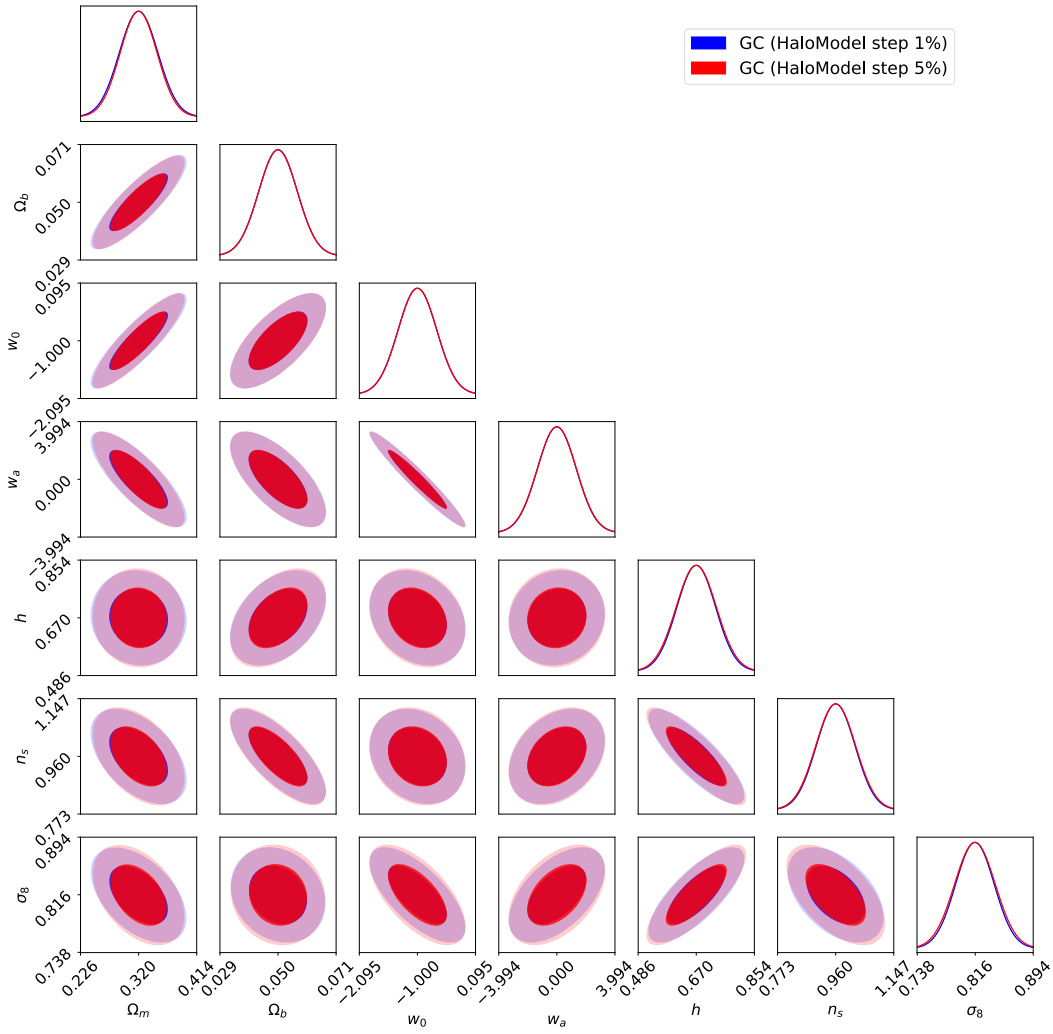

FIGURE A.22: 1σ and 2σ marginalized Fisher contours for the parameters of the w_0w_aCDM model using the baseline step of 1 % (blue) and a step of 5 % (red) for the numerical derivatives with the `HaloModel` non-linear recipe.

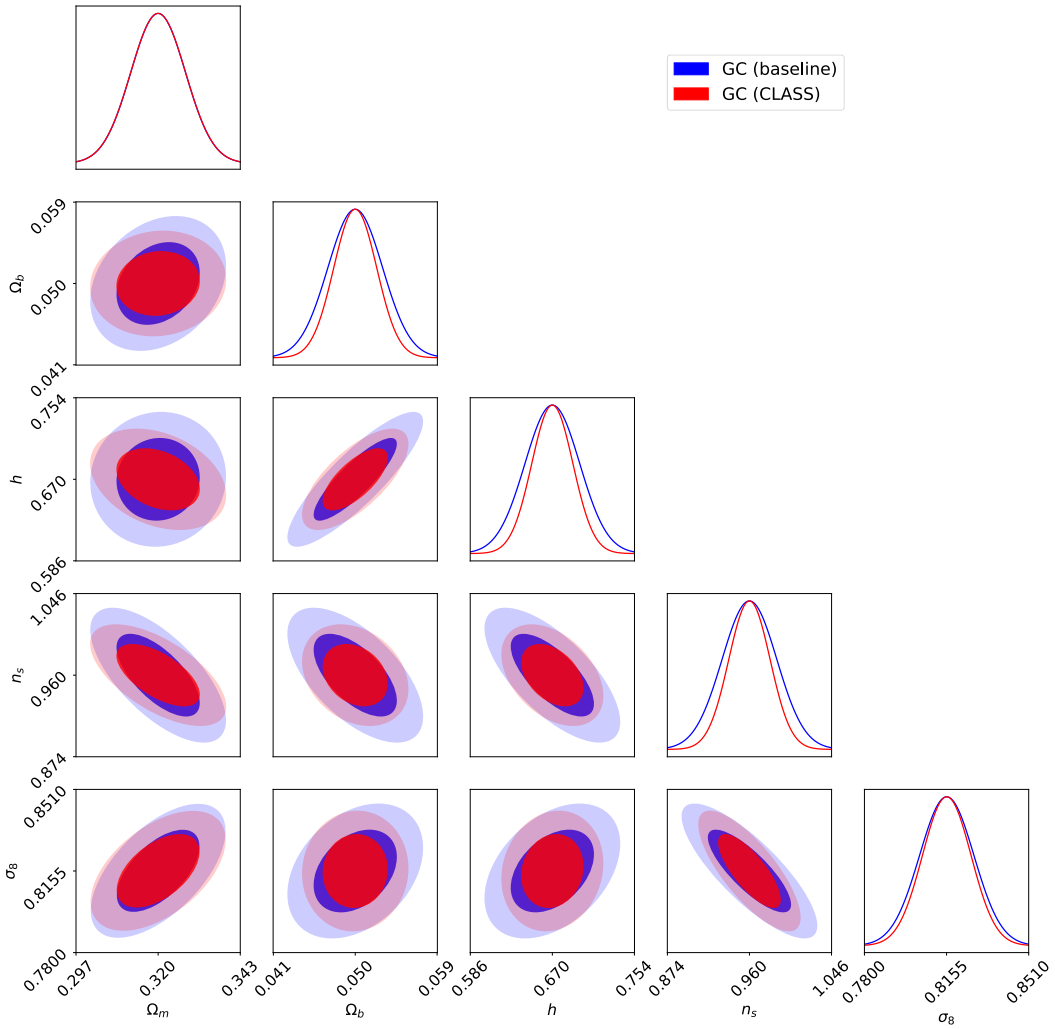

FIGURE A.23: 1σ and 2σ marginalized Fisher contours for the parameters of the ΛCDM baseline model using `CLASS` (red) and `CAMB` (blue) as Boltzmann solver.

A.4 Probe combination: photometric Euclid survey

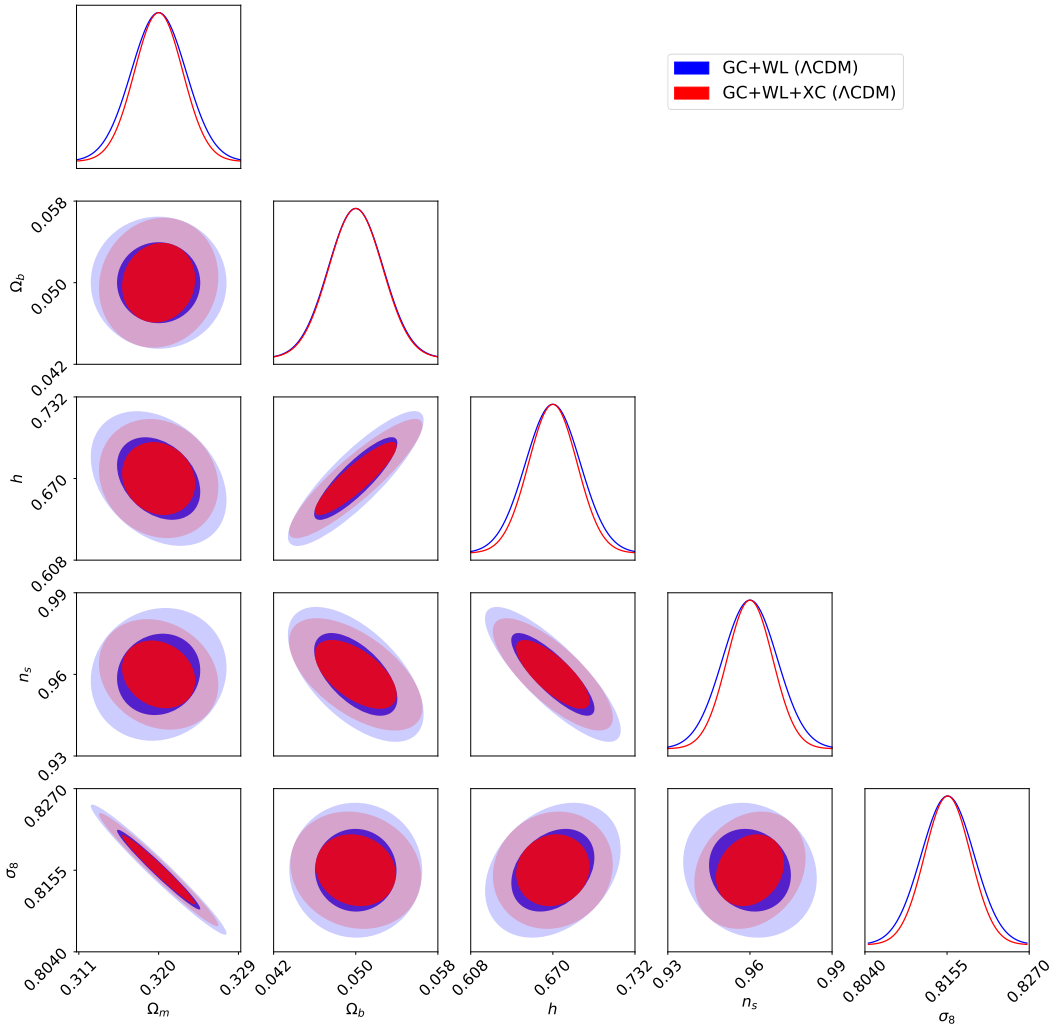

FIGURE A.24: Comparison of probe combination with (red) and without (blue) cross-correlations on the 1σ and 2σ marginalized Fisher contours for the parameters of the baseline ΛCDM model (see Sec. 6.5.1 for details).

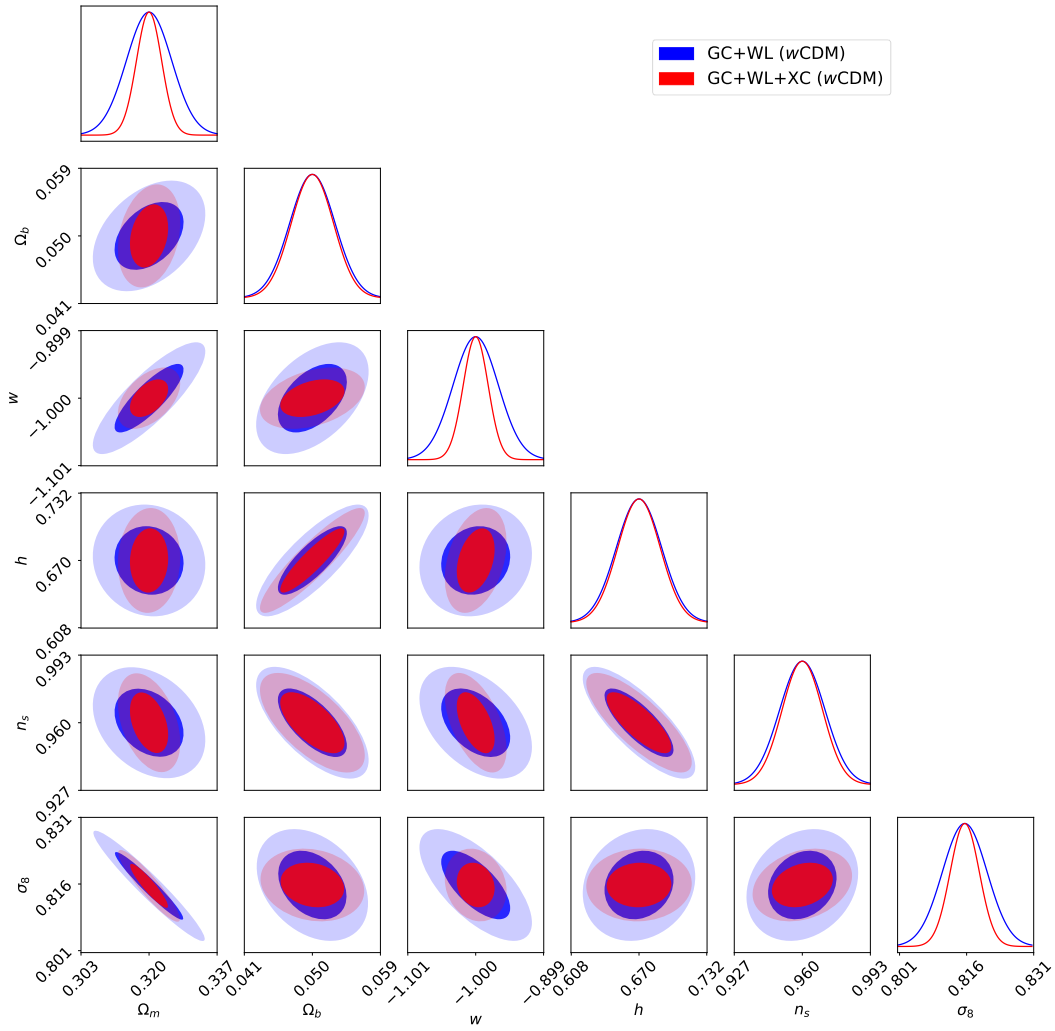

FIGURE A.25: Comparison of probe combination with (red) and without (blue) cross-correlations on the 1σ and 2σ marginalized Fisher contours for the parameters of the baseline wCDM model (see Sec. 6.5.1 for details).

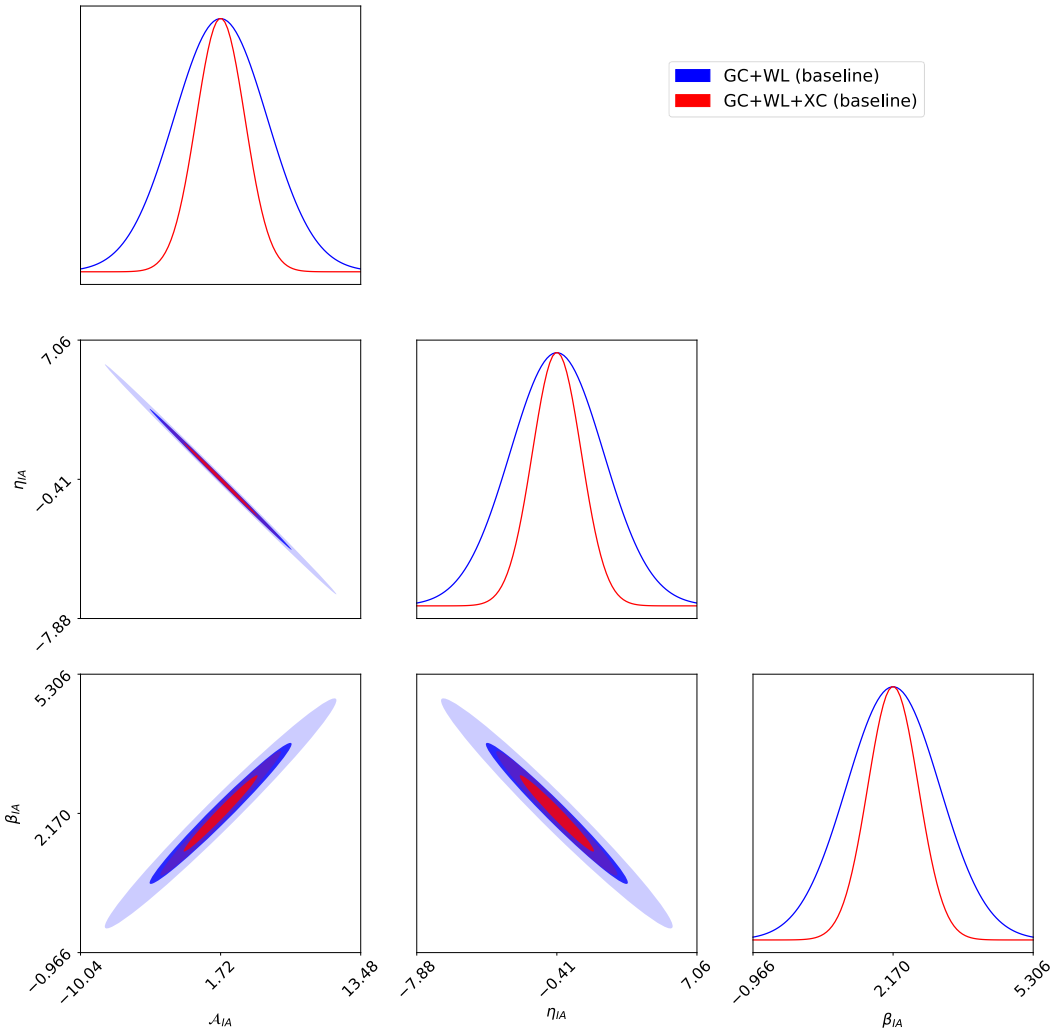

FIGURE A.26: Impact of cross-correlations on the intrinsic alignments nuisance parameters constraints for the baseline w_0w_aCDM model.

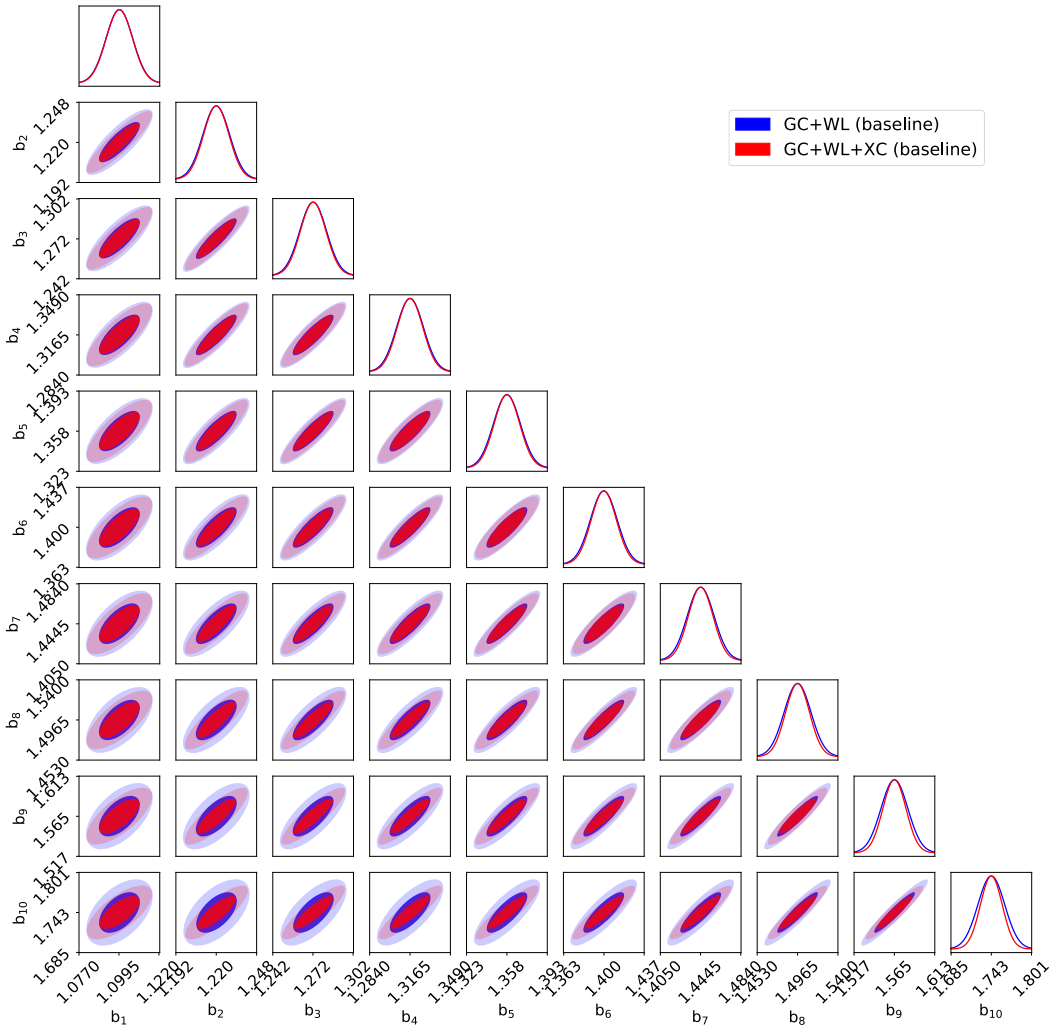

FIGURE A.27: Impact of cross-correlations on the galaxy bias nuisance parameters constraints for the baseline w_0w_aCDM model.

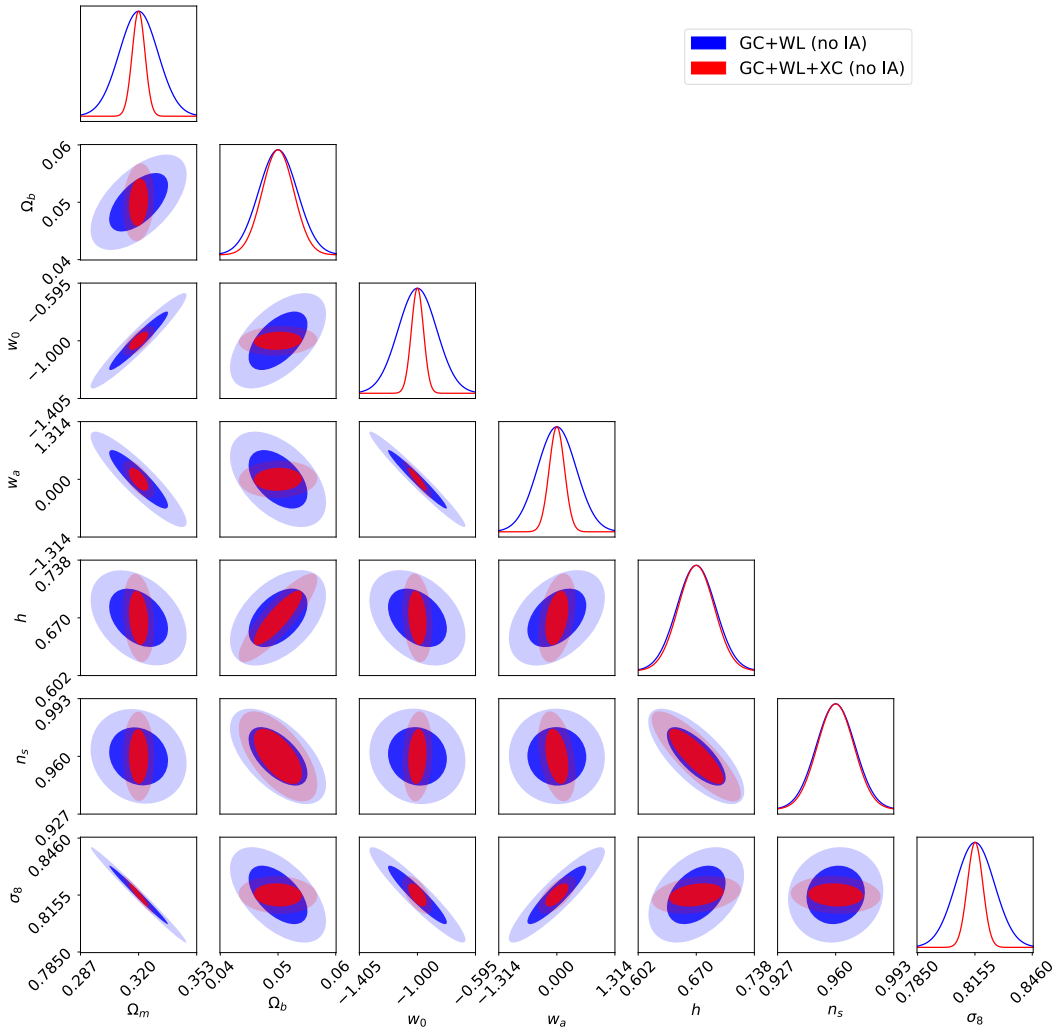

FIGURE A.28: Comparison of probe combination with (red) and without (blue) cross-correlations on the 1σ and 2σ marginalized Fisher contours for the parameters of the baseline w_0w_aCDM model when intrinsic alignments are not considered in the analysis.

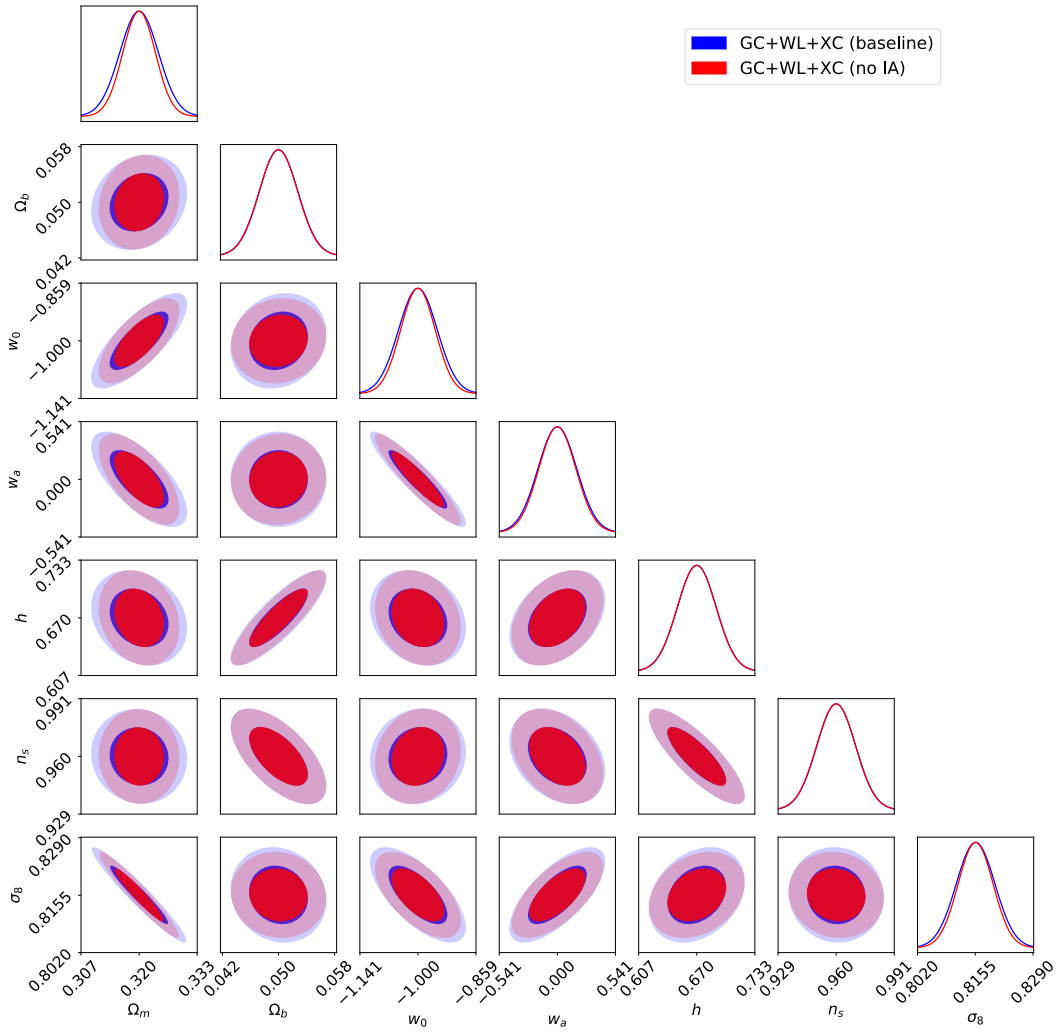

FIGURE A.29: Impact of intrinsic alignments on the 1σ and 2σ marginalized Fisher contours for the parameters of the baseline w_0w_aCDM model when we combine GCp and WL taking into account their cross-correlations.

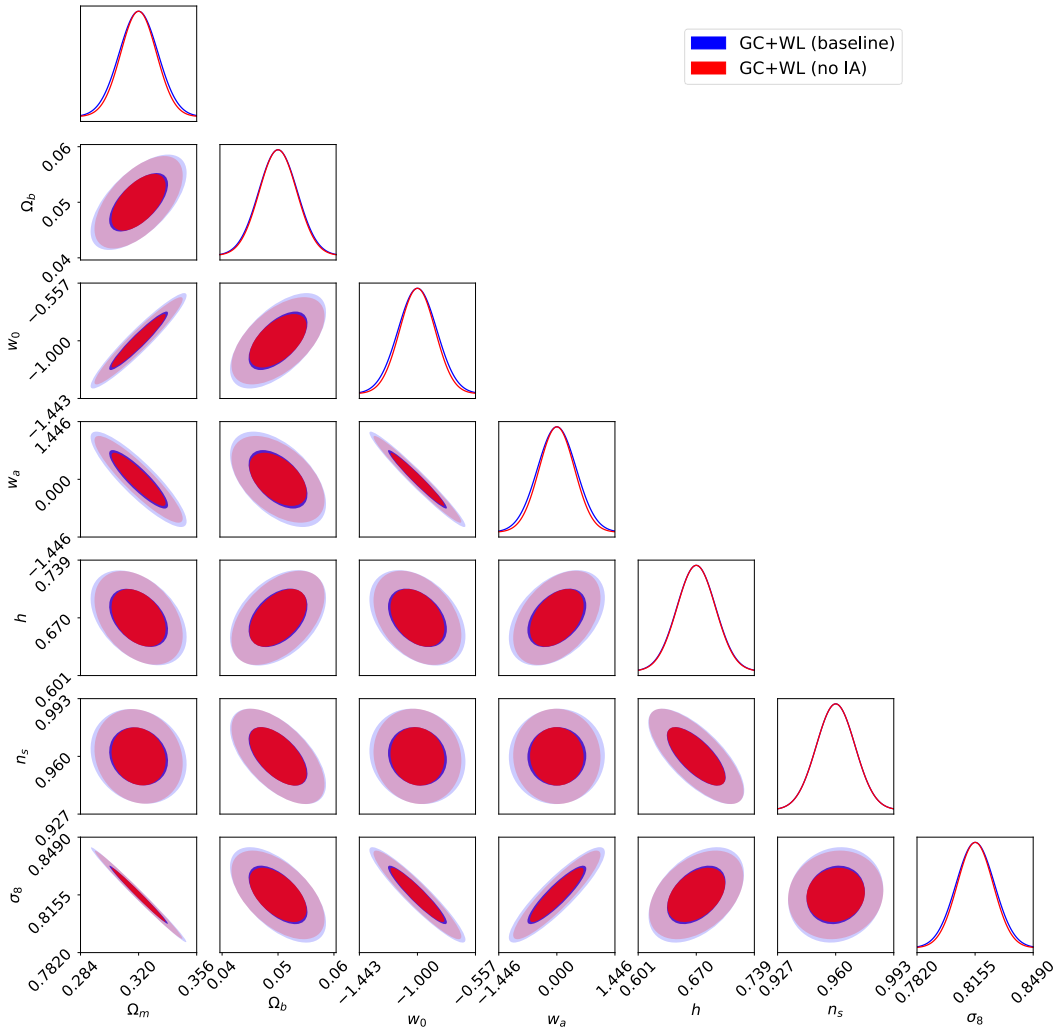

FIGURE A.30: Impact of intrinsic alignments on the 1σ and 2σ marginalized Fisher contours for the parameters of the baseline w_0w_aCDM model when we combine GCp and WL neglecting their cross-correlations.

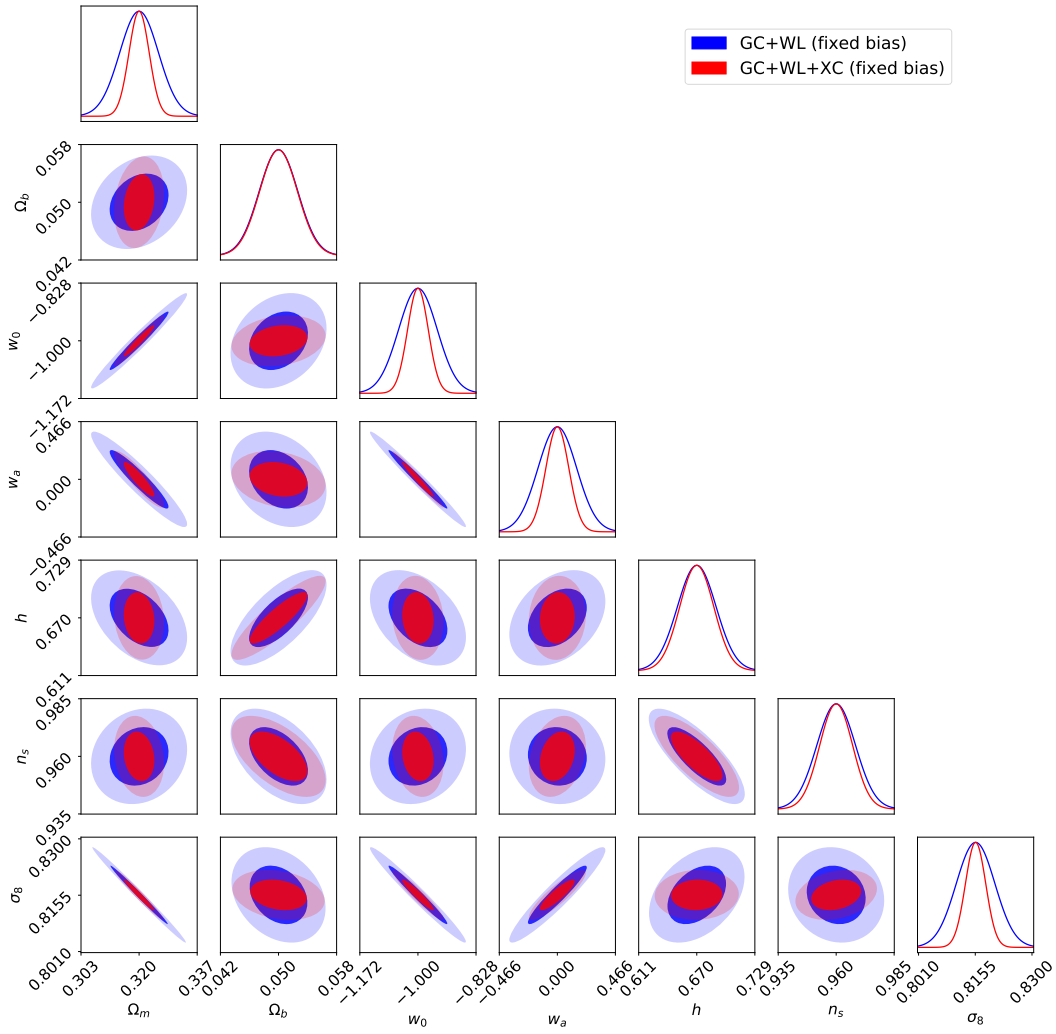

FIGURE A.31: Comparison of probe combination with (red) and without (blue) cross-correlations on the 1σ and 2σ marginalized Fisher contours for the parameters of the baseline w_0w_aCDM model when the nuisance galaxy bias parameters are fixed to their fiducial value.

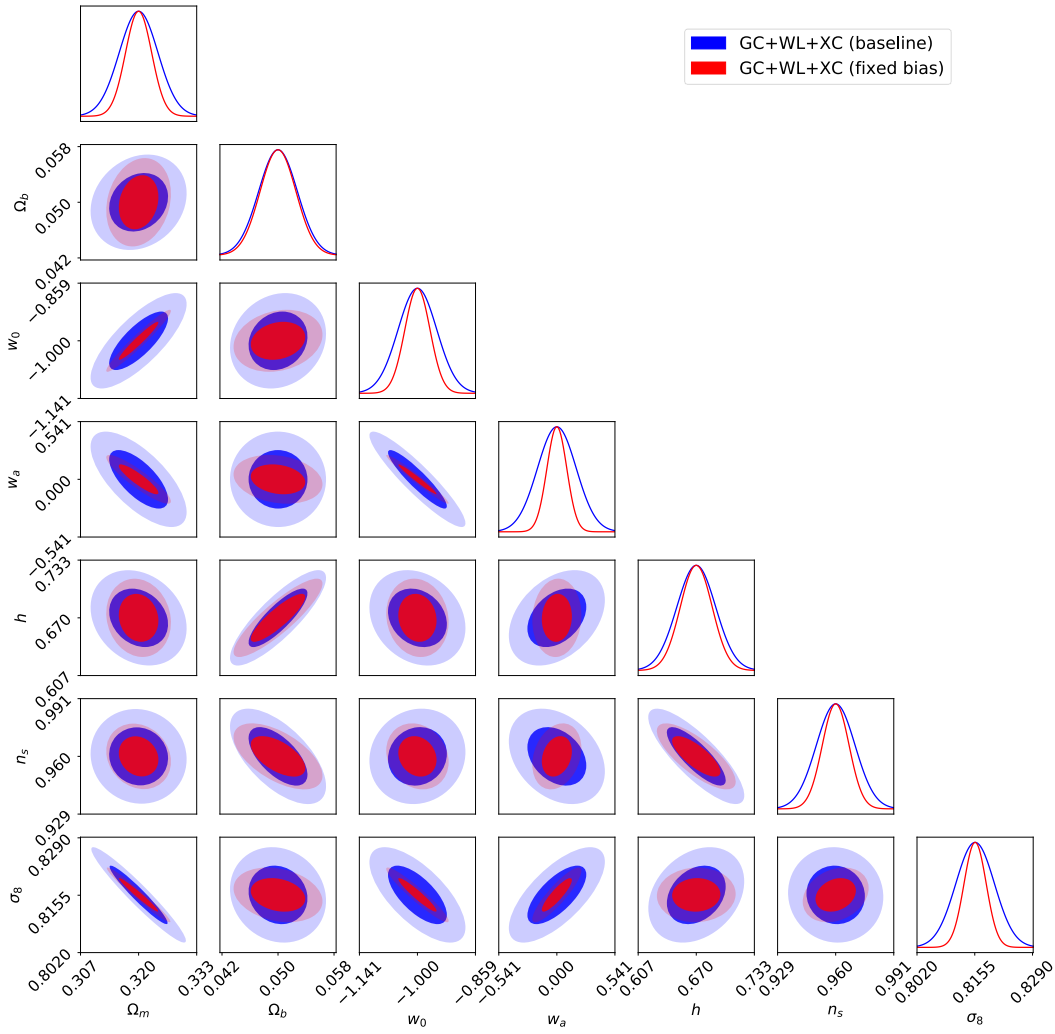

FIGURE A.32: Impact of fixed galaxy bias on the 1σ and 2σ marginalized Fisher contours for the parameters of the baseline w_0w_aCDM model when we combine GCp and WL taking into account their cross-correlations.

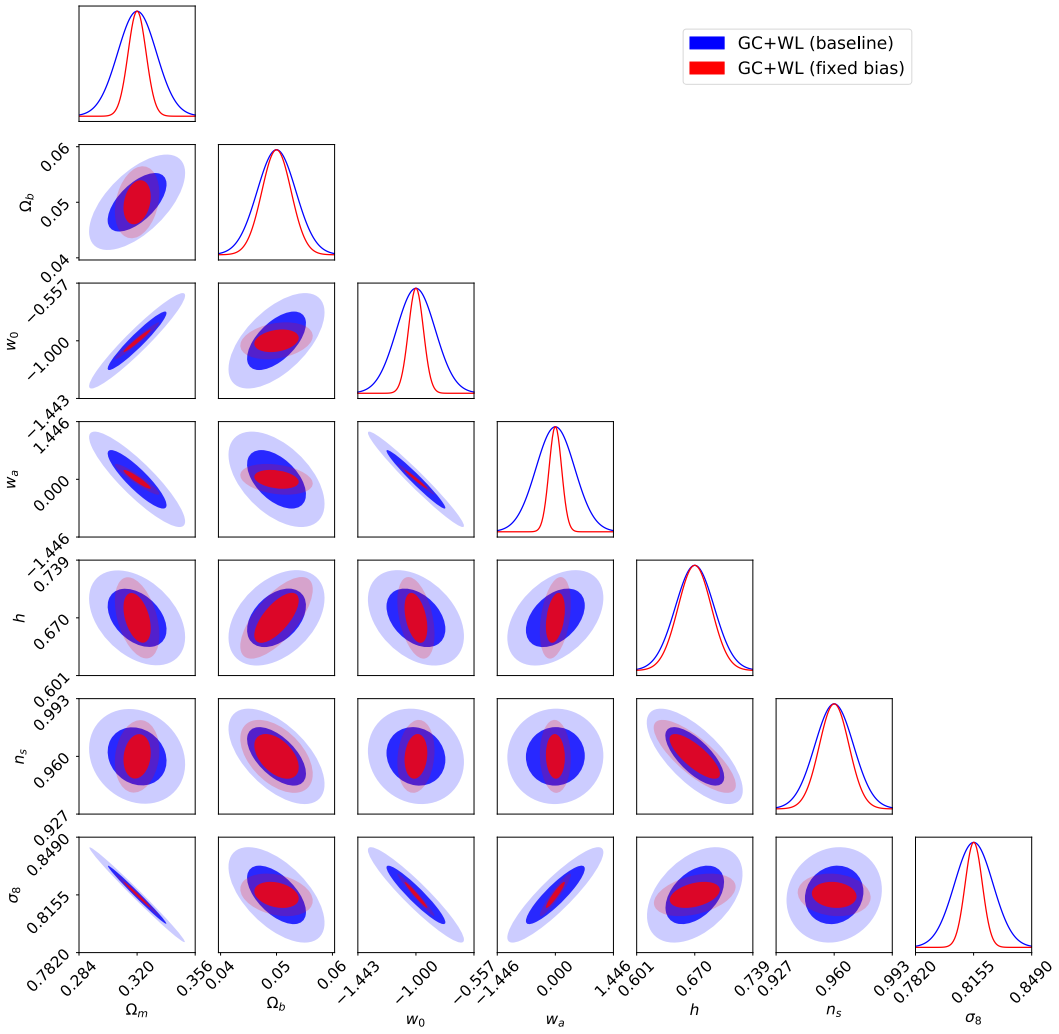

FIGURE A.33: Impact of fixed galaxy bias on the 1σ and 2σ marginalized Fisher contours for the parameters of the baseline w_0w_aCDM model when we combine GCp and WL neglecting their cross-correlations.

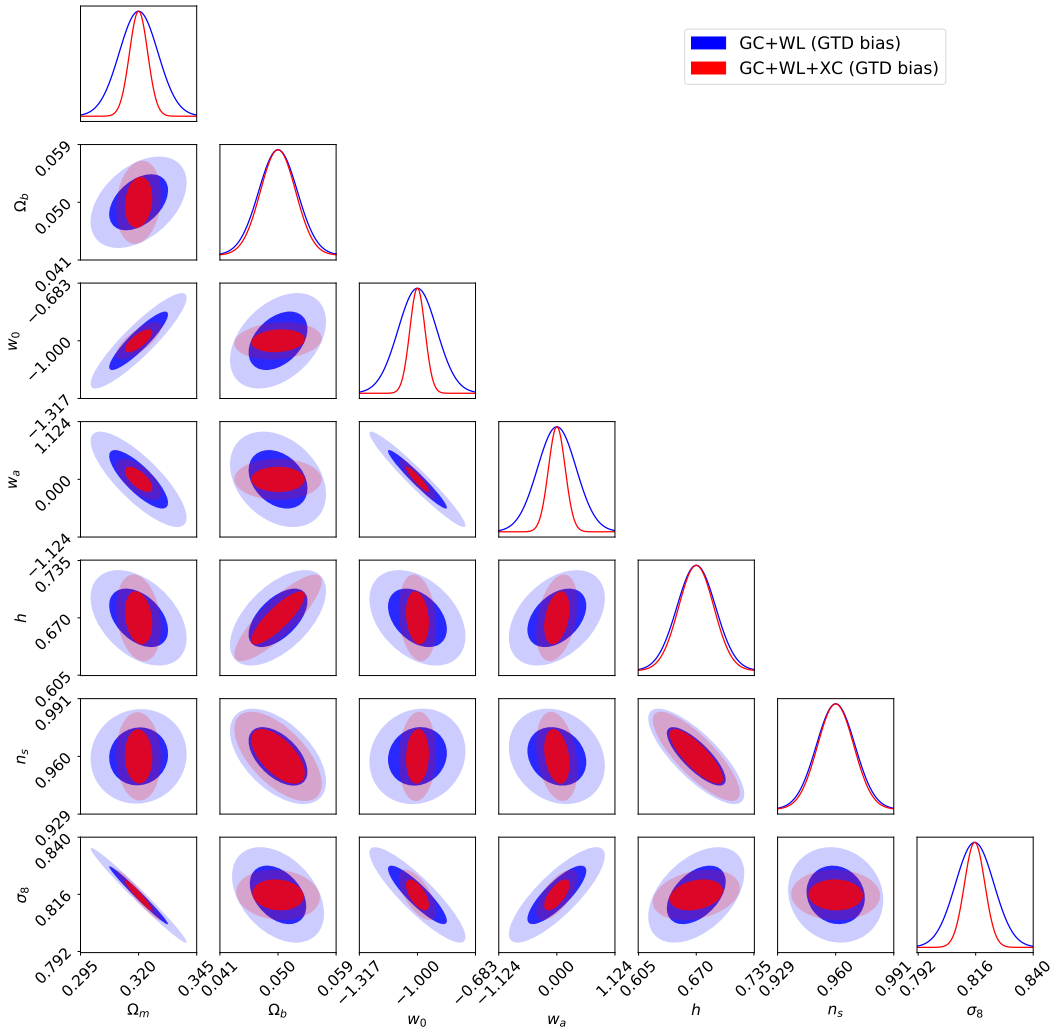

FIGURE A.34: Comparison of probe combination with (red) and without (blue) cross-correlations on the 1σ and 2σ marginalized Fisher contours for the parameters of the baseline w_0w_aCDM model when we consider the GTD model for the galaxy bias.

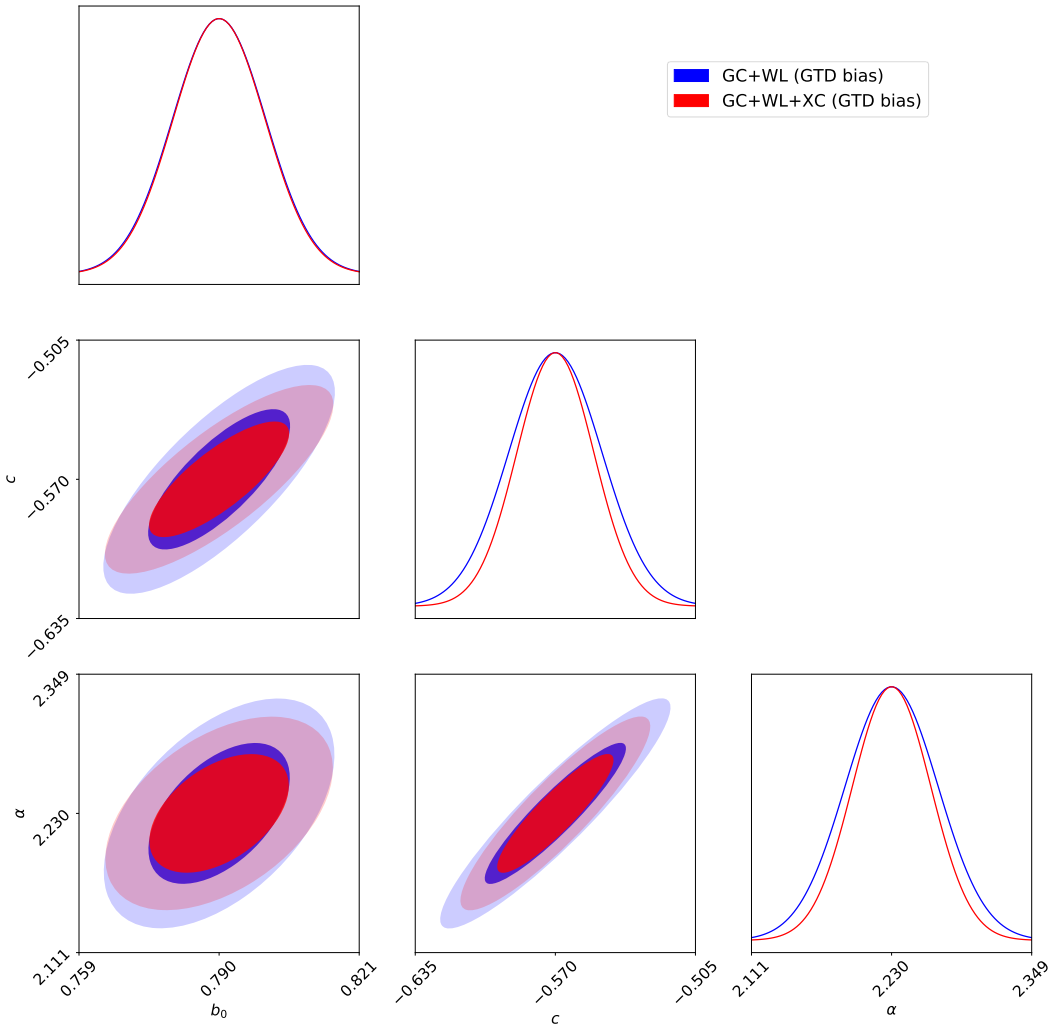

FIGURE A.35: Impact of cross-correlations on the GTD galaxy bias nuisance parameters constraints for the baseline w_0w_aCDM model.

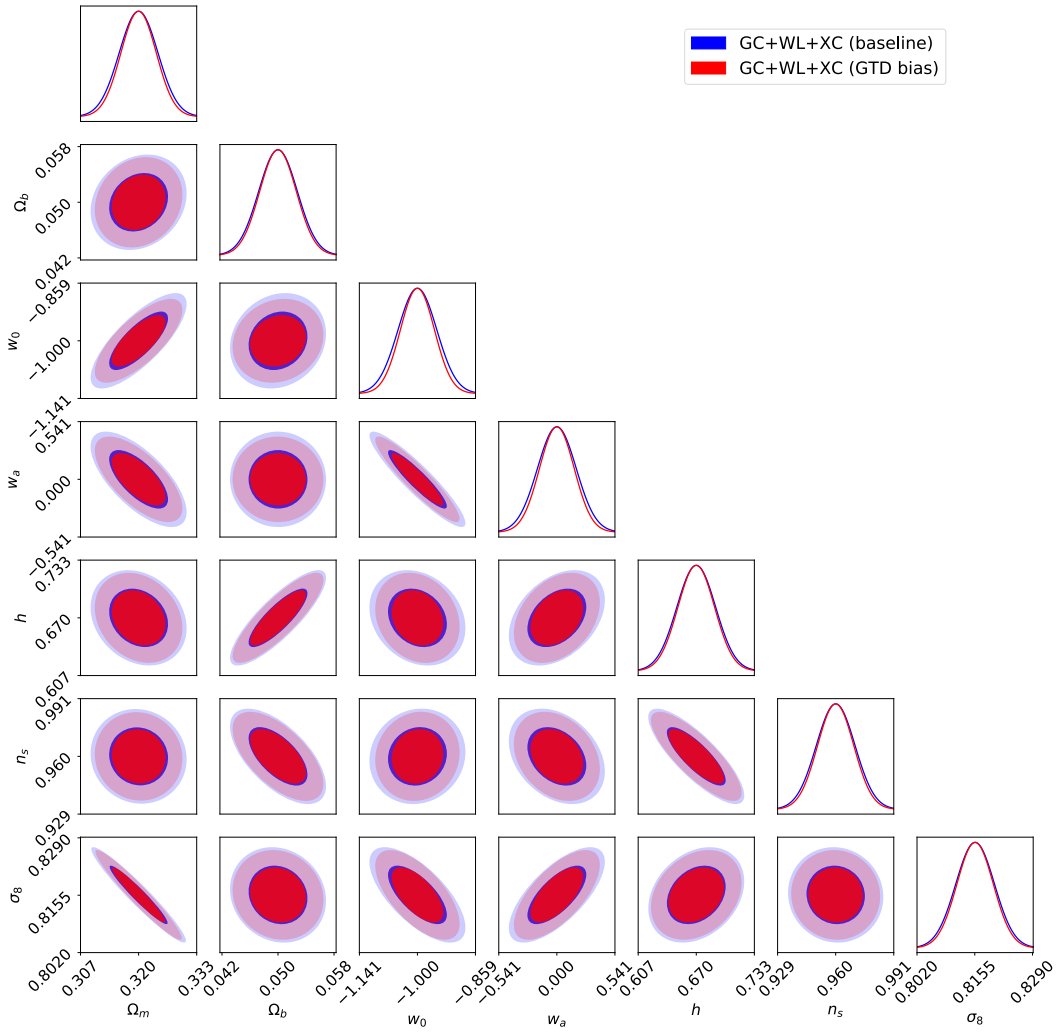

FIGURE A.36: Impact of GTD galaxy bias on the 1σ and 2σ marginalized Fisher contours for the parameters of the baseline w_0w_aCDM model when we combine GCp and WL taking into account their cross-correlations.

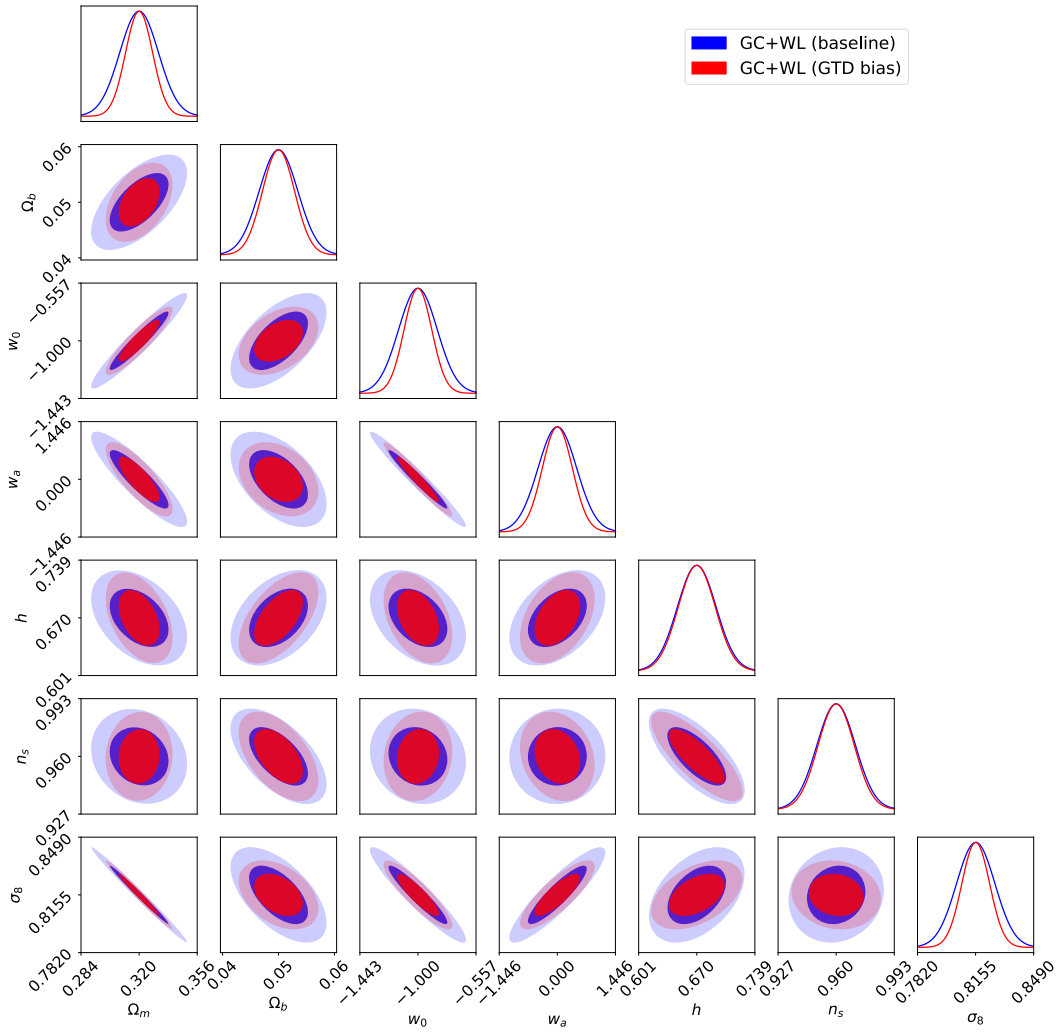

FIGURE A.37: Impact of GTD galaxy bias on the 1σ and 2σ marginalized Fisher contours for the parameters of the baseline w_0w_aCDM model when we combine GCp and WL neglecting their cross-correlations.

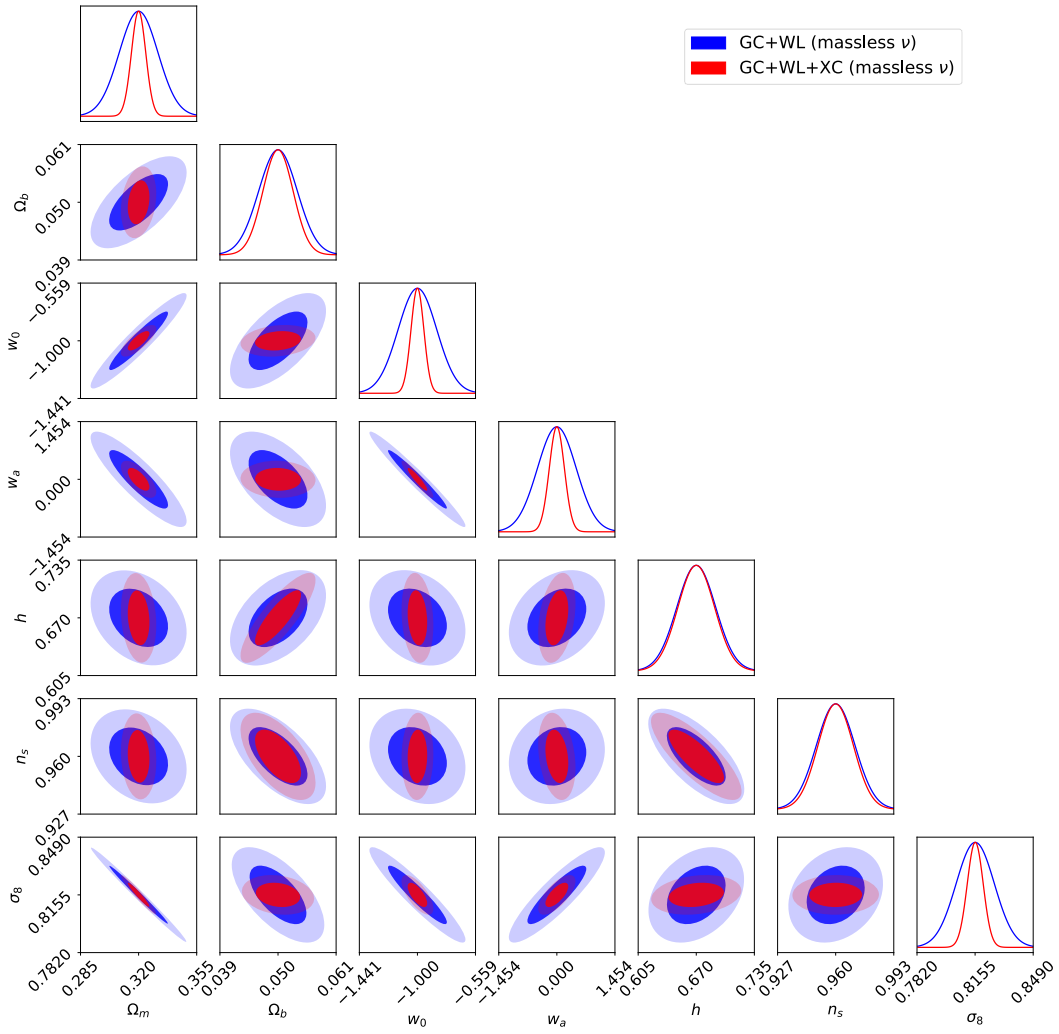

FIGURE A.38: Comparison of probe combination with (red) and without (blue) cross-correlations on the 1σ and 2σ marginalized Fisher contours for the parameters of the baseline w_0w_aCDM model when we consider 3 massless neutrinos.

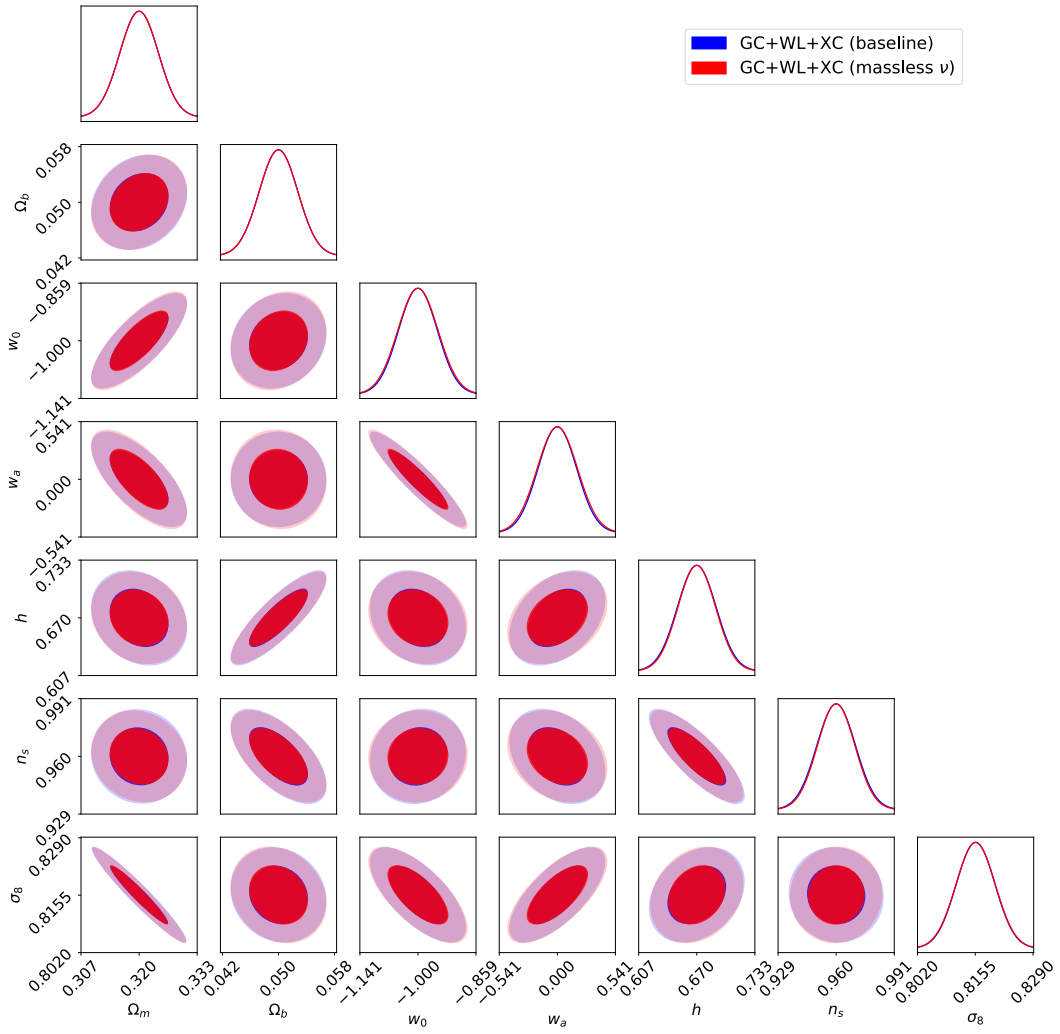

FIGURE A.39: Impact of massless neutrinos on the 1σ and 2σ marginalized Fisher contours for the parameters of the baseline w_0w_aCDM model when we combine GCp and WL taking into account their cross-correlations.

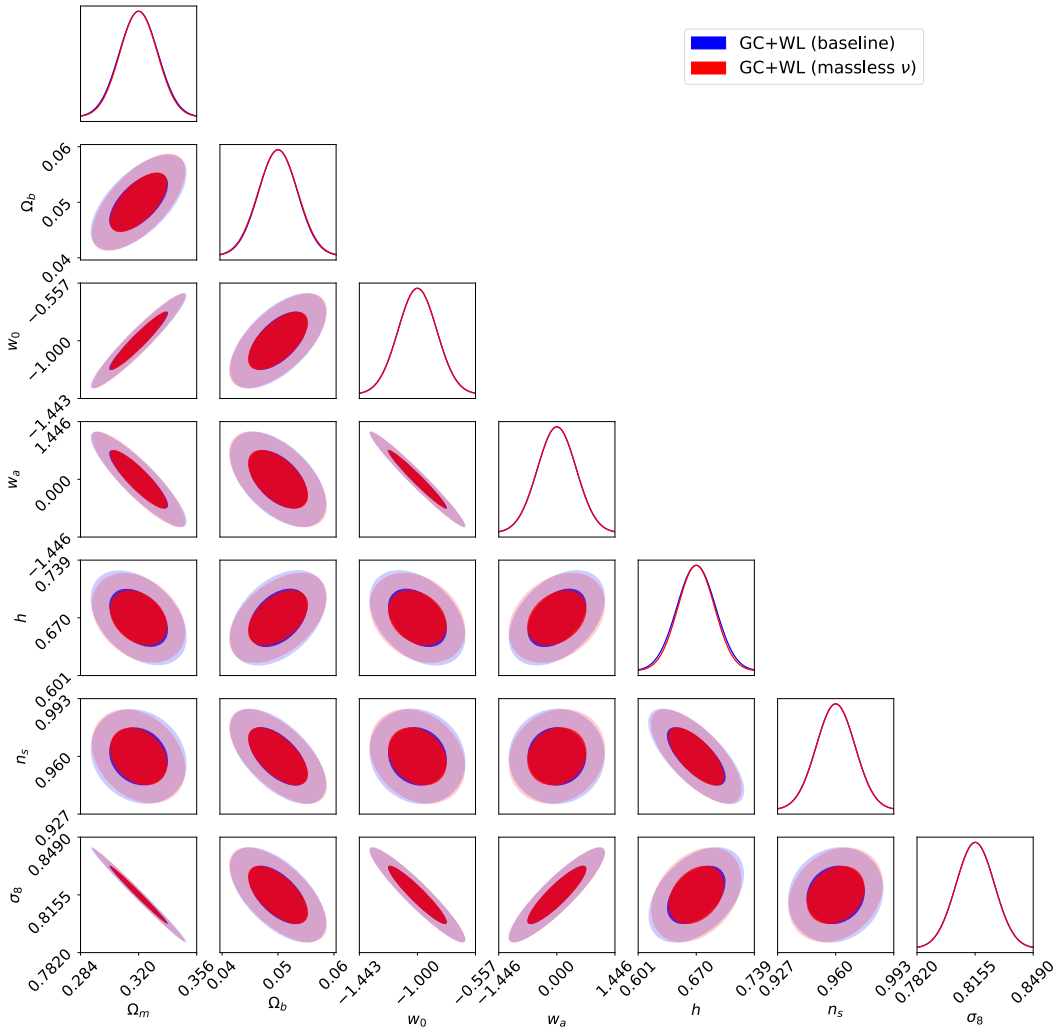

FIGURE A.40: Impact of massless neutrinos on the 1σ and 2σ marginalized Fisher contours for the parameters of the baseline w_0w_aCDM model when we combine GCp and WL neglecting their cross-correlations.

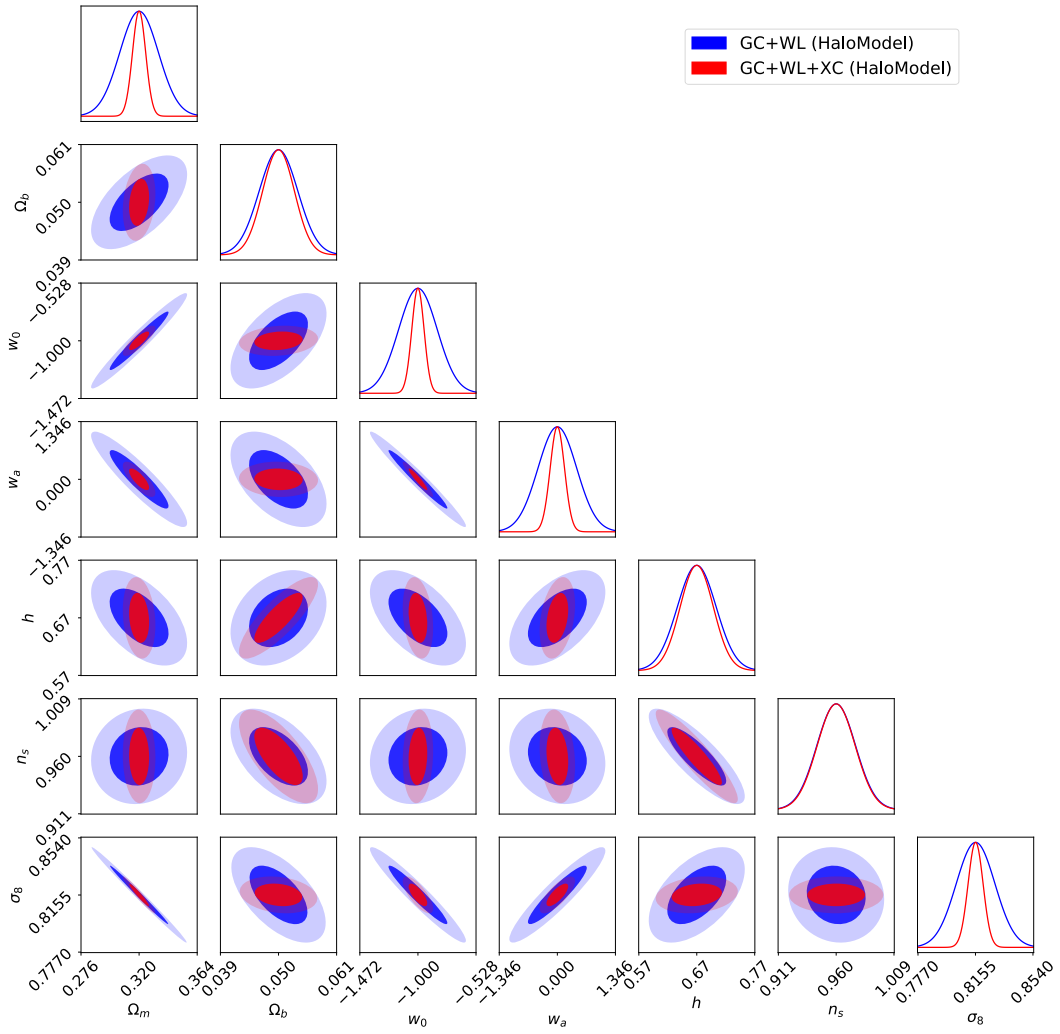

FIGURE A.41: Comparison of probe combination with (red) and without (blue) cross-correlations on the 1σ and 2σ marginalized Fisher contours for the parameters of the baseline w_0w_aCDM model when we consider the `HaloModel` non-linear correction.

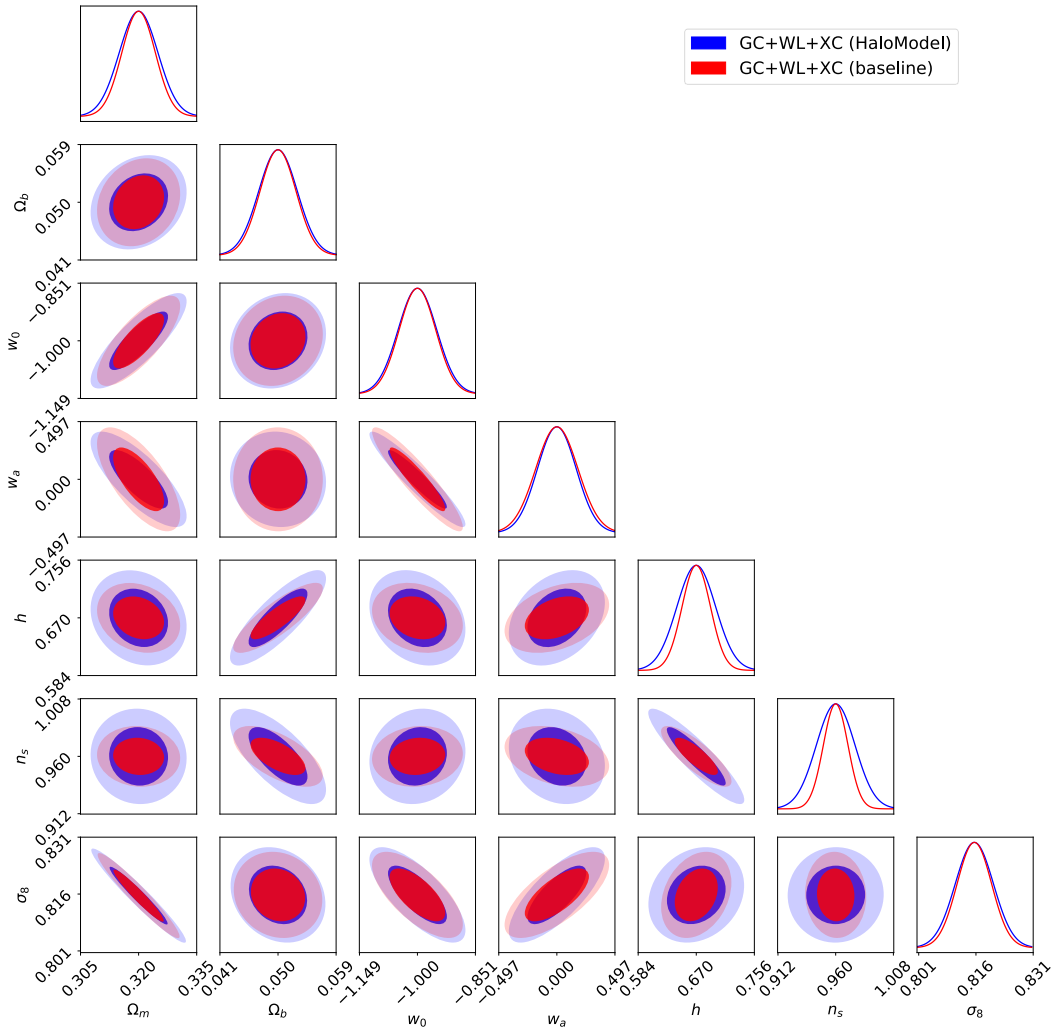

FIGURE A.42: Impact of the `HaloModel` non-linear correction on the 1σ and 2σ marginalized Fisher contours for the parameters of the baseline w_0w_aCDM model when we combine GCp and WL taking into account their cross-correlations.

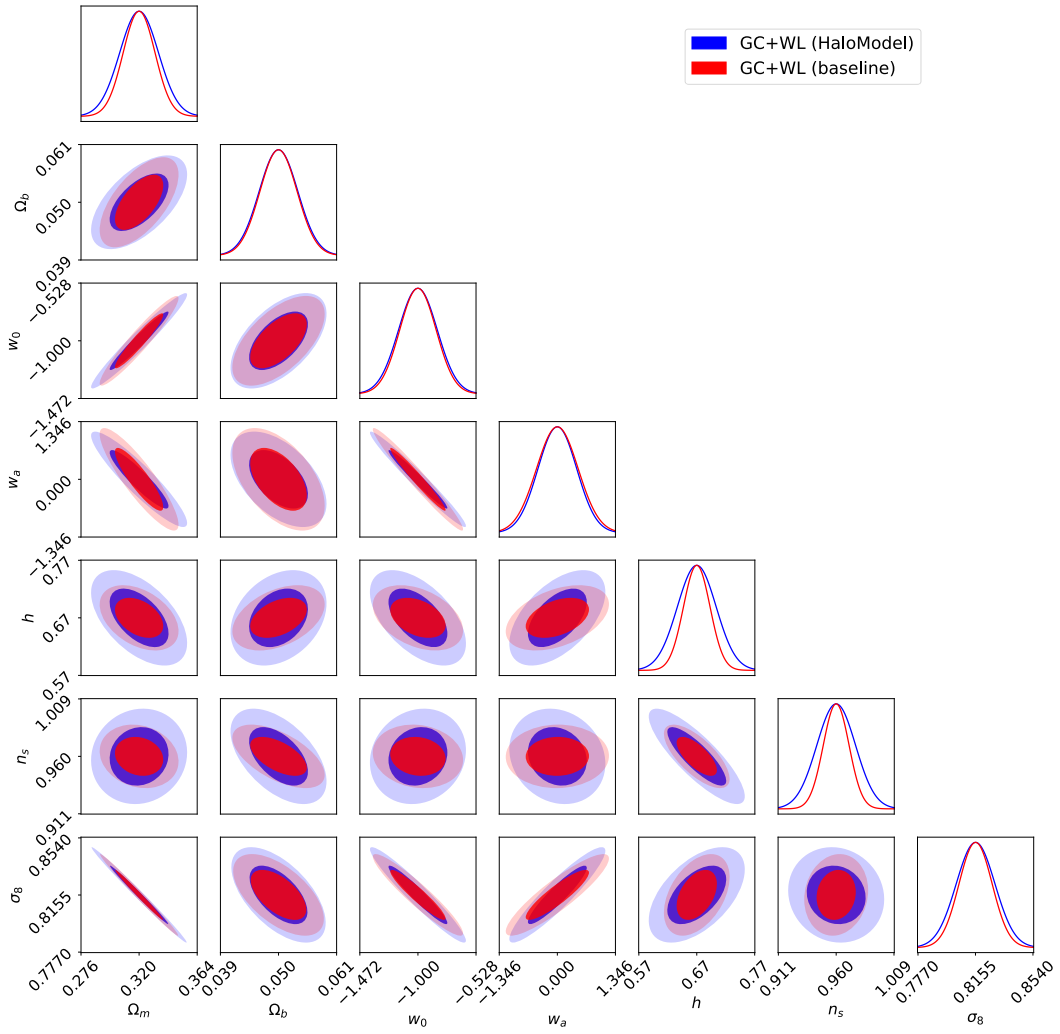

FIGURE A.43: Impact of the `HaloModel` non-linear correction on the 1σ and 2σ marginalized Fisher contours for the parameters of the baseline w_0w_aCDM model when we combine GCp and WL neglecting their cross-correlations.

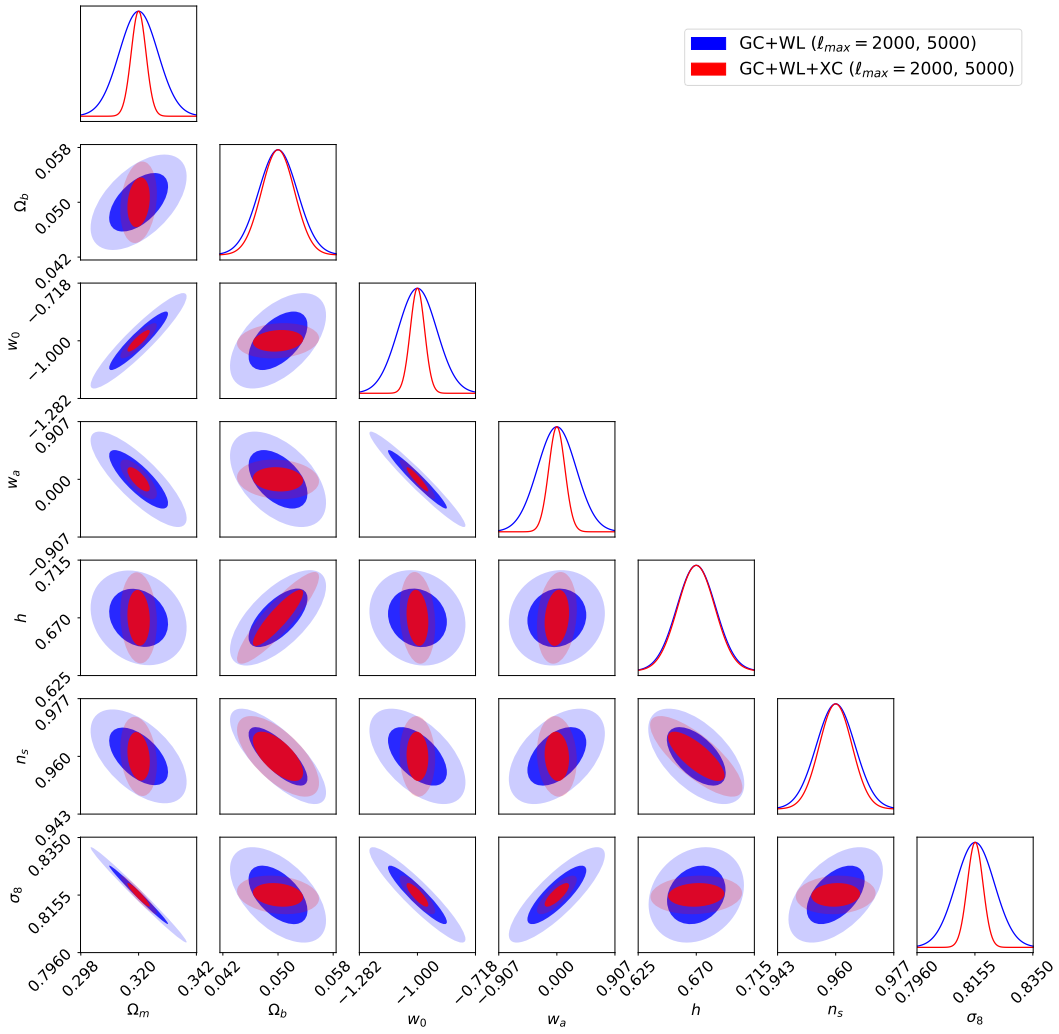

FIGURE A.44: Comparison of probe combination with (red) and without (blue) cross-correlations on the 1σ and 2σ marginalized Fisher contours for the parameters of the baseline $w_0 w_a$CDM model when we consider more non-linear scales with $\ell_{\rm max} = 2000$ for GCp and XC, and $\ell_{\rm max} = 5000$ for WL.

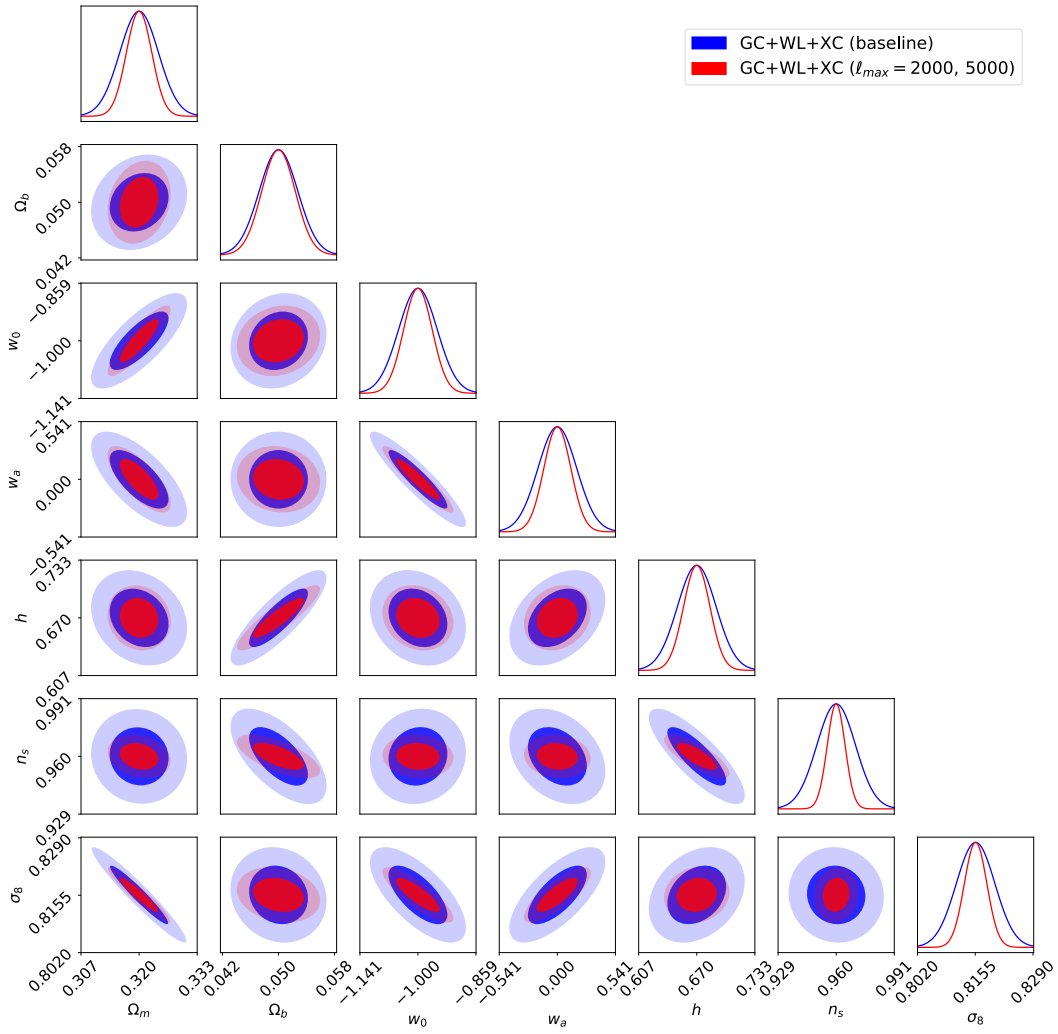

FIGURE A.45: Impact of a higher $\ell_{\rm max}$ cut (2000 for GCp and XC, and 5000 for WL) on the 1σ and 2σ marginalized Fisher contours for the parameters of the baseline w_0w_aCDM model when we combine GCp and WL taking into account their cross-correlations.

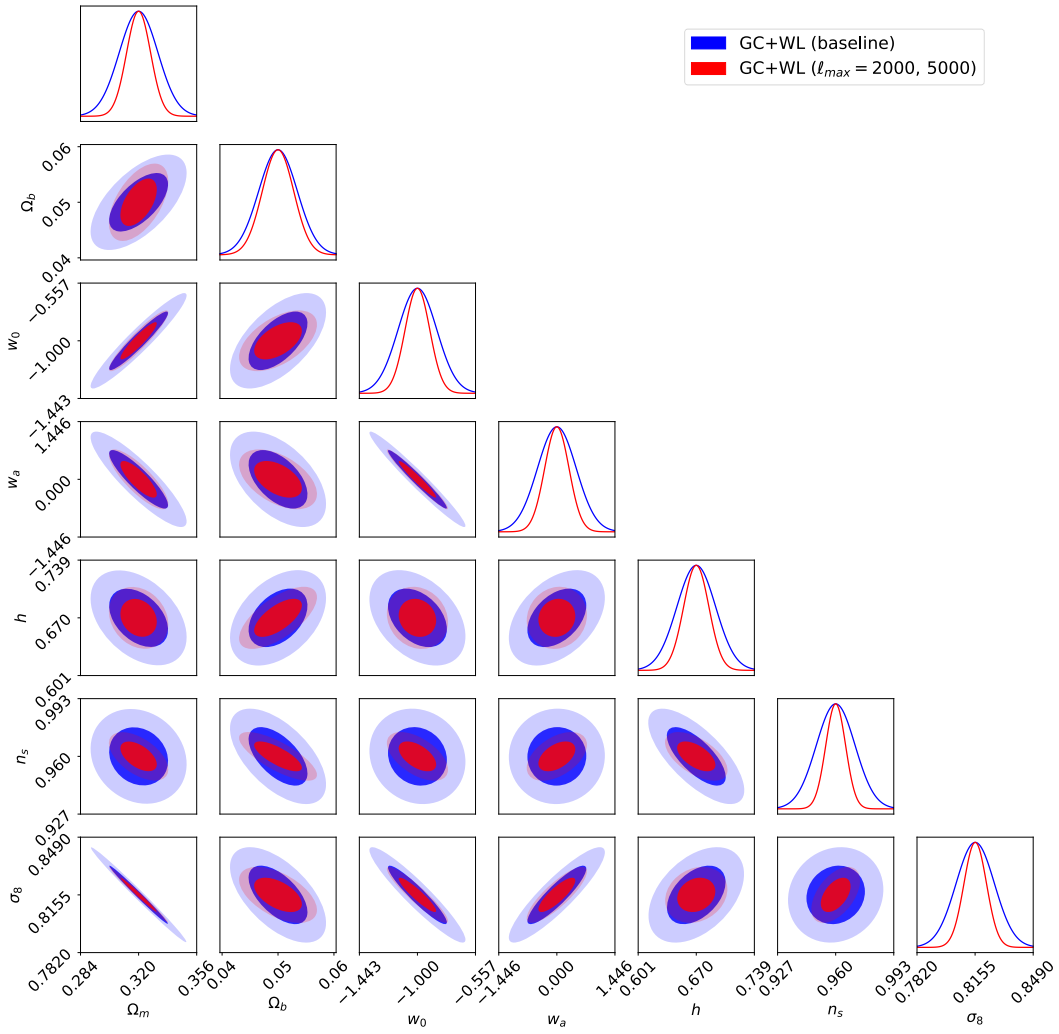

FIGURE A.46: Impact of a higher $\ell_{\max}$ cut (2000 for GCp and XC, and 5000 for WL) on the 1σ and 2σ marginalized Fisher contours for the parameters of the baseline w_0w_aCDM model when we combine GCp and WL neglecting their cross-correlations.

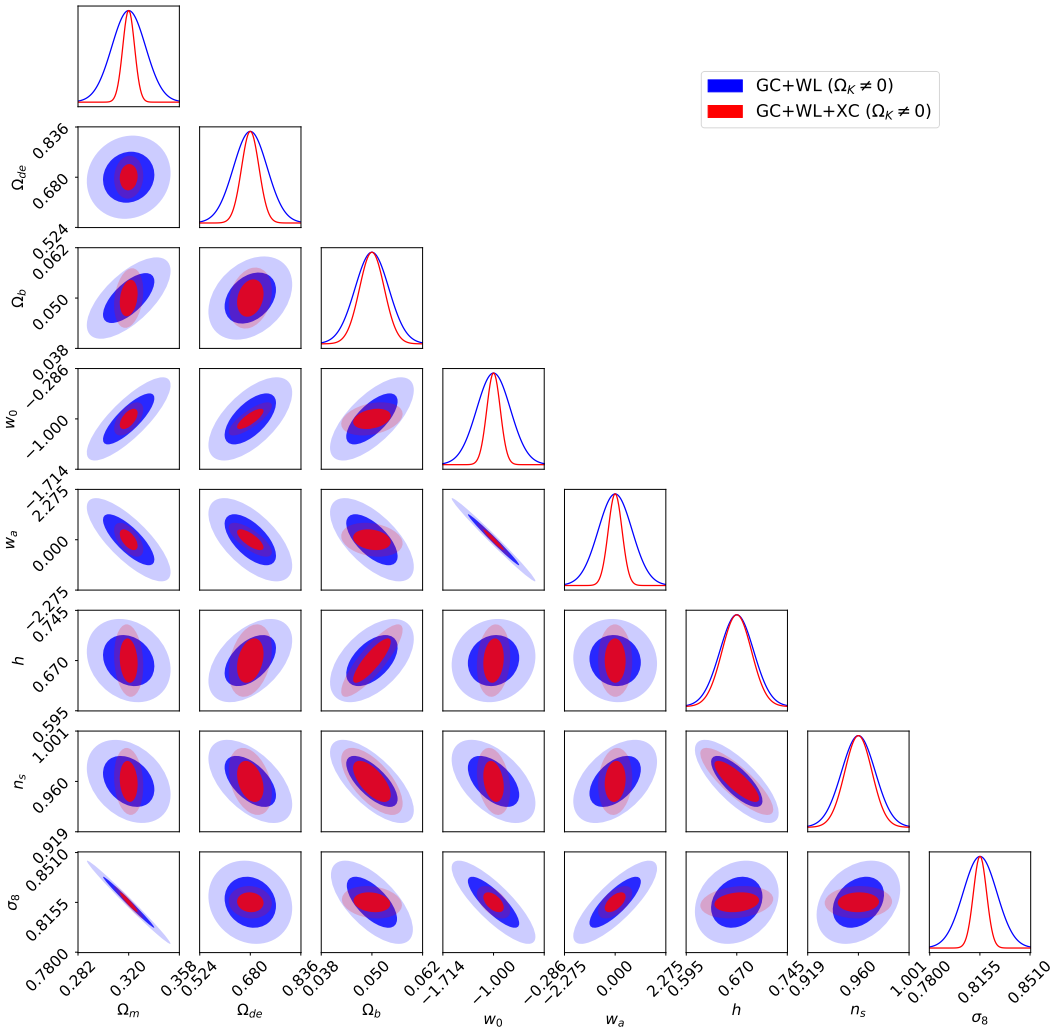

FIGURE A.47: Comparison of probe combination with (red) and without (blue) cross-correlations on the 1σ and 2σ marginalized Fisher contours for the parameters of the baseline $w_0 w_a$CDM model when we allow for a non-flat universe.

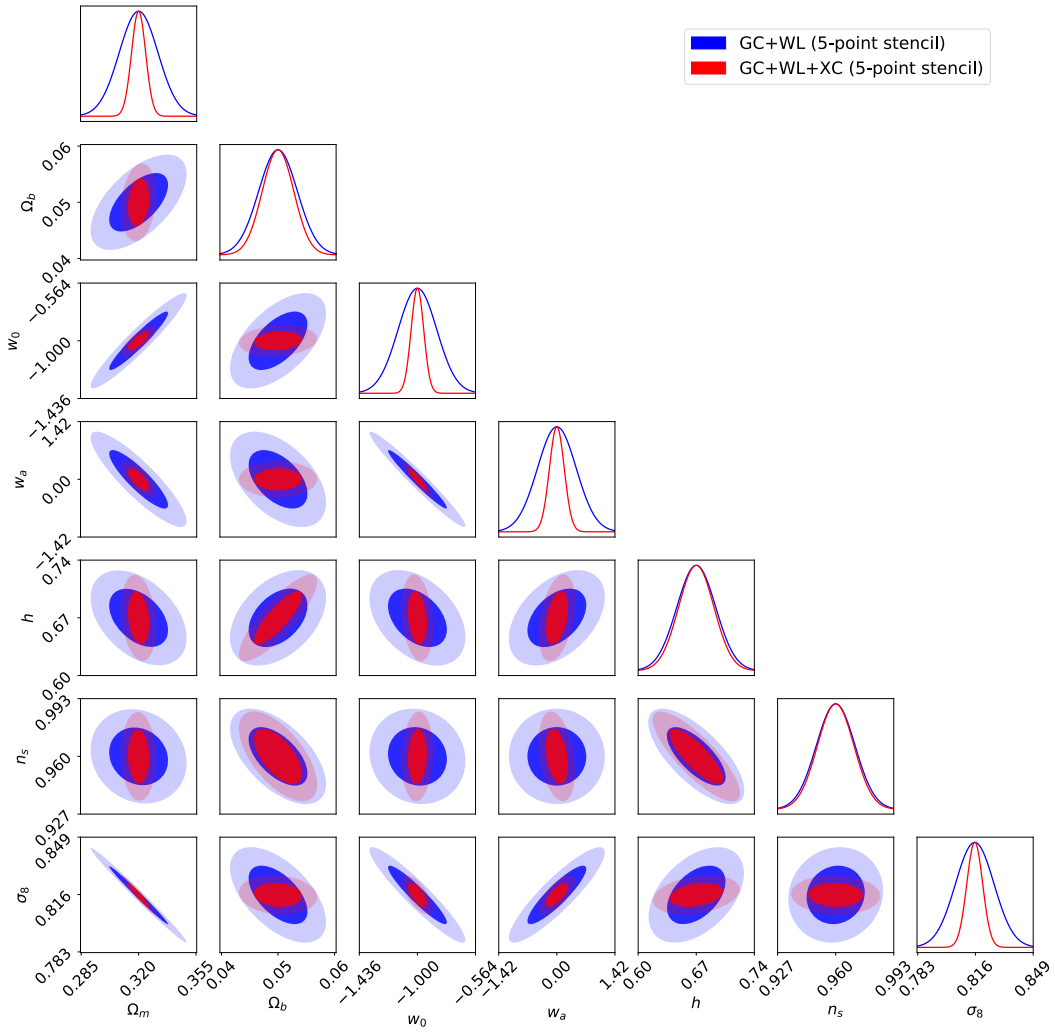

FIGURE A.48: Comparison of probe combination with (red) and without (blue) cross-correlations on the 1σ and 2σ marginalized Fisher contours for the parameters of the baseline w_0w_aCDM model when we use the 5-point stencil method for the numerical derivatives.

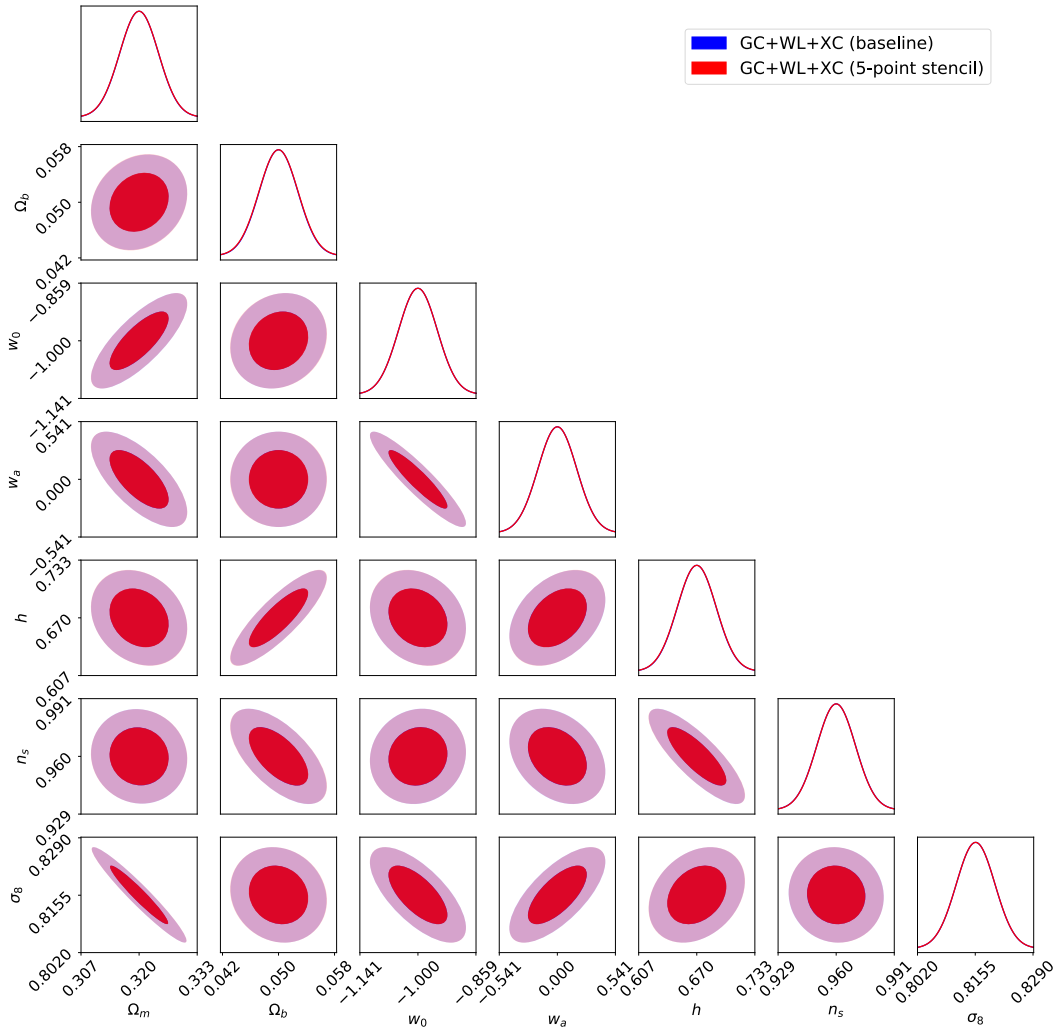

FIGURE A.49: Impact of 5-point stencil method derivatives on the 1σ and 2σ marginalized Fisher contours for the parameters of the baseline w_0w_aCDM model when we combine GCp and WL taking into account their cross-correlations.

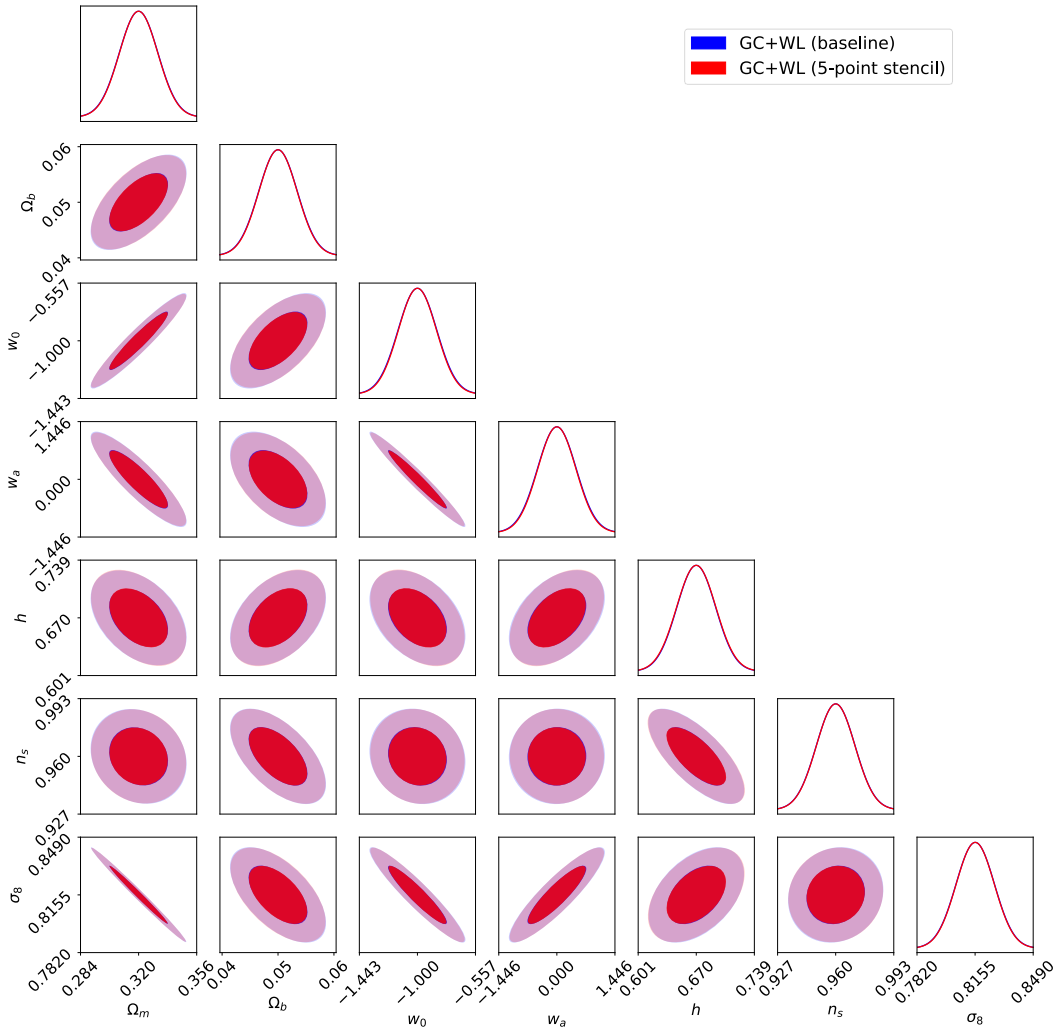

FIGURE A.50: Impact of 5-point stencil method derivatives on the 1σ and 2σ marginalized Fisher contours for the parameters of the baseline w_0w_aCDM model when we combine GCp and WL neglecting their cross-correlations.

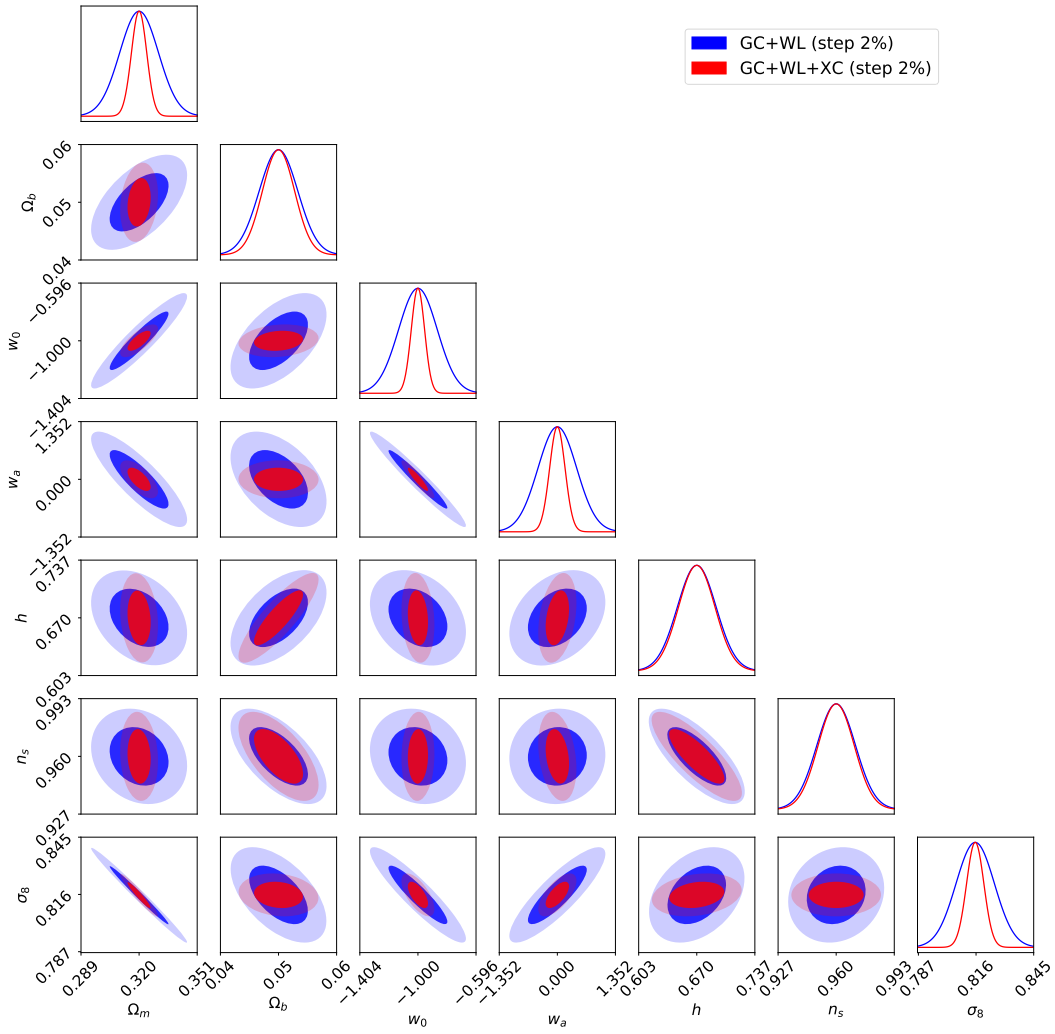

FIGURE A.51: Comparison of probe combination with (red) and without (blue) cross-correlations on the 1σ and 2σ marginalized Fisher contours for the parameters of the baseline w_0w_aCDM model when we use a step of 2 % for the numerical derivatives.

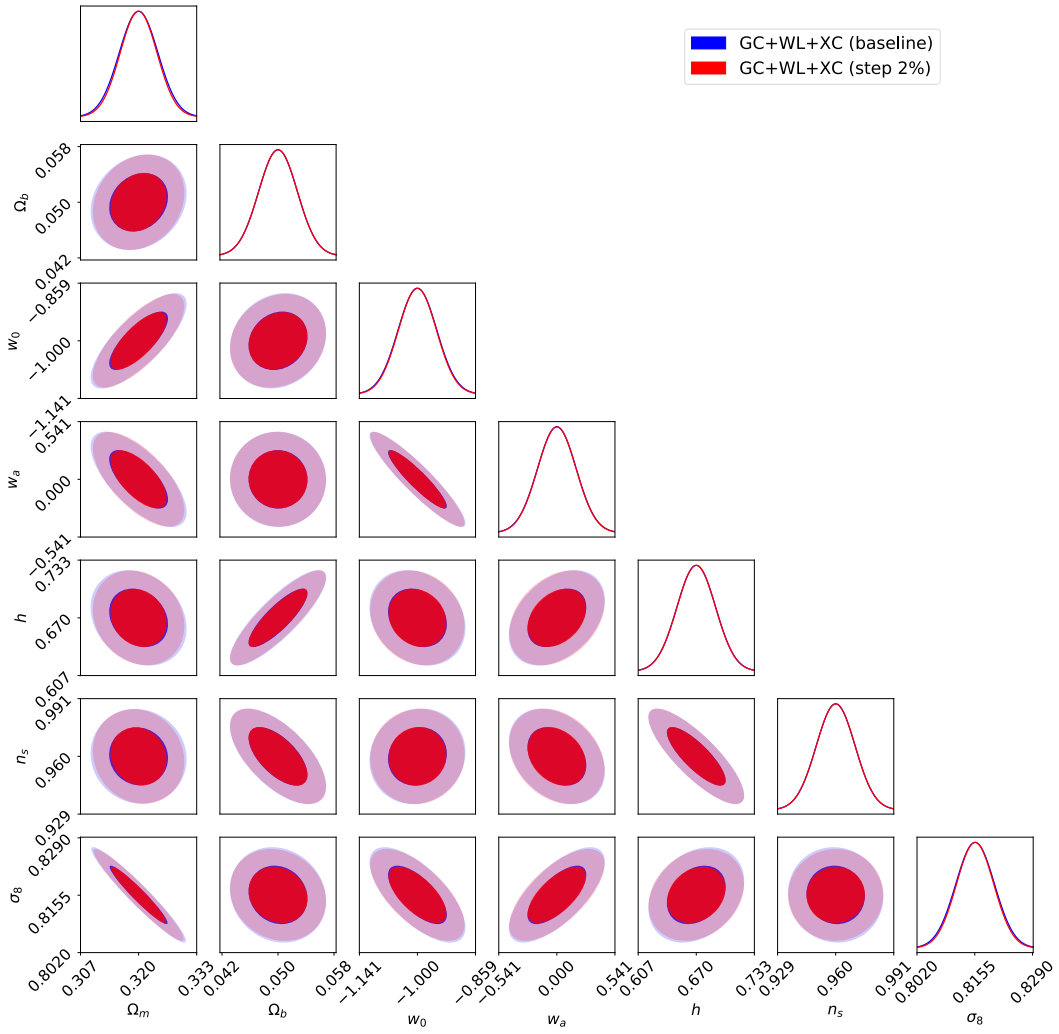

FIGURE A.52: Impact of a 2 % step in the derivatives on the 1σ and 2σ marginalized Fisher contours for the parameters of the baseline w_0w_aCDM model when we combine GCp and WL taking into account their cross-correlations.

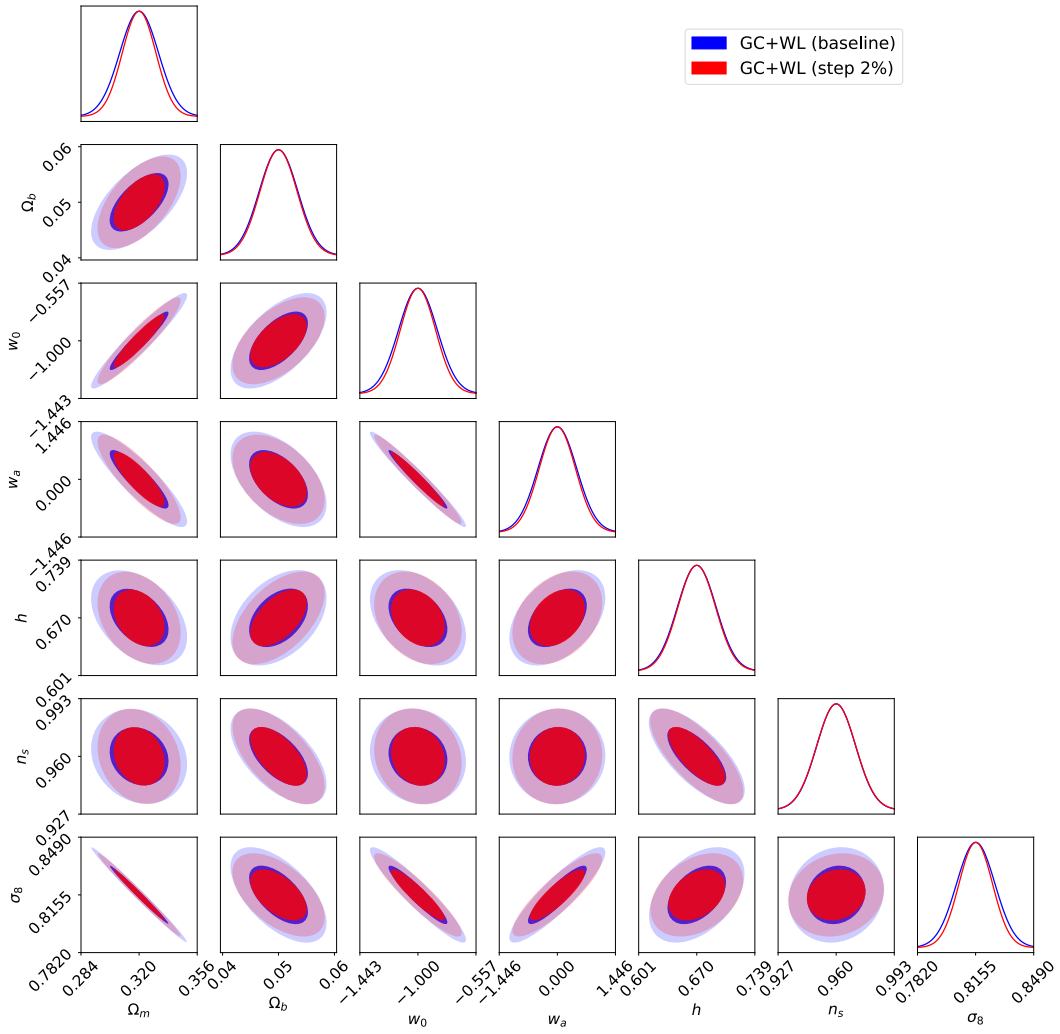

FIGURE A.53: Impact of a 2 % step in the derivatives on the 1σ and 2σ marginalized Fisher contours for the parameters of the baseline w_0w_aCDM model when we combine GCp and WL neglecting their cross-correlations.

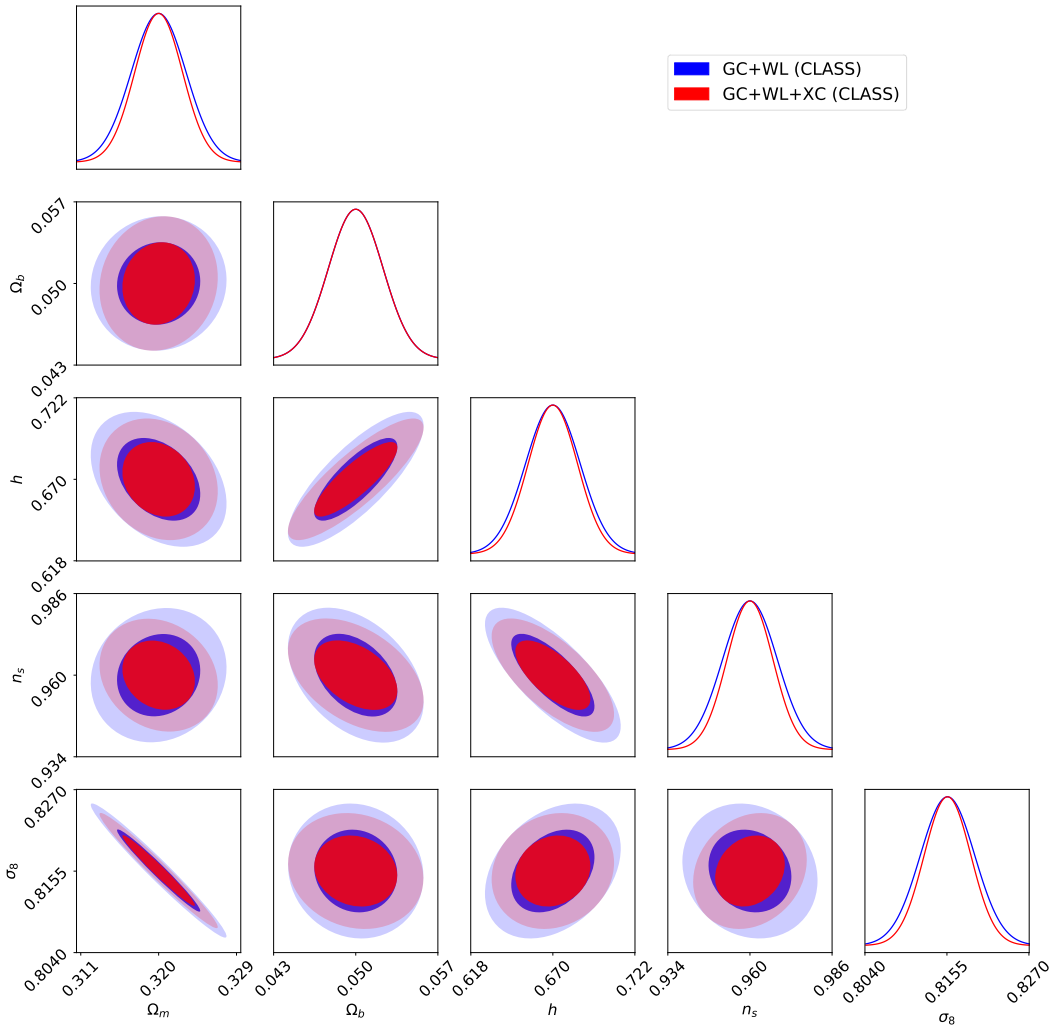

FIGURE A.54: Comparison of probe combination with (red) and without (blue) cross-correlations on the 1σ and 2σ marginalized Fisher contours for the parameters of the baseline ΛCDM model when we use `CLASS` as Boltzmann solver.

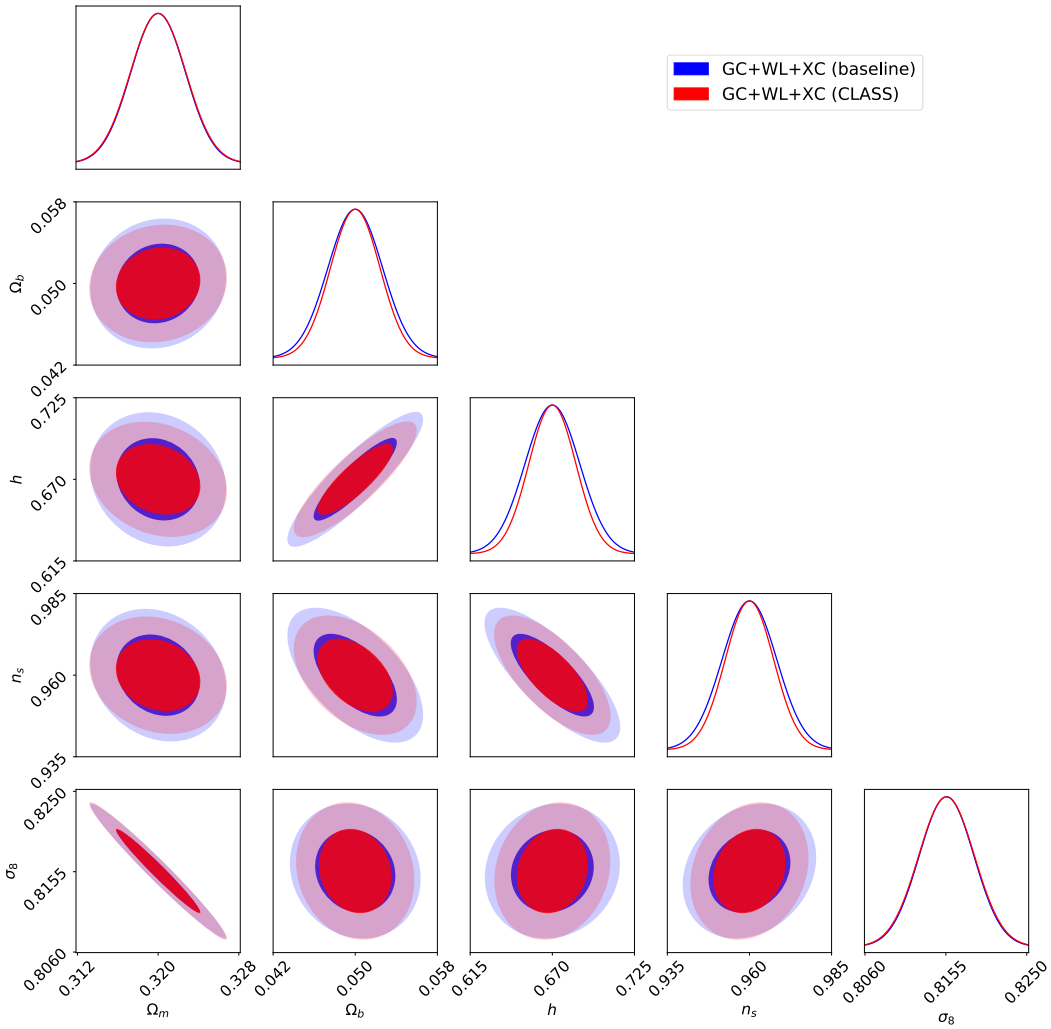

FIGURE A.55: Impact of `CLASS` as Boltzmann solver on the 1σ and 2σ marginalized Fisher contours for the parameters of the baseline ΛCDM model when we combine GCp and WL taking into account their cross-correlations.

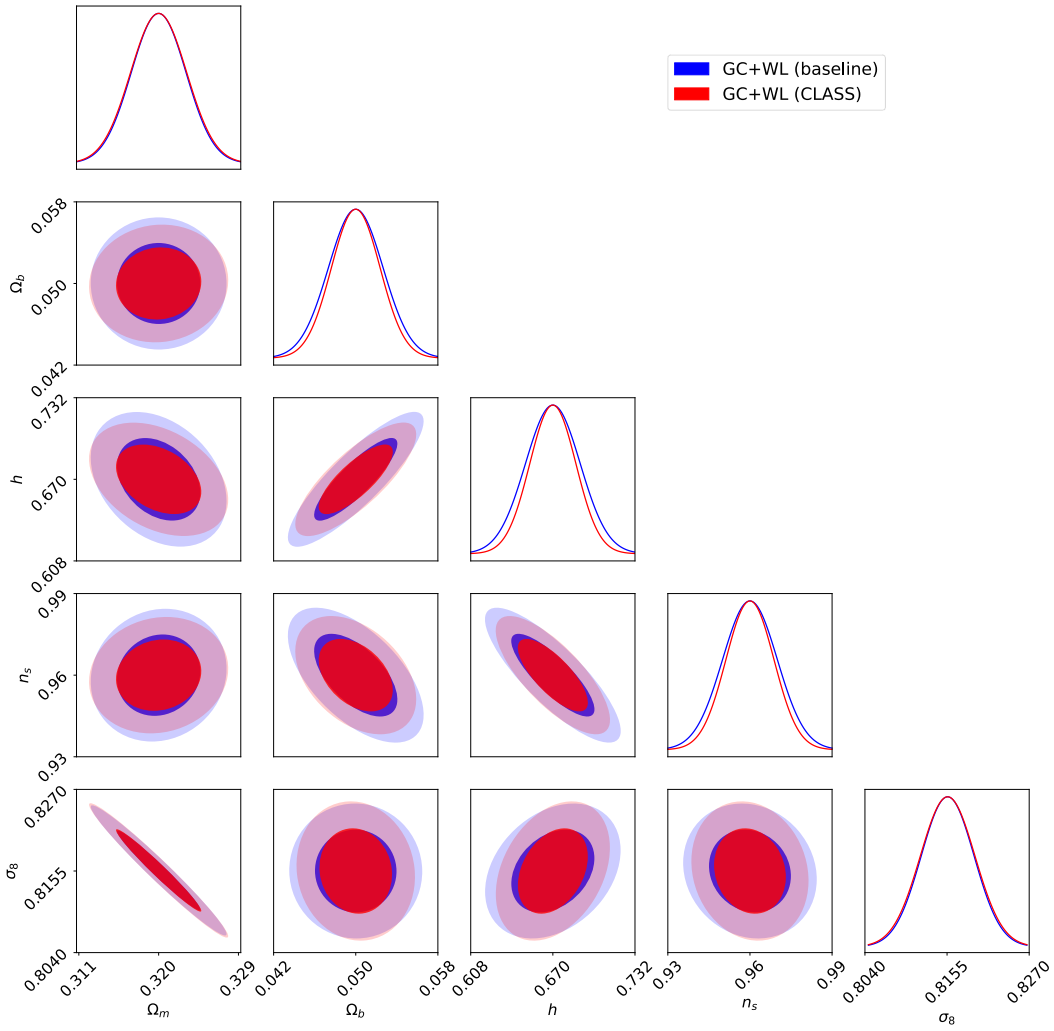

FIGURE A.56: Impact of `CLASS` as Boltzmann solver on the 1σ and 2σ marginalized Fisher contours for the parameters of the baseline ΛCDM model when we combine GCp and WL neglecting their cross-correlations.

A.5 CAMB and CLASS input files

```
*~~~~~~~~~~~~~~~~~~~~~~~~~~~~~~~~~*
*  CAMB input file  *
*~~~~~~~~~~~~~~~~~~~~~~~~~~~~~~~~~*
! Ranges of the redshift and matter power
! zmin = 0.0
! zmax = 4.0
! nz = 500
! kmin = 1e-6
! kmax = 50.
! nk = 10000

#Parameters for CAMB
output_root = test
get_scalar_cls = T
get_vector_cls = F
get_tensor_cls = F
get_transfer   = F
do_lensing     = F
do_nonlinear = 0

l_max_scalar      = 1200
l_max_tensor      = 1200
k_eta_max_scalar  = 2400
k_eta_max_tensor  = 2400

use_physical   = T
ombh2          = 0.022445
omch2          = 0.121203
omnuh2         = 0.000645145613
omk            = 0
hubble         = 67
w              = -1
cs2_lam        = 1

temp_cmb           = 2.726
helium_fraction    = 0.24

massless_neutrinos = 2.046
nu_mass_eigenstates = 1
massive_neutrinos  = 1
share_delta_neff = T
```

```
nu_mass_fractions = 1
nu_mass_degeneracies =

initial_power_num         = 1
pivot_scalar              = 0.05
pivot_tensor              = 0.05
scalar_amp(1)             = 2.181866264961206e-9
scalar_spectral_index(1)  = 0.96
scalar_nrun(1)            = 0
scalar_nrunrun(1)         = 0
tensor_spectral_index(1)  = 0
tensor_nrun(1)            = 0
tensor_parameterization   = 1

reionization          = T
re_use_optical_depth = T
re_optical_depth      = 0.058
re_redshift           = 11
re_delta_redshift     = 0.5
re_ionization_frac    = -1

re_helium_redshift = 3.5
re_helium_delta_redshift = 0.5

RECFAST_fudge = 1.14
RECFAST_fudge_He = 0.86
RECFAST_Heswitch = 6
RECFAST_Hswitch  = T

initial_condition   = 1
initial_vector = -1 0 0 0 0

vector_mode = 0

COBE_normalize = F
CMB_outputscale = 7.4311e12

transfer_high_precision = T
transfer_kmax           = 2
transfer_k_per_logint   = 0
transfer_num_redshifts  = 1
transfer_interp_matterpower = T
transfer_redshift(1)    = 0
```

```
transfer_filename(1)     = transfer_out.dat
transfer_matterpower(1) = matterpower.dat
transfer_power_var = 7

scalar_output_file = scalCls.dat
vector_output_file = vecCls.dat
tensor_output_file = tensCls.dat
total_output_file  = totCls.dat
lensed_output_file = lensedCls.dat
lensed_total_output_file  =lensedtotCls.dat
lens_potential_output_file = lenspotentialCls.dat
FITS_filename       = scalCls.fits

do_lensing_bispectrum = F
do_primordial_bispectrum = F

bispectrum_nfields = 1
bispectrum_slice_base_L = 0
bispectrum_ndelta=3
bispectrum_delta(1)=0
bispectrum_delta(2)=2
bispectrum_delta(3)=4
bispectrum_do_fisher= F
bispectrum_fisher_noise=0
bispectrum_fisher_noise_pol=0
bispectrum_fisher_fwhm_arcmin=7
bispectrum_full_output_file=
bispectrum_full_output_sparse=F
bispectrum_export_alpha_beta=F

feedback_level = 0
output_file_headers = T
derived_parameters = T
lensing_method = 1
accurate_BB = F
massive_nu_approx = 1
accurate_polarization   = T
accurate_reionization   = T
do_tensor_neutrinos     = T
accurate_massive_neutrino_transfers = T
do_late_rad_truncation   = T
halofit_version=
number_of_threads       = 0
```

```
high_accuracy_default=T
accuracy_boost          = 2
l_accuracy_boost        = 2
l_sample_boost          = 1
```

```
*~~~~~~~~~~~~~~~~~~~~~~~~~~~~~~~~~*
*  CLASS input file  *
*~~~~~~~~~~~~~~~~~~~~~~~~~~~~~~~~~*
# Ranges of the redshift and matter power
# zmin = 0.0
# zmax = 4.0
# dz = 0.01
# kmin = 1e-4
# kmax = 50*h
# nk = 100

------------------------------
----> background parameters:
------------------------------
h =0.67
T_cmb = 2.726
Omega_b = 0.05
N_ur = 2.046
Omega_cdm = 0.27
Omega_dcdmdr = 0.0
Gamma_dcdm = 0.0
N_ncdm = 1
ncdm_psd_filenames = psd_FD_single.dat
ncdm_psd_parameters = 0.3  ,0.5,  0.05
m_ncdm = 0.06
Omega_ncdm =
T_ncdm =
ksi_ncdm =
deg_ncdm =

Omega_k = 0.
Omega_fld = 0
Omega_scf = 0
w0_fld = -0.9
wa_fld = 0.
cs2_fld = 1
use_ppf = yes
c_gamma_over_c_fld = 0.4

attractor_ic_scf = yes
scf_parameters = 10.0, 0.0, 0.0, 0.0, 100.0, 0.0
scf_tuning_index = 0
```

```
-------------------------------------
-----> thermodynamics parameters:
-------------------------------------

YHe = BBN
recombination = RECFAST
reio_parametrization = reio_camb
tau_reio = 0.058
reionization_exponent = 1.5
reionization_width = 0.5
helium_fullreio_redshift = 3.5
helium_fullreio_width = 0.5
binned_reio_num = 3
binned_reio_z = 8,12,16
binned_reio_xe = 0.8,0.2,0.1
binned_reio_step_sharpness = 0.3
many_tanh_num = 2
many_tanh_z = 3.5,11.3
many_tanh_xe = -2,-1
many_tanh_width = 0.5
reio_inter_num = 8
reio_inter_z =    0,   3,   4,    8,    9,   10,   11, 12
reio_inter_xe = -2, -2, -1,  -1, 0.9, 0.5, 0.1,   0
annihilation = 0.
annihilation_variation = 0.
annihilation_z = 1000
annihilation_zmax = 2500
annihilation_zmin = 30
annihilation_f_halo= 20
annihilation_z_halo= 8
on the spot = yes
decay = 0.

-----------------------------------------------------
-----> define which perturbations should be computed:
-----------------------------------------------------

output = tCl,pCl,lCl
non linear =
modes = s
lensing = no
tensor method =
ic = ad
gauge = synchronous
```

```
-------------------------------------------------
----> define primordial perturbation spectra:
-------------------------------------------------
P_k_ini type = analytic_Pk
k_pivot = 0.05
A_s = 2.181866264961206e-9
n_s = 0.96
alpha_s = 0.
f_bi = 1.
n_bi = 1.5
f_cdi=1.
f_nid=1.
n_nid=2.
alpha_nid= 0.01
c_ad_bi = 0.5
c_ad_cdi = -1.
c_bi_nid = 1.
r = 1.
n_t = scc
alpha_t = scc
potential = polynomial
V_0=1.e-13
V_1=-1.e-14
V_2=7.e-14
V_3=
V_4=
H_0=1.e-13
H_1=-1.e-14
H_2=7.e-14
H_3=
H_4=
phi_end =
full_potential = polynomial
Vparam0 =
Vparam1 =
Vparam2 =
Vparam3 =
Vparam4 =
k1=0.002
k2=0.1
P_{RR}^1 = 2.3e-9
P_{RR}^2 = 2.3e-9
P_{II}^1 = 1.e-11
```

```
P_{II}^2 = 1.e-11
P_{RI}^1 = -1.e-13
|P_{RI}^2| = 1.e-13
special_iso =
command = cat external_Pk/Pk_example.dat
custom1 = 0.05      # In the example command: k_pivot
custom2 = 2.215e-9 # In the example command: A_s
custom3 = 0.9624    # In the example command: n_s
custom4 = 2e-10     # In the example (with tensors) command: A_t
custom5 = -0.1      # In the example (with tensors) command: n_t

-------------------------------------
----> define format of final spectra:
-------------------------------------

l_max_scalars = 2000
l_max_tensors = 500
P_k_max_h/Mpc = 50.
z_pk = 0
z_max_pk = 4.
selection=gaussian
selection_mean = 0.98,0.99,1.0,1.1,1.2
selection_width = 0.1
selection_bias =
selection_magnification_bias =
non_diagonal=4
dNdz_selection =
dNdz_evolution =
headers = yes
format = class
write background = no
write thermodynamics = no
k_output_values = #0.01, 0.1, 0.0001
write primordial = no
write parameters = yeap
write warnings =

-----------------------------------------------------
----> amount of information sent to standard output:
-----------------------------------------------------

input_verbose = 1
background_verbose = 1
thermodynamics_verbose = 1
perturbations_verbose = 1
```

```
transfer_verbose = 1
primordial_verbose = 1
spectra_verbose = 1
nonlinear_verbose = 1
lensing_verbose = 1
output_verbose = 1
```

List of Figures

List of Tables

Bibliography

Akaike, H. (1973). "Information Theory and an Extension of the Maximum Likelihood Principle". In: *Proceedings of the Second International Symposium on Information Theory, edited by B. N. Petro and F. Csaki (Akademiai Kiado, Budapest),* pp. 267 –281.

Akerib, D. S. et al. (2016). "Improved Limits on Scattering of Weakly Interacting Massive Particles from Reanalysis of 2013 LUX Data". In: *Physical Review Letters* 116, 161301 (16).

Alam, S. et al. (2017). "The clustering of galaxies in the completed SDSS-III Baryon Oscillation Spectroscopic Survey: cosmological analysis of the DR12 galaxy sample". In: *Monthly Notices of the Royal Astronomical Society* 470.3, pp. 2617–2652.

Albrecht, A. et al. (2006). "Report of the Dark Energy Task Force". In: *ArXiv Astrophysics e-prints*. eprint: astro-ph/0609591.

Ali-Haïmoud, Y. and C. M. Hirata (2010). "Ultrafast effective multilevel atom method for primordial hydrogen recombination". In: *Physical Review D* 82.6, 063521.

Amendola, L. (2000). "Coupled quintessence". In: *Physical Review D* 62, 043511 (4).

Amendola, L. and S. Tsujikawa (2010). *Dark Energy: Theory and Observations*.

Amendola, L. et al. (2013). "Cosmology and Fundamental Physics with the Euclid Satellite". In: *Living Reviews in Relativity* 16, 6.

Anderson, L. et al. (2012). "The clustering of galaxies in the SDSS-III Baryon Oscillation Spectroscopic Survey: baryon acoustic oscillations in the Data Release 9 spectroscopic galaxy sample". In: *Monthly Notices of the Royal Astronomical Society* 427, pp. 3435–3467.

Anderson, L. et al. (2014). "The clustering of galaxies in the SDSS-III Baryon Oscillation Spectroscopic Survey: baryon acoustic oscillations in the Data Releases 10 and 11 Galaxy samples". In: *Monthly Notices of the Royal Astronomical Society* 441, pp. 24–62.

Aprile, E. et al. (2012). "Dark Matter Results from 225 Live Days of XENON100 Data". In: *Physical Review Letters* 109, 181301 (18).

Aprile, E. et al. (2014). "First axion results from the XENON100 experiment". In: *Physical Review D* 90, 062009 (6).

Armendariz-Picon, C., V. Mukhanov, and P. J. Steinhardt (2000). "Dynamical Solution to the Problem of a Small Cosmological Constant and Late-Time Cosmic Acceleration". In: *Physical Review Letters* 85 (21), pp. 4438–4441.

— (2001). "Essentials of k-essence". In: *Physical Review D* 63.10, 103510.

Arnett, W. D. (1969). "Explosive Nucleosynthesis in Stars". In: *The Astrophysical Journal* 157, p. 1369.

Arnett, W. D., D. Branch, and J. C. Wheeler (1985). "Hubble's constant and exploding carbon–oxygen white dwarf models for Type I supernovae". In: *Nature* 314, 337 EP –.

Asorey, J. et al. (2012). "Recovering 3D clustering information with angular correlations". In: *Monthly Notices of the Royal Astronomical Society* 427.3, pp. 1891–1902.

Aubourg, É. et al. (2015). "Cosmological implications of baryon acoustic oscillation measurements". In: *Physical Review D* 92.12, 123516.

Audren, B. et al. (2013). "Conservative constraints on early cosmology with MONTE PYTHON". In: *Journal of Cosmology and Astroparticle Physics* 02, 001.

Avelino, A., N. Cruz, and U. Nucamendi (2012). "Testing the EoS of dark matter with cosmological observations". In: *ArXiv e-prints*. arXiv: 1211.4633.

Azzaro, M., F. Prada, and C. M. Gutiérrez (2004). "Motion Properties of Satellites around External Spiral Galaxies". In: *Satellites and Tidal Streams*. Ed. by F. Prada, D. Martinez Delgado, and T. J. Mahoney. Vol. 327. Astronomical Society of the Pacific Conference Series, p. 268.

Bahcall, J. N., C. Flynn, and A. Gould (1992). "Local dark matter from a carefully selected sample". In: *The Astrophysical Journal* 389, pp. 234–250.

Ballinger, W. E., J. A. Peacock, and A. F. Heavens (1996). "Measuring the cosmological constant with redshift surveys". In: *Monthly Notices of the Royal Astronomical Society* 282, p. 877.

Bardeen, J. M. et al. (1986). "The statistics of peaks of Gaussian random fields". In: *The Astrophysical Journal* 304, pp. 15–61.

Bassett, B. A and N. Afshordi (2010). "Non-Gaussian Posteriors arising from Marginal Detections". In: *ArXiv e-prints*. arXiv: 1005.1664.

Bassett, B. A. and M. Kunz (2004). "Cosmic distance-duality as a probe of exotic physics and acceleration". In: *Physical Review D* 69.10, 101305.

Baumann, D. et al. (2012). "Cosmological non-linearities as an effective fluid". In: *Journal of Cosmology and Astroparticle Physics* 07, 051.

Bautista, J. E. et al. (2017). "Measurement of baryon acoustic oscillation correlations at z = 2.3 with SDSS DR12 Lyα-Forests". In: *Astronomy and Astrophysics* 603, A12.

Baxter, E. J. et al. (2018). "Dark Energy Survey Year 1 Results: Methodology and Projections for Joint Analysis of Galaxy Clustering, Galaxy Lensing, and CMB Lensing Two-point Functions". In: *ArXiv e-prints*. arXiv: 1802.05257.

Bayes, T. (1958). "An essay towards solving a problem in the doctrine of changes (Reprint of 1763 original)". In: *Biometrika* 45, p. 293.

Begeman, K. G., A. H. Broeils, and R. H. Sanders (1991). "Extended rotation curves of spiral galaxies - Dark haloes and modified dynamics". In: *Monthly Notices of the Royal Astronomical Society* 249, pp. 523–537.

Benoit-Lévy, A. and G. Chardin (2012). "Introducing the Dirac-Milne universe". In: *Astronomy and Astrophysics* 537, A78.

Bernal, J. L., L. Verde, and A. G. Riess (2016). "The trouble with H_0". In: *Journal of Cosmology and Astroparticle Physics* 10, 019.

Bernardeau, F. et al. (2002). "Large-scale structure of the Universe and cosmological perturbation theory". In: *Physics Reports* 367, pp. 1–248.

Bertone, G., D. Hooper, and J. Silk (2005). "Particle dark matter: evidence, candidates and constraints". In: *Physics Reports* 405.5, pp. 279 –390.

Betoule, M. et al. (2014). "Improved cosmological constraints from a joint analysis of the SDSS-II and SNLS supernova samples". In: *Astronomy and Astrophysics* 568, A22.

Beutler, F. et al. (2011). "The 6dF Galaxy Survey: baryon acoustic oscillations and the local Hubble constant". In: *Monthly Notices of the Royal Astronomical Society* 416, pp. 3017–3032.

Beutler, F. et al. (2012). "The 6dF Galaxy Survey: z≈0 measurements of the growth rate and σ_8". In: *Monthly Notices of the Royal Astronomical Society* 423.4, p. 3430.

Bilicki, M. and M. Seikel (2012). "We do not live in the R_h=ct universe". In: *Monthly Notices of the Royal Astronomical Society* 425.3, pp. 1664–1668.

Bird, S., M. Viel, and M. G. Haehnelt (2012). "Massive neutrinos and the non-linear matter power spectrum". In: *Monthly Notices of the Royal Astronomical Society* 420, pp. 2551–2561.

Blake, C. et al. (2012). "The WiggleZ Dark Energy Survey: joint measurements of the expansion and growth history at $z < 1$". In: *Monthly Notices of the Royal Astronomical Society* 425, pp. 405–414.

Blake, C. et al. (2016). "RCSLenS: testing gravitational physics through the cross-correlation of weak lensing and large-scale structure". In: *Monthly Notices of the Royal Astronomical Society* 456.3, pp. 2806–2828.

Blanchard, A. (1984). "Angular fluctuations in the cosmological microwave background in a universe with a cosmological constant". In: *Astronomy and Astrophysics* 132, p. 359.

Blas, D., M. Garny, and T. Konstandin (2014). "Cosmological perturbation theory at three-loop order". In: *Journal of Cosmology and Astroparticle Physics* 01, 010.

Blas, D., J. Lesgourgues, and T. Tram (2011). "The Cosmic Linear Anisotropy Solving System (CLASS). Part II: Approximation schemes". In: *Journal of Cosmology and Astroparticle Physics* 07, 034.

Blas, D. et al. (2015). "Large scale structure from viscous dark matter". In: *Journal of Cosmology and Astroparticle Physics* 11, 049.

Blas, D. et al. (2016). "Time-sliced perturbation theory for large scale structure I: general formalism". In: *Journal of Cosmology and Astroparticle Physics* 07, 052.

Blazek, J., Z. Vlah, and U. Seljak (2015). "Tidal alignment of galaxies". In: *Journal of Cosmology and Astroparticle Physics* 8, 015.

Bloom, J. S. et al. (2012). "A Compact Degenerate Primary-star Progenitor of SN 2011fe". In: *The Astrophysical Journal Letters* 744, L17.

Boveia, A. and C. Doglioni (2018). "Dark Matter Searches at Colliders". In: *Annual Review of Nuclear and Particle Science* 68.1.

Boylan-Kolchin, M., J. S. Bullock, and M. Kaplinghat (2011). "Too big to fail? The puzzling darkness of massive Milky Way subhaloes". In: *Monthly Notices of the Royal Astronomical Society* 415, pp. L40–L44.

Bozdogan, H. (1987). "Model selection and Akaike's Information Criterion (AIC): The general theory and its analytical extensions". In: *Psychometrika* 52.3, pp. 345–370.

Branch, D. (1981). "Some statistical properties of type I supernovae". In: *The Astrophysical Journal* 248, pp. 1076–1080.

— (1998). "Type Ia supernovae and the Hubble constant". In: *Annual Review of Astronomy and Astrophysics* 36.1, pp. 17–55.

Branch, D. and G. A. Tammann (1992). "Type Ia Supernovae as Standard Candles". In: *Annual Review of Astronomy and Astrophysics* 30.1, pp. 359–389.

Buchert, T. and S. Räsänen (2012). "Backreaction in Late-Time Cosmology". In: *Annual Review of Nuclear and Particle Science* 62.1, pp. 57–79.

Buckley, J. et al. (2013). "Cosmic Frontier Indirect Dark Matter Detection Working Group Summary". In: *ArXiv e-prints*. arXiv: 1310.7040.

Burnham, K. P. and D. R. Anderson (2002). *Model Selection and Multimodel Inference: A Practical Information-Theoretic Approach*. Springer-Verlag, Berlin.

— (2004). "Multimodel Inference: Understanding AIC and BIC in Model Selection". In: *Sociological Methods and Research* 33.2, pp. 261–304.

Busca, N. G. et al. (2013). "Baryon acoustic oscillations in the Lyα forest of BOSS quasars". In: *Astronomy and Astrophysics* 552, A96.

Busti, V. C., C. Clarkson, and M. Seikel (2014). "Evidence for a lower value for H0 from cosmic chronometers data?" In: *Monthly Notices of the Royal Astronomical Society: Letters* 441.1, pp. L11–L15.

Caldwell, R. R., R. Dave, and P. J. Steinhardt (1998). "Cosmological Imprint of an Energy Component with General Equation of State". In: *Physical Review Letters* 80, pp. 1582–1585.

Carrasco, J. J. M., M. P. Hertzberg, and L. Senatore (2012). "The effective field theory of cosmological large scale structures". In: *Journal of High Energy Physics* 9, p. 82.

Carroll, S. M., S. Leichenauer, and J. Pollack (2014). "Consistent effective theory of long-wavelength cosmological perturbations". In: *Physical Review D* 90, 023518 (2).

Casas, S. et al. (2017). "Linear and non-linear Modified Gravity forecasts with future surveys". In: *Physics of the Dark Universe* 18, pp. 73–104.

Catelan, P., M. Kamionkowski, and R. D. Blandford (2001). "Intrinsic and extrinsic galaxy alignment". In: *Monthly Notices of the Royal Astronomical Society* 320, pp. L7–L13.

Cheng, C. and Q.-G. Huang (2014). "Dark side of the Universe after Planck data". In: *Physical Review D* 89, 043003 (4).

Chevallier, M. and D. Polarski (2001). "Accelerating Universes with Scaling Dark Matter". In: *International Journal of Modern Physics D* 10, pp. 213–223.

Chluba, J. (2010). "Could the cosmological recombination spectrum help us understand annihilating dark matter?" In: *Monthly Notices of the Royal Astronomical Society* 402.2, pp. 1195–1207.

Chluba, J. and R. M. Thomas (2011). "Towards a complete treatment of the cosmological recombination problem". In: *Monthly Notices of the Royal Astronomical Society* 412.2, pp. 748–764.

Chluba, J., G. M. Vasil, and L. J. Dursi (2010). "Recombinations to the Rydberg states of hydrogen and their effect during the cosmological recombination epoch". In: *Monthly Notices of the Royal Astronomical Society* 407.1, pp. 599–612.

Chuang, C.-H. and Y. Wang (2013). "Modelling the anisotropic two-point galaxy correlation function on small scales and single-probe measurements of H(z), D_A(z) and f(z)σ_8(z) from the Sloan Digital Sky Survey DR7 luminous red galaxies". In: *Monthly Notices of the Royal Astronomical Society* 435, pp. 255–262.

Clarkson, C. and C. Zunckel (2010). "Direct Reconstruction of Dark Energy". In: *Physical Review Letters* 104, 211301 (21).

Clerkin, L. et al. (2015). "A prescription for galaxy biasing evolution as a nuisance parameter". In: *Monthly Notices of the Royal Astronomical Society* 448, pp. 1389–1401.

Colgate, S. A. and C. McKee (1969). "Early Supernova Luminosity". In: *The Astrophysical Journal* 157, p. 623.

Colombi, S., S. Dodelson, and L. M. Widrow (1996). "Large-Scale Structure Tests of Warm Dark Matter". In: *The Astrophysical Journal* 458, p. 1.

Cooray, A. and R. Sheth (2002). "Halo models of large scale structure". In: *Physics Reports* 372, pp. 1–129.

Couchot, F. et al. (2017). "Relieving tensions related to the lensing of the cosmic microwave background temperature power spectra". In: *Astronomy and Astrophysics* 597, A126.

CRESST Collaboration (2015). "The CRESST Dark Matter Search - Status and Perspectives". In: *ArXiv e-prints*. arXiv: 1509.09124.

Crittenden, R. G., L. Pogosian, and G.-B. Zhao (2009). "Investigating dark energy experiments with principal components". In: *Journal of Cosmology and Astroparticle Physics* 12, 025.

Crocce, M. and R. Scoccimarro (2006). "Renormalized cosmological perturbation theory". In: *Physical Review D* 73.6, 063519.

Crocce, M., R. Scoccimarro, and F. Bernardeau (2012). "MPTBREEZE: a fast renormalized perturbative scheme". In: *Monthly Notices of the Royal Astronomical Society* 427, pp. 2537–2551.

Crocce, M. et al. (2015). "The MICE Grand Challenge lightcone simulation - II. Halo and galaxy catalogues". In: *Monthly Notices of the Royal Astronomical Society* 453, pp. 1513–1530.

Croom, S. M. et al. (2005). "The 2dF QSO Redshift Survey - XIV. Structure and evolution from the two-point correlation function". In: *Monthly Notices of the Royal Astronomical Society* 356, pp. 415–438.

Cypriano, E. S. et al. (2010). "Cosmic shear requirements on the wavelength dependence of telescope point spread functions". In: *Monthly Notices of the Royal Astronomical Society* 405.1, pp. 494–502.

Cyr-Racine, F.-Y. and K. Sigurdson (2013). "Cosmology of atomic dark matter". In: *Physical Review D* 87, 103515 (10).

Dam, L. H., A. Heinesen, and D. L. Wiltshire (2017). "Apparent cosmic acceleration from Type Ia supernovae". In: *Monthly Notices of the Royal Astronomical Society* 472.1, pp. 835–851.

Davis, M. and M. J. Geller (1976). "Galaxy Correlations as a Function of Morphological Type". In: *The Astrophysical Journal* 208, pp. 13–19.

de la Torre, S. et al. (2013). "The VIMOS Public Extragalactic Redshift Survey (VIPERS) . Galaxy clustering and redshift-space distortions at z = 0.8 in the first data release". In: *Astronomy and Astrophysics* 557, A54.

de Putter, R., O. Doré, and M. Takada (2013). "The Synergy between Weak Lensing and Galaxy Redshift Surveys". In: *ArXiv e-prints*. arXiv: 1308.6070.

Delubac, T. et al. (2015). "Baryon acoustic oscillations in the Ly-α forest of BOSS DR11 quasars". In: *Astronomy and Astrophysics* 574, A59.

DES Collaboration (2016). "Joint analysis of galaxy-galaxy lensing and galaxy clustering: Methodology and forecasts for Dark Energy Survey". In: *Physical Review D* 94, 063533 (6).

— (2017a). "Dark Energy Survey Year 1 Results: A Precise H0 Measurement from DES Y1, BAO, and D/H Data". In: *ArXiv e-prints*. arXiv: 1711.00403.

— (2017b). "Dark Energy Survey Year 1 Results: Cosmological Constraints from Galaxy Clustering and Weak Lensing". In: *ArXiv e-prints*. arXiv: 1708.01530.

Di Porto, C., L. Amendola, and E. Branchini (2012). "Growth factor and galaxy bias from future redshift surveys: a study on parametrizations". In: *Monthly Notices of the Royal Astronomical Society* 419.2, pp. 985–997.

Diamanti, R. et al. (2013). "Dark radiation and interacting scenarios". In: *Physical Review D* 87, 063509 (6).

Dodelson, S. (2003). *Modern Cosmology*. Amsterdam: Academic Press.

Dodelson, S. and L. M. Widrow (1994). "Sterile neutrinos as dark matter". In: *Physical Review Letters* 72 (1), pp. 17–20.

Doi, M. et al. (2010). "Photometric Response Functions of the Sloan Digital Sky Survey Imager". In: *The Astronomical Journal* 139.4, p. 1628.

Dolgov, A., V. Halenka, and I. Tkachev (2014). "Power-law cosmology, SN Ia, and BAO". In: *Journal of Cosmology and Astroparticle Physics* 10, 047.

Dolgov, A. D. (1997). "Higher spin fields and the problem of the cosmological constant". In: *Physical Review D* 55, pp. 5881–5885.

Drell, P. S., T. J. Loredo, and I. Wasserman (2000). "Type Ia Supernovae, Evolution, and the Cosmological Constant". In: *The Astrophysical Journal* 530.2, p. 593.

Dressler, A. (1980). "Galaxy morphology in rich clusters - Implications for the formation and evolution of galaxies". In: *The Astrophysical Journal* 236, pp. 351–365.

du Mas des Bourboux, H. et al. (2017). "Baryon acoustic oscillations from the complete SDSS-III Lyα-quasar cross-correlation function at z = 2.4". In: *Astronomy and Astrophysics* 608, A130.

Dyson, W., A. S. Eddington, and C. Davidson (1920). "IX. A determination of the deflection of light by the sun's gravitational field, from observations made at the total eclipse of May 29, 1919". In: *Philosophical Transactions of the Royal Society of London A: Mathematical, Physical and Engineering Sciences* 220.571-581, pp. 291–333.

Efstathiou, G. (2008). "Limitations of Bayesian Evidence applied to cosmology". In: *Monthly Notices of the Royal Astronomical Society* 388, pp. 1314–1320.

Einstein, A. (1915). "Die Feldgleichungen der Gravitation". In: *Sitzungsberichte der Königlich Preußischen Akademie der Wissenschaften (Berlin), Seite 844-847.*

— (1917). "Kosmologische Betrachtungen zur allgemeinen Relativitätstheorie". In: *Sitzungsberichte der Königlich Preußischen Akademie der Wissenschaften (Berlin), Seite 142-152.*

Eisenstein, D. and M. White (2004). "Theoretical uncertainty in baryon oscillations". In: *Physical Review D* 70, 103523 (10).

Eisenstein, D. J. and W. Hu (1998). "Baryonic Features in the Matter Transfer Function". In: *The Astrophysical Journal* 496.2, p. 605.

— (1999). "Power Spectra for Cold Dark Matter and Its Variants". In: *The Astrophysical Journal* 511, pp. 5–15.

Eisenstein, D. J. et al. (2005). "Detection of the Baryon Acoustic Peak in the Large-Scale Correlation Function of SDSS Luminous Red Galaxies". In: *The Astrophysical Journal* 633, pp. 560–574.

Euclid Collaboration (in prep.). "Forecast validation for the Euclid satellite". In: *TBD.*

Fang, W., W. Hu, and A. Lewis (2008). "Crossing the phantom divide with parametrized post-Friedmann dark energy". In: *Physical Review D* 78.8, 087303.

Farooq, O. and B. Ratra (2013). "Hubble Parameter Measurement Constraints on the Cosmological Deceleration-Acceleration Transition Redshift". In: *The Astrophysical Journal Letters* 766.1, p. L7.

Ferramacho, L. D., A. Blanchard, and Y. Zolnierowski (2009). "Constraints on CDM cosmology from galaxy power spectrum, CMB and SNIa evolution". In: *Astronomy and Astrophysics* 499.1, pp. 21–29.

Ferraro, S., B. D. Sherwin, and D. N. Spergel (2015). "WISE measurement of the integrated Sachs-Wolfe effect". In: *Physical Review D* 91.8, 083533.

Filippenko, A. V. (1997a). "Optical spectra of supernovae". In: *Annual Review of Astronomy and Astrophysics* 35.1, pp. 309–355.

— (1997b). "Type Ia supernovae: observational overview". In: *NATO Advanced Science Institutes (ASI) Series C.* Ed. by P. Ruiz-Lapuente, R. Canal, and J. Isern. Vol. 486. NATO Advanced Science Institutes (ASI) Series C, p. 1.

Fixsen, D. J. (2009). "The Temperature of the Cosmic Microwave Background". In: *The Astrophysical Journal* 707, pp. 916–920.

Fixsen, D. J. et al. (1996). "The Cosmic Microwave Background Spectrum from the Full COBE FIRAS Data Set". In: *The Astrophysical Journal* 473, p. 576.

Fletcher, R. (1970). "A new approach to variable metric algorithms". In: *The Computer Journal* 13.3, pp. 317–322.

Font-Ribera, A. et al. (2014). "Quasar-Lyman α forest cross-correlation from BOSS DR11: Baryon Acoustic Oscillations". In: *Journal of Cosmology and Astroparticle Physics* 05, 027.

Foreman, S. and L. Senatore (2016). "The EFT of Large Scale Structures at all redshifts: analytical predictions for lensing". In: *Journal of Cosmology and Astroparticle Physics* 04, 033.

Foreman-Mackey, D. et al. (2013). "emcee: The MCMC Hammer". In: *Publications of the Astronomical Society of the Pacific* 125, p. 306.

Friedmann, A. (1922). "Über die Krümmung des Raumes". In: *Zeitschrift fur Physik* 10, pp. 377–386.

— (1924). "Über die Möglichkeit einer Welt mit konstanter negativer Krümmung des Raumes". In: *Zeitschrift fur Physik* 21, pp. 326–332.

Fry, J. N. (1996). "The Evolution of Bias". In: *The Astrophysical Journal Letters* 461, p. L65.

Fry, J. N. and E. Gaztañaga (1993). "Biasing and hierarchical statistics in large-scale structure". In: *The Astrophysical Journal* 413, pp. 447–452.

Fu, L. et al. (2014). "CFHTLenS: cosmological constraints from a combination of cosmic shear two-point and three-point correlations". In: *Monthly Notices of the Royal Astronomical Society* 441, pp. 2725–2743.

Gaztañaga, E. (1992). "N-point correlation functions in the CfA and SSRS redshift distribution of galaxies". In: *The Astrophysical Journal Letters* 398, pp. L17–L20.

Gaztañaga, E., A. Cabré, and L. Hui (2009). "Clustering of luminous red galaxies – IV. Baryon acoustic peak in the line-of-sight direction and a direct measurement of H(z)". In: *Monthly Notices of the Royal Astronomical Society* 399.3, pp. 1663–1680.

Gelman, A., G. O. Roberts, and W. R. Gilks (1996). "Efficient Metropolis Jumping Rules". In: *Bayesian Statistics 5*. Ed. by J. M. Bernardo et al., pp. 599–607.

Gelman, A. and D. B. Rubin (1992). "Inference from Iterative Simulation Using Multiple Sequences". In: *Statistical Science* 7, pp. 457–472.

Gil-Marín, H. et al. (2018). "The clustering of the SDSS-IV extended Baryon Oscillation Spectroscopic Survey DR14 quasar sample: structure growth rate

measurement from the anisotropic quasar power spectrum in the redshift range $0.8 < z < 2.2$". In: *ArXiv e-prints*. arXiv: 1801.02689.

Goldhaber, G. et al. (2001). "Timescale Stretch Parameterization of Type Ia Supernova B-Band Light Curves". In: *The Astrophysical Journal* 558, pp. 359–368.

Gómez-Valent, A. and L. Amendola (2018). "H_0 from cosmic chronometers and Type Ia supernovae, with Gaussian Processes and the novel Weighted Polynomial Regression method". In: *ArXiv e-prints*. arXiv: 1802.01505.

Goodman, J. and J. Weare (2010). "Ensemble samplers with affine invariance". In: *Communications in Applied Mathematics and Computational Science* 5.1, pp. 65–80.

Grin, D. and C. M. Hirata (2010). "Cosmological hydrogen recombination: The effect of extremely high-n states". In: *Physical Review D* 81.8, 083005.

Guth, A. H. (1981). "Inflationary universe: A possible solution to the horizon and flatness problems". In: *Physical Review D* 23 (2), pp. 347–356.

Hamann, J., S. Hannestad, and Y. Y. Y. Wong (2012). "Measuring neutrino masses with a future galaxy survey". In: *Journal of Cosmology and Astroparticle Physics* 11, 052.

Hamilton, A. J. S. (1998). "Linear Redshift Distortions: a Review". In: *The Evolving Universe*. Ed. by D. Hamilton. Vol. 231. Astrophysics and Space Science Library, p. 185.

Hamuy, M. et al. (1995). "A Hubble diagram of distant type IA supernovae". In: *The Astronomical Journal* 109, pp. 1–13.

Hamuy, M. et al. (1996a). "BVRI Light Curves for 29 Type IA Supernovae". In: *The Astronomical Journal* 112, p. 2408.

Hamuy, M. et al. (1996b). "The Hubble Diagram of the Calan/Tololo Type IA Supernovae and the Value of HO". In: *The Astronomical Journal* 112, p. 2398.

Haridasu, B. S. et al. (2017). "Strong evidence for an accelerating Universe". In: *Astronomy and Astrophysics* 600, p. L1.

Harrison, I. et al. (2016). "SKA weak lensing - I. Cosmological forecasts and the power of radio-optical cross-correlations". In: *Monthly Notices of the Royal Astronomical Society* 463, pp. 3674–3685.

Hastings, W. K. (1970). "Monte Carlo Sampling Methods Using Markov Chains and Their Applications". In: *Biometrika* 57.1, pp. 97–109.

Heitmann, K. et al. (2014). "The Coyote Universe Extended: Precision Emulation of the Matter Power Spectrum". In: *The Astrophysical Journal* 780, p. 111.

Henrot-Versillé, S. et al. (2015). "Improved constraint on the primordial gravitational-wave density using recent cosmological data and its impact on cosmic string models". In: *Classical and Quantum Gravity* 32.4, 045003.

Henrot-Versillé, S. et al. (2016). "Agnostic cosmology in the CAMEL framework". In: *ArXiv e-prints*. arXiv: 1607.02964.

Heymans, C. et al. (2013). "CFHTLenS tomographic weak lensing cosmological parameter constraints: Mitigating the impact of intrinsic galaxy alignments". In: *Monthly Notices of the Royal Astronomical Society* 432, pp. 2433–2453.

Hirata, C. M. and U. Seljak (2004). "Intrinsic alignment-lensing interference as a contaminant of cosmic shear". In: *Physical Review D* 70.6, 063526.

Hlozek, R. et al. (2015). "A search for ultralight axions using precision cosmological data". In: *Physical Review D* 91, 103512 (10).

Hojjati, A., L. Pogosian, and G.-B. Zhao (2011). "Testing gravity with CAMB and CosmoMC". In: *Journal of Cosmology and Astroparticle Physics* 8, 005.

Holsclaw, T. et al. (2010). "Nonparametric reconstruction of the dark energy equation of state". In: *Physical Review D* 82, 103502 (10).

Hou, J. et al. (2018). "The clustering of the SDSS-IV extended Baryon Oscillation Spectroscopic Survey DR14 quasar sample: anisotropic clustering analysis in configuration-space". In: *ArXiv e-prints*. arXiv: 1801.02656.

Howlett, C. et al. (2012). "CMB power spectrum parameter degeneracies in the era of precision cosmology". In: *Journal of Cosmology and Astroparticle Physics* 04, 027.

Howlett, C. et al. (2015). "The clustering of the SDSS main galaxy sample – II. Mock galaxy catalogues and a measurement of the growth of structure from redshift space distortions at z = 0.15". In: *Monthly Notices of the Royal Astronomical Society* 449.1, pp. 848–866.

Hoyle, F. and W. A. Fowler (1960). "Nucleosynthesis in Supernovae." In: *The Astrophysical Journal* 132, p. 565.

Hu, W. (1998). "Structure Formation with Generalized Dark Matter". In: *The Astrophysical Journal* 506, pp. 485–494.

Hu, W. and D. J. Eisenstein (1999). "Structure of structure formation theories". In: *Physical Review D* 59, 083509 (8).

Hu, W. and I. Sawicki (2007). "Parametrized post-Friedmann framework for modified gravity". In: *Physical Review D* 76.10, 104043.

Hu, W. and N. Sugiyama (1996). "Small-Scale Cosmological Perturbations: an Analytic Approach". In: *The Astrophysical Journal* 471, p. 542.

Hubble, E. (1929). "A relation between distance and radial velocity among extra-galactic nebulae". In: *Proceedings of the National Academy of Sciences* 15.3, pp. 168–173.

Hurvich, C. M. and C.-L. Tsai (1989). "Regression and time series model selection in small samples". In: *Biometrika* 76.2, pp. 297–307.

Huterer, D. and G. Starkman (2003). "Parametrization of Dark-Energy Properties: A Principal-Component Approach". In: *Physical Review Letters* 90, 031301 (3).

Hwang, J. C. (1990). "Cosmological perturbations in generalized gravity theories: Formulation". In: *Classical and Quantum Gravity* 7, pp. 1613–1631.

James, F. (2006). *Statistical methods in experimental physics.*

James, F. and M. Roos (1975). "Minuit - a system for function minimization and analysis of the parameter errors and correlations". In: *Computer Physics Communications* 10.6, pp. 343 –367.

Jee, M. J. et al. (2014). "Hubble Space Telescope/Advanced Camera for Surveys Confirmation of the Dark Substructure in A520". In: *The Astrophysical Journal* 783.2, p. 78.

Jenkins, A. et al. (2001). "The mass function of dark matter haloes". In: *Monthly Notices of the Royal Astronomical Society* 321, pp. 372–384.

Jimenez, R. and A. Loeb (2002). "Constraining Cosmological Parameters Based on Relative Galaxy Ages". In: *The Astrophysical Journal* 573.1, p. 37.

Johansson, J. et al. (2013). "SN Ia host galaxy properties from Sloan Digital Sky Survey-II spectroscopy". In: *Monthly Notices of the Royal Astronomical Society* 435, pp. 1680–1700.

Kaiser, N. (1984). "On the spatial correlations of Abell clusters". In: *The Astrophysical Journal Letters* 284, pp. L9–L12.

— (1987). "Clustering in real space and in redshift space". In: *Monthly Notices of the Royal Astronomical Society* 227, pp. 1–21.

Kaplinghat, M., G. Steigman, and T. P. Walker (2000). "Nucleosynthesis in power-law cosmologies". In: *Physical Review D* 61, 103507 (10).

Kaplinghat, M. et al. (1999). "Observational constraints on power-law cosmologies". In: *Physical Review D* 59, 043514 (4).

Kauffmann, G. et al. (1999). "Clustering of galaxies in a hierarchical universe - II. Evolution to high redshift". In: *Monthly Notices of the Royal Astronomical Society* 307, pp. 529–536.

Kayo, I., M. Takada, and B. Jain (2013). "Information content of weak lensing power spectrum and bispectrum: including the non-Gaussian error covariance matrix". In: *Monthly Notices of the Royal Astronomical Society* 429, pp. 344–371.

Kazin, E. A. et al. (2014). "The WiggleZ Dark Energy Survey: improved distance measurements to z = 1 with reconstruction of the baryonic acoustic feature". In: *Monthly Notices of the Royal Astronomical Society* 441.4, pp. 3524–3542.

Kelly, P. L. et al. (2010). "Hubble Residuals of Nearby Type Ia Supernovae are Correlated with Host Galaxy Masses". In: *The Astrophysical Journal* 715, pp. 743–756.

Kilbinger, M. et al. (2010). "Bayesian model comparison in cosmology with Population Monte Carlo". In: *Monthly Notices of the Royal Astronomical Society* 405, pp. 2381–2390.

Kilbinger, M. et al. (2013). "CFHTLenS: combined probe cosmological model comparison using 2D weak gravitational lensing". In: *Monthly Notices of the Royal Astronomical Society* 430, pp. 2200–2220.

Kilbinger, M. et al. (2017). "Precision calculations of the cosmic shear power spectrum projection". In: *Monthly Notices of the Royal Astronomical Society* 472, pp. 2126–2141.

Kim, D. Y., A. N. Lasenby, and M. P. Hobson (2016). "Friedmann–Robertson–Walker models do not require zero active mass". In: *Monthly Notices of the Royal Astronomical Society: Letters* 460.1, pp. L119–L122.

Kim, J. et al. (2011). "The New Horizon Run Cosmological N-Body Simulations". In: *Journal of Korean Astronomical Society* 44, pp. 217–234.

Kitching, T. D. et al. (2014). "3D cosmic shear: cosmology from CFHTLenS". In: *Monthly Notices of the Royal Astronomical Society* 442, pp. 1326–1349.

Kitching, T. D. et al. (2017). "The limits of cosmic shear". In: *Monthly Notices of the Royal Astronomical Society* 469, pp. 2737–2749.

Klypin, A. et al. (2015). "Abundance of field galaxies". In: *Monthly Notices of the Royal Astronomical Society* 454.2, pp. 1798–1810.

Knuth, K. H. et al. (2015). "Bayesian evidence and model selection". In: *Digital Signal Processing* 47, pp. 50 –67.

Kodama, H. and M. Sasaki (1984). "Cosmological Perturbation Theory". In: *Progress of Theoretical Physics Supplement* 78, pp. 1–166.

Komatsu, E. et al. (2011). "Seven-year Wilkinson Microwave Anisotropy Probe (WMAP) Observations: Cosmological Interpretation". In: *The Astrophysical Journal Supplement* 192, p. 18.

Kopp, M., C. Skordis, and D. B. Thomas (2016). "Extensive investigation of the generalized dark matter model". In: *Physical Review D* 94.4, 043512.

Kopp, M. et al. (2018). "The Dark Matter equation of state through cosmic history". In: *ArXiv e-prints*. arXiv: 1802.09541.

Kunz, M. (2009). "Degeneracy between the dark components resulting from the fact that gravity only measures the total energy-momentum tensor". In: *Physical Review D* 80.12, 123001.

Kunz, M., L. Amendola, and D. Sapone (2008). "Dark Energy Phenomenology". In: *ArXiv e-prints*. arXiv: 0806.1323.

Kunz, M., S. Nesseris, and I. Sawicki (2016). "Constraints on dark-matter properties from large-scale structure". In: *Physical Review D* 94.2, 023510.

Kunz, M. and D. Sapone (2007). "Dark Energy versus Modified Gravity". In: *Physical Review Letters* 98, 121301 (12).

Kunz, M., R. Trotta, and D. R. Parkinson (2006). "Measuring the effective complexity of cosmological models". In: *Physical Review D* 74.2, 023503.

Lampeitl, H. et al. (2010). "The Effect of Host Galaxies on Type Ia Supernovae in the SDSS-II Supernova Survey". In: *The Astrophysical Journal* 722.1, p. 566.

Laureijs, R. et al. (2011). "Euclid Definition Study Report". In: *ArXiv e-prints*. arXiv: 1110.3193.

Lemaître, G. (1927). "Un Univers homogène de masse constante et de rayon croissant rendant compte de la vitesse radiale des nébuleuses extra-galactiques". In: *Annales de la Société Scientifique de Bruxelles* 47, pp. 49–59.

Lemos, P., A. Challinor, and G. Efstathiou (2017). "The effect of Limber and flat-sky approximations on galaxy weak lensing". In: *Journal of Cosmology and Astroparticle Physics* 5, 014.

Lesgourgues, J. (2011a). "The Cosmic Linear Anisotropy Solving System (CLASS) I: Overview". In: *ArXiv e-prints*. arXiv: 1104.2932.

— (2011b). "The Cosmic Linear Anisotropy Solving System (CLASS) III: Comparision with CAMB for LambdaCDM". In: *ArXiv e-prints*. arXiv: 1104.2934.

Lesgourgues, J. and T. Tram (2011). "The Cosmic Linear Anisotropy Solving System (CLASS) IV: efficient implementation of non-cold relics". In: *Journal of Cosmology and Astroparticle Physics* 09, 032.

Lewis, A. and S. Bridle (2002). "Cosmological parameters from CMB and other data: A Monte Carlo approach". In: *Physical Review D* 66, 103511.

Lewis, A. and A. Challinor (2006). "Weak gravitational lensing of the CMB". In: *Physics Reports* 429, pp. 1–65.

Lewis, A., A. Challinor, and A. Lasenby (2000). "Efficient Computation of Cosmic Microwave Background Anisotropies in Closed Friedmann-Robertson-Walker Models". In: *The Astrophysical Journal* 538, pp. 473–476.

Lewis, G. F. (2013). "Matter matters: unphysical properties of the Rh = ct universe". In: *Monthly Notices of the Royal Astronomical Society* 432.3, pp. 2324–2330.

Lewis, G. F., L. A. Barnes, and R. Kaushik (2016). "Primordial nucleosynthesis in the R_h = ct cosmology: pouring cold water on the simmering Universe". In: *Monthly Notices of the Royal Astronomical Society* 460, pp. 291–296.

Li, W. et al. (2011). "Exclusion of a luminous red giant as a companion star to the progenitor of supernova SN 2011fe". In: *Nature* 480, pp. 348–350.

Lin, H.-N., X. Li, and Y. Sang (2017). "The local probes strongly favor an accelerating universe". In: *ArXiv e-prints*. arXiv: 1711.05025.

Linden, S., J.-M. Virey, and A. Tilquin (2009). "Cosmological parameter extraction and biases from type Ia supernova magnitude evolution". In: *Astronomy and Astrophysics* 506.3, pp. 1095–1105.

Linder, E. V. (2003). "Exploring the Expansion History of the Universe". In: *Physical Review Letters* 90, 091301 (9).

— (2006). "Biased cosmology: Pivots, parameters, and figures of merit". In: *Astroparticle Physics* 26.2, pp. 102 –110.

Liu, A. et al. (2016a). "Eliminating the optical depth nuisance from the CMB with 21 cm cosmology". In: *Physical Review D* 93, 043013 (4).

Liu, Z.-E. et al. (2016b). "Direct reconstruction of dynamical dark energy from observational Hubble parameter data". In: *Physics of the Dark Universe* 14, pp. 21 –28.

Lonappan, A. I. et al. (2017). "Bayesian Evidences for Dark Energy models in light of current obsevational data". In: *ArXiv e-prints*. arXiv: 1707.00603.

Luković, V. V., B. S. Haridasu, and N. Vittorio (2018). "Cosmological constraints from low-redshift data". In: *ArXiv e-prints*. arXiv: 1801.05765.

Ma, C.-P. and E. Bertschinger (1995). "Cosmological Perturbation Theory in the Synchronous and Conformal Newtonian Gauges". In: *The Astrophysical Journal* 455, p. 7.

Ma, C.-P. and J. N. Fry (2000). "Deriving the Nonlinear Cosmological Power Spectrum and Bispectrum from Analytic Dark Matter Halo Profiles and Mass Functions". In: *The Astrophysical Journal* 543.2, p. 503.

Macaulay, E., I. K. Wehus, and H. K. Eriksen (2013). "Lower Growth Rate from Recent Redshift Space Distortion Measurements than Expected from Planck". In: *Physics Review Letters* 111, 161301 (16).

MacCrann, N. et al. (2015). "Cosmic discordance: are Planck CMB and CFHTLenS weak lensing measurements out of tune?" In: *Monthly Notices of the Royal Astronomical Society* 451, pp. 2877–2888.

Majerotto, E. et al. (2012). "Probing deviations from general relativity with the Euclid spectroscopic survey". In: *Monthly Notices of the Royal Astronomical Society* 424.2, pp. 1392–1408.

Mann, R. G., J. A. Peacock, and A. F. Heavens (1998). "Eulerian bias and the galaxy density field". In: *Monthly Notices of the Royal Astronomical Society* 293.3, pp. 209–221.

Martin, J. (2012). "Everything you always wanted to know about the cosmological constant problem (but were afraid to ask)". In: *Comptes Rendus Physique* 13, pp. 566–665.

Matarrese, S. et al. (1997). "Redshift evolution of clustering". In: *Monthly Notices of the Royal Astronomical Society* 286, pp. 115–132.

Mateo, M. L. (1998). "Dwarf Galaxies of the Local Group". In: *Annual Review of Astronomy and Astrophysics* 36, pp. 435–506.

Mead, A. J. et al. (2015). "An accurate halo model for fitting non-linear cosmological power spectra and baryonic feedback models". In: *Monthly Notices of the Royal Astronomical Society* 454, pp. 1958–1975.

Mead, A. J. et al. (2016). "Accurate halo-model matter power spectra with dark energy, massive neutrinos and modified gravitational forces". In: *Monthly Notices of the Royal Astronomical Society* 459, pp. 1468–1488.

Melia, F. (2013). "High-z Quasars in the R_h=ct Universe". In: *The Astrophysical Journal* 764.1, p. 72.

— (2015a). "Cosmological Implications of the CMB Large-Scale Structure". In: *The Astronomical Journal* 149.1, p. 6.

— (2015b). "On recent claims concerning the R_h = ct Universe". In: *Monthly Notices of the Royal Astronomical Society* 446, pp. 1191–1194.

— (2016a). "Constancy of the cluster gas mass fraction in the R_h=ct Universe". In: *Proceedings of the Royal Society of London Series A* 472, 20150765.

— (2016b). "Physical basis for the symmetries in the Friedmann-Robertson-Walker metric". In: *Frontiers of Physics* 11.11, 119801.

— (2017). "The zero active mass condition in Friedmann-Robertson-Walker cosmologies". In: *Frontiers of Physics* 12.12, 129802.

Melia, F. and M. Fatuzzo (2016). "The epoch of reionization in the R_h=ct universe". In: *Monthly Notices of the Royal Astronomical Society* 456, pp. 3422–3431.

Melia, F. and A. S. H. Shevchuk (2012). "The R_h=ct universe". In: *Monthly Notices of the Royal Astronomical Society* 419.3, pp. 2579–2586.

Metcalf, R. B. et al. (2004). "Spectroscopic Gravitational Lensing and Limits on the Dark Matter Substructure in Q2237+0305". In: *The Astrophysical Journal* 607, pp. 43–59.

Metropolis, N. and S. Ulam (1949). "The Monte Carlo Method". In: *Journal of the American Statistical Association* 44.247, pp. 335–341.

Metropolis, N. et al. (1953). "Equation of State Calculations by Fast Computing Machines". In: *The Journal of Chemical Physics* 21.6, pp. 1087–1092.

Moore, B. (1994). "Evidence against dissipation-less dark matter from observations of galaxy haloes". In: *Nature* 370, 629 EP –.

Moresco, M. et al. (2012). "Improved constraints on the expansion rate of the Universe up to $z \sim 1.1$ from the spectroscopic evolution of cosmic chronometers". In: *Journal of Cosmology and Astroparticle Physics* 08, 006.

Moustakas, L. A. and R. B. Metcalf (2003). "Detecting dark matter substructure spectroscopically in strong gravitational lenses". In: *Monthly Notices of the Royal Astronomical Society* 339, pp. 607–615.

Nesseris, S. and J. García-Bellido (2013). "Is the Jeffreys' scale a reliable tool for Bayesian model comparison in cosmology?" In: *Journal of Cosmology and Astroparticle Physics* 08, 036.

Nielsen, J. T., A. Guffanti, and S. Sarkar (2016). "Marginal evidence for cosmic acceleration from Type Ia supernovae". In: *Nature Scientific Reports* 6, 35596.

Nishimichi, T., F. Bernardeau, and A. Taruya (2016). "Response function of the large-scale structure of the universe to the small scale inhomogeneities". In: *Physics Letters B* 762, pp. 247–252.

Nock, K., W. J. Percival, and A. J. Ross (2010). "The effect of redshift-space distortions on projected two-point clustering measurements". In: *Monthly Notices of the Royal Astronomical Society* 407.1, pp. 520–532.

Nojiri, S. and S. D. Odintsov (2011). "Unified cosmic history in modified gravity: From F(R) theory to Lorentz non-invariant models". In: *Physics Reports* 505, pp. 59–144.

Nomoto, K., F.-K. Thielemann, and K. Yokoi (1984). "Accreting white dwarf models of Type I supernovae. III - Carbon deflagration supernovae". In: *The Astrophysical Journal* 286, pp. 644–658.

Nordin, J., A. Goobar, and J. Jönsson (2008). "Quantifying systematic uncertainties in supernova cosmology". In: *Journal of Cosmology and Astroparticle Physics* 02, 008.

Nugent, P. E. et al. (2011). "Supernova SN 2011fe from an exploding carbon-oxygen white dwarf star". In: *Nature* 480, pp. 344–347.

Nusser, A. and M. Davis (1994). "On the prediction of velocity fields from redshift space galaxy samples". In: *The Astrophysical Journal Letters* 421, pp. L1–L4.

Oldengott, I. M., C. Rampf, and Y. Y. Y. Wong (2015). "Boltzmann hierarchy for interacting neutrinos I: formalism". In: *Journal of Cosmology and Astroparticle Physics* 04, 016.

Olivari, L. C. et al. (2018). "Cosmological parameter forecasts for H I intensity mapping experiments using the angular power spectrum". In: *Monthly Notices of the Royal Astronomical Society* 473, pp. 4242–4256.

Padmanabhan, N. et al. (2012). "A 2 per cent distance to z = 0.35 by reconstructing baryon acoustic oscillations - I. Methods and application to the Sloan Digital Sky Survey". In: *Monthly Notices of the Royal Astronomical Society* 427, pp. 2132–2145.

Papastergis, E. et al. (2015). “Is there a "too big to fail" problem in the field?” In: *Astronomy and Astrophysics* 574, A113.

Passaglia, S., A. Manzotti, and S. Dodelson (2017). “Cross-correlating 2D and 3D galaxy surveys”. In: *Physical Review D* 95.12, 123508.

Patrignani, C. et al. (2016). “Review of Particle Physics”. In: *Chinese Physics* C40.10, 100001.

Peacock, J. A. and S. J. Dodds (1994). “Reconstructing the Linear Power Spectrum of Cosmological Mass Fluctuations”. In: *Monthly Notices of the Royal Astronomical Society* 267, p. 1020.

— (1996). “Non-linear evolution of cosmological power spectra”. In: *Monthly Notices of the Royal Astronomical Society* 280, pp. L19–L26.

Peacock, J. A. and R. E. Smith (2000). “Halo occupation numbers and galaxy bias”. In: *Monthly Notices of the Royal Astronomical Society* 318, pp. 1144–1156.

Peacock, J. A. et al. (2001). “A measurement of the cosmological mass density from clustering in the 2dF Galaxy Redshift Survey”. In: *Nature* 410, pp. 169–173.

Penzias, A. A. and R. W. Wilson (1965). “A Measurement of Excess Antenna Temperature at 4080 Mc/s.” In: *The Astrophysical Journal* 142, pp. 419–421.

Percival, W. J. et al. (2011). “Redshift-space distortions”. In: *Philosophical Transactions of the Royal Society of London A: Mathematical, Physical and Engineering Sciences* 369.1957, pp. 5058–5067.

Perlmutter, S. et al. (1997). “Measurements of the Cosmological Parameters Ω and Λ from the First Seven Supernovae at z >= 0.35”. In: *The Astrophysical Journal* 483, pp. 565–581.

Perlmutter, S. et al. (1999). “Measurements of Ω and Λ from 42 High-Redshift Supernovae”. In: *The Astrophysical Journal* 517, pp. 565–586.

Phillips, M. M. (1993). “The absolute magnitudes of Type IA supernovae”. In: *The Astrophysical Journal Letters* 413, pp. L105–L108.

Piazza, F., H. Steigerwald, and C. Marinoni (2014). “Phenomenology of dark energy: exploring the space of theories with future redshift surveys”. In: *Journal of Cosmology and Astroparticle Physics* 05, 043.

Planck Collaboration (2014a). “Planck 2013 results. XVI. Cosmological parameters”. In: *Astronomy and Astrophysics* 571, A16.

— (2014b). “Planck intermediate results. XVI. Profile likelihoods for cosmological parameters”. In: *Astronomy and Astrophysics* 566, A54.

— (2016a). “Planck 2015 results. XI. CMB power spectra, likelihoods, and robustness of parameters”. In: *Astronomy and Astrophysics* 594, A11.

— (2016b). “Planck 2015 results. XIII. Cosmological parameters”. In: *Astronomy and Astrophysics* 594, A13.
— (2016c). “Planck 2015 results. XIV. Dark energy and modified gravity”. In: *Astronomy and Astrophysics* 594, A14.
— (2016d). “Planck 2015 results. XV. Gravitational lensing”. In: *Astronomy and Astrophysics* 594, A15.
Prakash, A. et al. (2016). “The SDSS-IV Extended Baryon Oscillation Spectroscopic Survey: Luminous Red Galaxy Target Selection”. In: *The Astrophysical Journal Supplement Series* 224, p. 34.
Press, W. H. and P. Schechter (1974). “Formation of Galaxies and Clusters of Galaxies by Self-Similar Gravitational Condensation”. In: *The Astrophysical Journal* 187, pp. 425–438.
Pskovskii, Y. P. (1977). “Light curves, color curves, and expansion velocity of type I supernovae as functions of the rate of brightness decline”. In: *Soviet Astronomy* 21, p. 675.
— (1984). “Photometric classification and basic parameters of type I supernovae”. In: *Soviet Astronomy* 28, pp. 658–664.
Qin, H.-F. et al. (2015). “Reconstructing equation of state of dark energy with principal component analysis”. In: *ArXiv e-prints*. arXiv: 1501.02971.
Rani, S. et al. (2015). “Constraints on cosmological parameters in power-law cosmology”. In: *Journal of Cosmology and Astroparticle Physics* 03, 031.
Ratra, B. and P. J. E. Peebles (1988). “Cosmological consequences of a rolling homogeneous scalar field”. In: *Physical Review D* 37 (12), pp. 3406–3427.
Raveri, M. et al. (2016a). “CosmicFish Implementation Notes V1.0”. In: *ArXiv e-prints*. arXiv: 1606.06268.
— (2016b). “Information Gain in Cosmology: From the Discovery of Expansion to Future Surveys”. In: *ArXiv e-prints*. arXiv: 1606.06273.
Reyes, R. et al. (2010). “Confirmation of general relativity on large scales from weak lensing and galaxy velocities”. In: *Nature* 464, pp. 256–258.
Riess, A. G., W. H. Press, and R. P. Kirshner (1995). “Using Type IA Supernova Light Curve Shapes to Measure the Hubble Constant”. In: *The Astrophysical Journal* 438, p. L17.
— (1996). “A Precise Distance Indicator: Type IA Supernova Multicolor Light-Curve Shapes”. In: *The Astrophysical Journal* 473, p. 88.
Riess, A. G. et al. (1998). “Observational Evidence from Supernovae for an Accelerating Universe and a Cosmological Constant”. In: *The Astronomical Journal* 116, pp. 1009–1038.
Riess, A. G. et al. (2011). “A 3% Solution: Determination of the Hubble Constant with the Hubble Space Telescope and Wide Field Camera 3”. In: *The Astrophysical Journal* 730, p. 119.

Riess, A. G. et al. (2018a). “New Parallaxes of Galactic Cepheids from Spatially Scanning the Hubble Space Telescope: Implications for the Hubble Constant”. In: *ArXiv e-prints*. arXiv: 1801.01120.

Riess, A. G. et al. (2018b). “Type Ia Supernova Distances at Redshift >1.5 from the Hubble Space Telescope Multi-cycle Treasury Programs: The Early Expansion Rate”. In: *The Astrophysical Journal* 853.2, p. 126.

Ringermacher, H. I. and L. R. Mead (2016). “In Defense of an Accelerating Universe: Model Insensitivity of the Hubble Diagram”. In: *ArXiv e-prints*. arXiv: 1611.00999.

Ross, A. J. et al. (2011). “Measuring redshift-space distortions using photometric surveys”. In: *Monthly Notices of the Royal Astronomical Society* 415.3, pp. 2193–2204.

Ross, A. J. et al. (2015). “The clustering of the SDSS DR7 main Galaxy sample - I. A 4 per cent distance measure at z = 0.15”. In: *Monthly Notices of the Royal Astronomical Society* 449, pp. 835–847.

Rubiño-Martín, J. A. et al. (2010). “Estimating the impact of recombination uncertainties on the cosmological parameter constraints from cosmic microwave background experiments”. In: *Monthly Notices of the Royal Astronomical Society* 403.1, pp. 439–452.

Rubin, D. and B. Hayden (2016). “Is the expansion of the universe accelerating? All signs point to yes”. In: *The Astrophysical Journal* 833, p. L30.

Said, N. et al. (2013). “New constraints on the dark energy equation of state”. In: *Physical Review D* 88, 043515 (4).

Sakamoto, Y., M. Ishiguro, and G. Kitagawa (1986). *Akaike information criterion statistics*. Tokyo: KTK Scientific Publishers; Dordrecht; Boston: D. Reidel; Hingham, MA: Sold and distributed in the U.S.A. and Canada by Kluwer Academic Publishers.

Samushia, L., W. J. Percival, and A. Raccanelli (2012). “Interpreting large-scale redshift-space distortion measurements”. In: *Monthly Notices of the Royal Astronomical Society* 420.3, p. 2102.

Samushia, L. et al. (2011). “Effects of cosmological model assumptions on galaxy redshift survey measurements”. In: *Monthly Notices of the Royal Astronomical Society* 410.3, pp. 1993–2002.

Sánchez, C. et al. (2014). “Photometric redshift analysis in the Dark Energy Survey Science Verification data”. In: *Monthly Notices of the Royal Astronomical Society* 445, pp. 1482–1506.

Sapone, D. and M. Kunz (2009). “Fingerprinting dark energy”. In: *Physical Review D* 80, 083519 (8).

Sapone, D., M. Kunz, and L. Amendola (2010). "Fingerprinting dark energy. II. Weak lensing and galaxy clustering tests". In: *Physical Review D* 82, 103535 (10).

Schwarz, G. (1978). "Estimating the Dimension of a Model". In: *The Annals of Statistics* 6.2, pp. 461–464.

Scoccimarro, R. et al. (2001). "How Many Galaxies Fit in a Halo? Constraints on Galaxy Formation Efficiency from Spatial Clustering". In: *The Astrophysical Journal* 546, pp. 20–34.

Scott, D. (2018). "The Standard Model of Cosmology: A Skeptic's Guide". In: *ArXiv e-prints*. arXiv: 1804.01318.

Seager, S., D. D. Sasselov, and D. Scott (1999). "A New Calculation of the Recombination Epoch". In: *The Astrophysical Journal Letters* 523.1, p. L1.

Seikel, M., C. Clarkson, and M. Smith (2012). "Reconstruction of dark energy and expansion dynamics using Gaussian processes". In: *Journal of Cosmology and Astroparticle Physics* 06, 036.

Seljak, U. (2000). "Analytic model for galaxy and dark matter clustering". In: *Monthly Notices of the Royal Astronomical Society* 318, pp. 203–213.

Sellentin, E. (2015). "A fast, always positive definite and normalizable approximation of non-Gaussian likelihoods". In: *Monthly Notices of the Royal Astronomical Society* 453, pp. 893–898.

Sellentin, E., M. Quartin, and L. Amendola (2014). "Breaking the spell of Gaussianity: forecasting with higher order Fisher matrices". In: *Monthly Notices of the Royal Astronomical Society* 441, pp. 1831–1840.

Sellentin, E. and B. M. Schäfer (2016). "Non-Gaussian forecasts of weak lensing with and without priors". In: *Monthly Notices of the Royal Astronomical Society* 456, pp. 1645–1653.

Seo, H.-J. and D. J. Eisenstein (2003). "Probing Dark Energy with Baryonic Acoustic Oscillations from Future Large Galaxy Redshift Surveys". In: *The Astrophysical Journal* 598, pp. 720–740.

— (2007). "Improved Forecasts for the Baryon Acoustic Oscillations and Cosmological Distance Scale". In: *The Astrophysical Journal* 665, pp. 14–24.

Shafer, D. L. (2015). "Robust model comparison disfavors power law cosmology". In: *Physical Review D* 91.10, 103516.

Shapiro, C. et al. (2010). "Will multiple probes of dark energy find modified gravity?" In: *Physical Review D* 82, 043520 (4).

Shariff, H. et al. (2016). "BAHAMAS: New Analysis of Type Ia Supernovae Reveals Inconsistencies with Standard Cosmology". In: *The Astrophysical Journal* 827.1, p. 1.

Sheth, R. K. and G. Tormen (1999). "Large-scale bias and the peak background split". In: *Monthly Notices of the Royal Astronomical Society* 308, pp. 119–126.

Shi, X. and G. M. Fuller (1999). "New Dark Matter Candidate: Nonthermal Sterile Neutrinos". In: *Physical Review Letters* 82, pp. 2832–2835.

Shoji, M. and E. Komatsu (2010). "Erratum: Massive neutrinos in cosmology: Analytic solutions and fluid approximation [Phys. Rev. D 81, 123516 (2010)]". In: *Physical Review D* 82, 089901 (8).

Simon, J., L. Verde, and R. Jimenez (2005). "Constraints on the redshift dependence of the dark energy potential". In: *Physical Review D* 71.12, 123001.

Simpson, F. and J. A. Peacock (2010). "Difficulties distinguishing dark energy from modified gravity via redshift distortions". In: *Physical Review D* 81, 043512 (4).

Simpson, F. et al. (2013). "CFHTLenS: testing the laws of gravity with tomographic weak lensing and redshift-space distortions". In: *Monthly Notices of the Royal Astronomical Society* 429.3, pp. 2249–2263.

Skilling, J. (2004). "Nested Sampling". In: *American Institute of Physics Conference Series*. Ed. by R. Fischer, R. Preuss, and U. V. Toussaint. Vol. 735. American Institute of Physics Conference Series, pp. 395–405.

— (2006). "Nested sampling for general Bayesian computation". In: *Bayesian Analysis* 1.4, pp. 833–859.

Smith, R. E. et al. (2003). "Stable clustering, the halo model and non-linear cosmological power spectra". In: *Monthly Notices of the Royal Astronomical Society* 341, pp. 1311–1332.

Somerville, R. S. and J. R. Primack (1999). "Semi-analytic modelling of galaxy formation: the local Universe". In: *Monthly Notices of the Royal Astronomical Society* 310, pp. 1087–1110.

Spinelli, M. (2015). "Cosmological parameter estimation with the Planck satellite data : from the construction of a likelihood to neutrino properties". Theses. Université Paris Sud - Paris XI.

Stern, D. et al. (2010). "Cosmic chronometers: constraining the equation of state of dark energy. I: H(z) measurements". In: *Journal of Cosmology and Astroparticle Physics* 02, 008.

Sugiura, N. (1978). "Further analysts of the data by akaike' s information criterion and the finite corrections". In: *Communications in Statistics - Theory and Methods* 7.1, pp. 13–26.

Sullivan, M. et al. (2010). "The dependence of Type Ia Supernovae luminosities on their host galaxies". In: *Monthly Notices of the Royal Astronomical Society* 406, pp. 782–802.

Sullivan, M. et al. (2011). "SNLS3: Constraints on Dark Energy Combining the Supernova Legacy Survey Three-year Data with Other Probes". In: *The Astrophysical Journal* 737, p. 102.

Switzer, E. R. and C. M. Hirata (2008). "Primordial helium recombination. I. Feedback, line transfer, and continuum opacity". In: *Physical Review D* 77.8, 083006.

Takahashi, R. et al. (2012). "Revising the Halofit Model for the Nonlinear Matter Power Spectrum". In: *The Astrophysical Journal* 761, p. 152.

Tammann, G. A. and B. Reindl (2013). "The luminosity of supernovae of type Ia from tip of the red-giant branch distances and the value of H0". In: *Astronomy and Astrophysics* 549, A136.

Taylor, P. L. et al. (2018). "Testing the Cosmic Shear Spatially-Flat Universe Approximation with GLaSS". In: *ArXiv e-prints*. arXiv: 1804.03668.

Tegmark, M. (1997). "Measuring Cosmological Parameters with Galaxy Surveys". In: *Physical Review Letters* 79, pp. 3806–3809.

Tegmark, M. and P. J. E. Peebles (1998). "The Time Evolution of Bias". In: *The Astrophysical Journal Letters* 500.2, p. L79.

Thomas, D. B., M. Kopp, and C. Skordis (2016). "Constraining the Properties of Dark Matter with Observations of the Cosmic Microwave Background". In: *The Astrophysical Journal* 830, p. 155.

Tinker, J. L. et al. (2010). "The Large-scale Bias of Dark Matter Halos: Numerical Calibration and Model Tests". In: *The Astrophysical Journal* 724, pp. 878–886.

Tojeiro, R. et al. (2012). "The clustering of galaxies in the SDSS-III Baryon Oscillation Spectroscopic Survey: measuring structure growth using passive galaxies". In: *Monthly Notices of the Royal Astronomical Society* 424.3, p. 2339.

Tojeiro, R. et al. (2014). "The clustering of galaxies in the SDSS-III Baryon Oscillation Spectroscopic Survey: galaxy clustering measurements in the low-redshift sample of Data Release 11". In: *Monthly Notices of the Royal Astronomical Society* 440.3, pp. 2222–2237.

Tonry, J. and M. Davis (1979). "A survey of galaxy redshifts. I - Data reduction techniques". In: *The Astronomical Journal* 84, pp. 1511–1525.

Tripp, R. (1997). "Using distant type IA supernovae to measure the cosmological expansion parameters." In: *Astronomy and Astrophysics* 325, pp. 871–876.

— (1998). "A two-parameter luminosity correction for Type IA supernovae". In: *Astronomy and Astrophysics* 331, pp. 815–820.

Tutusaus, I., B. Lamine, and A. Blanchard (2016). "On the dark contents of the Universe: A Euclid survey approach". In: *Proceedings of the 51st RENCONTRES DE MORIOND*. Ed. by E. Augé, J. Dumarchez, and J. Trân Thanh Vân, pp. 117–120.

— (2018a). "Generalized dark matter with the Euclid satellite". In: *Proceedings of the 53rd RENCONTRES DE MORIOND*. Ed. by E. Augé, J. Dumarchez, and J. Trân Thanh Vân.

— (2018b). "Model-independent cosmic acceleration and type Ia supernovae intrinsic luminosity redshift dependence". In: *ArXiv e-prints*. arXiv: 1803.06197.

Tutusaus, I. et al. (2016a). "Dark sectors of the Universe: A Euclid survey approach". In: *Physical Review D* 94.12, 123515.

Tutusaus, I. et al. (2016b). "Power law cosmology model comparison with CMB scale information". In: *Physical Review D* 94.10, 103511.

Tutusaus, I. et al. (2017). "Is cosmic acceleration proven by local cosmological probes?" In: *Astronomy and Astrophysics* 602, A73.

Tutusaus, I. et al. (in prep.[a]). "Generalized dark matter and the tension between low-redshift and high-redshift data". In: *TBD*.

— (in prep.[b]). "Generalized dark matter with the Euclid mission". In: *TBD*.

Tyson, J. A., G. P. Kochanski, and I. P. Dell'Antonio (1998). "Detailed Mass Map of CL 0024+1654 from Strong Lensing". In: *The Astrophysical Journal Letters* 498.2, p. L107.

Verde, L. et al. (2017a). "Early cosmology constrained". In: *Journal of Cosmology and Astroparticle Physics* 04, 023.

Verde, L. et al. (2017b). "The length of the low-redshift standard ruler". In: *Monthly Notices of the Royal Astronomical Society* 467, pp. 731–736.

Vogt, S. S. et al. (1995). "Internal kinematics of the Leo II dwarf spherodial galaxy". In: *The Astronomical Journal* 109, pp. 151–163.

Walsh, D., R. F. Carswell, and R. J. Weymann (1979). "0957 + 561 A, B - Twin quasistellar objects or gravitational lens". In: *Nature* 279, pp. 381–384.

Wang, D. and X. Meng (2017). "Model-independent determination on H_0 using the latest cosmic chronometer data". In: *Science China Physics, Mechanics, and Astronomy* 60.11, 110411.

Wang, Y. (2012). "Robust constraints on dark energy and gravity from galaxy clustering data". In: *Monthly Notices of the Royal Astronomical Society* 423.4, pp. 3631–3637.

Wang, Y., C.-H. Chuang, and C. M. Hirata (2013). "Towards more realistic forecasting of dark energy constraints from galaxy redshift surveys". In: *Monthly Notices of the Royal Astronomical Society* 430.3, pp. 2446–2453.

Wang, Y. and P. M. Garnavich (2001). "Measuring Time Dependence of Dark Energy Density from Type Ia Supernova Data". In: *The Astrophysical Journal* 552.2, p. 445.

Wang, Y. and P. Mukherjee (2007). "Observational constraints on dark energy and cosmic curvature". In: *Physical Review D* 76.10, 103533.

Wang, Y. et al. (2010). "Designing a space-based galaxy redshift survey to probe dark energy". In: *Monthly Notices of the Royal Astronomical Society* 409.2, pp. 737–749.

Wei, J.-J. et al. (2015). "A Comparative Analysis of the Supernova Legacy Survey Sample With ΛCDM and the R_h=ct Universe". In: *The Astronomical Journal* 149.3, p. 102.

Wetterich, C. (1988). "Cosmology and the fate of dilatation symmetry". In: *Nuclear Physics B* 302.4, pp. 668 –696.

Wolz, L. et al. (2012). "On the validity of cosmological Fisher matrix forecasts". In: *Journal of Cosmology and Astroparticle Physics* 9, 009.

Wright, E. L. (2002). "Distant Supernovae and the Accelerating Universe". In: *ArXiv e-prints*. eprint: astro-ph/0201196.

Yang, Y. (2015). "Constraints on the basic parameters of dark matter using the Planck data". In: *Physical Review D* 91, 083517 (8).

Yu, H., B. Ratra, and F.-Y. Wang (2017). "Hubble Parameter and Baryon Acoustic Oscillation Measurement Constraints on the Hubble Constant, the Deviation from the Spatially-Flat Λcdm Model, The Deceleration-Acceleration Transition Redshift, and Spatial Curvature". In: *ArXiv e-prints*. arXiv: 1711.03437.

Zaritsky, D. et al. (1997). "Anisotropies in the Distribution of Satellite Galaxies". In: *The Astrophysical Journal Letters* 478.2, p. L53.

Zarrouk, P. et al. (2018). "The clustering of the SDSS-IV extended Baryon Oscillation Spectroscopic Survey DR14 quasar sample: measurement of the growth rate of structure from the anisotropic correlation function between redshift 0.8 and 2.2". In: *ArXiv e-prints*. arXiv: 1801.03062.

Zhang, C. et al. (2014). "Four new observational H(z) data from luminous red galaxies in the Sloan Digital Sky Survey data release seven". In: *Research in Astronomy and Astrophysics* 14, pp. 1221–1233.

Zhang, P. et al. (2007). "Probing Gravity at Cosmological Scales by Measurements which Test the Relationship between Gravitational Lensing and Matter Overdensity". In: *Physical Review Letters* 99, 141302 (14).

Zhang, T.-J. and C. Ma (2010). "Constraints on the Dark Side of the Universe and Observational Hubble Parameter Data". In: *Advances in Astronomy* 2010, 184284.

Zhao, G.-B. et al. (2009). “Searching for modified growth patterns with tomographic surveys”. In: *Physical Review D* 79.8, 083513.

Zuntz, J. et al. (2015). “CosmoSIS: Modular cosmological parameter estimation”. In: *Astronomy and Computing* 12, pp. 45–59.

Zwicky, F. (1933). “Die Rotverschiebung von extragalaktischen Nebeln”. In: *Helvetica Physica Acta* 6, pp. 110–127.

Index

Résumé

Le modèle de concordance de la cosmologie, appelé ΛCDM, est un succès de la physique moderne, car il est capable de reproduire les principales observations cosmologiques avec une grande précision et très peu de paramètres libres. Cependant, il prédit l'existence de matière noire froide et d'énergie sombre sous la forme d'une constante cosmologique, qui n'ont pas encore été détectées directement. Par conséquent, il est important de considérer des modèles allant au-delà de ΛCDM, et de les confronter aux observations, afin d'améliorer nos connaissances sur le secteur sombre de l'Univers. Le futur satellite Euclid, de l'Agence Spatiale Européenne, explorera un énorme volume de la structure à grande échelle de l'Univers en utilisant principalement le regroupement des galaxies et la distorsion de leurs images due aux lentilles gravitationnelles. Dans ce travail, nous caractérisons de façon quantitative les performances d'Euclid vis-à-vis des contraintes cosmologiques, à la fois pour le modèle de concordance, mais également pour des extensions phénoménologiques modifiant les deux composantes sombres de l'Univers. En particulier, nous accordons une attention particulière aux corrélations croisées entre les différentes sondes d'Euclid lors de leur combinaison, et estimons de façon précise leur impact sur les résultats finaux. D'une part, nous montrons qu'Euclid fournira d'excellentes contraintes sur les modèles cosmologiques qui définitivement illuminera le secteur sombre. D'autre part, nous montrons que les corrélations croisées entre les sondes d'Euclid ne peuvent pas être négligées dans les analyses futures, et, plus important encore, que l'ajout de ces corrélations améliore grandement les contraintes sur les paramètres cosmologiques.

Abstract

The concordance model of cosmology, called ΛCDM, is a success, since it is able to reproduce the main cosmological observations with great accuracy and only few parameters. However, it predicts the existence of cold dark matter and dark energy in the form of a cosmological constant, which have not been directly detected yet. Therefore, it is important to consider models going beyond ΛCDM, and confront them against observations, in order to improve our knowledge on the dark sector of the Universe. The future Euclid satellite from the European Space Agency will probe a huge volume of the large-scale structure of the Universe using mainly the clustering of galaxies and the distortion of their images due to gravitational lensing. In this work, we quantitatively estimate the constraining power of the future Euclid data for the concordance model, as well as for some phenomenological extensions of it, modifying both dark components of the Universe. In particular, we pay special attention to the cross-correlations between the different Euclid probes when combining them, and assess their impact on the final results. On one hand, we show that Euclid will provide exquisite constraints on cosmological models that will definitely shed light on the dark sector. On the other hand, we show that cross-correlations between Euclid probes cannot be neglected in future analyses, and, more importantly, that the addition of these correlations largely improves the constraints on the cosmological parameters.